Author:
Martin, Peter

Title:
The Fukushima Daiichi Nuclear Power Plant Accident: An Analysis Over 10 Orders of Magniture

The 2011 Fukushima Daiichi Nuclear Power Plant accident: an analysis over 10 orders of magnitude

PETER GEORGE MARTIN

Interface Analysis Centre, School of Physics
UNIVERSITY OF BRISTOL

A dissertation submitted to the University of Bristol in accordance with the requirements of the degree of DOCTOR OF PHILOSOPHY in the Faculty of Science.

MAY 2018

Word count: ~80,000

In memory of Peter Kirby.

Mum, Dad, David and Bert - without you I would not be where I am today. Thank you for all your support and encouragement.

ABSTRACT

The March 2011 events at the Fukushima Daiichi Nuclear Power Plant represented a radioactivity release of a similar "global severity" as the Chernobyl accident. Following the multiple reactor unit explosions that occurred, a total of 146,520 residents from across Fukushima Prefecture were evacuated from their homes. Today, with many years having passed since the event, there exists a greater commitment than ever to allow for those formerly displaced to return. Central to this resettlement is the combined remediation of the extensive swathe of contaminated land, but also a detailed understanding of the physiochemical nature and associated environmental affinity of the released radionuclides.

Regional radiation monitoring was first undertaken using newly-devised aerial and ground-based radiation mapping platforms. From this, it was observed that from an initially quasi-uniform radiocesium distribution in contaminated areas, that significant redistribution of contamination had occurred. For sites that had experienced recent remediation, contamination "hot-spots" were observed to quickly re-establish across such localities, occurring at positions where mobilised particulate would become readily trapped. At locations where no remediation had been performed, contamination was observed to be similarly mobile. These contamination transport results correlate with earlier works examining Cs sorption onto fine-scale clay and mica-type mineral particulates, which forms a ubiquitous and significant component of the Fukushima soil. This mobility is heightened by the regions sub-tropical climate with periodic typhoon events.

Alongside the Cs-sorbed material, the coarser particulate contributing to the radioactivity measured during this site-wide monitoring was examined. This material was classified into two groups; (i) particulate on the micron/sub-micron scale obtained from distances of up to 70 km from the site, and (ii) a grouping of larger particles (100's of µm in diameter), isolated from soils on the boundary of the facility (<2 km). The smaller particulate, found adhered to organic surfaces, was observed to be characteristically angular in form. Sub-micron U composition ejecta, as well as exhibiting a complex internal microstructure, also contained a determinable Cs component. The larger Si-rich particulate, in contrast, was characterised by a variable surface and internal form - in some instances being highly-porous. As well as occurrences of fragments of cement and iron, some of this material also contained micron-scale ^{235}U-enriched particles.

These results provide evidence that correlate with earlier studies, indicating that core material from Unit 2 was released in the accident as well as for the first time reporting the emission of U from the core of reactor Unit 1. The potential environmental implications of such fine and large particulate are investigated and discussed as part of this work, with recommendations detailed associated with the ongoing response and activities of the Japanese Government.

Author's Declaration

I declare that the work in this dissertation was carried out in accordance with the requirements of the University's Regulations and Code of Practice for Research Degree Programmes and that it has not been submitted for any other academic award. Except where indicated by specific reference in the text, the work is the candidate's own work. Work done in collaboration with, or with the assistance of, others, is indicated as such. Any views expressed in the dissertation are those of the author.

SIGNED: .... DATE: ....

ACKNOWLEDGEMENTS

PUBLICATIONS AND PRESENTATIONS

Work presented in this thesis has led to the following peer-reviewed publications. The personal contribution in each instance is additionally detailed.

Journal Publications - Available in Print

P.G. Martin, O.D. Payton, J.S. Fardoulis, D.A. Richards and T.B. Scott. "The use of unmanned aerial systems for the mapping of legacy uranium mines". *Journal of Environmental Radioactivity*, vol. 143, pp. 135-140, May 2015. *(Contribution: 90%, including; fieldwork, subsequent data analysis and production of the final published manuscript)*.

P.G. Martin, O.D. Payton, J.S. Fardoulis, D.A. Richards, T.B. Scott and Y. Yamashiki. "Low altitude unmanned aerial vehicle for characterising remediation effectiveness following the FDNPP accident". *Journal of Environmental Radioactivity*, vol. 154, pp. 58-63, January 2016. *(Contribution: 95%, including; fieldwork, subsequent data analysis and production of the final published manuscript)*.

P.G. Martin, I. Griffiths, C.P. Jones, C.A. Stitt, M. Davies-Milner, J.F.W. Mosselmans, Y. Yamashiki, D.A. Richards and T.B. Scott. "In-situ removal and characterisation of uranium-containing particles from sediments surrounding the Fukushima Daiichi Nuclear Power Plant". *Spectrochimica Acta Part B: Atomic Spectroscopy*, vol. 117, pp. 1-7, March 2016. *(Contribution: 80%, including; sample collection fieldwork, laboratory-based particle isolation, synchrotron analysis/data processing and production of the final published manuscript)*.

P.G. Martin and T.B. Scott. "Electron microscopy at the nano-scale to investigate the Fukushima Daiichi Nuclear Power Plant radiation releases". *Microscopy and Analysis*, vol. 26, pp. 27-31, October 2016. *(Contribution: 98%, full-contribution to the production of the magazine-style article based upon the above work)*.

P.G. Martin, S. Kwong, N.T. Smith, Y. Yamashiki, O.D. Payton, F.S. Russell-Pavier, J.S. Fardoulis, D.A. Richards and T.B. Scott. "3D unmanned aerial vehicle radiation mapping for assessing contaminant distribution and mobility". *International Journal of Applied Earth Observation and Geoinformation*, vol. 52, pp. 12-19, October 2016. *(Contribution: 75%, including; fieldwork, data processing and production of the final published manuscript. S.K. contributed to the 3D modelling using National Nuclear Laboratory (NNL) geospatial data manipulation software)*.

D. Connor, **P.G. Martin** and T.B. Scott. "Airborne radiation mapping: overview and application of current and future aerial systems". *International Journal of Remote Sensing*, vol. 37, pp.5953-5987, November 2016. *(Contribution: 35%, including; project guidance and assistance in producing the final published review article)*.

P.G. Martin, J. Moore, J.S. Fardoulis, O.D. Payton, and T.B. Scott. "Radiological Assessment on Interest Areas on the Sellafield Nuclear Site via Unmanned Aerial Vehicle". *Remote Sensing*, vol. 8 (11), p. 10, November 2016. *(Contribution: 95%, including; on-site fieldwork, subsequent data analysis and production of the final Sellafield-approved, published manuscript)*.

P.G. Martin, O.D. Payton, Y. Yamashiki, D.A. Richards and T.B. Scott. "High-resolution radiation mapping to investigate FDNPP derived contaminant migration". *Journal of Environmental Radioactivity*, vol. 164. pp. 26-35, November 2016. *(Contribution: 95%, including; fieldwork, subsequent data analysis and production of the final published manuscript)*.

P.G. Martin, Y. Satou, I. Griffiths, D.A. Richards and T.B. Scott. "Analysis of external surface irregularities on Fukushima-derived fallout particles". *Frontiers in Energy Research: Nuclear*

Energy, vol. 5. (25). p. 9, September 2017. *(Contribution: 80%, including; laboratory-based sample analysis and production of the final published manuscript. Y.S. contributed to the work by in-field sampling and subsequently extracting the particulate analysed in the study).*

P.G. Martin, N.G. Tomkinson and T.B. Scott. "The Future of Nuclear Security: Commitments and Actions Power Generation and Stewardship in the 21st Century". *Energy Policy*, vol. 110, pp. 325-330, November 2017. *(Contribution: 95%, including; background research, data analysis and production of the final published manuscript).*

A.C. Keatley, **P.G. Martin**, K.R. Hallam, O.D. Payton, R. Awbery, F. Carvalho, J.M. Oliveira, L. Silva, M. Malta and T.B. Scott. "Source identification of uranium-containing materials at mine legacy sites in Portugal". *Journal of Environmental Radioactivity*, vol. 183, pp. 102-111, March 2018. *(Contribution: 40%, including; fieldwork, subsequent data processing, generation of figure graphics and assistance in producing the final published manuscript).*

P.G. Martin, D.C. Connor, O.D. Payton, M. Leal-Olloqui, A.C. Keatley and T.B. Scott. "Development and validation of a high-resolution mapping platform to aid in the public awareness of radiological hazards". *Journal of Radiological Protection (IoP)*, vol. 38, pp. 329-342, February 2018. *(Contribution: 85%, including; design and calibration of the system, in-field platform validation, subsequent data analysis and production of the final published manuscript).*

Journal Publications - In-Press, Under Review, or In Preparation

P.G. Martin, C. Hutson, L. Payne, O.D. Payton, Y. Yamashiki and T.B. Scott. "Validation of a novel radiation mapping platform for the reduction of operator-induced shielding effects". *Journal of Radiological Protection (IoP)*, in-press. *(Contribution: 95%, including; design, construction and calibration of the system, in-field platform validation, subsequent data analysis and production of the final published manuscript).*

P.G. Martin, S. Cipiccia, D.J. Batey, K.R. Hallam, I.A.X. Ang, C.P. Jones, Y. Satou, I. Griffiths, C. Rau, D.A. Richards and T.B. Scott. "Internal analysis of a Fukushima-derived particle revealed using high-resolution synchrotron techniques". *ACS Environmental Science and Technology*, in-press. *(Contribution: 70%, including; laboratory-based material classification, subsequent data analysis, generation of manuscript figures and production of the final published manuscript. S.C. performed analysis on data obtained from the synchrotron. Y.S. contributed to the work by in-field sampling and subsequently extracting the particulate that was later analysed in the study).*

P.G. Martin, M. Davies-Milner, D.A. Richards, Y. Yamashiki and T.B. Scott. "Analysis of particulate following the Fukushima Daiichi Nuclear Power Plant accident reveals spatial depositional trends". *Atmospheric Environment*, under review. *(Contribution: 80%, including; sample collection fieldwork, laboratory-based material classification, subsequent data analysis, generation of manuscript figures and production of the final published manuscript. M.D.M. additionally assisted with the laboratory-based material classification during his MSci project).*

P.G. Martin, M. Louvel, S. Cipiccia, D.J. Batey, K.R. Hallam, I.A.X. Yang, Y. Satou, C. Rau, J.F. Mosselmans and T.B. Scott. "Evaluation of the distribution, state and composition of uranium contained within particulate derived from Unit 1 at the FDNPP". *Nature*, under review. *(Contribution: 65%, including; laboratory-based material classification, subsequent data analysis, generation of manuscript figures and production of the final published manuscript. S.C. performed analysis on the x-ray tomography and fluorescence data obtained at the synchrotron. M.L. assisted in the analysis of additional synchrotron-radiation absorption spectroscopy data. Y.S. contributed to the work by in-field sampling and subsequently extracting the particulate analysed in the study).*

Conference and Invited Presentations

Invited Presentation: "UAVs for Radiological Monitoring: Determining Ideal Operational Parameters From GEANT4 Simulations". Waste Management Symposium 2018 (WM2018). International Convention Centre, Phoenix, Arizona, USA. 18th - 22nd March 2018.

Oral: "High-Activity Microscopic Nuclear-Sourced Particles to Investigate Nuclear Release Scenarios". Waste Management Symposium 2018 (WM2018). International Convention Centre, Phoenix, Arizona, USA. 18th - 22nd March 2018.

Oral: "Robotics for Nuclear Monitoring and Inspection". Waste Management Symposium 2018 (WM2018). International Convention Centre, Phoenix, Arizona, USA. 18th - 22nd March 2018.

Oral: "What can microscopic fallout particulate tell us about nuclear accidents?". Defence and Security Doctoral Symposium 2017. United Kingdom Defence Academy, Cranfield University, Shrivenham, UK. 14th - 15th November 2017.

Invited Presentation: "Aerial Radiation Mapping for Nuclear Decontamination". Nuclear Security Science Network (NuSec) Development Grant Reception, Wellcome Trust, London, UK. 18th September 2017.

Invited Presentation: "Manipulator-based systems for nuclear forensic applications - The 2011 FDNPP accident". Kleindiek User Meeting 2017. Achalm Hotel, Reutlingen, Germany. 25th - 26th April 2017.

Oral & Poster: "High-Resolution Aerial Radiation Mapping for Nuclear Decontamination and Decommissioning". Waste Management Symposium 2017 (WM2017). International Convention Centre, Phoenix, Arizona, USA. 5th - 9th March 2017.

Invited Presentation: "Electron beam techniques for the analysis of Fukushima-derived fallout". Society of Electron Microscope Technology (SEMT) 2016 Annual Meeting. Natural History Museum, London, UK. 6th December 2016.

Oral: "Gaining novel insight into Fukushima Daiichi Nuclear Power Plant derived fallout". Co-Ordination Group on Environmental Radioactivity (COGER) 2016 Annual Meeting. University of Glasgow, Glasgow, UK. 5th - 7th April 2016.

Oral: "Low-Altitude Unmanned Aerial Vehicles as a Tool for the Remediation of Radiologically Contaminated Environments". Waste Management Symposium 2016 (WM2016). International Convention Centre, Phoenix, Arizona, USA. 6th - 10th March 2016.

Oral: "Investigating Fukushima Daiichi NPP fallout from 10^1 m to 10^{-7} m scale". Co-Ordination Group on Environmental Radioactivity (COGER) 2015 Annual Meeting. British Geological Survey (BGS), Keyworth, Nottingham, UK. 7th - 9th April 2015.

Invited Presentation: "UAVs for rapid radiological determination of contamination following dispersion events". 17th International CBRN Symposium, Defence Academy of the United Kingdom, Cranfield University, Shrivenham, UK. 11th - 13th November 2014.

PRIZES AND AWARDS

The work performed during this PhD has resulted in the following prizes and awards:

Innovus Nuclear Innovation Conference, February 2016 - Best Academic Abstract.

"Radiological contamination identified through high-resolution ground-based mapping".

P.G. Martin, O.D. Payton and T.B. Scott.

Waste Management Symposium, March 2016 - Roy G. Post Scholarship.

Conferences expenses and research fund prize.

Waste Management Symposium, March 2017 - Superior Paper Award.

"Autonomous unmanned aerial vehicles for examining current and evolving ditribution of contamination from the FDNPP accident".

P.G. Martin, Y. Yamashiki, T.B. Scott, O.D. Payton, D.A. Richards and J.S. Fardoulis.

Japan Society for the Promotion of Science, Summer 2017 - Research Fellowship.

Host: Professor Yosuke Yamashiki. Graduate School of Advanced Integrated Studies in Human Survivability (GSAIS), Kyoto University, Japan.

CONTENTS

LIST OF TABLES

ABBREVIATIONS

3D-APT   Three Dimensional-Atom Probe Tomography

AMS   Acceleration Mass Spectrometry

AUH   Autonomous Unmanned Helicopter

BGS   British Geological Survey

BSE   Backscattered Electrons

BWR   Boiling Water Reactor

CAA   Civil Aviation Authority

CCD   Charge-coupled device

CF   Carbon fibre

CMP   Cesium micro-particle

CPS   Counts per second

CZT   Cadmium Zinc Telluride (CdZnTe)

DLS   Diamond Light Source

DoE   Department of Energy

DU   Depleted uranium

DW   Dry Well

ECC   Emergency Core Cooling

EDS   Energy Dispersive Spectroscopy

EDX   Energy Dispersive X-ray

EM   Electromagnetic

ESRF   European Synchrotron Radiation Facility

EXAFS   Extended X-ray Absorption Fine Structure

FDNPP   Fukushima Daiichi Nuclear Power Plant

FEG	Field Emission Gun
FIB	Focused Ion Beam
FWHM	Full Width at Half Maximum
FSP	Fuel Storage Pond
GE	General Electric
GM	Geiger Muller
GPS	Global Positioning System
GSI	Geospatial Information Authority of Japan
GSJ	Geological Survey of Japan
HD	High Definition
HPGe	High-Purity Germanium
IAEA	International Atomic Energy Agency
IC	Isolation Condenser
ICP-MS	Inductively Coupled Plasma-Mass Spectrometry
IMU	Inertial Measurement Unit
INES	International Nuclear Event Scale
IRID	International Research Institute for Nuclear Decommissioning
JAEA	Japan Atomic Energy Agency
JST	Japan Standard Time
KB	Kirkpatrick-Baez
LA-ICP-MS	Laser Ablation-ICP-MS
LEU	Low-Enriched Uranium
LiPo	Lithium Polymer
LLW	Low Level Waste
LMIS	Liquid Metal Ion Source
LOCI	Loss of Coolant Incident
LoD	Limit of Detection
LWR	Light Water Reactor
METI	Ministry of Economy, Trade and Industry

MEXT	Ministry of Education, Culture, Sports, Science and Technology
MOX	Mixed Oxide
MS-SIMS	Magnetic Sector-Secondary Ion Mass Spectrometry
MWI	Municipal Waste Incineration
NDA	Nuclear Decommissioning Authority
NNL	National Nuclear Laboratory
NNSA	National Nuclear Security Administration
NORM	Naturally Occurring Radioactive Materials
NRA	(Japan) Nuclear Regulation Authority
NU	Natural Uranium
OD	Ordnance Datum
PC	Primary Containment
PCV	Primary Containment Vessel
PMT	Photomultiplier Tube
ppm	parts per million
PWR	Pressurised Water Reactor
RCIU	Reactor Core Isolation Unit
REE	Rare Earth Element
RF	Radiofrequency
RGA	Residual Gas Analysis
RHR	Residual Heat Removal
RIP	Radiocesium Interception Potential
RoI	Region of Interest
RPV	Reactor Pressure Vessel
SC	Suppression Chamber
SCRAM	Safety Control Rod Axe Man
SE	Secondary Electron
SEM	Scanning Electron Microscope
SIMS	Secondary Ion Mass Spectrometry

SR Synchrotron Radiation

TEM Transmission Electron Microscopy

TENORM Technologically Enhanced Naturally Occurring Radioactive Materials

TEPCO Tokyo Electric Power Company

TIMS Thermal Ionisation Mass Spectrometry

TIN Triangular Irregular Network

TMA Tokyo Metropolitan Area

UAH Unmanned Aerial Helicopter

UAV Unmanned Aerial Vehicle

WHO World Health Organisation

WW Wet Well

XANES X-ray Absorption Near Edge Spectroscopy

XAS X-ray Absorption Spectroscopy

XRD X-ray Diffraction

XRF X-ray Fluorescence

XRT X-ray Tomography

THE FUKUSHIMA DAIICHI NUCLEAR POWER PLANT AND ACCIDENT

The incident at the Fukushima Daiichi Nuclear Power Plant (FDNPP) represents one of the greatest ever radioactive release events to occur at a nuclear power generation facility. Classified as severe as the events that occurred at the Chernobyl facility 25 years earlier [1, 2], the radioactivity released from the Fukushima plant was rapidly detected as far away as Russia and mainland Europe [3, 4]. Alongside the development and application of radiation monitoring techniques to investigate the evolving distribution of contamination, this thesis presents a forensic examination of particulate samples (released into the environment) to attain a more detailed technical insight into events that occurred following the earthquake and ensuing tsunami, responsible for the catastrophic chain of events that occurred at the Japanese coastal facility.

This initial chapter provides an overview on each of the reactor units at the FDNPP, as well as an account of the on-site events that ensued from the afternoon of the 11th March 2011. A description of the monitoring activities performed to quantify the radioactive release(s) from the site is subsequently provided in Chapter 2.

Information on the plant is obtained from various sources, including the plant's operators - Tokyo Electric Power Company (TEPCO) [5–7], International Atomic Energy Agency (IAEA) [2, 8], Japanese Nuclear Regulators (NRA) [9] and World Nuclear Association [10, 11] as well as the reactor manufacturers - a consortium of General Electric (GE), Hitachi and Toshiba [12].

1.1 The Fukushima Daiichi Nuclear Power Plant (FDNPP)

Facing an increasing drive to become energy self-reliant, nuclear power was anticipated to account for 41% of Japan's domestic supply by 2019, with many new plants under construction (or in the planning stages) as of March 2011 [13, 14]. Home to some of the oldest reactors in Japan, the FDNPP consisted of six power-generating units, located on Japan's eastern Pacific coast, 225 km north-east of Tokyo. The complex was operated by the country's largest utility company, TEPCO. Combined, the total peak output of the FDNPP was 46 GWe - constituting 6 of the 54 reactors operational across the country at the time [8].

An annotated aerial photograph detailing the relative location of each of the reactors at the site is shown in Figure 1.1, with all of the units positioned several hundred metres back from the coastline at an elevation of 10 m ordnance datum (OD). Where it bordered the Pacific Ocean, the plant was protected by a concrete seawall, 5.7 m OD, that extended around its seaward perimeter - a consideration typical of the entirety of Japan's coastal nuclear plants [15]. This regulatory requirement was invoked as a result of the 1960 Chilean earthquake and tsunami - where a 3.1 m high protective seawall was recommended. A subsequent revision in 2002 saw the required height of the wall raised by 2.6 m, to 5.7 m. In addition to this, the seawater pumps that served to provide cool seawater for the main and auxiliary (emergency) condenser circuits, were environmentally-sealed to protect them against any tsunamis that could impact the site and reactor operations. These pumps were also relocated to a position 4 m above sea level.

With an estimated 20% of nuclear facilities worldwide operating in areas with "significant" seismic activity [8, 16], protection from earthquakes forms part of standard reactor design protocols. However, owing to the heightened seismic activity that occurs across Japan as a result of its proximity to the subducting "Japan Trench" (part of the larger "Pacific Rim of Fire") [17], seismic considerations are a significant component of Japanese reactor design [16].

Prior to March 2011, a number of earthquakes had occurred in close proximity to Japanese power reactors - the largest of which being the moment magnitude (M_W) 7.8 earthquake that occurred off the coast of Hokkaido in July 1993 [16]. Despite this large episode of seismic activity, the nearby Tomari 1 and 2 reactors (located 95 km from the epicentre), continued normal operation having not recorded ground accelerations necessary to "trip" the reactors and cause an automated shutdown. A lesser M_W 6.2 earthquake occurred offshore of Fukushima Prefecture on 13th June 2010 [18], however, the nearby Fukushima Daiichi, Fukushima Daini and Onagawa facilities were all unaffected. It was only in October 2004, however, following a M_W 5.2 earthquake with an epicentre 250 km north of Tokyo, that the first-ever "trip" (and automated shutdown) at a Japanese reactor occurred at Unit 7 of the Kashiwazaki-Kariwa nuclear plant [19]. Despite the regular seismic activity, no facilities had ever been inundated by tsunamis [16].
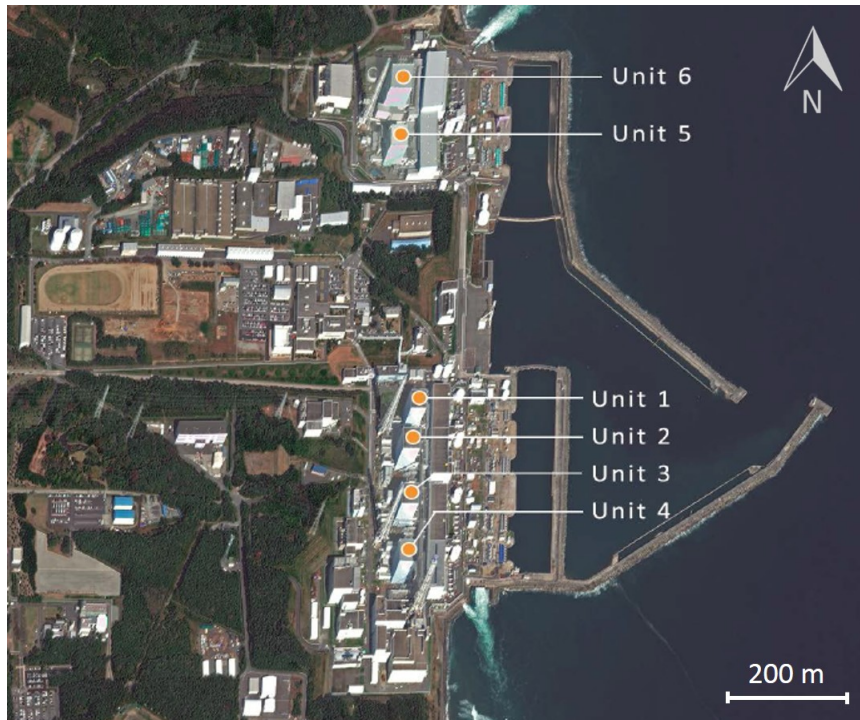
Figure 1.1: Annotated aerial photograph of the FDNPP - the location of its reactors is shown, set behind the protective seawall 5.7 m high and offshore perimeter breakwater. *From [2].*

As was typical of reactors within Japan, the units at the FDNPP were all of Boiling Water Reactor (BWR) design (a schematic of which is shown in Figure 1.2), each achieving criticality and entering into power generation over a ten year period between 1970 and 1979. All of the reactors were of GE design - supplied through a consortium of GE, alongside both Toshiba and Hitachi. A breakdown of the key attributes for each of the six reactors at the FDNPP, as well as the plant's central fuel storage facility, is shown in Table 1.1. Further details on the composition and state of the fuel, alongside other core properties, are shown in Table 1.2. Although features differed slightly between each reactor, the general construction and operation of each were near-identical. At the core of each reactor were a number of fuel assemblies (400 in the smallest Unit 1, with 764 in the largest Unit 6), each 4 m in length, with each assembly bundle containing 60 fuel rods - into these the fissile fuel (typically UO_2) was loaded.

To contain this fuel, it was encased within a high-purity (low Hf content) and low neutron-absorbing zirconium alloy (Zircaloy-4™) cladding. BWRs are the simplest light water reactor design by which to generate power - with the heat and resultant steam directed out of the top of the Reactor Pressure Vessel (RPV), where it drives a number of turbines. The steam is then condensed via a heat exchanger (using seawater supplied by the seawater pumps) before being returned to the reactor in a single (closed) loop. Control of the neutron flux, and hence
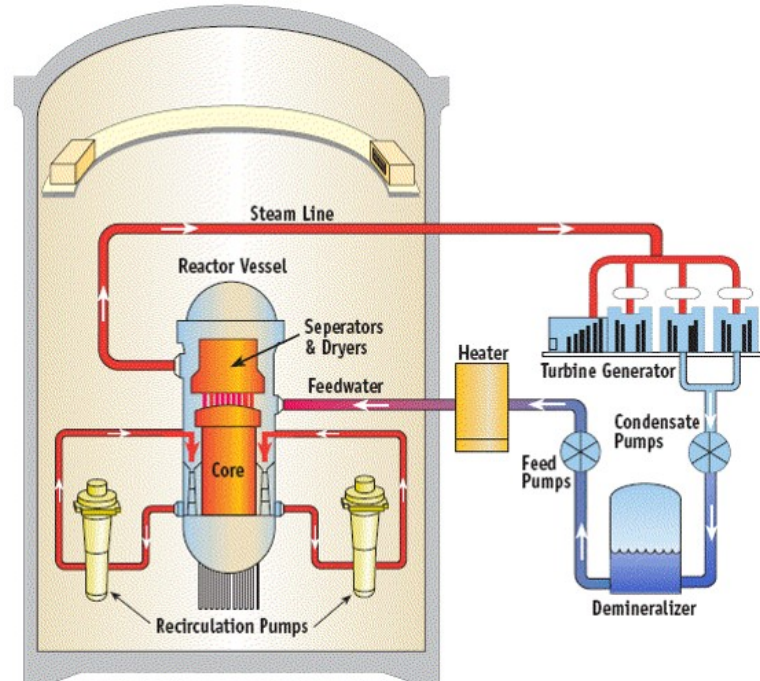
Figure 1.2: Illustrative schematic of the components within a light water BWR unit. *From [8].*

the reactor's power output, is performed via control rods composed of a high neutron-absorbing material (B_4C at Fukushima), with fine adjustments to operations undertaken by changes in the water recirculation flow rate. Water in these reactors also serves as a neutron moderator, producing "thermal" neutrons capable of fissioning U nuclei by slowing down "fast" neutrons, otherwise unable to induce fissions. Unlike the now favoured Pressurized Water Reactor (PWR) designs, the steam generated through the fission process is used to directly drive the turbines, whereas a secondary boiler loop is found within PWR systems.

Based around the "free-standing bulb-shape" design, five of the reactors (Units 1 - 5), including all those involved in the 2011 accident (Section 1.3) featured the older style of Mark-I Primary Containment (PC), a schematic of which is shown in Figure 1.3. Unit 6 conversely, employed a slightly different Mark-II Primary Containment. Contained within the reactors Dry Well (known also as the Primary Containment Vessel, or PCV), is the RPV. Connected below to the Dry Well is the torus-shaped Wet Well (or Suppression Chamber) - where water contained within a Suppression Pool acts as an energy absorbing medium in the event of a severe loss of coolant incident (LOCI); whereby excess heat is produced within the core-containing RPV [12]. Further details regarding the design and operation of nuclear reactors are detailed in Glasstone (1994) [20], and summarised with respect to the FDNPP in literature provided by the World Nuclear Association [11]. An illustrative schematic of a typical BWR is shown in Figure 1.2.

After its use within a reactor, nuclear fuel is both thermally as well as radiologically "hot" [21]. When removed from the core, a fuel assembly is routinely stored underwater for a period of around 3 years in dedicated fuel storage ponds (FSP), where it can be actively cooled and the ionising radiation that it emits safely shielded (whilst outside of the RPV) [20, 21]. To facilitate this, operations require an uninterrupted power supply to drive the recirculation pumps that distribute water and remove the considerable decay heat through the numerous heat exchangers. Typical of Japanese reactor designs and apparent from those at the FDNPP site, was the location of these fuel storage ponds (each maintained at specific chemical/pH conditions to allow for the safe long-term storage of the fuel [22]), positioned directly above each RPV (Figure 1.3). Their position allowed for the logistically simple routine transfer of fuel both in and out of the RPV while fully underwater. Both fresh (unirradiated) and spent (irradiated) fuel assemblies were stored in these ponds, above each of the reactors (a breakdown is presented in Table 1.1) - with additional material housed at the facilities central (wet) storage facility (before being transferred into long-term dry storage after sufficient cooling).

If a LOCI event were to occur at such a facility; with fuel still located within the RPV, the principal priority is to rapidly cool the fuel back to a safe temperature. As stated above, despite being shut down, a large amount of residual decay heat remains (approximately 1.5% of normal thermal output, or 3.0 MW [23, 24]). For the FDNPP reactors, this would be performed using a Residual Heat Removal (RHR) system and an Emergency Core Cooling (ECC) system - in the form of either an Isolation Condenser (IC) system, as in Unit 1, or a Reactor Core Isolation Unit (RCIU), for Units 2 - 6 [25]. These systems required only a limited amount of external power to recirculate cooling water, drawn by the coastal seawater pumps, through the reactors extensive heat exchanger network. In the case of Fukushima, this power was provided through a number of external high-voltage supply lines that ran to the site, in addition to several backup generators and batteries (located in the basement of each of the turbine halls). A number of unpowered systems also existed within each of the reactors to provide a "last chance" for emergency core-cooling in the event of powered systems failing.

1.1.1 Units 1, 2 and 3

As shown in Table 1.1, these were the first reactors to come into service, between 1970 and 1975 - with the first, Unit 1, being the smallest at the site. At the time of the accident, all three reactors were in power generation mode, with the cores of both Units 1 and 2 operating with a "standard" low-enriched ($\approx$3.5 wt% ^{235}U [25]) uranium dioxide (UO_2) loading. The neighbouring Unit 3 was, however, operating with a core composed of a mixture of both low-enriched UO_2 (total: 512 assemblies) and a plutonium-uranium mixed-oxide (or MOX) fuel (total: 32 assemblies) [25, 26]. MOX fuels represent a method through which to recycle Pu that had ingrown via the transmutation of fertile ^{238}U during neutron irradiation.

5
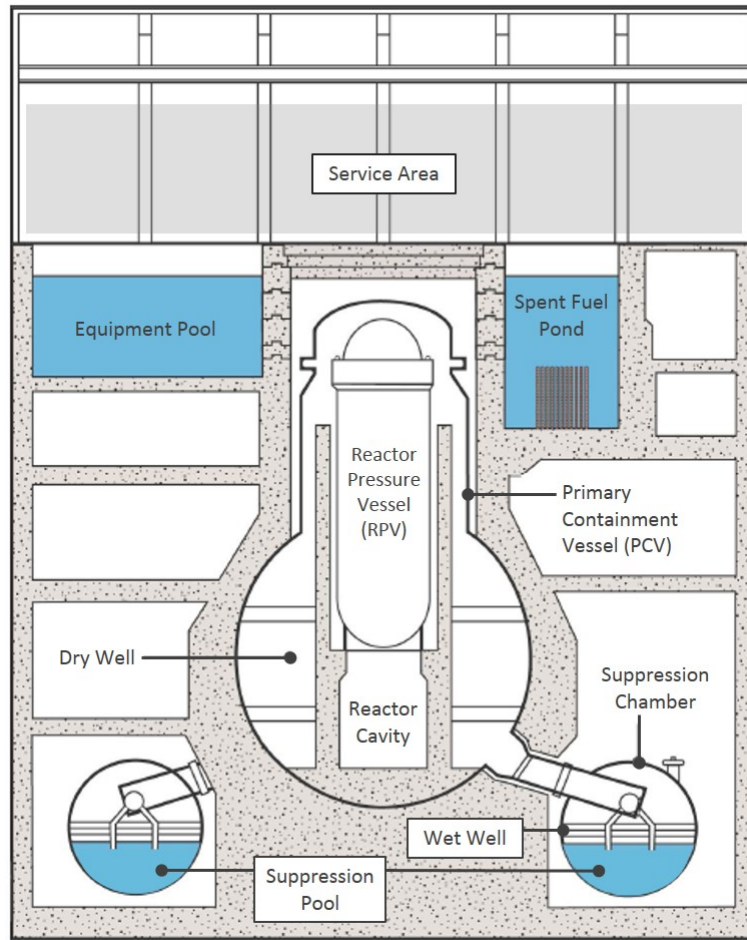
Figure 1.3: Schematic of BWR Mark-I Primary Containment (Units 1 - 5). *Modified from [2].*

	Unit 1	Unit 2	Unit 3	Unit 4	Unit 5	Unit 6	Central storage
Power output (MWe)	460	784	784	784	784	1100	-
First power	1970	1973	1974	1978	1977	1979	-
Fuel type	UO$_2$	UO$_2$	UO$_2$ / MOX	UO$_2$	UO$_2$	UO$_2$	UO$_2$
Reactor fuel assemblies	400	587	548	0	548	764	0
Stored fuel assemblies	292	578	514	1331	946	876	6375

Table 1.1: Operational parameters and fuel loadings at the six FDNPP reactors (and their associated fuel storage ponds) as well as the central fuel storage facility, at the time of the accident. *From [5, 11].*

	Unit 1	Unit 2	Unit 3
U mass (kg)	68	94	93
U enrichment (wt% ^{235}U)	3.4 - 3.6	3.8	1.1 - 3.8*
U burn-up - averaged (GWD/t)	39.5	45.0	45.0
U burn-up - maximum (GWD/t)	55.0	55.0	55.0
Cladding material	Zircaloy-4™		
Control material	B$_4$C		

Table 1.2: Core parameters for FDNPP reactor Units 1, 2 and 3 at the time of the incident on the 11th March 2011. *(*Unit 3 at the FDNPP also contained MOX fuel assemblies (32 in total), with 1.1 wt% - 1.3 wt% ^{235}U and 2.7 wt% - 5.3 wt% ^{239}Pu - the enrichment of the standard UO$_2$ fuel assemblies (516 in total), was 3.8 wt% ^{235}U). From [25].*

Due to limited space available at the sites central fuel storage facility, the above-reactor fuel storage pond in Unit 2 was abnormally full, resulting in a greater than normal thermal-loading on its heat-removal system.

1.1.2 Unit 4

Unlike Units 1, 2 and 3, the neighbouring Unit 4 was undergoing a planned outage at the time of the accident, prior to its refuelling and eventual restarting. As a result, the entirety of the core had been moved into the reactors FSP. Like Unit 2, this resulted in the facility being abnormally full, with a similarly high (but within tolerable limits) thermal-loading on both the recirculation and thermal extraction systems. Despite being much later in its construction than the earlier three reactor Units, a number of ventilation pipework connections were shared between it and the neighbouring Unit 3 - with similar pipework links existing between both Units 2 and 3.

1.1.3 Units 5 and 6

The northern-most and newest units at the FDNPP, Units 5 and 6, were in a period of prolonged "cold shutdown" at the time of the incident (Unit 5 had been shut down on 3rd January 2011, with Unit 6 on 14th August 2010) [25]. Contrary to Unit 4, where all of the nuclear material from the core had been removed into the above-reactor FSPs, the nuclear material from these reactor Units remained in its RPV and FSPs (as at the time of operation). Owing to the long period of time that these reactors had been in shutdown, its core material was not as thermally hot as the other Units [25]. As no events or radioactive releases occurred from either of these reactor units, they are not further discussed in this thesis.

1.1.4 Central fuel storage facility

Located close to Unit 4 (towards the southern-most part of the site), the plant's central fuel storage facility was near-full at the time of the accident, containing 6375 fuel assemblies (maximum: 6840, although reduced slightly due to some damaged assemblies being stored in this facility) [5]. The storage facility inventory comprised predominantly older fuel (with considerably less decay heat and radioactivity) and sustained no major damage during the March 2011 events. This facility did not contribute to any radiation emission and is not further discussed.

1.1.5 Site infrastructure

Like any electricity generating facility, significant infrastructure is required to connect it to the wider power distribution network, with the Fukushima Daiichi site being no exception to this. These extensive high-voltage lines transmit energy produced on the site out, to the national grid using a number of additional high-voltage lines supplying power to the facility, more importantly, should the need arise. In contrast to the majority of other countries, due to the extensive seismic activity typical of Japan [18], electricity (and other services) are transmitted above ground rather than buried at shallow depths [14]. Such a system allows for not only greater damage tolerance during earthquake events, but also a more efficient repair to infrastructure in such an aftermath.

1.2 The Great Eastern Japan Earthquake and Tsunami

At 14:46 on Friday 11th March 2011, a M_W 9.0 earthquake occurred 130 km offshore of the nearby city of Sendai, 100 km north of the FDNPP [27]. Resulting from the 20 m lateral movement of the sea-floor that occurred, the eastern part of Japan's main island, Honshu, shifted horizontally by several meters, and vertically by approximately half a meter [28]. The magnitude of this seismic event was unprecedented in modern human history and greater than almost all earthquakes formerly recorded in Japan - comparable to the M_W 9.1 Indian Ocean Earthquake in 2004 [29]. As a result of the earthquake's magnitude, the total amount of energy released was considerable. Estimates placed the total Joule equivalent at 3.0 EJ ($\times 10^{18}$ J), or the equivalent of 800 megatons of TNT (sixteen times the energy released from the worlds largest ever thermonuclear weapon, the "Tsar Bomba", tested in 1961 by the Soviet Union) [18].

Arsing from this vast vertical displacement, 41 and 50 minutes after the main earthquake (and during the hundreds of significant aftershocks), two tsunami waves up to 33 m high, inundated an area of coastline totalling over 560 km^2 (including that occupied by the FDNPP) - causing the loss of 19,000 lives, with many more reported missing [30].
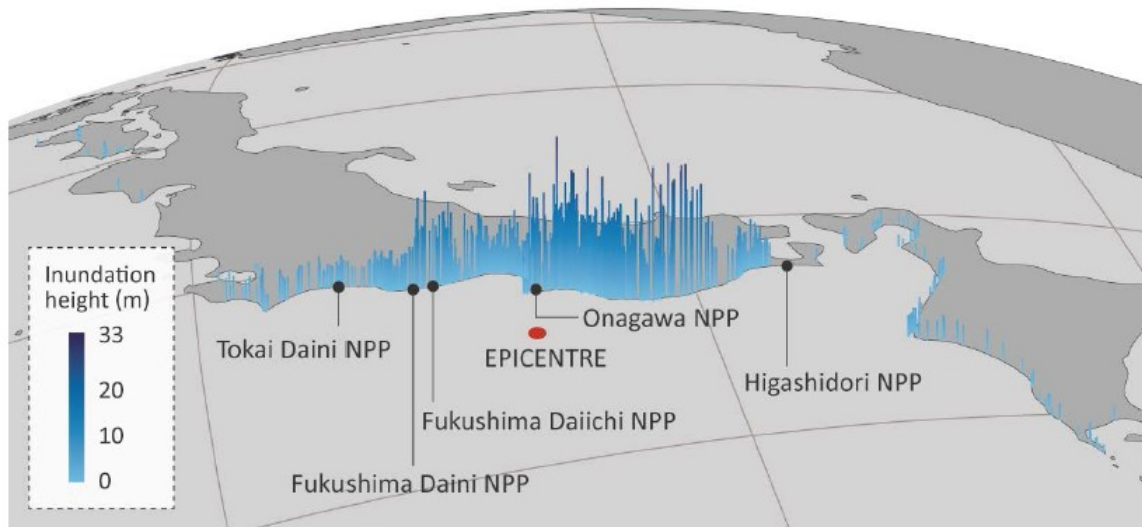
Figure 1.4: Map of north-eastern Japan nuclear facilities, with the 11th March 2011 tsunami inundation height and the location of the earthquake epicentre shown. *From [2].*

1.3 The Fukushima Daiichi Nuclear Power Plant Accident

The FDNPP was just one of a number of Japanese nuclear facilities impacted by the tsunami (Figure 1.4). However, all others (some impacted by greater inundations of up to 31 m) were better protected and able to successfully prevent any radioactive releases. Due to the extensive seismic monitoring network that exists across Japan, both the location and intensity of the earthquake were known instantly [17], and applicable tsunami warnings were issued - including to the area surrounding the FDNPP site [31].

This chronology of events is sourced from a number of official accounts, documents and press releases, shown graphically also in Figures 1.5 and 1.6. These were reported by the operators (TEPCO) [7, 32, 33] as well as detailed extensively within the IAEA 2015 Fukushima Report [2] alongside being further summarised by the World Nuclear Association (WNA) report on the event [34]. All times stated are Japan Standard Time (JST) (UTC +09:00).

1.3.1 11th March 2011

14:46. Immediately after the detection of the first seismic episode at the FDNPP (as well as many other reactors across the country), the operational reactors (Units 1 - 3) "tripped", entering into an immediate shutdown (or "SCRAM") with full insertion of control rods and initiation of the ECC systems. *(N.B. later analysis concluded that the earthquake itself did not cause any serious structural damage to the reactors)*. Almost instantly after this emergency shutdown and ECC system initiation, the external power to the plant was lost as a result of the earthquake - with supply instead drawn from generators located in the neighbouring turbine halls basements.

9
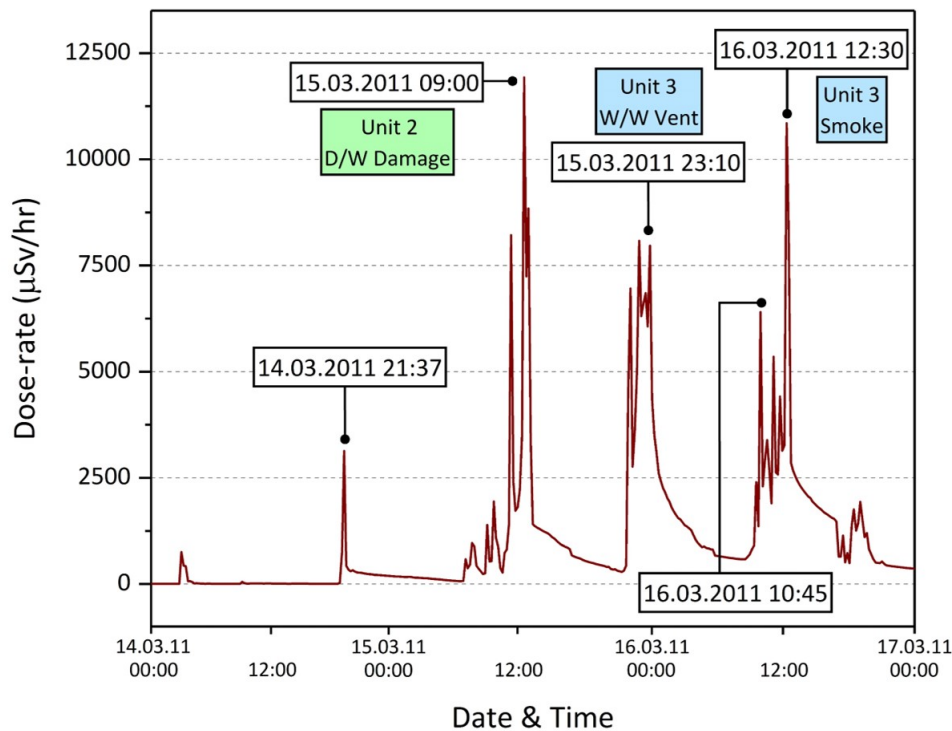
Figure 1.5: Variation in air dose-rate over the main release period as recorded at the FDNPP Main Gate. *Data obtained from [33].*

15:27 and **15:36**. Less than an hour after the main seismic event, two tsunami waves (4 and 15 m respectively) arrived at the site, causing damage which resulted in a station-wide power blackout. The tsunami waters flooded the basements where the back-up generators were housed; also destroying the seawater pumps (central to the heat-exchanger network), the RHR system and the electrical switchgear used to control and report on the condition of each of the reactors. Several backup batteries located in the basements of Units 1 and 2 were also flooded, leaving both without lighting or basic instrumentation. The batteries within Unit 3 survived, however, allowing readouts from limited instrumentation for a period of approximately 30 hours.

Following the tsunamis, all but 1 of the 24 static on-site radiation monitoring points were disabled, leaving the authorities with little or no knowledge as to the levels or spread of radioactivity. The only operating monitoring point was located at the plants Main Gate (to the far west of the site), with the variation in air dose-rate over the main 72 hour release period recorded by this monitor shown in Figure 1.5.

18:00. Without heat removal by circulation to an outside heat exchanger, extensive steam was produced (later directed into the PCV) - with the water-level in Unit 1 dropping below the top of
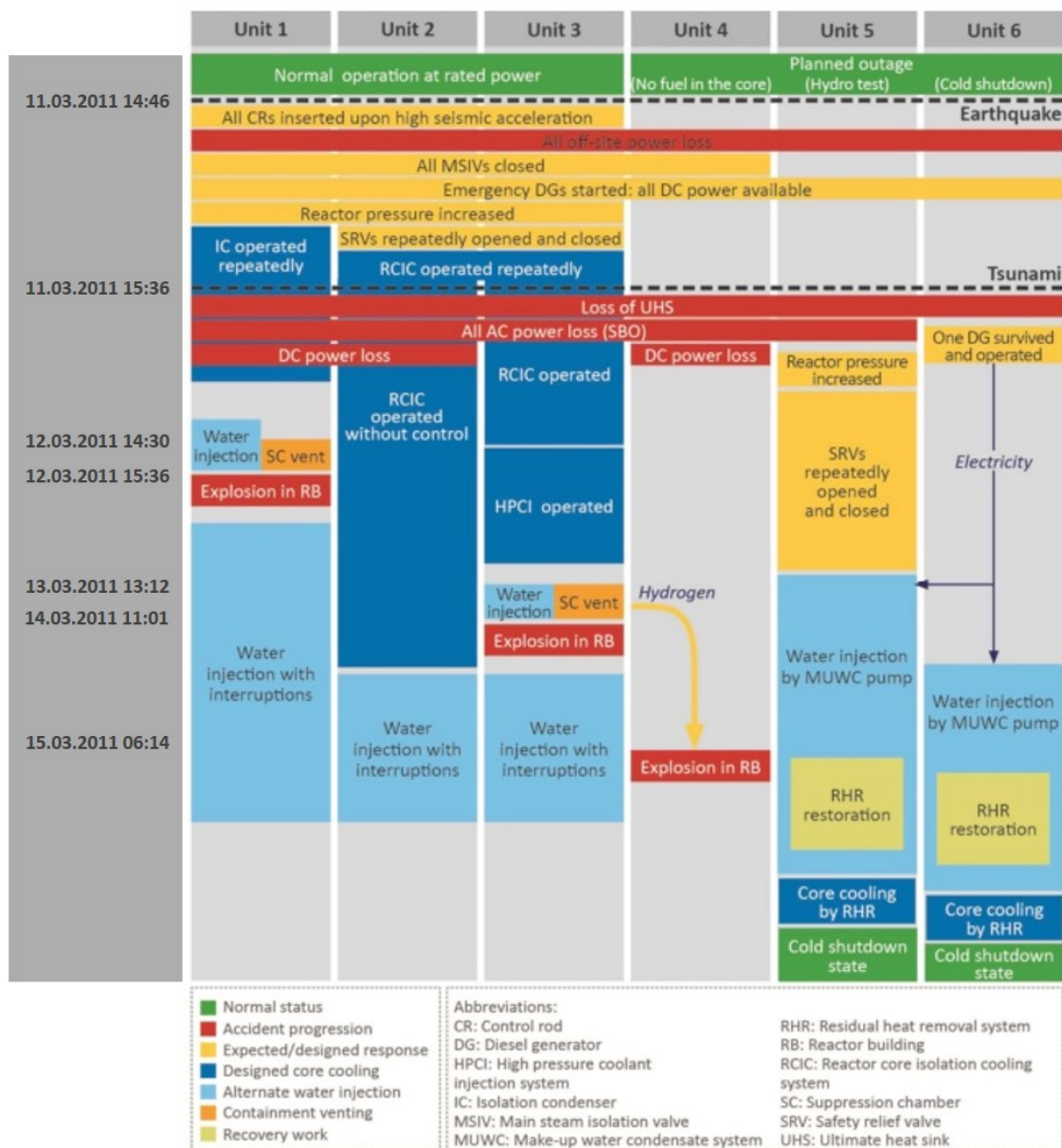
Figure 1.6: Chronology of events at the FDNPP. *Modified from the 2015 IAEA Fukushima Accident Report [2]*. A list of the acronyms contained within this schematic is provided.

the fuel, and by **19:30**, to below the bottom of the fuel assemblies. As a result, the fuel in the RPV began to increase in surface temperature and was estimated to have reached in-excess of 2800°C.

19:03. In light of the situation, the Government of Japan declared a Nuclear Emergency at the FDNPP site. At **20:50**, a 2 km evacuation order was issued for those living closest to the plant. This zone was extended to 3 km at **21:03** by the then Prime Minister, Mr Naoto Kan.

In the absence of adequate core-cooling, a large volume of steam was produced in each Units RPVs. This pressure of steam, as well as hydrogen gas, (produced as a result of the highly-exothermic oxidation of the zirconium (Zircaloy-4™) cladding at elevated temperatures in the presence of steam [35]), was subsequently released by venting the RPVs of reactor Units 1 and 2 into their respective Dry Wells (or PCVs).

However, during the incident, the pressure and temperature of each of the RPVs continued to rise, with reactor core water injection commencing through the various design mechanisms (as described in Section 1.1). Over time, each of these systems failed - with eventual decisions made for each of the reactors to be vented into their respective Wet Wells (Suppression Pools) to further relieve reactor pressure build-up and initiate seawater injection as a final core-cooling attempt.

1.3.2   12th March 2011

05:44. The estimated risk and likelihood of a radiation release was considered sufficiently high that under mounting pressure, Prime Minister Kan extended the mandatory evacuation zone to a 10 km radius from the sites western-most boundary.

07:00. Core melting in Unit 1 was estimated to have reached completion, with nearly all of the core having fallen to the base of the RPV and PCV before partly melting into the 5 m thick concrete pedestal below. *(N.B. quartz and other mineral components of concrete melt at temperatures of ≈1000°C [35–37] - well below the 2900°C melting point of UO_2 [35])*.

After earlier attempts failed at around **10:20**, the venting of the Unit 1 PCV through an external vent stack was again attempted at **14:30**. This vent, however, failed with a portion of the vented combustible gas flowing back into the service area, around the fuel storage ponds and other regions surrounding the reactor structure (Figure 1.3).

11:00. With the primary backup core cooling and water injection system having failed, as well as the secondary system (using the high-pressure return of condensed steam) in reactor Unit 3, the water level in the reactor had significantly dropped - alongside an associated increase in the reactors core temperature.

15:36. Following the failed venting of Unit 1 an hour earlier, an explosion occurred in the Unit 1 reactor building, producing large volumes of thick white smoke.

18:25 After visiting the plant, Prime Minister Kan further revised the evacuation radius, increasing it up to 20 km around the plant.

19:00. Seawater injection began into Unit 1 against the instructions of the Japanese Government (who shortly after, however, redacted this instruction).

The unknown whereabouts and condition of two TEPCO workers were reported by the company. Kazuhiko Kokubo and Yoshiki Terashima were in the basement of the Unit 4 turbine building undertaking an inspection for potential leaks caused by the earthquake when the tsunami hit. It was not until the 3rd April 2011 that the news of their deaths was finally released. These deaths, to date, are the only ones to have occurred as a direct result of events at the FDNPP [30].

1.3.3   13th March 2011

05:30. At this time, the melting of core material within reactor Unit 3 was believed to have initiated, with most of the core having undergone complete melting by 12:00 on the same day. As a result, like reactor Unit 1, most of the core material was believed to have fallen to the base of the RPV.

09:50. The RPV of Unit 3 was successfully vented into the Wet Well (Suppression Pool) to yield a reduction in the overall reactor core pressure. This venting was **not** through the PCV, but directly into the Wet Well through a dedicated vent line out of the top of the RPV.

10:15. Following high-pressure readings from Unit 2, a decision was made to vent the RPV into the PCV through the use of a small portable generator to open the required valves.

13:12. The RPV of Unit 3 was, again, successfully vented into the Wet Well (Suppression Pool), allowing for seawater injection (using a fire pump), to begin.

1.3.4   14th March 2011

11:01. Further attempted venting of the pressure that had subsequently built-up within Unit 3 was performed. However, shortly after, an explosion similar to that of Unit 1 occurred, demolishing the top portion of the reactor building. This venting effort was believed to have similarly failed as a result of the ignition of hydrogen that had accumulated/back-flown into the reactors service area.

The large amount of debris from the Unit 3 explosion, aside from being highly-radioactive, caused extensive damage to the other Units cooling systems, principally the neighbouring Unit 2.

13:00. The steam-driven systems that had provided cooling to the Unit 2 reactor, as a final back-up, eventually failed. From this time, there occurred a resultant rise in reactor pressure and a lowering of the RPV water level.

To avoid a repetition of the hydrogen explosion that had occurred at Unit 1 two days earlier, from **18:00**, the vent panels in the roof of the Unit 2 reactor building were opened.

19:05. Seawater injection into Unit 2 began after pressure was relieved via the venting of the PCV into the reactors Wet Well (Suppression Pool).

At approximately **20:00** on Monday 14th March, core damage to Unit 2 was likely to have begun, following the seven-hour break in cooling.

1.3.5   15th March 2011

00:01. Shortly after midnight, further venting of the Unit 2 RPV was performed, following an initial venting two days earlier on the morning of the 13th March.

06:14. An explosion was witnessed to have occurred from the top of Unit 4. The explosion caused extensive damage to the reactor building but also resulted in further damage to the neighbouring Unit 3. This explosion was believed to be the result of an explosive hydrogen gas mixture originating from Unit 3, that travelled into Unit 4 through the shared ducts from the venting process that had occurred earlier.

At around **09:00** on Tuesday 15th March, the highest levels of radiation since the start of the accident were detected. A dose-rate of 11,930 μSv hr^{-1} (0.1193 Sv hr^{-1}) was recorded at the radiation monitoring point at the Main Gate. Later analysis subsequently suggested that this spike in radioactivity was the result of a leak in the PCV of Unit 2. This release represented the largest to come from the site, and did not result from a physical reactor building explosion.

At around midnight on the 15th March, the reactor Unit 3 Wet Well was vented through an external stack into the atmosphere. Unlike the venting episodes that had occurred at reactor Units 1 and 2, the hot reactor gases had not passed through/contacted with the PCV (Dry Well) before leaving the reactor building.

Following the earlier explosion in reactor Unit 4, TEPCO began the injection of seawater into the Unit 4 FSP in an attempt to reduce its temperature. Later in the day, active cooling was started to the other reactor Units FSPs. Initial samples taken from the cooling waters in these ponds suggested that a number of fuel assemblies may have been damaged [38].

1.3.6   Beyond 16th March 2011

This timeline of events during the initial five days represents the most substantive releases from the site, with large mushroom-cloud style explosions from Units 1 and 3 and the believed PCV

breach from Unit 2. Over the period that followed, further, but less considerable releases occurred [33], with periodic and significant radiation releases occurring until the 31th March 2011 [39], and a further release occurring during August 2013 [40]. These emissions have been invoked to represent remediation and debris retrieval operations that were occurring on the site [40].

1.3.7 Meteoric conditions

Located on the countries border with the Pacific Ocean, as with any such coastal site, the meteoric (wind) conditions associated with the FDNPP site were highly-variable. The conditions measured at the plant over the twenty days from the 11th March 2011 are shown in the rose diagrams presented in Figure 1.7. From these plots, the predominant wind direction is observed as flowing from the plant in the west, out eastwards into the neighbouring Pacific Ocean. An additional (although less prominent) northerly wind direction is also apparent.

As shown by the rose diagram of Figure 1.7 depicting wind conditions on 12th March, at the time of the Unit 1 release (15:36), the wind conditions were such that radioactive material would be transported in a northerly direction. The wind conditions two days later, during the second site release from Unit 3 on the 14th March were, however, contrasting. During this contamination release at 11:01 JST, wind conditions resulted in emissions being transported towards the south. Conditions subsequently changed from mid-afternoon, with winds blowing offshore to the east.

The penultimate (and largest) radioactive release from the FDNPP site resulted from a believed leak of the reactor Unit 2 PCV. Invoked to have commenced at approximately 20:00 on the 14th March, the seaward wind direction from the afternoon through to the early evening meant that radiation released over this period was dispersed over the neighbouring Pacific Ocean. A change in the wind direction several hours later resulted in a component of this release being directed back onshore (westwards), towards the Chiba, Tsukuba and Tokyo Metropolitan areas - hundreds of km's to the south. However, a further change in the wind-direction within the Kantō Region overnight (into the morning of the 15th March), resulted in the transportation of air northwards - back towards the cities of Nihonmatsu and Fukushima. At the same time (morning of the 15th March), a light onshore wind occurred, alongside a more prevalent northerly wind - transporting material both on-land, but predominantly southwards and out to sea. With multiple contaminated air-masses now dispersed across the Japanese mainland, for the first time since the start of the incident on the 11th March, widespread precipitation occurred from 12:00 until 20:00 on the 15th March, across both the Kantō and Tōhoku Regions. This resulted in the deposition of once-airborne radioactive material across a large expanse of the Fukushima Prefecture [42].

As previously discussed, at 06:14 JST on the 15th March, during the explosion at the FDNPP Unit 4 reactor building (due to the inflow of highly-flammable Unit 3-derived hydrogen as a result
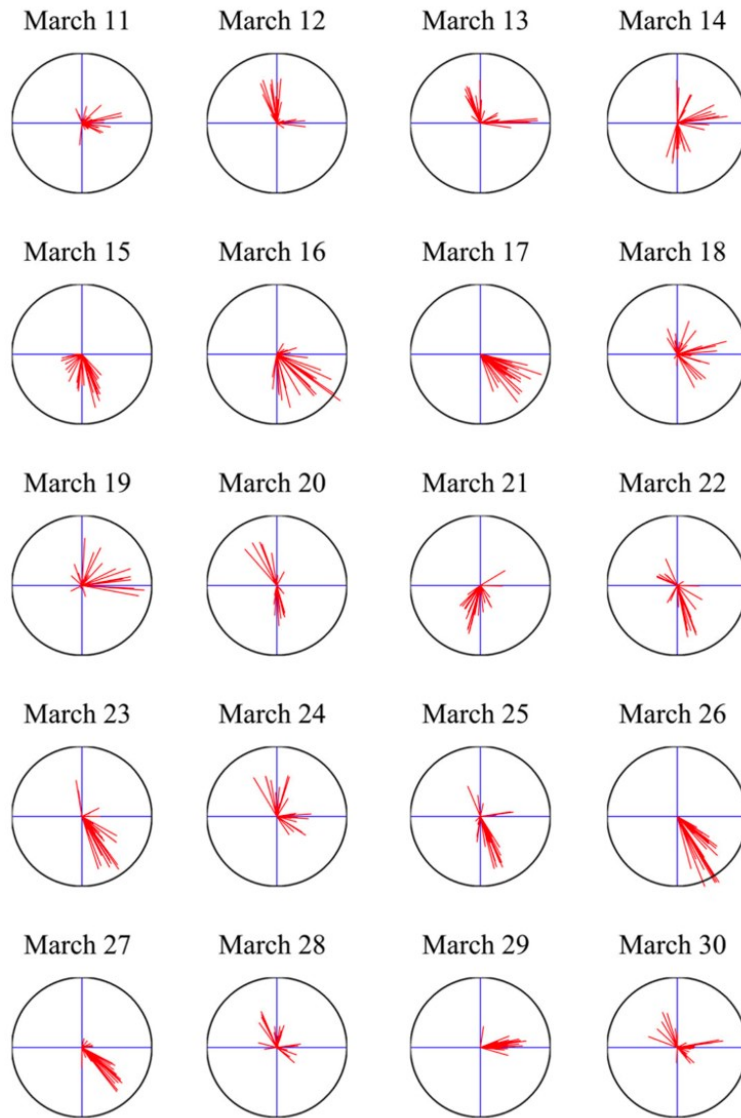
Figure 1.7: Schematic summary of wind fields during each day at the FDNPP. Red lines represent the wind directions (from the plant), with their length depicting the velocity. *From [41].*
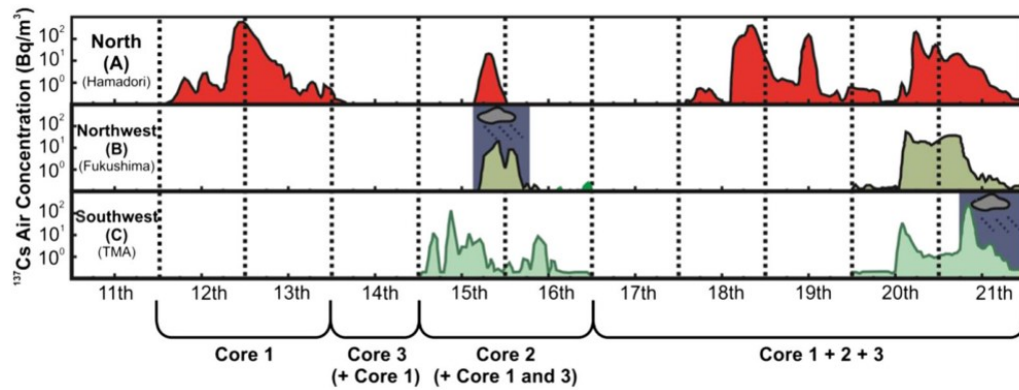
Figure 1.8: Time-resolved ^{137}Cs depositional concentrations monitored at three localities (A - Hamadori, Sendai; B - Fukushima, Fukushima City and C - TMA, Tokyo Metropolitan Area) over the ten day release period. Blue shaded areas illustrate the periods of precipitation that occurred at each geographically-distinct site. *From [43], with data from [42].*

of shared pipework), the prevailing wind direction was northerly - transporting contamination southwards, and out to sea. A light onshore wind also occurred early in the day.

A summary of the total ^{137}Cs depositional concentration releases that occurred over the initial ten-day emission phase is shown graphically in Figure 1.8. Also included in this plot from Snow et al., (2016) [43] (with data derived from Tsuruta et al., (2014) [42]) are illustrated; (i) the periods of prolonged precipitation that occurred at two of the sites (Fukushima (Fukushima City) and the Tokyo Metropolitan Area (TMA)) in addition to, (ii) the specific reactor Unit release event contributions attributed to have occurred.

1.4 Post-accident reactor assessment

1.4.1 International Nuclear and Radiological Event Scale (INES)

Owing to the *"major release of radioactive material with widespread health and environmental effects requiring implementation of planned and extended countermeasures"* [1], the events at the FDNPP were classified on the 12th April 2011 at Level 7 (the most severe) on the International Nuclear and Radiological Event Scale (INES) [44].

Representing the most significant of nuclear release scenarios, the only other event to be rated equally highly was that which occurred at the Chernobyl Nuclear Power Plant in 1986.

1.4.2 Reactor inventory modelling

To better inform the distribution of contamination arising from the different reactor sources at the FDNPP, reactor core inventory modelling for each of the reactors (Units 1 - 3) and associated

Source	$^{134}Cs/^{137}Cs$ (Activity)
Unit 1	0.94
Unit 2	1.08
Unit 3	1.04
FSP 1	0.54
FSP 2	0.64
FSP 3	0.74
FSP 4	0.68

Table 1.3: Characteristic $^{134}Cs/^{137}Cs$ activity ratios for reactor Units 1 - 3 and FSPs 1 - 4. *As determined by [50].*

FSPs (Units 1 - 4) involved/potentially influenced by the accident was undertaken. Owing to the differing ages and degrees of burn-up of the fuel within each of the reactors and FSP a specific radiocesium activity ratio ($^{134}Cs/^{137}Cs$), for each potential source was derived. Other activity ratios (e.g. $^{110m}Ag/^{137}Cs$) or isotope ratios ($^{134}Cs/^{137}Cs$ or $^{240}Pu/^{239}Pu$), are each similarly indicative of a specific reactor source (or release scenario) [45–47]. These radionuclide ratios have formerly been utilised for the attribution of other contamination sources (e.g. Three Mile Island and Chernobyl) [48, 49].

This work after Fukushima was undertaken by Nishihara et al. [50], of Japan Atomic Energy Agency (JAEA), using ORIGEN code for calculating the nuclide compositions and characteristics of nuclear materials [51]. The $^{134}Cs/^{137}Cs$ activity ratio results obtained from this work are shown in Table 1.3. As is apparent, all fuelled reactor Units possessed a $^{134}Cs/^{137}Cs$ ratio averaging 1. In each of the fuel storage ponds, however, owing to the age of the material and resultant decay of the shorter-lived ^{134}Cs ($t_{1/2}$ = 2.065 years [52]), ratios were less - varying from 0.54 to 0.74. These values, however, only represent an average for the entire fuel volume of that source, as within a fuel assembly, this Cs activity and atomic ratios are observed to vary considerably with height in a typical BWR fuel element [53]. The application of these activity ratios to fingerprint individual releases is utilised in later portions of this work (Section 2.2.5).

1.4.3   Core behaviour

Since the accident in March 2011, the plant's operators TEPCO, in collaboration with Japan's International Research Institute for Nuclear Decommissioning (IRID), have employed the highly penetrating properties of naturally-occurring sub-atomic muons to investigate the state of each of the three damaged reactor cores. Beginning with Unit 1 in 2015 [54], before Unit 2 in 2016 [55] and most recently Unit 3 in 2017 [56], the state of each of the cores (structure and location of fuel material) has been imaged and for the first time, assessed.

Figure 1.9: Photographs of the above-reactor spent fuel storage pond in Unit 4 obtained using a remotely-operated underwater vehicle by TEPCO. *From [59].*

Within Unit 1, the majority of the fuel material has been observed to no-longer exist in the RPV but is inferred to have melted to form a "corium" material and fallen onto the base of the PCV. Little material subsequently remains in the original core position. A similar scenario is apparent in Unit 3, however, more core material than Unit 1 has been shown to be located in its original position within the RPV (although collected at its base). Unit 2 on the other hand, whilst showing some core melting had occurred and escaped to the underlying PCV, most of the fuel material still remains within the RPV (also located towards its base). Only a limited amount of "corium" is believed to have reached the base of the PCV. This melting and relocation of material outside of the RPV has resulted in significant issues for the decommissioning of the FDNPP reactors and the efforts to retrieve this material for its final disposal are ongoing at the time of writing this thesis [57].

1.4.4 Fuel Storage Ponds

Over the months following the accident, the cooling facility to each of the Unit's FSPs was restored. Despite showing early signs of physical damage (Figure 1.9), after analysis of the material recovered from the storage pond in the most heavily-loaded (and thermally active) Unit 4, the fuel was observed to have suffered from no significant deformation or corrosion and has since all been removed [58]. Plans are currently set to commence with work to remove the stored fuel from Unit 3 in mid-2018 [56].

1.5 Background summary

As detailed within this chapter, the FDNPP accident of March 2011, caused by the M_W 9.0 Great Eastern Japan Earthquake and resultant tsunami, represents one of the most severe radiological releases to ever occur from a power generation facility. Whereas the 1986 Chernobyl accident

resulted in the emission of radioactive material from a single reactor, the releases from the FDNPP occurred from numerous reactor Units/FSPs - containing different composition fuel material over a week-long period, under changing meteoric conditions into a topographically extensive environment. Therefore, understanding; (i) the chain of events, (ii) the current form of the contamination, and (iii) the distribution of this radiological contamination associated with the Fukushima accident, represents a far greater analytical challenge than was the case formerly at Chernobyl. It is hence the aim of this thesis to attain a better understanding of the accident and associated radiological contamination than is currently available.

RESPONSE, CONTAMINATION AND RELEASE ESTIMATES

With the earthquake and subsequent tsunami crippling all but one of the static radiation monitors on the site, there existed little knowledge as to the extent of the numerous radiation releases, detailed formerly in Section 1.3. Immediately after the incident, operations were driven to attain data to aid in the establishment of suitable evacuation zones (Section 2.2.4). In the years after the accident, however, the focus has shifted to monitoring the spread and environmental transportation of radioactivity, its decline due to radioactive decay and the impact of the extensive remediation works [60–62]. A summary of these monitoring studies was presented within the Japanese Nuclear Regulation Authority (NRA) *Comprehensive Monitoring Plan* [63], and in Saito and Onda (2015) [64].

2.1 Radiation monitoring

In the immediate aftermath of a large-scale radiological release incident such as at Fukushima, with limited (or no) knowledge as to the distribution of radionuclides, the first monitoring surveys are typically undertaken using manned aircraft at the greatest altitudes and velocities to characterise the greatest land areas in the shortest time possible. Any number of subsequent survey types then follow - the fundamentals of each as well as their role after the FDNPP incident are hereby discussed, with a comparison detailed in Appendix A. The underlying principles behind various radiation interaction mechanisms and its detection are detailed in Chapter 3.

2.1.1 Airborne

Gamma-ray (γ-ray) intensity from an infinite source is observed to reduce rapidly via attenuation with the air through which it propagates. This attenuation of an infinite source by a homogeneous
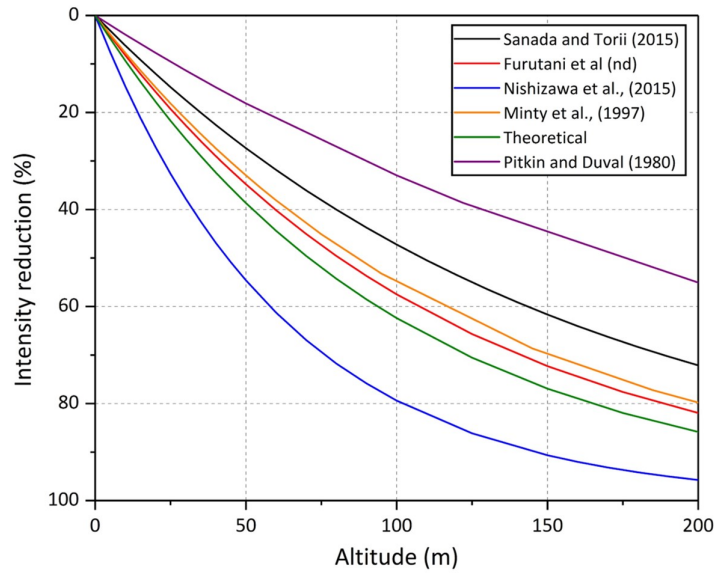
Figure 2.1: Attenuation slopes derived from previous airborne studies, detailing the exponential reduction in radiation intensity with altitude over a large area (planar geometry) source.

absorber can be described by Equation 2.1, where I_0 and I represent the initial radiation intensity and the attenuated intensity respectively. The attenuation is a function of μ - the mass attenuation coefficient, ρ - the density of the material and, x - the thickness through which it propagates. The mass attenuation coefficient ($cm^2\ g^{-1}$) is a combination of both the linear attenuation coefficient (cm^{-1}) [65, 66] and the density of the material (g cm^{-3}), with attenuation occurring as a result of the different energy and material dependent interaction mechanisms (detailed in Section 3.1.1).

$$I = I_0 e^{-\mu \rho x} \tag{2.1}$$

Apparent from Figure 2.1, is the rapid decline in radiation intensity as a consequence of detector altitude from such an infinite source, with results from a number of prior studies plotted (each employing a different experimental setup) [67–71], as well as from theoretical calculations (derived from Equation 2.1). Therefore, airborne surveys should not only contour topography as closely as possible but also maintain as low an altitude as safely achievable to attain the best possible sensitivity and on-ground spatial resolution [71, 72].

A number of calibration and review studies have concluded that airborne monitoring should ideally be performed at altitudes of less than 100 m - with sampling at altitudes of 600 m or greater representing data without "significant" ground influence [71–73]. Such rationale is consistent with the known half-distance (distance at which 50% attenuation occurs) of a ^{137}Cs γ-ray photon in air of $\approx$70 m, based on values presented within Grodstein (1957) [66] and Hubbell (1969), [74]. With the earth constantly bombarded by cosmic (solar) radiation, despite being

shielded from the vast majority of these strongly-ionising electromagnetic (EM) waves by our protective (ozone) atmosphere, a small proportion of this radiation is not attenuated and is incident onto the Earth's surface [75]. As such, at higher aerial survey altitudes (e.g. 600 m) - a greater proportion of cosmic background radiation would be detected than at lower survey heights (where increased interception and radiative attenuation would result [72]), significantly masking any underlying terrestrial radioactive signal [72]. Intuitively, if an aerial vehicle were to fly into an airborne radioactive plume, this represents a very different radiological situation (opposed to where radiation exists on the ground) and is resultantly not addressed in this discussion.

While the works of Minty (1997), Pitkin and Duval (1980) and Sanderson et al., (1995) [71–73] described above concluded that a 100 m survey altitude is the maximum height at which to undertake radiological mapping, this presents difficulties under current aviation guidelines. For nearly all countries, Civil Aviation Authority (CAA) regulations strictly prohibit manned aircraft from operating at less than 400 feet (122 m) OD [76], therefore, a special dispensation must be sought prior to such surveys (at 100 m) being undertaken.

To normalise for the effects of survey altitude back to a representative and meaningful air dose-rate (µSv hr^{-1}) 1 m above ground level, the equation for the slope of a calibration line (from Figure 2.1) is applied to the (at) altitude-derived data [71, 77].

In addition to the influence survey height has on the measured radiation intensity (via attenuation), the height at which the survey is performed further influences the "solid angle" (also termed the "field of view") between the detector and the ground; representing sampling from a larger on-ground region at greater survey altitudes [71, 73, 78]. This relationship is represented graphically in Figure 2.2 - derived through Equation 2.2, as presented within the work by Duval et al., (1971) [78]. In this equation, Y = radiation yield (or intensity), θ = half-angle of cone of incidence from detector to ground, H = height of the detector, A = a constant dependent upon the setup parameters, μ_e = linear attenuation coefficient of the ground within which activity is located, μ_a = linear attenuation coefficient of air, λ = Euler's constant (0.5772157), and x = ratio of the product of μ_a and height (H), to $cos\,\theta$.

$$Y\,(H, \theta) = \frac{A}{\mu_e}\cos\theta\left\{e^{-x} + x\left[\lambda + \log x + \sum_{n=1}^{\infty}\frac{x^n\,(-1)^n}{n\cdot n!}\right]\right\} \qquad (2.2)$$

Two further (user influenced) factors on the spatial resolution airborne surveys can attain are; (i) the velocity at which these surveys are conducted and, (ii) their grid-spacing (survey line separation). While flight velocity is highly-variable for manned helicopter surveys, fixed-wing (light aircraft) monitoring is typically performed at velocities of 50 ms^{-1} - 60 ms^{-1} [72],

23
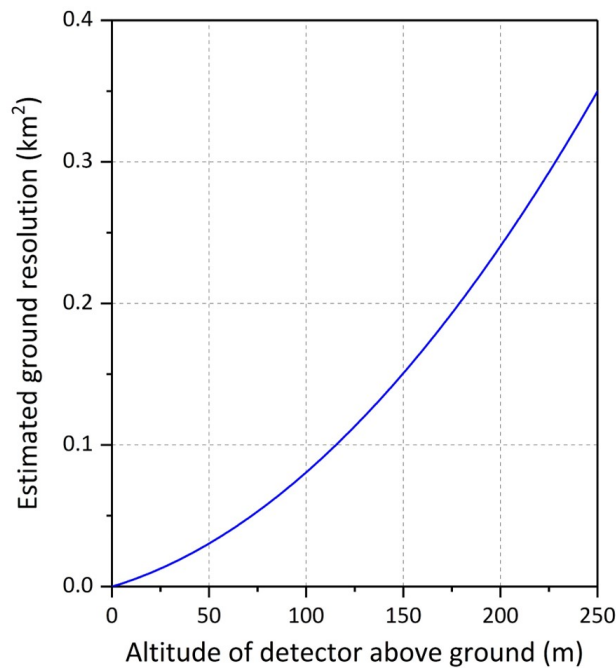
Figure 2.2: Estimated on-ground spatial resolution as a function of detector altitude (source-detector separation). *Modified from [78].*

with unmanned aerial methods operating at lower velocities (typically 10 ms^{-1} - 25 ms^{-1}) [79]. Therefore, the frequency at which data sampling occurs strongly dictates the spatial resolution through the total number of data points collected and the level (if any) of measurement overlap. Grid-spacing, in contrast to flight velocity, is one variable that can be readily-controlled (albeit at cost, especially in the case of manned aircraft monitoring), to directly influence the on-ground resolution attained [72]. With tighter grid-spacing, there occurs a greater inherent degree of data point overlap (between the sampling radii), as such - less inter-point inferencing and smoothing is required, hence improving the data accuracy and spatial resolution. The impact of these factors on spatial resolution for a number of previous environmental surveys are detailed in the review study by Sanderson et al., (1995) [73].

Between the numerous types of radiometric survey described in this chapter, the detector composition, but principally the volume of the solid-state detector varies considerably - and therefore influences its sensitivity for locating and mapping radioactive sources (the underlying physics of which are discussed in Section 3.1.1). Larger survey platforms (helicopters, light aircraft and also cars) are able to carry detector volumes of up to 45 L [72], whilst smaller unmanned systems are capable, however, of only transporting detectors with volumes typically less than 1 L [80, 81]. With larger detector volumes, a better ability to detect smaller (and less active) sources exists, owing to an increased overall detector sensitivity [82].

To obtain more than a basic "gross count-rate" from the data, an integration of specific regions of the spectrum (termed "windows") is performed. By analysing the number of counts (or relative proportions) in each of these discrete portions of the γ-ray energy spectrum, an isotopic composition of the radioactivity can be determined, as well as activity concentrations (Bq m^{-3}), with knowledge of the detectors basic characteristics [70, 71, 83, 84].

A number of additional, yet less significant, corrections to aerially-derived data are also routinely applied - including the removal of cosmic-ray background, anthropogenic sources that surround the detector (e.g. the aircraft and its occupants) and naturally-occurring radon, in addition to performing "spectral stripping". This "spectral stripping" serves to remove any contributions from elements that occur within the "windows" of others (most applicable during surveys of natural ore bodies with signals originating from Th, U and K γ-rays, and to a much lesser-extent from anthropogenic sources) [71]. Owing to this thesis, in-part, focusing on the mapping of these anthropogenically (nuclear) derived anomalies, the application of such "spectral stripping" is not considered, nor are other forms of minor data correction.

2.1.1.1 Manned airborne

The use of manned aircraft (helicopter and light aircraft) for radiological mapping was first employed, not in response to radiological release incidents, but for the geological mapping of radioactive mineral resources during the 1960's [77]. These early airborne surveys employed gas-filled Geiger-Muller (GM) detectors to rapidly gather information on the total "gross count-rate" in a survey area (without any spectroscopic data) to guide further analysis and ground sampling. Now, γ-ray spectrometers are used in-place of GM-based systems, providing the ability for isotopic differentiation formerly unattainable.

Following the earthquake and tsunami on the 11th March 2011 and the numerous radiation releases that occurred, it was not for six days until the first insight into the distribution and magnitude of radioactive contamination released from the plant was known - with full survey results not completed until the 5th April 2011 [85]. Prior to this, the only indication of the likely extent/transport of radionuclides and regions affected came from wind data recorded at the time [33], as well as a number of international monitoring projects [4].

Using a manned aircraft equipped with a high-volume NaI solid-state γ-ray detector (Figure 2.3), the first survey flight was performed directly over the plant and to its north in a joint exercise between the United States National Nuclear Security Administration (US NNSA)/United States Department of Energy (US DoE) and the Japanese Ministry of Education, Culture, Sports, Science and Technology (MEXT) [85, 86]. From this initial flight, high levels of radiation (>100 µSv hr^{-1}

25
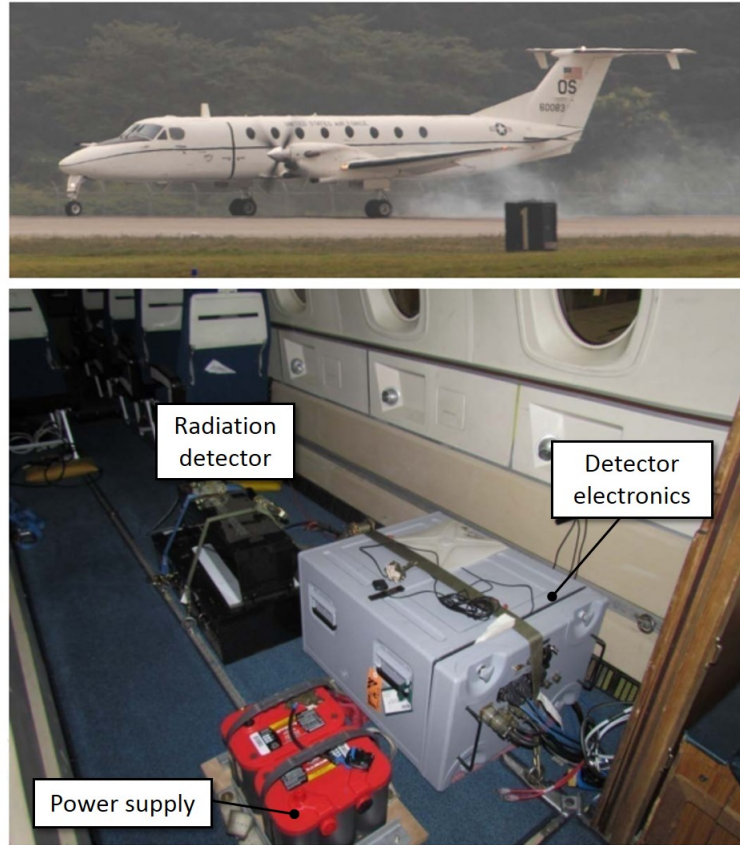
Figure 2.3: High-altitude (C12) manned aircraft (top), and radiation detection system (bottom), used during initial aerial surveys in March and April 2011 around the FDNPP. *From [86].*

as height corrected dose-rate) above the reactors were observed (shown in the maps of Figure 2.4). During the following three weeks, improved coverage was attained as a result of additional survey flights (42 in total), culminating in an 80 km landward radius from the FDNPP being mapped. This mapping highlighted the dominant NW-trending plume [85]. Operating at altitudes of 150 m - 700 m OD (due to considerable topographic variations across the region [62]), the resultant on-ground spatial resolution varied, with 300 m - 1500 m radius data points [85].

Further manned airborne studies over Fukushima Prefecture were regularly undertaken as part of the *Comprehensive Monitoring Plan* (CMP) introduced by the Japanese Nuclear Regulation Authority (NRA) [63], over the same 80 km radius from the plant [87, 88]. These surveys still continue on an annual basis under the CMP [89], with the results from all surveys to-date made publicly available via an online interactive platform [61]. It was this work that allowed for the full extent of both the contamination and resulting evacuation zone to be defined (Section 2.2.4).
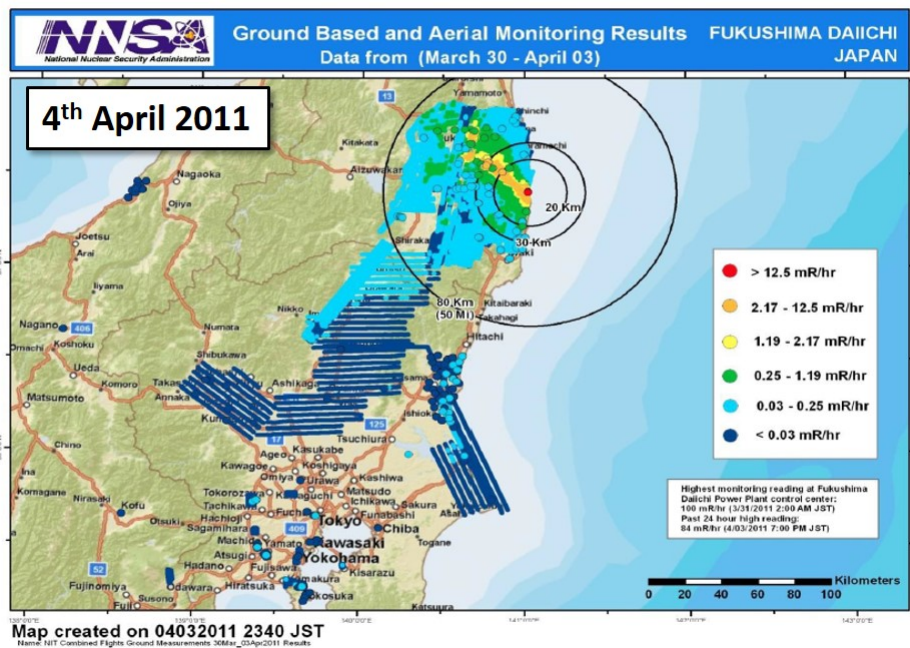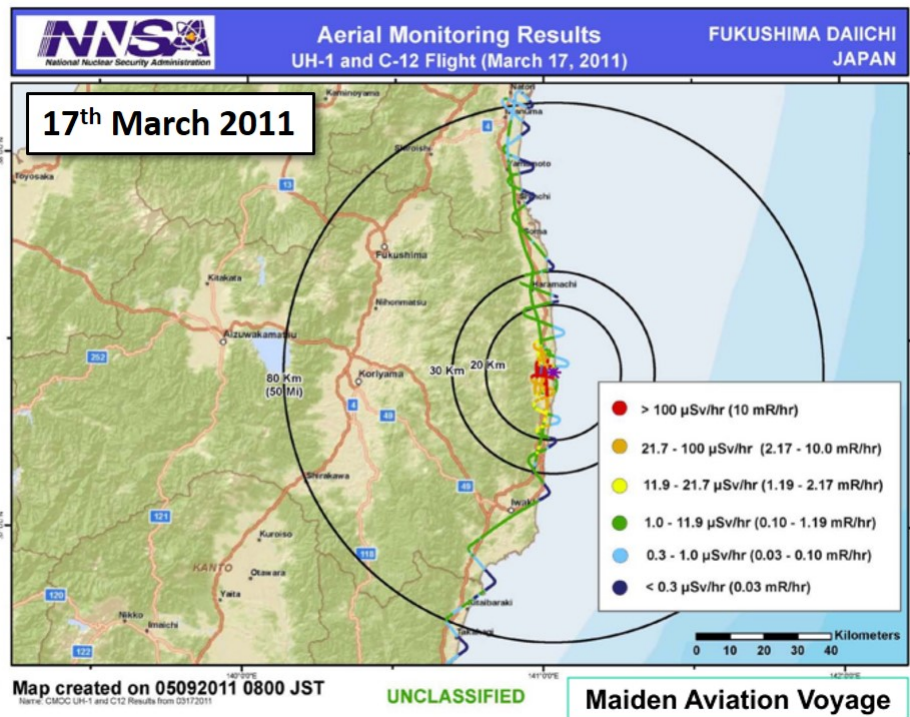
Figure 2.4: Initial height-corrected air dose-rate maps surrounding the FDNPP from 17th March 2011 (top), and 4th April 2011 (bottom). *From [86].*

2.1.1.2 Unmanned helicopter and fixed-wing

After the higher-altitude and rapid/large area coverage afforded by manned airborne surveys are performed, an additional survey type (and one that has been performed extensively in the region surrounding the FDNPP) is provided by unmanned helicopter or fixed-wing radiological surveys. Being unmanned, such surveys do not expose the operators to potentially significant doses of ionising radiation.

Accelerated greatly in their development as a consequence of the Fukushima accident, the current operational parameters of these platforms are detailed in Appendix A, with a number of such systems pictured in Figure 2.5. The first instances of radiological monitoring using these platforms (formerly used by hobbyists) were in the monitoring of legacy US nuclear facilities during the 1990's [90, 91]. Further advancements and development of these unmanned platforms were performed by Okuyama et al, (2014) [80] and Towler et al., (2012) [92], with the airframe employed by Okuyama and colleagues used formerly in agricultural crop-dusting [93].

The more common helicopter-style mapping platforms consist of a remotely operated airframe weighing approximately 70 kg, onto their underside a range of detector options are mounted [80, 90]. In contrast to their manned survey equivalents, these platforms are exempt for standard aviation laws and can operate autonomously at reduced altitudes (typically 50 m - 100 m) as long as they remain within the operators line-of-sight [76]. These systems also operate at both lower flight velocities (8 - 15 ms^{-1}) and tighter grid-spacings (less variance between transects). Whilst being able to attain greater spatial resolution, a number of a trade-offs are made, including the area it is possible to cover during one survey flight (3 km - 5 km of total flight distance), the size of the detector (<1 L) and also the requirement for operator training ahead of their operation [94].

The use of these systems in the wake of the Fukushima accident was pioneered by Sanada and co-authors [67, 95]. The autonomous unmanned helicopter (AUH) developed by the JAEA group attained an on-ground spatial resolution of 25 m^2 - and hence a more detailed visualisation of the contamination distribution when deployed to the region in the immediate vicinity of the plant. A comparison of the results obtained with this AUH platform and initial manned surveys are shown in Figures 2.6 (a) - (c). Whereas the monitoring results from manned aircraft shown in Figure 2.6 (a) (with 1.8 km grid spacing and average altitude of 300 m) depicts a single NW-trending emission plume, at lower altitudes and tighter grid-spacings, both of 80 m (Figure 2.6 (b)), the height corrected dose-rate map highlights multiple plumes out from the FDNPP site (Figure 2.6 (c)).

Figure 2.5: Images of various unmanned helicopter and fixed-wing platforms employed for radiation mapping. *From (clockwise from top left); Kurvinen et al., (2015), Towler et al., (2012), Pollanen et al., (2009), and Okuyama et al., (2014) [80, 92, 96, 97].*
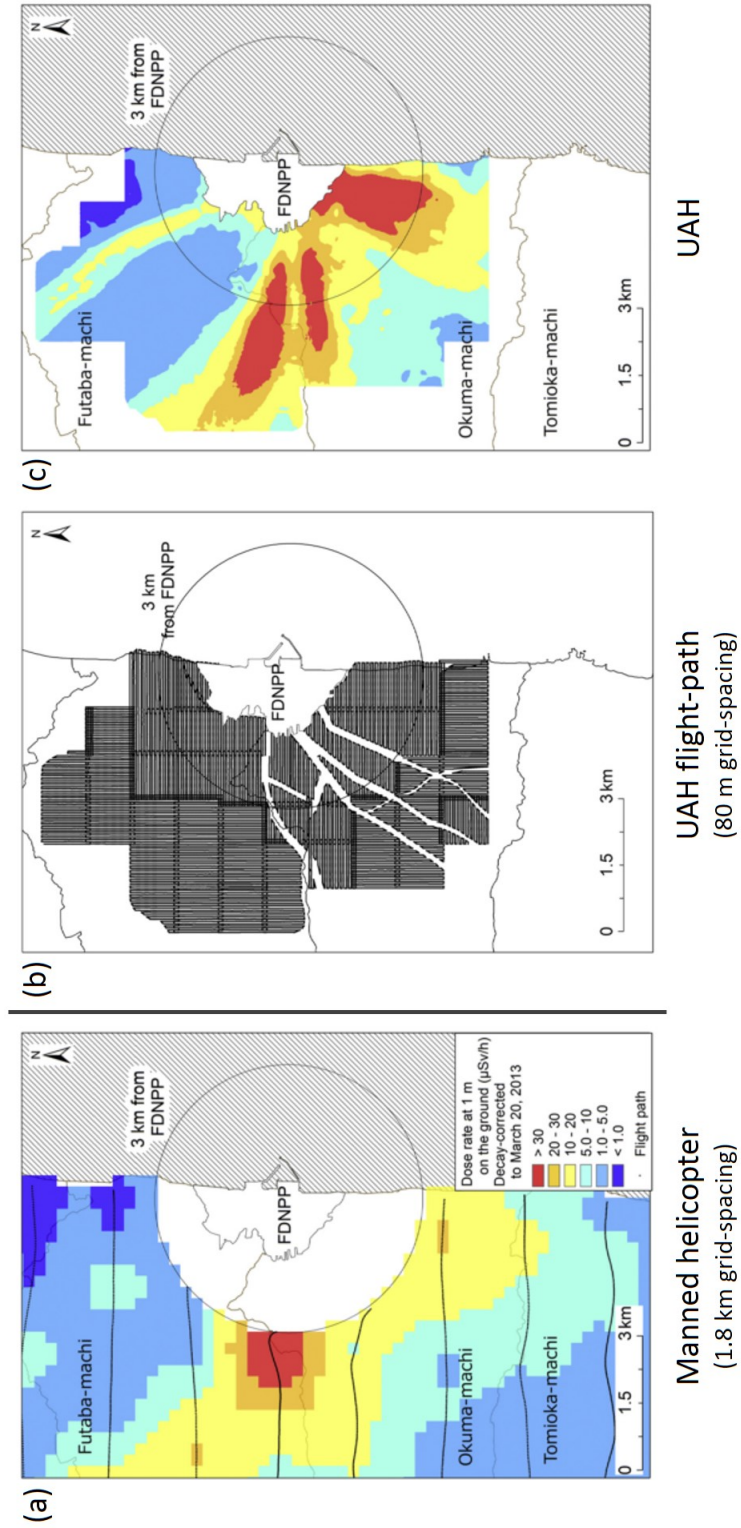
Figure 2.6: Comparison of radiological monitoring results performed using; (a) a manned helicopter, and the UAH through tighter (80 m) grid-line separation (b), to attain, (c) a greater spatial resolution dose-rate map. *From [67].*

2.1.1.3 Unmanned Aerial Vehicle (UAV)

A low-altitude unmanned aerial vehicle (UAV) represents an additional survey tool alongside the previously discussed manned survey platforms (Section 2.1.1.1) and unmanned helicopter/fixed-wing systems (Section 2.1.1.2), capable of achieving spatial resolutions comparable to traditional ground-based surveys (Section 2.1.2). These platforms consist of a lightweight airframe with multiple counter-rotating propellers onto which the radiation detection payload is mounted. The entire platform is controlled autonomously using pre-programmed geo-referenced waypoints and altitudes. One of the first radiation mapping systems was developed by Boudergui et al., (2011) [98], on the airframe and flight control systems devised by Guenard et al., (2006) [99]. Like the unmanned helicopter/fixed-wing platforms, it was not until the accident at Fukushima, however, that advancements in this survey method rapidly accelerated as a consequence of the increased requirements for such a system.

The first of the "post-Fukushima" systems was developed at the University of Bristol by MacFarlane et al., (2014) [100]. This platform used a commercially-available Mikrokopter™ of a "hex" configuration - consisting of six counter-rotating propellers to transport the radiation detection payload. A similar design was later produced by Aleotti et al., (2015) [101]. Both systems used a lightweight CdZnTe (CZT) miniaturised γ-ray spectrometer carried at survey heights of less than 15 m and variable flight velocities (less than 5 ms^{-1}). Typical parameters for UAV systems are presented in the comparison shown in Appendix A.

While capable of maintaining lower altitudes as well as conducting surveys at lower flight velocities - therefore achieving a much greater spatial-resolution as a result (typically sub-meter), these systems present with several limitations. The greatest of these is the total area possible to survey at this resolution - as current battery technology severely restricts the total area that may be covered on a single charge. In addition, whereas higher-altitude airborne surveys were able to navigate around obstacles (e.g. trees and buildings), such features present a significant hindrance to these smaller, lower-altitude systems.

Whereas limitations exist owing to the low spatial extent that is it possible to analyse using these UAV platforms, they do benefit, however, from a manoeuvrability and low operational altitude not possible with other aforementioned systems. Because of this, these systems have found extensive application across the fallout-affected Fukushima Prefecture for quantifying both remediation effectiveness and contaminant mobility [102, 103].

2.1.2 Ground-based

Without the need to devise an aerial mechanism through which to transport the detector setup, ground-based methods represent a simplistic means of capturing radiometric data. Shortly after

Figure 2.7: Images of typical low-altitude multi-rotor UAV systems employed for high spatial resolution radiation mapping. *From (top to bottom) MacFarlane et al., (2014), Aleotti et al., (2015), and FlyCamUAV Ltd (2017) [100, 101, 104].*

the FDNPP accident, the volunteer-based Safecast organisation was established, with the goal of crowd-sourcing radiometric data using a large number of portable GM-based GPS-enabled mapping units [105]. These units would be transported by citizens to generate a time-resolved dataset of radiological contamination. Being GM-based, however, spectroscopic data could not be obtained through this device.

Although a basic study using simple hand-held device allowing for spectroscopic analysis of the contamination was carried in a vehicle across Fukushima Prefecture by Imanaka et al., (2012) [108], it was the work of Ikuta et al., (2012) [106], and Tsuda et al., (2013) [107], that implemented and developed specific vehicle-based units. The former (larger) platform employed a cryogenically-cooled High-Purity Germanium (HPGe) detector, while the latter briefcase-sized
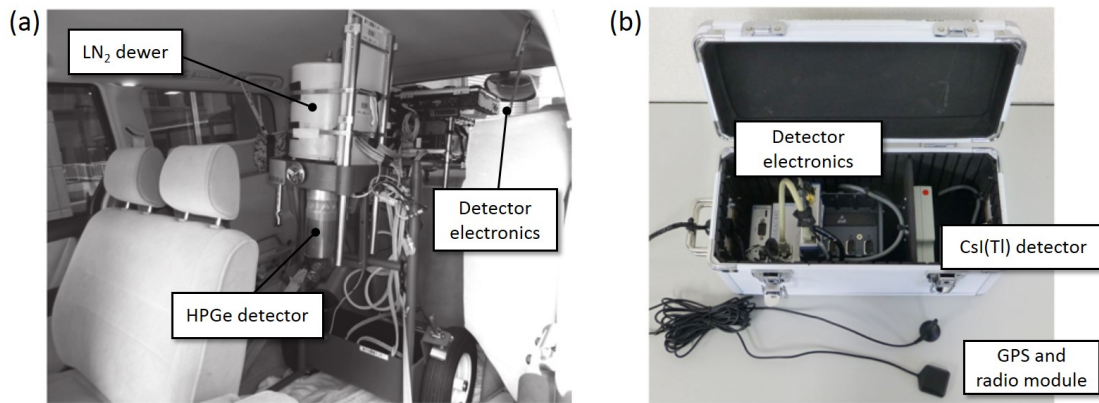
Figure 2.8: Vehicular-based radiation mapping platforms deployed across Fukushima Prefecture; (a) Car-borne cryogenically-cooled HPGe semiconductor-based detection system and, (b) CsI(Tl) detector based KURAMA-II survey platform. *From [106, 107].*

unit (termed KURAMA and later KURAMA-II), consisted of a small single-crystal CsI(Tl) detector that did not require active low-temperature cooling [109]. In both instances, the detector was connected to a GPS unit that allowed for its position to be paired with the corresponding radiation levels.

While simplistic in their nature, the limitations of vehicular-based systems are numerous; (i) their inability to deviate away from the road network significantly limits their overall coverage, (ii) the potentially complex shielding effects that differing vehicles and human occupants introduce on the results [82, 106], (iii) the varying impacts of topography (hills, trees and valleys) that surround the vehicle during such surveys [110] and, (iv) the potential contamination risk to the vehicle owing to material re-suspension and its entrapment [111, 112].

Conversely, using humans to perform on-ground manual radiation monitoring does allow for areas inaccessible to vehicles to otherwise be examined. However, this approach presents its own set of limitations - with some locations still being inaccessible due to challenging terrain and topography. As well as being slower than vehicular-based monitoring, the impacts of radiation attenuation by the human operator (as for vehicles) needs to be considered, quantified and corrected for [113, 114], in addition to dose considerations for the operator. As for low-altitude unmanned airborne surveys, the volume (and therefore the sensitivity) of the detector used in manned surveys is small in comparison to other monitoring methods. Despite these considerations, numerous ground-based surveys have been conducted around Fukushima Prefecture as a result of the March 2011 accident, often coinciding with physical sample collection for laboratory analysis [62, 115, 116].

Radionuclide	Half-life
^{85}Kr	10.76 yr
^{89}Sr	50.57 d
^{90}Sr	28.9 yr
^{129m}Te	33.06 d
^{132}Te	3.20 d
^{131}I	8.02 d
^{133}I	20.8 h
^{133}Xe	5.25 d
^{135}Xe	9.14 h
^{134}Cs	2.06 yr
^{136}Cs	13.16 d
^{137}Cs	30.07 yr

Table 2.1: Principal "short-lived" radionuclides of greatest environmental concern released as a result of a LOCI alongside their associated half-lives. *From [52, 127].*

2.1.3 Oceanic

As it bordered the Pacific Ocean, extensive radiation monitoring campaigns were performed at sea. To examine the concentration of radionuclide species within the seawater, as well as its uptake by aquatic organisms, various water sampling campaigns were undertaken [117, 118]. Due to the focus of this thesis being in the study of terrestrial radionuclides, the analysis and results of aquatic sampling are not discussed (but it is not to say that the topic is not important).

2.2 Contamination

2.2.1 Contaminant species

The principal radionuclides released from the reactors fuel rods at elevated temperatures following a LOCI scenario are the various noble gases and volatile fission product species (Table 2.1) [119].

Thankfully, the incidents to date from which such species have been released are rare, with those emitted by the Chernobyl accident having been extensively examined [120, 121]. However, to yield more/well-controlled data through which to understand releases from other severe and high-ranking INES level events - extensive empirical studies have been performed to simulate radioactive releases from nuclear facilities, including the French-led "VERCORS" programme [122–125], that followed from the successful "PHEBUS" fission product project [126]. Both studies utilised specially-constructed high-activity "hot cells" to subject previously irradiated UO_2 fuel assemblies to conditions representative of LOCI conditions.

Krypton. The majority of Kr isotopes are very short-lived (<1 day) - with the exception of ^{85}Kr, with a half-life of 10.76 years [52]. Due to Kr being chemically inert with a low fission product yield (0.286%) [128], and low energy γ-emission (being primarily a β-emitter), it presents a very limited contribution to external dose, becoming insignificant upon its rapid atmospheric dilution.

Strontium. In comparison to Kr, radio-Sr (^{89}Sr and ^{90}Sr) is produced in considerably greater fission product yields (4.9% and 5.9% respectively) [128]. Like Kr, however, Sr isotopes are both strong β-emitters and are undetectable via γ-ray spectroscopy. With ^{89}Sr having a short half-life of only 50 days [52], ^{90}Sr is the species of most environmental concern, is readily incorporated into the bone structure and hence representing a "risk over longer periods" after an accident if accumulated within the food chain [129].

Tellurium. The main isotope of Te, ^{132}Te, is produced with abundances just below ^{89}Sr, at 4.28% [128]. With a short half-life of 3.204 days, the isotope rapidly decays though β-emission into the unstable nucleus of ^{132}I, which itself decays within hours into the stable noble gas ^{132}Xe - with the ejection of four γ-rays.

Iodine. The two principal fission product isotopes of I are ^{131}I and ^{133}I, with yields of 2.88% and 6.59%, and half-lives of 8.02 days and 20.8 hours respectively [52, 128]. Both species decay via β-emission (with γ-ray emission as an intermediary step). As a species, I presents a health risk due to its uptake by the thyroid gland and resulting internal radiation exposure. Detectable via γ-ray spectroscopy, its short half-life results in its rapid decay and high activity - but associated rapid decline from the environment. Following a radioiodine release, it is currently best practice to disseminate non-radioactive I pills to affected populations to prevent the accumulation of radioiodine in the thyroid gland [75].

Xenon. Xe occurs with fission product yields close to 12% [128], and is therefore produced in the greatest quantities of all elements during reactor operation. As a noble gas, like Kr, Xe is also chemically inert and similarly decays principally through strong β-emission (alongside a low-energy γ-ray). Combined with a half-life of under a week, the radiological hazard posed by Xe, like Kr, is limited.

Cesium. The fission products of ^{134}Cs and ^{137}Cs are each produced with yields of $\approx$6% [128], and combined represent a significant contaminating radionuclide. The other fission product isotopes ^{135}Cs and ^{136}Cs are, however, produced with considerably less abundance. With the main isotopes of Cs decaying through γ-ray emission and each possessing moderate half-lives (Table 2.1), Cs represents a significant contaminant species. This is accentuated by its high solubility and capacity for bodily uptake, where it possesses no biological role [130].

With the noble gases of Kr and Xe not representing a radiological hazard once rapidly dispersed, and with both Sr and Te decaying through β-emission (with only limited γ-ray release), it is I and Cs that together contribute significantly to the ionising radiation hazard in the weeks, months and years after an accident [131]. Resulting from the shorter half-lives of I over Cs isotopes, it is Cs that is of the greatest concern with regards to external radiation dose exposure over periods beyond several weeks following such a release [132]. *(N.B. direct physical contact with β-emitting substances also represents a significant, yet acute, health concern).*

Low-volatility elements. The aforementioned radioisotope species represent the near entirety of the activity resulting from a release event, where elevated temperatures have caused full (or partial) fuel melting. Whilst their extensive release can be attributed predominantly to their high-volatility (low boiling-point), such an abundance can also be attributed to their fission product yield. Although other (less volatile) elements are produced at abundances equal to the highly-volatile species (e.g. Zr, Ru and Pd) [125, 133], their low volatility is considered to significantly limit the total amount of such elements released during a LOCI [125].

Also termed **refractory elements**, those species not fully-released at fuel-melt temperatures ($\approx$2400°C) are termed **semi-volatile**, **low-volatile** or **non-volatile** elements after the VERCORS classification study [125]. Whilst volatile species are released almost entirely from the fuel, these elements occur with release fractions ranging from 50% - 100%, 3% - 10% and «1% respectively (although variations in the exact reactor conditions at the time strongly influence these values). Elements classified as semi-volatile include Mo, Rh, Ba and Pd; whilst those in the low-volatile group include Ru, Nb, Sr, Y, La, Ce and Eu, with the non-volatile classification comprising Zr, Nd and Pr.

Actinides. Classified also as **refractory elements**, as a result of the VERCORS study, actinides can be subdivided into either of two groups based on their behaviour following fuel-melting associated with a LOCI. Owing to their low degrees of volatility (whereby high temperatures are required for their release) - both U and Np are emitted at fractions of up to 10%, with Pu in contrast, released at fractions of significantly less than 1%. Unlike the aforementioned fission products elements, actinides such as these decay initially through the emission of α-particles before subsequent γ-ray release from decay chain progeny.

Reactor materials. Work by Zinkle and Was (2013) [35], detailed the extensive suite of highly-specialised materials used in a BWR - including various forms of stainless steel and other bulk materials (e.g. concrete, thermal insulation and radiation shielding), to metals with specific in-reactor applications (e.g. B, Cd, Zr and Hf). With the high temperatures and energy densities associated with a LOCI, these materials are also readily-released during such an explosive event. This fragmentation and emission may also extend to the fuel elements, cladding material,

control rods and the reactors vast piping/heat-exchanger network [24, 127]. The extent of the release of such materials from the FDNPP reactors/reactor-building explosions is currently poorly constrained - with only minimal insight existing as to both the location and mass of residual core material in each of the RPVs (qualitatively ascribed via muon-scattering experiments of each reactor building) [54–56].

2.2.2 Fukushima release species

Due to the nature of the accident - with releases from numerous sources over a week-long period, estimates as to the total/individual reactor unit activity and species released vary considerably. Approximations by Steinhauser et al., (2014) [119], placed the total release at ≈520 PBq, or one-tenth of that from Chernobyl [134]. Estimates for the total release of the short-lived ^{131}I were first published by Chino et al., (2011) [135], at 150 PBq (or 8% of the Chernobyl value [136]), with estimates of ^{134}Cs and ^{137}Cs at 12 PBq each by both Steinhauser et al., (2014) [119], and Chino et al., (2011) [135] - (25% and 7% of Chernobyl values respectively [136]).

While the release from Fukushima can be characterised by a greater emission of ^{133}Xe [137], the Chernobyl accident, on the other hand, can be described by a more significant contribution of all other species [136] - as summarised in the work by Steinhauser et al., (2014) [119]. In the comparison of the FDNPP release with other documented radioactive emissions by Friese et al., (2013) [138], the absence of low-volatility species (including Zr, Ru, Nb, Ce and Mo) and actinides (U, Pu, Np and Am) emitted from Fukushima, at the time of writing, was attributed to a core temperature below that required to cause any degree of fuel melting. The differing incident and emission characteristics of Chernobyl and Fukushima have more recently been detailed in the comparison by Imanaka et al., (2015) [139]. Whereby the Chernobyl accident was the result of a power-surge in the graphite-moderated RBMK-1000 reactor (that instantly destroyed both the reactor and building), the FDNPP accident (as previously described in Section 1.3), resulted from a number of LOCI - leading to fuel melting, and a series of hydrogen explosions/PCV containment breaches/emergency venting scenarios.

Alongside the work of Friese et al., (2013) [138], other studies (employing mass spectrometry methods) have concluded that no U (via ^{235}U/^{238}U atomic ratios) was released from the FDNPP [140, 141] - or that any U composition material existed within the environment below detection limits of current Thermal Ionisation Mass Spectrometry (TIMS) instrumentation. In other studies, however, the existence of anthropogenic, Fukushima-derived U and/or Pu has been observed at sites across Fukushima Prefecture [142–144], identified using Inductively Coupled Plasma-Mass Spectrometry (ICP-MS) and Accelerator Mass Spectrometry (AMS). Owing to a combination of their inability to be detected using γ-ray spectroscopy, their long half-lives (low activity) and complicated/lengthy analytical procedures to be separated and subsequently quantified, these

actinide species are termed by Steinhauser et al., (2014) [145], as the "frequently forgotten" radionuclides. Whilst not representing as severe a radiological hazard as other fission products, such actinide elements represent an alternate and substantial hazard as a consequence of their substantially greater chemotoxicity [146, 147].

2.2.3 Distribution

As formerly discussed in Section 1.3.7, and illustrated in Figures 2.4 and 2.6, the main contamination plume extended to the north-west from the FDNPP for approximately 60 km, terminating shortly before the population centre of Fukushima City. The airborne radiological survey depicting the total height-corrected $^{134+137}$Cs ground deposition from April 2011 is shown in Figure 2.9. At this time, a month after the accident, nearly all of the ^{131}I contribution would have decayed into the stable ^{131}Xe. Not readily evident within Figure 2.9 are the smaller plumes of differing trend identified in the low-altitude UAH studies of Sanada et al., (2015) [67], shown in Figure 2.6.

Unlike the Chernobyl releases which dispersed radioactive fallout across large portions of mainland Europe [148, 149], following the Fukushima accident, estimates placed 80% of the total radiation release as having been deposited into the neighbouring Pacific Ocean [39, 150]. Also contrary to the 1986 accident is the topography that surrounds the Japanese site. Unlike the flat and heavily forested Pripyat region, at a distance of 5 km from the FDNPP lies a band of north/south trending mountains - which from the airborne surveys, were seen to significantly influence the distribution of contamination by capturing a large proportion of the airborne species [62]. This extensive topography is synonymous of the entirety of Fukushima Prefecture [151, 152].

2.2.4 Evacuation zones

Owing to the lack of static monitoring points to aid in the establishment of evacuation zones, a number of arbitrary radii of increasing size were introduced from the 12th March 2011 by the then Japanese Prime Minister Mr Naoto Kan (as detailed in Section 1.3). Following the results of early monitoring studies, this zone was subsequently redefined and enlarged to cover the severely contaminated Iitate Village area on the main north-westerly trending plume [154]. This revision of areas to which evacuation orders were issued came prior to the instigation of *The Act on Special Measures Concerning the Handling of Radioactive Pollution*, introduced by the Japanese national government [155]. Alongside a number of other topics concerning the remediation and associated handling of radioactively contaminated materials, this policy detailed the provision for radiological monitoring and establishment of specific zones surrounding the FDNPP.

Arising from this act, two land categories were defined based on the radiation level determined principally using aerial methods, combined with ground and vehicular-based surveys. The main zone was termed the *Special Decontamination Area*, and included the originally evacuated 20 km
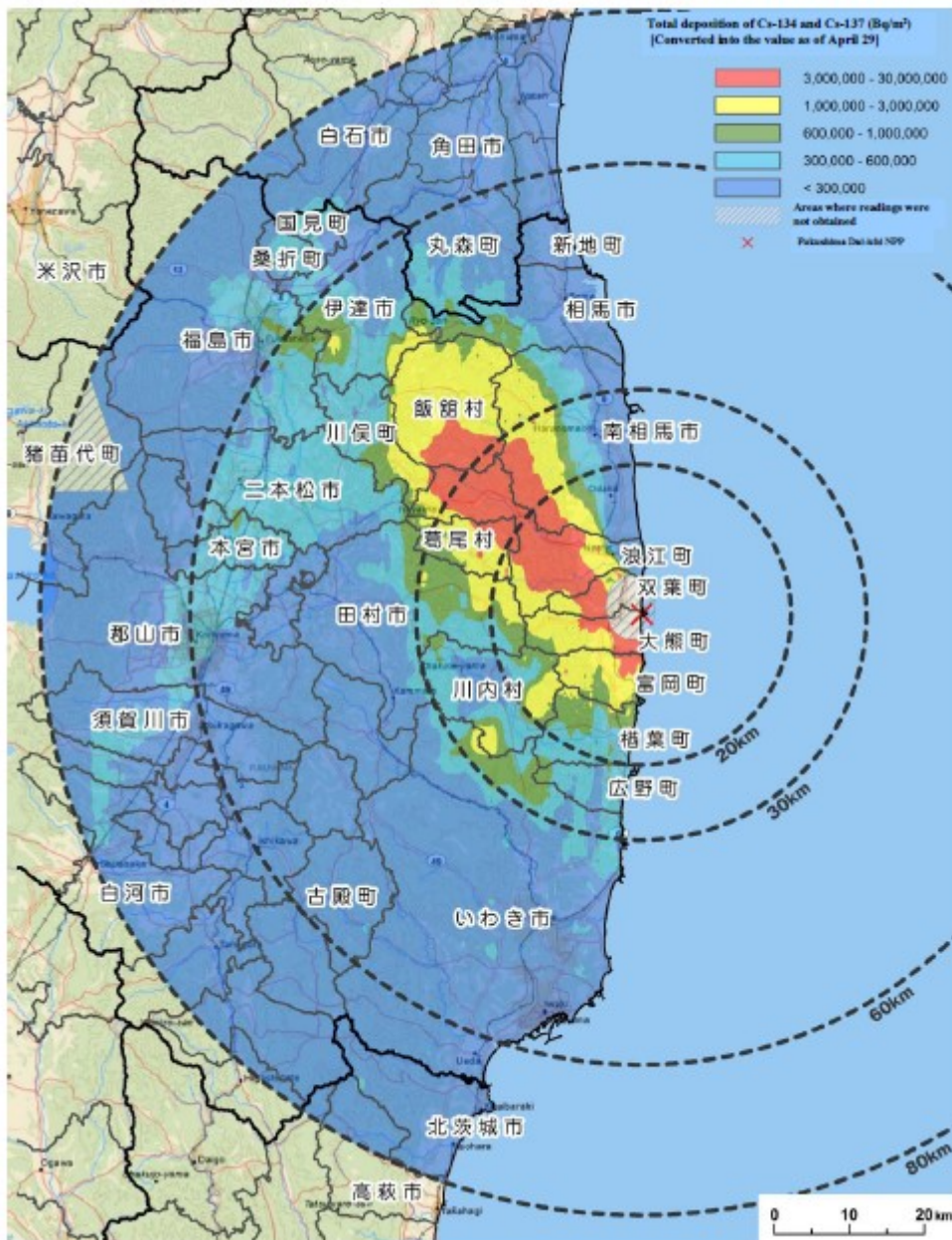
Figure 2.9: Total radiocesium ($^{134\,+\,137}$Cs) activity ground deposition within an 80 km radius of the FDNPP. The results were obtained during the first airborne (manned-aircraft) surveys of mid-April 2011. The primary (60 km) north-westerly trending contaminant plume (later attributed to reactor Unit 2 [69, 153]) is observed, as is a smaller (30 km) south-westerly area of radiological contamination. *From [85].*

radius *(Restricted Zone)* around the plant, as well as the additional 30 km north-westerly region including Iitate Village (hence termed the *Deliberate Evacuation Zone)*. Within this entirely evacuated area, national government-lead remediation activities would be undertaken (Section 2.4) [154, 155]. This *Deliberate Evacuation Zone* consisted of land where a cumulative dose would (at the time) exceed 20 mSv yr^{-1} [154, 155].

The second region defined under the *The Act on Special Measures Concerning the Handling of Radioactive Pollution* were *Intensive Contamination Survey Areas*. Covering large areas of western and central Japan where no evacuation orders were issued, this land presented an annual dose of less than 20 mSv. Any decontamination works in this area would be conducted under the direction of local municipality governance.

As shown by the assignment of these zones, it was determined by the Government of Japan that an acceptable annual radiation dose was 20 mSv yr^{-1} - with areas showing levels greater than this being evacuated and the subject of decontamination efforts (Section 2.4). This *Special Decontamination Area* is sub-divided into three areas; *Area 1*: 1 mSv yr^{-1} - 20 mSv yr^{-1}, *Area 2*: 20 mSv yr^{-1} - 50 mSv yr^{-1} and *Area 3*: >50 mSv yr^{-1}. The dose-rates in *Area 1* are now below those deemed safe by the Japanese Government and are shortly set to have evacuation orders revoked. For *Area 3*, it has been deemed that people will have "difficultly returning for some time" [156].

Due to the accident, a total of 146,520 people were evacuated from their homes. Published in a report by the Japanese bicameral legislature, *The National Diet* (or *Kokkai*), concluded that to-date, no deaths could be attributed due to radiation exposure as a result of the FDNPP accident. However, a total of 60 deaths had been deemed to have been caused by the evacuation of citizens out of the affected areas - brought about by increased stress and anxiety [30]. Such a figure is greater than might otherwise have resulted, owing to the age of those evacuated - with the majority being senior citizens, of an average age of 72 [157]. Through the mathematical assessment of the event, recent work by Waddington et al., (2017) [158], concluded that the greatest impact to human life was not the radiation exposure to populations - but the trauma caused by the evacuation itself.

By October 2014, following extensive monitoring and only limited remediation, both northern and southern portions of the original 20 km radius evacuation zone that surrounded the plant (introduced on the 12th March 2011) had been revoked (following earlier rescinding of orders in Naraha Town to the south). This removal permitted people who once resided less than 10 km north and south of the FDNPP to return. Despite the lifting of evacuation orders, however, very few of those once-displaced have returned [30]. This slow return of those rehoused following the incident is likely the result of both the age of the evacuees, but also the considerable mistrust that still exists towards the Japanese Government over the handling of the incident [159].
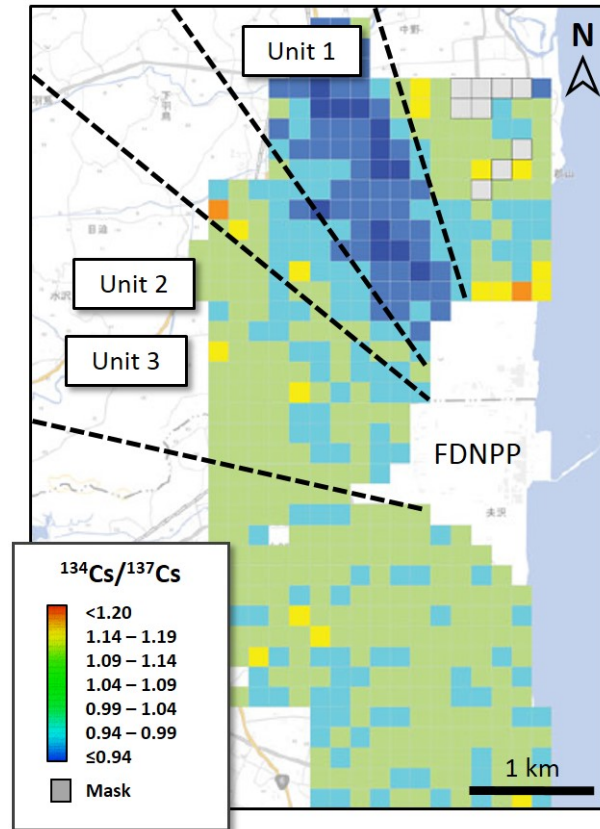
Figure 2.10: Distribution map of $^{134+137}$Cs activity ratio surrounding the FDNPP, determined using an AUH. *Modified from [69]*.

2.2.5 Source attribution

Resulting from radiation mapping and laboratory analysis (of physical samples), several studies have invoked specific reactor Unit sources to the different plumes observed in the radiation maps shown in Figures 2.6 and 2.9. Such attributions are based on comparisons to the modelling-derived ^{134}Cs/^{137}Cs activity ratio inventory results for each reactor Unit and associated FSP presented by Nishihara et al., (2012) [50] - shown in Table 1.3.

Environmental sampling from across Fukushima Prefecture and the subsequent γ-ray spectroscopy analysis by Yamamoto et al., (2014) [160], detailed slight, but notable variations in the measured ^{134}Cs/^{137}Cs activity ratios. After applying a decay-correction (to the time of the accident), the main north-west trending plume was shown to exhibit ^{134}Cs/^{137}Cs activity ratios >1.00 (average 1.06), with a smaller northerly-trending plume displaying contrasting ^{134}Cs/^{137}Cs activity ratios of <1.0 (average 0.94). By applying the inventory estimates of Nishihara et al., (2012) [50], these two plumes; north-westerly and northerly, were ascribed to reactor Units 2 ± 3 and 1 respectively.

The use of an AUH radiation mapping system by Nishizawa et al., (2015) [69], produced similar results. A short, northerly-trending plume was observed to display a ^{134}Cs/^{137}Cs activity ratio of less than 1.00 (average 0.95), whilst the remainder of the 2 km survey radius out from the FDNPP site displayed a ^{134}Cs/^{137}Cs activity ratio $\geq$1.00. Both studies were further compounded by the combination of radiometric sample analysis and an AUH survey by Chino et al., (2016) [153], who also identified a contrasting northerly-trending ^{134}Cs/^{137}Cs ratio plume - similarly invoking its provenance also to Unit 1, following the predicted core inventories from Nishihara et al., (2012) [50]. The radiocesium mapping results of Nishizawa et al., (2015) [69], are shown in Figure 2.10.

A number of additional studies have employed mass spectrometric analysis of physical samples to more accurately quantify the radiocesium distribution via the ^{135}Cs/^{137}Cs atomic (isotopic) ratio across the region. Like the activity ratios, these studies all reported the same contaminant distribution and likely source attribution [43, 161–163].

While the prevailing wind direction at the time of the Unit 2 release (Section 1.3.7) supports this contamination of a large region to the north-west of the facility on the 15th March; owing to the similarity between both the inventory modelled radiocesium activity ratios and the mass spectrometry-derived atomic (isotopic) ratios for both Units 2 and 3 (Table 1.3 and Figure 2.11) - it has not been possible to unequivocally discriminate land contaminated to a component sourced from Unit 3. As a result, the region to the west-north-west of the facility (Figure 2.10) has been ascribed to have resulted from contamination originating from both release events (but primarily from reactor Unit 2).

Stemming from the differences in the cooling histories [7], and the known/estimated time of contamination release from each of the reactor Units - the use of environmental ^{110m}Ag/^{137}Cs activity ratios have also been utilised in an attempt to potentially attribute the primary plume (or regions thereof), to differing release events (Unit 2 from 3) [164]. The application of this activity ratio centres on the higher volatilisation temperature of Ag (2212°C), in contrast to Cs (678°C) [165]. Therefore, earlier core release events (where a high level of decay heat existed) would comprise a greater component of the γ-ray emitting ^{110m}Ag.

As the first release to occur; ^{110m}Ag/^{137}Cs values (decay corrected) of approximately 0.01 were attributed to the (shorter) northern-most contamination plume produced by the Unit 1 hydrogen explosion on the 12th March by Satou (2016) [164], following distribution measurements by Saito et al., (2014) [116] and Mikami et al., (2015) [166]. Through the application of this ratio, however, Satou (2016) [164], invoked that a thin, southerly portion of the main north-west trending plume was the result of contamination derived for Unit 3 - alongside the more extensive release from Unit 2. With both the Unit 2 and 3 release events occurring later on the 15th March 2011 and
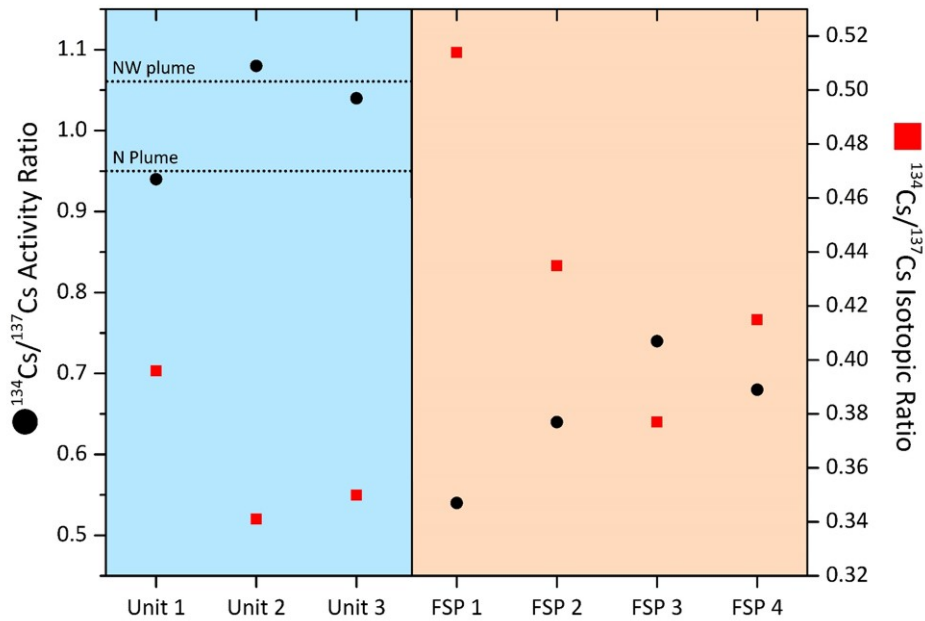
Figure 2.11: Comparison of the calculated ^{134}Cs/^{137}Cs activity (black circles) and isotopic ratios (red squares) for reactor Units 1 - 3 and associated FSPs 1 - 4. *Data obtained from [50]*. The ^{134}Cs/^{137}Cs activity ratios corresponding to both the north and north-west trending plumes are additionally shown. *Values from [69, 153]*.

14th March 2011, ^{110m}Ag/^{137}Cs values were determined to average 0.0060 and 0.0023 for both reactor Units respectively.

Whereas this Ag-based plume sub-division has yet to achieve widespread acceptance, and owing to the radiocesium releases from Units 2 and 3 not allowing for Unit-specific contamination areas to be attributed in contrast to that arising from Unit 1, a source of the material from the FSPs can be excluded based upon a comparison to the estimated radiocesium ratios published in the work of Nishihara et al., (2012) [50]. Consistent with observations made following the accident (Section 1.4.4) [5], and as depicted graphically in the plot of Figure 2.11 - all of the ^{134}Cs/^{137}Cs activity ratios for the older material located in the FSPs fall below those observed across the contaminated area. The wind directions at the time of each release event further support these source attributions [33].

2.3 Particle forensics

The preferential sorption of ionic Cs over other elements (e.g. K, Mg and Na) onto the highly-reactive frayed-edge sites of mica and clay-type minerals (where it is subsequently transported) is well known and understood, having been extensively-studied as a consequence of the Chernobyl accident in 1986 [167, 168]. Similar sorption of radiocesium within the Fukushima environment

has been identified, with the work of Mukai et al., (2014) [169], employing focused ion beam (FIB) systems to quantify specific amounts of such mineral uptake.

Alongside the release of gaseous species from Chernobyl, there also occurred the release of differing forms of radioactive particulate, some of which were found far from the facility [170, 171].

Two types of radioactive particle (ranging in size from 0.5 - 150 μm) were identified - classified as either "Group A" or "Group B" [171–173]. The former consisted of fragments of the fuel elements (UO_2) alongside differing intermediate volatility and other refractory elements; identified via high-resolution α-particle and γ-ray spectroscopy. These particles were observed, however, to be depleted in the more-volatile species such as Cs, I and Ru. Particles within "Group B" on the other hand, were termed "mono" or "bi-elemental" in response to their limited compositional variance (identified through γ-spectroscopy). Being composed almost exclusively of $^{103+106}Ru$ or $^{140}Ba/^{140}La$, this material contained little or more frequently no actinide material and was invoked to represent inclusions formed within the fuel matrix over standard reactor operation.

No strong relationship in the materials form was observed to permit differentiation between the two types of particle, although those within "Group B" typically appeared more rounded and slightly smaller than the marginally larger and more angular material of "Group A" [172, 173]. The particle sizing of "Group A" material was also observed to be consistent with the known crystal sizes in UO_2 fuel - whereby the constituent grains (approximately 10 μm in mean diameter [23]) represent inherent weaknesses within the materials microstructure [23, 174]

In addition to Chernobyl, a number of other release events have occurred to introduce particulate into the environment. Resulting from extensive atmospheric, underground and underwater nuclear weapons testing prior to the Partial Nuclear Test Ban Treaty being enacted in 1963, large quantities of radioactive material were released into the global environment [175–177]. With what is believed to have amounted to over 2,000 tests conducted at locations around the world, their influence has been felt across the planet - with a background Pu fallout signature produced that will be preserved in the near-surface record for tens of thousands of years [178]. This extensive global testing program is estimated to have produced several orders of magnitude more radioactivity than resulted from the Chernobyl accident [179].

Additional anthropogenically-derived species have been introduced into the environment as a result of both the 1966 and 1968 aircraft incidents involving the transportation of nuclear warheads at Palomares (Spain) and Thule (Greenland) respectively [180–182]. Further particulate emissions have also occurred as a result of the widespread use of depleted uranium (DU) within armour-penetrating munitions - starting in the 1991 Gulf War, with their usage continuing in present-day conflicts in the Middle-East [183]. In addition, releases from power generating and

reprocessing facilities, including those at the Sellafield (UK) and Le Hague (France) sites, are well documented [184, 185]. In each of these scenarios, a particle of characteristic form and composition was produced, illustrative of the waste precursor and processing activity [186, 187].

Since the first studies were undertaken to analyse radioactive particulate, the methods available and the resolutions attainable have increased markedly. From basic electron microscopy techniques, autoradiography and alpha-spectroscopy utilised to identify and evaluate the composition of fallout material, current state of the art methods now include high-intensity synchrotron radiation alongside a range of high-precision/sensitivity mass-spectrometric techniques. A review of such advancements and methods are presented in various review works [186, 188, 189].

Like the events that occurred before it, a range of particulate material was emitted into the terrestrial (and oceanic) environment as a result of the FDNPP accident. This material (like that arising from Chernobyl) can additionally be classified into either one of two groups, in this work (and the limited prior studies [164, 190]), differentiated wholly on size - existing as micron-scale *atmospheric particulate* or the considerably larger (>100 µm) *ejecta particulate*. Alongside their size difference, a number of distinctions associated with the form of this particulate can be made. The former particle type is more rounded in appearance, whereas the latter are considerably less well-rounded. Both particle types are, however, different to those produced as a consequence of the 1986 Chernobyl accident [171, 172].

2.3.1 Atmospheric material

The first reported isolation and analysis of these highly-spherical emission particles, colloquially termed "Cs-balls", averaging 2 µm in diameter, (shown in Figure 2.12) was reported by Adachi et al., (2013) [191], on material collected from aerosol filters located 170 km south-west of the FDNPP in Tsukuba. Amongst other constituents (including O, Si, Fe, Na, S, Ca, Zn and Pb) these particles were found to contain a notable radiocesium ($^{134+137}$Cs) content when analysed via γ-ray spectroscopy and subsequently via energy dispersive x-ray spectroscopy (EDS). This work was succeeded by the study of Abe et al., (2014) [192] on the materials internal structure through the application of synchrotron radiation micro-focus x-ray fluorescence (SR-µ-XRF) analysis at the Japanese Spring-8 facility. As well as confirming the existence of Cs, this study also identified U at the cores of a number of these particles - suggesting that the FDNPP "sustained sufficient damage to emit U fuel outside of the reactors PCV".

Yamaguchi et al., (2016) [193], further examined this plant-distal spherical particulate material, using transmission electron microscopy (TEM). During this study (at greater resolutions attainable than in the prior synchrotron studies), an internal variation in the distribution of Cs was identified; with the Cs concentration increasing from the centre towards the outer circumference.

45
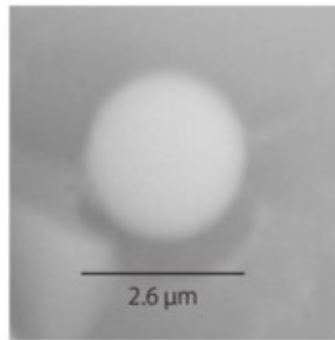
Figure 2.12: Secondary electron image of a Cs-bearing aerosol particle (informally termed "Cs-balls"), recovered in Tsukuba, 170 km south-west of the FDNPP. *From [191].*

The spherical particle was identified as formed of a silicate glass matrix containing additional elements (Al, Cl, K, Fe, Zn, Rb and Sn). A depletion in alkali elements (including Cs) around the very outermost rim of one of the samples raised concerns as to the potential release of radiocesium due to species leaching by meteoric conditions. In work by Kogure et al., (2016) [194], in addition to replicating the study undertaken by Yamaguchi et al., (2016), here on particulate specimens retrieved from fabric samples exposed at the time of the accident, attempts to artificially synthesise the spherical fallout particles within a laboratory setting were attempted. Proving unsuccessful, the authors attributed this to the materials complex formation conditions - namely the extremes of pressure, temperature and gas volume that existed in the reactor environment.

Following the collection of soil (and road-side sediment) before extracting the radioactive particles contained within, work by Satou et al., (2016) [195], found that similar form micron-scale radioactive particles possessed a greater average diameter closer to the plant - with this particulate type measuring up to a maximum of 6.4 µm at 20 km from the plant. It was also observed that whilst a large portion of material existed in the previously reported highly-spherical form, a component also occurred with a slightly more angular appearance. As well as the characteristic Cs contribution detected via EDS, the major component of this material was similarly Si-based. These results were corroborated by the later work of Higaki et al., (2017) [196].

A study by Furuki et al., (2017) [197], employing TEM on material obtained closer-still to the plant (4 km) further confirmed Si to be the dominant component of this material, occurring alongside strong compositional heterogeneity shown by the other elements. However, despite being similarly isolated from the near-identical source material as that of Satou et al., (2016), the particles within this study were found to be marginally smaller (ranging from 2.0 to 3.4 µm) - invoked to represent a different phase in the large-scale release event.
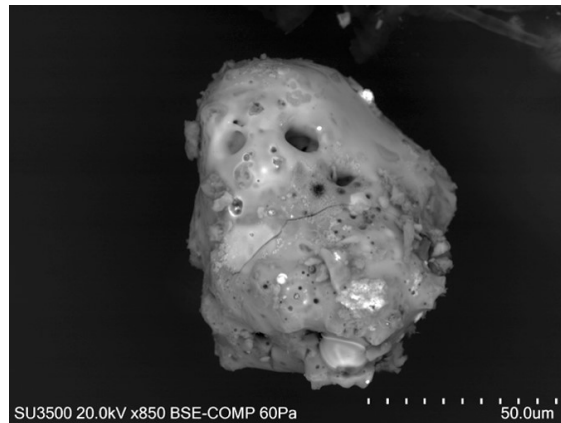
Figure 2.13: Secondary electron image of a typical *ejecta particle*. *From [164].*

Termed "Type A" by Satou (2016) [164], the γ-ray spectroscopy of this individual micron-scale *atmospheric particulate* revealed its $^{134}Cs/^{137}Cs$ activity was analogous to that estimated for reactor Unit 2 in the core inventory modelling work of Nishihara et al., (2012) [50]. This provenancing of such fine-scale particulate is again supported via the prevailing (onshore) meteoric conditions that existed at the time (Section 1.3.7).

2.3.2 Ejecta material

A contrasting suite of particles has also been identified - termed "Type B" by Satou (2016) [164]. Whereas the *atmospheric material* possesses dimensions of <10 μm, this *ejecta material* is an order of magnitude larger in its maximum dimension - isolated from material collected near to the northern boundary of the plant, 2 km from the site of the six reactors. An electron microscope image of a typical isolated *ejecta particle* is shown in Figure 2.13. Arising from the individual particulates $^{134}Cs/^{137}Cs$ activity ratio aligning with that of reactor Unit 1 (as determined by the inventory modelling of Nishihara et al., (2012) [50]), this sub-mm material has been attributed to have been sourced from the FDNPP reactor Unit 1 [164], following the explosive events that occurred on the 12th March 2011.

Whereas this larger material has also received some analysis to date, it has been much less extensive than the *atmospheric material*, owing to its smaller spatial extent - being dwarfed by the main north-westerly plume produced from Unit 2 (and potentially a small component of Unit 3) (Figures 2.9 and 2.10). After isolating the material and performing initial γ-ray spectroscopy, Satou (2016) [164], conducted SEM imaging and EDS compositional analysis of the particulate. Analogous to the *atmospheric material*, this material was also primarily Si in composition - occurring alongside additional elements including; Na, Mg, Al, Cl, K, Ca, Ba and Zn. In contrast to the micron-scale particulate, however, no characteristic Cs emission peak was identified, nor the significant contribution of Fe, itself a major contributor within the smaller particulate.

Synchrotron radiation analysis, similar to that performed on the *atmospheric material* by Abe et al., (2014) [192], has also been performed on a small sub-region of this larger fallout material, employing SR-μ-XRF to attain a two-dimensional map the internal distribution of the constituent elements, not possible with EDS. Within this work by Ono et al., (2017) [190], Cs was again observed to occur - distributed heterogeneously throughout the sample volume. High concentrations of Pb, Zr, Sr, Cd, Sb and Ag (also heterogeneously dispersed throughout the sample), not formerly identified via the earlier EDS analysis, were also encountered. U was also located, dispersed throughout the sample, although at low concentrations as small, isolated regions.

This absence of a detectable Cs signal via EDS analysis of these larger particles can be ascribed to two factors. One of which is the limited sampling depth (interaction volume) that the electron beam has with a material - generating characteristic x-ray emissions from only ≈2 μm depth [66]). Hence, if Cs were to occur at depths within the sample greater than this, it would simply not be detected. This could occur alongside the second factor, being the techniques detection sensitivity - with a limit of detection (LoD) of 0.01 wt%. This value is less than synchrotron-based x-ray or secondary ion mass spectrometry (SIMS) techniques, whereby parts per million (ppm) concentrations of an element can be determined [198]. A thorough description of EDS and other experimental methods is contained within Chapter 5.

The rationalisation provided by Satou et al., (2016) [164], to account for the detection of Cs within the smaller *atmospheric material* whilst not within the larger *ejecta material* by EDS, results from the low concentration of the γ-emitting radioactive species that the different particle-types contain. Despite containing up to two orders of magnitude more ^{137}Cs than the smaller, spherical, particles, the larger and more angular "Type B" particles are on average 5 orders of magnitude greater in volume - therefore representing a considerable "species dilution", below the EDS LoD.

A summary comparison of the physical and compositional differences between the *atmospheric* (Unit 2) and *ejecta material* (Unit 1) is presented in Tables 2.2 and 2.3 respectively. Whilst a radiation release from Unit 3 is known to have occurred [2, 7], alongside a contamination footprint for the reactor having been invoked to exist to the south of the major Unit 2 plume [164] (Section 2.2.5), no particulate from the 15th March release of the MOX-burning reactor Unit 3 has yet been identified/isolated.

As has been described, both the form and composition of the two particle types (*atmospheric* and *ejecta*) are significantly different, with each possessing discernible and unique characteristics. Whilst a notable volume of work has been undertaken on this material to derive its characteristics

(almost exclusively by Japanese research groups), there is still a great amount of research effort required to elucidate; (i) the mechanism(s) behind its release, (ii) the subsequent occurrence of this material in the environment, and (iii) the environmental legacy of this particulate material. It is therefore the aim of this thesis to advance the current understanding of the multiple (and intricate) release events that resulted in the widespread dispersion of radiological particulate contamination through the application of advanced materials analysis methods.

	Unit	Diameter (µm)	Average volume (cm³)	Activity (Bq / particle)	^{134}Cs/^{137}Cs Activity	Release date
Atmospheric material	2	<10	10^{-11}	$10^0 - 10^2$	>1.0 (1.04)	15.03.2011
Ejecta material	1	>100	10^{-6}	$10^1 - 10^4$	<1.0 (0.93)	12.03.2011

Table 2.2: Comparison of physical characteristics of *atmospheric* and *ejecta* particulate material. *Data obtained from [164].*

	Cr	Mn	Fe	Ni	Zn	Rb	Sr	Zr	Nb	Mo	Pd	Ag	Cd	In	Sn	Sb	Te	Cs	Ba	Pb	U
Atmospheric material	O	O	O	X	O	O	X	O	X	O	X	O	X	O	O	O	O	O	O	O	O
Ejecta material	O	O	O	O	O	O	O	O	O	O	O	O	O	O	O	O	O	O	O	O	O

Table 2.3: Comparison of elemental constituents of both *atmospheric* and *ejecta* particulate material (O = observed, X = not observed). *Data obtained from [164, 190]*

2.4 Decontamination

As formerly discussed in Section 2.2.4, two distinct regions were combined shortly after the incident, encompassing both the 20 km radius surrounding the plant (*Restricted Area*) as well as the area extending north-west impacted by the contamination plume (*Deliberate Evacuation Area*) (Figure 2.14 (a)). Under *The Act on Special Measures Concerning the Handling of Radioactive Pollution* [155], these together formed the *Special Decontamination Area*. This area is characterised by locations whereby a cumulative annual dose would likely exceed 20 mSv. This resulted in an area of approximately 1,170 km^2, and affected 85,000 people from 11 municipalities [199].

The other *Intensive Contamination Survey Areas* (Figure 2.14 (b)) formed a larger region away from the plant, where radiation levels ranged from 1 mSv yr^{-1} - 20 mSv yr^{-1}; below those set for both evacuation and any government-led remediation. As a result, any decontamination activities deemed necessary in this area fell upon individual municipalities to fund, manage and perform.

The *Special Decontamination Areas*, on the other hand, are the subject of government-lead actions. The remedial work undertaken within this area is detailed within *The Japanese Ministry of the Environment - Decontamination Guidelines* [60], published shortly after the incident, in response to the *Act on Special Measures Concerning the Handling of Radioactive Pollution* and the Japanese Nuclear Regulators (NRA) *Comprehensive Monitoring Plan*, [63, 155].

During the remedial work, all hard surfaces such as roads and buildings were to be scrubbed/pressure-washed, organic material (such as trees, bushes and plants) would be removed or cut back and combined with other stripped surface materials (soil, earth and grass) and sent for disposal. This disposal consisted of packaging such wastes into 1 m^3 high-density black plastic waste bags and depositing them into one of the thousands of specially-constructed waste stores located across the Prefecture. From these temporary sites, these bags would eventually be relocated into a long-term storage facility, where they would remain for a period of 30 years [200]. As of March 2018, the construction of neither long-term or interim facilities had begun [200].

A comparison between the Chernobyl and Fukushima accidents was published by Fesenko et al., (2016) [201], which analysed many mechanistic and environmental parameters. Whilst a number of differences exist between the two locations (including the usage of potassium-based fertilisers, agricultural land application and population density), the most notably contrasting factors between Fukushima Prefecture and Pripyat are the extensive topography and associated rates of soil/sediment transport around Fukushima. This is enhanced relative to Pripyat by the sub-tropical and typhoon-type environment of the region (average rainfall $\approx$1,500 mm yr^{-1}) [31].
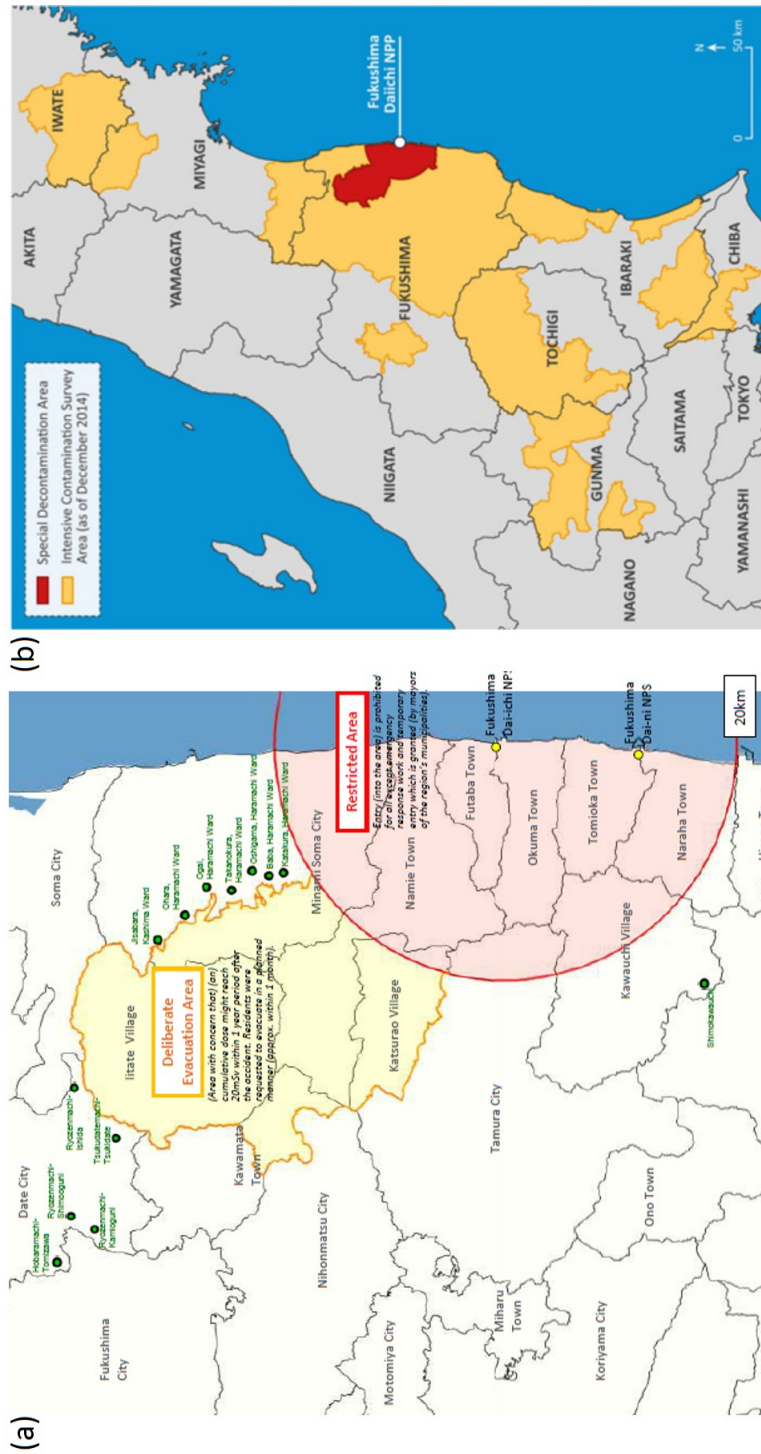
Figure 2.14: Maps detailing; (a) the initial 20 km radius exclusion zone and north-west trending *Deliberate Evacuate Area* (as of November 2011), and (b) the location of the *Special Decontamination Areas* and *Intensive Contamination Survey Areas*. From [57, 154].

Aided by the progressive decay of the γ-ray emitting radiocesium, the progress of the clean-up in the *Special Decontamination Area* has been extensive around the periphery of the main plume. Increasing regions are determined to exist with dose-rates of <20 mSv yr^{-1} and now have been reclassified to fall into *Area 1* - where evacuation orders are ready to be lifted, allowing those displaced to return [156]. In contrast, the heavily contaminated central region of the plume *(Area 3)*, still exhibits dose-rates of >50 mSv yr^{-1} despite the radioactive decay. As a result, the size of this area remains unchanged and decontamination has yet to commence - having been deemed that people will "have difficulties in returning (to their homes) for a long time" [156]. Remediation continues in *Area 2* ("habitation restricted areas", originally 20 mSv yr^{-1} - 50 mSv yr^{-1}), within the *Special Decontamination Area*, following the decay-related reduction in dose rate [202]. The progress of this remediation is shown in Figure 2.15, with activities progressively moving inwards towards the central *Area 3* (shown in grey).

With only *Area 3* and a small region defined as *Area 2* yet to be decontaminated (as of March 2018), only 3% of the entire Fukushima Prefecture will remain under an evacuation order (413 km^2). The cost of this extensive decontamination, not including the final storage of the wastes generated, is estimated to range from ¥2.55 to ¥5.12 trillion (£20 to £40 billion) depending upon the amount of vegetation removed [203]. This assessment by Yasutaka et al. (2016), however, concludes that if complete remediation were to occur - with the removal of all contaminated forest areas, then these costs would be significantly higher - up to ¥16 trillion (£110 billion). This cost difference arises due to the large (90% of the Prefecture) and currently unremediated forested areas, that may require decontamination. The total volume of wastes generated even for the lower cost option is approximated at 30 million m^3 [200]. For context - in the UK, the disposal of 30 million m^3 would be £90 billion, based on a Nuclear Decommissioning Authority (NDA) stated cost of £3,000 per m^3 of low level waste (LLW) [204].
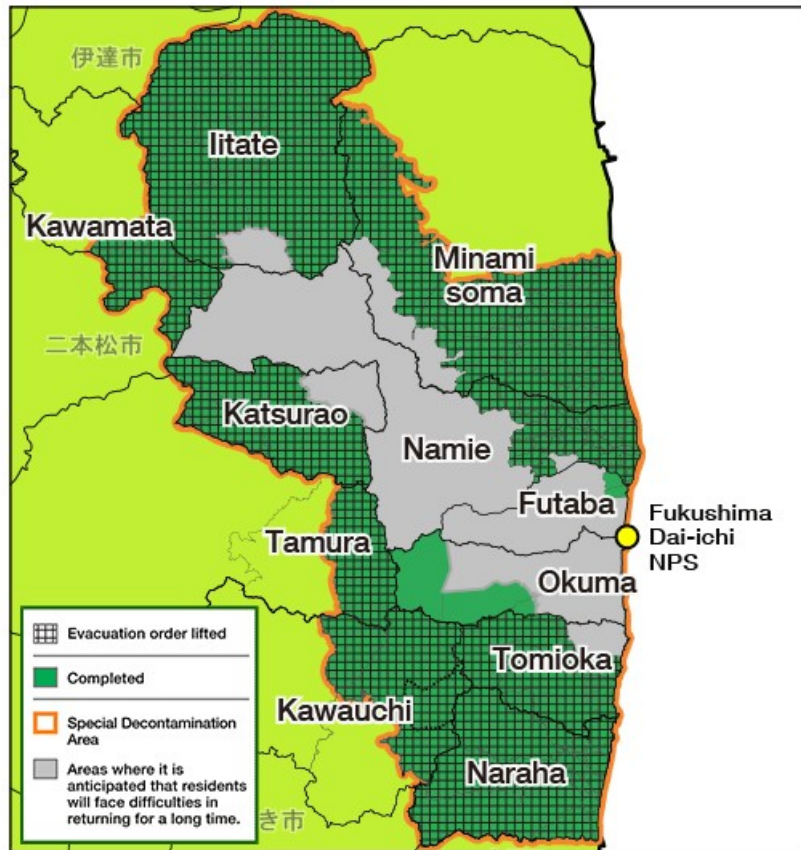
Figure 2.15: Map of the *Special Decontamination Area* (as of April 2017), where evacuation orders have been rescinded, as well as the locations where high levels of radiological contamination still exist. *From [205].*

3

FIELD-BASED METHODS

During the fieldwork component of this study, a number of radiation detection and characterisation methods were utilised. Some of these represented conventional methods employed for routine on-site characterisation, others, however, were developed for, or in response to specific challenges and environments that presented during this work.

Alongside an overview of radiation interactions and the principles governing its detection, details of both the ground-based and low-altitude unmanned aerial vehicle (UAV) characterisation systems are presented. The details of how each platform was calibration are discussed alongside normalisation parameters to derive the correct on-ground air dose-rate.

Methods and results presented in this chapter have been previously published in the peer-reviewed literature in a number of specific works:

P.G. Martin, O.D. Payton, J.S. Fardoulis, D.A. Richards and T.B. Scott. "The use of unmanned aerial systems for the mapping of legacy uranium mines". *Journal of Environmental Radioactivity*, vol. 143, pp. 135-140, May 2015.

P.G. Martin, O.D. Payton, J.S. Fardoulis, D.A. Richards, T.B. Scott and Y. Yamashiki. "Low altitude unmanned aerial vehicle for characterising remediation effectiveness following the FDNPP accident". *Journal of Environmental Radioactivity*, vol. 154, pp. 58-63, January 2016.

P.G. Martin, S. Kwong, N.T. Smith, Y. Yamashiki, O.D. Payton, F.S. Russell-Pavier, J.S. Fardoulis, D.A. Richards and T.B. Scott. "3D unmanned aerial vehicle radiation mapping for assessing

contaminant distribution and mobility". *International Journal of Applied Earth Observation and Geoinformation*, vol. 52, pp. 12-19, October 2016.

P.G. Martin, J. Moore, J.S. Fardoulis, O.D. Payton, and T.B. Scott. "Radiological Assessment on Interest Areas on the Sellafield Nuclear Site via Unmanned Aerial Vehicle". *Remote Sensing*, vol. 8 (11), p. 10, November 2016.

P.G. Martin, O.D. Payton, Y. Yamashiki, D.A. Richards and T.B. Scott. "High-resolution radiation mapping to investigate FDNPP derived contaminant migration". *Journal of Environmental Radioactivity*, vol. 164, pp. 26-35, November 2016.

D. Connor, **P.G. Martin** and T.B. Scott. "Airborne radiation mapping: overview and application of current and future aerial systems". *International Journal of Remote Sensing*, vol. 37 (24), pp. 5953-5987, November 2016.

A.C. Keatley, **P.G. Martin**, K.R. Hallam, O.D. Payton, R. Awbery, F. Carvalho, J.M. Oliveira, L. Silva, M. Malta and T.B. Scott. "Source identification of uranium-containing materials at mine legacy sites in Portugal". *Journal of Environmental Radioactivity*, vol. 183, pp. 102-111, March 2018.

P.G. Martin, D. Connor, O.D. Payton, M. Leal-Olloqui, A.C. Keatley and T.B. Scott. "Development and validation of a high-resolution mapping platform to aid in the public awareness of radiological hazards". *Journal of Radiological Protection (IoP)*, vol. 38. pp. 329-342, February 2018.

D. Connor, **P.G. Martin**, N.T. Smith, L. Payne, C. Hutson, O.D. Payton, Y. Yamashiki and T.B. Scott. "Application of airborne photogrammetry for the visualisation and assessment of contamination migration arising from a Fukushima waste storage facility". *Environmental Pollution*, vol. 234. pp. 610-619, March 2018.

An additional work is currently under peer-review:

P.G. Martin, C. Hutson, L. Payne, O.D. Payton, Y. Yamashiki and T.B. Scott. "Validation of a novel radiation mapping platform for the reduction of operator-induced shielding effects". *Journal of Radiological Protection (IoP)*.

3.1 Radiation detection

For radiation to be quantified, it must first be detected. To detect the longest-range form of radiation, γ-rays, a number of different instrument types exist - using a range of different detector materials.

3.1.1 Principles of radiation detection

Whereas the laboratory-based techniques employed in this work (described subsequently in Chapter 5) are "active" methods, the detection of radioactive emissions (specifically γ-rays) does not require an external stimulus and can be conversely classified as a "passive" technique.

In addition to the release of γ-rays, the two other primary mechanisms of radioactive decay occur via the emission of either positively and negatively charged sub-atomic alpha (α) and beta (β) particles. These emissions typically occur, alongside the release of γ-rays as a result of the decay of large, neutron-heavy and unstable nuclei as they seek to approach a stable ground-state. Due to the limited range of both α and β particles in air, their detection is difficult and cannot easily be performed within regional environmental monitoring/mapping scenarios.

Gamma-ray photons interact with matter through three mechanisms, dependent on both their energy and also the atomic (Z) number of the material with which they interact. These interactions are; (i) the *photoelectric effect* (low energies and low-Z number materials), (ii) *Compton scattering* (moderate energies and atomic densities), and (iii) *pair-production* (highest energies and absorber densities) [66, 74, 206, 207]. A graph illustrating these three interaction mechanisms at the differing γ-ray energies and detector material densities is shown in Figure 3.1. Highlighted is the energy range over which the majority of environmentally-sourced γ-rays exist [72], as well as the effective atomic densities of the detector types used in this work (Section 3.1.2).

As discussed formerly in Section 2.1.1.1 with reference to FDNPP monitoring activities, alongside the traditional (and basic) gas-filled Geiger-Muller (GM) detectors, a number of different types of solid-state detector exist. Unlike GM detectors, however, this type of system is able to provide spectroscopic data on the incident radiation. These types of detectors can be classified as either the more common and widely-used scintillator type, or the more recently developed semiconductor type. A full review of the current state of the art types, geometries and electronic configurations of such radiation detectors is included within Connor, Martin and Scott (2016) [79].

Consisting of the largest group of radiation detectors - different types of organic, plastic, gaseous, glass and inorganic scintillator-type units exist. These are materials that are notionally fully or semi-transparent, which permits for the transmission of near-UV or visible light generated via
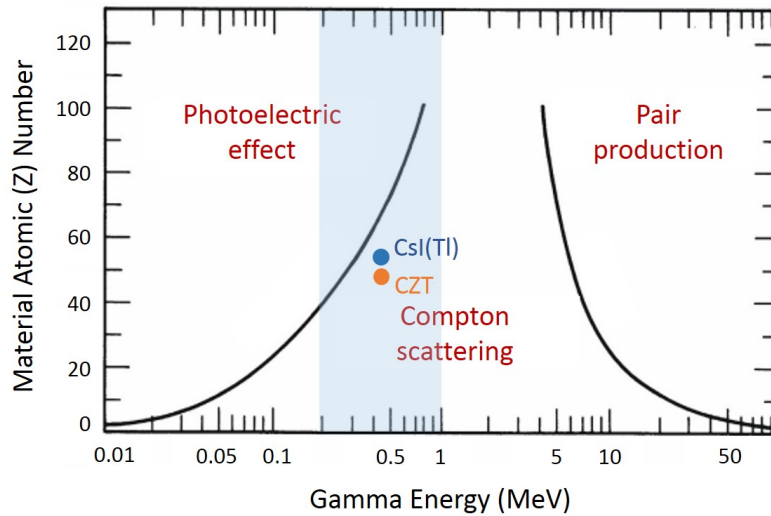
Figure 3.1: Plot depicting the three differing radiation-material interactions that occur as a function of both atomic (Z) number and incident γ-ray energy. The atomic (Z) numbers for the two detectors used in this work are also plotted, further highlighted is the energy window over which the majority of anthropogenic γ-rays are observed. *Modified from [207].*

the materials interaction with incident γ-ray photons. The most common of the inorganic high Z-number scintillator crystal materials are; $LaBr_3$, NaI and CsI (all of which typically contain a dopant species to enhance or modify the photo-emission produced - typically Tl). Scintillator detectors operate whereby a gamma-ray photon incident on an atom, ejects an electron from the lower-energy valence band (comprising numerous orbital shells) into the higher-energy conduction band (also with numerous electron shells) resulting in the production of an "electron-hole" pair. The subsequent infilling of this hole through the de-excitation (demotion) produces light (tuned to the near-UV or visible range where photo-multipliers are at their most efficient). This light emitted by the crystal leads to the production of photoelectrons by a photo-multiplier tube (PMT), or diode, via the photoelectric effect. The multiplication of these electrons and their analysis then follows, allowing for an assessment of the energy of the original gamma-ray photon that struck the detector - being proportional to that of the photo-electron population produced.

Semiconductor detectors operate via a method similar to scintillator-type devices. Upon interaction with ionising γ-rays, both "electron-hole" pairs are produced when electrons are promoted to the conduction band from the valence band. The number of pairs produced is proportional to the energy of the incident ionising radiation, and in the presence of an electric field, these pairs travel to two opposingly charged electrodes - generating a measurable electronic signal pulse. Semiconductor materials used for radiation detection are not as numerous as scintillator-type materials, with typical detectors being comprised of Si, diamond, high-purity Ge (HPGe) and more recently, the direct band-gap semiconductor CdZnTe (CZT).

While α and β particles are easily detected (at short measurement distances) due to their charged nature, γ-rays in contrast, are more difficult to detect with the ultimate efficiency of a detector being a function of both its volume and also its sensitivity (or counting efficiency), which itself is partly dictated by its density, band-gap and the energy of the interacting γ-ray photon. For the incident gamma radiation to be registered and counted, it must have a sufficient interaction with the detector [206]. As no detector material exists that is 100% efficient, not all γ-ray energy will be absorbed and hence radiation detected.

A quantity termed the "intrinsic counting efficiency" is hence defined - existing as the ratio of radiation incident onto a detector to that registered (and counted). This efficiency is the physical density of the detector material, and its associated electron density. It is these electrons, that migrate through the detector (as electron-hole pairs), that underlies radiation detection.

With radiation detection relying on the interaction between the incident γ-ray and the detector material, the attenuation of radiation results from the similar, yet undesired, interception and absorption of this radiation. As one of the most abundant compounds of the planets surface, water is extensively utilised in the shielding of the ionising radiation that is emitted from spent nuclear fuel in facilities worldwide alongside providing cooling owing to its high specific heat capacity. Water has a high linear attenuation coefficient (μ) and therefore, is a strong absorber and attenuator of γ-ray radiation [20, 74].

This property represents an issue, however, within environmental radiological surveys for a number of reasons. The primary issues results from the majority of the human body being constituted by water, with the male and female body on average being composed of 58% and 49% water (as bodily tissues) respectively [208]. Work by Jones and Cunningham (1983) [113], placed the total reduction of incident radiation resulting from its attenuation by the human body at approximately 30%, with recent work by Buchanan et al., (2016) [114], attained a comparable value at between 20% and 30% attenuation of a radiocesium source. While the human body can be represented by a volume of water, this is a gross simplification, with the body composed of many different materials - all with differing attenuation coefficients (Section 2.1.1) [74].

3.1.2 Detector instrumentation

The in-field characterisation of radiation described in this thesis was performed using one scintillator and one semiconductor detector. Specifications of both are detailed in Table 3.1.

Both detectors (GR1 and SIGMA-50) were manufactured by Kromek™ Ltd., with their signal outputted through a mini-USB as a series of channel numbers (1 - 4096) proportional to the

	SIGMA-50	GR1
Type	Scintillator	Semiconductor
Detector material	CsI(Tl)	CdZnTe
Detector volume (cm^3)	32.8	1
Mass (g)	300	60
Maximum CPS	5,000	30,000
Energy range	50 keV - 1.5 MeV	30 keV - 3.0 MeV
Energy resolution (at 662 keV)	<7.2% FWHM	<2.5% FWHM
Channels	4096	

Table 3.1: Comparison of γ-ray detectors used during this study. *From [209, 210].*

individual γ-ray photon energies incident onto the detector. Each unit can be controlled through the KSpect™ software provided by the manufacturer, however, for this work an alternative control program was produced at the University of Bristol for the purposes of controlling either detector during radiation mapping - described in MacFarlane et al., (2014) [100]. Within this alternative code, the string of channel numbers obtained during the previous 0.5 seconds (2 Hz sampling rate) was combined with positional information obtained from a GPS unit (Adafruit™ Ultimate GPS Breakout - connected to an external GPS antenna) onto an Arduino™ Mega ADK micro-controller board, before being written to a micro-SD card in near real-time (0.5 second processing delay). Positional accuracy stated by the manufacturer was ±1 m, however, a resolution of ±0.5 m was determined to be generally obtained. The entire system was powered by an internal high-capacity lithium-polymer (LiPo) battery, all of which was encased within a protective ABS plastic case with externally-mounted connections. Through the collection of the channel numbers corresponding to the γ-rays incident onto the detector, an energy spectrum could be produced at every position.

In addition to the detector control software that was developed at the University of Bristol, the software used to display, post-process and export the data for further analysis was also constructed in-house, using the LabView™ environment from National Instruments™ (NI).

Prior to in-field deployment, an energy vs. channel number calibration was performed for each of the detectors. A number of calibration sources were held in front of each detector (GR1 energy range: 30 keV - 3.0 Mev and SIGMA-50 energy range: 50 keV to 1.5 Mev) to derive a value for the specific emission energies corresponding to each of the detectors 4096 channels. While the GR1 was able to detect a greater energy range of γ-rays than the SIGMA-50, this larger energy range was not required, as the principal radiocesium γ-ray photon energy is only 662 keV [52], and therefore well within the range of the more sensitive SIGMA-50 - with twice the energy resolution.
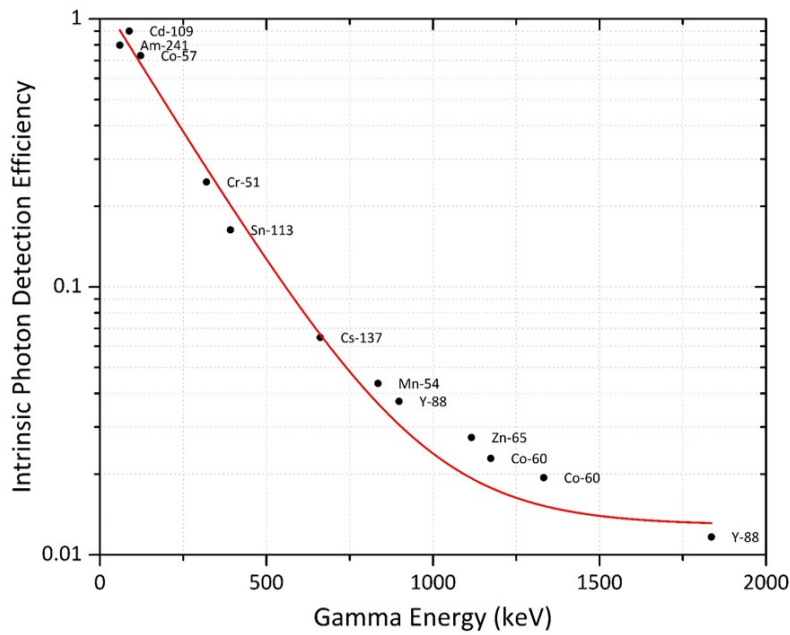
Figure 3.2: Detection efficiency of the CZT-based GR1 detector with incident γ-ray energy. Optimum efficiencies are experienced at the lowest photon energies. *From [211]*.

To permit the conversion of the measured counts per second (CPS) into a meaningful value of dose-rate, an additional processing step and a further calibration were required. For this calibration, each of the solid-state detectors was exposed to a number of different radiocesium dose-rates, as quantified by a hand-held Tracerco™ PED dose-meter. Linear plots were produced detailing the response from both detectors in comparison to values obtained from the dose-meter.

Existing as a cubic centimetre volume (1 cm^3) of CZT detector material, encased within a uniform thickness of Al with electronics positioned behind the crystal - the sensitivity of the GR1 detector to incident radiation was determined to be almost independent of its orientation [211]. In contrast, the prismatic volume of the SIGMA-50 detector (25 mm × 25 mm × 51 mm) resulted in significant sensitivity differences dependent upon its orientation [212]. Within this work by the UK National Physical Laboratory (NPL), a 40% increase in count-rate was observed when the detectors long-axis was positioned parallel (facing) to the ^{152}Eu source.

As formerly mentioned, the "intrinsic counting efficiency" is a further property of the detector that requires an assessment to allow for quantitative results to be derived. A plot detailing the exponential reduction in detection efficiency with increasing γ-ray energy, for a GR1 detector, is shown in Figure 3.2. Evident from this plot is the rapid reduction in CZT photon detection efficiency - from 0.79 at 59.5 keV (^{241}Am), reducing to only 0.012 at 1,836.1 keV (^{88}Y). The

CsI-based SIGMA-50 is conversely characterised by a slightly improved detection efficiency at higher incident photon energies (0.2 at 1,500 keV) [213]. Through applying the approximately linear reduction in detection efficiency that is derived for either the GR1 or SIGMA-50 unit (when graphed onto a log-linear scaling), a compensation for this energy-dependent efficiency of the detector can be corrected for. This correction was performed during subsequent post-processing, whereby the mathematically derived function describing the trend was applied to correct for such detector efficiencies [214].

Having quantified the energy-dependent efficiency of the detector, the activity of the source/sample can subsequently be determined using a number of additional setup/environmental parameters, alongside values derived from the γ-ray spectrum. The equation used to derive a samples activity is given in Equation 3.1, whereby in this equation; A = activity concentration of a specific radionuclide in the decay series, N_{net} = net background-subtracted peak count area (from the γ-ray spectrum), ϵ = energy specific efficiency of the detector, $I_{(\gamma)}$ = emission probability (branching ratio) of the specific energy photo-peak (0.851 for the ^{137}Cs emission at 662.94 keV [52]), t = sample collection time, and m = mass of the sample.

$$A = \frac{N_{net}}{I_{(\gamma)} \, \epsilon \, m \, t} \tag{3.1}$$

The minimum detectable activity (MDA) of a counting system can also be derived using these values, with the equation describing the lowest activity possible for a specific detector to accurately measure shown in Equation 3.2. Where N_B represents the total count under the photo-peak of interest.

$$MDA = \frac{4.653 \, \sqrt{N_B}}{I_{(\gamma)} \, \epsilon \, m \, t} \tag{3.2}$$

3.2 Ground-based surveys

Several on-ground surveys have been performed to characterise radiation across discrete areas within Fukushima Prefecture alongside airborne mapping surveys (Section 3.3). In comparison to sites examined via airborne survey, those sites examined using ground-based methods were topographically simplistic and did not present access limitations that would otherwise require an airborne survey. Such limitations are depicted in one of the initial radiation maps produced around the Kawamata Town area of Fukushima Prefecture by Kinase et al., (2015) [215], shown in Figure 3.3. While providing valuable information on the distribution of radiological contamination, these results highlight the absence of spatial data coverage, away from the road network. Despite this limited coverage, ground-based surveys are powerful in initially locating regions of interest.
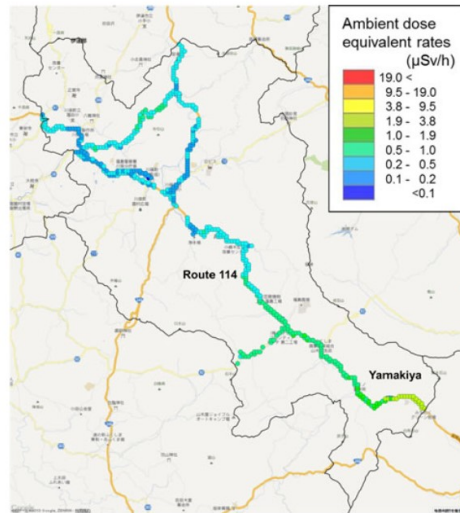
Figure 3.3: Map of ambient dose equivalent rates through vehicular surveys at Kawamata Town (Fukushima Prefecture). *From [215].*

3.2.1 Detector setup

Two forms of ground-based radiation survey were performed as part of this thesis using slightly differing derivatives of the base-setup formerly described and depicted in Figure 3.4. Within one method, the setup as described was deployed - consisting of system electronics, GPS antenna and a single GR1 or SIGMA-50 radiation detector placed within an operator's backpack - positioned at 1 m above the ground. Due to the directional sensitivity of the SIGMA-50 unit, it was placed at the base of the backpack with its long-axis positioned parallel to the ground's surface. To maintain consistency, the same operator conducted all radiological surveys via this method.

As discussed previously (Section 3.1.1), and as shown in the various studies - the influence of water (and the human body) on radiation attenuation is significant - greatly impacting on results of radiological surveys [113, 114]. To address this limitation, a new form of radiation detection system was deployed.

A schematic of this new dual-detector system is shown in Figure 3.5. To remove the approximately 30% reduction in intensity associated with nearby human operators, two SIGMA-50 units were mounted at either end of a plastic pole mounted under the operator's backpack, each extending out a distance of 1 m. Two GPS units were used to independently record the position of each of the detectors - with the system electronics modified to incorporate measurements from both systems onto two Arduino™ Mega ADK micro-controller boards. As per the single unit system, both detectors were held at 1 m above the ground surface to avoid the requirement to perform the otherwise required height-correction.
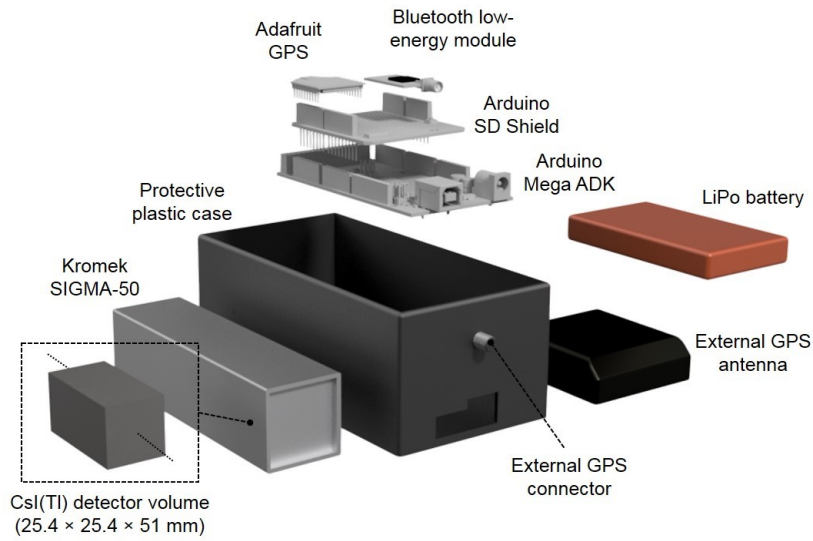
Figure 3.4: Exploded schematic of the base unit setup used during radiation mapping (a SIGMA-50 detector is shown).
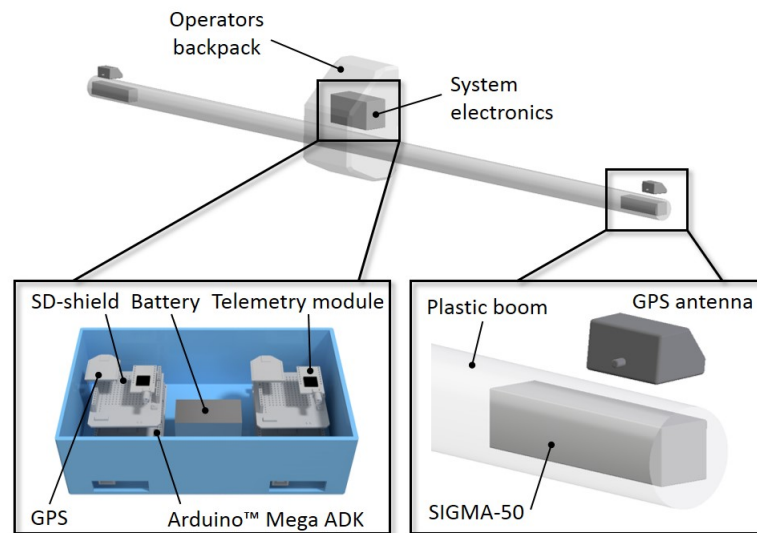
Figure 3.5: Schematic of the backpack-mounted ground survey platform.

Resulting from the two detectors being deployed by a single operator, the survey efficiency of this method is considerably greater than in conventional surveys, therefore permitting for increased ground coverage. However, as the nearby positioning of multiple GPS units is widely-regarded to produce erroneous position readings due to radio-frequency (RF) interference, a prior study was performed. The resulting position derived from both GPS units during this test survey are shown
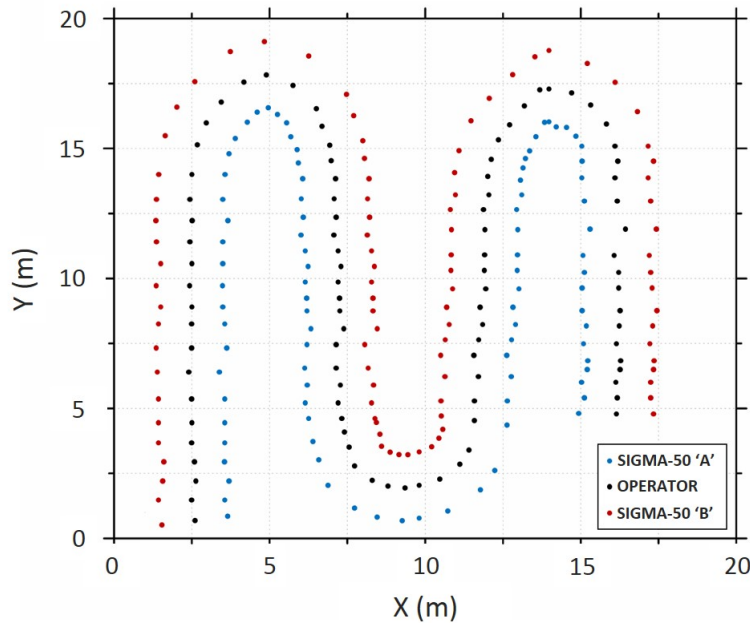
Figure 3.6: Influence of one GPS units position, as reported by the other neighbouring unit.

in Figure 3.6. From these results, however, neither GPS unit is seen to suffer from any form of positional irregularity - suggesting sufficient separation of the units and no RF interference.

A further calibration was also undertaken to more accurately quantify the radiation reduction as a result of bodily attenuation, and therefore the benefits of this system in comparison to "traditional" survey methods. The results of this exercise are shown in Figure 3.7. Within this calibration, the SIGMA-50 detector was progressively moved away from a central radiocesium source, with the measured radiation levels recorded. A subsequent set of measurements were made by placing a human volunteer (of typical build) between the source and detector. From these measurements, an average reduction of 30% is calculated - identical to values determined during earlier works [113, 114]. By therefore positioning the detector away from this source of attenuation, a more representative account of true air dose-rate is recorded. As a result, for the subsequently detailed ground-based detection setup whereby measurements were undertaken with the detection unit held in close proximity to the body - a correction factor of 1.3 was applied to the results.

A final calibration of the system to ensure repeatability between both SIGMA-50 units of the dual-mapping system was undertaken within an established radiological environment. Over a 50 m length, a series of varying activity radioactive sources were positioned. During the first pass of the platform, one detector (SIGMA-50 "A") passed directly over the sources, during the
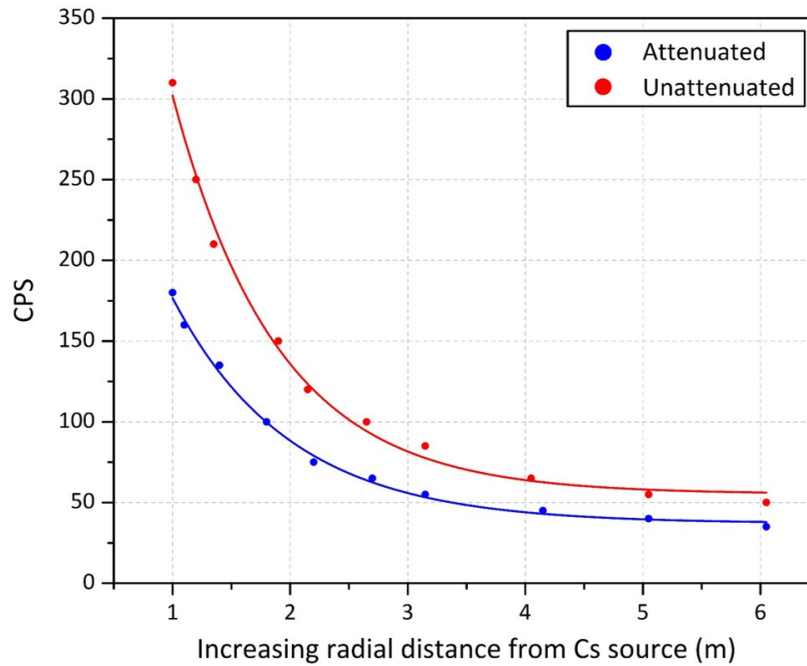
Figure 3.7: Influence of human attenuation on radiation intensity recorded by a detector.

return pass, the second detector (SIGMA-50 "B") travelled directly over each of the sources. A comparison of each detector's response to this radiation field is shown in Figure 3.8. Between the two detectors, for measurements taken at the same location but with differing detectors, a maximum difference of only $\pm 5\%$ was observed. Resulting from such a small degree of inter-detector variation, the measurements attained via either of the SIGMA-50 units can be directly compared, without the requirement for any normalisation be applied.

3.2.2 Survey setup

For radiation surveys within open areas, the operator would walk in a number of parallel survey transects, each equally spaced. When using the single-detector (backpack-contained) unit, a grid spacing of approximately 1.5 m was attempted, increased to 3 m, however, when the dual-detector (boom-mounted) system was employed. In each case, a closer grid-spacing served only to enhance the level of measurement overlap. If surveys were conducted in areas where space was limited or where numerous obstructions existed, smaller survey grids comprising the full area were used.

To establish if any system "drift" (variation between time-resolved measurements from the same location) had occurred, deliberate repeats of the same survey lines, at both the start and end of the survey were made. This provided assurances of the accuracy of the system.
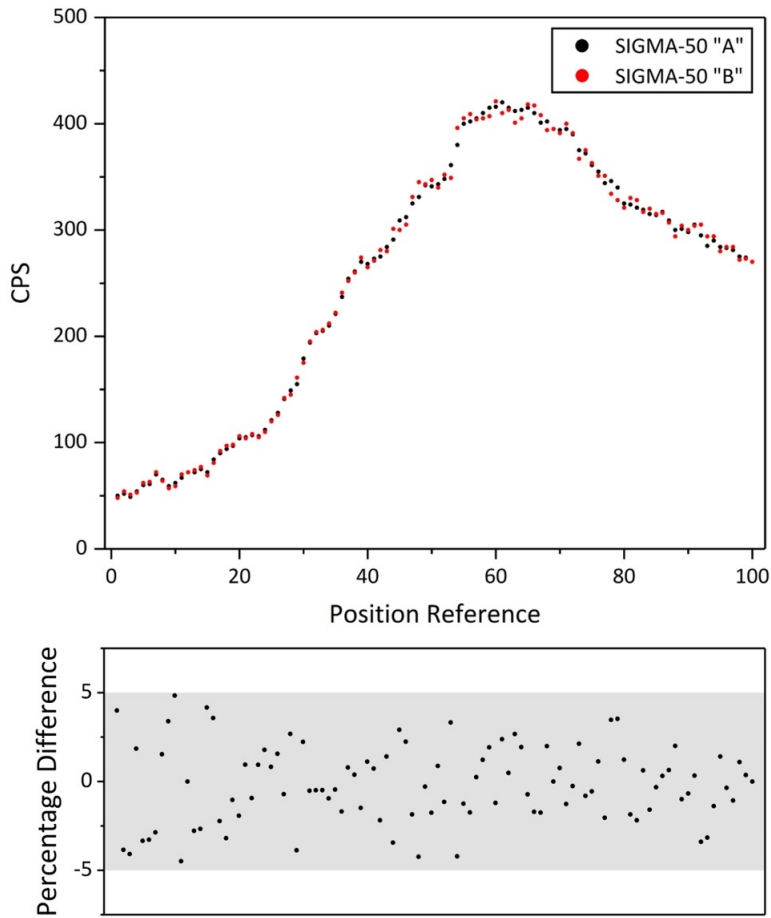
Figure 3.8: Repeatability comparison of both SIGMA-50 units comprising the dual-detector ground-based mapping system.

The measurement data was captured at a slow walking pace (approximately 1.0 ms^{-1}), at a 2 Hz sampling frequency. Data was subsequently uploaded from the systems micro-SD card into the processing and analysis software. Within this software, the number of the γ-rays incident onto the detector during each 0.5 second sampling window were summed (and multiplied by two for a per-second value), before being plotted as a user-defined colour-scaled (CPS or calibrated dose-rate) overlay onto a satellite base-map of the area, using the GPS-derived position of the unit.

The circles that formed the radiation overlay were scaled to both the intensity of the radiation (colour), but also in size to represent the region on the ground that this signal could originate. The radius of these circles existed as a combination of the height at which the detector was held (1 m), its velocity of travel, as well as the physical aperture (of the detector) for incident radiation. These circles are here defined as 1 m in diameter, in-line with common practice - comparable to earlier survey systems and collection methods [105, 216]. In regions where data point overlap occurred, a "nearest-neighbour" smoothing filter was applied to the data to remove any inconsistencies that

existed. The same nearest-neighbour filter was also used to interpolate measurements into areas where the data density was lower or where a grid-separation greater than 1 m existed.

3.2.3 Platform testing, calibration and initial application

Prior to its deployment across Fukushima Prefecture, system testing of the single-unit ground-based platform was performed at sites both in the UK and abroad, including;

- Geevor Tin Mine, Cornwall, UK

- South Bristol, UK

These test sites were selected to represent locations where there existed a known, but low-activity, radiological signature, however, the extent of the contamination in each case was not fully known/understood.

The survey undertaken in Cornwall represents an area formerly of extensive resource extraction, with resulting legacy contamination. Investigations within Bristol were used to investigate the deployment of the platform within a contrasting urban area, where low-activity geological exposures and prior underground coal workings present radiological anomalies with a more limited spatial extent.

The results of these initial studies and the associated calibrations can be found within the peer-reviewed literature:

P.G. Martin, D. Connor, O.D. Payton, M. Leal-Olloqui, A.C. Keatley and T.B. Scott. "Development and validation of a high-resolution mapping platform to aid in the public awareness of radiological hazards". *Journal of Radiological Protection (IoP)*, vol. 38, pp. 329-342, February 2018.

Geevor Tin Mine

Existing within a rich and extensive granite-derived mineral vein network, the county of Cornwall in south-west England has long since exploited its metalliferous reserves for economic gain; with the region formerly the worlds largest supplier of tin and tin-ores at the start of the 19th Century [217]. One such mine to exploit these rich mineral reserves was the Geevor Mine, located on the north-west Cornish coast - approximately 10 km north-east from Lands End, neighbouring the numerous other mines found across the area, including its sister mine - Levant. The Geevor Mine principally extracted tin ores (however, the Levant and other nearby mines also extracted Cu, Ag, Au and As) formed as a result of the intrusion of the Lands End Granite and the associated mineralisation dating from 223 ± 7 Ma [218, 219].
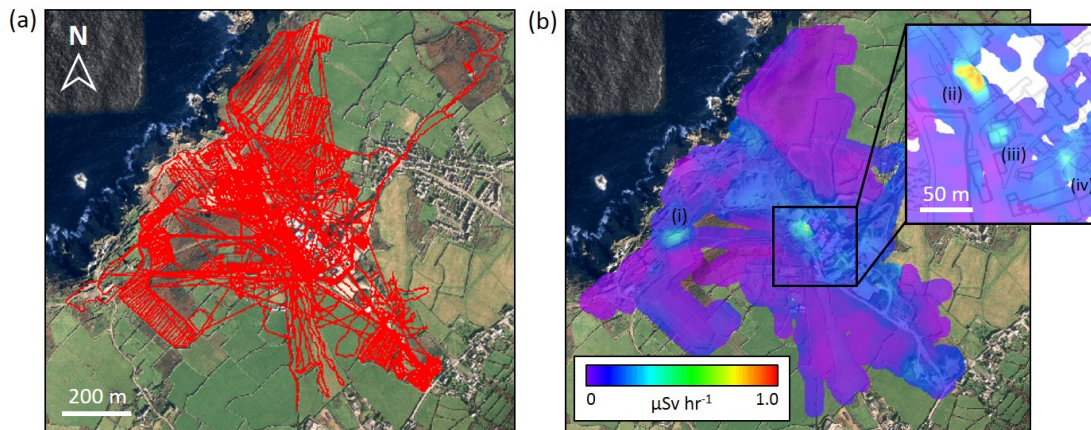
Figure 3.9: Dose-rate calibrated air dose-rate maps obtained using the single unit ground-based system at the Geevor Tin Mine, Cornwall.

In addition to these primary tin phases, extensive later-phase uranium mineralisation also occurred across the region [218]. After extraction, this uranium-containing material was treated as gangue (waste) material and disposed of as large spoil heaps across the site. Since the demise of the Cornish industry and the mine's closure in 1990, these spoil piles have been removed and the estate has since opened as a popular visitor attraction. However, low-levels of localised legacy contamination were known to occur across the site, and therefore represented a useful system test site for assessing platform sensitivity and resolution. The only prior radiological assessment of this site was conducted as part of the Tellus SW Project [220], where a light-aircraft was used to overfly the region (56 m - 200 m altitude) obtaining geophysical alongside radiometric data.

Radiological data from the site was obtained using a SIGMA-50 detector attached to the single-unit backpack-contained setup, held at the standard 1 m above the ground, as detailed in Section 3.2.1. To enhance ground coverage in the time available, three units were deployed concurrently. To attain consistency between each of the units, operators were chosen with similar builds - full details of inter-unit calibrations are included within Martin et al., "Development and validation of a high-resolution mapping platform to aid in the public awareness of radiological hazards". *Journal of Radiological Protection (IoP)*, vol. 38, pp. 329-342, February 2018.

Methods employed to survey the site were identical to those described in Section 3.2.2, with the operators each walking in a grid pattern of consistent survey-line separation. The plotting of survey data was performed as described in Section 3.2.2, with radiation levels corrected by a factor of 1.3 to account for human-induced shielding of the detector. Calibration points were made across the site using a RADEX™ hand-held dose-meter (Moscow, Russia) to permit for conversion between dose-rate and system produced CPS output.
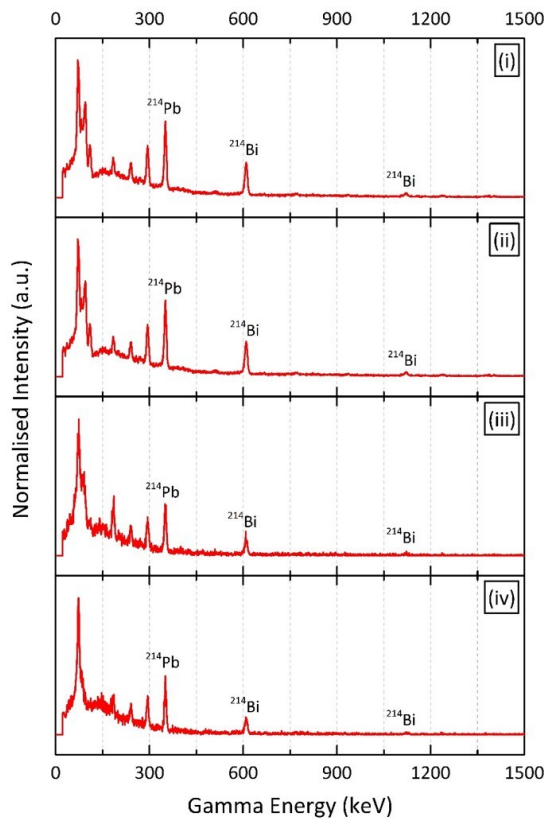
Figure 3.10: Gamma-ray spectrum produced using the single unit ground-based systems at locations (i) - (iv), as identified in Figure 3.9.

The calibrated dose-rate map of the site is shown in Figure 3.9, with the four points of increased activity ((i) - (iv)) identified. Position (i) was determined to represent the location of a small legacy spoil heap near to the coast, whilst (ii), (iii) and (iv) marked the locations of former extraction and processing activities at the sites centre. A region with elevated activity trending NW-SE through the site is also observed, coincident with a downwards slope where contaminant material is ascribed to have progressively migrated. Resulting from this survey, the ability to identify points that are both spatially limited in their extent as well as low in their activity is proven. Whilst elevated in activity, these points are all well below levels defined as safe [221].

Analysis of the γ-ray spectra attained at the four points, (i) - (iv) shown in Figure 3.10, including; the relative heights of each of the peaks, highlights the identical isotopic signature ($\pm 2\%$ peak height difference) at each of these locations. As expected from a uranium-ore material, the contributing peaks result from the radioactive decay of the daughter products that have over-time ingrown after the materials emplacement. The peaks identified in Figure 3.10 are from the
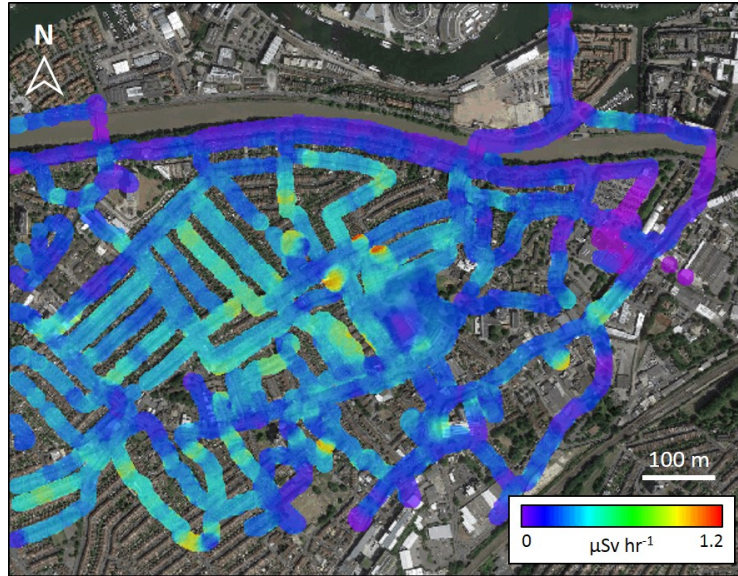
Figure 3.11: Calibrated air dose-rate maps obtained using the single unit ground-based system across a region of South Bristol.

radioactive decay of ^{214}Bi and the parent ^{214}Pb - with ^{214}Bi decaying via strong gamma-emission into the very short-lived ^{214}Po, which following a number of intermediary decay steps reaches the stable ^{206}Pb. However, these intermediary steps are dominated by α and β decays, with only limited (and difficult-to-detect γ-ray emission). Such spectral similarity shows a commonality to the source material and the absence of preferential species transport/mobilisation.

South Bristol

The City of Bristol in south-west England, like Cornwall to its south, also has a rich history of underground resource extraction resulting from its extensive buried resources, however, for coal rather than various metalliferous ores [222]. These workings, sometimes at depths of <5 m below the ground surface, have long presented issues for new construction as well as the subsistence of existing properties across the city [223]. However, as is typical for coal, a radiological signature is evident due to concentrations of naturally-occurring radioactive species (K and U) present within the material [219, 224], accumulated during deposition and/or the subsequent interaction of U and K carrying waters. Where past mining activity had occurred across south Bristol, the surface manifestations are evident through the location of vents extending to the surface.

With the sensitivity and spatial resolution of the system already demonstrated by its application at the Geevor Tin Mine, the deployment across south Bristol sought to further test and quantify these attributes, and in addition examine the performance of the system within an urban environment - where issues relating to GPS shielding and signal reflection/scattering events could serve to produce measurement/locational errors.

As per the surveys at the Geevor site (and detailed in Section 3.2.2), the single unit ground-based system was used, with the more-sensitive SIMGA-50 unit attached. The system was again carried in the operator's backpack (1 m above the ground), with a factor of 1.3 applied to the results to remove the influence of human attenuation. Like at the Geevor site also, a series of dose-rate measurements were also obtained to allow for a CPS to dose-rate conversion. Unlike Geevor, however, where evenly spaced grid-lines could be used to construct the survey, mapping was undertaken by walking along either side of the road along the pavement. The calibrated dose-rate map produced over the south Bristol area is shown in Figure 3.11.

From these results, a greater maximum dose-rate than at the Geevor site is evident, with a larger number of "hot-spot" locations. The highest levels of radiation are associated with the central portion of the survey area, correlating with the location of the greatest density of both coal seams and resulting former mine workings [223]. The land to the north (close to the river) and the east were not extensively exploited, and show levels of radioactivity up to 70% lower than measurements obtained 200 m to the south - corresponding to the location of the Dean Lane Colliery (closed in 1906) [222].

From these results, the spatial resolution (with meter-scale anomalies identifiable) and the low limit of detection of the unit (<0.1 μSv hr^{-1} resolvable difference) shown previously at the Geevor site are further evaluated. The lack of anomalous data points (representative of poor GPS signal or RF "signal interference") supports the system for use within built-up environments such as these. This system shows comparable results to other ground-based systems [64, 216], whilst being both lighter, fully-spectroscopic and considerably more portable. Hence, this interchangeable detector system represents a significant capability advancement over existing platforms.

3.3 Airborne (UAV) surveys

While ground-based surveys were suited to and undertaken at smaller sites that were readily-accessible on-foot and exhibited limited topographic obstructions, unmanned aerial vehicle (UAV) surveys were utilised in areas where such obstructions presented access limitations or where it was undesirable/impractical to send humans to perform such work.

3.3.1 Airframe

The low-altitude UAV used within this work is pictured in Figure 3.12, alongside a schematic of the total system in Figure 3.13 - a full description of the airframe is contained within prior works [102, 103, 225–227].
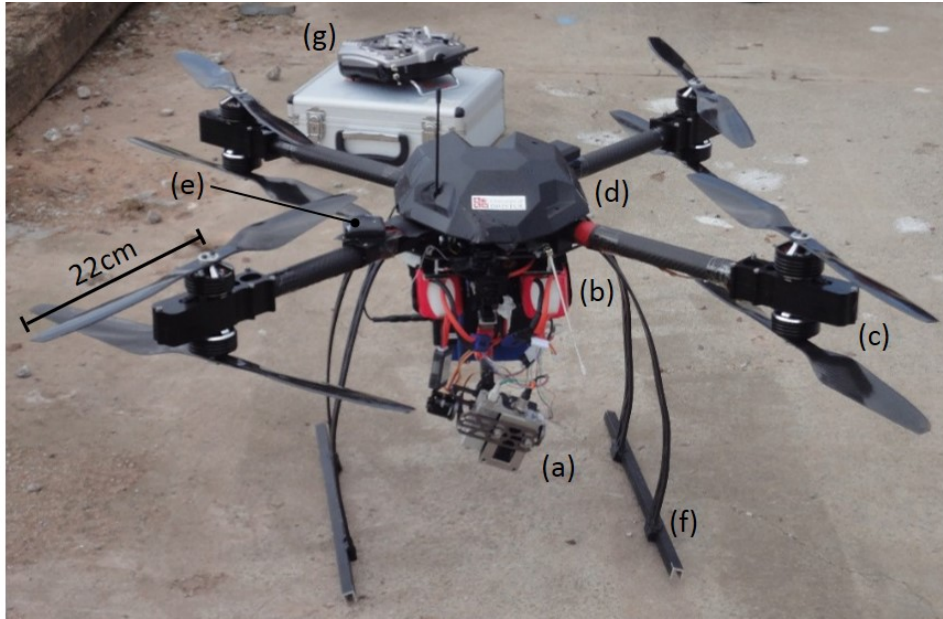
Figure 3.12: Labelled photograph of the UAV with associated payload used for low-altitude radiation mapping, consisting of; (a) detector payload, (b) LiPo batteries, (c) motors and propellers, (d) tubular CF arms, (e) payload GPS, (f) legs, (g) radio-controls. *From [102]*.

Consisting of an "X8" configuration with motors and propellers mounted both above and below its four tubular carbon-fibre (CF) arms, the entire system was collapsible for transportation - with the main central body of the system also constructed from a lightweight CF composite. The platform was powered by two high-capacity LiPo batteries mounted under the main central electronic systems to ensure an even weight distribution. These electronics (located under a protective cover) consisted of a PixHawk™ or APM flight-control board containing an onboard inertial measurement unit (IMU), compass, barometer and GPS (all for navigation), alongside power distribution and speed control systems for the UAVs motors. Whilst being able to operate fully autonomously during flights, control of the UAV was also possible using conventional hand-held radio controls. Mounted under the UAV, between its flexible aluminium legs, was the radiation detection payload - modified from the basic system described previously in Section 3.1.2.

3.3.2 Detector setup

Within ground-based surveys previously discussed in Section 3.2.2, the low height (1 m) above the ground at which they were conducted permitted for the simplistic apportioning of a 1 m diameter field of view from whereby the radiation incident onto the detector was sourced. However, due to the varying distances from a surface that a UAV-mounted detection system would be deployed, an enhancement to the basic detection system, shown formerly in Figure 3.4, was made. This addition was the inclusion of a single-point (905 nm wavelength eye-safe infra-red) laser range-
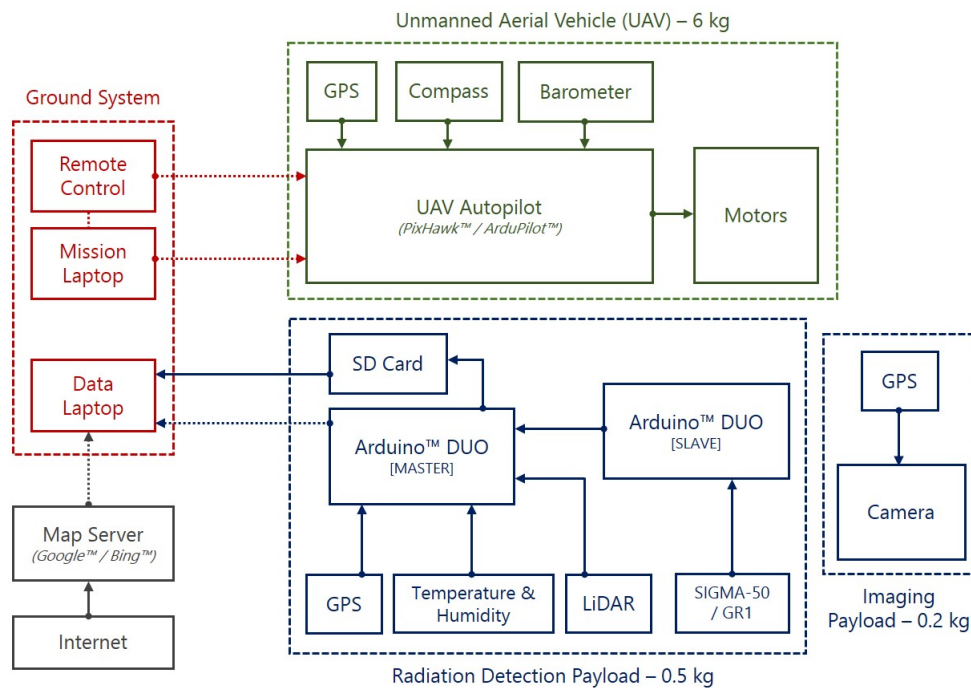
Figure 3.13: Schematic overview of the UAV and associated detection payload(s) - radiological and imaging. *From [225].*

finder. The AR2500™ time-of-flight sensor from Acuity™ [228], possessed an accuracy of ±1 cm over its 100 m operational range.

Alongside the series of channel numbers (corresponding to the energies of the individual incident γ-rays) and GPS position information (latitude, longitude and altitude), a value for the height of the unit above a surface (ground, roof or trees) was also concurrently recorded - sampled at the same frequency of every 0.5 seconds (2 Hz).

Due to its lower mass and smaller size, the GR1 detector was employed for the majority of the airborne survey work. The heavier, yet more sensitive SIGMA-50 was, however, used within later portions of fieldwork across Fukushima Prefecture due to the decline in radiocesium activity over the duration of this study. For either of the detection units, to ensure they remained in the same orientation throughout the flight irrespective of the attitude of the UAV, they were mounted onto a gyroscopically-stabilised three-axis gimbal. Alongside the detector on the gimbal was the laser range-finder unit, itself also gimballed to ensure it remained normal to the ground's surface. The orientation of either detector when mounted onto the airborne system was the same as that used during ground-based surveys.

3.3.3   Detector field of view calibration

As presented in the work by Duval et al., (1971) [78] (and as previously discussed in Section 2.1.1), the height at which airborne surveys are conducted is central not only to the degree of attenuation experienced, but also the spatial resolution attainable, termed in this work as the "circle of investigation". While this work by Duval et al. accurately describes the typical on-ground resolutions produced via higher-altitude survey methods such as planes and helicopters, this rationalisation does not hold for lower-altitude radiometric surveys. Via this equation (Equation 2.2), an aerial survey performed at 10 m altitude would sample radiation from a radius of 39 m. As before, in this equation, Y = radiation yield (or intensity), θ = half-angle of cone of incidence from detector to ground, H = height of the detector, A = a constant dependent upon the setup parameters, μ_e = linear attenuation coefficient of the ground within which activity is located, μ_a = linear attenuation coefficient of air, λ = Euler's constant (0.5772157), and x = ratio of the product of μ_a and height *(H)*, to *cos θ*

An alternative function to describe the on-ground sampling radius of an aerial detection system, applicable to lower altitudes was subsequently provided by Pitkin and Duval (1980) [71], shown in Equation 3.3. Where, H = height of the detector, R = radius of the "circle of investigation" (ground sampling radius), θ = half-angle of the cone of response from detector to the ground, and n = a constant dependent upon the detection setup.

$$\tan \theta = \frac{R}{H} = n \tag{3.3}$$

From this function, the on-ground radius *(R)* from which radiation is sampled is dependent upon both the height of the detector *(H)*, but more critically its half-angle *(θ)*. The influence of both factors is shown in the plots of Figures 3.14 (a) and (b). From Figure 3.14 (a), for a detector with a large theta angle (sampling aperture), the radius of investigation is shown to be strongly influenced by the detector height - illustrated here by a linear trend. This function is further shown by Figure 3.14 (b), whereby for a specific survey altitude - detectors of widening θ half-angles produce an ever-increasingly ground sampling radii ("circle of investigation").

To determine the specific half-angles of the two detectors, the GEANT4 software platform was used [229]. GEANT4 is a simulation tool-kit constructed using the C++ programming language at CERN for simulating the passage and interactions of differing sub-atomic particles through various forms of matter and under a range of environmental conditions. For each detector in its standard survey configuration, a radiocesium point source was positioned 2.5 m directly beneath the detector - before being moved horizontally to attain a range of half-angles (±90°), with the

75
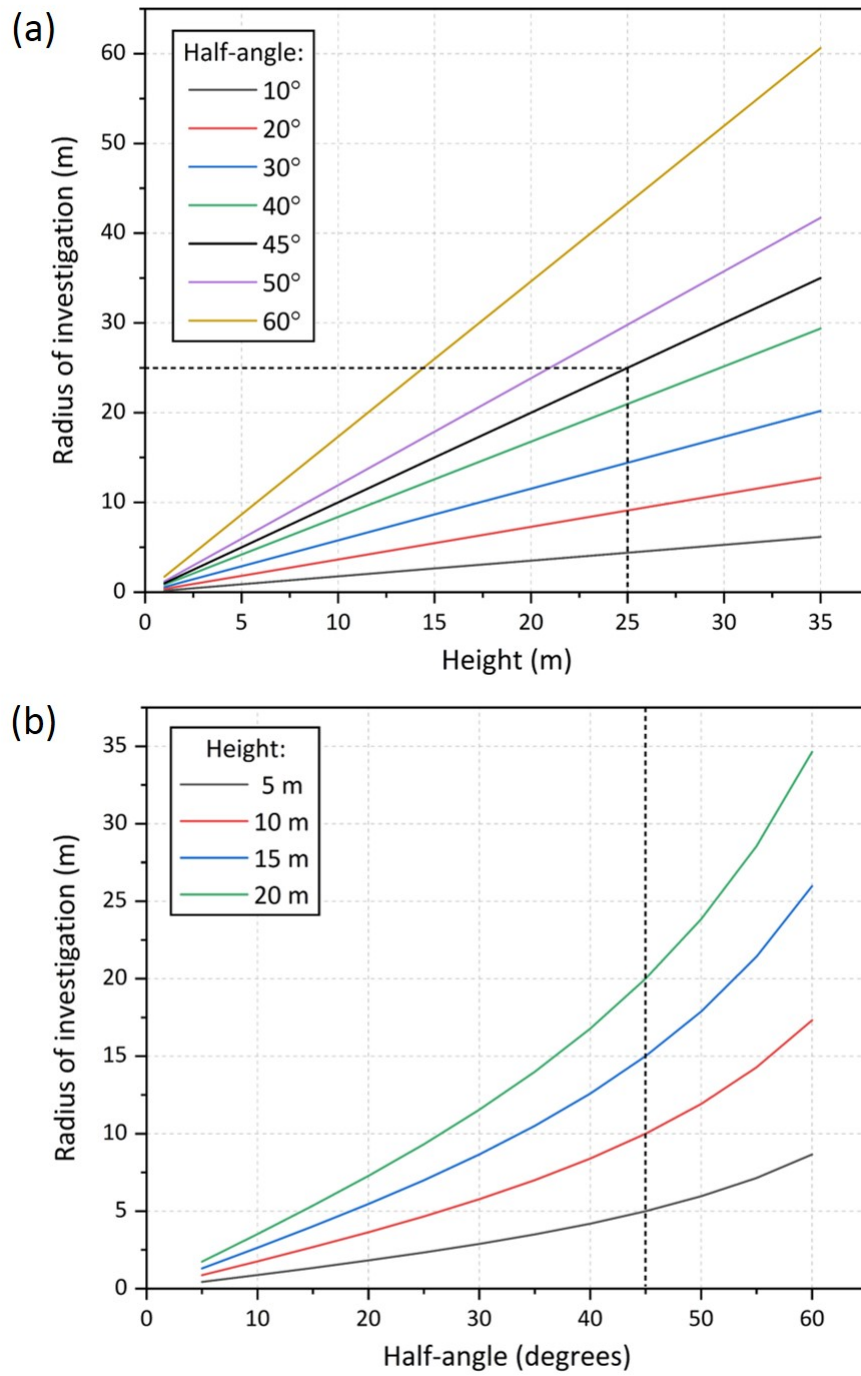
Figure 3.14: Plots detailing the influence of; (a) detector height *(H)*, and (b) detector half-angle *(θ)*, on the radius of investigation.

resultant radiation intensity recorded. A height of 2.5 m was selected to represent the lowest altitudes at which surveys would be performed. A graph of the GEANT4 simulation results for both detectors is shown in Figure 3.15. This plot details the strongly-normal distribution and hence the crucial influence altitude and detector half-angle plays on the spatial resolution of airborne surveys.

For both detectors, at approximately 45° half-angle, the measured intensity falls to below 90% of the maximum. This value of θ can, therefore, be taken to represent the characteristic angle of the detectors - shown with dashed lines in Figures 3.14 (a) and (b). As shown in these plots, for such a half-angle, the height at which the detector is positioned above the ground directly corresponds to the radius of the "circle of investigation" on the ground. Therefore, for a survey at 10 m altitude, a 20 m sampling diameter would be attained. However, if survey flights were to be performed at lower altitudes than 10 m, such a "circle of investigation" would be similarly reduced.

These modelling-derived results were subsequently verified through an in-field calibration, whereby a 5 MBq ^{137}Cs source was positioned on the ground, away from the UAV and its detector (outside of the on-ground "circle of investigation"). By incrementally increasing the height of the platform (hovering at differing altitudes over the same initial location), the height (and resultantly the detector half-angle) at which the source became visible, was mathematically determined.

The inclusion of the single-point laser range-finder as a component of the airborne detection payload allows for the UAVs height above a surface to be determined over the duration of the survey. From this altitude value, the "circle of investigation" and hence the diameter of the on-ground sampling radius for each measurement can be derived.

Operating at such limited distances from the ground, the influence of surrounding topographic features on measurement uncertainties is a further, required, consideration. To address this, in work by Malins et al., (2015) [110], the influence of a number of spatial geometries (e.g. valleys, hillsides, mountains and trees) on the detected air dose-rate, obtained via high-altitude, low-altitude or ground-based systems, were each simulated. Following these works, it was concluded that whilst high-altitude manned surveys may encounter significant uncertainties in the determined on-ground dose-rate as a result of topographic features, UAV systems are significantly less susceptible to such influences - therefore affording a greater measurement accuracy. This study ultimately concluded that a greater influence on radiation levels (determined via low-altitude aerial platforms including UAVs) was the result of source heterogeneity.
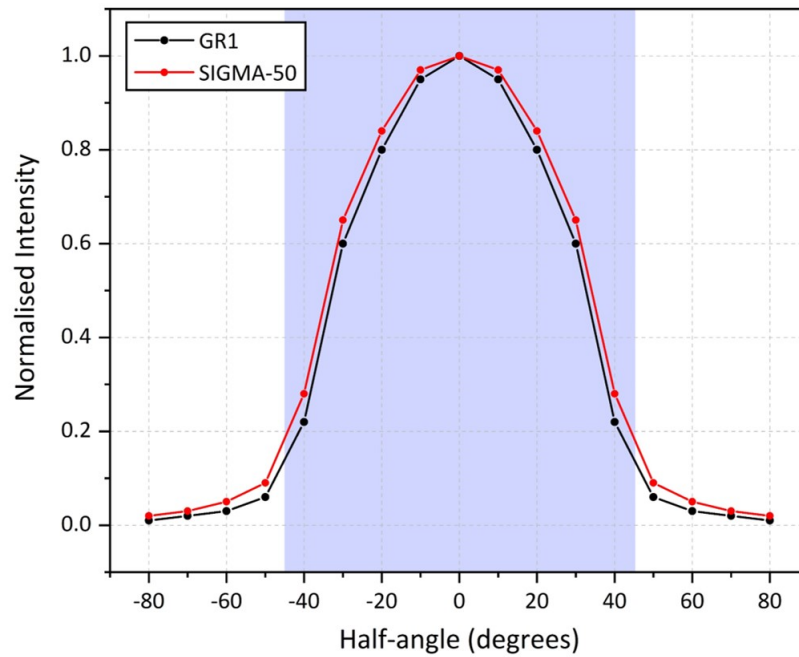
Figure 3.15: Results of GEANT-4 simulations on both GR1 and SIGMA-50 detectors, illustrating the field of view (θ half-angle) of the two detector units.

3.3.4   Survey setup

To conduct a radiation survey of a site, the area to be assessed was first inspected to ensure there existed no unforeseen or obscured obstructions with which the UAV could collide when flying autonomously. After determining the height at which the survey should be performed following a measurement of the heights of any buildings or structures to be overflown, a GPS "geo-fenced" area was set within the UAV Mission Planner™ control software [230]. Within this software, the velocity and grid-spacing at which the survey was to be performed were also selected. Although both take-off and landing were performed manually, the operation of the UAV during radiation mapping flights was conducted using the platforms autopilot system - combining inputs from the units onboard GPS, barometer and compass.

With measurement sampling at a frequency of 2 Hz, UAV radiological surveys were performed at altitudes of 3.0 m - 10.0 m (up to 15 m in circumstances with considerable on-ground features), velocities of 1.5 ms^{-1}, and with resultant grid-spacings of 1.5 m - 5.0 m using a raster survey pattern. Obstructions were overflown at a minimum height of 1 m. These parameters allowed for data collection as a number of height-scaled overlapping "circles of investigation" (Section 3.3.3), with subsequent nearest-neighbour smoothing and infilling performed, as used previously for ground-based survey results (Section 3.2.2).

3.3.5 Platform calibration and prior application

With the relationship formerly described by Duval et al., (1971) [78], equating both the detector height and the on-ground radius ("circle of investigation"), not holding at these lower survey altitudes (Section 3.3.3), the normalisation method through which data is corrected for reduced altitudes requires consideration. As discussed in Section 2.1.1, this normalisation to derive the air dose-rate at 1 m above the ground surface due to the attenuation from the air through which it passes is performed using an exponential function - a number of which are shown in Figure 2.1.

To determine if the routine exponential normalisation method was applicable to surveys at these lower altitudes (as well as to investigate a largely uncharacterised site), a study was undertaken at South Terras - a former uranium mine located 22.5 km south-west of St. Austell, Cornwall, UK.

Associated with the extensive contact metamorphism that occurred following the emplacement of the St. Austell granite, it is one part of the larger Cornubian batholith which also formed the Land's End Granite, responsible for the mineralisation at the Geevor Tin Mine and numerous other sites across south-west England. Prior to its abandonment in 1927, it is estimated that approximately 750 tons of uranium ore were produced at the South Terras site - most of which was of a particularly high grade, with up to 30% uranium by weight at many points within the primary lode [219]. Post-extraction, all processing was undertaken at the mine site, within the numerous buildings. Owing to the absence of any environmental legislation at the time, a considerable degree of legacy contamination exists across the site.

Owing to the significant topographic features that occurred across the entire site, a range of operational altitudes were employed, from 3 m - 15 m. However, in each case, an identical grid spacing of 3 m was employed alongside a velocity of 1.5 ms^{-1}. Due to the size of the site, a number of individual surveys were undertaken and combined to produce the radiological intensity map of the entire site. From the known higher-activities at South Terras than at Geevor, and to improve the overall survey duration possible with the UAV - the less-sensitive but lighter GR1 detector was attached to the gimballed aerial detection payload. To similarly permit the calibrated conversion between CPS recorded by the γ-ray spectrometer and dose-rate, a RADEX™ (Moscow, Russia) hand-held dose-meter was used to obtain measurements at points alongside the GR1.

The CPS and calibrated dose-rate map with height normalisation performed via the alternative inverse-square law of radiation dispersion from a point-source (with the intensity of radiation decreasing with the square of the distance from the source) is shown in the plots of Figure 3.16. Also identified in these plots are positions where corresponding ground measurements of radiation intensity were made to assess the differences in normalisation method (inverse-square vs. exponential). A graph detailing these results is shown in Figure 3.17.
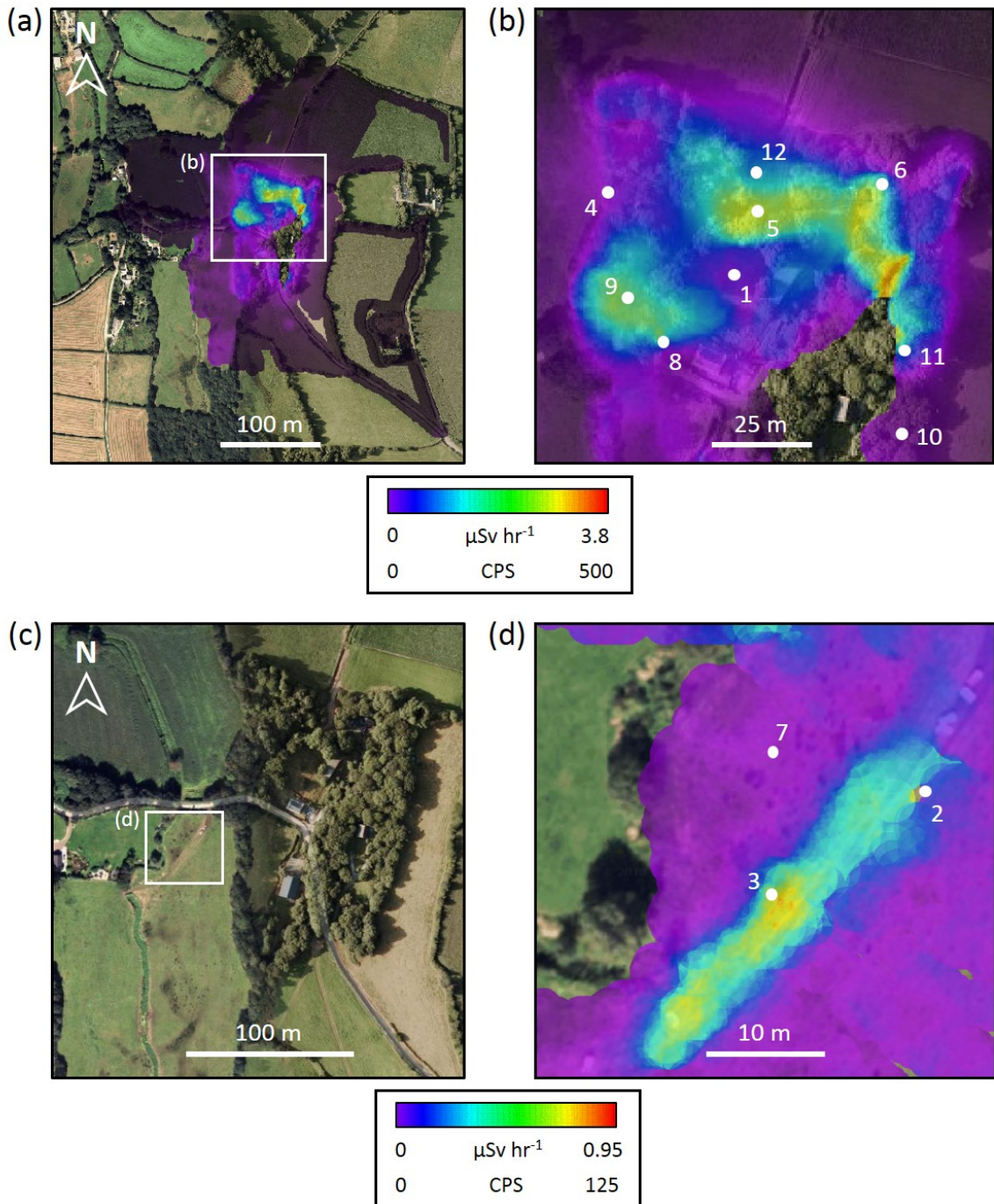
Figure 3.16: Height-normalised air dose-rate maps obtained using the UAV at the South Terras site in Cornwall, UK. A site-wide map is shown in (a), with an enlarged view of the sites centre shown in (b), alongside the location of the ground measurement points. An area to the south-west of the main site is shown in (c), corresponding to the location of a hardcore track, the results of radiation mapping over this area are shown in (d).
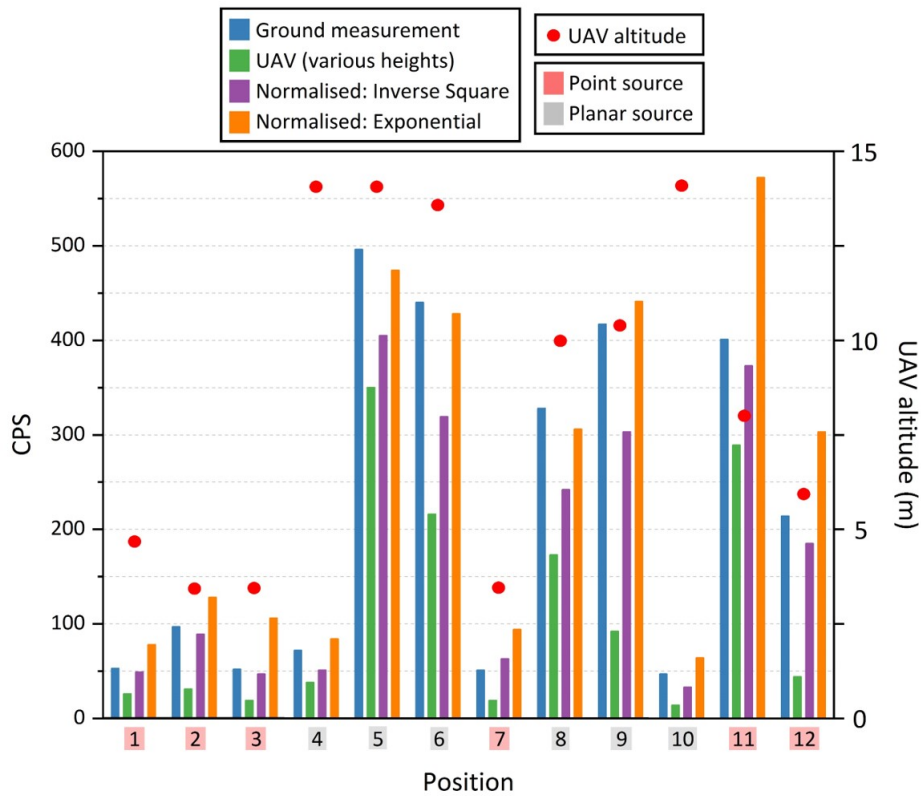
Figure 3.17: Radiation intensity and height-normalisation results from positions 1 - 12, identified in Figure 3.16.

$$intensity \propto \frac{1}{dis\tan ce^2} \qquad (3.4)$$

In this figure, values for both the on-ground CPS obtained at a height of 1 m, and the raw CPS measured by the UAV are shown. Alongside these values are shown the normalisation of this aerial data via both the inverse-square law (Equation 3.4), as well as via an exponential function, (Equation 2.1). From this plot, while a number of the measurement positions taken using the UAV were normalised accurately to ground-level readings via the inverse-square law (positions 1, 2, 3 and 12), a range of the data points were conversely better corrected via the more commonly utilised exponential function (positions 4, 8, 9 and 10).

When the location and altitude at each of these positions across the South Terras survey are analysed, however, a trend is apparent as to the most applicable height normalisation formula. For measurements taken at lower altitudes (<10 m) (position 7) and where the radiation is emitted from concentrated areas (positions 2, 3 and 11) the inverse-square law better normalises the UAV

data - defined as a "point-source" in Figure 3.17. In contrast, at locations monitored at greater altitudes - typically >10 m (positions 4 and 10), and where the radiation was more laterally extensive/diffuse (positions 5, 8 and 9), the exponential function provides a more appropriate normalisation of the airborne data - defined in Figure 3.17 as a "planar-source".

While these two height normalisation functions are applicable for the correction of data with differing source attributes (point, or the much larger, planer) and survey heights (<10 m to >10 m), the over or under-estimation provided by the alternate correction method (in comparison to the more accurate method) is not greater than ±32% in any instance. Such variations in measured activities are expected during typical airborne surveys due to source heterogeneity [110].

As the aerial surveys forming this work (in the Fukushima Prefecture region of eastern Japan) will be conducted near-exclusively at altitudes of <10 m above various surfaces, the use of point-source normalisation is, therefore, more appropriate. With these aerial radiation mapping flights focused on identifying small regions of radioactivity resulting from contaminant transport or left as an artefact following remediation activities, the sources of radiation will occur in the form of more isolated regions rather than more laterally extensive contamination bodies. In contrast to the sites examined in the UK (South Bristol and Cornwall), the "hotspot" localities within Japan will all exist within environments where a significantly elevated background activity occurs. This can be interpreted as isolated point sources superimposed onto larger (lower-activity) planar geometry sources.

By utilising these UAV systems, allowing measurements to be made at locations formerly inaccessible/impractical to workers or where dose-rate considerations for the operative may have occurred - this work details the adoption of this novel aerial mapping platform (alongside the associated ground-based system) at localities across Fukushima Prefecture. The key topics addressed as part of this thesis pertain to, (i) the mobility of contamination within the environment - including its residence, transport and likely entrapment, and (ii) the impact of restorative works - rapidly, safely and efficiently quantifying their effectiveness. Together, both topics are important in the long-term remediation of extensive portions of Fukushima Prefecture, contaminated by the March 2011 FDNPP accident.

SAMPLES AND PREPARATION

Samples analysed during this work fall into either one of two distinct categories; those smaller than 10 μm in maximum dimension (down to several hundreds of nm), and those considerably larger - greater than 100 μm in typical dimensions. These smaller particles are henceforth termed *atmospheric material* or *particulate*, while the larger are conversely termed *ejecta material* or *particulate*. *Atmospheric material* was sampled via the collection of organic species onto which the fine-scale particles became trapped or adhered. The larger material, however, was sampled directly from the ground (dust and sediment samples). Details of both sampling strategies and isolation methods are hereby discussed.

Methods presented in this chapter relating to the extraction of individual atmospheric-type particles from a bulk sample ahead of subsequent analysis have been previously published in the peer-reviewed literature:

P.G. Martin, I. Griffiths, C.P. Jones, C.A. Stitt, M. Davies-Milner, J.F.W. Mosselmans, Y. Yamashiki, D.A. Richards and T.B. Scott. "In-situ removal and characterisation of uranium-containing particles from sediments surrounding the Fukushima Daiichi Nuclear Power Plant". *Spectrochimica Acta Part B: Atomic Spectroscopy*, vol. 117, pp. 1-7, March 2016.

4.1   Atmospheric material (<10 micron)

This form of particulate consisted of fine-scale material obtained at numerous sampling localities across the Fukushima Prefecture. As a result of its small mean particle size and resulting ability to be readily-transported by an entraining air mass, the material of this type is encountered at a wide-range of distances extending out from the power plant. The distribution of this material

Figure 4.1: Photograph of typical samples from which *atmospheric material* was isolated; (left) moss samples and (right) roadside sediments.

is apparent from the previously discussed contamination plume map produced [85, 86, 154] - identified by the numerous surveys that have been performed since, and are still to this day ongoing [156, 231].

4.1.1 Sampling strategy

To obtain sufficient material for detailed analysis, multiple sampling visits were made to the Fukushima Prefecture region of western Japan. Consideration was given to ensure as best as possible that a wide-range of samples were collected from across the entire fallout-affected area. In order to fully analyse the spatial and depositional trends of the radioactive fallout, samples were taken from a variety of depositional settings, e.g. forested areas, valley floors and roadsides.

To minimise/negate the impact of both naturally-occurring and legacy contamination species from compromising the sample set, the material for analysis consisted of organic substrates found more than 1 m above the ground. Bulk samples selected for analysis were those that showed elevated levels of radioactivity when examined using a hand-held Geiger-counter. Occurring as natural "particle filters" due to their fibrous nature, these surfaces included; lichens, tree bark, mosses and dead leaves. A number of highly-textured anthropogenic surfaces (or those where radioactive material was witnessed to collect) were also sampled, these included concrete walls, gutter/drainage networks, rooftops and air-conditioning intakes (from abandoned settlements). Images of a selection of typical bulk organic samples are shown in Figure 4.1.

For organic substrate collection, a razor blade or metal spatula was used to gently loosen material from the underlying surface before being removed using a pair of sterile disposable plastic tweezers. A typical sample was approximately 3 cm × 3 cm. Additional sample material from walls, roofs and drainage networks was collected directly using disposable plastic spatulas. Each sample was then double-bagged, inventoried and a dose-rate measured before being securely packaged and shipped back to the UK for analysis using a specialist hazardous materials courier.
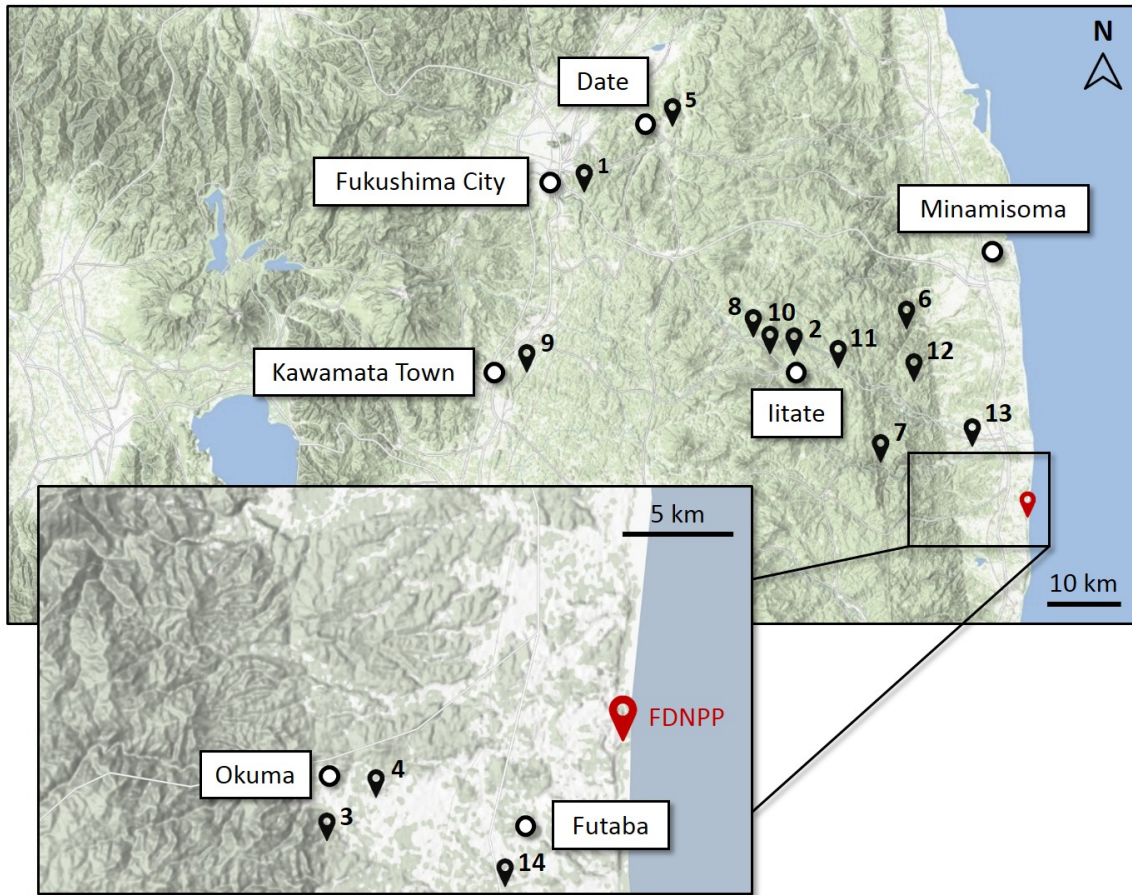
Figure 4.2: Locations at which *atmospheric particulate*-containing bulk samples were obtained. *Base-map from Geospatial Information Authority of Japan (GSI) [152].*

Prior to sampling at each locality, permission was sought from either the property owner or local official. Full protective equipment, including; FFP3 respirators, gloves and disposable outer-jackets were used whilst undertaking sampling. Such precautions were emplaced owing to the easily inhalable nature of this material [232] - consistent with precautions employed by remediation operatives within the region [155].

4.1.2   Sample inventory

A large number of organic samples were collected over the multiple visits to Fukushima Prefecture. The details of these samples are presented in Table 4.1, with the locations shown graphically within Figure 4.2. Characteristics of each of these samples are further documented in Table 4.2.

Ref.	Location	Town / City	Latitude (°N)	Longitude (°E)
1	Emataira	Fukushima	37.724482	140.487234
2	Shimohiso	Iitate	37.614174	140.708123
3	Okuma (I)	Okuma	37.400413	140.950743
4	Okuma (II)	Okuma	37.404197	140.971492
5	Kamiibuchi	Date	37.797488	140.619856
6	Dai	Minamisoma	37.604078	140.914587
7	Katsurao	Futaba	37.512471	140.816988
8	Yamakiya School	Kawamata	37.602655	140.676441
9	Kitaosawa	Kawamata	37.545626	140.427948
10	Hirokuboyama	Kawamata	37.580838	140.716738
11	Shiobite	Namie	37.565656	140.796706
12	Odakaku Kanaya	Minmisoma	37.553426	140.873597
13	Teramae	Namie	37.491576	140.981855
14	Mukaihata	Futaba	37.394940	141.004750

Table 4.1: Locations from which *atmospheric particulate*-containing bulk samples were collected.

Ref.	Distance to FDNPP (km)	Sample medium
1	58.8	Leaf/Moss
2	35.7	Lichen/Moss
3	6.0	Leaf/Moss
4	3.1	Moss
5	60.3	Leaf
6	22.8	Lichen/Moss
7	20.3	Moss
8	37.4	Lichen/Leaf
9	55.7	Lichen/Moss
10	32.9	Moss
11	25.9	Moss
12	20.3	Lichen/Moss
13	8.9	Moss
14	3.6	Lichen/Moss

Table 4.2: Characteristics of *atmospheric particulate*-containing bulk samples.

4.1.3 Sample precautions and preparation

Resulting from the largely unknown elemental and isotopic composition of the *atmospheric material* contained within the organic filter-type materials, a methodical and step-wise approach to their preparation was employed.

As for any work in which radioactive material is handled, special sample handling and processing procedures were required to comply with University of Bristol Health and Safety requirements. Due also to the fine size of the radioactive particulate contained within the samples, further care was taken to ensure any particulate was not inhaled during handling, thereby avoiding any internal expose issue. It is widely accepted that material <2.5 µm also presents a range of other potential health implications [233]. When not being analysed, all bulk samples were stored double-bagged inside a locked, shielded container. During handling of the material, to produce a sub-sample for particle isolation (Section 4.1.4), the radiation-controlled area was cleaned and monitored prior to manipulating the sample to establish background levels of radioactivity before being covered in multiple layers of a non-absorbent protective Bench-coat (VWR Ltd.). After sample manipulation, the area was thoroughly monitored and cleaned as necessary to achieve the formerly determined background.

For each of the samples, a new (sterilised) plastic spatula was used to extract a small volume (approximately 0.1 g) of the sample material onto a filter paper disc. Using the spatula alongside a pair of plastic tweezers, portions of the sample material exhibiting elevated count-rates on a GM-counter were separated from the bulk. These sub-samples were placed onto a new electron microscope pin-stub that had been ultra-sonically cleaned using acetone, HPLC grade isopropyl alcohol and finally methanol. These sub-samples of the bulk material were adhered to a microscope pin-stub using low elemental background Spectro Tab™ double-sided adhesive carbon discs (TED PELLA Ltd.). Each of these pin-stubs was then placed within its own sealed plastic sample tube to provide effective containment of the sample.

4.1.4 Particle isolation

A complete description of the methods used for the location of individual *atmospheric particulate* material from within these sub-samples is included within Section 8.3.1, as well as extensively within the aforementioned publication. This section also describes the isolation/manipulation of these isolated particles for the subsequently applied analysis methods. Details of the compositions of the particulate removed from these bulk samples are included in Chapter 7, with the subsequent analysis of U composition fragments in Chapter 8.
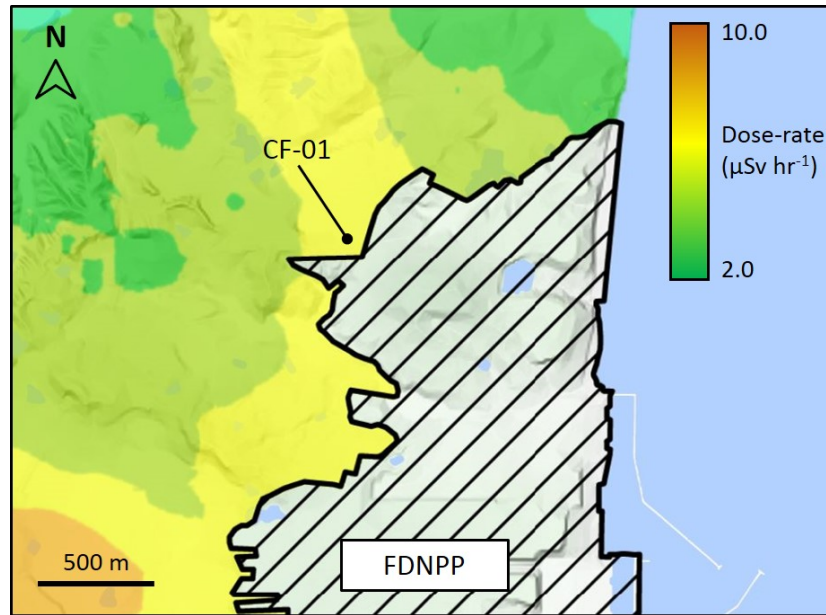
Figure 4.3: Location at which *ejecta particulate*-containing samples (CF-01) were obtained. Overlain onto the air dose-rate map as of October 2014. *From [234].*

4.2 Ejecta material (>100 micron)

The second form of particulate material, termed *ejecta material*, was also analysed as part of this thesis. This material consisted of fragments at least an order of magnitude greater in size than the *atmospheric material* formerly discussed.

4.2.1 Sampling and extraction

The sediment and dust samples containing these larger fallout particles were collected close to the FDNPP boundary (less than 2 km) in October 2014, during the fieldwork of Dr Yukihiko Satou (Japan Atomic Energy Agency - JAEA). The two sampling locations for this material are shown in Figures 4.3 and 4.4.

Identical to the sampling performed to obtain the *atmospheric material*, the bulk samples containing *ejecta material* were those that displayed notably higher radiation intensity when scanned with a hand-held radiation monitor. A series of ≈100 g samples were collected from these plant-proximal sites to extract the radioactive particles they contained.

To isolate each individual sub-mm particle, a multi-stage autoradiography process was used, the full details of which are presented in Onda et al., (2015) and Satou et al., (2016) [195, 235]. In summary; after an initial homogenisation of the clear plastic bag containing the bulk dust or sediment, it was placed onto an autoradiography scanner (imaging plate - IP). After a brief
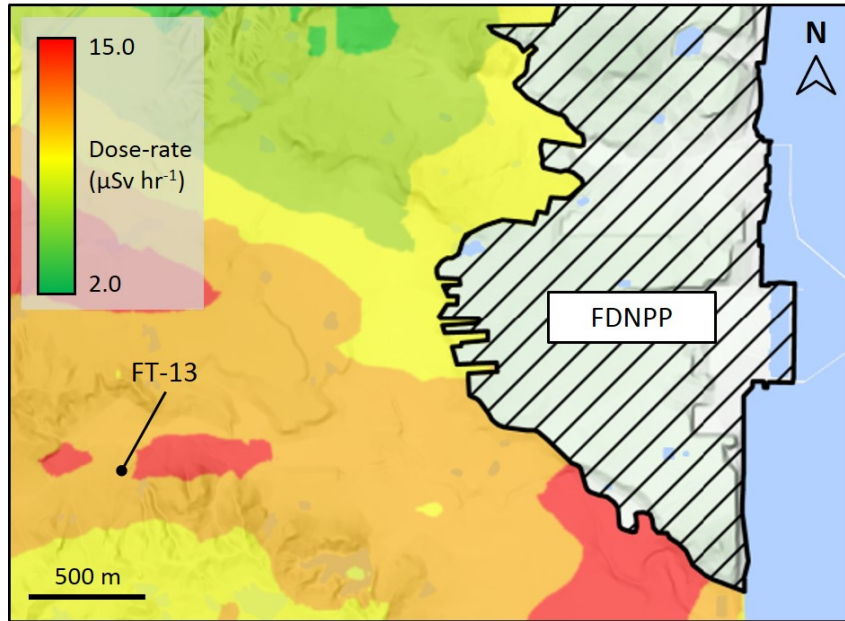
Figure 4.4: Location at which *ejecta particulate*-containing samples (FT-13) were obtained. Overlain onto the air dose-rate map as of October 2014. *From [234].*

exposure of only 5 minutes of the systems phosphor screen to the sample, only the most radioactive regions within the sample were apparent - shown as small regions of local darkening when this film was rastered by the systems detection laser. By hand, the areas not exhibiting radioactive emission were removed - with this reduced sample being then rescanned before further division and re-exposure were performed. When only a limited volume of material remained, an optical microscope alongside a manipulation arm were used to remove these most-radioactive fragments. Final confirmation of the radioactive nature of the material was made using a hand-held radiation meter. These fragments were then secured onto a piece of adhesive Kapton™ film (DuPont Ltd.) or an adhesive carbon disc for the advanced characterisation techniques discussed subsequently in this work.

4.2.2   Sample inventory

The particles provided by Dr. Satou for analysis were sourced from two sampling sites during October 2014. One group of samples (CF-01) were collected from the former Cambridge Filter Company Limited (Location: 37.437662° N, 141.022131° E) to the north-north-west of the FDNPP site. The second suite of samples (FT-13) were obtained from the west of the facility (37.471410° N, 140.999804° E), further from its perimeter boundary (in Futaba Town), but from a region shown to exhibit significantly higher levels of radiological contamination (than the sampling site of CF-01) during the proceeding aerial radiation mapping surveys [234]. This study has focused near-exclusively on the CF-01 particulate, which was observed to show a highly-complex external

morphology, alongside being invoked to have resulted from the more-northerly trending reactor Unit 1 contamination plume. Owing to the more spatially-limited extent of this plume, it has been considerably understudied in comparison to the more spatially-extensive and greater magnitude emission that is observed more westerly from the plant - invoked to have resulted from reactor Unit 2 (Section 2.2.5) [2, 236]. The ability of the *atmospheric material* to become entrained in such transporting air masses, in contrast to this significantly larger *ejecta particulate* which would rapidly fall/settle-out of any entraining air mass, provides a mechanism to explain this materials existence only at localities close to the FDNPP perimeter boundary.

5

EXPERIMENTAL METHODS

The results presented in this thesis were obtained using a wide-range of analytical equipment and an extensive suite of physical samples. This chapter details the instrumentation used as well as the specialist sample handling and preparation methods/steps.

To examine the surface, internal structure (morphology) and composition of fallout samples, the analytical techniques applied typically involve subjecting the sample to high energy beams of either electrons, ions or x-rays - with the resultant secondary signals being measured and processed as part of the analysis (with the exception, however, of the "passive" γ-ray spectroscopy).

5.1 Gamma-ray spectroscopy (γ-spec)

The physics of γ-ray spectroscopy and the detectors employed during this work were described previously in Section 3.1. The same detectors as those used during fieldwork were also employed in the laboratory to undertake sample characterisation. Both detectors were solid-state (crystal-based) and were manufactured by Kromek Ltd., the two units were:

- **GR1** - a new-generation of semiconductor-type detector composed of Cadmium Zinc Telluride (CdZnTe or CZT), 1 cm^3 in volume. Operating at room-temperature, this detector has a maximum throughput of 30,000 CPS across the energy range of 30 keV to 3.0 MeV (over 4,096 channels) and a high energy resolution of <2.5% Full Width at Half Maximum (FWHM) at 662 keV [210].

- **SIGMA-50** - a scintillator-type detector composed of thallium-doped cesium iodide - CsI(Tl). Like the GR1, the SIGMA-50 operates at ambient temperatures but possesses a greater total interaction volume of 32.8 cm^3. More sensitive than the GR1 and therefore better in

lower-activity situations, the SIGMA-50 has a maximum throughput of 5,000 CPS across the energy range of 50 keV to 1.5 MeV (over the same 4,096 channels). The energy resolution of this unit is considerably wider than the GR1 at <7.2% FWHM at 662 keV [209].

5.2   Scanning Electron Microscopy (SEM)

The fundamental principle that determines the resolution at which an image can be obtained is a direct consequence of the wavelength of the medium used to attain that image [237]. Due to the shorter de Broglie wavelength of the electron (circa. 1 nm) compared with that of visible light (400 nm - 700 nm) [238], the scanning electron microscope is able to produce images of material surfaces with nano-meter resolution - whilst optical systems are unable to surpass length-scales much below a micron.

Since their first invention in the early 1940's ahead of widespread manufacturing commencing around 1965 [237], considerable advancements have been made to the technology. Despite the progression in electron source type, the general principle and configuration of the instrument remains largely unchanged. The following sections describe the generation of the primary electron beam, its interaction with the sample and the subsequent detection of a secondary signal - including the information that this interaction can provide about the sample.

5.2.1   Theory

After the highly-focused beam of electrons exit the vertical column (described in Section 5.2.2) it interacts with the sample in the area it strikes to produce five different detectable signals, each originating at different depths from within the sample - up to ≈5 µm, (Figure 5.1) [239]. These interactions and the resultant emissions are detected by a number of different detectors, installed within the SEM. Occurring at progressively greater depths are; Auger electrons, secondary electrons, backscattered electrons, characteristic x-rays, continuous (Bremsstrahlung), and cathodoluminescence (visible) light. The three most-studied emissions and those used in the analysis in this thesis are secondary electrons (SE), backscattered electrons (BSE) and characteristic x-rays (EDX), the interaction mechanism responsible for the generation of each is shown in Figure 5.2.

The image resolution attainable by the SEM is further demonstrated in Figure 5.1. Combined with the beam current; which controls the spot size and therefore the diameter of the surface interaction, the accelerating voltage additionally determines the electron beams interaction volume (depth penetration) that occurs. Although also largely dependent on the material, a higher beam current and accelerating voltage will produce lower resolution and less surface-sensitive images than if lower values for both parameters were used.

Electron beam

Auger electrons
(≈1 nm)

Sample surface

Secondary electrons (SE)
(≈10 nm - 50 nm)

Backscattered electrons
(≈1 μm)

Characteristic x-rays (EDX)
(2 μm)

10 kV

Continuous x-rays
(Bremsstrahlung)
(3 μm - 5 μm)

Cathodoluminescence (CL)
(>4 μm)

20 kV
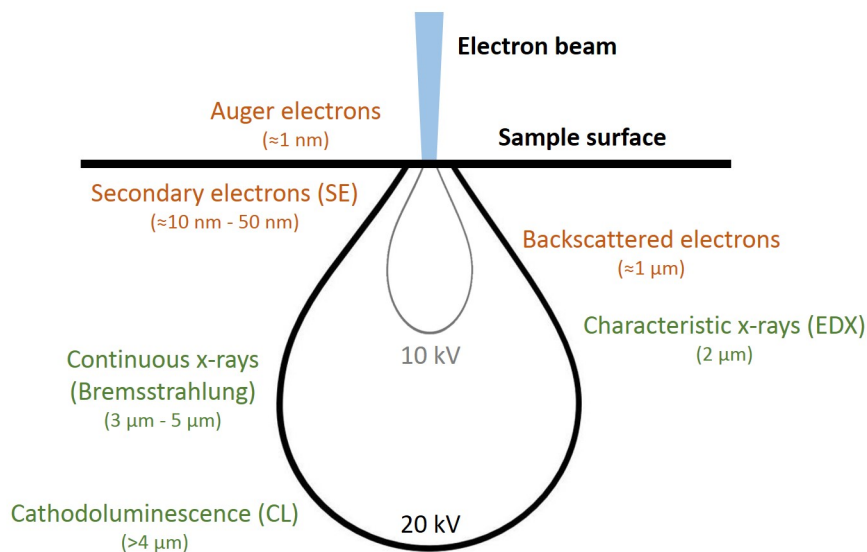
Figure 5.1: Schematic of the various depths from which the different emission signals are generated by the primary (incident) electron beam. *Modified from [239].*

Secondary electron (SE) imaging

When the high-energy incident electron beam collides with the electron cloud that exists at the samples surface, inelastic scattering occurs as secondary electrons are ejected - with the parent atom ionised as a result, (Figure 5.2 (a)). Due to the high kinetic energy of the primary beam and the incomplete transfer of this energy to the secondary electrons, these electrons possess only a fraction of energy of the primary beam (<50 eV), which itself loses very little in comparison. Multiple low-energy secondary electrons can be generated and released from the sample as a result of the collision cascade that occurs in the uppermost 10 nm of the sample. Due to their shallow depth of this interaction, the influence of surface topology greatly influences the generation of the secondary electrons. When rastering the electron beam across an area of the surface, it is possible to generate a grey-scale (secondary electron yield) image of the sample that depicts its fine-scale topography.

Backscattered electron (BSE) imaging

Whereas SE imaging relies on measuring the ejection of excited secondary electrons from a sample, backscattered electrons are the result of the re-emission of the same primary incident electron back out from the sample. Instead of colliding with an atoms electron (and resultantly ionising the atom), if the high energy incident electron of the primary beam is "scattered" back out of the sample upon interaction with the atom's nucleus, then it is termed to have been "backscattered" (Figure 5.2 (b)). The size of the nucleus being impinged will determine the amount of backscatter
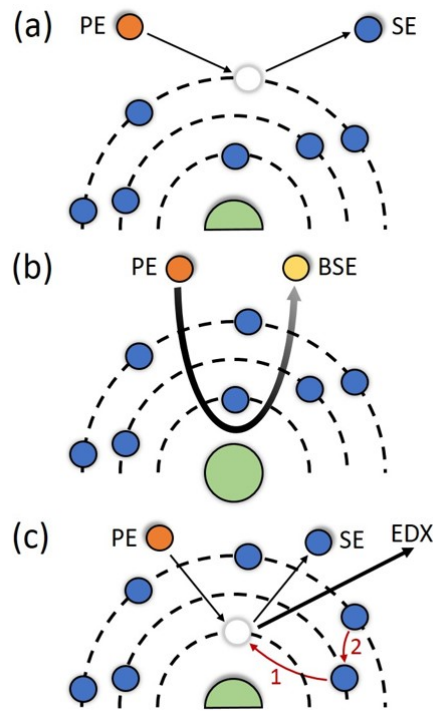
Figure 5.2: Schematic of the three principal electron beam producing signals; (a) secondary electrons (SE), (b) backscattered electrons (BSE), and (c) characteristic x-rays (EDX).

that will occur, with larger nuclei (great atomic number) producing more electron scattering. These backscattered electrons are characterised by an escape energy >50 eV and originate from depths of approximately 1 μm. Resulting from the varying amounts of backscatter that occurs from different mass atoms, such backscattered electrons provide an imaging method that is highly sensitive to the sample's composition and is ideally suited to identifying high Z-number elements/particles (e.g. U and Pu) contained in a low Z-number background.

Energy dispersive x-ray (EDX) analysis

Originating from depths deeper than both secondary and backscattered electrons (circa. 2 μm), characteristic x-rays (or EDX) provide quantifiable compositional information relating to the elemental make up of the sample (Figure 5.1). Upon interaction with the primary electron beam, a secondary electron is ejected, resulting in a production of valency (electron vacancy) that is rapidly filled by an electron relaxing from a higher energy orbital (Figure 5.2 (c)). This demotion of an electron to a lower energy state yields a surplus of energy which is released in the form of an x-ray. The x-ray will have a characteristic energy specific to the electron orbital and therefore the atom from which it originated. With electrons ejected from all atomic shells, there exists a characteristic energy spectrum for each element.

Electron source

Electron path

Condensor

ESB detector
Filter grid

Beam-booster ™

In Lens detector
Objectives

Magnetic lens

Electrostatic lens

Scan coils

Sample
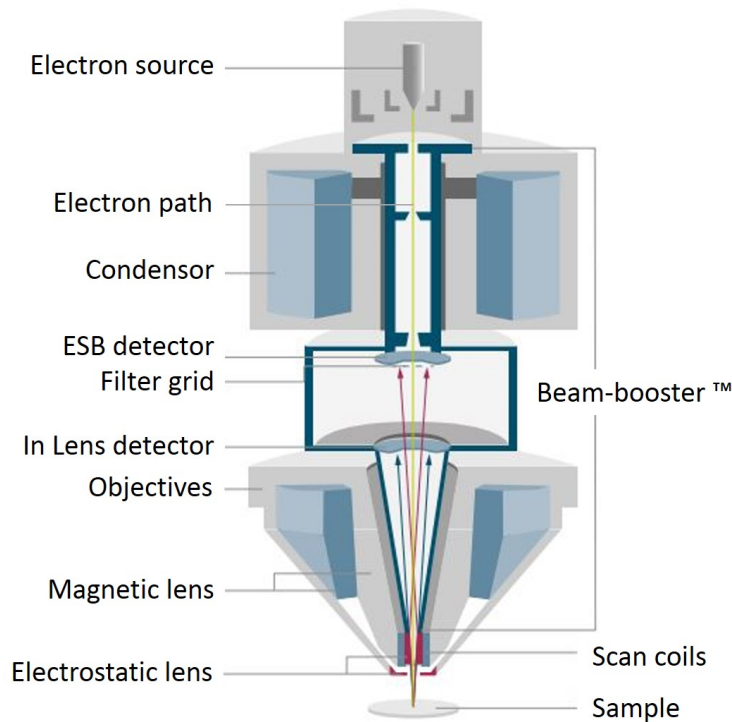
Figure 5.3: Schematic of a field emission gun (FEG) scanning electron microscope column.
Modified from [240].

5.2.2 Experimental instrumentation

Electron generation and beam control

Although able to attain highly-detailed images with nanoscale resolution, the principles behind the operation of an SEM are inherently simple. At the top of the column, electrons are generated in a concentrated beam and accelerated down the column, passing through a number of focusing lenses to be electronically rastered over the sample's surface - a schematic is shown in Figure 5.3.

The entirety of an electron microscope is held under a vacuum (of varying levels) to allow for the uninterrupted primary electron beam to travel through the system to the sample while also allowing for the various secondary signals produced to be transmitted and detected without (significant) losses. As is typical of most modern instruments, the source used to generate the incident electron beam is a field emission gun or tip (FEG). Through a process known as "tunnelling", a sharp (<50 nm) chemically etched tip, typically of W coated in a 5 nm thickness of zirconium oxide, is strongly biased with a high negative potential (-9 kV) while a nearby alternately charged anode is used to strip (draw) electrons away in order to produce the initial (unrefined) electron beam [239].
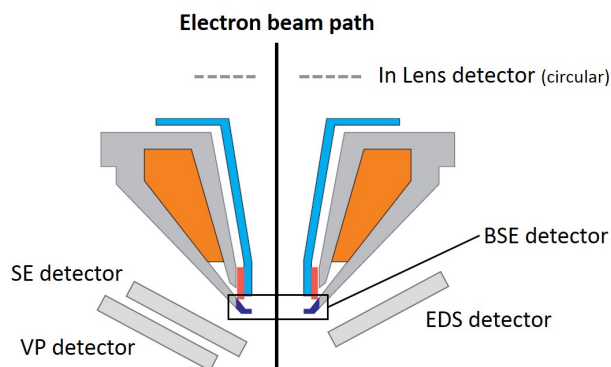
Figure 5.4: Schematic of the detectors installed within the Zeiss SIGMA™ HD SEM, showing their position relative to the lower portion of its optics. *Modified from [240].*

The acceleration of this beam down the column towards the sample then occurs, where it is focused and shaped using a condensor lens before passing through the desired physical aperture, milled into a Pt film. This selection of apertures both refines the beams size (and hence the beam current) incident onto the sample as well as removing any stray electrons that remain after passing through the large condensor lens. Magnetic objectives (and for this instrument a "beam-booster™") are used to further refine and accelerate (or decelerate in some circumstances) the beam [240]. Scan coils and magnetic lenses positioned near the base of the column control both the rastering of the electron beam over the samples surface, and also its stigmation (roundness). An electrostatic lens at the very base of the column serves to further refine the electron beam.

Signal detection

To analyse the sample, the emissions that are produced following the primary electron beams interaction must be detected and quantified. A schematic of the detector setup installed within the electron microscope used for this PhD research is shown in Figure 5.4.

Secondary electrons

The secondary electrons (those with energies less than 50 eV) are detected using a standard Everhart-Thornley detector [241]. By applying a low bias voltage (+300 V to -300 V) to a grid across the front of the detector, the higher energy (backscattered) electrons are not attracted - in contrast to the secondary electrons, which having entered the detector, are rapidly accelerated by a high bias voltage (circa. 15 kV) to a scintillator detector. After impacting the scintillator near the front of the detector, photons are produced which then travel along the detectors cylindrical light-guide towards a photomultiplier. This photomultiplier then amplifies and converts the photon signal into an electronic one, allowing for an image to be constructed [239].

An Everhart-Thornley detector, however, cannot operate outside of a high-vacuum environment. To detect secondary electron emissions within a reduced-vacuum, a Variable Pressure (VP) detector is alternatively used (Figure 5.4). Rather than detecting secondary electrons, this system detects the photons that are generated as a result of the ion cascade when electrons collide (and ionise) residual gas molecules within the microscopes chamber. A greater volume of water, air or nitrogen in the chamber results in an increased likelihood of such collisions and therefore an enhanced signal [240].

Backscattered electrons

To detect the higher energy (>50 eV) backscattered electrons, an Everhart-Thornley detector is insufficient, due principally to the angle at which it exists - but also its bias grid [241].

Typical of backscattered electron detectors, the Carl Zeiss four-quadrant backscattered electron detector (Four-quadrant CZ-BSD™) consists of a ring of silicon dioxide semiconductor pixels located at the base of the electron column (shown in Figure 5.4). Identical to the means by which characteristic x-rays are detected (detailed below), the detector uses the production of electron-hole pairs within the material and their corresponding energies to generate a grey-scaled image. A thin coating on the detector surface discriminates against lower energy electrons interacting with the SiO_2 detector by shielding their passage [240].

With backscattered electrons ejected near-vertically from the sample, the detector is positioned horizontally - as a consequence, both sample tilt and topographic imaging are not possible [239]. Unlike the Everhart-Thornley detector for secondary electrons, the backscattered electron detector can operate in low-vacuum/environmental modes.

Characteristic x-rays

The characteristic x-rays that are produced via the interaction of the electron beam with the sample are analysed via energy dispersive spectroscopy (EDS). To traditionally detect the emitted x-rays, a Peltier-cooled single-crystal of lithium-doped silicon (now increasingly replaced with silicon drift detectors - or SDD) is used, shown schematically in Figure 5.5. When the incident x-ray enters the crystal, its energy is absorbed through an ionisation event - leading to the production of an "electron-hole" pair. By applying a high bias voltage to the contacts on either side of the crystal, these hole and electron pairs are drawn to alternate faces of the crystal, resulting in the production of an electrical signal pulse. This signal (pulse) voltage is directly proportional to that of the energy of the x-ray that produced it, with a plot of this intensity (x-ray energy) versus frequency constituting an EDS spectrum. This EDS analysis is quantifiable for elements with an atomic (Z) number greater than Li. Cooling of the crystal is required to reduce
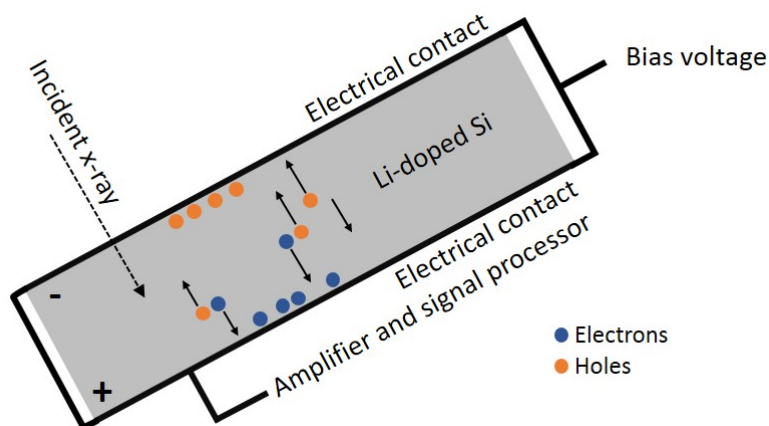
Figure 5.5: Schematic of a traditional Li-doped EDS detection system, now more commonly replaced with SSD-based units.

the electrical noise that would otherwise saturate the detectors counting electronics. Previously undertaken cryogenically, it is now more typically performed via Peltier (thermoelectric) stages.

Operating alongside the beam control software of the SEM, the EDS system used in this study was operated in three modes:

- **Point**: obtains a spectrum at a point (single or multiple) or a defined region of interest on the sample surface.

- **Line-scan**: moving the beam along a pre-selected linear portion of the sample to determine changes in elemental concentrations.

- **Mapping**: systematically rastering the beam over a user-defined region of the sample to map an elemental (or phase) distribution.

Instrument

The instrument used during this work was a Zeiss SIGMA™ HD Variable Pressure (VP) system controlled using the SmartSEM™ software. Attached to which was an Octane Plus™ Si-drift EDS detector from EDAX (Ametek) Ltd., with control and data analysis performed via the TEAM™ software platform. This software contained the necessary algorithms to undertake the required ZAF (atomic number, matrix-related x-ray absorption, and internal fluorescence) spectrum/compositional correction of the EDS results [242]. Also installed onto this instrument, within the microscope chamber, was an MM3A™ Micromanipulator from Kleindiek GmbH [243]. Capable of movement steps of the systems fine needle in increments of mm down to nm, the usage of this manipulation system and the SEM instrument are detailed extensively in the subsequent experimental chapters.
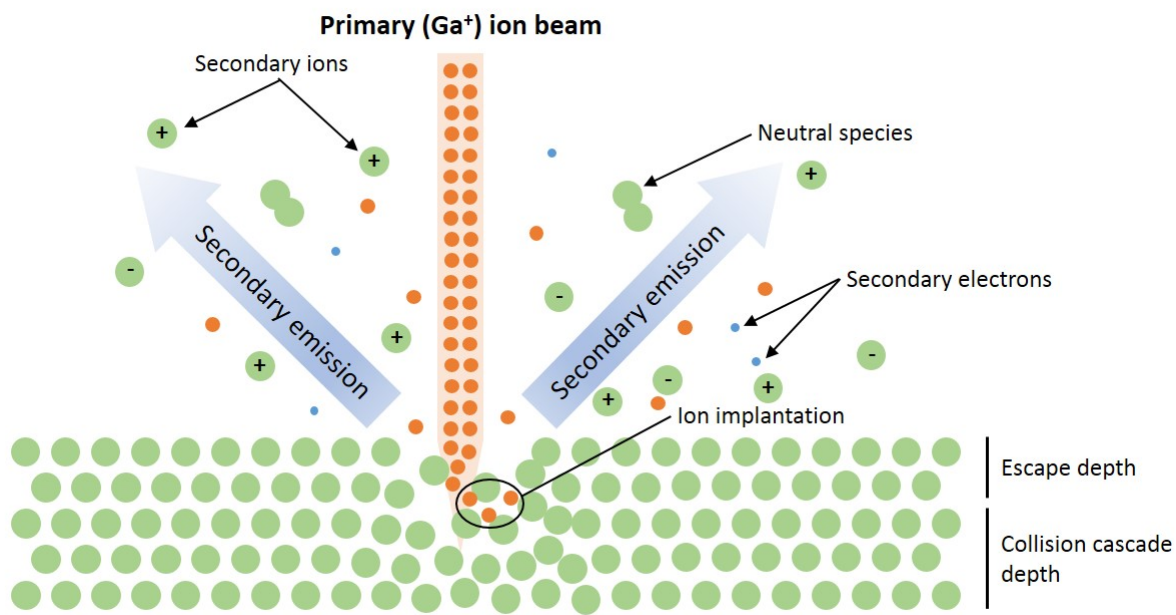
Figure 5.6: Schematic illustration of the interaction of a primary ion beam with a surface, with resultant secondary emissions.

5.3 Focused Ion Beam (FIB)

Focused ion beam (FIB) instruments entered commercial manufacturing approximately a decade after electron microscopes, with their development employing liquid metal ion sources (LMIS) pioneered in the work of Seliger et al., (1979) [244]. Unlike an SEM, a FIB uses ions, typically Ga^+ [245], although other ions are becoming increasingly widely utilised (e.g. He^+, Ne^+, Xe^+ ,and Ar^+). Due to their greater mass (and size) than electrons, the incident ion beam has a greater kinetic energy, therefore is destructive and is subsequently used for removing small volumes (nm^3 to μm^3) of material from a surface to "mill" a section often with a smooth, damage-free face to investigate a samples interior structure.

5.3.1 Theory

Like an SEM instrument, a FIB must also operate under a vacuum for the primary beam to travel unimpeded to the sample as well as for the secondary emissions generated to be detected. Through a mechanism near identical to that of an SEM, the incident ion beam bombards the samples surface, with the interactions (elastic and inelastic) and ionisations, resulting in a cascade of a range of secondary particles - including secondary electrons and ion fragments (Figure 5.6) [246].

Of the range of material ejected, the "lightest" portion - the secondary electrons, can be detected as per a scanning electron microscope to obtain an ion-contrast image of the sample. The other
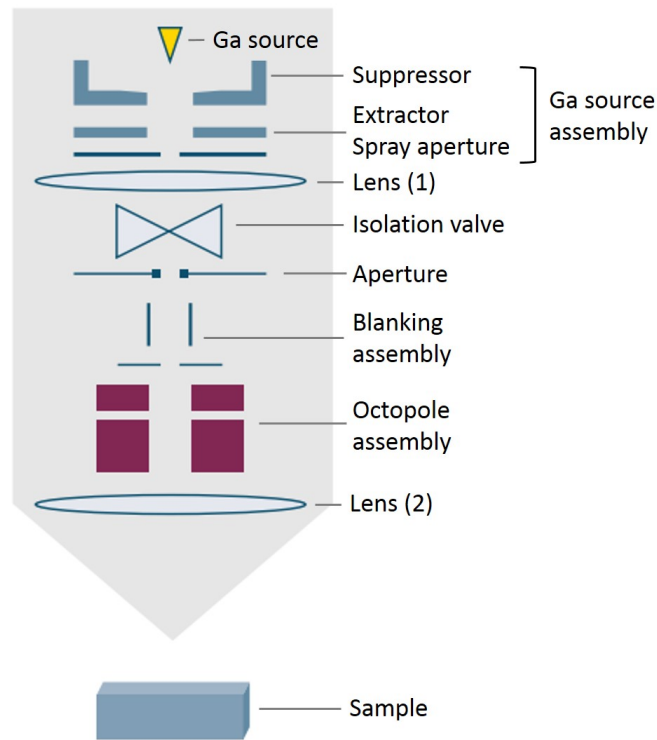
Figure 5.7: Schematic of a focused ion beam column. *Modified from [250].*

(heavier) ejecta species consist of neutral atoms or charged ions. These charged secondary particles can be detected and analysed (a technique known as secondary ion mass spectrometry - SIMS, to determine isotopic composition), or used in surface etching, material deposition or for ion-implantation [247]. This implantation (Figure 5.6) is desired within some applications (i.e. semiconductor fabrication doping [248]) but is an undesirable artefact in the compositional analysis of an ion beam prepared sample surface. Owing to its versatility, the FIB instrument is a widely utilised tool within materials science and wider industry [246], principally as a method through which to prepare samples for further analysis - the primary being transmission electron microscopy (TEM).

5.3.2 Experimental instrumentation

Ion beam generation and control

With a similar setup to an SEM, the schematics of a FIB column are shown in Figure 5.7. Like an SEM, the instrument is held under a vacuum to allow for the production of a highly-focused beam and to permit for its passage all the way to the sample's surface. Unlike an SEM, however, the ion beam formed at the top of the column is obtained from a liquid metal source [245, 249].

Such a LMIS is formed of a filament of the high melting point element tungsten, that is connected to a microscopic source of solid Ga metal. By applying a high voltage between the source and the nearby extractor (heating the Ga metal), a Taylor cone is formed, with the metal "flowing" to the filaments tip [251, 252]. This high-voltage (approximately 8 kV) results in the generation of an electric field, with the ionisation and subsequent emission of the Ga^+ ions [253].

After the release of Ga^+ ions, they are accelerated down the instrument column through a number of components to focus and refine the beam (Figure 5.7) [245]. After passing through the first set of Einzel lenses (which control the resultant beam current by applying a voltage between plates through defining a magnetic field), there occurs both physical apertures to define the beam size as well as an assembly to "blank" the destructive beam from further progressing down the column without having to suspend source emission. A magnetic assembly consisting of a quadrupole and an octopole (or two octopole magnets) are then used to manipulate the beams stigmation as well as raster the beam onto the sample. A final set of Einzel (plate) lenses act to finally focus and refine the incident ion beam.

As for an SEM, by increasing the current of the beam - greater degrees of sample interaction occur. Described more comprehensively within Section 5.3.3, at low beam currents (pA), good quality sample imaging is possible without significantly degrading the material's surface by material removal. Using higher beam currents (nA), however, results in the extensive milling of the sample - with greatest extraction (removal) rates at the highest attainable beam currents (approximately 20 nA).

Signal detection

The signals detected within a FIB to yield an image of the sample are the same as those for SEM imaging. Upon interaction of the primary ion beam with the surface, secondary electrons are ejected alongside a range of other particles (Figure 5.6). These are detected using a side-mounted Everhart-Thornley detector.

Instrument

The instrument used during this work was an FEI Helios™ NanoLab 600i DualBeam system, controlled using the FEI NanoLab™ software interface. This system incorporated a vertical FEG electron column with a coincident side-mounted Ga^+ ion source allowing for the simultaneous ion-milling and electron beam imaging of samples. Like the Zeiss SIGMA™ HD SEM, both an EDS detector (XMAX™ 50 mm^2 from Oxford Instruments Ltd.) was installed onto the instrument for compositional analysis of samples as well as a Kleindiek GmbH MM3A™ Micromanipulator [243] - used extensively in the in-situ preparation of TEM (foil) samples (Section 5.3.3).

5.3.3   Sample fabrication

The primary use of the FIB instrument during this work was the ion beam sectioning of samples. A further use centred on the related preparation of thinned TEM foils. A sequence of steps was performed to produce a high-quality surface suitable for both imaging and compositional analysis.

To protect the surface of the region of interest from the highly-damaging ion beam, a thickness of Pt (approximately 0.5 μm) was first deposited at low beam currents of approximately 90 pA, and 15 kV accelerating voltage. For the succeeding bulk material removal, a high-energy (2.7 nA - 6.5 nA, and 30 kV) stepped ion beam cut was used - ending some distance from the desired final vertical surface. A series of progressively reduced ion beam energies were then used to remove progressively smaller volumes of material and any "curtaining" artefacts produced from proceeding high-energy sectioning, gradually approaching the desired final vertical (cut) surface.

5.4   X-ray analysis

Existing at the higher energy portion of the electromagnetic (EM) spectrum, x-rays were famously first discovered by the German physicist and mechanical engineer Willhelm Röntgen at the end of the 19th century, using a simple cathode-ray tube setup [198]. Over the last 100 years, however, considerable advancements have been made in x-ray generation and associated x-rays optics - allowing for better-focused, higher energy and more intense (brighter) x-ray beams to be attained. Owing to the wide range of analytical techniques that employ highly-penetrating x-rays to probe a sample, applications extend out into the medical, aeronautical and materials research fields. During electron or light microscopy analysis of a sample, only the outermost surface of a material can be studied. The application of penetrating x-rays, however, allows for the three-dimensional visualisation of a sample that would only be possible through destructive FIB sectioning.

Consisting of electromagnetic radiation, x-rays are formed of transverse waves with perpendicular electric and magnetic component vectors, like all other forms of radiation that exist as part of the EM spectrum. While some debate exists, x-rays are classified as having wavelengths (λ) between 0.01 nm and 10 nm, an energy (E) of 100 eV - 100 keV, and frequencies (f) of 3×10^{16} Hz - 3×10^{19} Hz. A further division between "soft" (<5 keV) and "hard" (>5 keV) x-rays also exists.

5.4.1   Theory

When x-rays are incident onto a solid sample, one of three phenomena may occur; (i) *absorption*, or scattering, which can be subsequently described as either, (ii) *coherently (elastically)*, or (iii) *incoherently* (also known as *Compton scattering*). These phenomena are the result of the interaction between the rapidly-oscillating electric field of the propagating x-ray and an atoms surrounding electron orbitals.

Absorption

If the energy possessed by the photons of the incident x-ray is absorbed by the electrons of the sample, then the transmitted (outgoing) x-ray will exhibit a lower energy (and longer wavelength). If the atom is ionised, then the interacting (impinging) photon will cause the ejection of an outer-shell electron. Existing briefly in a state of surplus energy, the atom will return to its stable ground-state configuration through the emission of a photoelectron alongside the demotion of a higher energy electron into a lower energy orbital (this mechanism is the same as for radiation detection, described formerly in Section 3.1).

Coherent (elastic) scattering

During this interaction mechanism, if the electrons orbiting the atoms of the sample oscillate at the same frequency as the electric field of the incident x-ray (photon), then simultaneous acceleration and deceleration of these electrons will occur. These electrons will resultantly emit x-rays at the same wavelength and frequency as the incident beam. With no energy being lost as a result of this interaction, it can also be termed *elastic*.

The term *coherent* arises from the way through which the scattered photons interact with one-another, emitted as spherical waves away from the centre of each atom. When each of these waves are "in-phase" with one another, constructive interference results - producing a greater wave amplitude. Out of phase waves, in contrast, result in destructive interference. It is this constructive interference produced by the surface of a crystalline solid that results in the signal analysed through x-ray diffraction (XRD).

Incoherent (Compton) scattering

While *coherent (elastic)* scattering results in the complete transfer of incident photon energy - with the emission of a photon with the same wavelength and frequency, during *incoherent (Compton)* scattering, however, kinetic energy is lost in the photon-electron energy transfer. This results in the emission of a photon of lower energy (and correspondingly longer wavelength).

5.4.2 X-ray Fluorescence (XRF)

As a consequence of the multiple electron shells (and sub-shells) that surround an atom (e.g. K, L, M and N), numerous characteristic emission peaks exist, each occurring at discrete energies.

To generate this fluorescence emission from a sample, the incident x-ray beam must exist at an energy greater than the ionisation energy of that atom [239], an energy of 20 kV is typically used to excite atoms up to and including the actinides. For the detection of a fluorescence (photon) signal as the incident x-ray beam is translated over the sample, solid state detectors (over older

gas-filled units) are typically employed - with single-crystal Si-drift detectors used extensively in both laboratory and synchrotron-based studies. Identical to detector systems used for EDS analysis, the energy of the incident (ejected) photon, absorbed by an atom within the detector (and transmitted through the crystal) is directly proportional to the charge output by the detector.

5.4.3 X-Ray Tomography (XRT)

Whereas serial FIB sectioning combined with electron imaging and EDS analysis represents one method through which to derive information about the internal form and composition of a sample [250], it is not only destructive but possible only on relatively small sample volumes. Such three-dimensional visualisations are potentially unrepresentative of the bulk sample material. Rather than using electrons or ions, x-ray computed tomography - typically referred to as x-ray tomography (XRT) has become an established and highly-versatile technique through which to non-destructively study the microstructure and composition differences within samples [254].

To generate a three-dimensional XRT rendering, the sample is positioned within a collimated x-ray beam, in front of a solid-state x-ray detector/camera. Owing to the previously described absorption phenomena, a change in the intensity ratio of the x-ray transmitted through the sample will occur due to its interactions with regions of different density within a heterogeneous sample. Microstructural features (of low density) such as cracks, pores and voids within the sample will display significantly less attenuation than regions composed of solid (denser) material. By rotating the sample through 180° (or 360°), the two-dimensional radiograph images (slices) from each projection can be computationally rendered to yield a volumetric reconstruction of the entire sample [254].

A property central to XRT is the materials *linear attenuation coefficient* (μ), which is employed within the *Beer-Lambert Law* (Equation 5.1), where I_0 = incident beam intensity, I = transmitted beam intensity, and x = sample thickness. The linear attenuation coefficient is a function of the energy of the x-ray beam in addition to the density of the material and atomic (Z) number. Such coefficients have been determined for a range of materials, compounds and mixtures [65].

$$\frac{I}{I_0} = e^{(-\mu \cdot x)} \tag{5.1}$$

Alongside both the x-ray source and detector, all tomography instruments include a rotating stage to accurately position the sample through the full range of orientations. Combining accurate positioning of the sample with better-focused x-rays and greater numbers of radiograph projections (employing increased computing power) has allowed for the spatial resolution attainable via both lab and synchrotron-based XRT to increase significantly, to voxel (pixel) resolutions of below 10 nm [255].
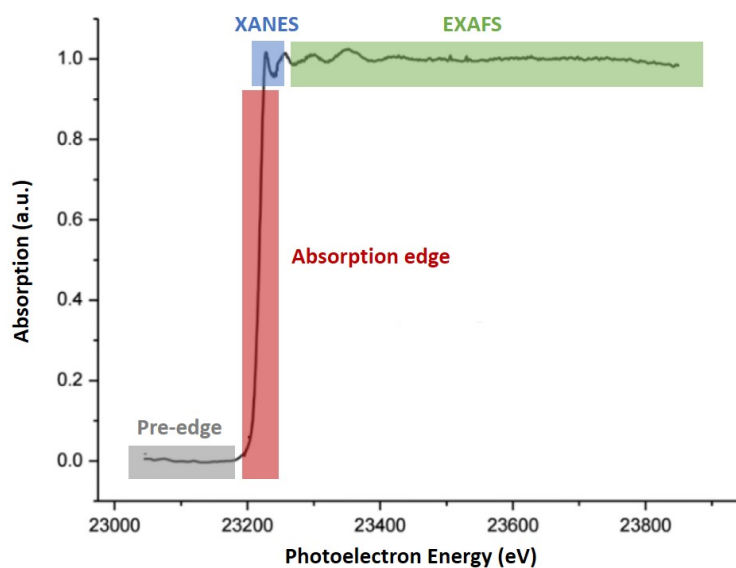
Figure 5.8: Schematic representation of a typical XAS spectrum (at the Rh K-edge), illustrating the pre-edge, absorption edge, XANES and EXAFS regions. *Modified from [257].*

5.4.4 X-ray Absorption Spectroscopy (XAS)

Owing to the intricate energy-dependent behaviour associated with an atoms atomic structure, inter-atom bonding and coordination chemistry; x-ray absorption spectroscopy (XAS) permits for the fine-scale differences associated with an elements absorption edge to be examined [256]. Despite such an atomic property having first been observed in 1918 and quantified in the years that followed [257], it was the mainstream usage of XRD as well as the absence of synchrotron facilities to offer XAS analysis that led to its usage being dwarfed by diffraction studies.

Contrary to XRD, XAS does not require a long-range crystallographic order to attain a signal, being able to determine the atomic ordering of a material irrespective of its chemical or physical state [258]. This spectroscopy method provides details of the inter-atomic spacings (up to an atom-atom separation of 5 Å), the oxidation states as well as the number and type of the atoms that surround the central, absorbing atom (its coordination environment). The ability to finely tune the incident x-ray energy allows for XAS to be a highly-selective technique, permitting the analysis of the state of individual elements within a sample. Alike to other x-ray analysis techniques, XAS relies on the photoelectric effect (described with respect to radiation detection in Section 3.1.1), resulting from the ejection of a photo-electron in response to an x-ray stimulus.

Unlike previous x-ray techniques, however, a double-crystal (typically Si) monochromator is used to precisely vary the energy of the photons incident onto the sample across a user-specified energy range. When this energy is equal to an atoms core-shell binding energy, a marked rise in the

energy absorption occurs (shown graphically in Figure 5.8), with the production of the *absorption edge*. Such edges are observed for each of the core electron sub-shells [256]. Centred around this rapid rise in absorption, the XAS spectrum can be divided into three separate regions; *pre-edge* (of limited use), *x-ray absorption near edge structure (XANES)* and *extended x-ray absorption fine structure (EXAFS)*.

The **Pre-edge** is the energy region immediately proceeding the absorption edge and is the least-informative of all the regions, whereby the impinging photons do not possess the energy required to induce an ionisation event. These photons do, however, have sufficient energy to cause the excitation of a low-energy 1s electron into a vacancy within a higher energy orbital. Only information pertaining to coordination chemistry on the very local scale (<3 Å) from the excited atoms can be obtained from this portion of the spectrum [257]. As a consequence, this portion of the spectrum is seldom examined.

5.4.4.1   X-ray Absorption Near-Edge Structure (XANES)

At energies immediately above the sharp absorption edge (up to approximately 30 eV above the peak), occurs the region defined as the XANES. This region is representative of the photoelectron transitions into various unoccupied, higher energy bound (but not continuum) states [198]. As a consequence, XANES is indicative of chemical bonding, in addition to the absorbing atoms oxidation state [257]. This is important in the current work, for example, defining the oxidation state of U in an unprovenanced sample to invoke its likely origin.

5.4.4.2   Extended X-ray Absorption Fine Structure (EXAFS)

Extending into the higher energy portion of the XAS spectrum, the EXAFS incorporates energies from 30 eV up to 1,000 eV above the absorption edge (Figure 5.8) [198]. At these higher energies, the promotion of the photoelectron into the higher energy continuum band is observed. Representing greater separations (distances) from the absorbing atom, the EXAFS portion of the XAS spectrum is independent of the influences contained with the XANES region (chemical bonding). EXAFS conversely provides information on the atoms coordination number, interatomic spacings as well as details of the host material structure and order/disorder [257].

5.4.5   X-ray sources and experimental instrumentation

To attain x-rays for use in experiments, two types of source exist; either laboratory-based or the larger, higher fluence and greater resolution synchrotron sources. During this study, both forms of x-ray source were used.

5.4.5.1 Laboratory-based

Despite being significantly smaller than synchrotron sources - therefore producing considerably lower source intensity, otherwise termed flux (photons per second); modern laboratory-based systems are capable of providing not only highly-focused x-rays for sample analysis but also tunable energies, often over ranges exceeding those available at synchrotron facilities [254, 259].

X-rays are produced in a laboratory system using x-ray tubes - with the resultant radiation being highly monochromatic (of a single wavelength) [260]. Through accelerating, under vacuum, electrons from a high-temperature and high-voltage cathode towards a positively charged anode (typically composed of W, Mo or Re), interactions occur to yield x-rays with a discrete energy spectrum (dependent upon this anode "target" material). The primary mechanism ($\approx$80%) by which x-rays are produced, is via Bremsstrahlung (or "Braking") radiation [260]. As a fast electron emitted from the cathode approaches the nucleus of the target metal anode, it is slowed, with this loss in energy resulting in the emission of an x-ray photon equal to that energy. If an electron, however, interacts with the targets nucleus, then a characteristic x-ray is produced (Section 5.2.1), with these x-ray energy peaks superimposed onto the energy continuum of the Bremsstrahlung.

Zeiss Xradia-520 Versa™

Laboratory-based XRT was performed using a Zeiss Xradia-520 Versa™ x-ray microscope - a photograph of which is shown in Figure 5.9. With a true spatial-resolution of <700 nm, a minimum attainable voxel of 70 nm is possible on the instrument [261]. Samples were positioned onto the instruments three-axis rotational stage and irradiated with a collimated x-ray beam produced by a micro-focus Mo x-ray source at incident energies of up to 160 kV. Transmitted x-rays were detected and quantified using a Zeiss high-efficiency x-ray detector mounted behind the sample. One of twelve source filters is used to tune the energy spectra of the incident beam by removing low energy tails (via attenuation).

A user-defined step-size of the stage is selected to achieve the appropriate level of spatial resolution in the desired time-frame with appropriate exposure times to 1 second - 40 seconds. The level of detector, sample and source separation is also tuned to facilitate the desired spatial resolution (increased beam divergence occurs at larger separations). Control of the microscope was undertaken using the instruments Scout-and-Scan™ control software, with the associated XM3D-Viewer™ software used to render and visualise the results in the instruments native "Xradia" data format.
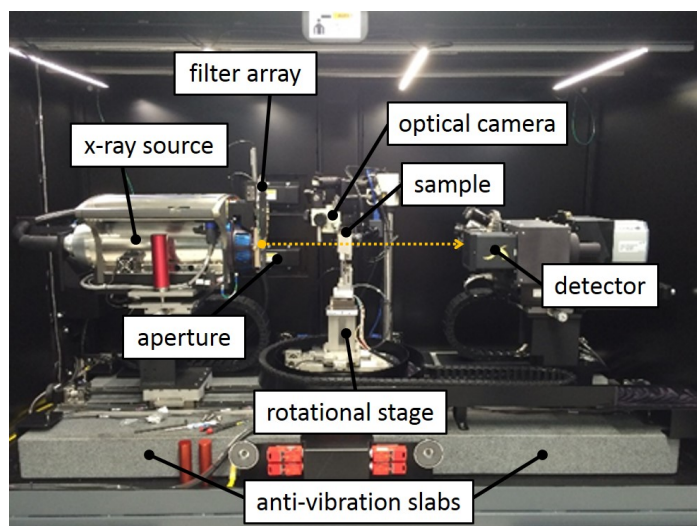
Figure 5.9: Schematic of the Zeiss Xradia-520 Versa™ x-ray microscope - both source and detector are shown fully-retracted. The yellow dashed line represents the path of the x-rays from source to detector (left to right).

Niton™ 950 Field X-ray Lab (FXL)

Whereas the Zeiss Xradia Versa™ is able to derive the internal structure of a sample, it is unable, however, to determine compositional information beyond discriminating high and low atomic density materials. The Niton™ 950 Field X-ray Lab (FXL), in contrast, is able to attain a bulk XRF elemental breakdown of a material. Consisting of a Ag x-ray (anode) tube, the system can quantify x-ray emissions up to 60 keV (25 keV in this work) using four overlapping energy sweeps (main, low, high and light range) before employing one of a number of in-built peak fitting and identification algorithms (e.g. "Soil", "Mining" and "TestAll Geo"). Over a 240 second acquisition period, a stated limit of detection less than 5 ppm (2 ppm for U) was attainable for most transition metals and rare earth elements [262]. The analysis of spectra obtained using the instrument was performed through the Thermo Scientific Inc. NDT™ software.

5.4.5.2 Synchrotron

The synchrotron source used in this work was the Diamond Light Source (DLS) in Harwell, Oxfordshire, UK. As a third generation synchrotron, using insertion devices as well as traditional bending magnets to produce synchrotron light, the facility is classified as "medium-energy", with the production of a 3 GeV beam. In contrast to laboratory x-ray sources, the light produced by synchrotron facilities is 10 orders of magnitude brighter (more intense), as well as being highly-collimated - with typical fluxes at the DLS of 2×10^{12} photons per second (at 10 keV) [263].

A labelled schematic of components of a third generation synchrotron, such as the DLS, are shown in Figure 5.10 [263]. To produce the intense synchrotron light, electrons are accelerated
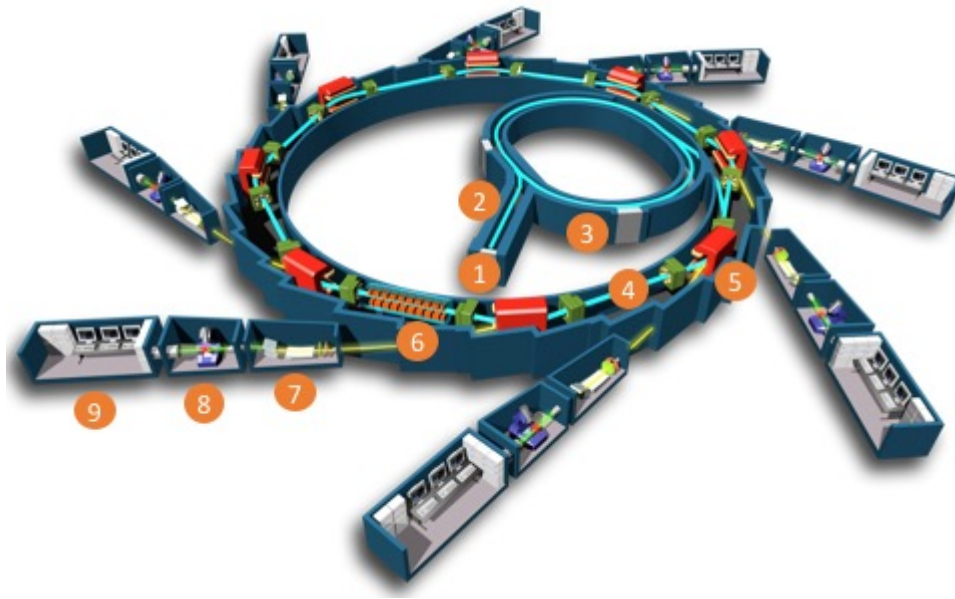
Figure 5.10: Schematic of the component parts of a third generation synchrotron facility such as the Diamond Light Source. *Modified from [263].*

to relativistic velocities before being manipulated using powerful magnetic arrays. After being first produced via the heating of a high-voltage cathode maintained within a high-vacuum (*(1)* in Figure 5.10), the electrons are accelerated down a 10 m linear accelerator, or LINAC (*2*), where their energy is increased from 90 keV to 100 MeV using a succession of radio-frequency (RF) cavities. These electrons are then injected into the near-circular booster ring (*3*), where additional RF cavities and hexapole magnetics focus and accelerate the electron beam up to 3 GeV. Having reached this energy, the electrons are then injected as discrete, equally spaced "bunches" into the 562 m circumference storage ring (*4*), where further magnets and RF cavities focus and curve the electron beam (*5*). Whilst circular in appearance, the DLS is, however, comprised of 24 straight sections separated by curved (bending) sections - all of which is maintained under ultra-high vacuum ($\times 10^{-11}$ mbar) to prevent against loses from collisions with residual air molecules.

X-rays are produced at synchrotrons from the orbiting electron beam using either one of two methods: bending magnets and insertion devices - consisting of wigglers and undulators (*6*). Bending (dipole) magnets are used to curve the electron beam around the synchrotron ring but are also used to produce a broad spectrum of synchrotron light (from x-rays to infra-red). The more advanced insertion devices are conversely located on the straight sections of the storage ring. These consist of arrays of opposing magnets that surround the orbiting electron beam - producing more intense light over bending magnets. By modifying the separation of the magnets, the energy of the x-ray beam can be tuned. Experiments at synchrotrons are conducted at various end-stations or beamlines, each established for specific experimental conditions. After being

109
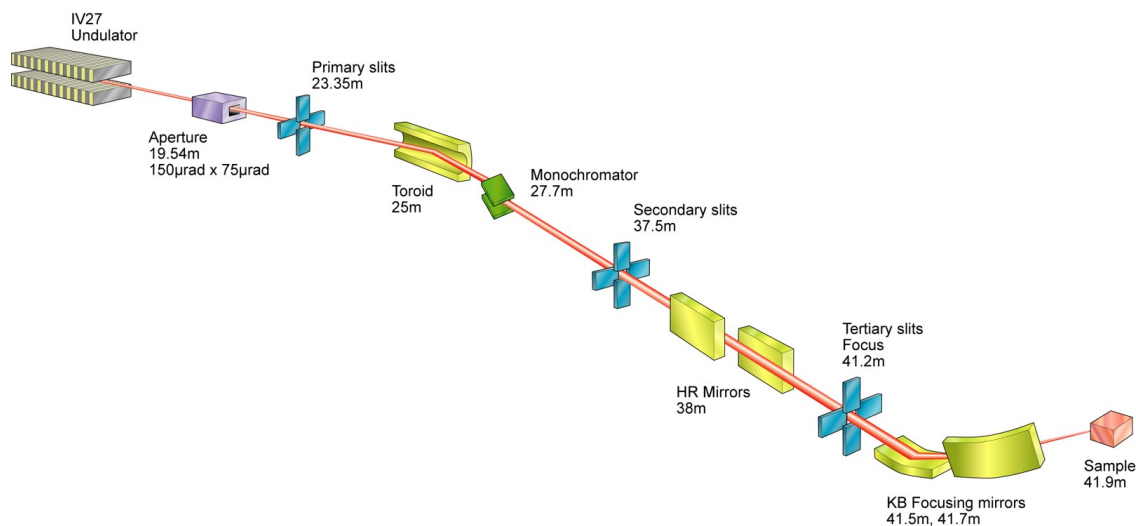
Figure 5.11: Schematic of the I18 beamline optics setup. The distances quoted are referenced from the beamlines undulator. *From [263].*

generated, the x-ray beam passes through the beamlines optics cabin (*7*) where focusing and tuning occurs before it enters the experimental hutch (*8*). Control of the experiment is performed in the beamlines control cabin (*9*), protected from the scattered radiation field inside the hutch.

In this thesis, two different beamlines at the DLS were employed - both using insertion devices (undulators) to generate the x-ray beam. Micro-focus spectroscopy and x-ray fluorescence were conducted on beamline I18, whilst further fluorescence imaging, as well as x-ray tomography, was performed on the I13-1 (coherence) beamline.

I18

Following the production of the initial x-ray beam using a 2 m in-vacuum undulator located within the storage ring, the x-ray beam undergoes extensive focusing before reaching the sample. A schematic of the I18 setup is shown in Figure 5.11. After passing through an initial aperture, the beam is then focused in the horizontal plane using a Rh-coated Si mirror, before progressing onto a liquid nitrogen-cooled double-crystal Si[111] monochromator - defining the energy (2.05 - 20.5 keV) of the resulting beam. The second set of mirrors serves to provide harmonic rejection of low-energy noise before being directed onto the sample using Kirkpatrick-Baez (KB) mirrors after passing through a final set of slits [264].

The resultant x-ray beam has dimensions and a spatial resolution of 2 μm × 2 μm, with a typical flux of 2×10^{12} photons per second. A core energy range of 5 keV - 15 keV permits the analysis of most elements, including Cs and the actinide elements [260, 264].
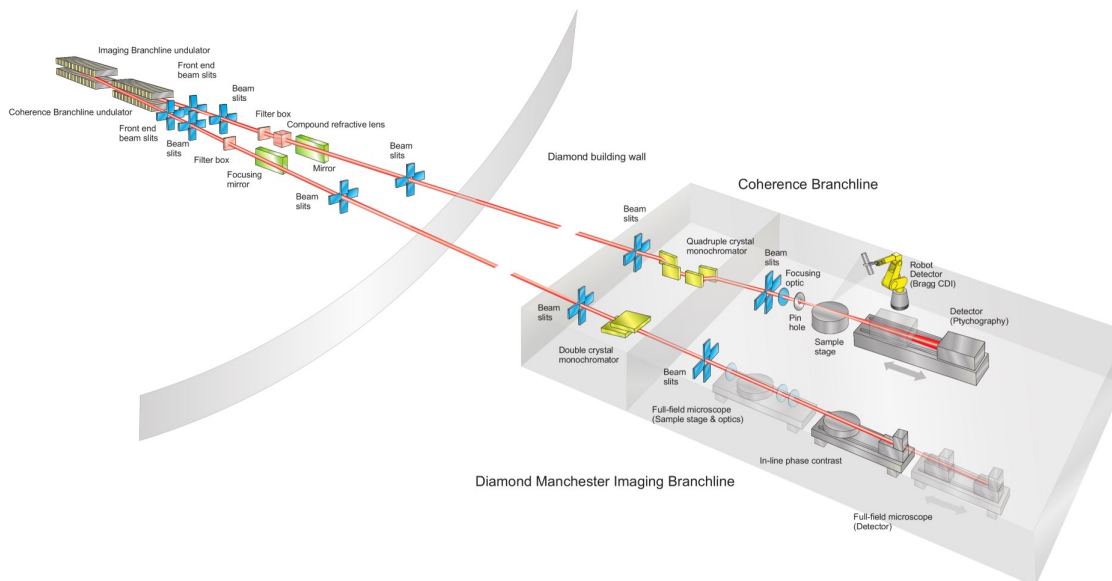
Figure 5.12: Schematic of the I13-1 (coherence branchline) optics setup alongside the neighbouring imaging branch. The distances quoted are referenced from the beamlines in-vacuum undulator. *From [263].*

I13-1

The initial x-ray beam is again attained through an undulator (although canted), like I18. However, the I13 beamlines (I13-1 and I13-2) are the longest at Diamond, with the experimental stations located 250 m from the source [265]. As a result, the coherent (strongly in-phase) nature of the source and resultant x-rays can be exploited. Dependant upon the experimental setup, a spatial resolution identical to I18 can be achieved over an energy range of 4 keV - 19 keV. A similar array of apertures and slits, as well as a water-cooled Si[111] monochromator, are employed on the I13-1 beamline shown in the beamline schematic of Figure 5.12. Unlike I18, all deflection optics are installed in the horizontal plane to maintain the coherence of the source. Final focusing of the x-ray beam (flux = 7×10^{14} photons per second) is achieved using either Kirkpatrick Baez (KB) mirrors or Fresnel (plate) lenses (termed "focusing optic" in Figure 5.12).

5.5 Magnetic Sector-Secondary Ion Mass Spectrometry (MS-SIMS)

Contrary to studying the outer electronic structure of an atom, spectrometric techniques, of which Magnetic Sector-Secondary Ion Mass Spectrometry (MS-SIMS) (herein referred to as just SIMS), represents a powerful tool to analyse a materials isotopic composition - via its mass (m)/charge (z) ratio. To derive a mass spectrum of a sample (a plot of abundance vs. m/z ratio),

it must first be ionised - therefore all forms of mass spectrometry are destructive, consuming a portion (or entirety) of the sample material. Whereas other techniques utilise laser-ablation or dissolution (aqueous) chemistry to generate material/for material introduction, SIMS uses a highly-focused primary ion beam. This magnetic sector SIMS instrument differs from other time-of-flight systems, whereby a magnet is used to separate ions of differing m/z ratio, rather than recording the duration of their flight time down an accelerator tube.

Regardless of the type of mass spectrometry system, each instrument comprises three core components: a mechanism through which to generate ions, a mass analyser to differentiate the ions based on their m/z ratio and finally a means through which to detect this range of ions.

Despite the first experimental SIMS instrumentation being developed during the mid-1930's [266], it was not for another thirty years that the first commercialised instruments were produced [267, 268] and employed, for both routine elemental and isotopic analysis. Unlike the surface analysis afforded by EDS, SIMS is advantageous in being extremely surface sensitive, as well as providing isotopic data, with the signal produced resulting from the uppermost few nm of the material. This data can be used to derive not only a simplistic mass spectrum of the sample to reveal its composition but depth profiles through several 10's of nm to a couple of μm of a sample's surface can be achieved, in addition to selective ion surface mapping.

SIMS can be sub-divided into two types: static or dynamic. The lesser-used, static method employs a lower energy primary ion beam (usually pulsed) to sputter material from the sample's surface. This method is only readily utilised in the characterisation of monolayer samples, where the surface is of uniform composition and limited sample etching is required. Dynamic SIMS, in contrast, uses a considerably higher energy incident ion beam, and as a result is far more destructive. This method allows for a greater sample volume to be analysed, down to ppb concentrations. Because of the ability to study a greater, three-dimensional, sample volume - this method is hence referred to as dynamic [269].

In addition to the implantation of the primary ion beam into the sample's surface at depths of up to 10 nm (depending upon the incident energy) [269], a range of other surface processes occur to produce complex ion emissions and uncertainties for the subsequent analysis of the derived spectrum. One of the greatest factors to introduce complications during SIMS analysis is the ion yield achieved from a sample's surface. This yield, defined as the number of secondary ions successfully sputtered, ionised and detected, depends upon a number of factors, and results in yield differences over several orders of magnitude [269]. The principal factors include the element's electron affinity (for anion-forming species), its ionisation potential (for cation-forming species) in addition to influences such as those attributable to local-scale chemical variations in the sample and also primary beam interactions with the secondary ions [269].

Local-scale compositional variation may also introduce what are termed matrix effects [268]. These interferences are produced when the secondary ion yield from one species is affected (generally increased) by the presence of an additional species within the material. Species responsible for this enhanced secondary ion generation are reactive species such as oxygen or the halogens (positive-bias SIMS) and the alkali metals (negative-bias SIMS) (detailed within Section 5.5.2). Surface topography is a further factor to influence secondary ion generation (and detection) due to a combination of inconsistent or inhomogeneous surface sputtering, alongside potential re-absorption or shielding of emitted ions by the materials surface features. In practice, this limits the data reliability of depth profiles up to approximately 20 μm.

Like all other mass spectrometric methods, SIMS is capable of determining the isotope ratios within a material - rather than just the elemental composition. Difficulties arise with such techniques, however, in separating species (e.g. oxides and hydrides) that occur with the same total atomic mass. This is highlighted in the mass spectrometry of uranium, whereby the many isotopes of uranium (^{234}U, ^{235}U, ^{236}U and ^{238}U) can occur alongside a range of uranium oxide, hydride and hydroxide compositions in what are termed isobaric interferences. Contributions from other elements within the Periodic Table further serve to complicate routine analysis - with smaller ions summing together to equal the masses of larger isotopes [268, 269]. Alongside numerous O^{2-} and H^+ interferences for U masses, the potential occurrence of Pu within a sample presents mass attribution issues for SIMS - with the mass at 239 amu representing both ^{239}Pu but also ^{238}UH. The careful setup of the instrument can, however, remove or significantly reduce these influences [246]. Modern inductively coupled plasma-mass spectrometry (ICP-MS) instruments now employ collision-cell technology to react-out undesired species before the ions reach the detection portion of the instrument [270]. As this technology relies on the carrier plasma (typically Ar) to permit for these reactions to occur, such cells do not exist for SIMS systems.

5.5.1 Theory

With an ion beam used as part of standard FIB sample preparation to investigate a material's internal composition and morphology (Section 5.3.1), SIMS utilises the associated secondary ion ejecta to determine sample composition. A typical MS-SIMS instrument can be broken down into a number of core components, shown schematically in Figure 5.13.

Standard for most analytical equipment is the vacuum system, with the operation of any SIMS instrument performed under ultra-high vacuum (UHV) levels, at pressures lower than $\times 10^{-6}$ mbar. This reduces the likelihood of primary and secondary ions being removed through collisions with any residual air molecules and hence increases the systems detection efficiency. In order to easily maintain such a high vacuum level within the system, and protect against potential
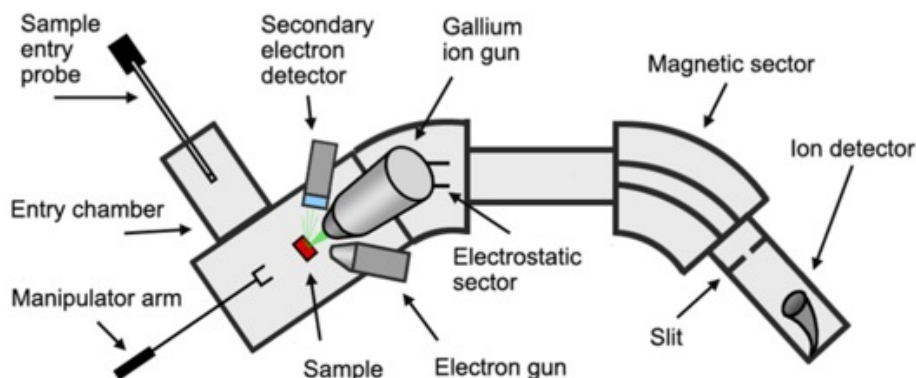
Figure 5.13: Schematic of the custom-built MS-SIMS used in this work. *From [271].*

system and specimen contamination, an entry chamber is used to load the samples, and evacuate them to a suitable transfer pressure before admitting them into the main analytical portion of the instrument, without having to repeatedly expose the entire system to atmosphere. The samples are transferred onto a multi-axis stage for analysis.

There exist multiple ion sources to produce the primary ion beam used for SIMS analysis. These can fall within three categories; (i) gas-phase sources (O^- and Ar^+), (ii) surface ionisation sources (Cs^+) or the more common, (iii) liquid metal ion sources (LMIS) (Ga^+). The selection of a LMIS source is typical for dynamic-type instruments due to the high sputter-rates that can be achieved. After being generated, arising ions and ion clusters must then be extracted, focused and accelerated towards the sample. The primary optics used to achieve this are identical to those within a FIB column, as described in Section 5.3.2 and represented schematically within Figure 5.7. After sputtering the sample, secondary ion extraction occurs using a bias formed by an electric field to draw charged particles away into the systems mass spectrometer - of which a magnetic sector is used in this work. Before this, however, an energy filter is used to remove undesired ion species and improve the resolving power of the system [269]. At the end of the instrument are located the detectors of which there are multiple types - typically operating within a pulse-counting mode to detect the signal generated by single ions. In addition to Faraday cups, the most commonly used detectors are electron multipliers (EM) - of which the channeltron-type detector is the most common [269].

All of this instrumentation is controlled using a dedicated, combined data acquisition, control and evaluation system. Typically one or more computers serve to control the various instrument components as well as record, plot and process the arising data.

5.5.2 Experimental instrumentation

Instrument

The instrumentation used during this work was custom-built at the University of Bristol. Consisting of an FEI Ga^+ LMIS source to produce the primary ion beam, typical parameters of 25 keV accelerating voltage and 3 nA beam current are used. Beyond the ion source, a Vacuum Generators 7035 double-focusing magnetic sector mass analyser was used to screen the secondary ion products. Typical of mass spectrometry instruments, results of this instrument are reported as atomic mass units (amu), in Da or u.

To initially locate the region of interest (RoI) on a sample, an SE image is acquired using the instruments Everhart-Thornley SE detector. Within this instrument, an operational vacuum of better than 5×10^{-7} mbar is maintained at all times to ensure sufficient secondary ion yield. Prior to Ga^+ ion beam exposure, the sample is first biased with a high voltage of ± 4.5 kV. This user-defined bias polarity determines the proportions of either positive or negative ions that are generated by the incident beam.

Instrument control, data acquisition and analysis

With the instrument having been constructed in-house, the entire control software for the system was also produced specifically for this application, written by Dayta Systems Ltd. Three methods of operation were possible, depending on the desired results; (i) mass spectrum, (ii) depth profile, and (iii) ion mapping. The acquisition of a mass spectrum was performed initially in each instance to quantify the instruments mass calibration and confirm the surface composition. Depth profiling or ion mapping followed once a general knowledge of the sample was attained.

During the generation of a mass spectrum, an area of the sample is rastered by the primary Ga^+ ion beam. The m/z ratios of the ejected secondary ions are screened by the magnet (sweeping through the user-specified m/z ratios), before being analysed downstream. As alluded to previously; at increased m/z ratios, there exists a greater number of ionic combinations through which it is possible to form each of the mass peaks. This results in peak broadening across the spectrum, with the instruments curved magnet unable to efficiently discriminate between the heavier ions and molecules. To reduce this peak width, permitting for different masses to be distinguished/separated, therefore attaining an enhanced mass resolution, the size of the physical apertures (or slits) located before and after the magnet were reduced. By refining the size of these slits, while the quality of the spectrum is enhanced - the total signal is reduced.

The destructive nature of SIMS can be employed for investigating compositional variations through depth profiling. After selecting an area of the sample and a number of masses of interest

(five for this instrument), their secondary ion concentration is measured as the primary beam etches through the material. If the etch rate of the material is known, then it is possible to convert from this ion count rate to etch depth. This etch rate is a function of the total area etched (nm^2), beam current (nA) and ion yield (s^{-1}), shown in Equation 5.2.

$$etch\ rate\ =\ \frac{sputter\ rate\ \times\ beam\ current}{scan\ area} \tag{5.2}$$

Sputter rates (the thickness of material removed from the surface) vary from less than 1 nm s^{-1} to 5 nm s^{-1}, yielding 5 - 15 secondary ions per primary ion [268]. Whilst typical of most materials, factors such as the primary ion beam current, the samples composition and the materials crystallographic orientation all influence the rate at which secondary ions are generated. A computational approach to predicting sputter rates (alongside ion-ion interactions within matter) can be derived using The Stopping Power and Range of Ion in Matter (SRIM) software [272].

A highly-visual representation of sample composition can be produced using ion mapping. By rastering the primary beam over a micron-sized region of interest, the SIMS instrument is set up to detect a single atomic mass unit (ion or molecule), with the signal intensity (brightness) at each pixel scaled to represent the concentration of that ionic species. The distribution of multiple ions can be studied whilst repeatedly rastering the sample - detecting the contrasting mass units. A three-dimensional compositional rendering can also be derived by repeatedly rastering/etching through the sample.

5.6 Experimental methods summary

As detailed in this chapter, each of the different analytical techniques employed as part of this thesis allows for contrasting information on the form, structure and composition of a sample to be determined. In isolation, the information gained from a single technique does not contribute to the complete characterisation of a sample. Hence, this multi-technique and sequential approach permits for a more extensive sample evaluation - facilitating the inter-technique correlation of both results and hypotheses.

To ensure that the precious particulate samples examined during this thesis were analysed to their fullest extent, non-destructive characterisation methods were first performed (and exhausted) - prior to any destructive methods, deemed worthwhile, were employed. It is only as a result of the cutting-edge techniques available both at the University of Bristol and other national facilities, that this highly-detailed sample analysis was possible.

CONTAMINATION DEPOSITION, TRANSPORTATION AND REMEDIATION

Results and methods presented in this chapter have formerly been published in the peer-reviewed literature:

P.G. Martin, O.D. Payton, J.S. Fardoulis, D.A. Richards, T.B. Scott and Y. Yamashiki. "Low altitude unmanned aerial vehicle for characterising remediation effectiveness following the FDNPP accident". *Journal of Environmental Radioactivity*, vol. 154, pp. 58-63, January 2016.

P.G. Martin, S. Kwong, N.T. Smith, Y. Yamashiki, O.D. Payton, F.S. Russell-Pavier, J.S. Fardoulis, D.A. Richards and T.B. Scott. "3D unmanned aerial vehicle radiation mapping for assessing contaminant distribution and mobility". *International Journal of Applied Earth Observation and Geoinformation*, vol. 52, pp. 12-19, October 2016.

P.G. Martin, O.D. Payton, Y. Yamashiki, D.A. Richards and T.B. Scott. "High-resolution radiation mapping to investigate FDNPP derived contaminant migration". *Journal of Environmental Radioactivity*, vol. 164. pp. 26-35, November 2016.

D. Connor, **P.G. Martin**, N.T. Smith, L. Payne, C. Hutson, O.D. Payton, Y. Yamashiki and T.B. Scott. "Application of airborne photogrammetry for the visualisation and assessment of contamination migration arising from a Fukushima waste storage facility". *Environmental Pollution*, vol. 234. pp. 610-619, March 2018.

6.1 Introduction

Beginning on the 12th March 2011, and continuing over the succeeding six days, an estimated 520 PBq of radioactivity was released from the FDNPP [119]. Despite estimates that 80% of this material was dispersed eastwards into the neighbouring Pacific Ocean [39, 150], such a combined activity represents one of the largest ever on-land contamination release events from a nuclear facility (behind the 1986 accident at Chernobyl) [236].

Over the days and weeks after the release, the shorter-lived radioisotopes that comprised the majority of the release inventory, including; ^{131}I, ^{133}I, ^{129m}Te, ^{132}Te, ^{136}Cs and ^{133}Xe rapidly decayed into stable species (Table 2.1) [119]. Consequently, the current radionuclides responsible for the detectable γ-ray radiation across the affected Fukushima Prefecture (and the source to the extensive decontamination effort) are the two longer-lived, high fission product yield isotopes of Cs - ^{134}Cs ($t_{1/2}$ = 2.065 years) and ^{137}Cs ($t_{1/2}$ = 30.17 years).

As presented in Chapter 2, the primary land contamination exists as a plume extending north-west from the FDNPP, a result of the radioactive release from reactor Unit 2 on the 15th March 2011 [153]. This radioactive plume extended for 50 km, approaching (but fortunately not reaching) the densely-populated Fukushima City [85], the capital of the Prefecture with a population of over 300,000 [152]. This contamination, although decreasing in its activity with distance from the FDNPP, was observed to have occurred as a homogeneous covering across typical local-scale survey sites [85], with such measurements supported by the modelling undertaken by Malins et al., (2016) [273]. Since the accident, numerous mapping surveys, conducted using a range of mapping systems and carrier platforms, have been undertaken under the Japanese Nuclear Regulator (NRA) *Comprehensive Monitoring Plan* [63]. A detailed review of Prefectural and regional mapping was provided by Saito and Onda, (2015) [64].

In addition to the vast number of regional and site-specific contamination monitoring surveys [57], there has also been a considerable volume of work assessing the behaviour of radiocesium within the environment. As well as being densely populated with a large land-use dependency, the Fukushima region is typified by high mean annual precipitation and extensive volcanogenic topographic variation [31, 151, 236]. These factors have resulted in studies modelling the transport and fate of Fukushima-related Cs in soils [137, 274–276], as well as within the larger catchment-scale systems [277, 278]. This anthropogenic radiocesium represents a powerful means to perform large-scale tracer experiments, where environmental transport cycles in sub-tropical zones can be studied - applicable for the assessment of residence times and associated transport rates. Following its initial application by Rogowski and Tamura (1965) [279], Walling et al., (1991) [280], used the radiocesium input into the environment as a consequence of the Chernobyl accident to investigate soil erosion across arable land across the UK.

During September 2011, Typhoon Roke (one of many typhoons to impact the region annually), mobilised a total of 10.08 TBq of radiocesium within the Abukuma Basin as suspended particulate material. This output represented close to 2% of the total input into the catchment [277].

Studied extensively following the Chernobyl accident, the behaviour of ionic Cs and its high sorption affinity with ion exchange minerals (e.g. clays such as Illite and Montmorillonite) has been well-characterised [167, 168, 281]. As an ionic species, it is observed to become strongly sorbed onto the highly-reactive frayed-edge sites of such microscopic clay and mica-type minerals, with the formation of inner-sphere complexes, whereby Cs is strongly-bound and difficult to remove. It is therefore readily transported under fluvial conditions, bound to colloidal clay and mica (mineral) material. [280, 282, 283].

The similarity, in addition to the physio/chemical nature, of the soil profile across the majority of Fukushima Prefecture (including areas close to sites in this study) has been reported in the work of Konoplev et al., (2016) [284]. Following from the work of Rosen et al., (1999) [285] , who observed a high degree of Cs absorption within the typical soil horizons surrounding the Chernobyl reactor site, Konoplev et al., concluded that a higher partition-coefficient (K_d) was typical for Fukushima soils. At 1 - 2 orders of magnitude greater than that of Chernobyl soils, this elevated K_d value was attributed to the high radiocesium interception potential (RIP) - a result of the soils higher clay component (in part also a consequence of the glassy and highly-insoluble nature of the fallout [191]). This high soil clay component results from the volcanically-derived terrain of Fukushima Prefecture [151], in contrast to the thick sedimentary sequences of poorly-compacted clastic deposits that constitute the Chernobyl region [286].

Despite what has been shown to be highly-mobile contamination, remediation of the affected regions continues, via methods detailed within the Japanese Ministry of the Environment *Decontamination Guidelines* [60]. However, the overall effectiveness and value of this current work in manually reducing the dose-rate to below 20 µSv hr^{-1} to allow for re-population has been questioned in several works [287–289], all of which cite the remobilisation of material or input derived from additional long-term sources as challenges to remediation targets.

Forming a baseline from which to quantify the level of contamination that has occurred, Abe et al., (1981) [290] undertook an extensive nationwide radiological survey during the late 1970's. Advancing previous dose-rate estimations by sampling at localities representing every 100,000 inhabitants (approximating to a 30 km^2 mesh) through a hand-held survey-meter, the work assessed influences of both sub-surface geology and atmospheric fallout. Whilst identifying marginally-elevated dose-rates in south-west Japan, a mean national dose-rate of 0.097±0.013 µSv hr^{-1} was determined, marginally less (at 0.090±0.013 µSv hr^{-1}) across Fukushima Prefecture.

119

Such dose-rates corresponded to an annual dose of 0.8 mSv (<25% of the UK average [221]).

As discussed formerly in Chapter 2, with the total cost of both the land remediation and disposal of the radioactive wastes generated estimated at between ¥2.55 trillion and ¥16.0 trillion [203], the cost-effectiveness of these actions has been questioned in achieving a permissible dose-rate. This high-cost per unit dose-rate reduction for differing types of radiologically contaminated site has been detailed in the numerous works by Yasutaka and co-workers [199, 203, 287].

These works highlighted the combined influences of the Fukushima topography and meteoric conditions (sub-tropical precipitation) alongside the highly mobile nature of the contamination, in re-contaminating remediated sites. Compounded by this analysis, such large-scale stripping of areas located on or close to valley floors is increasingly viewed as futile, with contamination promptly replenished onto these remediated sites from the bordering slopes and forested areas.

A more pragmatic approach to this decontamination effort would be based on that employed during "traditional" nuclear reactor decommissioning [204], where a comparable radionuclide activity is encountered. Termed "delay (entry) and decay" - this method involves waiting for periods of approximately 30 years (although this can be as much as 50 years) from the shutdown of a reactor to allow for the short and medium-lived (mostly γ-ray emitting) species to decay into stable species. Only once this period has passed will full-scale decommissioning commence.

This approach is currently being implemented as part of the UK's ongoing decommissioning of its fleet of legacy Magnox reactors, and could also be utilised in the Fukushima remediation. In the case of Fukushima, as well as allowing for the similar decay-related reduction in the total radioactivity, a delay before the commencement of remediation/a break from current activities would permit for the downwards movement of a large volume of the radiocesium contamination, ahead of the onset of the costly clean-up program. As a result, not only would the dose experienced by the operator be reduced, but also the total volume of contaminated wastes generated.

6.2 Aims

The work detailed in this chapter sought to investigate site-wide variations in radiological contamination as a result of material transport, as well as focusing on assessing the impact of remedial works on formerly contaminated sites and the success in reducing radiation levels. This was undertaken through the application of the newly developed low-altitude UAV alongside the ground-based mapping platform. Through which, an increased spatial-resolution over former aerial methods was possible in addition to affording the ability to survey locations formerly inaccessible to human survey personnel.

Using the results of these surveys to identify regions of elevated activity, targeted sampling could be undertaken to identify material for subsequent, laboratory-based, analysis.

6.3 Survey methods

At each of the five sites, each subsequently described, a radiological survey was performed using either the ground-based or the UAV radiological mapping platform. A full account of the methods and calibrations for each of these systems was detailed previously in Chapter 3. Both the GR1 and SIGMA-50 detectors were used, with the calibrations undertaken to allow for the CPS output of each detector to be converted to a meaningful unit of dose-rate described in Section 3.1.2.

6.4 Survey sites

The sites investigated as part of this work were all located at the northern-western most extent on the main north-west trending contamination plume, within the *Exclusion Zone* established to contain *Areas 1 and 2* [156]. All survey sites were located in *Area 2* at the commencement of the study, within 3 km of the border with *Area 3* and the *Restricted Zone* - where habitation is not permitted and residents will "unlikely be able to return (to their homes) for the foreseeable future" [155]. In contrast to the *Restricted Zone*, following successful decontamination and dose-rate reduction (to <20 μSv hr^{-1}), the evacuation orders pertaining to each of these sites will be removed [155]. An air dose-rate map of the region (from May 2014) detailing the locations of each of the sites is shown in Figure 6.1, alongside the survey date(s) and the Area 3 northern-most perimeter. Contamination following the March 2011 releases has been observed to be spatially uniform in its extent [85], with the sites studied in this work receiving a total (homogeneous) radiocesium deposition of 1 MBq m^{-2} - 3 MBq m^{-2}.

6.4.1 Irikuboyama

(Latitude: 37.586248°, Longitude: 140.701586°). Comprising a strip of inclined farmland 200 m × 50 m running north-south, formed from a series of smaller near-horizontal fields all of differing size is shown in Figure 6.2, an aerial photograph of the site. Prior to the accident, the site was used for rice production, with 30 cm wide irrigation channels bounding each of the smaller sub-fields. To allow for farming, between each of the fields, cut into the hillside, were a number of steeply-inclined (near-vertical) banks ranging from 1 m to 5 m in height (forming a terraced or stepped appearance). The height difference between the northern extent (topographic high) and southern extent (topographic low) of the site was approximately 25 m. At the time of the site survey (May 2014), no remedial work on the site had been performed.
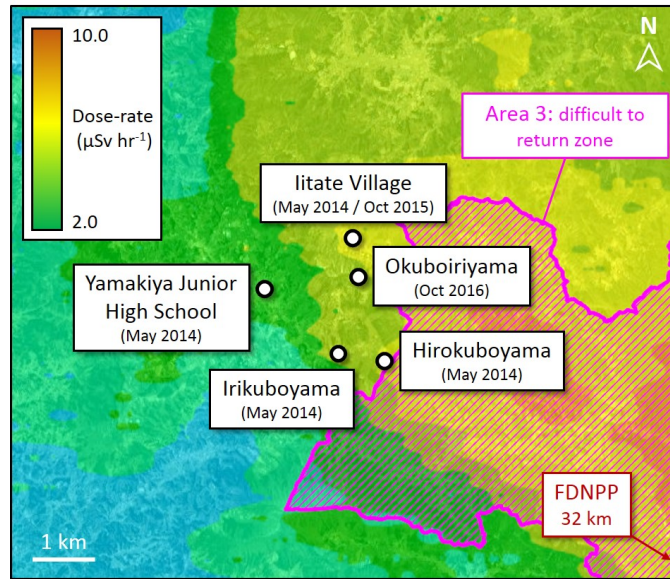
Figure 6.1: Location of survey sites at the north-west extent of the main plume-line, alongside survey dates, overlain onto the air dose-rate map as of October 2014. *From [234].*

Figure 6.2: Aerial photograph showing the location of the Irikuboyama site (date of imagery: May 2012), the survey area is highlighted (green region). *From Google Earth™.*

Figure 6.3: Aerial photograph showing the location of the Iitate Village site (date of imagery: May 2012), the survey area is highlighted (green region). *From Google Earth™.*

While capable of performing the survey during one UAV flight, due to the height variation over the extent of the site, a number of smaller mapping flights were undertaken, modifying the GPS-derived altitude for each flight. Every survey was undertaken with a grid-spacing of 2 m, a velocity of 1 ms^{-1} and above-ground heights ranging from 1 m - 10 m. The lighter GR1 γ-spectrometer was used - mounted onto the UAVs gimballed detection payload. As well as being advantageous for aerial surveys due to its low mass, the GR1 was capable of operating in higher radiation environments, where the larger volume SIGMA-50 detector would saturate [209].

6.4.2 Iitate Village

(Latitude: 37.614125°, Longitude: 140.708053°). Larger in extent than Irikuboyama, the site in Iitate Village was dissected by both a small river trending east-west as well as a tarmac road - entering the site from the north before crossing the river and bending to the west to run parallel to the river, as shown in Figure 6.3. Across the site, there occurred differing fertiliser usage between areas. Like Irikuboyama, this site (and much of the rest of Iitate Village) had not received any remediation during May 2014, however, prior to the second survey during October 2015, remedial activity had commenced at areas of the site. During this decontamination, crops had been removed alongside soil to a depth of 15 cm (as per the *Japanese Ministry of the Environment Decontamination Guidelines* [60]). Extensive surface scrubbing was also undertaken.

Typical of much of populated Fukushima Prefecture, this site existed on the base of a valley floor (500 m wide) bounded by parallel (forested) valley sides (200 m high). Aside from the 5 km north-south trending coastal plain bordering the Pacific Ocean where the FDNPP is located, the

123

region is typified by extensive igneous, metamorphic and sedimentary sequences - all extensively faulted and deformed [151], providing such a rugged terrain and extreme topography.

Unlike the aerial survey at Irikuboyama, however, both mapping works at Iitate Village were performed using the ground-based survey platform, with the miniaturised GR1 γ-spectrometer attached. This ground-based method was selected (over aerial mapping) due to the strong wind that occurred down the valley in which the site was located. Both surveys were undertaken by the same operator - with the device held in their backpack, 1 m above the ground. As before, a factor of 1.3 was applied to the data to correct for the influence of bodily-attenuation to derive a corrected CPS value prior to converting this value to a more applicable dose-rate.

Resulting from the seventeen-month separation between surveys, numerous site features had changed, the greatest of which is the initiation of remediation at portions of the site prior to the latter October 2015 visit. Additional features of this Iitate Village site included a small river, a tarmac-covered road (routinely washed during clean-up activities) and differing fertiliser usage (prior to the accident). As such, this locality served as a powerful validation experiment to quantify the dose-rate reduction between surveys potentially attributable in-part or entirely due to; (i) radioactive decay, (ii) soil infiltration (depth attenuation) and, (iii) contaminant migration. This was achieved through the selection of 14 arbitrary points located across the site from both survey dates, representative of the various land uses and conducting the subsequently described dose-rate modelling. From personal communications with the land-owner, the sole crop-type produced across the site was identical (winter wheat) - having since become overgrown since the radioactive release and resulting evacuation.

Decay-only modelling. As formerly discussed in Section 2.2.1, in the years after such a radiological release incident, the principal radionuclides contributing to external dose are radiocesium; the shorter-lived ^{134}Cs ($t_{1/2}$ = 2.065 years) and the longer-lived ^{137}Cs ($t_{1/2}$ = 30.17 years). These nuclides were produced following the FDNPP accident with a characteristic 1 to 1 (equal) activity ratio [50]. Because of such species dominance, contributions from other radionuclides were considered insignificant and excluded from calculations as part of this study. Both forward and back modelling of measurement values determined in May 2014 from the 14 on-site data-points was performed using a weighting factor calculation to account for the difference in half-lives of ^{134}Cs and ^{137}Cs (28 years). The formula used for backwards activity calculations is shown in Equation 6.1, with the forward modelling values obtained via Equation 6.2. In both, λ = the decay constants (yr^{-1}) for either ^{134}Cs and ^{137}Cs, N_0 = initial dose-rate, and N_t = dose-rate at time *(t)* years.

$$N_{0\,(Cs134+Cs137)} = \frac{N_t^{(Cs134)}}{e^{-\lambda(Cs134)\times t}} + \frac{N_t^{(Cs137)}}{e^{-\lambda(Cs137)\times t}} \tag{6.1}$$

$$N_{t\,(Cs134+Cs137)} = N_{0\,(Cs134)}\, e^{-\lambda(Cs134)\times t} + N_{0\,(Cs137)}\, e^{-\lambda(Cs137)\times t} \qquad (6.2)$$

Depth attenuation modelling. Invoked by Malins et al., (2016) as the main mechanism through which a reduction in air dose-rate is achieved alongside radioactive decay, is the downward migration of radiocesium into the soil profile - with a resulting enhanced attenuation of γ-rays with increasing radiocesium depth (burial) [273]. Values for Cs infiltration from a number of studies undertaken across Fukushima Prefecture in the wake of the accident were used to describe the Cs distribution within the soil profile [291–293], and are shown in Figure 6.4.

A mass attenuation coefficient (μ) from Hubbell and Seltzer (2004) [65], was used to describe the associated attenuation that occurred at Cs γ-ray energies for soil compositions (silt, clay and sand) described in the work of Teramage et al., (2014) [293]. The equation used to calculate the theoretical dose-rate assuming losses from both radioactive decay and depth-related attenuation (of May 2014 data), is shown in Equations 6.3 and 6.4. Where $N_{t\,(depth)}$ = dose-rate at time *(t)* incorporating depth-related attenuation, Δ = the proportion (%) of radiocesium at depth *x* (cm), μ = the linear attenuation coefficient (cm^{-1}), and ρ = the soils bulk density (g cm^{-3}) - also at depth (*x*). The value of N_t represents the dose-rate at time *(t)* (in years), as determined previously for the position in Equation 6.2.

With the sites crop type entirely uniform and therefore shown to not represent a factor through which differential Cs fixation or soil penetration could occur, another factor that could produce differences across the site may result from the differing application of fertiliser species (principally K-based), resulting in ionic Cs-K competition within clay-type minerals. However, no such compounds were applied to any portion of the site since May 2010 (personal communication with land-owner) and can, therefore, be discounted as a possible influence on the retention of ionic Cs.

Extensive ploughing activities to homogenise the upper 45 cm of the soil profile have further served to disrupt the occurrence of organic-rich horizons. It is these heterogeneous layers that contribute to a reduction in Cs retention in a soil - comprising a proportion of the soil otherwise constituted by clay-type minerals that would strongly absorb ionic Cs [294, 295]. This regolith homogenisation (termed "soil-burying") is a common remediation strategy to reduce dose-rates at agricultural sites across Fukushima Prefecture - burying the uppermost contaminated soil surfaces below unaffected horizons [87, 296]. Despite not physically removing the Cs like other remediation strategies, a dose-rate reduction factor of 2.3 is typically achieved through this method. No ploughing, however, had been performed at the Iitate Village site since similar agricultural ploughing in May 2010.
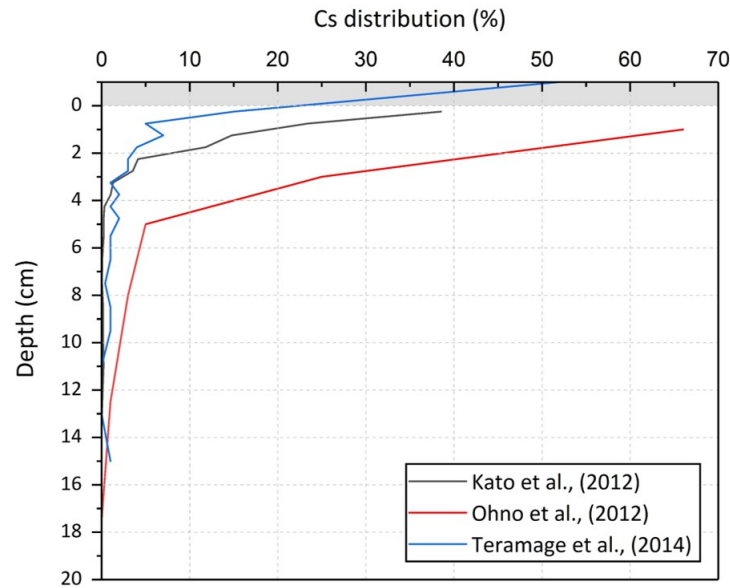
Figure 6.4: Depth distribution of radiocesium within the soil profile. As determined in earlier works *[291–293]*.

Due to the universal crop-type, negligible fertiliser usage and extensive ploughing prior to the accident (but **not** following the accident) - both the site and underlying soil characteristics were considered to be consistent across the site.

$$N_{t\,(depth)} = N_t \times depth\,attenuation\,factor \tag{6.3}$$

$$N_{t\,(depth)} = N_t \times exp^{-(\Delta_1(\mu_1 \cdot x_1 \cdot \rho_1)) + (\Delta_2(\mu_2 \cdot x_2 \cdot \rho_2)) + ((...))} \tag{6.4}$$

6.4.3 Yamakiya Junior High School

(Latitude: 37.60226°, Longitude: 140.676035°). Located the greatest distance away from the centre of the plume than any of the other sites surveyed during this work, the Yamakiya Junior High School (YJHS) site was the least radiologically contaminated [85]. Because of this, the YJHS also existed as a JAEA study/test site for remediation strategies and as a result, had seen a range of decontamination activities as of May 2014 [297]. Such actions included the removal of surface material from the schools playing field, the removal of vegetation, clearance of gutters and drains, in addition to the high-pressure washing/scrubbing of surfaces. An aerial photograph of the site during early remediation in 2012 is shown in Figure 6.5, highlighting the rooftop survey area investigated in this work. To evaluate the effectiveness of this roof clearance (where solar-panel arrays had been installed prior to the accident), a UAV survey was undertaken (in addition to an accompanying ground survey of the site, although not discussed in this thesis).

Figure 6.5: Aerial photograph showing the location of the Yamakiya Junior High School site (date of imagery: May 2012), the survey area is highlighted (green region). *From Google Earth™.*

Like the survey performed at Irikuboyama, a flight velocity of 1.0 ms^{-1} was used employing the radiation mapping payload equipped with the GR1 γ-ray spectrometer. Unlike the survey that took place at Irikuboyama, however, where post take-off, the flight was performed fully-autonomously, here the whole flight was conducted using conventional hand-held remote controls. Hence, the pitch of the roof could be mirrored at varying altitudes maintaining a 1.0 m separation throughout. To compensate for this reduced height and therefore the smaller "circle of investigation" (Section 3.3.3), the grid-spacing was reduced from 2.0 m to between 0.5 m and 1.0 m.

6.4.4   Hirokuboyama

(Latitude: 37.581745°, Longitude: 140.716527°). In addition to being the largest of the sites studied during this work, the former livestock farm at Hirokuboyama was the closest to the north-western border with *Area 3* and the Namie Town region. This boundary is shown in Figure 6.6, an aerial photograph of the site, detailing also the study area described in this work. As a result of its closest proximity to the FDNPP site, it was the most heavily contaminated by the accident out of all the sites mapped - receiving an estimated 3.0 MBq m^{-3} of radiocesium, with a resulting total dose-rate of 15.0 μSv hr^{-1} in May 2014 [85].

As a location that was not only heavily contaminated but also extensive in size, a new method of dose-rate reduction was trialled to negate against the requirement to otherwise remove extensive volumes of contaminated surface material. With the exception of a small dwelling and a number of farm buildings around its northern-most perimeter, the site consisted of flat open grassland 300 m × 300 m in size - bounded by thick forests to its south, with a steep hillside rising to its

127

Figure 6.6: Aerial photograph showing the location of the Hirokuboyama site (date of imagery: May 2012). The survey area is highlighted (green region), as is the position of the border with the restricted Namie Town. *From Google Earth™.*

south-east. Approximately 30 of the now infamous 1 m^3 waste bags had also been placed at the entrance to the site, close to the location of the farm buildings.

For this experimental method of dose-rate reduction, the central portion of the site (an area 80 m × 100 m) was covered by a 15 cm thickness of sand, with the remainder of the site left unremediated.

Being both the flattest and least obstructed of any of the sites, the entire site survey was performed autonomously using the UAV with the GR1-equipped detector payload attached. Monitoring was performed as a series of separate, overlapping flights due to the size of the location. Typical of standard unmanned aerial surveys, a flight velocity of 1.5 ms^{-1} was used alongside an altitude of 5 m and grid-spacing of 2 m to ensure adequate on-ground coverage.

6.4.5 Okuboiriyama

(Latitude: 37.592393°, Longitude: 140.700477°). A large number of storage sites exist throughout Fukushima Prefecture to contain the contaminated materials removed from decontaminated sites until final disposal facilities are constructed. One such facility - located on the site of former rice fields is at Okuboiriyama, in the Yamakiya District of Fukushima Prefecture. An aerial photograph of the study site and surrounding area is shown in Figure 6.7. After the original top-soil had been removed, the site was covered with an impermeable polymer and covered with a 10 cm depth of clean (imported) sand. The 1 m^3 bags of contaminated soil collected in the surrounding contaminated region were then stacked on the site. Surveyed in October 2016, this

Figure 6.7: Aerial photograph showing the location of the Okuboiriyama site (date of imagery: May 2012), the survey area is highlighted (green region). *From Google Earth™*.

site had been constructed, and was part-filled with waste material. The first bags installed at the site were emplaced ten weeks prior to the survey - with a total of approximately 250 bags having been positioned (up to three units high in places). Over the course of the lengthy process of installing the waste bags, a temporary, impermeable material was used to protect the bags against water ingress (and the resultant outflow of contamination).

To survey this site, the dual-unit ground-based mapping system was used - comprising the two SIGMA-50 units mounted 1 m from the operator, again at a height of 1 m above the ground. Owing to the specifics of the platform (detailed in Section 3.2.2), an increased separation of 2 m was used - yet still providing a high degree of data-point overlap. In order to survey the entire site, the operator walked both the ground that surrounded the waste material, as well as directly on top of it. Resulting from the low radioactivity levels at the site, the more sensitive SIGMA-50 detector was used opposed to the higher throughput (yet less sensitive) GR1 detector.

6.5 Environmental transport of contamination

The γ-ray radiation detected within this study arose exclusively from radiocesium (^{134}Cs and ^{137}Cs). The ratios (activity and atomic) of ^{134}Cs to ^{137}Cs varied depending on the survey date, decreasing with the decay of the shorter-lived ^{134}Cs.

6.5.1   Irikuboyama

Results of the aerial surveys conducted at the terraced farm site in Irikuboyama are shown in Figures 6.8 (a) - (c). Owing to data obtained by the UAV containing information relating to both its altitude (from the units onboard GPS) and its distance from a surface immediately below the detection payload (from the single-point laser range-finder), a numerical subtraction of distance from altitude allowed for a crude elevation model of the overflown surface to be constructed. A full description of this method using the National Nuclear Laboratory (NNL) produced *EnVi* software to digitalise the three-dimensional surface by combining both data-streams is included within the previously published works [298]. This topographic surface is shown as an altitude heat-map in Figure 6.8 (a) - agreeing with the in-field observations. The plots depict the decline in site elevation from north to south - in addition to an elevated area along the sites western-most extent.

During post-processing of the results derived from the Irikuboyama test site, a number of irregularities were observed within the data stream recorded by the range-finder (distance). These anomalous laser returns (deriving both negative and extreme height values for the platform), were identified to result from survey positions whereby differing thicknesses of water were encountered - the results of subsequent laboratory tests are shown in Figure 6.9. The ns-pulsed laser return from the water body is shown to occur from its surface, for water thicknesses of up to 0.4 m, producing an accurate measurement of the platforms altitude (distance to a surface). However, in situations where the thickness of the water is greater than 0.4 m, the altitude determined by the UAV is shown to be highly-erroneous. This error is likely the result of the increased scattering for within a larger depth of fluid [299], combined with the "piling-up" of the various returns to the range-finder from the water and underlying surfaces.

To account for the small number of erroneous points within the resultant site topography model, the nearest neighbour correction (smoothing filter) was applied. This correction replaced <0.5% of the data-points from across the site, but succeeded in removing such spurious data points.

Translating Figure 6.8 (a) to generate a triangular irregular network (TIN) representing the sites topographic surface, followed by overlaying the radiation map obtained by UAV produces the three-dimensional radiation map shown in Figures 6.8 (b) and (c). From these two plots, low levels of activity are seen across the higher western and northern portions of the site. In contrast, elevated levels of radioactivity are apparent, distributed over the rest of the downwards (southwards) sloping site, with highly-localised areas of increased radioactivity corresponding to the irrigation (drainage) network. Forming a local sink of transported material, dose-rates averaging 5.1 µSv hr^{-1} are evident at these points - above the site average of 4.5 µSv hr^{-1}. Both differ from the mean dose-rates at the northern and western portions of the site, of 2.8 µSv hr^{-1}, with local minimum values in these areas between 1.3 µSv hr^{-1} and 1.5 µSv hr^{-1}.

(a)

N

31.5

Height
(m)

0

25 m

(b)

6.0

μSv hr^{-1}

0

(c)

N

0   6.0
μSv hr^{-1}
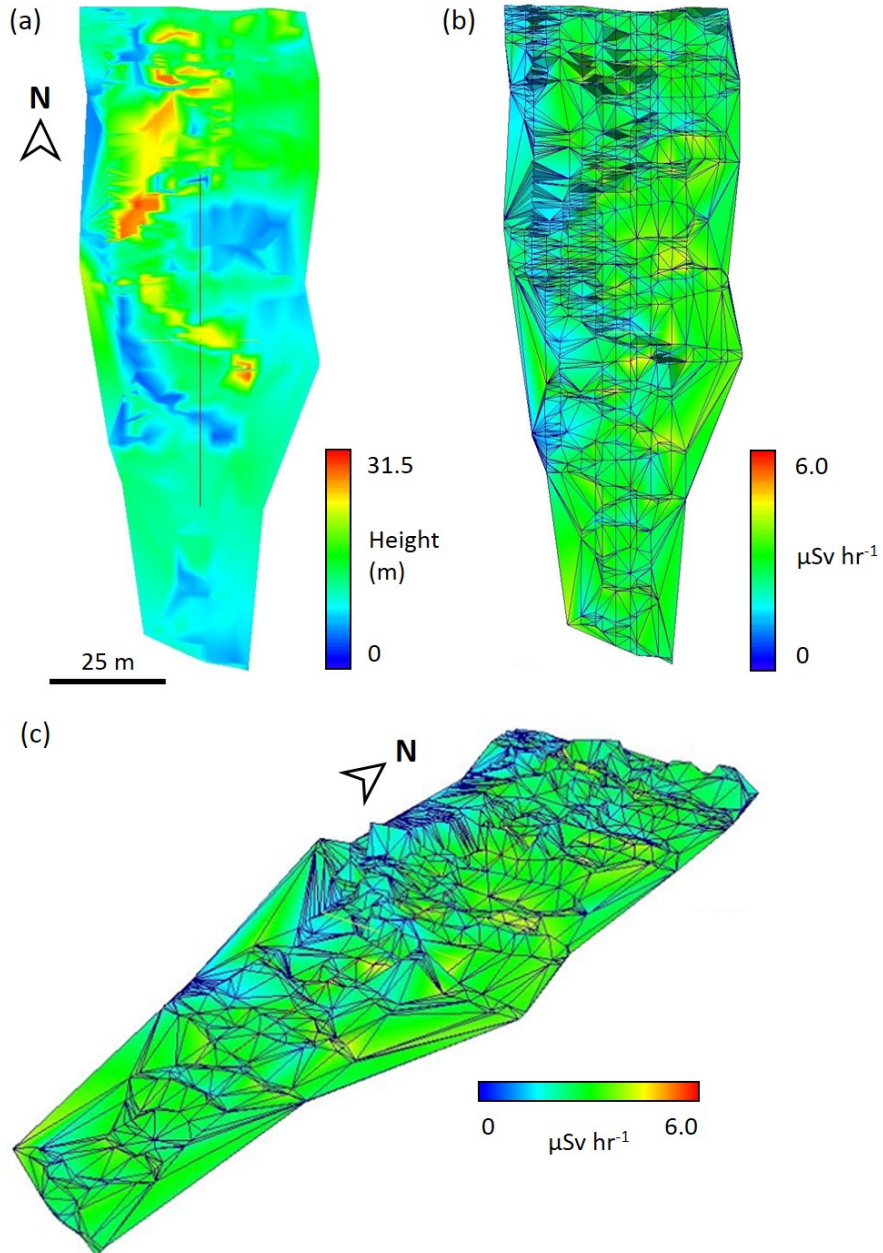
Figure 6.8: Results of the UAV survey at Irikuboyama; (a) height variation recorded across the site, alongside (b) and (c), air dose-rate radiation map overlain onto this topographic data.
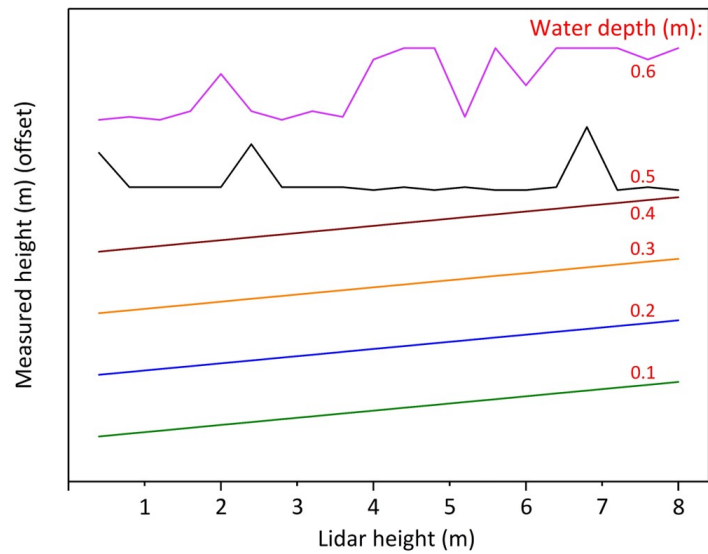
Figure 6.9: Influence of water depth on range-finder return. *Modified from [298].*

With radioactive material having originally been deposited uniformly [85] - owing to both overland and channel flow, extensive volumes of fallout Cs have since been re-distributed. This movement correlates with the numerous studies on the form of Fukushima-derived radiocesium - highlighting its affinity and significant transport potential when bound to the surfaces of clay and mica-sized material [300–302].

6.5.2   Iitate Village

Results of the two radiation surveys at the Iitate Village site are shown in Figures 6.10 (a) and (b) - obtained during May 2014 and October 2015 respectively. Shown in Figure 6.10 (a) also, are the locations of the fourteen geo-referenced points. While no remediation had occurred prior to the May 2014 survey, the influence of vehicular activity along the road dissecting the site, as shown in Figure 6.10 (a), depicts a band of reduced activity with respect to the surrounding fields - whereby contamination was likely removed upon adhesion to transiting vehicles. Also apparent from the May 2014 data is the contrasting dose-rate north and south of the road and stream. A site-wide activity average in May 2014 was determined to be 400 CPS (4.8 μSv hr^{-1}), with the lowest levels of contamination found on the road (2.9 μSv hr^{-1}) - a 40% overall activity reduction. The radiation levels in the southern field (site maximum) were determined to be 5.8 μSv hr^{-1}, unlike the northern fields where a dose-rate of 4.4 μSv hr^{-1} was measured.

An elevated dose-rate south of the road (and river) was similarly observed in survey results from October 2015 (Figure 6.10 (b)). Identified in these results also, are the locations where remediation work had commenced at the site, in addition to the area where this removed

material was temporarily stored (identified as "Bail Store"). The site average 17 months later was determined at 267 CPS or 3.0 μSv hr^{-1}, with a similar disparity between northern and southern fields - with dose-rates of 2.7 μSv hr^{-1} and 3.0 μSv hr^{-1} respectively.

The activities and calibrated dose-rates at the fourteen reference localities, derived from both May 2014 and October 2015 are plotted in Figure 6.11. Also plotted are the values resulting from both back and forward modelling of May 2014 values produced using Equations 6.1 and 6.2. Location numbers are shown for the October 2015 data. From the average site-wide value of 398 CPS (4.8 μSv hr^{-1}) in May 2014, backwards modelling calculations placed the total activity at the Iitate Village site in the immediate aftermath of the release at 820 CPS (9.7 μSv hr^{-1}). This level is consistent with formal radiation monitoring results of 9.0 μSv hr^{-1} - 11 μSv hr^{-1} [85]. Forward modelling of the May 2014 data to October 2015 yields a mean value of 323 CPS (or 3.4 μSv hr^{-1}) - a reduction over the 17 month period of 33%, this calculation, however, produced a greater value than the average actually determined at the site of 3.0 μSv hr^{-1}.

Shaded within Figure 6.11, identified amongst the data from the May 2014 surveys, are the blue data-points, corresponding to the positions on the dissecting road. The activity measured at these locations (reference 1, 2 and 3 on Figure 6.10 (a)) prior to any formal remediation, all plot below the main clustering. The additional divergence of data between values measured and those calculated to have existed in October 2015 are depicted by the spread of red data-points in Figure 6.11 - away from the anticipated (predicted) activities in black. A comparison of the measured and calculated values from each of the 14 points for the October 2015 data is shown in Figure 6.12.

As highlighted in Figure 6.12, and apparent from the two maps in Figure 6.10, remediation activities prior to October 2015 had contributed to dose-rate reductions at a number of locations (9, 11 and 12) - as well as on the road (1, 2 and 3). Storage of this removed material at locality 10 had produced a contrasting activity increase.

Represented graphically in Figure 6.12, a dose-rate reduction is observed at other survey points across the site beyond that ascribable only to radioactive decay or site remediation activities (4, 5, 6, 7, 8, 13 and 14). The results of modelling the γ-ray attenuation resulting from the infiltration (burial) of radiocesium into the soil regolith at these seven positions are shown in Figure 6.13. With the measured value only slightly below the calculated value at point 4, this position is not subsequently discussed. At a number of points (5, 6, 13 and 14), the application of this depth-related attenuation to the October 2015 calculated values yields results equatable to those yielded by actual on-site monitoring - with reductions in intensity through the application of this attenuation factor ranging from 10.9% to 15.5%. As such, the influence of Cs infiltration can be viewed as the likely mechanism by which the dose-rate has been reduced. Despite this mechanism contributing to appreciable reductions in calculated radiation intensity (allowing for
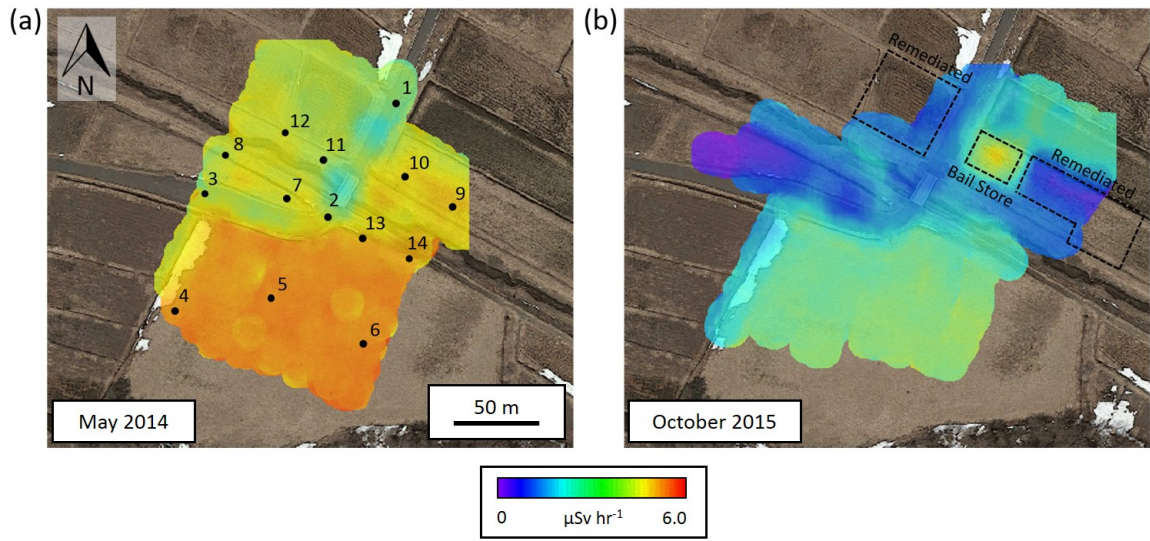
Figure 6.10: Ground-based air dose-rate maps of the Iitate Village site obtained during, (a) May 2014 and, (b) October 2015. *Modified from [103].*
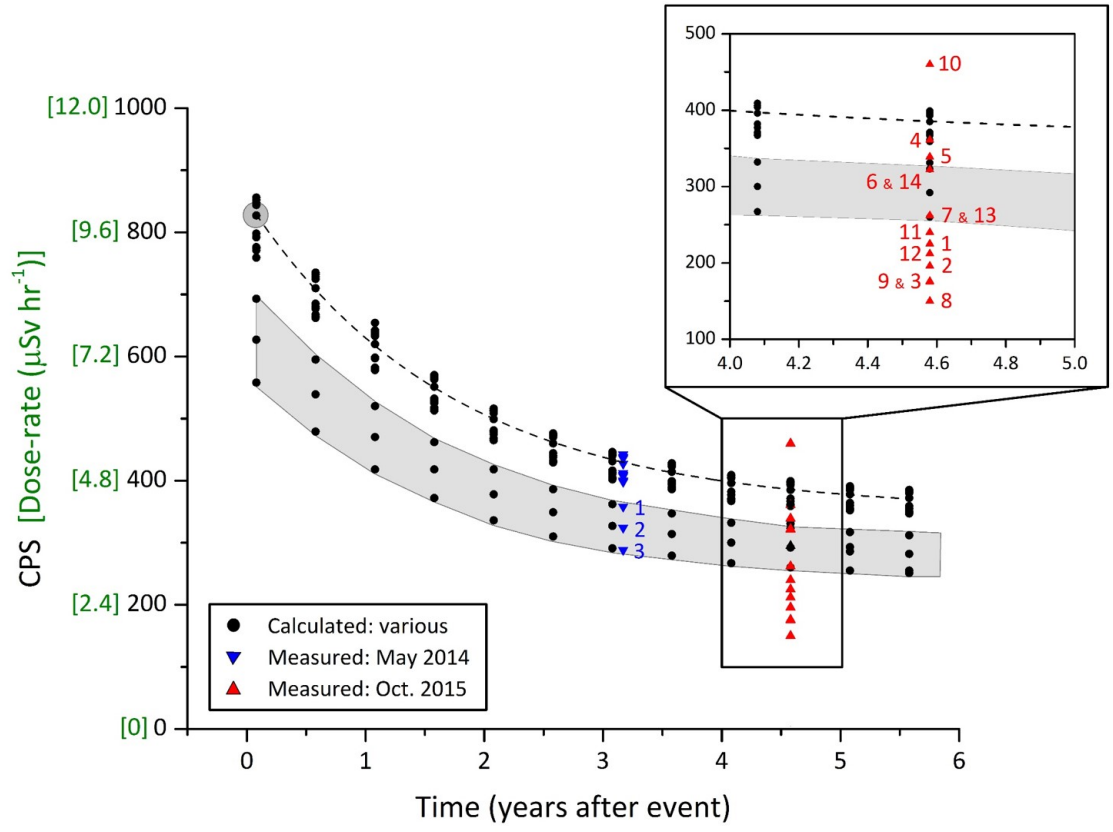
Figure 6.11: Calculated and measured activity levels (CPS and dose-rate) for the 14 points across the Iitate Village study area. *Modified from [103].*
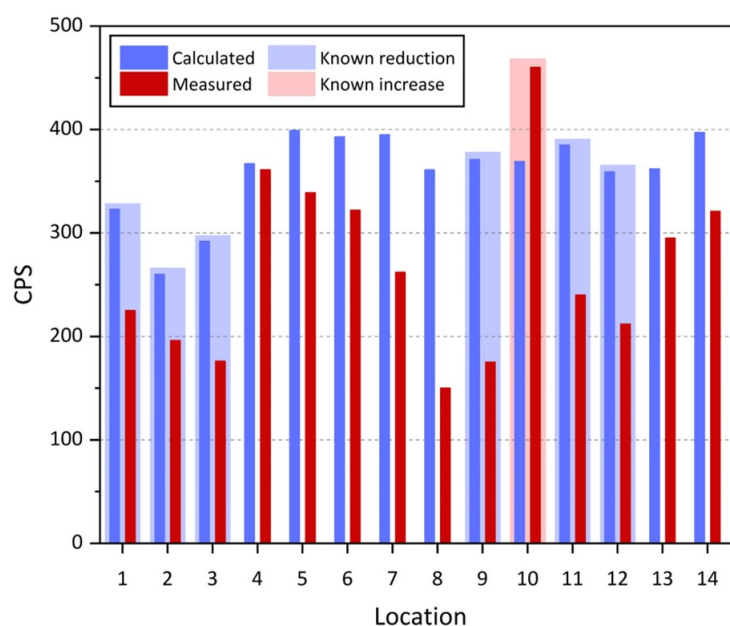
Figure 6.12: Site reference point comparison between calculated and measured radiation levels in October 2015. *Modified from [103].*

a comparison to physically measured values), lower levels of radiation, not rationalised by this mechanism were, however, determined at other points - both positions 7 and 8.

Both of these survey points contrast to the majority of the other positions in their proximity to the river - itself 1.5 m wide and within a 2.0 m incised channel. Points 7 and 8 are located 9 m and 13 m respectively from the rivers southern-most bank. With both surveys being performed using the instrument maintained at 1 m above the ground, combined with the small size of the river - no attenuating effects from the small volume of water contained within the channel are envisaged.

Typical of many environments, and especially one located within an area typified by typhoon-type conditions [31], soil erosion and transportation (together with surface run-off and overland flow) are prevalent as illustrated previously at Irikuboyama (Section 6.5.1). Following the deposition and absorption of radiocesium onto fine-scale mica and clay-type minerals - its transport as particulate (over a dissolved ionic species) has been determined in a number of studies [303–305]. The extensive output of suspended Cs-containing material into the Pacific Ocean has been reported in Yamashiki et al., (2014) [277] - exacerbated by the region weather conditions. Consistent with these observations, this reduction in dose-rate is likely the result of the fluvial transport of Cs-containing particulate - introduced following erosion of the contaminated banks.

135
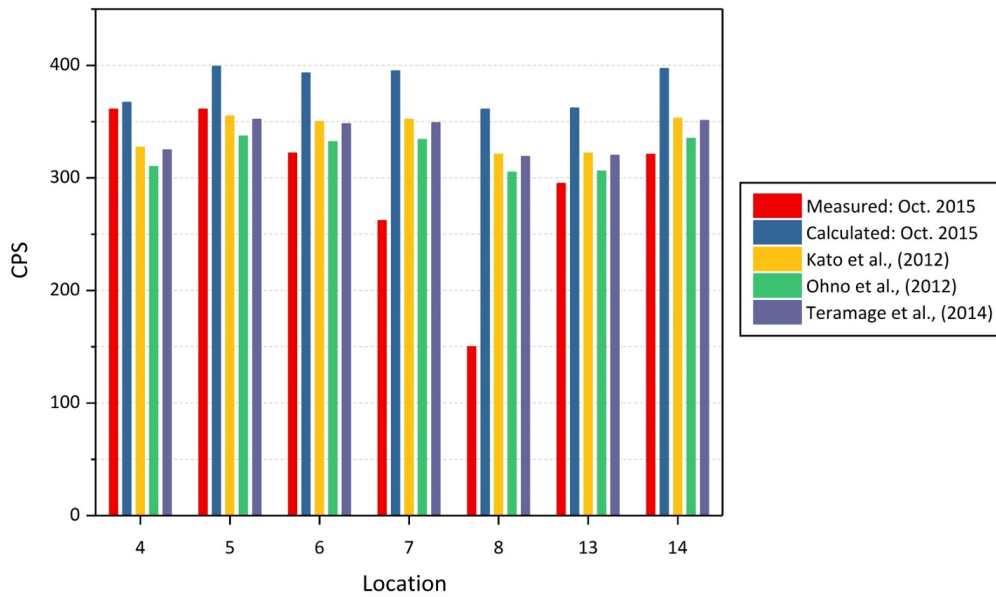
Figure 6.13: Comparison of October 2015 measured radiation intensity values with those derived from forward modelling of May 2014 values, also shown are results of additional depth-attenuation modelling of the May 2014 results. *Modified from [103].*

6.6 Environmental remediation

6.6.1 Yamakiya Junior High School

The maps depicting both the UAV flight path and radiation dose-rate from the airborne survey at the YJHS are shown in Figures 6.14 (a) and (b) respectively. Despite the manual control of the UAV during this work, in contrast to the survey at Irikuboyama (Section 6.5), the consistent grid-line spacing of the survey is evident in Figure 6.14 (a).

Whereas extensive remediation had been performed on the buildings prior to the survey in May 2014 [297], two regions of elevated activity are apparent. Even though these highly-localised areas exhibit dose-rates of 0.75 μSv hr^{-1} and 0.8 μSv hr^{-1} - many times greater than the mean radiation level across the remainder of the roof (of 0.3 μSv hr^{-1}), such dose-rates are only one third of those requiring remediation under the *Act on Special Measures Concerning the Handling of Radioactive Pollution*, instigated by the Government of Japan [155].

The contamination anomalies in this instance are associated with; (i) the location of a large solar-panel array (installed shortly before the accident) - close to the apex of the roof, and (ii) a drainage downpipe on the south-eastern corner of the roof. While following any remediation of part of this Act, extensive characterisation is performed to ensure the removal of all traces of radioactivity [60], the intricate nature and inaccessible nature of the solar panels, however,

136
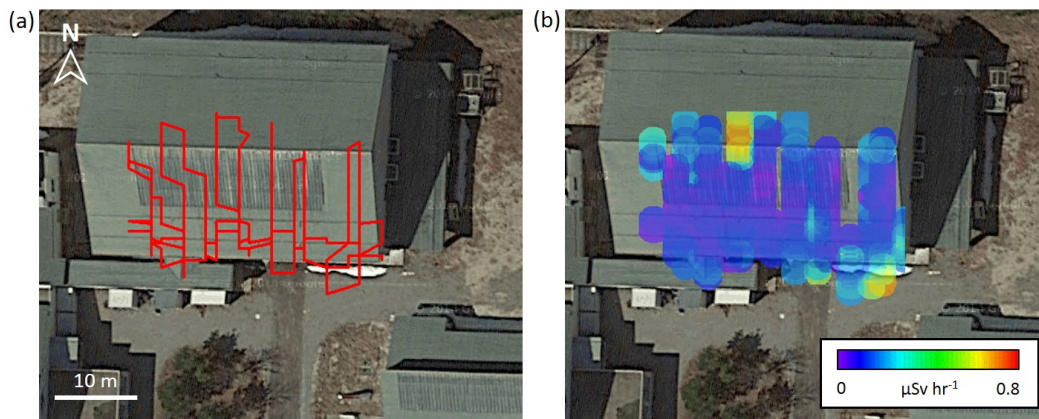
Figure 6.14: Results of UAV radiation surveying at the Yamakiya Junior High School, showing; (a) the flight-path of the system and (b) height-corrected dose-rate map. *Modified from [102].*

presents difficulties in this final assessment step. The report by Miyahara et al., (2012) [296], details the extensive contamination and remediation challenges surrounding drainage pipes and sewage networks - where large source areas feed into/are pre-concentrated. Such areas may therefore be easily omitted or hard to fully decontaminate.

An additional source of material, however, likely arose from the neighbouring forest on the hillside to the east of the school. The influence of the regions extensive forests as a long-term source of (particulate) contamination (and hence radiological dose) since the accident has been the focus of a number of studies [289, 306, 307], with this site in Kawamata Town having been left untreated to allow for the through-flow study, presented in Cresswell et al., (2016) [308]. In this study fallout material was shown to have been initially trapped by the highly textured surfaces of leaves and bark, with the subsequent downwards redistribution resulting from wind and/or rain, re-contaminating areas/sites/buildings once remediated.

Despite presenting only a minimal radiological hazard in this instance due to; (i) the isolated nature and, (ii) the low activity of the contamination - the importance of not only ensuring complete initial site remediation, but also performing continued site monitoring to determine the extent of any contamination migration/recontamination is shown to be essential. Also further demonstrated, is the ability of the system to resolve radiation anomalies at the meter-scale - comparable to that performed through human monitoring, however, at localities inaccessible or impractical for human operatives to study.

6.6.2 Hirokuboyama

In addition to the cumulative flight-path map of the airborne surveys - shown in Figure 6.15 (a), the resultant radiation (dose-rate) map of the site is presented in Figure 6.15 (b). Due

to the sites large size, the total flight-path of the UAV is extensive - formed from a series of 20-minute to 30-minute duration flights, with irregularities in its path due to on-site obstructions.

Apparent from the radiation map of Figure 6.15 (b), are a number of elevated radiation intensity features. To the north and west of the site (highlighted) were located two areas where surface (stripped) waste material was stored, alongside dense forest around the southern boundary of the site. While the UAV did not enter into the forest, the influence of contamination adhered to its numerous physical surfaces is observed (as was the case at Yamakiya Junior High School). This woodland represents a secondary radiation emitter, existing perpendicular to the radiologically contaminated ground and the primary source of dose encountered.
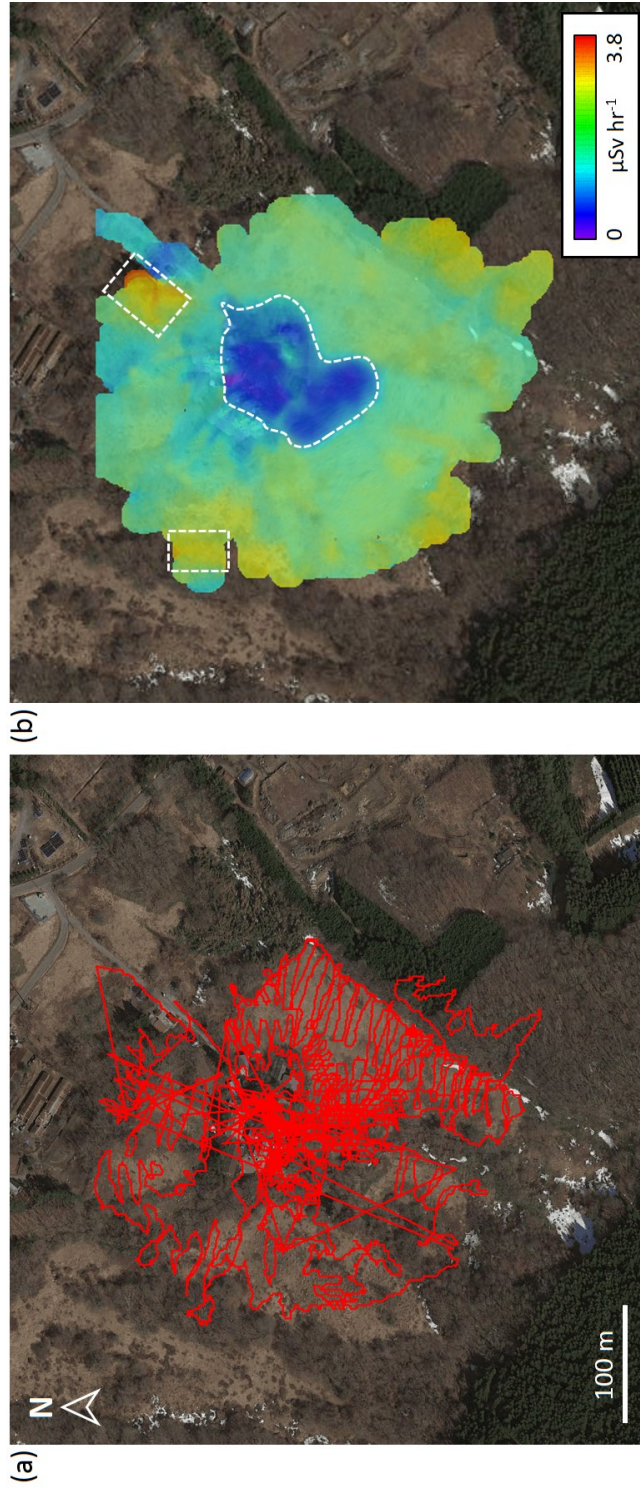
Figure 6.15: Cumulative results of UAV radiation surveys at the Hirokuboyama livestock farm, showing; (a) the total flight-path of the system and, (b) the height-corrected air dose-rate map. *Modified from [102].*
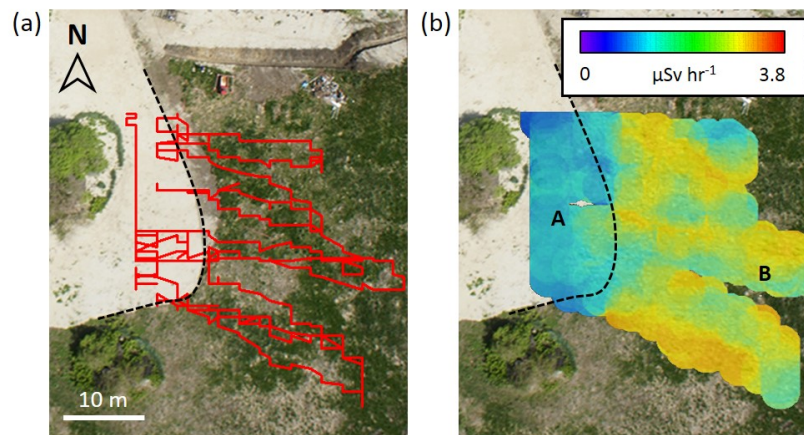
Figure 6.16: Portion of the UAV radiation mapping survey from Figure 6.15 (b), showing; (a) the path of a single flight and, (b) the height-corrected air dose-rate map. *Modified from [102].*

Observed also in Figure 6.15 (b), is an area at the centre of the farm where a considerable dose-rate reduction exists. This local activity minimum corresponds to the location of the contrasting method of remediation employed at this site. Whereas all other sites in this study were remediated through the removal of material, at this locality, however, as previously stated a 15 cm thickness of coarse sand was applied as a blanket directly over the contaminated land. A portion of the survey flight over the transition that exists between the remediated (sand-covered) area and the remainder of the uncovered field is shown in Figure 6.16, detailing in (a), the systems flight path, and in (b), the resultant dose-rate map. The clear and rapid drop-off in activity, as determined by the sub-meter resolution attained by the UAV is apparent, as is also shown graphically in Figure 6.17. Over a distance of 10 m from A to B (Figure 6.16 (b)), a two-fold increase in activity is measured - with an average dose-rate increase from 1.8 µSv hr^{-1} to 3.5 µSv hr^{-1}. This increase is observed around the entire area overlain by sand.

While this experimental remediation method has yielded a dose-rate reduction to levels below those defined as sufficient under the *Act on Special Measures Concerning the Handling of Radioactive Contamination* [155], at 2.3 µSv hr^{-1}, this reduction is not as substantial as those resulting from conventional decontamination methods. Similar to the ploughing of affected agricultural fields, this strategy is advantageous in dose-rate reduction as it does not produce material that requires final disposal, rather relying on the attenuation from the overlying material. Hence, this method would be cheaper to administer.

Unlike "traditional" methods, this technique does not physically remove contamination from the affected area - where it continues to exist distributed within the uppermost soil horizons, as such, public acceptance is likely to be lesser than if the contamination were to be completely removed. This strategy, although a rapid and low-cost means through which to "decontaminate" a large
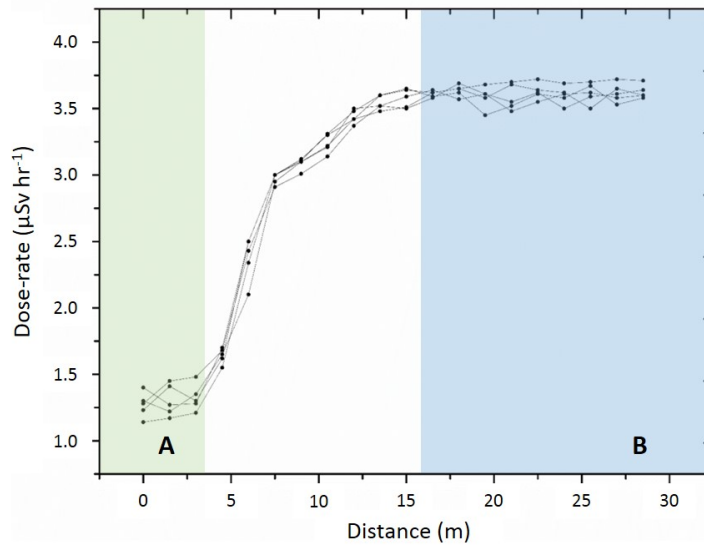
Figure 6.17: Dose-rate variation outwards from the sand-covered portion of Hirokuboyama site, between points A and B (Figure 6.16 (b)). *Modified from [102].*

area of agricultural land, does require greater upkeep over the succeeding years. The impact of not providing adequate care and maintenance to this site was evidenced during a subsequent visit in June 2017. With no actions undertaken to control plant growth beyond the deposition of sand that occurred shortly before the May 2014 survey, extensive re-growth of plants had occurred. Because of this, the dose-rate measured across the sand-covered portion of the site was identical to that determined elsewhere across the survey site. This re-establishment of pre-remediation dose-rates is likely the result of (sand) buried Cs becoming bound to plant surfaces, which have grown through the covering sand layer. The study by Tanaka et al., (2012) [309], and Niimura et al., (2014) [310], detailed the high level of Cs incorporation into the physical structure of such organic material, and explains such an observation.

6.6.3 Okuboiriyama

Representing the final step within the extensive remediation process, the radiation map from the $1 \, m^3$ bags located across the interim waste storage site at Okuboiriyama, determined using the ground-based dual-unit system, is shown in Figure 6.18.

Despite having only been placed onto the newly-prepared (and formerly contamination free) site for a maximum of ten weeks, an apparent "plume" of contamination away from the known (marked) position of the waste storage bags was observed. Whilst a dose-rate high of 2.5 $\mu Sv \, hr^{-1}$ was found at the location of the waste storage bags, dose-rates greater than 2.0 $\mu Sv \, hr^{-1}$ occurred over a 100 m area to the south of the under-construction storage facility. This apparent movement of radioactivity is consistent with the location and topography of the site, existing on a hillside,
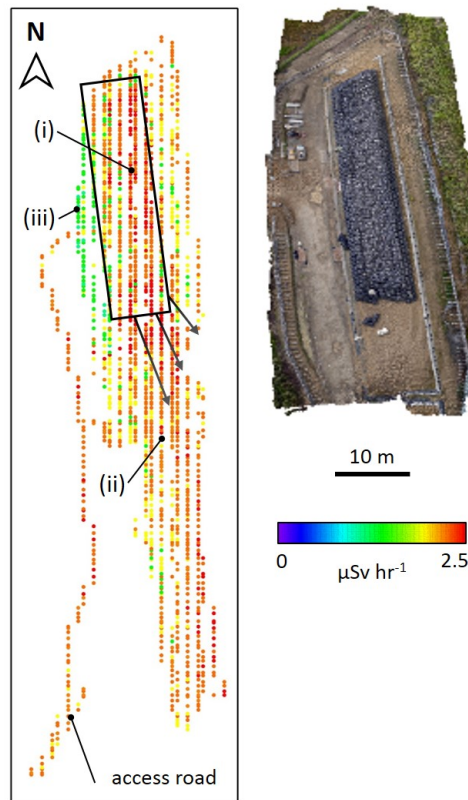
Figure 6.18: Air dose-rate map of the Okuboiriyama waste storage site. Identified is the location of the area containing the bagged waste material, the direction of apparent contaminant migration and also positions at which γ-ray spectra were obtained ((i) to (iii) in Figure 6.19). A photogrammetry rendering, corresponding to the location of the waste bags, produced through stitching overlapping aerial photographs is additionally shown.

with the site gently inclined to the south. While considerable care was employed to minimise water ingress into the waste bags during the site's construction, the eventual outflow of species under hydrological conditions was likely to be the result of precipitation through-flow - subsequently carrying radiocesium out either as an ionic species or associated with solid particulate. The escape of fluids originally contained in the storage bags is an additional, potential source of the highly-mobile radiocesium.

Following γ-ray spectroscopy of the storage bag heap and associated radioactive plume (Figure 6.18, points (i) and (ii)), the contamination signature was determined to be identical to the other sites - comprised exclusively of ^{134}Cs and ^{137}Cs (Figure 6.19 (a)). Additional spectroscopic analysis of the imported sand used to overlie the site (Figure 6.18, point (iii)), however, detailed the existence of other, non-accident attributable, γ-ray emitting radioisotopes.
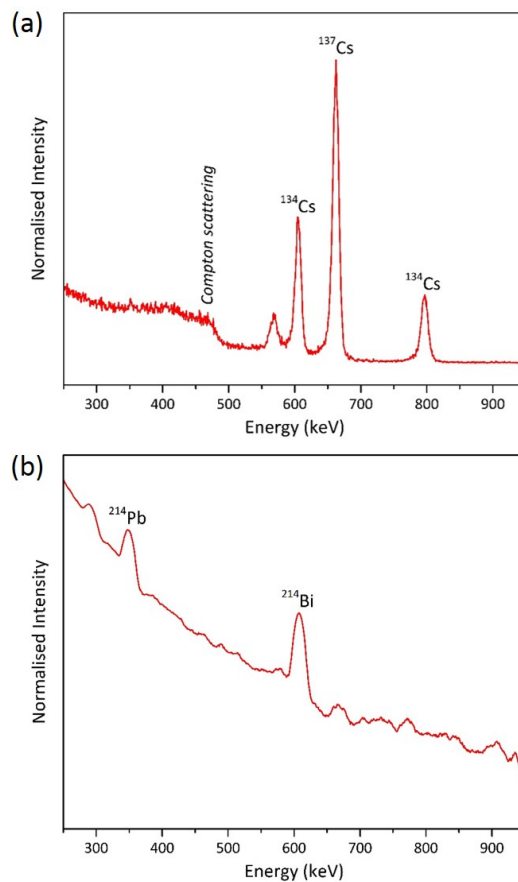
Figure 6.19: Gamma-ray spectra from Okuboiriyama representing; (a) locations containing/contaminated with radiocesium (positions (i) and (ii)), and (b) newly-imported sand, (position (iii)).

Contrasting to the waste materials, the γ-ray spectrum of the uncontaminated "clean" sand is shown in Figure 6.19 (b). While not containing any radiocesium, the spectrum shows the emission peaks from ^{214}Pb and ^{214}Bi - isotopes within the uranium-series decay chain. This sand is sourced from localities in neighbouring regions of Japan (personal communication with remediation site manager), all of which contain a (small) natural uranium component [151].

Through the application of the γ-ray spectrum to activity conversion equation detailed in Equation 3.1, an approximate activity for a subsequently sampled volume of both the stripped (and now stored) radiocesium-containing organic material and the imported sand could be quantified. This collection of additional in-field γ-ray spectra was similarly performed (as per the aerial mapping) using the hand-held GR1 miniaturised γ-ray spectrometer, however, employing a counting time of 30 minutes on a 1 kg mass of sample. The results of this analysis determined the Cs-containing (bagged) wastes to exhibit an activity of approximately 27,300 Bq kg^{-1}, with the sand showing an activity an order of magnitude less at 2,570 Bq kg^{-1} (2.57 Bq g^{-1}).

While remediation activities continue to actively reduce dose-rates to below the prescribed limits [155], the site-wide addition of sand at this particular site has conversely resulted in the addition of radioactivity. Although the total duration of the uranium-series decay-chain is many orders of magnitude greater than even the longest-lived Cs isotope (^{137}Cs) [52] (with a correspondingly lower activity), this addition of naturally-occurring radioactive material (U, Th and K) contradicts with the governments goal of significantly reducing radiation levels across Fukushima Prefecture. It should be noted, however, that this U decay-series containing material is not only naturally-occurring [311], but has a γ-ray activity below levels deemed acceptable (in the UK) [221].

6.7 Discussion

This chapter sought to apply two types of newly-devised radiation monitoring platform to determine the time-resolved spatial extent, migration behaviour and environmental impact of Fukushima-derived radiocesium at a number of analogue sites. These sites were characterised as either having been remediated (or are in various stages of remediation) or having been untouched since the March 2011 radiation release.

Through the high-resolution mapping results, at sites where little or no remediation had occurred (Irikuboyama and Iitate Village), extensive contaminant transport was evidenced. This movement of material away from an initially uniform radiocesium distribution to generate markedly concentrated hotspots of radioactivity was seen to result from its readily-mobilised nature, transported under the influence of water; a result of both precipitation and fluvial action (in the case of Iitate Village). Material from Irikuboyama was observed to have travelled tens or hundreds of meters in the three years post-release, with material from Iitate Village having likely travelling tens of kilometres, feeding into the Pacific Ocean through the Abukuma river. As shown in the numerous formerly described studies, with the radiocesium strongly bound to the highly-reactive edge sites of clay and mica-sized particles, it is not only difficult for it to become desorbed from its host colloidal sized particle, but also for this material to settle out from the fluid that transports it - requiring near-still fluid transporting conditions.

Contaminant transport and reintroduction was also observed at remediated sites. The Yamakiya Junior High School in Kawamata Town highlights the likely influence of material sourced from neighbouring un-remediated areas, re-contaminating locations previously cleaned. This material was likely mobilised by the wind, being further transported by rain - transport mechanisms typical of the typhoon-type sub-tropical environment within which Fukushima Prefecture exists. The extensive fluid-related movement has also caused notable migration at the Okuboiriyama

waste storage site - a location established to contain material for the period prior to the instigation of interim and permanent disposal facilities. At the time of writing, following the presentation of these results to the company charged with the construction and maintenance of this storage site, it has since been remediated. This remediation has seen the contaminated hard-stand sediment replaced and the bag pile covered with an impermeable geo-polymer (with welded seams) to prevent against water ingression.

6.8 Conclusions and implications for Fukushima

Both the newly-devised UAV and ground-based radiation detection systems have further proven their ability to determine the spatial extent and isotopic composition of radioactive contamination across a series of test sites. The units ability to monitor regions of interest with challenging/difficult access, or those sites dangerous for human operatives to work (due to the risk of radiation exposure) therefore represents significant advantages of these low altitude UAVs over "traditional" human-based (ground) surveys methods.

The readily-mobilised nature of radiocesium, sorbed onto particle surfaces, has large-scale implications for the distribution of residual radioactive contamination across the entirety of Fukushima Prefecture. While a concern prior to the onset of remediation, the pre-concentration of material and the production of highly contaminated "hot-spots" are of equal concern at sites where remediation has occurred. There hence exists the requirement for the continued monitoring of sites in the years after the main clean-up activities to fully assess the need for any supplementary remedial actions. With a large number of both remediated and un-remediated areas across Fukushima Prefecture alongside hundreds of tonnes of contaminated material, there exists a significant challenge ahead for the Japanese authorities.

As has been shown in this work, UAVs represent a powerful tool for the radiological monitoring of contaminated sites - especially those where accessibility for human operatives is a limitation. Being autonomous, utilising a series of predefined way-points and altitudes, UAVs are able to offer a repeatability that ground-based human surveys cannot simply match. Using UAVs also results in theoretically no ionising dose being experienced by the operator. While primarily advantageous from a radiation protection viewpoint, the impact of differing amounts of bodily radiation attenuation by the operator (that would otherwise be incident onto the detector and therefore require an intricate correction be applied), can be excluded.

Work as part of this study on the Okuboiriyama waste storage site highlighted the challenges in providing a suitable, long-term storage facility for the contaminated material generated by the remediation. With material observed to have leached from its original location after a period of only ten weeks; when a longer-term facility is (eventually) constructed, both an improved

containment design as well as continued care and maintenance of the facility will have to be considered.

Having analysed the spatial extent and behaviour of the radiocesium contamination, more "scientifically sensible" approaches to the current clean-up operations could be invoked - with not only a reduced cost but also resulting in a lower radiation exposure to operatives undertaking such work:

1. **"Delay and decay"**. Assuming the contamination were to result exclusively from the γ-ray emitting radiocesium, bound to fine-scale particulate - which itself is highly-mobile, then one approach would be "delay and decay" (a technique associated with the decommissioning of nuclear facilities [204]). After waiting for a sufficient period for; (i) natural radioactive decay to reduce the total activity and, (ii) for particle-bound contamination contained within the regions hill-sides to migrate to the valley floors - only one phase of decontamination would therefore be required.

2. **Do nothing**. Again assuming the contamination were to result entirely from radiocesium - immobilised as an ionic species by its sorption onto solid fine-scale solid particulate, another (and considerably cheaper) approach would be to do nothing - allowing for the dose-rate to reduce naturally. With dissolved Cs shown to exhibit only a limited toxicological risk in comparison to other release species [179, 312], and with radiocesium having been immobilised through its sorption to the surfaces of solid particulate, the element does not represent a toxicity risk whilst in the environment via its biological uptake - rather a radiological hazard.

   Resulting from the majority of the contaminated (and currently habitation restricted) region displaying dose-rates below those observed to occur naturally (Section 3.2.3), remediation activities could be avoided in their entirety.

However, both of these more "scientifically sensible" approaches assume that the species responsible for the contamination is the volatile and high-yield fission product of radiocesium. These approaches, however, would not be valid if other species (e.g. actinides) were to exist as a component of the contamination - whereby greater toxicity considerations would have to be considered [147].

7

PARTICULATE DISTRIBUTION

7.1 Introduction

Nuclear reactor cores contain a range of materials with contrasting compositions and properties, each serving to perform specific functions, including; (i) structural and shielding materials, (ii) boilers and heat exchangers and, (iii) the physical (fissile) fuel and the associated control rod material [35, 128, 174].

As discussed formerly in Section 2.2, with the majority of the work on nuclear fallout having focused on the volatile fission products (principally radiocesium [313–315]) and to a lesser extent that of several actinide elements [145], the environmental impact of particulate of other compositions has yet to receive consideration within the peer-reviewed literature. While some of this material potentially ejected from the FDNPP is radioactive, many of the reactor products are, however, only very weakly or nominally non-radioactive. Despite not presenting a radiological hazard, many elements and materials associated with the FDNPP pose an environmental concern as a result of their chemotoxicity - as defined by the World Health Organisation [316]. The likely micron length-scale of this ejecta material (if comparable to that of the emission material already encountered) presents additional issues owing to its easily inhalable nature - consequently resulting in respiratory issues if smaller than 3 μm in diameter [233].

Complications arise, however, with respect to the analysis of this non-radioactive particle analysis owing to the number of additional anthropogenic sources from which this material could be sourced. Extensive analysis has been performed on both trace and rare earth elements (REE) encountered in the environment at sampling sites around the world; with the foremost number of studies having been undertaken within Japan. These works have investigated anthropogenically-

derived material incorporated into soils [317, 318], contained within meteoric precipitation (rainwater) [319, 320], or entrained as aerosol particulate [321, 322].

In contrast to many European countries, the United States of America and Canada, the limited available undeveloped rural and urban space suitable for development in Japan means that nearly all waste (both industrial and domestic) is incinerated at a large number of plants, rather than being directed to landfill [323]. Recent values placed on wastes generated by the Japanese Ministry of the Environment [324] determined that 70% of all of Japan's waste was incinerated, with only 20% being recycled and 10% directed to landfill. This value is only marginally down on the 74.3% reported by Sakai et al., (1996) [323], two decades earlier. During this period, considerable advancements have been made in the efficiency of capturing the fly ash otherwise released by the incineration process alongside the more efficient (complete high temperature) combustion of the waste material [325].

Owing also to the strong manufacturing and technological industries located across Japan and the surrounding Asian sub-continent (e.g. China, South Korea and more recently India), alongside the limited environmental legislation to control emissions and wastes - aerosol-derived particulate contamination has been witnessed to occur extensively across the region [326]. Much of this particulate has been associated with the production of electronic components, or their end-of-life recycling to recover the highly-valued REEs and other precious metals owing to the record high prices that such elements currently command.

7.2 Aims

The work detailed in chapter sought to undertake a detailed examination of both the composition and size distribution of high Z (atomic) number, micron-scale *atmospheric particulate* fragments distributed across Fukushima Prefecture - potentially released as a consequence of the FDNPP accident. With no prior studies having examined such a suite of non-active material, this work sought to first establish whether material from the FDNPP existed within environmental samples collected from different locations, alongside an analysis of any resulting depositional trends.

If the observed particulate was not able to be definitively attributed to result from the FDNPP accident, an alternative source provenance was required to exist alongside additional (and as-yet unevaluated) considerations for the potential environmental and/or anthropogenic risk.

7.3 Experimental methods

7.3.1 Sample material

A full description of the sampling undertaken across Fukushima Prefecture is detailed in Section 4.1, with site information presented in Table 4.1. To obtain the micron-scale *atmospheric material* potentially released by the incident, naturally occurring organic substrate materials were collected from positions above ground level. These bulk material samples consisted of lichens, mosses, leaves and bark - a number of roadside sediment samples (informally termed "black substances" [327]) obtained from within drainage channels, gutters and culverts were also collected. Each was associated where elevated levels of activity were detected.

For sample analysis (detailed extensively also in Section 4.1), a small portion of each bulk sample (approximately 0.1 g) was placed onto a low elemental background Spectro Tab™ adhesive carbon disc (TED PELLA Ltd.), itself then mounted onto a standard SEM pin-stub. This bulk sub-sample was then placed into the SEM and maintained under vacuum at better than $\times 10^{-5}$ mbar for two hours to permit for sufficient sample out-gassing.

7.3.2 Sample classification

An initial characterisation of a bulk sample from each of the 14 sampling locations was obtained prior to SEM analysis using γ-ray spectroscopy. To afford the best spectral resolution possible (at a detriment to the total γ-ray energy range) the GR1 miniaturised γ-ray spectrometer was used. To derive such a location-specific spectrum, a sample of approximately 10 g was placed within a flat-bottomed (cup-shaped) sample container with the energies of the emitted γ-rays recorded over a 4 hours counting period. A background spectrum with no sample present was also obtained over the same collection period to permit for an appropriate background subtraction to be performed - subtracting the background signal from that obtained from the bulk sample. The γ-ray spectroscopy analysis presented herein was performed during November 2014, corresponding to the passing of one half-life of the shorter-lived ^{134}Cs.

7.3.3 Particle identification and analysis

The examination of the sub-samples after sufficient time held under vacuum was conducted using a Zeiss SIGMA™ Variable Pressure (VP) SEM with attached EDS instrumentation (Octane Plus™ Silicon Drift Detector) and TEAM analysis software supplied by EDAX (Ametek) Ltd. Through the use of the microscopes VP-mode, the negation of electron beam-induced sample charging was achieved through the introduction of a nitrogen-rich atmosphere at low-vacuum conditions (approximately 1×10^{-1} mbar). This setup removed the requirement for a conductive coating (e.g. C or Au) to be applied to the sample - maintaining an "as collected" sample composition.
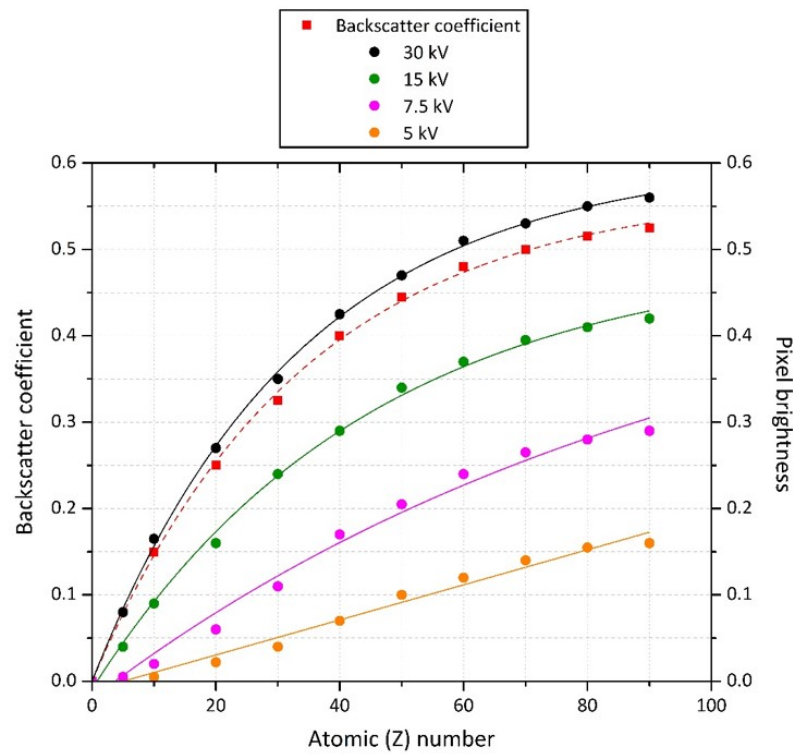
Figure 7.1: Influence of atomic (Z) number on electron backscatter coefficient, calibrated for pixel brightness across a range of accelerating voltages (5 kV, 7.5 kV, 15 kV and 30 kV) in the Zeiss SIGMA™ HD SEM. *Coefficient data obtained from [240].*

During analysis, a consistent working distance of 9.5 mm - 10.5 mm in addition to an accelerating voltage of 25 kV and 1.7 nA beam current (120 μm diameter beam aperture) were maintained throughout. To both rapidly locate and subsequently analyse the elevated atomic (Z) number particles, over mm^2 areas, the instruments backscattered electron detector (Carl Zeiss AsB™) was used alongside high-speed EDS mapping. Using the high-contrast imaging mode alongside a threshold value for pixel brightness, as determined via the calibration results presented in Figure 7.1, upon automatically scanning the sample and moving the microscope's stage accordingly, particles with elevated atomic (Z) number above the background matrix material were identified - evident as bright (white) spots. After the particulates stage-referenced location was recorded by the automated system, the composition of the particles was classified using EDS.

When performing EDS acquisitions of individual particles, the electron beam was rastered over a rectangular region containing no less than two-thirds of the particle - with a background spectrum also acquired of the surrounding substrate area immediately neighbouring the particle for comparison. A collection period of 250 seconds was used to maximise the signal to noise ratio in each instance. Resulting from the interaction depth (approximately 2 μm [239]), from which EDS analysis samples the material, for particles with a thickness less than this, then a contribution

from the underlying matrix was known to arise. This "dilution" of the particles signal with that arising from the substrate resulted in the reduction of the true elemental concentration observed for each of these particles, with an enhanced light element (e.g. C, Si, S and P) contribution.

In addition to analysing the weight percentage (wt%) composition of each high Z-number particle, measurements for the two observable perpendicular (major) axes of the fragment were recorded, as well as the particles surface area and approximate volume - all automatically determined by the microscopes control and analysis software (following the similarly automated identification and compositional quantification). The smallest particles identifiable were determined to be approximately 80 nm in diameter.

A total of 12,000 individual particles were identified and subsequently analysed during this work, across 10 - 15 sub-samples from each of the 14 localities, representing different background (substrate) matrices (bark, leaf, moss etc.). A number of "particles of interest" were later extracted from the samples for subsequent analysis, as described in Section 8.3.1.

7.3.4   Location convention

The convention employed during this work to describe the location of the sampling sites in relation to the FDNPP is shown graphically in Figure 7.2. The distance of each sampling site to the FDNPP was measured directly "as the crow flies" (irrespective of the compass bearing) to the centre of the coastal reactor site.

7.4   Results

7.4.1   Bulk gamma-ray spectroscopy

Arising from the identical source of the radioactive contamination (reactor Unit 2), the γ-ray spectrum resulting from each of the 14 samples were identical - with a representative background-subtracted spectrum shown in Figure 7.3. Corresponding to the earlier spectroscopic results attained by the UAV (Chapter 6 and Figure 6.19), the radionuclides responsible for the γ-ray emitting contamination are those of radiocesium (^{134}Cs and ^{137}Cs). A slight difference in the peak ratios of the two isotopes exists as a result of the difference in their collection (and analysis) date. As a result of the greater count-rates recorded by the GR1 micro γ-ray spectrometer, the laboratory-based γ-ray spectroscopy results contain a considerable number of "double-energy" peaks - whereby the dead-time of the spectrometer was insufficient to differentiate between closely-spaced γ-ray (photon) arrivals.
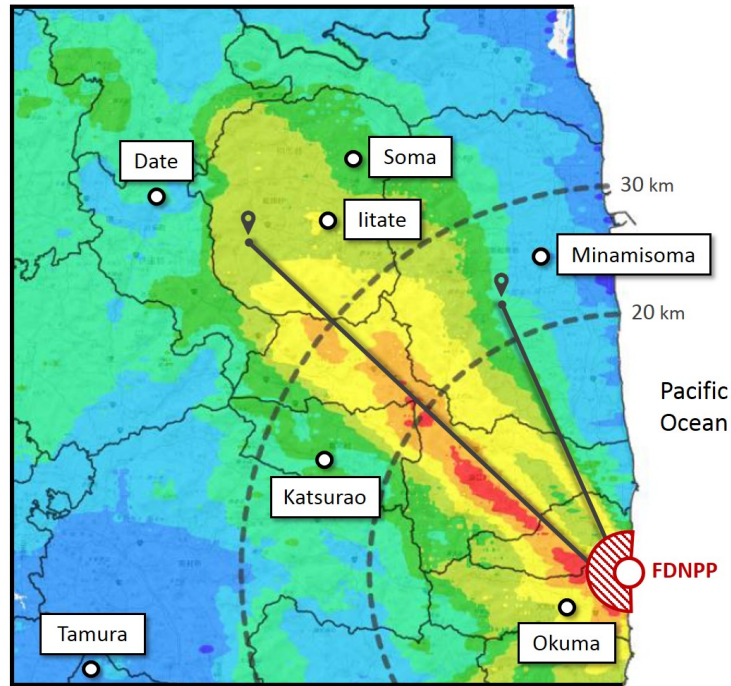
Figure 7.2: Radiation intensity map showing the height-corrected air dose-rate resulting from the FDNPP release. The direct-distance convention (from the FDNPP to each sampling site) used in this work, is shown. *Modified from [231].*
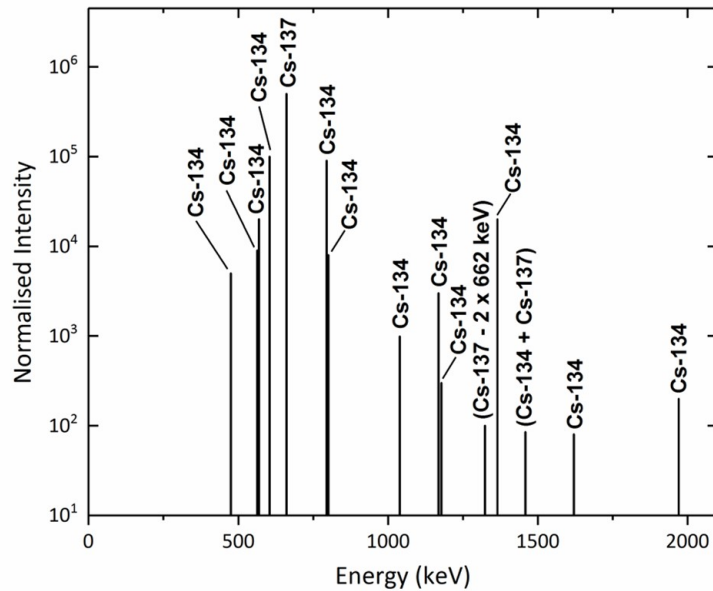
Figure 7.3: Representative γ-ray spectrum for bulk samples obtained from the 14 sampling sites.

152

	33 As	39 Y	40 Zr	44 Ru	46 Pd	47 Ag	48 Cd	50 Sn	51 Sb	52 Te	56 Ba	72 Hf	73 Ta	74 W	79 Au	82 Pb	83 Bi
Site 1			x			x											x
Site 2						x	x	x			x				x	x	
Site 3				x		x					x				x		
Site 4		x	x	x		x					x		x		x	x	x
Site 5			x		x	x					x		x		x	x	x
Site 6				x		x		x		x	x		x	x	x	x	x
Site 7		x	x	x		x		x			x		x		x		x
Site 8			x			x	x	x			x	x		x	x	x	
Site 9			x			x		x	x		x				x		x
Site 10				x		x		x	x	x	x				x	x	x
Site 11			x			x					x				x	x	x
Site 12				x		x		x	x				x		x	x	
Site 13	x			x		x		x			x				x	x	x
Site 14		x	x	x		x					x		x		x	x	

Table 7.1: Elemental composition of *atmospheric particulate* (elements As - Bi) observed at each of the sampling sites, 1 - 14.

7.4.2 Particle composition

The elemental composition of the various particulate encountered at the 14 sampling sites, as identified via EDS, is shown within Tables 7.1 and 7.2 for elements Bi through As, and La through U respectively. Each of the particles were characterised by only containing a single element (with the exception of some particles whereby Ce, La and Nd occurred together, each at equal wt%concentrations) in addition to any number of lighter elements, including; O, S, Na, K, P, C, Si, Al, Fe, Mn, Ti, Cu and Zn - at varying wt% proportions. Apparent from both tables is the commonality that exists for a number of elements observed across most/all sampling locations (e.g. Zr, Ru, Ag, Ba, Au, Pb, Bi, Ce and U). In contrast, the distribution of other elements was markedly less extensive - with particles of As, Pd and Hf encountered at only one locality. Particles containing U were observed at all localities except Site 5 (Date City) - the furthest from the FDNPP, with all of the REEs (Table 7.2) present at numerous (albeit differing) sites.

A plot illustrating the variation in observed wt% composition of the entire particle inventory is presented in Figure 7.4. Apparent is the wide variability in the proportion of the particles principle component; with Ag ranging from 5.5 wt% up to 92.8 wt%, and Au from 4.2 wt% to 81.7 wt%. A similarly large range in principle component of 66.3 wt% and 63.9 wt% is observed for Ce and U respectively. In contrast, smaller ranges in weight percentage composition are observed for species including; As, Sb, Te and Th. Also shown in Figure 7.4 (as green boxes) is the wt% range of these elements present within known naturally-occurring mineral species [328]. For many of the elements, this range of known mineral compositions encompasses all of the particles

	57 La	58 Ce	59 Pr	60 Nd	62 Sm	63 Eu	64 Gd	65 Tb	66 Dy	67 Ho	68 Er	70 Yb	90 Th	92 U
Site 1		x												x
Site 2		x										x		x
Site 3														x
Site 4		x			x									x
Site 5		x			x			x	x					
Site 6	x	x	x	x	x	x	x	x	x	x		x	x	x
Site 7		x	x	x		x	x	x	x	x	x	x	x	x
Site 8		x												x
Site 9	x	x	x		x		x	x	x	x	x			x
Site 10			x		x		x	x	x			x	x	x
Site 11		x												x
Site 12						x							x	x
Site 13														x
Site 14		x			x									x

Table 7.2: Elemental composition of *atmospheric particulate* (elements La - U) observed at each of the sampling sites, 1 - 14.

encountered in this work - with Zr, Ru and Te, for example, all bound by these known mineral compositions. Mobilisation and re-deposition of such mineral particles is one mechanism by which some of this material could exist within the environment [329]. This mechanism could account for this particulate material, including particles composed of Au, Ba, Au and U - observed across the largest number of the sampling sites. As it is discussed subsequently in Chapter 8, the results are not presented nor discussed here, however, U particulate was shown to exist with the fewest (and smallest) contributions from other (accessory) elements.

The wt% composition of some of the particles identified within the environment, however, plot firmly outside those of recognised mineral compositions - with some elements existing at concentrations considerably beyond those attributable to geological minerals. The particles exhibiting such a significant elemental enrichment are the REEs (Ce to Yb) - with Tb, Ho and Er showing no overlap with the elemental wt% of known mineral material. Tb exists with a maximum particle weight percentage of 63.8 wt%, while its naturally-occurring (in-mineral) concentrations vary only between 0.03 wt% and 0.57 wt%. Such elemental concentrations represent direct evidence for this material resulting from anthropogenic processes. The most of which is manufacturing, but this does not alone provide a conclusive mechanism to account for how this material came to exist as aerosol sized fragments. Images of typical fragments are shown in Figure 7.5, illustrating their highly-angular form and embedded/adhered nature onto the surfaces of their containing substrate materials.
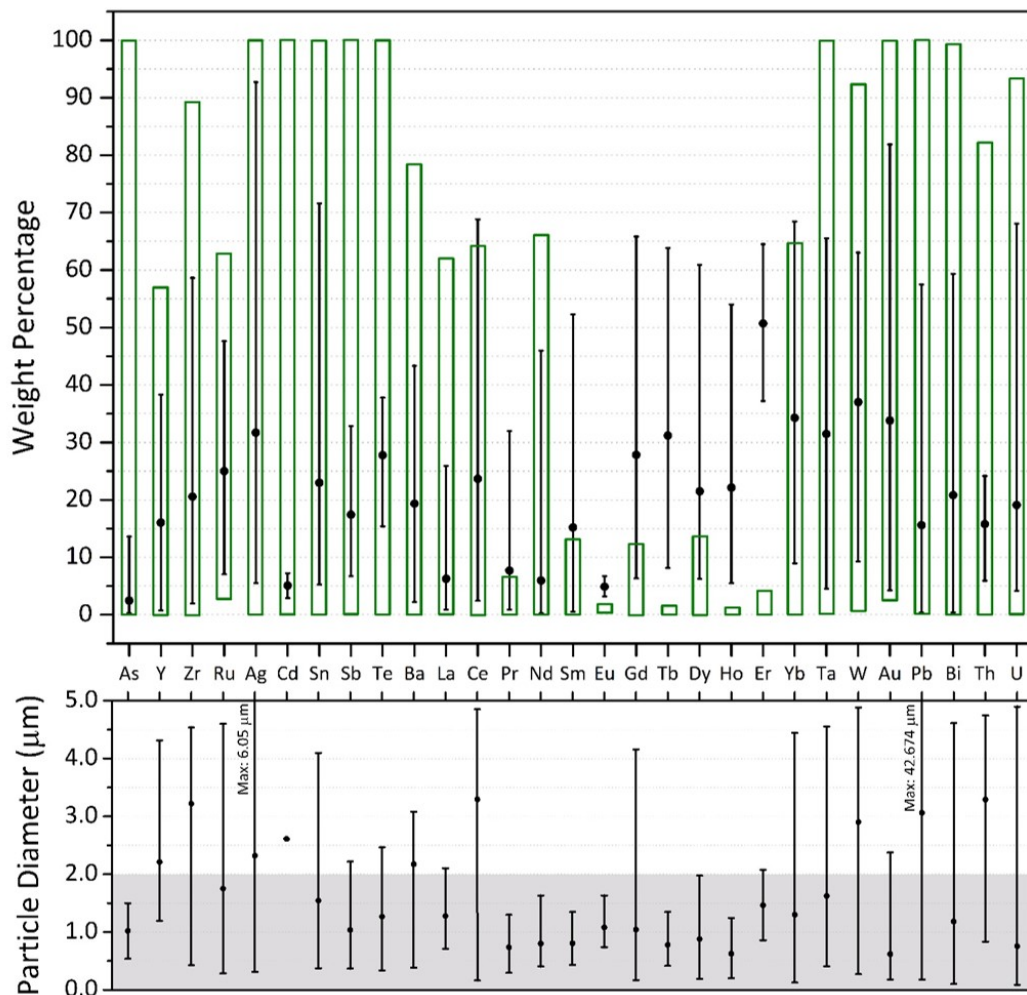
Figure 7.4: (Top) elemental weight percentage composition of particulate across all sampling sites (black lines), alongside the compositional range of elements observed within known mineral species (green boxes). *Mineral composition data obtained from [328]*. (Bottom) average diameter for particulate of each elemental composition. The sampling depth of EDS (circa 2 µm) is highlighted (grey), whereby the influence of substrate interaction/sampling would dilute the compositional analysis results derived from the particulate.
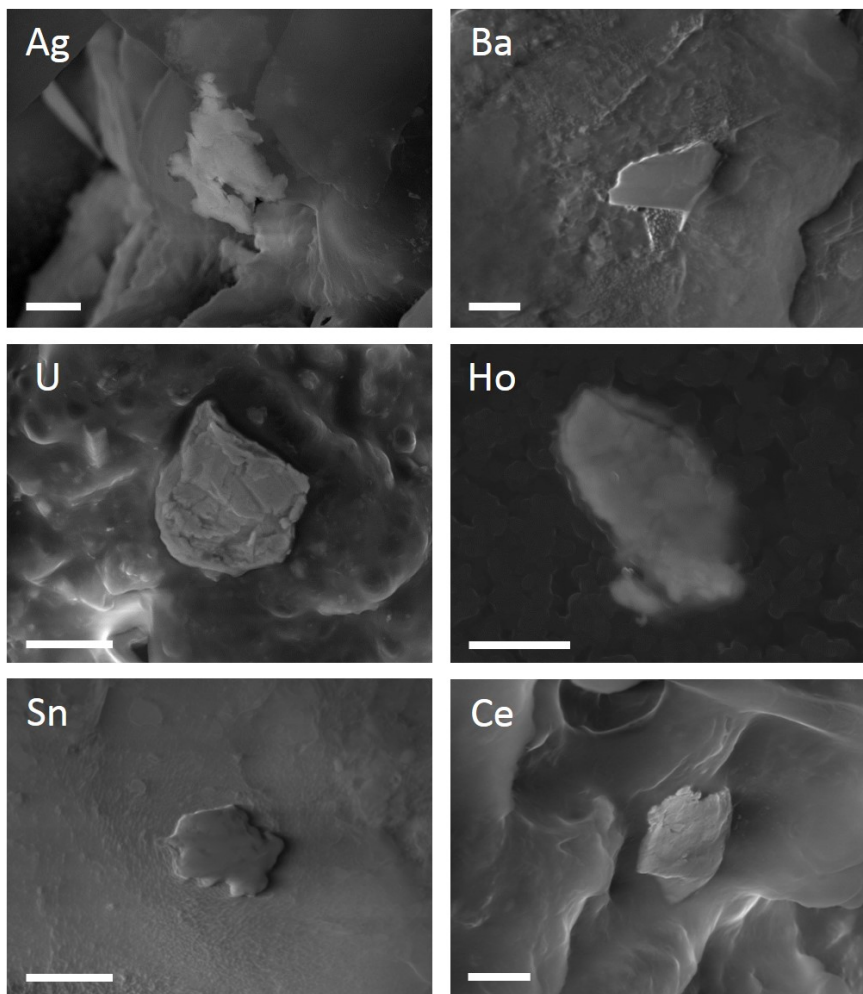
Figure 7.5: Secondary electron images of *atmospheric particulate* material observed on organic substrate surfaces obtained across the 14 sampling sites. Scale bars = 1 μm.

7.4.3 Elemental size average

The mean diameter for each of the particles (of differing elemental composition) is shown in Figure 7.6, averaged across all 14 of the sampling sites. With the exception of two outlier points (Y and Hf), there is a gradual reduction in particle size with increasing atomic mass - with particles of U being some of the smallest observed (average size = 1.07 μm), distributed across the plume-affected area.

Many REEs, circled in Figure 7.6, are seen to group together - existing below the trend-line derived for the particulate of other compositions. Based on such a grouping of the REE, this could invoke that fragments constituted principally of these elements were derived from a specific formation scenario potentially associated with events at the FDNPP, or conversely, a source entirely unrelated to the 2011 release.
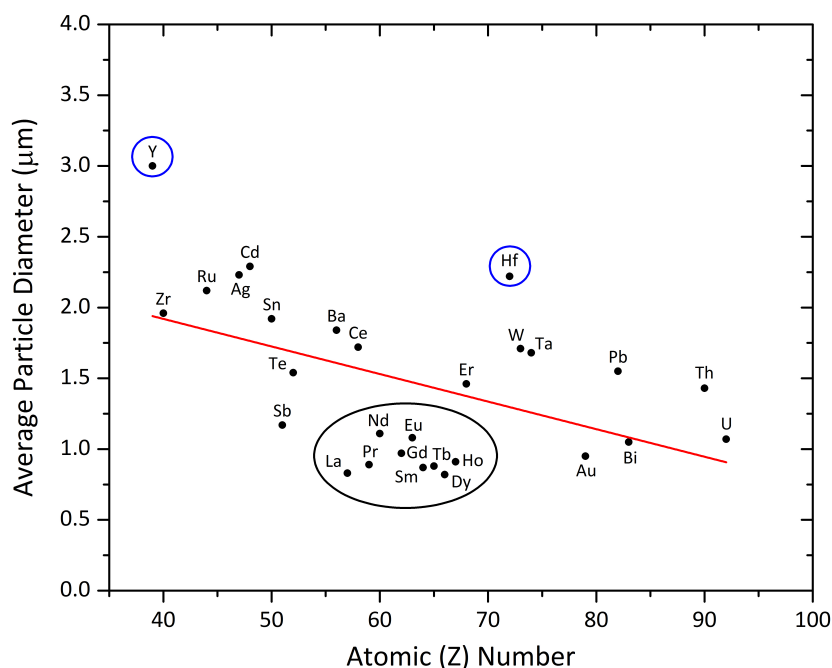
Figure 7.6: Variation in particle diameter with differing principle elemental component. Y and Hf outliers are highlighted, as is a grouping containing the REEs.

This plot, however, does not factor the influence that differing site location (distance from the source) has on the particles diameter - rather illustrating the reduction in average particle size with composition. Whereas a reduction in particle size is apparent for atomic (Z) number, such a trend would not be observed if elemental density were, in contrast, plotted against average particle diameter. The variations in density for both native elements and typical metal-oxide species is detailed within the CRC Handbook of Chemistry and Physics [165]. While representing an interesting yet unexpected trend, as the densities of the most frequently observed oxide species of the two end-member elements (Zr and U) are near-identical [165], the average diameters of these particles should be comparable - for which, as shown in Figure 7.6, they are not. More appropriate and meaningful representations of the distributions of this particulate data, however, are hereby subsequently presented.

7.4.4 Average particle size

A plot showing the diameter of all particulate as well as the weighted average value (blue) for fragments of all compositions sampled at all 14 localities, is presented in Figure 7.7. Apparent from this plot is the small range that exists between these average particle size values, with
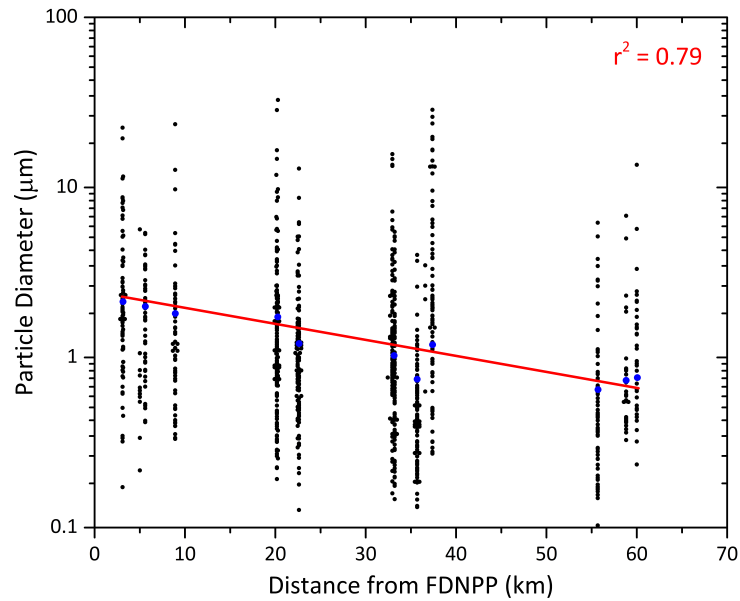
Figure 7.7: Mean particle diameter for all composition material, plotted against distance from the FDNPP.

diameters occurring between 0.93 μm and 2.62 μm - alongside a mean value for all particulate of 1.61 μm. When plotted on this log-linear axis scaling, the trend-line applied to the data follows a linear relationship, with the mean particle diameter showing a decreasing size with increasing distance from the plant. Over the near 64 km distance, a reduction in particle diameter equal to the mean, of 1.61 μm is observed (a 64.6% overall decrease).

7.4.5   Elemental size average

In addition to the linear relationship (when plotted on log-linear axes) shown by the average particle diameter vs. distance plots for all elemental compositions (Figure 7.7), similar trends are observed for specific elements - with the average particle diameter declining markedly over the length of the north-west trending plume. These plots, detailing the average particle diameter for specific elements with distance from the FDNPP are shown in Figures 7.8 and 7.9.

Ag composition material has been extensively studied and quantified in a number of earlier works [330, 331]. It is shown here to exhibit a strongly negative correlation - with fragments located within 10 km of the plant being some of the largest material encountered during this entire study (>3 μm in diameter).
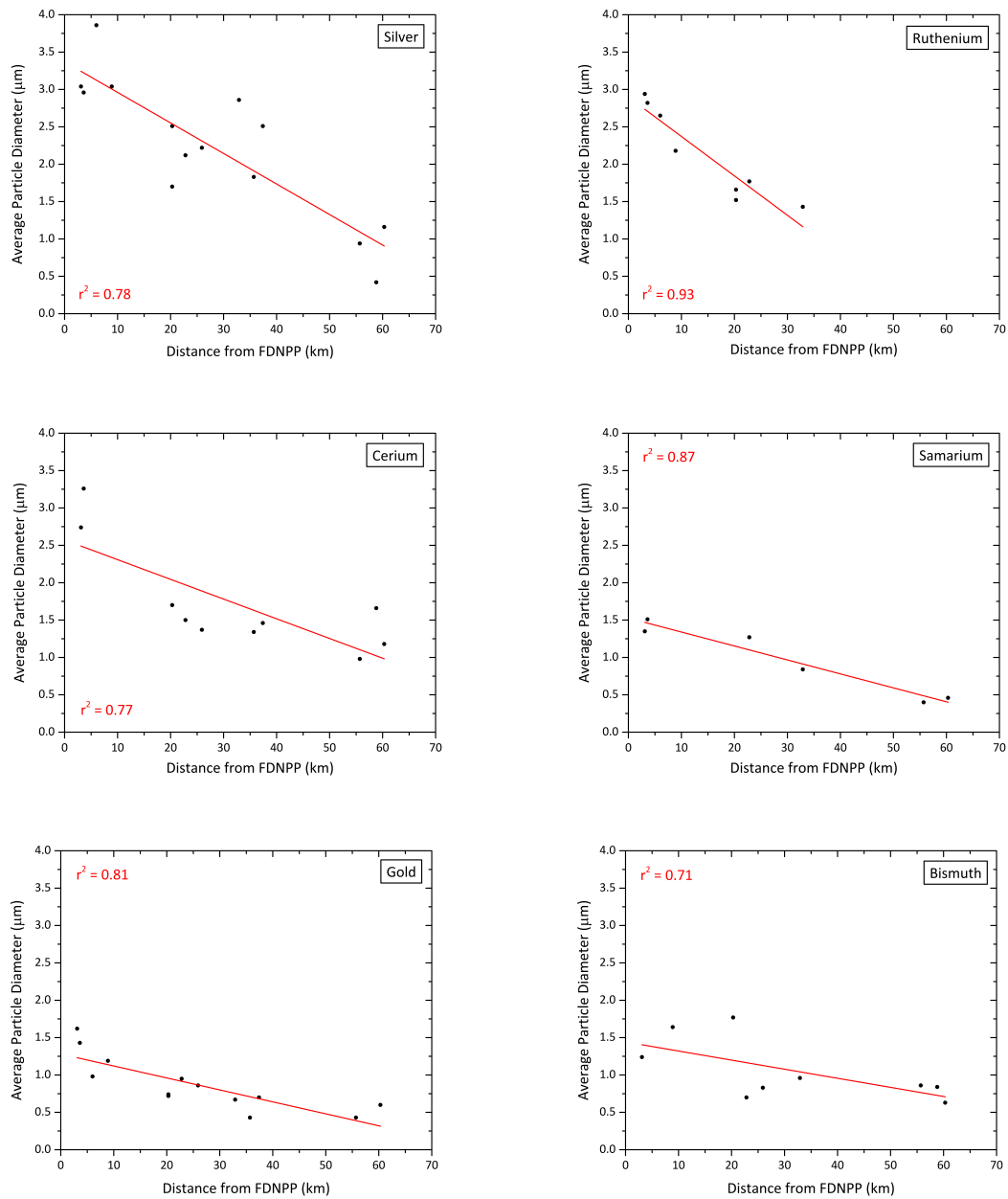
Figure 7.8: Average particle diameter with distance from the FDNPP, for elements: Ag, Ru, Ce, Sm, Au and Bi. The coefficient of determination (r^2) is shown where a correlation is observed.
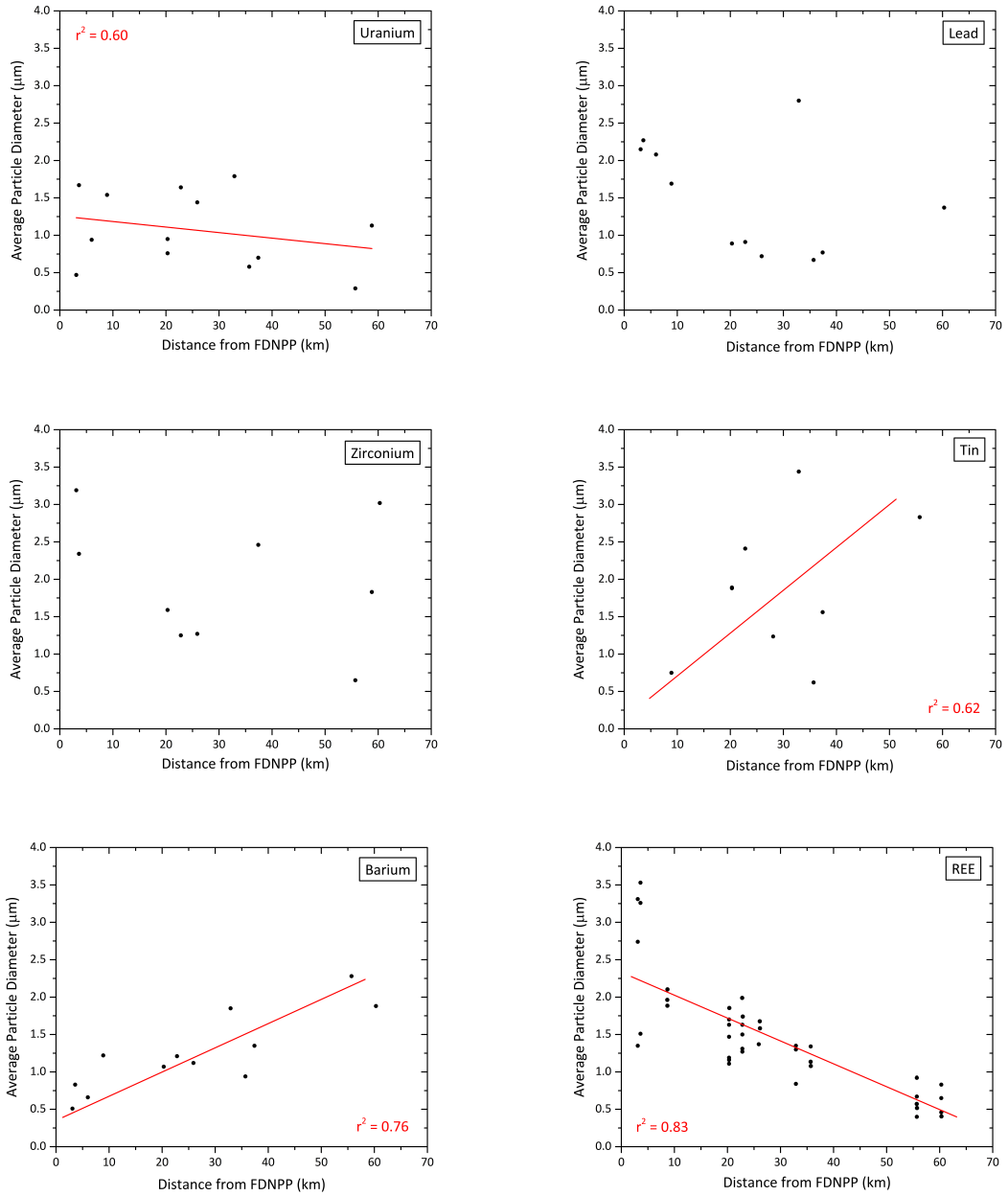
Figure 7.9: Average particle diameter with distance from the FDNPP, for elements: U, Pb, Zr, Sn, Ba and REEs. The coefficient of determination (r^2) is shown where a correlation is observed.

Exhibiting with a similar gradient to Ag, particles of Ru composition, were also identified to show the same decline in particle diameter with increasing distance from the FDNPP site. Unlike Ag and fragments of other compositions, however, the density of Ru is significantly greater than other elements. Such a density (12.1 g cm^{-3} [165]) may provide a mechanism to account for the occurrence of Ru fragments only at localities less than 35 km from the FDNPP - representing the first to be deposited, having only remained entrained within the transporting air-mass (plume) for a more limited period. Additional potential (Fukushima-related) mechanisms exist to account for this more spatially limited extent of Ru-containing material. One such rationalisation could result from an inherent degree of sampling bias - whereby despite the extensive examination of multiple samples (collected >35 km from the FDNPP), no particles of Ru composition were identified - despite existing within the containing matrix. An additional FDNPP-related explanation could result from the minimum size at which Ru-based particulate exists - with no such composition particulate occurring with diameters below circa. 1.5 μm.

A similar trend to Ag for the Ce fragments is also observed, with an appreciable decline in mean particle diameter over the extent of the sampled sites. In contrast to Ag, Ru and Ce, however, Sm, Au and Bi are all characterised by considerably smaller average particle diameters at sampling localities close to the boundary with the FDNPP site (circa. 1.2 μm - 1.5 μm). While a reduction in the average particle size is similarly apparent along the 60 km plume, the size of this material and resulting gradient of the trend-line are both smaller and shallower respectively.

Occurring as one of the few elements observed at a large number of the sampling sites (Table 7.2), U is also seen to display a particle diameter reduction over the 60 km length of the plume. While displaying a shallower trend-line gradient, comparable to both Sm and Au, the spread of the U data laterally away for the calculated trend-line is the greatest of all of the composition particles encountered - indicating a weaker degree of correlation in comparison to the other data.

The elements Ag, Ru, Ce, Sm, Au, Bi, and U are all shown to display a negative linear trend - with the average diameter of particles composed of these elements decreasing over the 60 km distance north-west from the FDNPP site. Such a linear relationship, however, is not apparent for Pb-containing particulate - whereby no such correlation is observed. The same absence of any mean particle diameter reduction (with distance from the FDNPP) is observed for particles of Zr composition. The material of both compositions is employed extensively for roles within nuclear facilities - the implications for the particulates source attribution is subsequently discussed.

In contrast to the aforementioned particulate whose mean dimensions show either a negative correlation or no correlation with distance from the FDNPP site, material containing Sn and Ba is seen to exhibit positive linear correlations - with size increasing over the length of the plume.
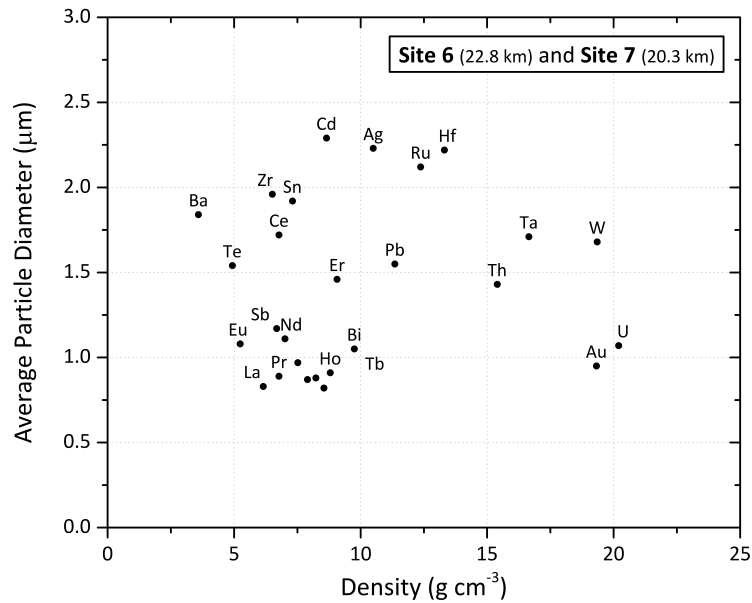
Figure 7.10: Average particle diameter vs. density (corrected for their mean composition - from Figure 7.4) for Sites 6 and 7, located 22.8 km and 20.3 km from the FDNPP site respectively. No correlation to the micron-scale particulates distribution is, however, observed.

Whereas the strength of the fit is not as great for Sn as it is for Ba, a notable disparity with the formerly discussed particulate is clearly evident. This dissimilar trend strongly invokes a different origin of this material to other particulate.

While no correlation is observed for both Pb and Zr containing material and with a highly contrasting positive correlation, however, existing for the particulate containing Sn and Ba - the combined REEs exhibit a strongly-negative correlation, analogous in gradient and fit to both Ag and Ru. In contrast to the various composition particulate, the mean particle size distributions of which are shown in Figure 7.8, the REEs exhibit a degree of size variability closest to the FDNPP.

A plot detailing the average particle diameter at two similarly located sites (Sites 6 and 7) in which the influence of the materials composition (from Figure 7.4) and hence its density are corrected for, is presented in Figure 7.10. For the two sites, located 22.8 km and 20.3 km from the FDNPP respectively, no degree of statistical correlation is observed. If such particulate material were to be sourced exclusively from a release at the FDNPP, then it could be reasoned that material with the lowest density would possess the largest diameter - with the greatest density material, however, forming the smallest diameter particulate encountered at these two sampling sites. These results, therefore, invoke an additional source contribution to this particulate. As

discussed formerly with respect to Ru-containing material, factors may exist, however, to yield particulate across only limited size ranges - therefore contributing to this apparent absence of an observed density vs. particle diameter correlation.

7.5 Discussion

As evidenced by the various distance, size and composition-based plots shown in Figures 7.7, 7.8 and 7.9, in a number of instances there exists a correlation between the average diameter of the particulate and the distance (from the FDNPP) at which it was obtained.

While the negative linear trend shown by the average particle diameter versus atomic number (Z) in Figure 7.6 could invoke a compositionally induced decline in mean particle diameter, as previously alluded, the influence of the particles density is, however, not considered within this plot. As such, these results serve only as an unusual peculiarity. Whereas the densest element observed during this study was in-fact U - possessing one of the smallest mean particle sizes (1.07 µm), other elements with a comparable high density (e.g. W, Au and Ta), were observed to exist with a smaller mean particle diameter than fragments of a much lower density (e.g. Bi, Dy, as well as the majority of the highlighted REE). When a density correction is applied to account for the summed wt% contributions from each constituent element in the total particle, no statistically significant correlation between the micron-sized particles total density and its site-wide diameter was observed (shown in Figure 7.10).

This grouping of REE-containing particulate below the trend-line in Figure 7.6 suggests a commonality of the source. The likely anthropogenic nature of the material is further illustrated due to a large component of the particles containing elemental abundances above those of known naturally observed minerals (average 30 wt%) - as shown in Figure 7.4.

Owing not only to the wide compositional range of particulate associated with a nuclear facility, but also the highly-variable topographic nature of the contaminated region - the analysis of material by site illustrates an improved and less-erroneous mechanism through which to explore the distribution of particulate via its diameter - excluding the influence of composition.

Shown in Figure 7.7 by the blue data points, is the statistically significant linear correlation (when plotted using log-linear axes) between the mean particle diameter (for all composition fragments) and the distance at which the particulate was obtained from the plant. Such a trend represents strong evidence for this material having been derived from a common emission source - one located to the east of Fukushima City - towards the coast, and likely the FDNPP, to generate such a mean particle size reduction over distributed sampling sites.

163

While the decline in mean particle size for a number of elements used within (or produced by) standard nuclear reactor operation (e.g. Ag, Ru, Ce, Sm and U) serves to further support these conclusions, the lack of a distinctive negative correlation shown by Pb and Zr in addition to the absence of other elements expected to occur within the fallout (e.g. Rb, Sr, Rh and Pd [133]) suggests that some/a component of the particulate is, however, not sourced from the FDNPP. A non-Fukushima contribution of particulate is evidenced by the occurrence (and comparable negative linear trend) of Au and Bi material - neither of which are associated with nuclear operations. In contrast, while both Sn and Ba are elements associated with (produced as a result of) nuclear energy generation, particulate of both elements shows a trend indicative of a source in the opposing direction to the FDNPP - centred inland. The distribution of REEs is statistically significant and similarly invokes a sourcing of material from a location coinciding with the position of the FDNPP.

Exhibiting one of the best-defined particle diameter vs. distance correlations of all elements, therefore strongly invoking its provenance from the FDNPP, Au is an element that is neither used nor produced within a nuclear reactor during its operation [133]. The same is also true for Bi, whereby a strongly linear trend is also observed (despite not resulting from a nuclear source). Being both chemically inert (in all but a small number of instances) as well as being corrosion resistant and electrically conductive results in the majority of Au being utilised in the electronics (and to a lesser extent) the jewellery industry [332]. Bismuth, on the other hand, possesses a considerably smaller number of commercial/industrial applications - the main ones are high-temperature ceramics, industrial castings and specialist alloy manufacturing [333, 334].

Despite occurring as known fission products, produced following the thermal neutron irradiation of standard uranium-dioxide (UO_2) fuel [133], the occurrence of Ag and Ru at significant concentrations and spatial distributions when considered alongside those of Au and Bi further strengthens the requirement for an additional anthropogenic source of particulate. The case for material input from a contrasting non-Fukushima related source is strengthened by the spatially limited occurrence of additional elements - unattributable to a nuclear origin. Such particles include those composed principally of W, Ta and Cd (Table 7.1). With the main application of W being the production of super-hard metals, both Ta and Cd are utilised extensively, and near-exclusively, within electronics and electrical component fabrication [332, 334]. The existence of a number of particles containing As at Site 13 (Teramae, Namie Town) could represent fission product material [133], however, its sole occurrence combined with the low fission product yield of [75]As, hence implies a contrary (non-Fukushima) source of this material.

Owing to their unique properties, the REEs are utilised in the manufacturing of a large number of specialist products and materials [333, 334]. Several of these REE are also produced at notable abundances as fission products [133], including; Ce, Nd, La, Pr, Sm, Eu and Gd (decreasing

in natural elemental abundance through this sequence). Despite Ce and Sm both showing a correlation between particle diameter and distance along the main plume - the combination of; (i) the absence of any other fission product REE-containing particles (e.g. Nd, La and Pr) at comparable concentrations - despite equatable fission produce yields [133], (ii) a contrasting diameter between both particle compositions (Figure 7.8), in addition to, (iii) being amongst the most naturally abundant of the REEs [335], invokes an origin for such material unrelated to the numerous Fukushima release events. Finally, (iv) the proportion of these elements contained within some of this particulate is very high (Figure 7.4) for elements that initially exist at negligible concentrations - being "ingrown" over the UO_2 fuels in-reactor lifetime.

The most characteristic species resulting from a nuclear release scenario is that of the U fuel - originally contained within the facilities core and fuel storage pond(s). Like many of the other particle diameter vs. distance relationships shown in Figures 7.8 and 7.9, the trend of U is similarly linear - albeit with a greater degree of data spread away from the applied trend-line. The mean particle diameter of U-composition material is also one of the smallest encountered, despite exhibiting one of the largest ranges in wt% component composition of all fragment material - with an average U content across all material of 19.6 wt%. In contrast to particles of other compositions, those containing U were observed as part of this work to contain a reduced number (component) of accessory (accompanying) elements. Owing to the small diameter (<2 µm) of these U particles, as discussed previously and illustrated graphically in the bottom portion of Figure 7.4, their EDS compositional analysis will result in the electron beam interaction and resultant sampling of the underlying (containing) bulk material [239]. This quantification will resultantly introduce a background (and additional species) into the spectrum and subsequent quantification determined for the particle.

In the works of Kikawada et al., (2009 and 2012) [336, 337], both enrichments and depletions in U isotope ratios ($^{235}U/^{238}U$) for atmospheric deposits obtained at localities across Japan were determined. Despite not analysing particulate material as part of this study (rather bulk material via solution analysis), the enrichment and depletion were suggested to result from nuclear testing fallout (from East Asia) and depleted uranium munitions (from the 1991 Gulf War) respectively. This material was blown across from the source regions by prevailing winds. The application of phosphate fertilisers as invoked by Yoshida et al., (1998) [338], is a further mechanism through which elevated concentrations of U were reasoned to exist, with Hirose and Sugimura (1981) [339], attributing the atmospheric burn-up of the Russian COSMOS-954 in 1978 as a further source of anomalous U ratios. The global influence of the 1986 Chernobyl accident has also been recorded across the entirety of Japan as a result of bulk material isotopic analysis by Aoyama et al., (1987) [340], and later by Hirose et al., (1990) [341]. Highly-localised U isotope anomalies associated with the criticality accident at the JCO campus (Ibaraki) in September 1999 have been further cited as a source of anthropogenic uranium in the environment by Yoshida et al.,

165

(2000) [342]. None of these sources, however, can singularly describe the existence, and more importantly, the decreasing particle size observed away from the FDNPP.

Aside from the atmospheric release events at the FDNPP, and as mentioned previously, a range of alternative sources exist to account for the existence of some of the particulate types - associated with specific industries/processes. One such source is the suspension/resuspension of elements, including REE, sourced from soils and geological deposits [329, 343]. Major sources of this material, some from significant distances from where they are eventually recovered, arise from the increased use of motor vehicles and urban activities [344]. However, the underlying geology of the Fukushima Prefecture region - much like the rest of the country, is typified by a contrasting REE signature to that particulate compositions observed in these works [151, 338, 345].

Japan's lengthy history of extensive municipal waste incineration (MWI) is another potential source of these particulate species, occurring with a wide range in compositions owing to the material feed-stock that is consumed [325, 346, 347]. A further, related, source of particulate arises from the consumption of fossil fuels for electricity production. As a result, numerous studies have been performed on the various micron-scale aerosols, "fly-ash" and "bottom-ash" produced during the combustion processes [348–350]. Despite the nearby proximity of a number of coal, gas and oil-fired power stations to the FDNPP site [14], as well as likely location to one of the several thousand waste incineration facilities distributed across Japan [346]; major advancements in particulate capture have ensured that such material is not readily released into the environment [323].

Analytical work by Ault et al., (2012) [351], on various forms of urban particulate derived from Ohio (USA), determined that combustion products near-exclusively occurred with a highly-spherical geometry. The resuspended mineral dust originating from the erosion of geological material was observed, however, in this study by Ault et. al., to be 5× the mean particle diameter as well as possessing a significantly different form to the samples analysed in this work.

The occurrence of this material adhered to the outermost surfaces of living bulk moss, lichen and leaf samples implies that this highly-angular material is recent in its origin - whereby meteoric alongside other natural processes would have otherwise resulted in its removal. Despite considerable care being taken during the initial sampling to ensure that bulk material samples were obtained from locations significantly above the ground (Section 4.1), the influence of a component of particulate resuspension cannot be excluded.

It could be invoked, that such an observed particle size vs. distance from the FDNPP trend could rather represent a particle size vs. distance from the coast trend - with major industrial facilities (located neighbouring the FDNPP along the Pacific coast) generating such particulate.

However, after searching for the locations of industrial activities within the 3 km - 6 km wide north-south trending coastal band (that transitions into the regions characteristic mountainous topography to the west) [152], only a single such site was observed.

Located 4 km south-east of Minamisoma City (and 17 km north of the FDNPP), this chemical plant (Ouchi Shinko Chemical Industrial) researched and produced various S-containing synthetic (rubber) and agricultural products - not, however, the composition of particulate material encountered during this study. This particulate could therefore not have originated from activity located within this coastal belt, despite the prevailing wind directions readily transporting such material onshore, and north-westwards towards the populated Fukushima City [41, 352].

7.6 Conclusions and future work

Resulting from the analysis of over 12,000 individual particles through combined SEM-EDS analysis, patterns pertaining to the spatial and/or compositional distribution of such material were observed in a number of instances. For some particulate, however, no such correlations were encountered - with many species absent or depicting contrasting depositional trends.

In-spite of the observed trends for many elements - when combined with a range of other indicative factors including the absence of other (nuclear-sourced) elements, an identical correlation of these (likely nuclear-derived) species with non-nuclear particulate, in addition to vastly differing particle size between different composition (but potentially nuclear-origin) material, would strongly suggest a non-Fukushima source for the bulk of this material. Owing to the wide compositional variance displayed by this particulate, alongside the extensive occurrence of REE species; electronics fabrication (and/or its subsequent recycling and processing), specialist metallurgical production and non-ferrous smelting plants are ascribed as the most likely sources of this particulate. The declining particle-size with distance from the FDNPP would imply a source location geographically similar to that of the coastal nuclear facility - despite no such site (as yet) having been identified.

While potentially unrelated to Fukushima, the environmental impact of this particulate is still of concern. Being readily-inhalable due to its micron length-scale, the material of this size is irritant to the respiratory tract and represents *"a long-term exposure risk contributing to a heightened risk factor for cardiopulmonary and lung cancer mortality"* [233]. The composition of these particles themselves also represents a hazard (resulting from their chemical toxicity) beyond just respiratory distress. A breakdown of elements and common pollutants by the World Health Organisation (WHO) details the 10 chemicals (or groups of chemicals) of major (global) public concern [316]. In addition to general air pollution - As, Cd and Pb are included within this classification - having been encountered as particulate at sites across Fukushima Prefecture.

167

Future work will first seek to isolate a range of particles of interest from these bulk samples, in addition to U - the analysis of which is described in Chapter 8. After their extraction, standard mass-spectrometric techniques will be employed to determine their true isotopic composition alongside Three-Dimensional Atom Probe Tomography (3D-APT) to derive isotopic information as well as details on the position sensitive distribution of the materials constituent atoms. It is only then that material can unequivocally be apportioned to the Fukushima accident or another, specific, emission source. In either case, as a result of much of the particulate materials inherent chemotoxicity, it is of considerable importance to determine its likely source provenance in order to reduce the future volume/impact of such material released into the environment. It should be noted, however, that the total volume of all such particulate, irrespective of its composition, is very small - requiring extensive electron microscope examination to identify its existence within the containing (bulk) material. Unless "considerable" volumes of this micron-scale particulate were to be inhaled, ingested, or sufficiently pre-concentrated via the food-chain, then a detrimental exposure/dose, however, is unlikely to be encountered [311]. The observed entrapment/adhesion of this material onto surfaces will further serve to reduce its aerosol mobility (as shown in Figure 7.5). Therefore, citizens currently residing, or set to shortly return, should not be adversely impacted by the existence of such material.

Additional future work will explore samples obtained from other sites across Fukushima Prefecture - located both within as well as outside of the radioactive plume. This will hopefully enable the potential source(s) of the particle material to be located, in addition to identifying sites where inherent sampling bias (non-detection of particulate despite its existence) may have formerly occurred.

8

URANIUM PARTICULATE ANALYSIS

8.1   Introduction

As shown previously in Chapter 7, U-containing material (alongside material of a wide range of other compositions) has been observed to exist distributed across the majority of Fukushima Prefecture. This U-rich *atmospheric particulate* was shown to be some of the smallest to exist (with a mean diameter of 1.07 μm), while containing the fewest additional elemental constituents (i.e. predominantly composed of just U and O).

In addition to being the fuel material used near-exclusively at the FDNPP (alongside a number of Pu-containing MOX assemblies) and the thousands of other nuclear reactors around the world [8], U also exists with a considerable natural (crustal) abundance. With a total annual production of approximately 75,000 tons in 2016 [353], U exists with an average crustal concentration of 2 parts per million (ppm) - therefore making it the 51st most abundant element [332]. This concentration is in contrast to both Ag (65th most abundant) and Au (72nd most abundant), which are considerably less-enriched within the crust, despite being perceived by many to be significantly more abundant than the actinide element [332].

Not occurring as native U metal, naturally-occurring U has been identified to exist as a component of over 350 minerals [36, 354] - with the U displaying a wide wt% variation across the mineral inventory, shown formerly in Figure 7.4. Alongside U, a considerable number of other cations comprise these minerals, however, only one "hyper-rare" mineral contains both U and the alkali metal Cs in its structure [36]. This yellow monoclinic, Carnotite Group mineral known as *Margaritasite* $((Cs,K,H_3O)_2(UO_2)_2(VO_4)_2 \cdot H_2O)$ is observed only at a single type-locality in north-west Mexico. Several anthropogenically-produced minerals have also been observed to contain both U and Cs - the principal species being *Chernobylite* (a variety of Zircon); containing U from the fuel elements and Zr ± Cs, found within the "corium" produced during the Chernobyl accident.

While U occurs with a considerable natural abundance, the species interactions associated with actinides (e.g. U, Am, Pu and Cm) in the environment and their inherent chemotoxicity is well-known and significant for both humans and other biological organisms [147, 355]. Owing to their low radiological activities in comparison to the γ-ray emitting fission products, the concern for human exposure is chemical, over radiological, toxicity [146, 355]. The development of cancers (such as leukaemia) after exposure to depleted uranium (DU) munitions was determined by Hamilton (2001) [356], to result after seven to ten years of environmental exposure. Alongside this U-containing material, there may also exist other species (e.g. Cd, Pb and Pa), which represent further chemotoxicity issues [355].

With the results of geological mapping undertaken by the Geological Survey of Japan (GSJ) unable to identify the existence any significant U-mineralisation (across all but a few minor and commercially unexploitable/unviable sites across the entirety of Japan (Section 7.5)) [354], the source of this material is unlikely to represent the resuspension of U-containing mineral species. This material therefore likely represents material derived from an anthropogenic source. To irrefutably discriminate any potentially natural material from anthropogenically-derived actinides, an in-depth analysis of not only the materials structure but also its composition, is required. This analysis would further permit for the discrimination between different types of anthropogenically-derived U material that may exist.

8.2 Aims

This chapter sought to provide further analysis of a suite of U-containing particles - both compositionally as well as through the examination of their internal form and structure. With such actinide-containing particles having been found at nearly all of the 14 sampling localities, it is crucial to understand whether this material is the result of the 2011 FDNPP accident, the result of another (potentially anthropogenic) source or if it is conversely entirely natural. If originating from the FDNPP accident, a number of questions arise pertaining to; (i) its long-term

stability within the environment, (ii) the potential existence of other reactor-sourced species, and (iii) if the provenance of such material may be attributed to specific FDNPP reactor Units as per the studies using radiocesium to ascribe the source of the material described in Chapter 2.

8.3 Experimental methods

Following their extraction from the containing bulk organic substrate, a range of complementary techniques were employed to analyse the U-containing particulate, these included both non-destructive and destructive methods.

8.3.1 Sample preparation

U-containing particles, adhered/entrapped onto the surfaces of organic substrates identified using combined SEM-EDS analysis (described previously in Section 7.3.3), were first removed to enable their sole analysis - independent of this background material. To remove these micron-scale particles, a Kleindiek MM3A™ Micromanipulator (Kleindiek Nanotechnik GmbH) [243, 357], was used - mounted inside the chamber of the Zeiss SIGMA™ HD SEM, used formerly to identify the fragments. This instrument was similarly operated in low-vacuum (Variable Pressure) mode to negate against specimen charging under the incident electron beam. Using a polar (circular) coordinate system, the MM3A™ Micromanipulator was capable of moving the associated probe/needle with steps of 0.5 mm (S6) down to 1.0 nm (S1), alongside providing full rotation of the tip. A labelled image of the electron microscope's chamber detailing the relative positions of the source, stage, detectors and MM3A™ Micromanipulator is shown in Figure 8.1.

After performing exploratory EDS analysis at high(er) beam currents (2.7 nA) and accelerating voltages (25 kV), a lower beam current 90 pA (30 μm aperture) and reduced accelerating voltage (10 kV) were used for the subsequent removal of the particle of interest. Using the Micromanipulator, either tungsten probe-tips (PT-4-10, Picoprobe Industries Inc.) or thermally-extruded borosilicate capillaries (needles) were used to remove the material. To adhere the micron-scale U-containing particles to the tips of these needles, an electron beam hardened adhesive (SEMGlu™ Kleindiek Nanotechnik GmbH) was used [358, 359]. After applying a small volume of this vacuum-compatible adhesive to the end of either tip type while in the SEM (at the lower energy beam conditions) it was then contacted onto the particle - where an increase in both the beam current and accelerating voltage (to those typically used for EDS analysis) caused its rapid (30 second) polymerisation. A graphical depiction of the steps used in the removal of such a particle is shown in Figure 8.2.

The needle containing the particle was then carefully withdrawn and removed from the electron microscope before being stored in an air-tight sample container. Subsequent analysis of the
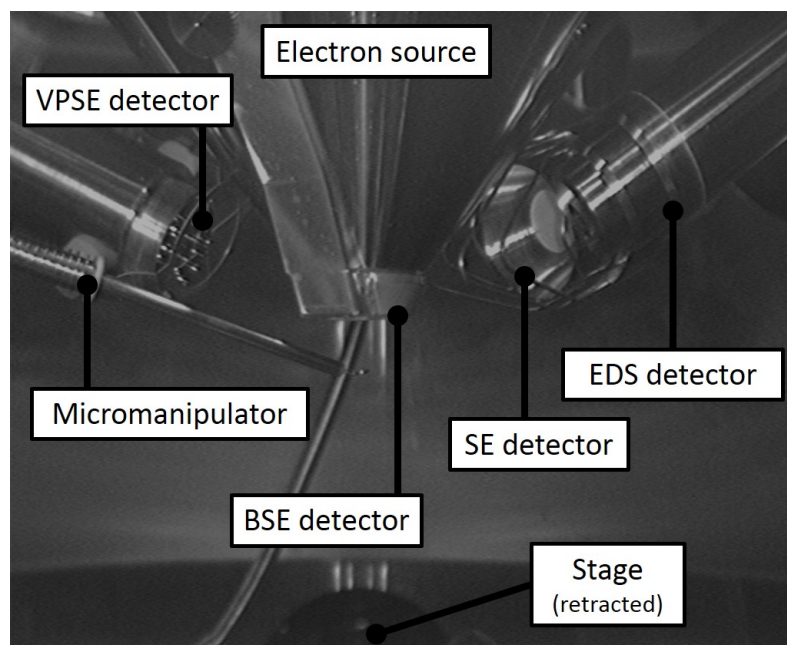
Figure 8.1: Labelled image of the Zeiss SIGMA™ HD scanning electron microscope chamber.

bond-strength of the adhesive yielded results consistent with those specified by the manufacturer at 2 mN [359]. Subsequent exposure analysis additionally showed the glue to be resistant to dissolution with water and dilute (1M) HCl and HNO_3 acids after 24-hour exposure.

Using SEMGlu™ over the Pt deposition from a gaseous organometallic precursor (Trimethyl-methylcylopentadienyl Platinum-IV) routinely used as an adhesive within FIB/SEM systems [252], was advantageous not only in the increased bond-strength it afforded but also in preventing the need to deposit additional high atomic mass (Z) number elements onto the sample. The incorporation of any such higher mass elements would serve to generate considerable atomic interferences during any subsequent mass spectrometry analysis.

During this study into the large number of U-containing particles formerly identified (Chapter 7), material from a single location, representative of an area with significant Fukushima-derived radiocesium contamination (Site 2: Shimohiso, Iitate Village - Table 4.1) was selected owing to experimental time constraints. This site, located 35.7 km north-west from the FDNPP on the main plume line, exhibited dose-rates of >19.0 µSv hr^{-1} during initial aerial surveys in the period that immediately followed the accident [85].

8.3.2 Ion beam slice and view

Following their isolation from the bulk material, ion beam sectioning was employed to destructively analyse a number of these U-containing fragments to ascertain structural and compositional
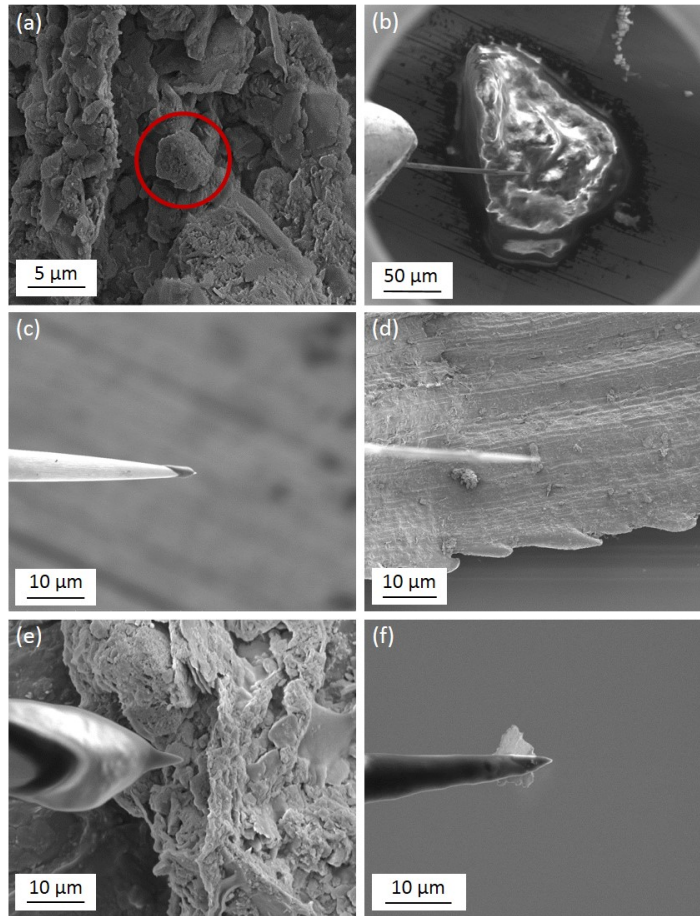
Figure 8.2: Steps detailing the removal of a particle from sediment material; (a) the particle is located and referenced within the microscope, (b) and (c) applying a small quantity of SEMGlu to the tip of the needle, before, (d) and (e) progressively moving the tip towards the particle, and (f) lifting out a particle from the surrounding material - adhered to the needle. *Modified from [227].*

information on the particle. The high adhesion strength of the particle to the needle afforded by the SEMGlu™ allowed for the sectioning to be performed without the need to otherwise remount the particle onto another support mechanism (e.g. Si-wafer or Cu/C support grid).

Using the FEI Helios™ NanoLab 600i DualBeam system consisting of a vertical electron beam and a side-mounted co-incident Ga^+ ion beam, a low current (0.9 nA) Ga^+ ion beam was used to remove sequential "slices" through the U particles. This was achieved using the automated "Slice and View" software installed within the Helios™ NanoLab control system; whereby a user-defined depth of section and slice thickness was sequentially removed from the sample. After each FIB cut, the sample was rotated from 52° to the horizontal (used for FIB sectioning) back to the horizontal, for a secondary electron (SE) image to be obtained using the systems vertically-mounted electron beam, before then being rotated back to 52° for further milling.
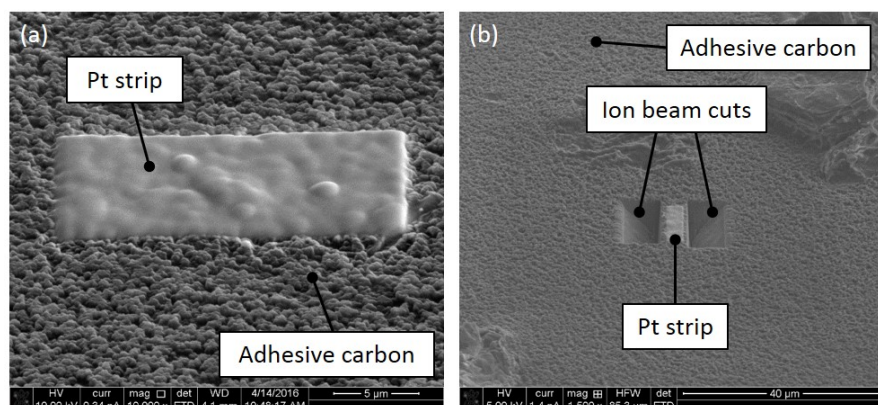
Figure 8.3: Process of manually ion beam sectioning a U-containing particle; (a) initial deposition of a protective Pt strip, and (b) progressive ion beam cuts towards the central particle.

During several points in the automated process, EDS compositional mapping of the particle was also performed. To undertake this analysis, the automated serial-milling was paused - with the sample-containing needle rotated back to the horizontal. Using the Oxford Instruments Ltd. XMAX™ EDS detector mounted onto the instrument, the electron beam was rastered over the sample with the characteristic x-ray emissions from the particles cut surface mapped and concentrations quantified. A consistent 20 kV accelerating voltage, 2.7 nA beam current and 4.12 mm working distance were used during all EDS analysis within the DualBeam instrument.

Manual ion beam sectioning and imaging were also undertaken, with the U-containing particle prior deposited onto a low elemental background adhesive carbon Spectro Tab™ disc (TED PELLA Ltd.) - itself mounted onto a standard SEM pin-stub. To ensure that the particle emplaced onto the adhesive surface remained in place, a thin (200 nm thick) Pt strip was deposited using electron beam ionisation of a Pt precursor. Alongside ensuring adhesion, the Pt served to protect the sample's surface from the incident ion beam (Figure 8.3 (a)). Initially, a high energy Ga^+ ion beam (30 kV and 6.0 nA) was used to make the primary cuts, before lower beam currents (down to 90 pA) were progressively used to obtain a surface free from substantial Ga^+ implantation and the effects of ion beam "curtaining" due to the non-uniform cutting afforded by differences in the samples internal structure.

Owing to the greater range of stage/sample movement, in addition to the greater detector volume, the EDAX (Ametek) Ltd. Octane-Plus™ Si-drift EDS system within the Zeiss SIGMA™ HD SEM was used to undertake the compositional analysis of this particle "wafer". As per its previous operation, a 25 kV accelerating voltage and 2.7 nA beam current (120 μm aperture) were used. The sample was, however, located at a smaller working distance (5 mm) and was additionally angled at 45° from the horizontal, directed towards the EDS detector.
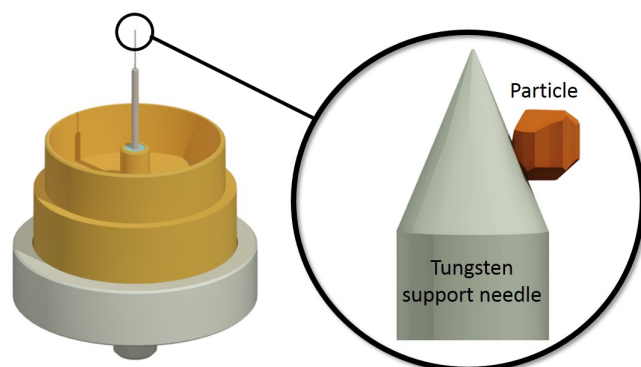
Figure 8.4: Illustration of the synchrotron beamline sample setup, with the sub-micron U-containing particle adhered onto the tip of a fine tungsten support needle.

8.3.3 Synchrotron micro-focus spectroscopy

Unlike ion beam analysis which results in the destruction of the particle, synchrotron radiation micro-focus x-ray absorption spectroscopy (SR-µ-XAS) is non-destructive, but also benefits in providing compositional, species and bonding-state information not attainable using ion beam lithography combined with EDS.

To undertake the XAS study, the I18 beamline at the Diamond Light Source was used (capable of producing monochromatic tuned x-rays in 0.5 eV increments over an energy range of 2.05 keV - 20.5 keV), operating at the nominal beam current of 300 mA using a "standard mode" fill pattern of 900 contiguous electron "bunches", each 2 ns apart, with a total "bunch-charge" of 0.33 mA [263]. For the analysis of the individual U-containing particles, each was left adhered to the tip of the tungsten needle (via SEMGlu™), onto which they were originally removed from their containing substrate. A graphical rendering of this particle-needle setup, as mounted onto the I18 beamline, is shown in Figure 8.4, with the full setup within the beamlines experimental cabin shown in Figure 8.5. During the experiment, steps were undertaken to prevent against the radioactive particles from being lost into the beamline setup if they were to become dislodged due to the effects of local heating brought about by the x-ray beam. To achieve this, an envelope made from x-ray transparent Kapton™ film (DuPont ®) was used to enclose the particle in its plastic mount.

The standard beamline optical setup was used to attain the 2 µm × 2 µm x-ray beam incident onto the sample, as detailed previously in Section 5.4.5.2. During the analysis of each needle-mounted particle, the samples approximate location was determined using a camera mounted within the experimental setup - used to assist with preliminary positioning. For optimal signal
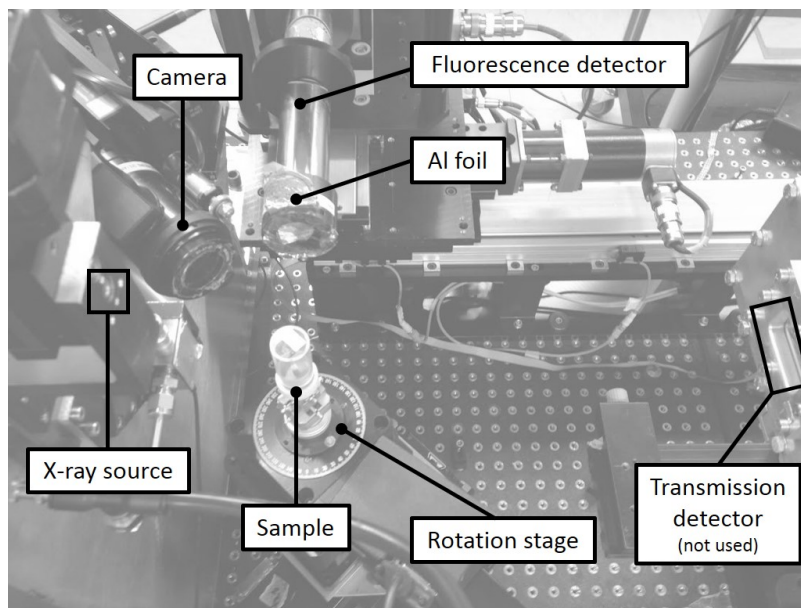
Figure 8.5: Experimental cabin setup on the I18 micro-focus spectroscopy beamline at the Diamond Light Source with the various components labelled.

generation and collection, as shown within Figure 8.5, the fluorescence detector was mounted at 90° to the incident beam - with the needle-mounted sample conversely positioned at 45° to the source. Owing to the high flux of the beam (2×10^{12} photons per second) combined with the small size of the sample to generate signal absorption, the transmission detector (mounted directly behind the sample) would have become over-saturated, was hence was not used in this work. The obliquely mounted x-ray fluorescence (XRF) detector also suffered from high count-rates (due to its high signal sensitivity), however, a 0.1 mm Al foil was inserted to reduce these effects in addition to screening out lower-energy fluorescence peaks. A high-precision three-axis (+ rotation) piezoelectrically-driven stage from Thorlabs Inc. was used to accurately manipulate the sample.

Each of the samples was initially mapped using XRF to derive the correct position from which to subsequently obtain both x-ray absorption near-edge structure (XANES) and extended x-ray absorption fine structure (EXAFS) data. All of the XRF, XANES and EXAFS analysis was performed using a six element SGX Sensortech Si-drift fluorescence detector (Xspress-3) controlled by software constructed in-house at Diamond. These XRF maps were obtained at an energy of 18,000 eV, above the U-L_3 edge at 17,166 eV, using a dwell of 30 seconds per point to enhance the resulting signal quality. Additional U edges (with higher fluorescence yields) also exist, however, all are encountered at energies greater than those attainable on the I18 beamline. The interpretation of these 2D fluorescence maps was conducted using the Python multichannel analyser (PyMCA) [360].

Having identified the 2 µm × 2 µm area on the needle from which the U signal originated - the subsequent collection of the µ-XAS was performed at that point. Data were obtained using the same Xspress-3 Si-drift detector, with the pre-edge data collected at 5 eV energy steps from 17,014 eV to 17,139 eV, before reducing to 0.5 eV steps up to 17,300 eV and finally coarsening to 1.0 eV to the upper limit at 17,412 eV. Each of these energy "sweeps" was performed over the same region a total of three times to enhance signal quality and suppress spurious noise.

The processing of the XAS data - including normalisation, deconvolution and linear combination peak-fitting to known standards was performed using the Demeter software package (version 0.9.24) [361]. This package included the Athena and Artemis programs (for XANES and EXAFS analysis respectively), based upon the IFEFFIT code [362, 363]. Spectroscopy standards were obtained from the International X-ray Absorption Spectroscopy (IXAS) Database [364], with data derived from a number of global facilities (e.g. SSRL, CHESS and NSLS).

8.4 Results

8.4.1 SEM and EDS

Secondary electron images from the Zeiss SIGMA™ HD SEM (operated in low vacuum mode) of three of the smallest U-containing particles (A, B and C) obtained from organic substrate material in Site 2: Shimohiso (Iitate Village) are shown in Figures 8.6 (a), (b) and (c) respectively. An elemental map of Particle A (obtained using the electron microscopes associated EDAX EDS system), confirming the location of the U corresponding to the exact position of the sub-micron particle is shown additionally, in Figure 8.6 (d). For each of the three particles, a complete EDS spectrum is shown in Figure 8.6 (e). As was observed during the initial in-situ quantification of the particulates composition and as was discussed formerly in Section 7.5 - the sample interaction volume associated with EDS analysis (circa. 2 µm) incorporated the underlying bulk substrate material into the quantification of such very fine particles (<2 µm). This "sampling" consequently resulted in the increased Si, Al and Ca spectral contributions in Figure 8.6 (e).

Despite occurring with an elevated background contribution, the compositional analysis of the particles in Figure 8.6 highlights not only a large inherent similarity between the material, but also the absence of any elements strongly indicative of a nuclear reactor origin (e.g. fission products such as; Cs, Sr, I and Rb, activation products including; Co, Ni, Nb and Ag, or other actinide species; Am, Cm and Pu). The elemental breakdown of this analysis - detailing the compositional similarity between the particles, is shown in Table 8.1.
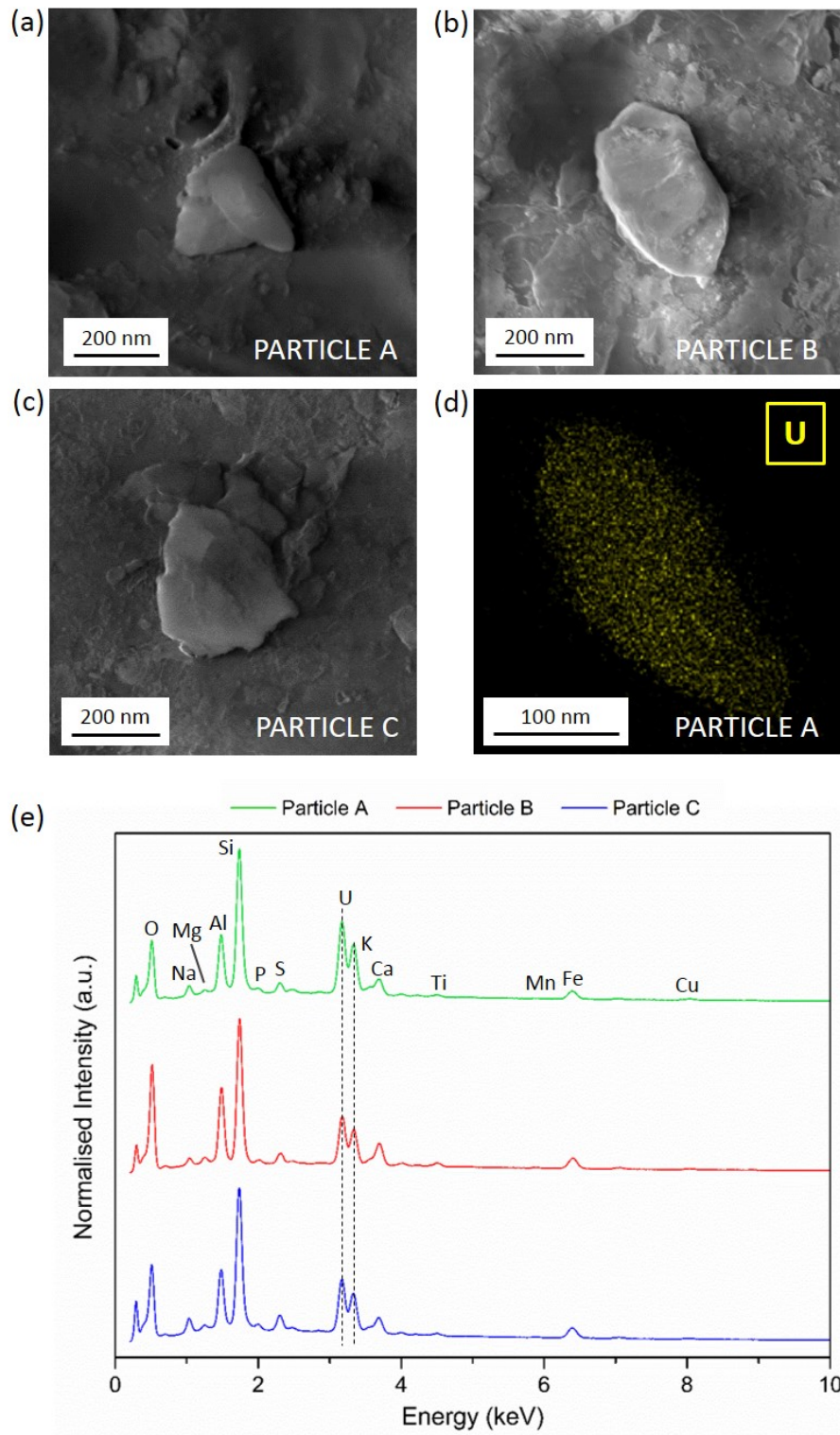
Figure 8.6: Secondary electron images (a), (b) and (c) of three U-containing particles, alongside (d) an EDS U map for Particle A, and, (e) the EDS spectra of the three particles shown in (a), (b) and (c). *From [227].*

	Weight percentage		
Element	Particle A	Particle B	Particle C
O	26.66 ± 0.61	36.44 ± 0.81	29.88 ± 0.68
Na	1.53 ± 0.06	1.39 ± 0.05	2.86 ± 0.07
Mg	0.08 ± 0.01	0.16 ± 0.02	0.74 ± 0.04
Al	7.82 ± 0.19	8.99 ± 0.23	8.09 ± 0.35
Si	18.74 ± 0.44	15.59 ± 0.39	17.68 ± 0.51
P	1.26 ± 0.04	1.08 ± 0.03	2.07 ± 0.06
S	1.79 ± 0.05	2.02 ± 0.07	3.04 ± 0.10
U	31.45 ± 0.77	17.33 ± 0.21	23.01 ± 0.36
K	-	-	1.12 ± 0.06
Ca	4.38 ± 0.09	6.77 ± 0.11	4.44 ± 0.18
Ti	0.43 ± 0.02	-	0.54 ± 0.03
Mn	0.14 ± 0.01	-	0.25 ± 0.02
Fe	4.44 ± 0.13	9.35 ± 0.15	2.76 ± 0.20
Cu	1.28 ± 0.07	0.89 ± 0.11	0.92 ± 0.08

Table 8.1: EDS weight percentage (wt%) elemental composition of the three particles: A, B and C, with the associated measurement error for each sample shown.

8.4.2 Ion beam analysis

The results of ion beam sectioning and subsequent compositional analysis of a typical U-containing particle are shown in Figures 8.7 (a) to (d). Within Figure 8.7 (a), obtained using the backscattered electron detector installed onto the Zeiss SIGMA™ HD SEM, is shown the high atomic number (Z) nature of this micron-scale particle - located within the adhesive carbon disc (low atomic number (Z) to backscattered coefficient ratio) and overlain by the thickness of deposited Pt (moderate backscattered electron yield). It was this high backscatter coefficient that enabled the particle(s) to be initially identified. As apparent from the homogeneous white colour displayed by the particle, the elemental distribution of material appears, before compositional analysis, to be spatially consistent. The secondary electron image taken of a slice located in the centre of the particle is also shown in Figure 8.7 (b). Not only is the highly-irregular morphology of the particle apparent, but also evident is the texture at the samples centre - occurring as nano-crystallites, each ten's of nm in size. Their appearance, raised above the FIB cut surface, suggests that these features are significantly harder than the surrounding particle.

Supporting the earlier compositional analysis of such material (Figure 8.6 (a)), a strong U signal was observed via EDS mapping over the sectioned particle - the results are shown in Figure 8.7 (c). Although not presented here, sample mapping results also detailed the occurrence of the numerous accessory elements identified (and quantified) in Table 8.1. As per the EDS mapping results of a typical particles surface shown in Figure 8.6 (d), the distribution of U in this section, alongside all of the other elements, are homogeneously distributed throughout the sample.
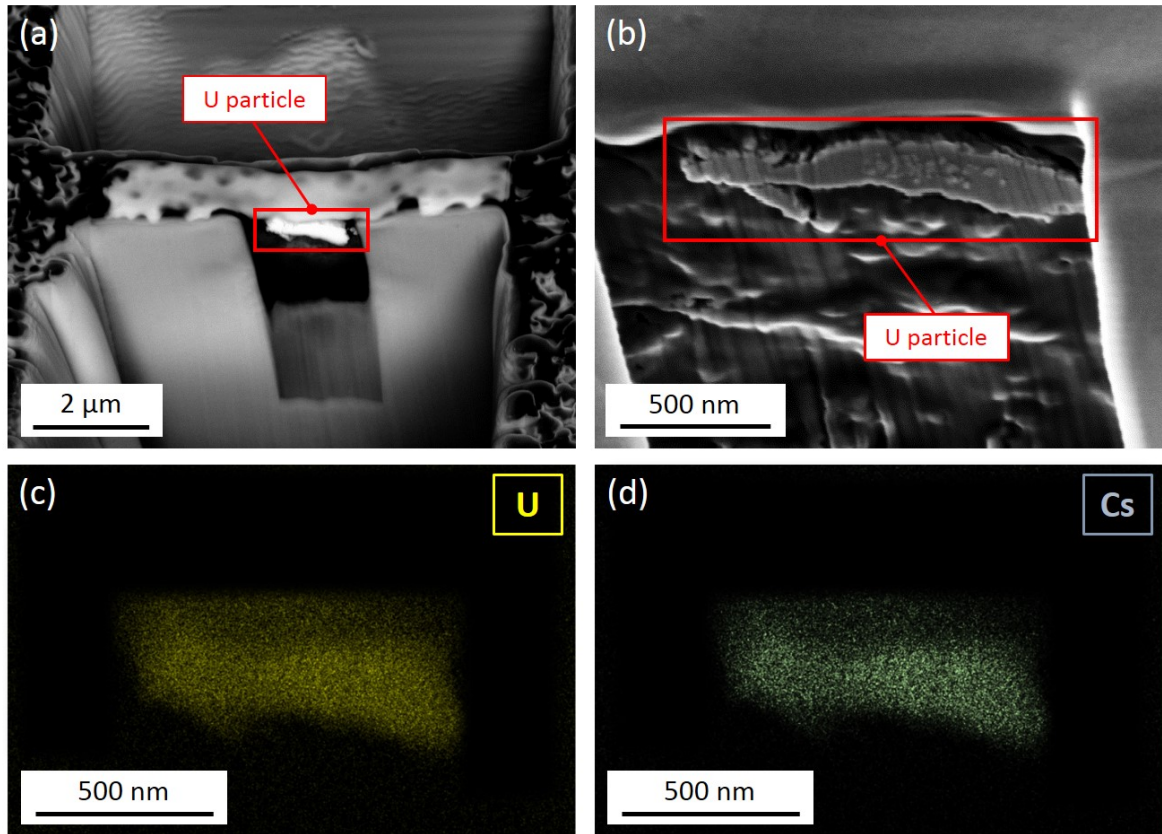
Figure 8.7: SEM-derived analysis of the particle; (a) backscattered electron image of the FIB-cut particulate, (b) secondary electron image detailing the existence of nm-scale particle inclusions, (c) U EDS elemental map, and (d) Cs EDS elemental map.

While the EDS results acquired from both the external surface and sectioned face of the U-containing particle are consistent in their composition, the mapping results of the ion beam sectioned internal surface of the sample, however, highlighted the presence of Cs - albeit at low concentrations of 1.2 wt% - similarly homogeneously distributed. The Cs EDS map from the region containing the sectioned particle is shown in Figure 8.7 (d).

Despite additionally identifying the existence of Cs within the sectioned particle, EDS mapping (and later single-point analysis) was unable to resolve the composition of the raised (likely harder) surface features present on the samples cut surface. Such results are, however, expected owing in part to the greater interaction volume (circa. 2 µm) of the incident electron beam (with the sample) than the features subjected to analysis (10's of nm) [239], but also the ultimate spatial resolution (precision of beam positioning) attainable by the SEM instrument. Hence, the spectrum derived is not solely the result of these sub-micron features, but in the majority of cases from the surrounding bulk sample interaction.
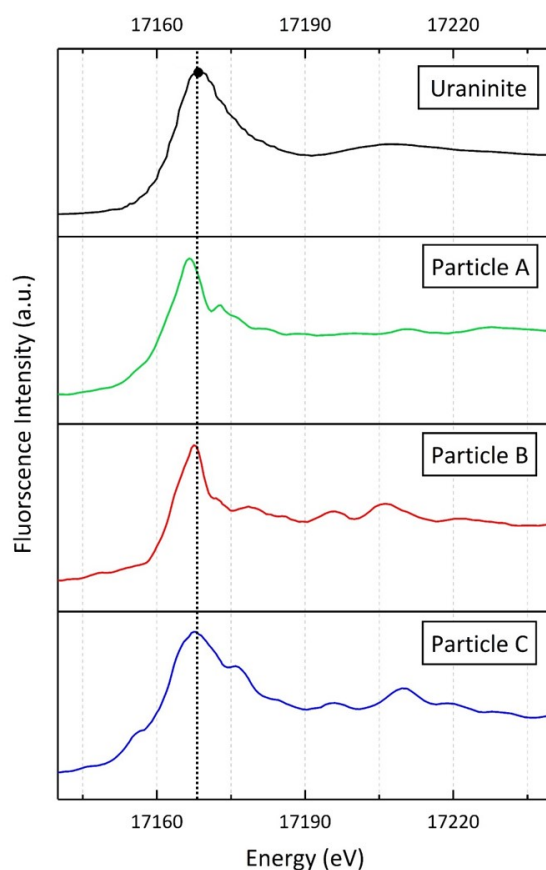
Figure 8.8: Results of SR-µ-XANES analysis of particles A, B and C at the U-L$_{III}$ edge. A reference spectrum for Uraninite (UO$_2$) is shown for comparison.

8.4.3 Micro-focus spectroscopy

Results derived through SR-µ-XANES on three separate U-containing particles (A, B and C) are shown in Figure 8.8 (alongside a Uraninite (UO$_2$) reference spectrum). As is shown in this plot, these results confirm the existence of U as a core component of the particle - with a clear peak at 17,167 eV, corresponding to the position of the U-L$_{III}$ absorption edge.

When the SR-µ-XANES spectra from each of the three particles (A, B and C) are directly compared with a (UO$_2$) reference spectrum, a high degree of similarity between each of the isolated particles and the material standard, are observed. Uraninite is one of the primary U minerals with a chemical composition that is near-entirely UO$_2$ (although some degree of hyper-stoichiometry will occur to yield a small additional component of triuranium octoxide - U$_3$O$_8$), with U existing within the thermodynamically stable and insoluble U(IV) oxidation state. Notably, UO$_2$ and the Uraninite structure, is also the form in which nuclear fuel exists. Therefore, provenancing this

material to either source represents a challenge for SR-µ-XANES analysis. Hence, knowledge of the differences in the U atoms coordination chemistry determinable through the succeeding EXAFS portion of the absorption spectrum - brought about by the effects of the materials irradiation and incorporation of fission product species is required [258].

However, owing to the high thermal effects of the x-ray beam imparted onto the sample, difficulties were experienced whereby the poor thermal conductivity of the tungsten needle onto which the particle was mounted thermally drifted (in some instances by several microns) over the duration of the experiment. When combined with the size of the incident beam (2 µm × 2 µm) being greater than the material analysed, this vibration resulted in significant spectral noise. As such, quantification of the subsequent and delicate EXAFS portion of the absorption spectrum (that follows the main absorption edge and succeeding XANES region of the spectrum) - providing information on bonding-state and coordination chemistry, was not possible.

8.5   Discussion

As invoked formerly in Chapter 7, one of the potential sources of this U-containing material (and the other varying composition micron-scale *atmospheric particulate*), is the resuspension of naturally-occurring mineral material [329]. The compositional results of this chapter, however, firmly suggest that this mechanism is most likely not the source of this particulate.

From the EDS results of particles A, B and C - shown graphically in Figure 8.6 (e) and quantified in Table 8.1 are detailed; (i) the high wt% U component, but also (and most distinctively), (ii) the absence of other constituent elements contained at wt% concentrations within most other commonly encountered U-bearing minerals [36, 354]. Such "accompanying" elements include As, Th, Y, Ba, Zr and most of the REEs including; Ce, Sm, La, Nd, Dy and Gd. While these elements have not been detected during this EDS analysis at the wt% abundances they would exist at in naturally-occurring minerals, this does not constitute their complete absence from the particulate at concentrations below the techniques lower limits of detection (LoD).

Owing to the low activities of the principal U isotopes (^{235}U and ^{238}U) - with half-lives of hundreds of millions and billions of years respectively [52], if this material was formed of primordially-aged, naturally-occurring U, then since its formation, there should exist a small component of ingrown daughter product Pb. However, none of these were observed from the EDS analysis. This, therefore, implies that the state secular equilibrium (the quantity of a radioactive isotope remains constant as its production rate is equal to its decay rate) had recently been reset - with this material either; (i) naturally-occurring - having been newly-formed and therefore yet to undergo decay (and such daughter product ingrowth) or more likely, (ii) being non-natural in origin, with the U having similarly yet to decay into an EDS-detectable quantity of these daughter products.

Although the LoD of EDS analysis is poor in comparison to other analytical quantification techniques (with a sensitivity of >0.01 wt%, or 100 ppm) its application would still be suitable in this instance. If primordial in origin, ^{235}U would have passed through 0.65 half-lives, while ^{238}U would have conversely decayed through exactly one half-life - resulting in the production of both ^{207}Pb and ^{206}Pb, for ^{235}U and ^{238}U respectively (after passing through a number of intermediary decay steps). *N.B. it is through measurements of Pb isotopes in U-rich Zircon minerals that it has been possible to accurately determine the age of the Earth* [365].

Despite the limited results provided by the SR-μ-XANES analysis of particles A, B and C - the synchrotron findings do, however, support those of the EDS compositional analysis of the same material. Alongside such compositional results, from this synchrotron analysis, the structure of the samples is observed as analogous to the Uraninite (UO_2) - with U existing near-entirely within the U(IV) oxidation state. In nature, numerous other U-containing minerals also exist - displaying an extensive compositional range, varying oxidation state, and differing atomic structure [354]. A comparison of the differing U oxidation states and their influence on the XANES spectrum is detailed (with respect to U contained within sub-mm *ejecta particulate*) in Section 10.4.2 of Chapter 10. Alongside being the structure of naturally-occurring Uraninite, both the structure (U(IV)) and composition (UO_2) of this mineral are identical to the pressed and sintered fuel employed almost universally in the global nuclear reactor inventory [21, 366].

An intricate microstructure observed within one of the ion beam sectioned particles, consisting of a clustering of nano-scale crystallites at its centre, was shown in the electron microscope image of Figure 8.7 (b). This observation further promotes a non-natural (anthropogenic) source of this material. While compositional analysis of these features was not possible via EDS due to a combination of the inadequate spatial resolution attainable by the instrument, as well as the bulk dilution effect from the surrounding (enclosing) particle - the raised form of such inclusions implies their elevated hardness over the bulk.

The anthropogenic nature of the ion beam sectioned particle (which extends to the other similarly sourced U-containing particles) is further confirmed through its EDS compositional analysis. As was shown in Figure 8.7 (d), alongside the homogeneous distribution of U (Figure 8.7 (c)), was a similar Cs distribution - albeit at an expected lower wt% abundance. With only one naturally-occurring mineral (found only in north-west Mexico) containing both U and Cs as component cations [36, 354], a source other than Fukushima is therefore very unlikely. A number of anthropogenically-derived minerals otherwise not encountered naturally, containing both U and Cs, have been found close to the reactor as well as across the nearby Ukrainian environment - produced by the 1986 Chernobyl accident [354].
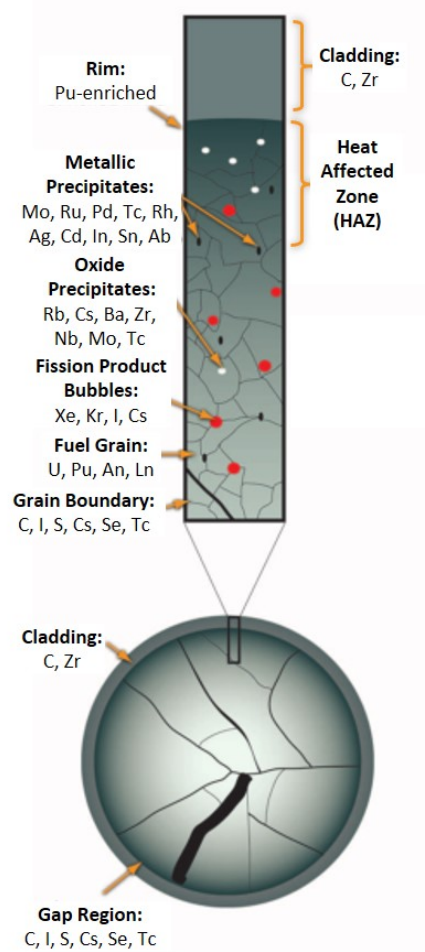
Figure 8.9: Schematic representation through an irradiated UO_2 fuel pellet (11 mm in diameter). *Modified from [24], after the initial work by [23].*

Whereas EDS analysis of the sectioned U particle was able to detect the existence of Cs, the corresponding exterior surface analysis of the particles when adhered to the containing substrates, however, was unable to detect (and quantify) any such Cs existence. This can, again, be attributed to result from the larger than particle of interest electron beam-sample interaction volume, generating characteristic x-ray emissions from depths of circa. 2 µm (Figure 5.1), hence masking/diluting the low intensity Cs signal. With such thinned samples possessing thicknesses of <100 nm, there is no bulbous sampling volume present beneath the particle - with the x-ray signal and compositional analysis resulting only from the characteristic x-rays generated by the particle.

These Cs-containing U particles, are therefore almost certainly the result of the environmental dispersion of fragmented, irradiated fuel, ejected from the FDNPP facility over the duration of, or in the period following the accident. While both the U and O found within the particle arise from the initial UO_2 fuel material, the homogeneous distribution of Cs within the particle

results from the incorporation of the major fission product species over power generation operations. Such a distribution is consistent with numerous earlier works, exploring both the structure and composition of post-irradiation nuclear fuel during standard operation as well as following emergency/LOCI scenarios [23, 24, 367]. As shown within Figure 8.9, in addition to existing at increased concentrations towards the outer-most portion of the non heat-affected/Pu-enriched/high burn-up zone of the fuel pellet as intra-granular fission product gas bubbles and oxide precipitates, Cs (as well as other fission product species) occurs also (at greater concentrations) between the micron-scale grains as an inter-granular (grain-boundary) species.

Due to the "inter-granular" nature of the Cs, it (and other highly-volatile fission product gas species), contained between the crystal grains as well as within the "gap region" between the fuel element and the C and Zr-based cladding, are unlikely to represent the Cs encountered within these micron/sub-micron particles. This inter-granular and "gap region" Cs not contained within the physical lattice structure of the UO_2 fuel, would be easily volatilised and liberated from the material - therefore accounting for the large activity of radiocesium released by such a LOCI [119, 135]. These gaseous and fine-scale ionic nature of this contamination has seen it sorbed and strongly-bound onto the frayed-edge sites of various clay and mica-type minerals [167, 169].

In contrast, it is the intra-granular (lattice-bound) Cs that is the form of the fission product most likely to exist within these micron-scale U-based particles, this "entrapped" Cs is difficult to liberate from the UO_2 crystal structure, hence providing a rationalisation to account for why the full inventory of such volatile species are not fully-released during such a LOCI event - instead existing contained within a "corium" composition volume formed during the event [24, 127, 368].

The existence of these micron-scale U-containing particles is consistent with the centrally located and similarly sized material observed to exist at the centres of spherical "Cs-balls" by Abe et al., (2014) [192]. These balls (approximating 2.6 µm in diameter, isolated following air-sampling in Tsukuba - 170 km south-west of the plant), are considered to have formed after the fragmentation and Si-incorporation of the U fuel. With the high-pressure of Cs contained within the RPV being readily incorporated into the outermost circumference of the partially-molten spherical reactor-sourced Si before being transported away in the buoyant (super-heated) air-mass [193, 194].

With the large north-west trending plume, responsible for contaminating the sampling site at Iitate Village having been formerly determined as resulting from the radiological release of Unit 2 [69, 153, 160] (Section 2.2.5), this material is able to further substantiate claims and support the current hypotheses that exist - that the PCV had indeed been compromised/breached by the incident [2, 7, 34]. Alongside the leak of volatile species, actinide-containing material was additionally released and deposited at localities up to 36 km from the site. Whereas the events at reactor Units 1 and 3 were both violent explosions that resulted in large mushroom-cloud

style emissions, the non-explosive emission from Unit 2, in contrast, was only evident at the time of the release as a result of increased radioactivity levels detected by the (limited) on-site monitoring network that survived the tsunami [33].

8.6   Conclusions and future work

This multi-technique analysis of micron-scale U-containing particulate has served to near definitively attribute its provenance to result from the FDNPP accident, emitted from reactor Unit 2 on the site. Not only is the form of each particle highly-indicative of such an anthropogenic provenance, but also the coexistence of Cs distributed homogeneously within the UO_2 material.

Although a number of studies have formerly identified the occurrence of a non-natural $^{235}U/^{238}U$ atomic ratio across Fukushima Prefecture [142, 144] - the existence, isolation and microscopic analysis of such actinide-bearing material from amongst bulk material had, until now, to be undertaken. Despite representing only a small sub-sample of particulate derived from a single, yet initially highly-contaminated site, these results compound earlier works - that core material had been released from the FDNPP site [192], reaching distances of at least 40 km. Further work will analyse additional U-containing material from other sampling sites across Fukushima Prefecture to explore its similarity to that currently examined.

A further set of synchrotron experiments on this micron-scale material is planned on the I14 (nano-focus XAS) beamline at the Diamond Light Source to further quantify both composition, phase and internal elemental distribution within either ion beam sectioned or unprepared samples. To prevent the previously encountered beam-induced heating-related movement of the particles while attached to the tips of the tungsten composition support needles, a different particle preparation setup will be employed during this future work. This setup will again the needle-mounted micron-scale particulate (sectioned or unprepared) being contained/wrapped within adhesive Kapton film, however, the particles will only be mounted onto the tip of extruded glass capillary needles and not the tungsten composition needle tips.

Subsequent TEM is proposed on a suite of samples after first exhausting all non-destructive analytical methods. Having suitably ion beam thinned each particle sample, the materials structure, as well as the phases present, can be derived. Such analysis would be focused towards looking for evidence of nano-scale non-volatile fission product precipitates and heavier actinides (e.g. Am, Pu and Cm). To determine high-accuracy isotopic information from each particle, both Three-Dimensional Atom Probe Tomography (3D-APT) and/or Laser Ablation-Inductively Coupled Plasma-Mass Spectrometry (LA-ICP-MS) are being explored as potential analytical tools for interrogating such fine-scale material.

From such isotopic analysis, the material can be further and more-strongly attributed to the FDNPP accident. Not only confirming the anthropogenic nature of this material as a result of the March 2011 accident, atomic ratios (e.g. ^{235}U/^{238}U, ^{135}Cs/^{137}Cs, ^{134}Cs/^{137}Cs, ^{240}Pu/^{239}Pu, and ^{241}Pu/^{239}Pu) and the presence of non-natural isotope abundances/activities (e.g. ^{234}U and ^{236}U [144, 145], in addition to various other indicative transition/REE species [330]), will enable this particulate material to be independently confirmed as originating from a specific source on the site when compared to the results derived by core inventory modelling [38, 50, 369].

STRUCTURAL AND COMPOSITIONAL ANALYSIS OF EJECTA MATERIAL

Results and methods presented in this chapter have previously been published in the peer-reviewed literature:

P.G. Martin, Y. Satou, I. Griffiths, D.A. Richards and T.B. Scott. "Analysis of external surface irregularities on Fukushima-derived fallout particles". *Frontiers in Energy Research: Nuclear Energy*, vol. 5. (25). p. 9, September 2017.

9.1   Introduction

In addition to the micron and sub-micron scale *atmospheric particulate* identified through combined electron microscopy and characteristic x-ray (EDS) analysis (as described formerly within Chapter 8), a suite of considerably larger particles were also released into the environment - the analysis of which is herein described.

Alike to the earlier studies that occurred shortly after the accident which identified the micron-scale "Cs-balls" within bulk aerosol and environmental samples through the application of autoradiography [191, 192, 195], the same methods were also used to locate these sub-mm *ejecta particles* - similarly discernible via their characteristic fissionogenic radiocesium γ-ray emission. Contrasting to the significantly smaller *atmospheric material*, this larger *ejecta material* has been sourced from sites located less than 2 km from the FDNPP, within *Area 3* - or the region defined as that where displaced inhabitants "are not expected to return (to their homes) for some time" [156]. Owing to the more spatially limited extent of this sub-mm material, it has to-date been

greatly understudied - with much still be to determined. While the spherical "Cs-balls" have been located at sites of considerable distances (some as much as 170 km south-west) from the FDNPP [191], where populations currently exist (or will shortly return under planned repopulations) - the analysis of this more plant-proximal material, although distributed across localities where people are not set to inhabit "for some time" is still of crucial importance in understanding the accident scenario as well as any long-term environmental consequences that may likely result.

Despite the very limited works to date on such large-scale material [164, 190, 370], a number of preliminary differences have been identified between this *ejecta particulate* and the vastly size contrasting "Cs-balls". As mentioned earlier within the background provided in Section 2.3, during the study by Satou (2016) [164], the smaller (1 µm - 10 µm) spherical "Cs-ball" material was referred to as "Type A", while the larger (70 µm - 400 µm) particulate as "Type B". Whereas their size and the locations at which they were collected represented two macro-scale characteristics for subdividing the particulate, their contrasting radiocesium (^{134}Cs/^{137}Cs) activity ratios served as an objective indicator as to the materials contrasting provenance. From γ-ray spectroscopy measurements during this work by Satou (2016) [164], the smaller "Type A" particulate was attributed to Unit 2, with "Type B" material, conversely ascribed to having been released from the neighbouring reactor Unit 1. These attributions were based on the comparison to core inventories of radiocesium as predicted by the modelling of Nishihara et al., (2012) [50].

9.2   Aims

This chapter sought to provide an enhanced insight into the nature of "Type B" (Unit 1) derived sub-mm *ejecta particulate* collected (and subsequently isolated) from a locality neighbouring the FDNPP. Alongside information on its interior/exterior structure, when combined with information on the particles composition and its elemental distribution, it is hoped that an initial hypothesis into the mechanism(s) responsible for the formation of the material can be alluded to.

In addition to this Unit 1 *ejecta particulate* (designated CF-01), this chapter also sought to perform a similar (albeit less extensive) analysis on Fukushima-derived particulates with a comparable length-scale to "Type B" (Unit 1) material, but obtained, however, from a region attributed to contamination from reactor Unit 2 [69, 153]. Not only do the area-wide contamination mapping results illustrate a radiocesium signature indicative of reactor Unit 2, but this newly isolated mm-scale radiocesium containing particle (designated FT-13) was sourced from a region that has been shown to contain the highly-spherical "Type A", "Cs-balls" [193, 197, 371] - attributed to reactor Unit 2 [164]. As a result, this chapter subsequently aimed; (i) to establish if this material was sourced from reactor Unit 2 - despite being several orders of magnitude greater in size than the typical "Cs-ball" particulate, or, (ii) if the material resulted from the reactor Unit 1 release - although being located within an area contaminated with reactor Unit 2 fallout.

Despite only being able to perform a highly-detailed analysis on a small sub-set of Fukushima-derived *ejecta particulate* as part of this thesis, the wider aim of this work was to devise a sequential analytical methodology, through which the subsequent analysis of further particulate material could be based. Such an increased sample examination would not only provide an improved statistical basis to the conclusions herein, but would also for the suitability of methods and techniques applicable to the study of other environmentally-derived particulate to be fully evaluated.

9.3 Experimental methods

9.3.1 Sample preparation

The *ejecta particulate* sample studied during this work is described fully in Section 4.2, with the majority of this work centred on material sourced from the bulk dust sample collected at the Cambridge Filter Company (termed "Type B" [164]), denoted herein as CF-01. This site was located less than 100 m from the site boundary, approximately 2 km north-north-west from the facilities six reactor Units - with reactor Unit 1 invoked to be responsible for the release of this material [164]. The latter, subsequent, portion of analysis was conducted on the mm-scale *ejecta material* isolated from bulk sediment material collected from Futaba Town (designated FT-13) - located directly west of the site within contamination attributed to reactor Unit 2.

Also detailed within Section 4.2 is the multi-stage process employed to isolate such particles from the bulk substrate material (dust in this instance), to produce a sample either; (i) contained within a "sandwich" of x-ray transparent adhesive Kapton™ film (DuPont ®), or (ii) securely bonded to an adhesive and conductive carbon disc (Spectro-Tab™, TED PELLA Ltd.).

While numerous isolated particle samples of both CF-01 and FT-13 designation existed, owing to combined time constraints and equipment availability (primarily synchrotron-based techniques), only a representative suite of selected particles were analysed. Therefore, only a single particle from the Cambridge Filter Company was analysed using all of the techniques subsequently described, however, additional particles (three in total) extracted from the same bulk sediment were used to contribute to γ-ray spectroscopy, combined scanning electron microscope (SEM) and energy dispersive (x-ray) spectroscopy (EDS) surface analysis and bulk compositional analysis via laboratory-based x-ray fluorescence (XRF). Only a single particle from Futaba was analysed, although unlike the Unit 1 sourced CF-01 material, this particle was only subjected to γ-ray spectroscopy, combined SEM-EDS surface analysis and laboratory-based x-ray tomography (XRT). While this analysis was performed on only a small number of the total *ejecta particles* isolated from each site, care was taken to ensure that the material analysed was representative of the
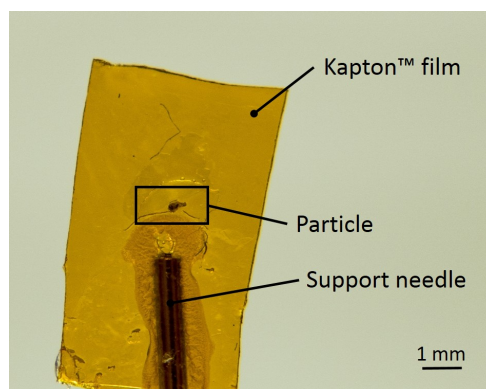
Figure 9.1: X-ray analysis experimental setup, with the sub-mm CF-01 radioactive particle enclosed within a double-layer thickness of Kapton™ film, mounted onto a support needle.

entire suite of material isolated from a localities bulk sample. This was achieved by pre-screening each particle in the SEM, before selecting those on which to perform the succeeding and more extensive body of analysis.

To further prepare either sample (CF-01 or FT-13) for x-ray characterisation (XRT and XRF), additional layers of Kapton™ film were placed around the sample to provide a double thickness of the film to securely contain the particle while in the instrument. Any surplus Kapton™ that surrounded each of the particles was removed and an aluminium support pin mounted to the Kapton™ using a quick-drying adhesive to produce a sample setup as shown in Figure 9.1. The entire 5 mm × 12 mm pin-supported sample was subsequently secured onto a magnetic holder.

9.3.2   Gamma-ray spectroscopy

Prior to its extensive analysis, initial γ-ray spectroscopy of the particulate was undertaken using methods identical to those described for the characterisation of bulk organic samples (Chapter 7), obtained from the 14 localities extending along the north-westerly plume from the FDNPP. For this quantification, the GR1 γ-ray spectrometer from Kromek Ltd. was used - positioned 1 cm from the sample. A total counting time of six hours for each of the particles was used to ensure sufficient signal quality. In addition to the spectra of the particulate, a background spectrum of the detector within the shielded sample environment was also obtained to allow for background subtraction and contributing peak identification.

9.3.3   Surface examination

Following the detailed analysis of the structure and composition of the micron-scale (*atmospheric particulate* using combined focused ion beam (FIB) milling alongside high-resolution SEM and EDS (Section 8.4.1), the same methods were also applied in the analysis of the outer surfaces

of both forms of this larger *ejecta particulate*. Three of the CF-01 designation particles were studied via this technique alongside the one mm-scale FT-13 particle. To perform this surface analysis, one side of the Kapton™ film enclosing the particle was removed - with the remaining side adhered to the surface of an adhesive carbon disc before being mounted on an SEM pin-stub.

As per the analysis of the *atmospheric material*, an FEI Helios™ NanoLab 600i DualBeam system was used to perform the ion beam lithography (sectioning) of the various surface features existent across the sample. After depositing a protective Pt strip to prevent any ion beam induced surface damage, a succession of reducing Ga^+ ion beam energies were used to remove progressively finer amounts of material (as well as to protect against any surface "curtaining" that may occur). The electrically conductive nature of both the sample and mount resulted in a conductive coating (Au, Pt or C) need not be applied. Subsequent imaging and EDS analysis was performed within the Zeiss SIGMA™ SEM with associated EDS (Octane Plus™ Si-drift and TEAM control/analysis software) from EDAX Ltd.

9.3.4   Laboratory x-ray fluorescence

Initial compositional XRF quantification of the *ejecta material* samples was performed using the Niton™ FXL 950 X-ray Lab, with the particulate sample securely contained within the Kapton™ film envelope. Positioned as close as possible to the instruments x-ray source (<1 mm) using the systems inbuilt optical camera, the sample was irradiated with 25 keV x-rays for 500 seconds through the four overlapping energy ranges (main, low, high and light). To analyse and quantify the full range of potential elements within the sample (from C to U), the "TestAll Geo" peak-fitting algorithm was used within the Thermo Scientific Inc. NDT™ analysis software. Three successive scans were conducted and results combined for noise reduction through averaging each of the recorded spectra.

9.3.5   Laboratory tomography

Alongside synchrotron tomographic reconstructions of the material, x-ray (absorption) tomography was additionally performed using the Zeiss Xradia 520 Versa™ to attain structural and phase-contrast data. The identical sample setup to the Niton™ XRF and subsequently described synchrotron-based methods was employed, with the *ejecta particulate* enclosed within the double-layer Kapton™ envelope (Figure 9.1).

Using the instruments Scout-and-Scan™ control software, a total of 3,601 rotational angles (through 180°) were used, each scanned with a pixel resolution of 0.2410 µm over a 30-second total exposure per point. An incident beam energy of 140 kV and 8.0 W was used to attain maximum image contrast between the full range of elements (phases) likely to exist within the
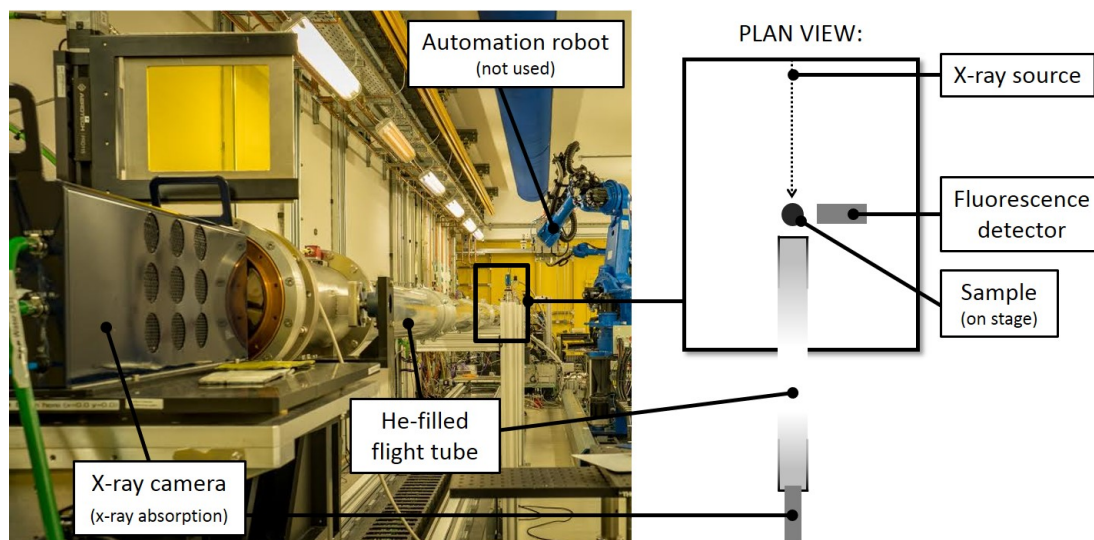
Figure 9.2: Experimental setup of the I13-1 experimental end-station.

sample. In order to attain the highest-possible spatial resolution, a ×40 optical magnification was used alongside source-sample and sample-detector separations of 0.8 mm and 0.9 mm respectively. A refinement of the source energy profile (specific for the sample) was made through the insertion of the LE1 filter, upstream of the particle. Both three-dimensional reconstructions and tomographic slices were performed using the instruments XM3D-Viewer™ software.

9.3.6 Synchrotron analysis

Further extending the surface analysis afforded through the FIB-SEM/EDS examination of the material, the synchrotron radiation (SR) x-ray analysis of the large-scale internal structure and elemental distribution within the *ejecta material* was performed on the I13-1 (coherence branch) beamline at the Diamond Light Source (DLS). With 250 m distance between the insertion device (undulator) and the experimental end-station, the beamline benefits from highly-coherent x-rays (in-phase) with an energy range of 4 keV - 23 keV (19 keV used in this study). Full details of the beamline are described in Section 5.4.5.2 as well as within [372], with a schematic shown in Figure 9.2.

Owing to time constraints, only one of the particles isolated from the dust sample obtained from the Cambridge Filter Company was analysed using synchrotron radiation - with separate scans of the material undertaken using both SR-μ-XRT and SR-μ-XRF mapping.

Synchrotron tomography

The initial synchrotron scans of the material undertaken were SR-μ-XRT to derive the material's structure. Here, the sample was illuminated with a 19 keV collimated x-ray beam and rotated

through a total of 180° in 1800 incremental steps to acquire a series of grey-scale images which could be subsequently rendered into a three-dimensional volumetric projection. These absorption (phase contrast) images were obtained using an optical microscope coupled to a 26 µm GGG:Eu scintillator, providing a ×20 sample magnification. This resulted in a 0.45 µm pixel size.

An x-ray camera placed downstream (behind) the sample was used to acquire data on the degree of sample absorption (transmission) that occurred at each of the stage positions (rotations) using a dwell-time (exposure) of 0.5 seconds per stage position.

Synchrotron fluorescence

Synchrotron XRF was performed, with the same incident 19 keV x-ray beam, however, focused using Kirkpatrick-Baez (KB) mirrors rather than being sourced directly from the beamlines insertion device (undulator). A 10 µm pinhole located upstream of the sample was used to remove any undesired "wings" from the focal spot. Unlike the XRT, the sample was scanned (using this refined beam) in a raster (snake) pattern - translated through the incident beam at 10 µm steps while additionally rotated through 180°in a reduced number of only 40 incremental steps to derive a three-dimensional image with each pixel composed of a complete fluorescence spectrum. Limited by the diameter of the upstream focusing aperture - a 10 µm pixel size was achieved. The step size of the stage during these raster scans was selected to match this spot size, at 10 µm.

A single element Vortex™ (Hitachi High Technology) fluorescence detector, positioned perpendicular to the sample and incident beam (Figure 9.2), was used alongside custom-built control and data acquisition software, developed in-house at the DLS. An increased dwell-time for XRF, of two seconds per acquisition (pixel), was used to derive the highest possible intensity fluorescence signal with minimal noise contribution.

Reconstructions

From the series of thousands of iterative projections, a three-dimensional volume for each element was reconstructed using the ordered-subset penalised maximum likelihood algorithm, with weighted linear and quadratic penalty algorithms in the TomoPy framework [373]. An iterative algorithm to correct for the level of sample self-absorption was also employed during the processing of tomography results (publication in preparation by the I13-1 beamline scientists).

The combined x-ray fluorescence (XRF) and x-ray absorption tomography (XRT) signals were both reconstructed and graphically rendered using the FEI Avizo™ software package [374]. Sole XRT renderings were processed using the open-source ImageJ software package with the HDFS plugin (to interrogate the stack of outputted .HDF files).

195
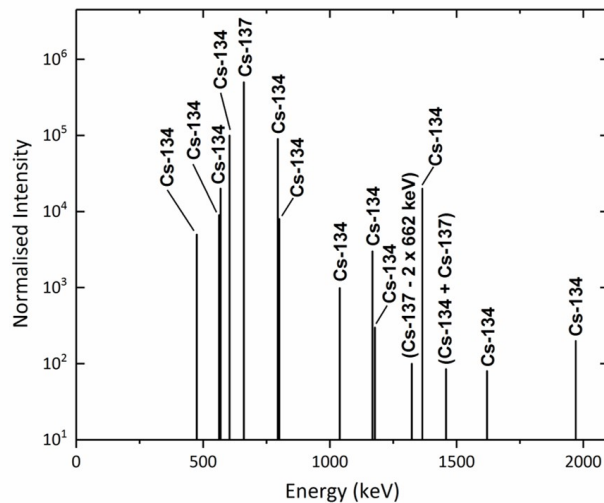
Figure 9.3: Typical background subtracted γ-ray spectrum for one of the sub-mm *ejecta* particles with contributing peaks identified.

9.4 Results

The results presented in Sections 9.4.1 through 9.4.5 represent those obtained from the analysis of the CF-01 *ejecta particulate*, for which Satou (2016) [164], attributed to have originated from the FDNPP Unit 1, and the reactor building hydrogen explosion that occurred on the afternoon of the 12th March 2011 [2]. The analysis of the larger FT-13 *ejecta particle* is subsequently presented in Section 9.4.6.

9.4.1 Gamma-ray spectroscopy

Due to their identical source provenance, the γ-ray spectra obtained from the three CF-01 *ejecta particles* were identical - with the background subtracted spectrum shown in Figure 9.3. Despite only depicting the sole contributions from radiocesium (^{134}Cs and ^{137}Cs) - with the production of a near-identical γ-ray spectrum to the bulk organic material obtained at the sampling sites 60 km north-west of the plant (Figure 6.19) - there exists a slight difference in the ^{134}Cs to ^{137}Cs (primary) peak ratios when decay corrected to March 2011, between these plant-proximal individual particles and the more plant-distal bulk material.

With the decay-corrected activities of each of the CF-01 *ejecta particles* averaging 35 kBq, the ^{134}Cs/^{137}Cs activity ratio of these particles (determined through peak intensity subtraction) is 0.94, less than the 1.05 determined for the samples obtained from along the primary north-westerly plume. This serves to confirm the provenance of this material as having been derived from the FDNPP Unit 1, as invoked in the earlier works [153, 164] - having matched the reactor core inventory modelling values published in the works of Nishihara et al., (2012) [50].

9.4.2 Surface irregularities and composition

A secondary electron image of one of the entire CF-01 particles is shown in Figure 9.4 (a). Observable is the highly angular form and irregular surface texture. While the majority of the samples outer surface is smooth, a considerable portion, however, is characterised by numerous pits or recesses - each sub-micron to several microns in diameter, all typically rounded in their form (Figure 9.4 (b)). Also distributed across the surface are numerous elongate fibrous features (Figure 9.4 (c)). These fibres all vary in their thickness; occurring with dimensions from less than 10 μm, through to bulbous portions averaging 30 μm - 35 μm in maximum diameter. The total length of these fibres also varies, from short lengths of 50 μm through to longer sections over 100 μm. Observable from Figure 9.4 (a) is the fibres attachment mechanism to the body of the particle (yellow dashed region), where each of these strands is physically fused at its ends to the particle's surface.

An EDS spectrum acquired over the entire sample is shown in Figure 9.5. As observed in earlier works [164, 190], the constituents comprising the majority of the particle are Si, O, C and Na. Further component elements consistent with these earlier studies include P, K, Ti, Ca, Mn, Fe and Zn. Also observed is the higher atomic (Z) number element Ba (albeit at low concentrations) - a fission product readily-volatilised and released in the reducing atmosphere typical of a nuclear reactor [125]. The work by Ono et al., (2017) [190], also detected Pb and Cr in some particles - although none was detected in this large-area raster scan. The existence of such elements agrees with the results of studies on the smaller, spherical material, derived from Unit 2 [191, 192].

The supplementary results of EDS point analyses taken across the entirety of all three CF-01 samples are shown in the three compositional plots of Figure 9.6. Of the elements present within the samples, the most abundant is Si - with the weight percentage - wt% (or mass fraction), component of this element ranging from 24.9 wt% to 53.8 wt%. Within this range, two distinct clusters can be observed - with Si compositions ranging between 24.9 wt% to 37.1 wt% and 44.6 wt% to 53.8 wt%. This upper range of data points was determined from the fibres that lay across the surface of the particle, whereas the lower values were all associated with the surrounding bulk of the particle. A similar elemental enrichment associated with the fibrous component of the material is also apparent for Al - where a clear compositional difference is observed between the bulk particle and the associated surface fibre. As shown in Figure 9.6, the fibre contains more than four times the concentration of aluminium than the material that surrounds it. Also enriched within the particle, although not at levels as high as for both Si and Al, is the halogen-group element Cl. As highlighted within Figure 9.6, the fibres all displayed an elevated Cl content (average 2.02 wt%), whereas the remainder of the particle contains comparatively little Cl (average 0.27 wt%).

197
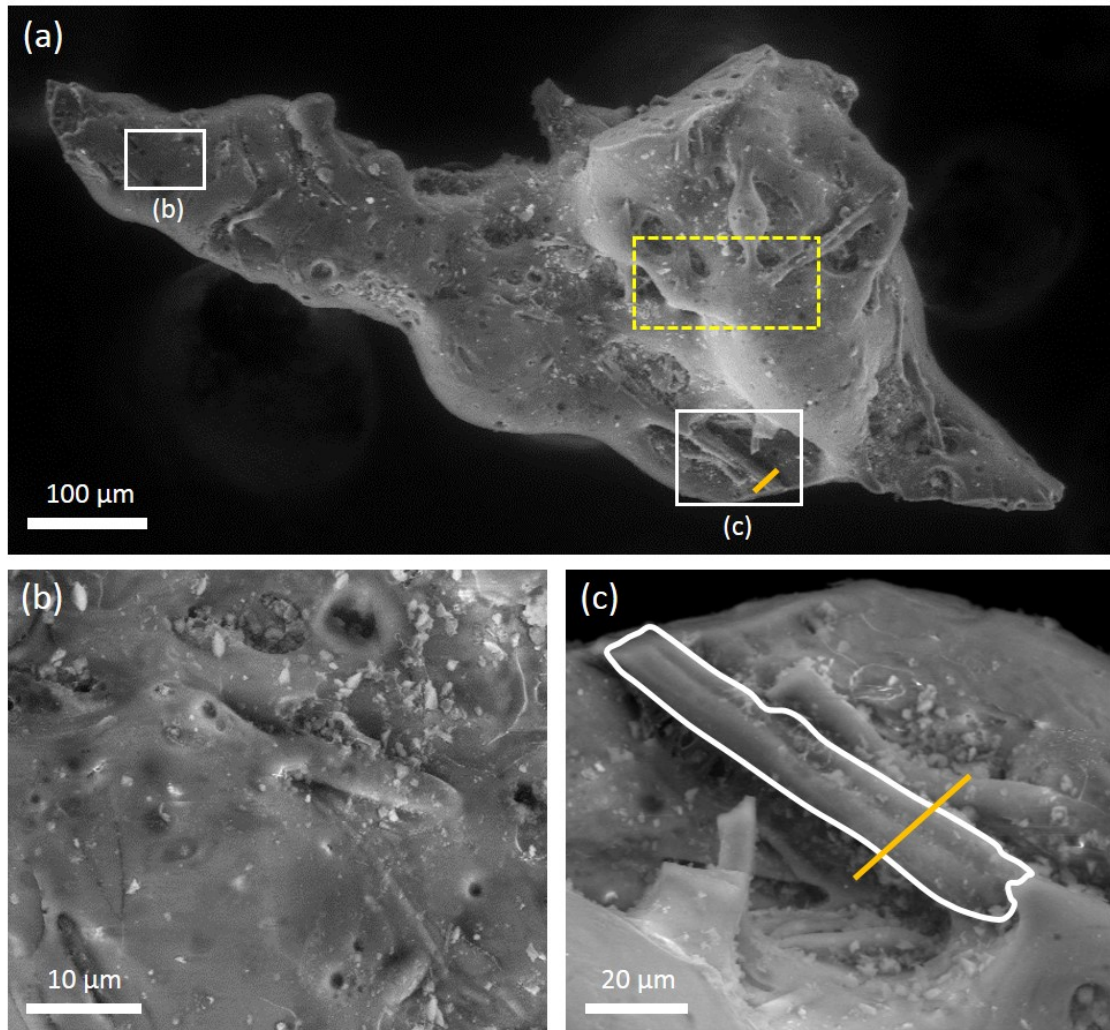
Figure 9.4: Secondary electron images of; (a) one of the entire sub-mm CF-01 designation particles, (b) smooth surface region showing micron and sub-micron sized recesses and, (c) fibrous surface feature - with line of section (Figure 9.7 (a)) shown.
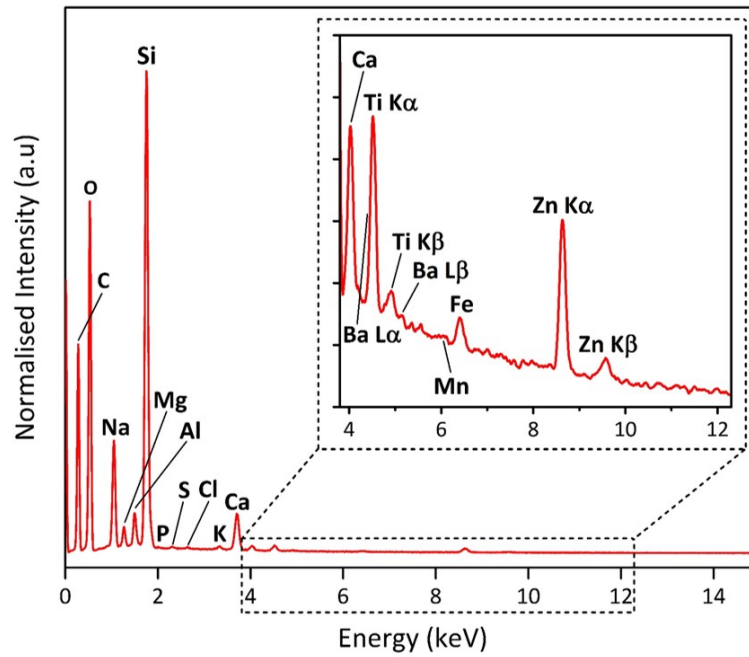
Figure 9.5: EDS spectrum derived for the entire sub-mm sized *ejecta particle*.
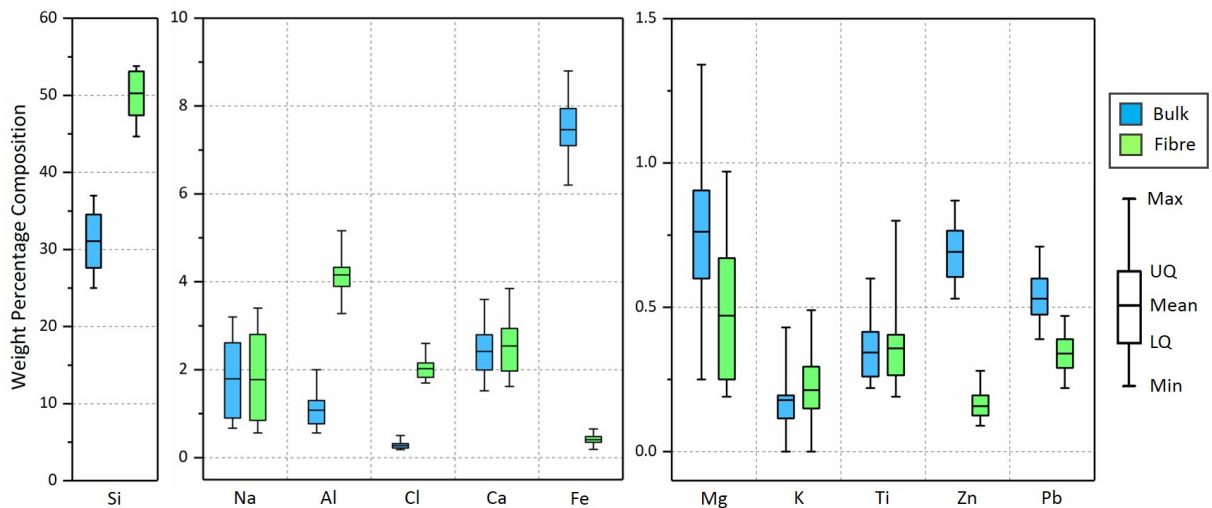
Figure 9.6: Elemental comparison of both the fibrous and surrounding bulk particle. Values are derived from the compositional analysis of three separate *ejecta particles*.
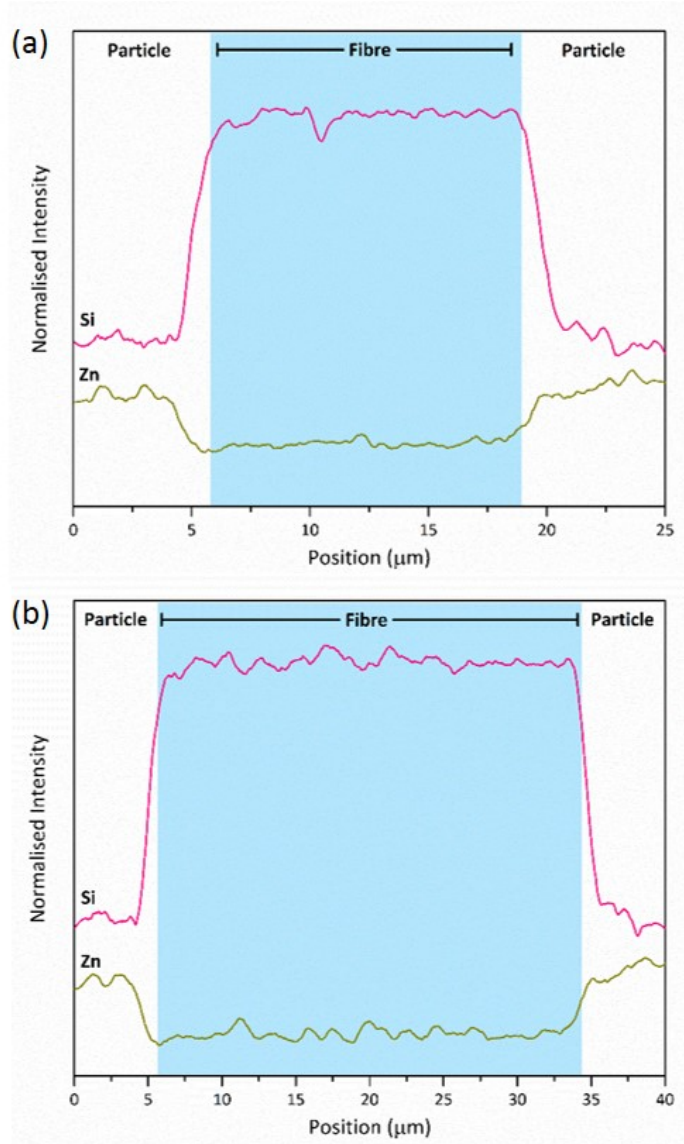
Figure 9.7: EDS line scans (Si and Zn) across the fibrous features on particle surfaces; (a) line scan over a smaller diameter fibre (as identified in Figure 9.4 (a)), and (b) line scan over a larger-diameter Si-rich fibre.
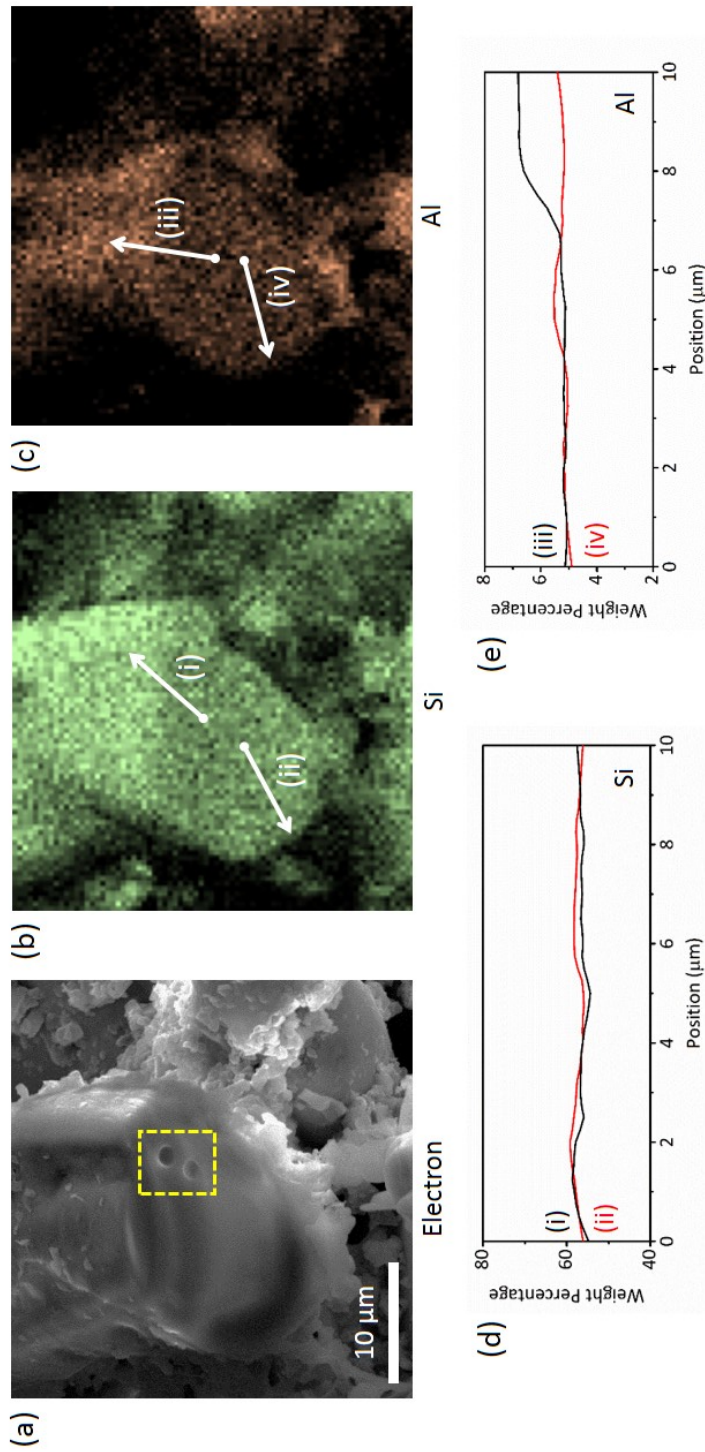
Figure 9.8: Internal compositional analysis of a surface fibre; (a) a secondary electron image through an ion beam sectioned fibre. The highly amorphous/structure-less internal form of the material is apparent alongside two small voids (highlighted), (b) an EDS elemental map of Si distribution, (c) an EDS map of Al distribution, (d) Si compositional line scans - (i) and (ii) delineated in (b), and, (e) Al compositional line scans (iii) and (iv), as shown in (c).

In contrast, however, some elements show an observable depletion within the fibrous features in relation to the surrounding bulk particle. The transition elements of Fe and Zn both show a large reduction in their relative concentration across the fibre features. Fe occurs within the fibres with a mean value of 0.41 wt%, whereas away from these structures, the average mass fraction is 7.47 wt%. Similar compositional variation is observed for Zn, however, to a much lesser extent - with the particle containing an average of 0.16 wt%, and the surrounding bulk particle 0.69 wt%.

Several elements do not display any discernible difference in their abundance between the enclosing particle and the fibres. Both Ca and Na exhibit a wide compositional variation of several wt%, however, neither element shows a marked difference in abundance between EDS results obtained from the particle or the fibres. The other elements; Mg, K and Ti, all show a much smaller spread in their composition (<1 wt%), with no significant difference observable between EDS results obtained over either region. A small amount of compositional difference is, however, observed for Pb between the contrasting regions of the sample (having not previously been identified in the large area EDS raster analysis). However, the degree of overlap is small and could be invoked as insignificant given the low concentrations of this element (between 0.22 wt% and 0.70 wt%) within either region. While Pb is used extensively within nuclear facilities as a shielding material [35], its ductility has additionally afforded its usage as cladding for the various thermally insulated pipes of the heat-exchanger network (personal communication with TEPCO engineer).

The results of an EDS line scan across a fibrous structure (position identified in Figure 9.4 (c)) are shown in Figure 9.7 (a), detailing the compositional variance for both Si and Zn. As is shown graphically in Figure 9.6, a considerable enrichment in Si exists across the width of the fibre, above the lower levels observed within the surrounding particle bulk. A similar depletion of the fibre in Zn, as again shown quantitatively in Figure 9.6, is also shown within the line scan across the raised fibre. Results from an identical line scan over a thicker diameter fibre (28 μm) are shown in Figure 9.7 (b). These results are consistent with the smaller fibre, (Figure 9.7 (a)), with a considerable enrichment in Si, and a corresponding depletion in Zn.

EDS analysis of both the bulk particle and the fibrous features showed no discernible emission peaks for Cs (Figure 9.5), however, the γ-ray spectrum derived from the particulate, as shown in Figure 9.3, shows the characteristic radiocesium emission (it is these γ-ray emissions that were used to initially locate the material through autoradiography). The low sample penetration depth (circa. 2 μm) afforded by EDS analysis [239], therefore dictates that the Cs contained within the particle may be contained at depth below the surface of the particle, or more likely, present at concentrations below that detectable by EDS (Limit of Detection = 0.01 wt%). An inhomogeneous distribution of radiocesium has previously been identified through synchrotron analysis of the finer-scale (circa. 2 μm) spherical "Cs-ball" (Unit 2) material [192, 194], with the Cs concentrated
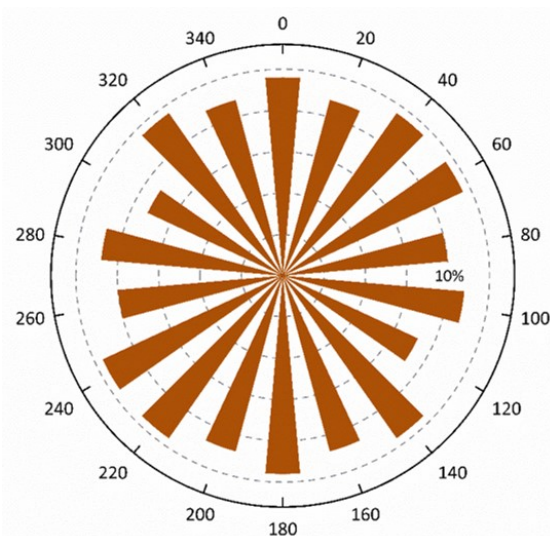
Figure 9.9: Rose diagram detailing the orientations of the fibres found on the surfaces of the three CF-01 (Unit 1) *ejecta particles* studied.

exclusively around the particles circumference. Owing to the potential commonality in their formation mechanism, a comparable (inhomogeneous) spatial distribution of Cs is hence expected.

A secondary electron image of a fibre following focused ion beam sectioning is shown in Figure 9.8 (a). From this image, the lack of internal structure within the fibres is apparent - with no micro-scale crystals or discernible external outer rim or rind around its circumference. Towards the top right of the image are two small micron-sized voids, most-likely representing the location of gaseous inclusions associated with the materials formation or the exsolution of formerly contained volatile species.

The glassy and amorphous nature of the principally Si-based CF-01 *ejecta particle* was confirmed through the application of Raman spectroscopy. A broad spectrum, absent of any specific peaks, was observed - illustrating the materials long-range structural disorder [375].

Elemental EDS mapping of the region imaged in Figure 9.8 (a) is shown in Figures 9.8 (b) and (c), for Si and Al respectively. From these maps, the uniform distribution of Si along the external surface as well as through the fibre's interior is apparent. The reduced concentrations of Si present within the bulk region immediately surrounding the particle is also evident - supporting the earlier line scan EDS results shown formerly in Figures 9.7 (a) and (b). Whereas Al was observed to have an enrichment within the fibre in contrast to the containing bulk particle (as shown formerly in the plot of Figure 9.6), a contrast is apparent in Figure 9.8 (c), between the fibres outermost surface and its interior.

To assess this, additional EDS line scans were performed - outwards from the fibre centre, to quantify their compositional consistency. The resultant line scan over the particles end-section for Si, is shown in Figure 9.8 (d) and supports the earlier findings - with the concentration of Si consistent (average 58 wt%) from the fibre's centre through to its exterior surface. However, while the line scan of Al shows that the concentration of Al within the fibre's sectioned core is constant (Figure 9.8 (e)) - a 40% increase in Al concentration is associated with its external surface (increasing from 5 wt% to 7 wt%).

Acting also as an indicator of the provenance of the material, although not as powerful as assessing composition, the orientation of these features across the surface of the particulate could yield information regarding the conditions of formation. A rose diagram detailing the orientation of the fibres encountered across the surface of these three samples is shown in Figure 9.9. From this plot, the spread of fibre orientations appears highly-uniform. This directionality distribution may, therefore, suggest that these fibrous features result from a source material that is itself highly-heterogeneous in form. Conversely, this material may exist as the result of an event that served to generate a wide orientation variance. While an examination of the structure across the *ejecta particles* surfaces has been performed, a contrasting texture may exist within its interior.

9.4.3 Tomographic reconstructions

Unlike the analysis of the outermost regions of the particles(s) afforded by combined FIB and SEM-EDS, the application of XRT provides not only a non-destructive means through which to study a material but also a method to investigate its internal structure alongside its basic phase/density composition.

Iso-surface renderings showing views of the "front" and "back" (defined as the long axis of the particle perpendicular to the source) of a CF-01 *ejecta particle* derived from the SR-µ-XRT are shown in Figures 9.10 (a) and (b) respectively. Apparent from both renderings is the highly-complex and heterogeneous internal structure of the material, with many near-spherical voids existing over a wide range of sizes - the largest of which measures 80 µm, while the smallest occurs with a diameter of less than 0.8 µm. A total of 24% of the particle is constituted by such void space. The particle can be viewed as foam-like internally, but with a solid, and generally smoothed, outer-surface.

In addition to this considerable porosity, a large solid fragment (subsequently identified as Fe-based via SR-µ-XRF) is observed to exist, embedded in the outer surface of the sample, closely surrounded by several of these large-diameter pores. The location of this fragment is highlighted (orange) within Figure 9.10 (a), and is further detailed in the corresponding tomographic slices
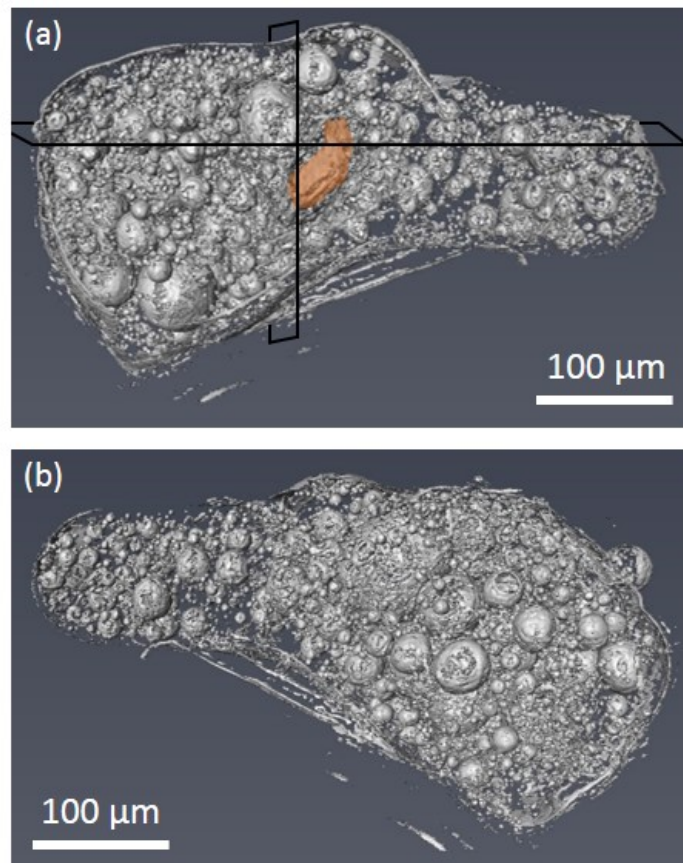
Figure 9.10: SR-µ-XRT renderings of; (a) the "front" face of the particle, with the location of the Fe-rich inclusion highlighted alongside lines of section (Figure 9.11), and (b) the "back" surface.

through the sample in both Figures 9.11 (a) and (b). In these sections, taken vertically and horizontally through the sample, the fragment (composed near-exclusively of Fe) is observed to represent the only prominent surface extrusion aside from the fibrous features and surface pitting.

As well as the discontinuous (unconnected) nature of the majority of the voids, an approximately bi-modal size distribution of the pore-space is evident, illustrated through the tomographic slices shown in Figures 9.11 (a) and (b). With mean diameters of the larger voids at 70 µm, the smaller voids occur with diameters ranging between 5 µm and 20 µm (a small number of vesicles also occur as small as 1.5 µm). Both are generally distributed homogeneously throughout the material apart from a slight edge enrichment in the smaller voids. Several areas exist, however, where very few (or none) of any size void exist (shaded green in Figures 9.11 (a) and (b)).

Identified in Figures 9.11 (a) and (b) by dashed white boxes, are the locations that interactions occur between the various voids. In each case, the smaller voids are observed to impinge upon the larger ones - resulting in a slight degree of deformation (of the larger voids) as well as highlighting
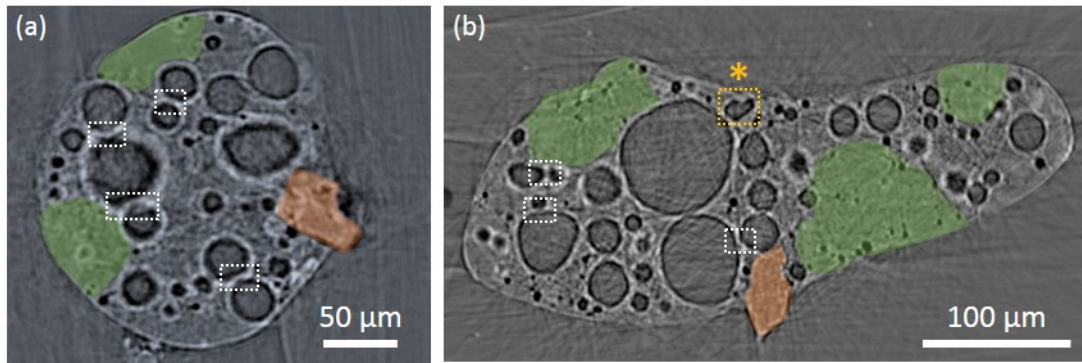
Figure 9.11: SR-µ-XRT sections; (a) vertically and (b) horizontally through the particle (as identified in Figure 9.10). The location of the Fe-rich particle (orange) and regions of low void component (green) are also identified, as are the locations at which neighbouring voids interact.

Oxide	Reference composition [376]	CF-01 ($\pm\sigma$)
CaO	60.2 - 66.3	62.5 ± 0.76
SiO$_2$	18.2 - 23.4	25.1 ± 0.33
Al$_2$O$_3$	2.4 - 6.3	2.3 ± 0.02
Fe$_2$O$_3$	1.3 - 6.1	6.8 ± 0.05
MgO	0.6 - 4.8	1.4 ± 0.02
Na$_2$O	0.05 - 1.2	0.3 ± 0.01
K$_2$O	0.05 - 1.2	0.1 ± 0.01
SO$_3$	1.7 - 4.6	1.5 ± 0.02

Table 9.1: Comparison of the reference wt% composition of Portland Cement *(from [376])*, with EDS wt% results from the green highlighted regions (as identified in Figures 9.11 (a) and (b)).

the relative order of formation (with the larger voids emplaced initially, ahead of the smaller ones). The likely, yet uncommon amalgamation of these smaller pores, identified with a yellow box and * in Figure 9.11 (b), details their potential parallel formation - potentially contributing to the production of the larger diameter voids.

The results of EDS elemental analysis (plotted as oxide ratios) taken over the low void density exterior regions of the sample, highlighted in green in Figures 9.11 (a) and (b), are detailed in Table 9.1 alongside those of a reference Portland Cement (from [376]). This compositional similarity of the low void density regions within the CF-01 particle with that of the reference Portland cement clearly illustrates these fragments as having originated as former structural material, associated with the reactor. Their existence, alongside the Fe-based particle, would be expected from such a reactor building explosion, which served to explosively produce such composition ejecta species. A contrasting hardness between the Fe and concrete could serve to explain the difference in the surface form of both included "fragment" types.
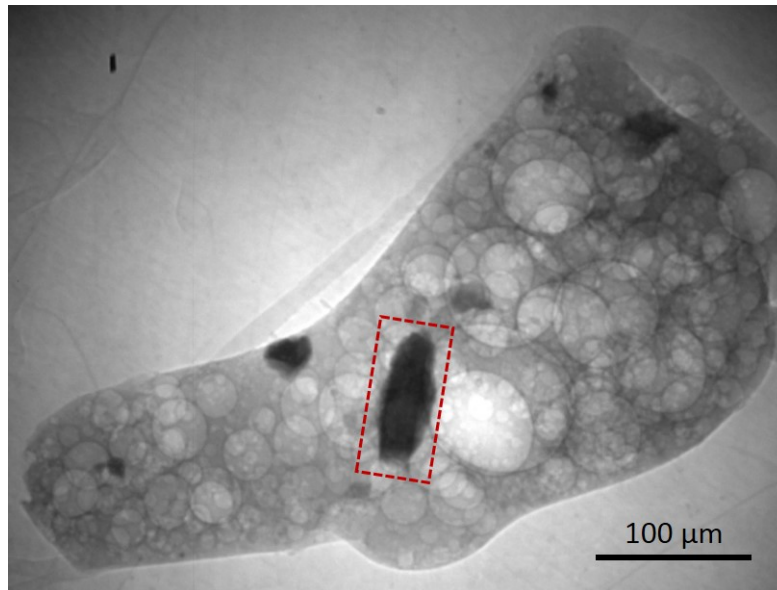
Figure 9.12: Zeiss Xradia Versa™ two-dimensional (flat) x-ray absorption image through the particle, the location of the formerly identified Fe-rich particle is highlighted.

Of the two materials, structural concrete (as used in nuclear reactor facilities) has a typical value for Mohs Hardness of between 5.0 and 6.0 [37, 376, 377]. In contrast, the Fe-based particle which through EDS is shown to have a composition equatable to a steel possesses a hardness of between 7.0 and 8.5, brought about by its heat treatment/fabrication process [35, 377]. As a consequence of these hardness differences, during as well as after the explosion, the "softer" concrete material that would have likely existed extruded from the surface of the particle, would have been easily eroded/abraded to produce a rounded particle surface, contrasting to the "harder" Fe-rich material - which in contrast, did not.

In addition to the SR results, a two-dimensional slice of the particle is shown in Figure 9.12, obtained using the lab-based Zeiss Xradia Versa™ system. As well as both the extensive void volume (previously calculated at 24%) and the previously discussed, extruding Fe-rich particle (highlighted in Figure 9.12), despite representing only a single vertical slice taken across the length of the sample - a number of additional, smaller and higher-density (dark) particles are observed, not otherwise identified in the lower-resolution SR analysis. While the SR analysis afforded both tomography combined with fluorescence (elemental) mapping (whereas the Xradia Versa™ could only perform three-dimensional absorption contrast imaging); the increased time available, maximum spatial resolution (pixel size) attainable as well as the number of rotational tomographic slices, together enabled for an improved internal sample visualisation over the internal imaging performed on the I13-1 synchrotron beamline during the initial beam-time.

A number of renderings, based on the computed tomographic absorption derived from the Xradia Versa™ system, are shown in Figure 9.13. In each of the four visualisations of the particle, alongside the large surface projecting Fe-rich fragment (highlighted in each case), there exists a significant number of additional (albeit smaller) high-density particles.

Analogous to the bimodal distribution observed for the voids contained within this particle - a similar size deviation is apparent for these solid inclusions. The largest of the fragments occur within maximum dimensions between 25 µm and 100 µm. The smaller, grouping comprises particles ranging from 1 µm - 3 µm in maximum dimension. Whereas the grouping of larger fragments occurs exclusively with a significant degree of observed angularity, the smaller material occurs with a variable morphology from angular to highly-spherical in nature. In addition, the frequency at which the fragments (classified into these two groups) occur within the sub-mm particle are very different - with five times the number of smaller (angular to rounded) material existing over the order of magnitude larger, and solely-angular, material.

As well as the increased frequency of the material, a further disparity is associated with the location at which these smaller fragments exist. Highlighted within the tomographic renderings (Figure 9.13), the larger material is strongly associated with the very outer circumference of the particle, whereas the considerably smaller material is found located at positions marginally closer to the centre of the CF-01 *ejecta particle* - away from its surface. Supporting the SR-µ-XRT results, the results from the Xradia Versa™ XRT also highlights the majority of this larger material existing protruding from the *ejecta particles* surface. Identical also to the distribution of voids within the sub-mm particle (Figure 9.11), there also exist locations whereby neither of the two particle size groupings is observed to exist as has been associated with the locations of the cement composition regions within the CF-01 sample.
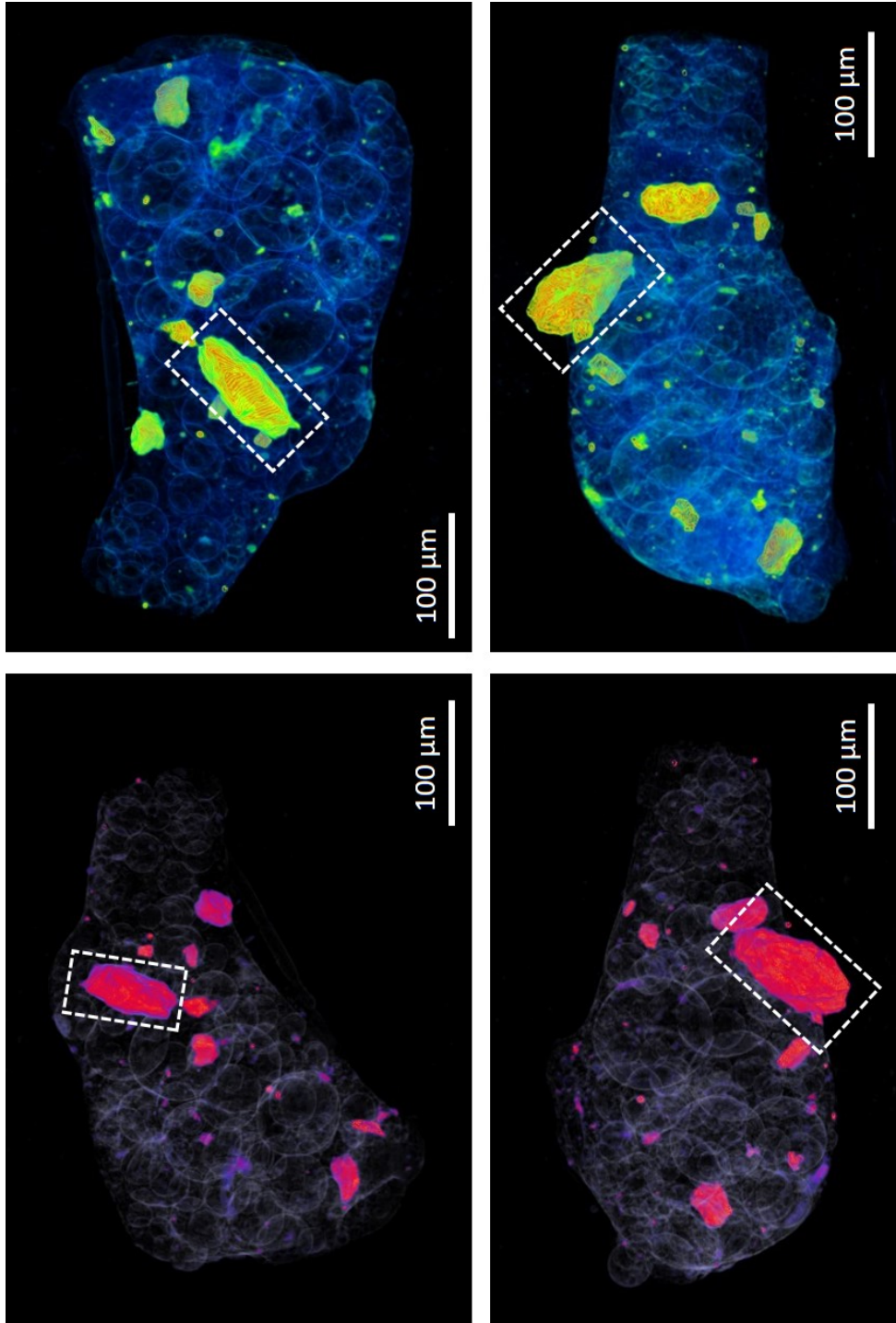
Figure 9.13: Zeiss Xradia Versa™ three-dimensional renderings of the sub-mm particle, the location of the formerly identified Fe-rich fragment is identified. A number of other particles with elevated density are also observed as is the extensive void network.

209
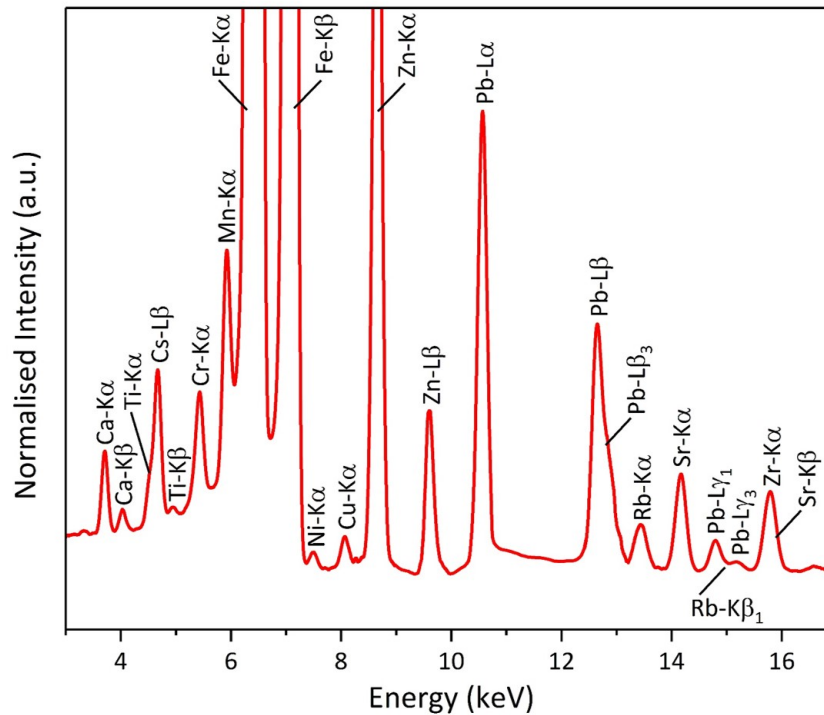
Figure 9.14: SR-μ-XRF spectrum obtained from the entire sub-mm *ejecta particle*, with contributing emission peaks identified.

9.4.4 Fluorescence spectroscopy

A representative SR-μ-XRF spectrum from the CF-01 *ejecta particle* is shown in Figure 9.14. While the characteristic emissions at <3 keV (principally the bulk elements Na, Mg, Al and Si), are below the energies attainable on the beamline, a compositional agreement with prior SR analysis on Unit 1 material is attained [190], showing a considerable Fe and Pb component. While EDS is capable of attaining abundance sensitivities of >100 ppm, XRF is conversely able to quantify elemental concentrations down to ppm levels [262, 378]. XRF is further advantageous over EDS, as no vacuum is required to ensure the unimpeded path of the incident electron beam onto the sample through which the characteristic x-rays (EDX) are generated.

Unlike the results obtained via EDS analysis of the material (Section 9.4.2), the x-ray emission peaks from SR-μ-XRF additionally detail the existence of Cr, Ni, Cu, Rb, Sr, Zr alongside the principal fission product, Cs. Whereas EDS identified both Ba and Mn within the particulate, these elements were not encountered during this SR compositional analysis. The study by Ono et al., (2017) [190], also identified the presence of additional elements, however, these were not identified during this work due to either their potential absence/low concentration/spectral overlap with other elements (Nb, Mo and U), characteristic emissions beyond that achievable on the beamline (Ag, Cd, Sn, In, Pd, Sb, Te, and Ba), or their highly-limited spatial extent.
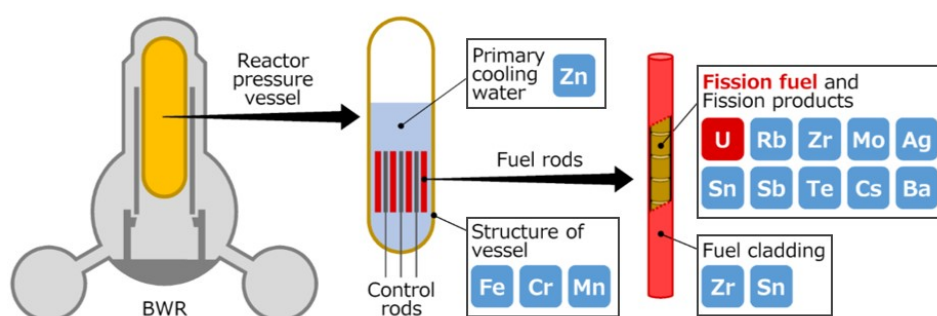
Figure 9.15: Sources of the various composition materials occurring within (and around) a nuclear reactor. *Modified from [192].*

All of the elements contained within this *ejecta particulate* have been formerly assigned in the work of Abe et al., (2014) [192], to originate from either the reactor pressure vessel (PRV), its neutron-absorbing control rods, the fuel elements themselves or their Zr-Sn based (Zircaloy-4™) cladding material. A schematic of which is shown in Figure 9.15 - consistent with the materials application in nuclear facilities as described in the review by Zinkle and Was (2013) [35].

The subsequent bulk fluorescence spectrum produced from the laboratory-based Niton™ XRF system is shown in Figure 9.16. Whilst able to attain fluorescence emissions at greater energies (25 keV) - after collection, normalisation and quantification of the results with the Thermo Scientific Inc. NDT™ software, an energy window between 10.0 keV and 16.0 keV (highlighted grey in Figure 9.16) was observed to contain no characteristic emission peaks, owing to a fault with the systems x-ray detector over that energy range.

Despite the absence of any emission peaks from this 6 keV window; the confirmation of previously determined elements as well as the existence of additional elements beyond those previously identified through either EDS or SR-μ-XRF, are apparent within this spectrum. An approximate quantification provided by the platforms peak-fitting and signal intensity correction algorithms was also possible, as shown in Table 9.2. This spectrum and associated quantification shows the occurrence of a near-identical suite of elements as determined by Ono et al., (2017) [190], derived through SR-μ-XRF analysis, including; Fe, Zn, Cr, Mn, Zr, Nb, Mo, Ag, Cd, Cs, Rb, Ni, Pd and U. The Niton™ laboratory-based XRF analysis also determined contributions from Cl and Ca - alongside a significant signal from Si. These three elements all occur with x-ray emissions below those quantifiable in the preliminary study (on similar material) by Ono et al., (2017) [190]. Like the SR-μ-XRF spectroscopy provided by the I13-1 beamline, the upper energy limit of this laboratory-based system (25 keV) does not permit the detection and quantification of the primary x-ray emissions of In, Sn, Sb, Te, and Ba, all of which may have existed within this
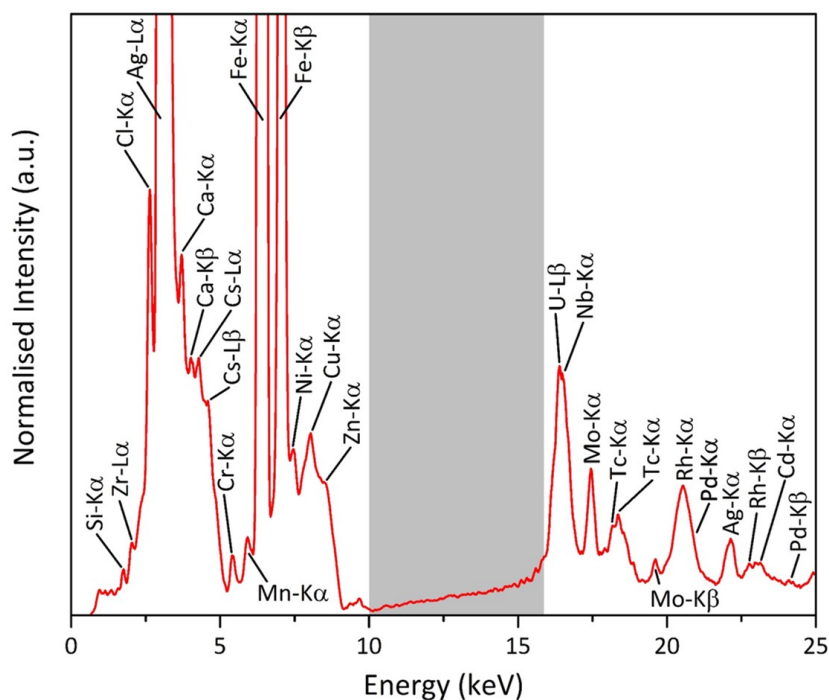
Figure 9.16: XRF spectrum derived from the entire particle using the Niton™ FXL 950 X-ray Lab with contributing emission peaks identified. The region absent of x-ray emissions is highlighted.

particulate. The measurement errors as determined by the instrument for each of the elements are shown in Table 9.2 alongside the results of the materials compositional quantification. These values (like the peak-fitted quantification) will feature a considerable level of inaccuracy due to the absence of emissions between 10 keV and 16 keV. As a consequence of this uncertainty, the Niton™ XRF analysis is, therefore, more appropriately considered as a qualitative representation of the particles composition over a quantitative one.

In contrast to this previous study, however, the emission peaks observed at the higher-energy portion of the spectrum (Figure 9.16) detail the existence of Tc and Rh. Both elements are known fission products, generated with yields of around 6% and 3.6% respectively [133]. The main isotope of Tc is ^{99}Tc - with a low activity and lengthy half-life (211,000 years) [52], it would still exist at an abundance close to original levels long after a release event. Two isotopes of Rh are produced as fission products - ^{103}Rh and ^{105}Rh. Whereas ^{103}Rh is radiologically stable, ^{105}Rh conversely exists with a half-life of only 35.36 hours [52], before decaying into the stable ^{105}Pd - the form that would now exist. Alongside ^{105}Pd, other isotopes are also produced (^{105}Pd, ^{106}Pd, ^{107}Pd, ^{108}Pd, ^{109}Pd and ^{110}Pd), with a combined fission product yield of circa. 8% [133]. The Pd primary (Kα) emission peak (in Figure 9.16), exists as a higher-energy shoulder and broadening of the Rh Kα signal (approximately 21 keV), representing the entire contribution of Pd isotopes.

Element	Oxide Weight Percentage* (wt%)	Error in Measurement (wt%)
Si	46.63	1.49
Na	13.04	0.42
Ca	7.57	0.24
Al	5.27	0.17
Ag	2.67	0.09
Ti	4.07	0.13
Zr	2.73	0.09
Sn	2.77	0.09
Pb	2.33	0.07
Cs	1.43	0.05
Zn	1.18	0.04
Cd	0.99	0.03
Cr	1.26	0.04
S	2.12	0.07
Ni	0.94	0.03
Tc	0.74	0.02
Au	0.73	0.02
U	0.77	0.02
Cu	0.51	0.02
Rh	0.53	0.02
K	0.39	0.01
Fe	0.37	0.01
Pd	0.26	0.01
Mo	0.32	0.01
Nb	0.26	0.01
Cl	0.13	0.01

Table 9.2: Average weight percentage quantification of the CF-01 *ejecta particulate* as determined via the Niton™ FXL 950 X-ray Lab and associated Thermo Scientific Inc. NDT™ peak fitting and quantification software. * The results are plotted as oxide wt% for applicable elements and as pure elements for native species. The measurement errors on these values is shown.

Despite being known fission products, neither Tc or Rh have been identified in the Fukushima-derived *ejecta particulate* material until now. Resulting from the earlier reactor inventory studies of Pontillon et al., (2010) [125], as part of the large French-led multinational VERCORS project, both Rh and Pd were similarly classified within the "semi-volatile" group - one of four fission product emission categories (the others being "volatile", "low-volatility" and "non-volatile"). Elements within this group include Mo, Ba and Pd - all of which have also been observed to exist within these Fukushima-sourced *ejecta particles*. Such "semi-volatile" elements are released at levels of 50% - 100% of their total core-inventory, with deposition occurring at locations "close to their source".

Element	Volume (μm^3)
Cs	1.40×10^4
Mn	1.42×10^6
Sr	4.74×10^5
Zr	4.70×10^4
Ti	5.00×10^4
Pb	1.81×10^6
Fe	3.88×10^6
Total	7.70×10^6
XRT volume	**8.76×10^7**

Table 9.3: Elemental volumes of the total CF-01 *ejecta particle* as determined via SR-µ-XRF mapping on the I13-1 beamline. The total particle volume, derived through SR-µ-XRT analysis - also performed on the I13-1 beamlines, is additionally shown.

Such an inconsistent occurrence of both Tc and Rh within the *ejecta particulate* not only supports the results of the VERCORS test-studies; highlighting the incomplete release (<100%) and subsequent deposition of such composition material close to the plant, but also compounds the conclusions of Ono et al., (2017) [190], that there exists an extreme amount of compositional heterogeneity within this particulate. The results of other fuel post-irradiation and reactor release studies have provided additional insight into the inconsistent elemental distribution that exists throughout the fuel matrix [23, 24, 379]. Such low concentrations of Tc and Rh, in this instance, most likely represents; (i) the low concentration of these elements in a typical burn-up nuclear fuel and, (ii) the spatial distribution at which these species are located - hence not being fully represented within this particulate sample set. Unlike species such as Cs, I, Xe, Kr and C which exist within either the void space between the fuel pellet/cladding or as discrete gas bubbles within the fuel matrix [23, 24], both Rh and Tc (alongside other elements) occur as inter-granular precipitates, and are therefore less easily liberated from the irradiated fuel.

9.4.5   Species distribution

Applying the SR-µ-XRF mapping results to the SR-µ-XRT rendering of the particle, yields the full three-dimensional compositional rendering shown in Figure 9.17. From these reconstructions, a high-degree of internal species heterogeneity is observed.

Of note is the distribution of Cs. From prior studies on the circa. 2 µm spherical "Cs-ball" particulate attributed to having been released from reactor Unit 2 at the FDNPP, Cs was observed to be spatially inhomogeneous within the Si-glass matrix - concentrated radially around the particle [193, 194, 197]. From Figure 9.17, the Cs is observed to occur in a few limited, but highly-concentrated locations. As well as surrounding the internal surface of the smaller voids, the Cs is principally associated with the locations of the larger, yet spatially discrete Fe-rich
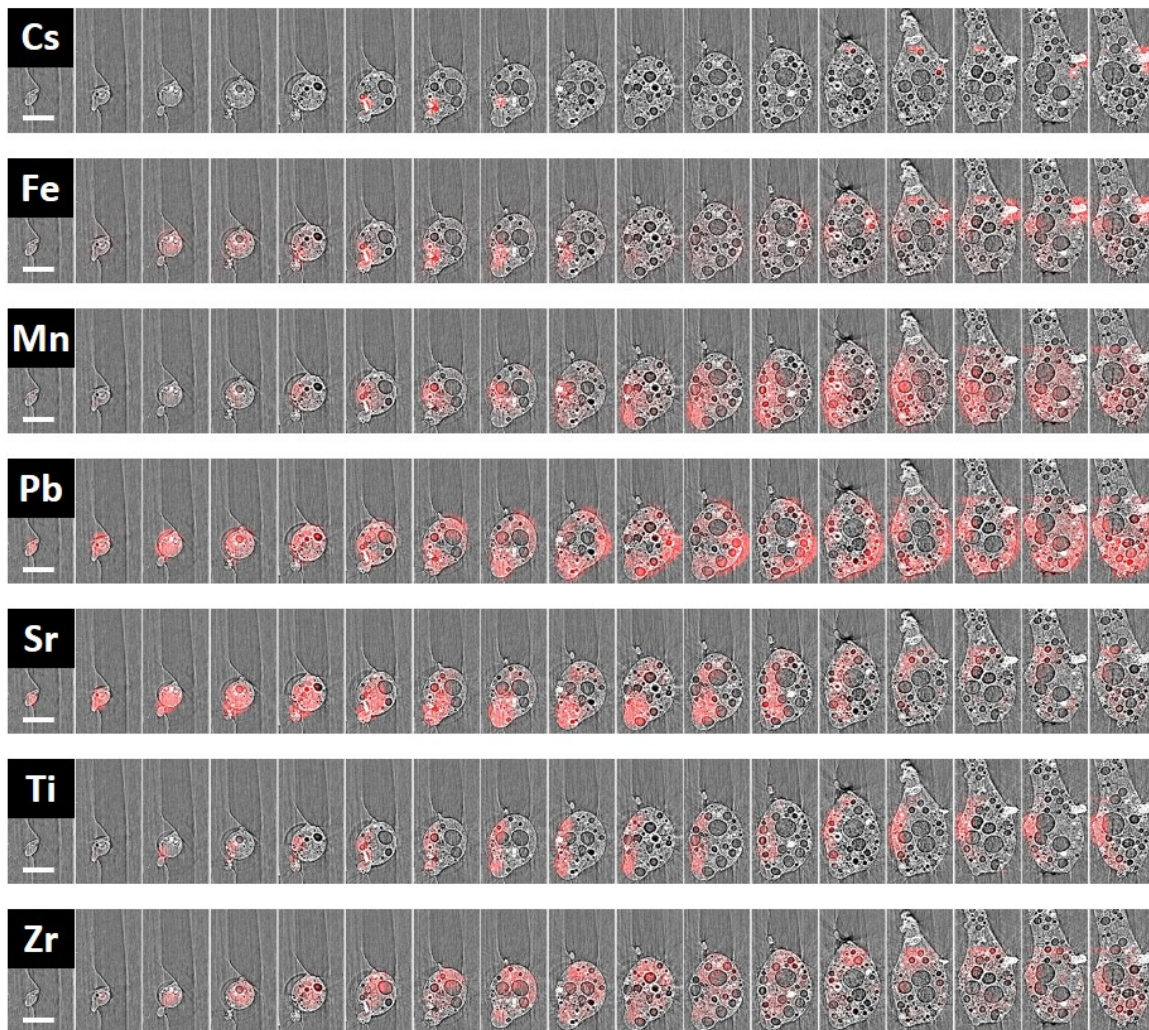
Figure 9.17: SR-μ-XRT rendering of the particle, overlain with compositional data derived via SR-μ-XRF mapping. Scale bar = 100 μm.

regions. The same highly-concentrated and heterogeneous distribution is also observed for a number of the other elements, as shown in Figure 9.17, including; Fe and Ti. In contrast, a more spatially extensive elemental distribution is shown by the additional species of Sr, Mn, Pb and Zr, yet all are still distributed heterogeneously throughout the *ejecta particle*. All of these elements, however, are observed to occur at higher concentrations radially around the external perimeter of the sub-mm particle, with little (or none) existing towards the particles centre.

With the preliminary results obtained on a small (circa 70 μm) sub-region of a similar reactor Unit 1 particle by Ono et al., (2017) [190], likewise exhibiting a circumference enrichment in Cs, a similar origin for this species as a component of the material can be instigated. A mechanism to account for this peripheral distribution of Cs in Unit 2 "Cs-ball" material (classified as "Type A"

by Satou (2016) [164]) has been provided by Kogure et al., (2016) [194]. Kogure and co-authors invoked that gaseous Cs (as Cs_2O and CsOH etc.) was "diffused into the Si glass particles from outward to inward after the formation of the glass particles in the atmosphere of the reactor". This work continued by speculating, that such Cs diffusion would likely have occurred after the onset of solidification of the Si matrix at high temperature. If such a matrix were to be molten at the time of Cs exposure, then enhanced diffusion would occur to yield Cs at greater depths within the material than otherwise observed [380].

In relation to the previously discussed bi-modal void structure of the particle, while no Cs (and to a lesser-extent, Sr) were observed associated with the larger diameter pores - distributed homogeneously throughout the sample, the converse was observed for the smaller, µm-scale voids. These more circumference-concentrated voids were observed to exist with elevated levels of both Cs and Sr - suggesting both species occur as a result of the coating of/condensation onto the interior surfaces of such micron-scale voids.

A volumetric breakdown of the various elemental components contained within the CF-01 *ejecta particle* are shown in Table 9.3, as determined through the SR-µ-XRF mapping performed on the DLS I13-1 beamline. The total particle volume as derived through the co-incident SR-µ-XRT is also included in Table 9.3. From these values, these seven specific elements (Cs, Mn, Sr, Zr, Ti, Pb and Fe) together constitute circa. 9% of the particles total internal volume. Owing to the differing degrees of elemental co-existence that occurred across the pixels used to derive these values, the resultant errors associated with the signal contribution deconvolution is approximated to represent ±5% for each of these elements.

From this compositional volume analysis, the total Cs contained within this representative CF-01 *ejecta particle* is shown to constitute 0.002% of the sample's total (XRT-derived) volume. Immediately prior to the combined SR analysis, γ-ray spectroscopy of this sample (against radiocesium reference standards) found it to exhibit a total activity of 18,600 Bq - associated with radiocesium isotopes $^{134+137}$Cs. The majority of such activity was associated with the longer-lived ^{137}Cs (16,800 Bq) over the much shorter-lived ^{134}Cs (1,800 Bq), which had decayed through approximately three half-lives since its environmental release. Converting this activity (of Cs) to a mass (assuming 1 g of ^{134}Cs has an activity of 48.10 TBq and the same 1 g of ^{137}Cs has an activity of 3.215 TBq [75]), yields a value of approximately 4.7×10^{-9} g of ^{137}Cs alongside a much smaller 3.74×10^{-11} g of ^{134}Cs.

The volume of this fissionogenic Cs contained within this *ejecta particle* can be approximated (assuming a Cs density of 1.93 g cm^{-1} [165]). This yields a total radiocesium volume of 14,240 µm^3 - of which ^{137}Cs constitutes 10,170 µm^3 and ^{134}Cs comprises 70 µm^3. Assuming a ^{135}Cs/^{137}Cs ratio for reactor Unit 1 of 0.35 - 0.40, as calculated from the ORIGEN modelling by Nishihara

et al., (2012) [50], this yields a ^{135}Cs volume of approximately 4,000 μm^3. Such an assumption, that Cs exists as a native (metallic) element rather than as one of its various oxides (e.g. $Cs_{11}O_3$, Cs_4O, Cs_7O, and Cs_2O), is likely to introduce a degree of uncertainty to these constituent (isotope) volumetric values.

The final main isotope of Cs to contribute to the total XRF signal would be the primordial ^{133}Cs - also being produced at very low fission product yields [133] - several orders of magnitude less than ^{134}Cs, ^{135}Cs and ^{137}Cs. In the isotopic analysis undertaken by Imoto et al., (2017) [371], a substantial ^{133}Cs component within similar Fukushima-derived particulate was highlighted. From the combined γ-ray spectroscopy and secondary ion mass spectrometry (SIMS) analysis on a suite of samples sourced from around the perimeter of the plant, a ^{137}Cs/^{133}Cs isotopic ratio of ≈1.0 was determined - illustrating approximately equal quantities of both Cs isotopes. However, the approximate Cs budgeting presented above accounts for the entirety of the Cs to exist as radiocesium; either ^{134}Cs, ^{135}Cs or ^{137}Cs - with no contribution remaining for ^{133}Cs. This contrasting absence of any such primordial ^{133}Cs is supported through the subsequent SIMS analysis detailed in Section 10.4.3.

9.4.6   FT-13

Gamma-ray spectroscopy

The γ-ray spectrum obtained from the single FT-13 *ejecta particle* is shown in Figure 9.18. Alike to the background subtracted γ-ray spectrum of the CF-01 particulate presented previously in Figure 9.3, the emission energies detected correspond solely to those of the fission product isotopes of radiocesium - ^{134}Cs and ^{137}Cs. After a decay correction of both isotopes activities to the March 2011 release date, a ^{134}Cs/^{137}Cs (activity) primary peak ratio of 1.05 is observed. The total activity of this particle (at the time of measurement in October 2017) was determined to be 2,600 Bq - an order of magnitude less than the CF-01 (reactor Unit 1) material.

In contrast to the ^{134}Cs/^{137}Cs activity ratio of 0.94 that was derived for the CF-01 *ejecta particulate*, this value for the FT-13 sample is consistent with the radiocesium core inventory value of Unit 2, as estimated through the ORIGEN modelling undertaken by Nishihara et al., (2012) [50]. While statistically different to the CF-01 *ejecta particulate*, this radiocesium activity ratio is not unforeseen, as the bulk sample from which this particle was isolated was obtained from a site (Futaba Town) located at the base of the main north-west trending contamination plume, attributed by regional radiation mapping to result from reactor Unit 2 [69, 153, 162]. These attributions are also, however, based upon the reactor radiocesium inventories as predicted in the work of Nishihara et al., (2012) [50], although these values have achieved wide acceptance in the scientific community.
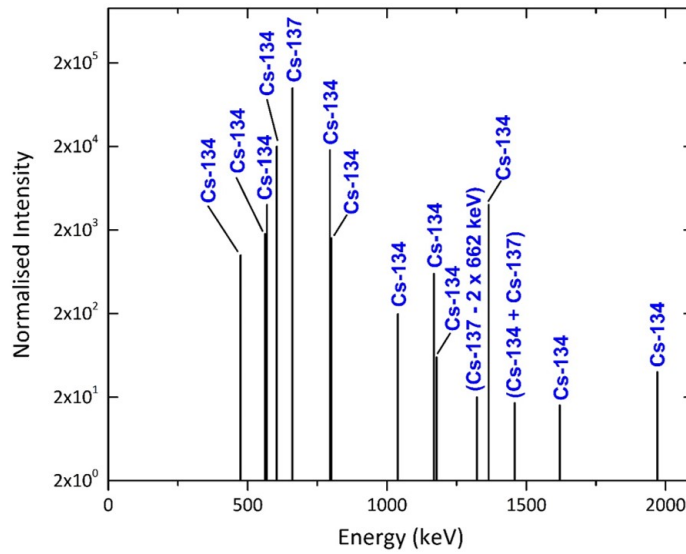
Figure 9.18: γ-ray spectrum obtained from the FT-13 particle, with contributing peaks identified.
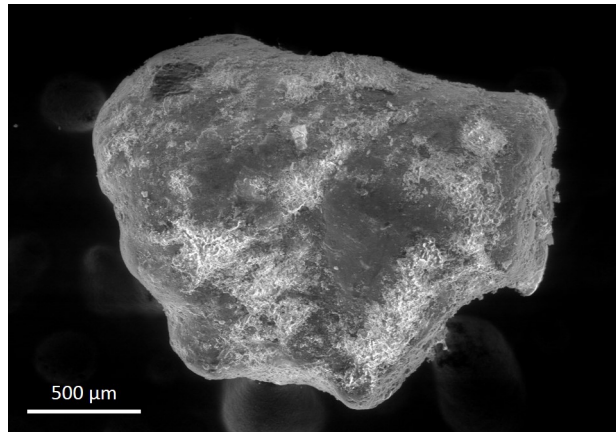
Figure 9.19: Secondary electron image of the entire mm-scale FT-13 *ejecta particle*.

Surface examination

A secondary electron image of the surface of this Unit 2 derived FT-13 *ejecta particle* is shown in Figure 9.19. Apparent from this image is not only the size of the particle (2 mm in maximum dimension) but also its smooth exterior - contrasting to the extensive fibrous surface morphology observed for the CF-01 material (Figure 9.4). Whereas the Unit 1 sourced CF-01 material was characteristically angular in its form, the exterior of the FT-13 material is considerably well-rounded - with no pronounced points or distinctive angular edges.

An EDS spectrum acquired over the entire surface of the particle is shown in Figure 9.20. From this spectrum, like the sub-mm CF-01 material, the primary component of the sample is observed to be Si - existing alongside significant contributions from C, O, Na, Al, Mg, Ca and Ti. Whereas
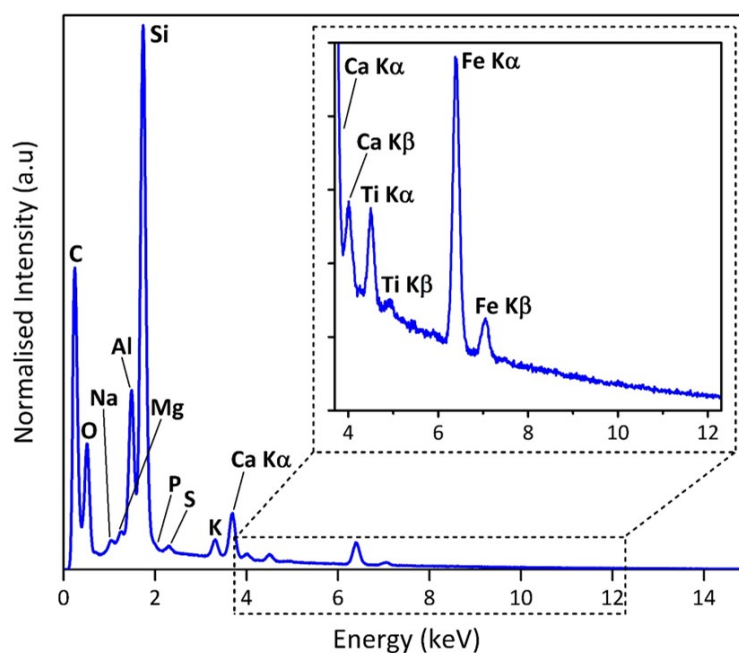
Figure 9.20: EDS spectrum derived from the entire surface of the FT-13 *ejecta particle*.

the EDS analysis of the CF-01 particulate revealed the additional contribution of Zn and trace quantities of Ba within the more angular particle, these species were absent from the EDS analysis of the FT-13 material. While the CF-01 material contained low concentrations of Fe, the FT-13 particle is shown to contain notably more of the transition metal. From EDS elemental mapping of both particle types (not shown), this Fe is observed to be distributed homogeneously across the entirety of the larger FT-13 material - having conversely being concentrated as angular sub-particles within the CF-01 *ejecta particulate*.

X-ray tomography

With the surface of the FT-13 particulate being homogeneous with respect to both its form and composition, its internal structure and composition were subsequently evaluated through the application of the laboratory-based Zeiss Xradia™ Versa XRT system. A series of three-dimensional computational renderings of the particle shown in a number of orientations are displayed in Figure 9.21.

In contrast to the XRT results obtained on the smaller, sub-mm CF-01 *ejecta particulate* presented in Figure 9.13, the internal form of the FT-13 particle is vastly different. Whilst the Unit 1 particulate exhibited a considerable internal porosity (24% void volume), such a texture is not apparent within the FT-13 particle. The entire internal volume of this sample is shown to be

constituted by an amorphous solid material, within which no porosity exists. Although the outer surface of this particle details none of the fibrous structure apparent across the surface of the CF-01 material, some internal artefacts of similarly fibrous material exist - the locations of which are additionally highlighted with yellow boxes in Figure 9.21.

As well as the isolated regions containing these fibres, a number of high-density inclusions are also observed. Opposed to the CF-01 particle, where a large number of contrasting density fragments (existing across a wide size range) were observed both within as well as extruding from the surface of the sample, the FT-13 particle contains a significantly smaller component of elevated density fragments none of which are observed to protrude from the particles exterior. These inclusions are represented in the tomographic renderings and volumetric cross-sections shown in Figure 9.21 by the areas with red colouration. In addition to their more limited occurrence as well as complete containment within the main particle, these inclusions are not angular in form like those associated with the outermost surfaces of the CF-01 *ejecta particle*. As shown in Figure 9.21, the high-density sub-particles within the FT-13 sample are concentrated within a small region, located towards the flat base of the particle.

Furthermore, in contrast to the strongly bi-modal size distribution of the particle inclusions within the CF-01 *ejecta particulate*, the inclusions contained within the FT-13 particle are strongly uni-modal in size. These particles occur with comparable dimensions to the larger suite of high-density material associated with the CF-01 *ejecta particle*, existing over a size-range of 40 µm - 100 µm in maximum dimension. Ion-beam milling into the surface of the FT-13 sample at positions corresponding to the locations of several of these high-density particles was subsequently undertaken, prior to performing EDS elemental analysis. This quantification confirmed that the particulate, like those contained within the CF-01 sample, was similarly Fe-based.

As per the Raman spectroscopy analysis of the CF-01 sample, the similar analysis of this larger FT-13 sample yielded identical results - with the amorphous nature of the sample confirmed by the broad spectrum devoid of any clearly-defined (sharp) peaks [375].
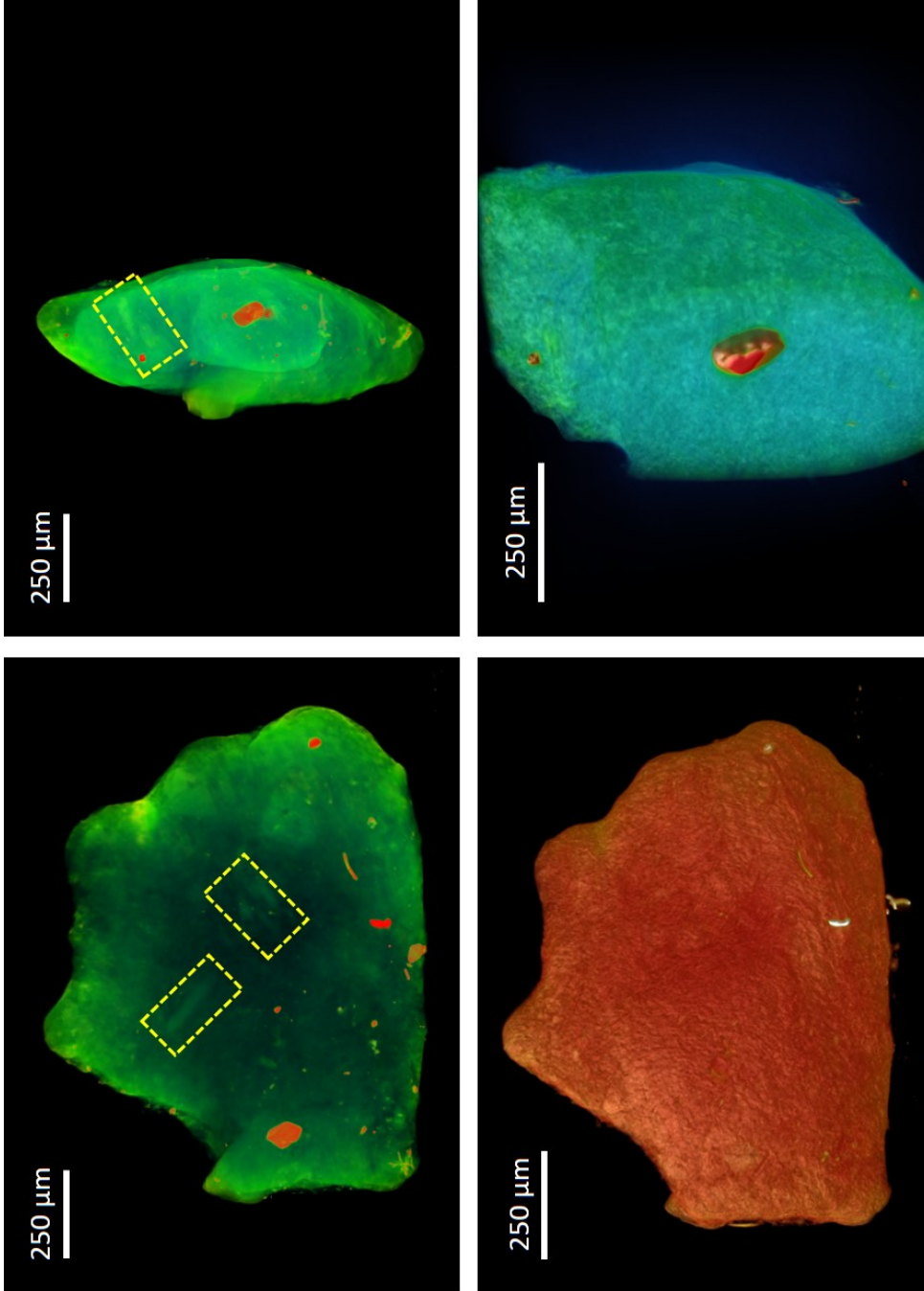
Figure 9.21: Zeiss Xradia Versa™ three-dimensional renderings of the FT-13 *ejecta particle*. The isolated (high-density) regions correspond to the location of Fe, with the regions representing the position of former fibrous structures contained inside the Si-based particle shown by the yellow boxes.

221

(Not to scale)
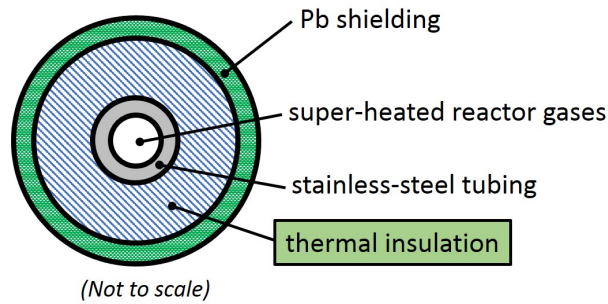
Figure 9.22: Schematic of a typical thermally-insulated stainless-steel pipe used to transmit steam around the various reactor components.

9.5   Discussion

CF-01 (Unit 1)

The highly-fibrous nature of the Si-rich material is synonymous with a thermal insulation-type material. This insulation is encountered in numerous positions within a nuclear reactor; surrounding large portions of a typical reactor pressure vessel (RPV), it's associated heat-exchanger/piping network, as well as within the reactor building structure itself.

Opposed to a pressurised water reactor (PWR) system, where the high-pressure steam produced within the RPV is used to supply steam to a secondary boiler circuit which subsequently feeds steam into generator turbines, BWRs (as at Fukushima) do not possess this secondary loop - supplying steam generated in the reactor directly to the power-generating high-speed turbines [20]. Being older in their design (with the reactor at the FDNPP dating from the 1970's), BWRs are now not a common type of LWR design - having been globally dwarfed in number by PWR systems [8]. Despite PWR units operating at twice the pressure of BWRs (15 MPa, rather than around 7.5 MPa) - therefore requiring substantially thicker piping to transfer reactor-generated steam, the secondary loop design of PWRs means that unlike BWRs, water and other downstream components, are not radiologically contaminated. Resultantly, a greater length of stainless-steel pipework at the FDNPP would have carried, and therefore been exposed, to various types of (largely γ-ray emitting) radioactive material.

As shown in the schematic cross-section of Figure 9.22, one such use of this fibrous material is to provide thermal insulation to the kms of stainless-steel tubing that serves to transfer the steam and pressurised water around the various components of the facility. At Fukushima, this Si-clad network was surrounded by a layer of Pb shielding - for both radiological protection and to also ensure that the insulation completely enclosed the pipe.
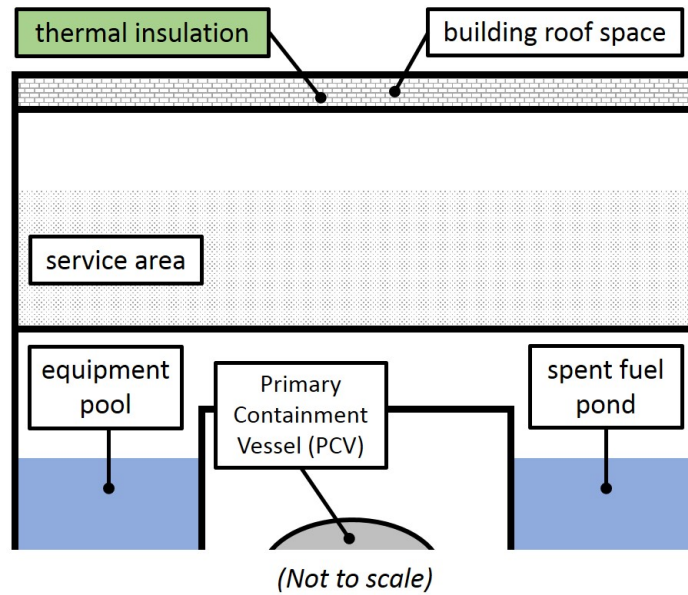
Figure 9.23: Schematic of the FDNPP Unit 1 reactor building, detailing the location of the Si-composition thermal insulation material.

Alongside this thermal insulation material utilised in close proximity to the reactor vessel, an additional source of this fibrous material is shown in the Figure 9.23 schematic - conversely located away from the RPV and PCV. This material is located in the building's roof space, surrounding the extensive concrete and steel superstructure that housed the reactors themselves. As shown in Figure 9.23, a service area many meters high (containing cranes used to transfer the fuel assemblies in and out of the reactor) in addition to the water-filled fuel storage ponds served to separate the underlying RPV from this roof space (void) located material. Owing to differences in their final designs, eventual construction and subsequent upkeep of each of the FDNPP reactor buildings at the site, the Unit 1 reactor hall was significantly different (and much more structurally robust) than each of the other reactor Unit buildings [5, 11]. Whereas reactor Units 2 - 6 all comprised a simpler and less extensive concrete roof with no such insulation, the roof of Unit 1 was not only painted extensively with a Zn-based paint (to afford a level of corrosion resistance) but also contained a 0.5 m thickness of the fibrous Si-composition insulation material.

A third and final location within reactor Unit 1 where such fibrous Si-based thermal insulation material was located is shown in the Figure 9.24 schematic. This application of Si-based material represents its greatest volumetric use within the entire reactor Unit, employed as a 30 cm thickness to provide thermal insulation around the stainless steel PCV/dry well. Alongside being the greatest volumetric use of this material, this insulation was located within the closest proximity to the reactor core and the greatest potential heat intensities.
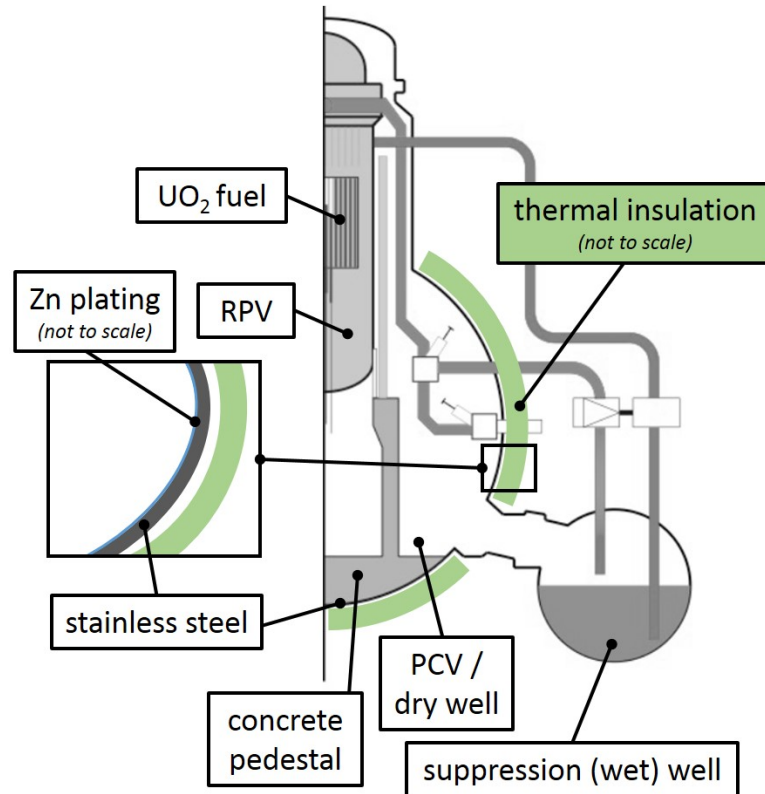
Figure 9.24: Schematic of the FDNPP Unit 1 RPV, PCV (dry well) and suppression (wet) well, with the location of the fibrous Rockwool™ thermal insulation shown.

Following personal communications with Dr Y. Satou (JAEA) and TEPCO engineers at the FDNPP, the insulation material located within the roof space, cladding the pipes of the reactors heat exchanger network as well as enclosing the PCV, was of the Rockwool™ type.

A comparison of the characteristics of typical (melted, and subsequently extruded) geologically-sourced fibrous material, as determined in a number of studies, alongside the current technical data provided by the original Rockwool™ brand, are presented in Table 9.4. From these results, a strong similarity is apparent between the fibres observed in this study, and published/manufacturers technical values for such rock-sourced material.

The average fibre diameter measured in this study was 12 µm (range: 6 µm - 32 µm), with the reported diameters of insulation-type materials varying from 2 µm - 25 µm. This contrast between the size of many of these fibres and the typical values of the insulation material presented in Table 9.4 may result from the partial melting of the Si fibres - permitting for the material to flow under the elevated temperatures experienced during the reactor Unit 1 LOCI (and ensuing reactor building hydrogen explosion). The existence of the extensive micron-sized pits across the surface of the particle and fibres (Figure 9.4 (b)) may represent the location of vesicles, or gas

Study	Mean Fibre Diameter (µm)	Reference
Öztürk (2010)	8 - 20	[381]
Zihlif and Ragosta (2003)	2 - 25	[382]
Rockwool™ Limited (2017)	4 - 5	[383]
IARC Working Group on the Evaluation of Carcinogenic Risk to Humans (1988) *"General Thermal Insulation"*	6 - 15	[384]
IARC Working Group on the Evaluation of Carcinogenic Risk to Humans (1988) *"High-Temperature Thermal Insulation"*	<3	[384]
Klingholz (1977)	4 - 6	[385]
This Study	6 - 32 (average: 12)	[386]

Table 9.4: Mean fibre length of Si-based insulation materials obtained from prior studies on their physical form.

pockets, formed during the materials initial production, or during the accident - whereby either reactor and fission product gases were incorporated into the sample, or more likely, the exsolution of (volatile) species contained within the material produced an extensive internal gas volume.

Of the three potential sources of the Si-based insulation material that could account for the form and composition of this reactor Unit 1 particulate (Figures 9.22, 9.23 and 9.24) - the source of this fibrous material can, however, be best attributed to the thickness of material that surrounded the PCV. During the LOCI and associated fuel melting that occurred at reactor Unit 1 [7], this insulation would have; (i) reached the highest temperatures of any of the insulation material, and (ii) was located closest to the reactor materials in addition to the high temperature and pressure reactor-sourced gases.

Although located close to the reactor core, the elevated temperatures associated with the melting of the reactor Unit 1 fuel assemblies (and relocation to the base of the PCV and underlying concrete pedestal) alongside the large volumes of reactor steam would not have caused the heating and melting of the insulation that existed around the peripheral piping network above what is considered normal operational conditions [2, 20]. This integrity was confirmed in the subsequent post-accident analysis of the facility [9, 59], which verified that no melting of this component had occurred. The third volume of Rockwool™ type insulation - located in the Unit 1 roof space, and the greatest distance (>10 m) from the heat associated with the LOCI in the RPV below, would also not have been adversely impacted by the elevated temperatures associated with the core-melting that occurred some distance below, within the RPV/PCV [9]. An analysis of

the temperature values recorded during the incident within the above-reactor fuel storage ponds further confirmed that temperatures were within normal operational bounds [33].

While considerably more radiation was released from reactor Unit 2 as a consequence of the substantial (yet non-explosive) breach of the reactors PCV [7, 30] (where a high temperature and pressure state existed until its eventual damage on the morning of the 15th March), the source of radiation from reactor Unit 1 was the dramatic reactor building hydrogen explosion [7]. Despite numerous episodes of RPV venting to relieve the elevated pressure in Unit 1, the structural integrity of the PCV was eventually lost in the hours proceeding the explosion [7].

Resulting from this critical loss of structural integrity, a substantial quantity (and pressure) of highly-combustible hydrogen gas (approximately 130 kg [387]) was released into the region around the PCV and base of the reactor assembly, to a position where fuel was subsequently determined to have relocated [54]. This hydrogen gas originated from the steam-driven auto-catalytic H_2-O breakdown of the reactors coolant water in the presence of the Zr cladding that reached elevated temperatures during the LOCI. In addition to the H_2 gas, numerous fission product species, including; Cs, I, Xe, Kr and Te would have all existed closely associated with this region of the reactor. The resultant combustion of this gaseous volume resulted in the explosive fragmentation (and release) of this structural component, with a proportion of this gas also having been incorporated into the partially-melted Si-based material with the elevated temperatures.

The internal morphology of these sub-mm particles, as observed via SR-μ-XRT, compliments the observations of the particulates external (fibrous) structure - having likely been formed from the considerable thickness of fibrous Rockwool™ insulation alongside the reactors pedestal (structural) concrete and stainless-steel from the reactor vessel itself. A comparison of the internal form of this representative particle with naturally-occurring volcanically-derived pumice highlights their high degree of structural similarity [388], and provides a mechanism to account for the observed bi-modal void distribution. Upon the accident-related heating and partial melting of the source silicate material (originally produced itself through the melting and extrusion of basaltic rocks), volatile (low boiling-point) species originally contained as solids were exsolved to produce a considerable gaseous pore volume, and the larger of the internal voids. The well-formed and highly-spherical nature of these larger voids suggests that they were not produced by gases flowing into what would have been a highly-viscous material (where non-spherical pores would be produced) - rather growing in-situ, via the exsolution of dissolved gases and volatiles as the molten silica was heated (and depressurised) with the intense heat of the LOCI.

In contrast, the smaller suite of voids are ascribed to result from later stage incorporation of the reactor-sourced gases from the FDNPP. With SR-μ-XRF identifying the location of Cs and Sr to be located around the periphery of the particle, at positions corresponding to locations of the

smaller-sized voids, the significant hydrogen and fission product overpressure associated with the reactor Unit 1 is highly likely to be responsible for developing these voids. This is supported by the Cs and Sr coatings observed on the surfaces of these (smaller) voids, ascribed to species condensation upon incorporation into the parent particle. The locations at which interactions occur between the two void types is shown in Figures 9.11 (a) and (b). In each case, the smaller voids are observed to "impinge" into the larger ones - resulting in a slight amount of deformation, as well as highlighting the relative order of formation (with larger voids emplaced initially). The amalgamation of these voids (∗ in Figure 9.11 (b)) may also contribute to the formation of larger voids, from the subsequent (smaller) gaseous volumes. A component of the Cs is additionally associated with the Fe-based (surface protruding) fragment. This co-existence supports the known affinity of ionic Cs for Fe-based surfaces examined in the work of Al Rayyes et al., (1993) [389].

The explosion of the reactor building, as well as fragmenting the Si-based insulation material to yield the sub-mm particles, will also have resulted in the destruction of the other structural materials comprising the reactor Unit and surrounding building. Identified within the *ejecta particle* tomographic slices (Figures 9.11 (a) and (b)) are distinct regions (75 µm - 150 µm in maximum dimension) where neither voids nor high-density particles (of either of the two distinct size groupings) were observed to exist. Such regions were shown to represent cement fragments, embedded within the partially-molten Si-based material during its violent ejection. This material has been rounded through their attrition with other particulate and surfaces during their release.

The smaller diameter (included) elevated density particulate could, like the smaller-sized component of the particle's voids, result from pre-existing material contained within the Si-based source material. Like the concrete material discussed above, the composition and peripheral nature of the larger steel fragments "embedded" into the particle advocates that this component is sourced from the reactor building hydrogen explosion, "adhered" to the surfaces of the softened material. Further supported by the diameter of such material being considerably larger than even the greatest sized fibre diameter for the Rockwool™ material (presented in Table 9.4), a provenance of having originated within the insulation fibre can be disregarded. This difference between the protrusive Fe and the smoothed cement surfaces were described previously in Section 9.4.3 - resulting from their contrasting levels of hardness.

While not detailed in the XRF spectrum obtained via SR analysis on the I13-1 beamline (Figure 9.14), the occurrence of U was, nonetheless, identified within the XRF results provided by the lab-based Niton™ system (Figure 9.16). Combining the high-density of the smaller (approximately micron-scale) particles, located towards the exterior of the sub-mm particle (Figure 9.13), with similarly-sized and smaller U composition material having been formerly identified to originate from the FDNPP (Chapter 8) albeit from reactor Unit 2, this signal could potentially result from a U component existing in this reactor Unit 1 particulate.

Such high-density, micron-scale material could have existed as a component of the original Si-based insulation material. In the work of Morgan and Lovering (1965) [390], the basaltic (mafic) rock precursor used to produce the standard Rockwool™ was shown to contain approximately 0.2 ppm U. Such species, despite being homogeneously distributed throughout the source basalt, were determined to become heterogeneous and concentrated during the Rockwool™ production as a consequence of the melting and extrusion process due to the strong incompatibility for U within a geological fluid (melt).

Despite being a potential source of this material, the size of these particles is significant in relation to that of the source fibres within which they are found; with the high-density material possessing diameters of circa. 1 μm - this would therefore constitute a large component of the entire cross-sectional area of the Rockwool™ insulation (Table 9.4).

To analyse these potentially U-containing micron-sized particles, further SR analysis was applied to the sample. As well as further utilising the coherence imaging (I13-1) beamline at the Diamond Light Source, the higher-resolution micro-focus spectroscopy (I18) beamline was additionally used. The results of this spectroscopic analysis are presented in Chapter 10, alongside the complementary SIMS analysis of the same embedded material.

FT-13 (Unit 2)

This material represents the largest diameter particulate encountered from reactor Unit 2 to-date when compared to the highly-spherical "Cs-ball" material and the small volume of other micron-scale material analysed by other authors [164, 196, 371]. At 2 mm in maximum dimension, this particle is greater in size (by an order of magnitude) than any of the formerly discussed CF-01 (Unit 1) *ejecta particulate*. Despite being comparable in its size to material from reactor Unit 1, the 1.05 ^{134}Cs/^{137}Cs activity ratio of this FT-13 particle ascribes it to reactor Unit 2, when evaluated with respect to the core-specific values defined by Nishihara et al., (2012) [50].

As documented in official accounts of the accident [2, 9], in addition to the description of the accident in Chapter 1, the events at the Unit 2 reactor were not only the last within the series of catastrophic release events to occur - but were also the greatest in magnitude. Also contrasting to reactor Unit 1 was the mechanism of the Unit 2 release; representing an eventual (but rapid duration) failing of the PCV - having existed at elevated temperatures for 100 hours prior to release, opposed to the Unit 1 rapid (24 hours after SCRAM) PCV breach and H_2 gas explosion.

These dissimilar release conditions combined with their timings after the seismic activity, SCRAM and tsunami, together provide an explanation to account for why this large-scale *ejecta particulate*
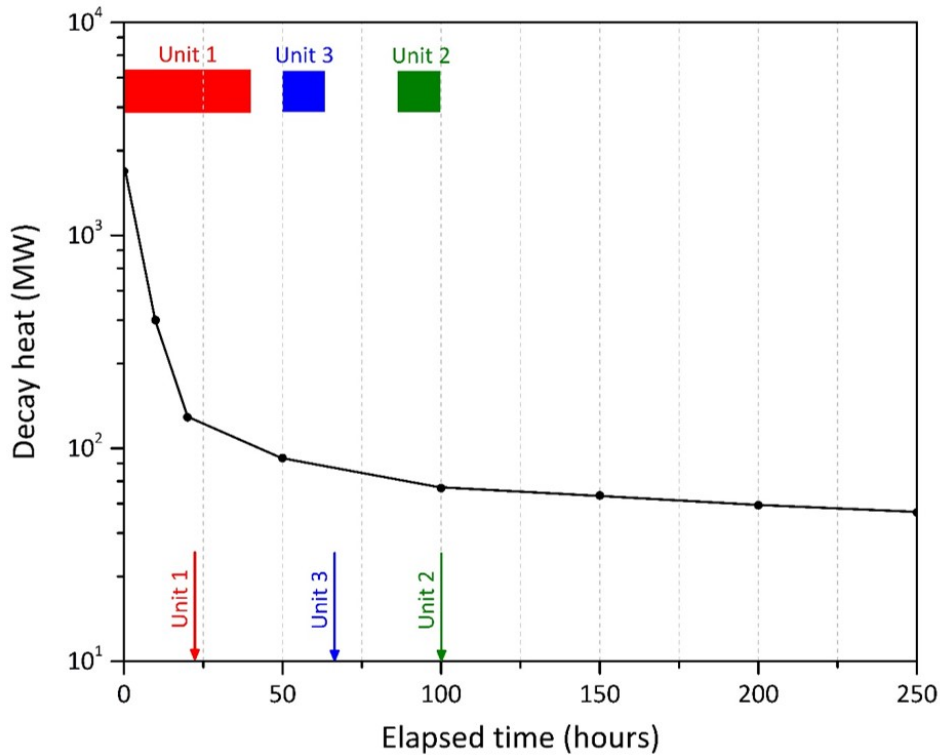
Figure 9.25: Decay heat for a typical FDNPP BWR following shutdown (SCRAM). The periods over which continuous cooling (provided by water injection) was suspended at each reactor is illustrated by solid blocks, with the timing of each reactor Units environmental discharge shown by the arrows along the horizontal axis.

from reactor Units 1 and 2 is so characteristically different. A plot summarising the release events from each reactor Unit at the FDNPP is shown in Figure 9.25 (arrows), alongside solid bars depicting periods during which interruptions to each reactors core cooling provision occurred. These events are plotted alongside the residual decay heat that would have existed within an FDNPP BWR loaded with an LEU fuel after the initiation of such a SCRAM event.

As illustrated in Figure 9.25, unlike reactor Unit 1, where core-cooling was lost immediately after the tsunami inundated the site (when residual core thermal output would have been at its highest), adequate cooling of reactor Unit 2 was maintained for close to 100 hours (during the greatest thermal output of the reactor), until the morning of the 15th March - when eventual core and reactor damage was sustained. While the reactor core of reactor Unit 1 would have been considerably hotter at the time of the radioactive release, less extensive melting (and volatile exsolution) of the fibrous Si material would have occurred than associated with the reactor Unit 2 thermal insulation. This difference in duration at which elevated temperatures were experienced in each reactor can be viewed as one factor to rationalise the difference in particle morphology between that produced by reactor Units 1 and 2.

At the time of the Unit 1 reactor building explosion, the Si-based thermal material is likely to not have reached an entirely molten state - illustrated by the strongly fibrous form of the *ejecta particle*. Although some degree of core cooling was maintained, in contrast, the Si matrix that constitutes the Unit 2 *ejecta particulate* would likely have achieved a near fully-molten state. This is demonstrated by the largely structure-less form of the Unit 2 (FT-13) material. Such an extensive degree of melting permitted the full out-gassing of the volatile species contained within the Rockwool™ material.

The disparity observed between the fragment-rich surface of the Unit 1 particulate and the featureless surface of the Unit 2 material can be rationalised by; (i) the nature of the release event alongside, (ii) the physical state at which the Si-rich Rockwool™ existed. Whereas the Unit 2 release was a non-explosive breach of the primary containment (and therefore did not result in the generation of the extensive volume of reactor-sourced fragment species), the H_2 gas explosion of reactor Unit 1 on the other hand, resulted in the production of vast quantities of material fragments. As the Rockwool™ was softened (partially-melted) under the conditions of the Unit 1 LOCI, these fragments became incorporated into the surface of the material, which itself became ejected during the explosion. This material "softening" also permitted for the rapid decompression enabling for the exsolution of volatile species contained within the Rockwool™ (producing the large diameter voids), in addition to the inwards diffusion and condensation of both H_2 gas and various fission product species contained within the region encompassing the reactors PCV.

The absence of porosity within the Unit 2 (FT-13) particulate supports such a hypothesis, that this PCV enclosing insulation material underwent a significant (if not complete) degree of melting during the LOCI. This melting would have permitted for volatile gases to exsolve entirely out of the material - resulting in the solid particulate, observed through XRT analysis. The absence of fission product species within this insulation-containing environment, until the PCV integrity compromise occurred, would not have resulted in the formation of pores within the sample. Instead, these radioactive species would only have become incorporated within the very outermost surface of the particle (shortly ahead of its reactor Unit 2 release).

Despite being considerably larger in diameter than all other Unit 2 derived particulate material described in the literature [164, 196, 371], a comparable internal structure consisting of a glassy Si matrix with no internal porosity, has been observed during this study. Having been isolated from closer to the facility (2 km from the site boundary) than any of the other material, its size (2 mm) is the result of having been deposited earlier (closer to the source) as a gravity-fall deposit in contrast to the smaller material capable of being transported further distances whilst entrained within the transporting plume.

Although no high-density actinide composition inclusion material was seen to exist within the Unit 2 *ejecta particle* material, as was observed in a number of the *atmospheric particulate* samples by Abe et al., (2014) [192], the inconsistent occurrence of U was described in the same work, as was also discussed in that of Ono et al., (2017) [190]. Therefore, the absence of actinide material is not entirely unexpected within such a small sampling of this material.

9.6 Conclusions and future work

The analysis of material in this chapter has allowed for a greater understanding as to the likely source of these radioactive *ejecta particles* found immediately in the immediate proximity of the FDNPP. This analysis has also afforded a better insight into the events that occurred in March 2011 as the reactors experienced severe Loss Of Coolant Incidents (LOCI), with subsequent reactor building hydrogen explosions or PCV structural failure.

The large size of the CF-01 particulate collected near the reactor site, coupled with the highly angular nature of the embedded fragments is illustrative of a highly-energetic mechanism of formation - explosive in nature and consistent with the events described as part of the numerous accounts of the incident by organisations such as the International Atomic Energy Agency (IAEA) [2] and the plants operators the Tokyo Electric Power Company (TEPCO) [7]. As is now widely-accepted, this incident represents a large-scale reactor building hydrogen explosion resulting from the combustion of hydrogen gas following the exothermic oxidation of the Zircaloy-4™ fuel cladding at elevated reactor core temperatures. The incorporation of structural cement, alongside extrusive and angular particles of metallic Fe (as steel), supports such a formation mechanism [2, 7, 30].

The complementary analysis of the FT-13 particle confirmed that this material was likely derived as a consequence of the PCV breach/leak associated with reactor Unit 2 - the specific nature and location of which (inside the PCV) is still the topic of much debate [34]. With a maximum diameter of 2 mm, this sample represented the first large *ejecta particulate* possessing a ^{134}Cs/^{137}Cs signature attributable to reactor Unit 2 to be analysed. Having in all likelihood been sourced from the same precursor Si-based Rockwool™ insulation material, the contrasting conditions associated with its formation (PCV breach over an extended time period rather than a reactor building H_2 explosion) resulted in the production of a material with an internal form contrasting with the CF-01 (reactor Unit 1) *ejecta particulate*.

Future work shall investigate any specific compositional variance in samples containing voids. One such future experiment planned on this highly-porous *ejecta material* will seek to analyse the composition of the voids/void surfaces that comprise 24% of the total sample. Employing

the FIB system with a residual gas analyser (RGA) attached, the low operational pressure of the instrument ($\times 10^{-6}$ mbar), and the destructive Ga ion-beam - this process will selectively ablate the sample's surface. The material released by this targeted FIB milling can then be characterised by the associated RGA system.

10

Spectroscopy and isotopic analysis of ejecta material

10.1 Introduction

The results of Chapter 9 identified the existence of a number of micron-scale particles of considerable density contained within the CF-01 (Unit 1) *ejecta particulate*. In addition to these surface and sub-surface fragments, Cs (as well as other elements, including Pb, Sr and Zr) were observed to be strongly-heterogeneous - located as spatially discontinuous regions at elevated concentrations. Despite exhibiting a spatially heterogeneous occurrence of these elements (within the Si-based particle) - the location of such constituents was shown to be concentrated greatest around the exterior circumference of the sub-mm sample.

In contrast, the FT-13 (Unit 2) material was shown to be homogeneous in its internal form - comprising no internal void volume and showing only a limited number of sub-surface fragments. These fragments were additionally of lower bulk density in comparison to those in the CF-01 *ejecta particulate* sample. Although constituted by the same bulk (Si) matrix material, the differing release dynamics associated with the Unit 1 and Unit 2 events were hence ascribed as being responsible for the dissimilar structural (and compositional) characteristics of the two forms of *ejecta particulate*.

While the events that occurred at the FDNPP Unit 2 have been shown (in this work) to have likely resulted in the emission of core material (Chapter 8) - the radiological release from Unit 1 has (to-date) only been observed to have been constituted by fission-product species condensed from a vapour - and not any actinide material (e.g. U, Pu or Am) [164, 190]. As such, if this sub-mm Unit 1 particulate were to contain reactor-sourced U, this would invoke a situation whereby similar actinide release and contamination to Unit 2 has occurred. Although U, as the UO_2,

would represent the actinide encountered at the greatest concentrations within the environment should such a core-compromise occur - a number of additional actinide elements (e.g. Pu, Am and Np) associated with nuclear transmutations, would also be anticipated. As discussed in earlier chapters, whereas fission products are typically characterised as possessing a greater (γ-ray) radioactivity (with shorter half-lives), actinides have considerably longer half-lives - on the orders of hundreds of thousands to millions of years [52]. Over a hazard resulting from their γ-ray (and their α-particle) activity/emission, the actinides present an increased toxicological concern over elements such as Cs and Sr owing to their direct chemotoxicity to humans (and other species) [311, 332, 355], of which the anthropogenically-derived Pu is of an extreme concern [391].

If derived from a reactor source, it is essential to determine the physiochemical state and abundance of the actinide material within this *ejecta material*. The form and oxidation state of this particulate, like the micron/sub-micron U and Cs containing particles studied in Chapter 8, has important environmental implications. With differences in their oxidation state, the solubility of uranyl ions varies considerably [147, 392] - resulting in material entering solution, with the potential for such material to be readily environmentally transported and subsequently up-taken by species including plants and animals. As a consequence, such material may become pre-concentrated in the food-chain.

Previous "nuclear forensics" studies on material derived from around the world have utilised both spectroscopic and isotopic analysis methods as part of the standard "tool-kit" to examine nuclear fallout material. Following advancements in synchrotron radiation (SR) sources, enabling them to provide greater intensity (fluence) x-ray beams and at ever-decreasing beam profiles (emittance) - the x-ray analysis afforded by these large-scale and multi-technique facilities has become a central part of fallout analysis. The first instance of x-ray microanalysis techniques applied to nuclear fallout is described in the work of Salbu et al., (2001) [393]. Using the ID22 beamline at the European Synchrotron Radiation Facility (ESRF), the team employed SR-μ-XANES and SR-μ-XRD to derive information pertaining to the oxidation state and respective phases of U contained within Chernobyl-derived particulate. This work also employed a high-resolution charged-coupled device (CCD) x-ray detector camera (with a spatial resolution of 0.6 μm) to generate a three-dimensional representation of the structure of the sample, as well as a physical volume onto which the other data could be overlain.

Synchrotron-based x-ray imaging and μ-XANES analysis on U-based particulate have seen further application since this initial work by Salbu et al., (2001). Works by García López et al., (2007) [182], and Lind et al., (2007) [180], both applied these synchrotron techniques to material distributed in the environment from the 1966 Palomares (Spain) release event, following on from the work of Lind et al., (2005) [394], having undertaken the corresponding analysis of particles produced by the 1968 nuclear weapons transportation accident in Thule (Greenland).

Source	$^{135}Cs/^{137}Cs$ (Atomic)	$^{134}Cs/^{137}Cs$ (Activity)
Unit 1	0.40	0.94
Unit 2	0.34	1.08
Unit 3	0.35	1.04
FSP 1	0.52	0.54
FSP 2	0.44	0.64
FSP 3	0.38	0.74
FSP 4	0.42	0.68

Table 10.1: Characteristic $^{135}Cs/^{137}Cs$ atomic ratios and $^{134}Cs/^{137}Cs$ activity ratios for reactor Units 1 - 3 and associated fuel storage ponds (FSP) 1 - 4 at the time of the accident and release. *As determined by [50].*

These high-energy x-ray based techniques have more recently been applied to the oxidation state analysis (and environmental stability assessment) of U composition particulate material encountered as Naturally Occurring Radioactive Material (NORM) and Technologically Enhanced Radioactive Material (TENORM) by Lind et al., (2013) [395]. Works by Crean et al., (2014) [183], and Crean et al., (2015) [396], have again used these x-ray techniques - analysing the oxidation state chemistry of U associated with depleted U (DU) munitions and uranium ore concentrate (UOC) particles, both obtained from the environment, respectively.

SIMS has also been an extensively deployed tool within the nuclear forensics analysis portfolio, allowing for the analysis of single particles of interest [397–399]. One of the initial uses for SIMS for single particle nuclear forensics analysis, was on material derived from the 1986 Chernobyl accident by Tamborini et al., (2000) [400]. Unlike synchrotron-based methods which are entirely non-destructive (although a certain amount of beam-induced sample alteration may occur [401]), SIMS results in the particles consumption, but unlike x-ray methods, SIMS yields isotopic information on the sample, which provides information critical for determining material provenance.

Further applications of SIMS have included the analysis of DU particles [402, 403], surface/near-surface nuclear weapons testing particulate [404–406], radioactive fragments generated by nuclear weapons transportation accidents (Palomares, Spain), in addition to particles associated with the storage and reprocessing of nuclear wastes (Kola Bay, NW Russia) [407]. Owing to the simple sample preparation afforded to SIMS, in addition to the selectivity of the analysis (targeting only individual identified spots) and low limits of detection (LOD) [246, 408], SIMS is one of the methods of choice for particle analysis by the IAEA [409].

As shown formerly in Table 1.3, the $^{134}Cs/^{137}Cs$ activity ratios (produced through the modelling work of Nishihara et al., (2012) [50]) of each of the reactor units and fuel storage ponds are
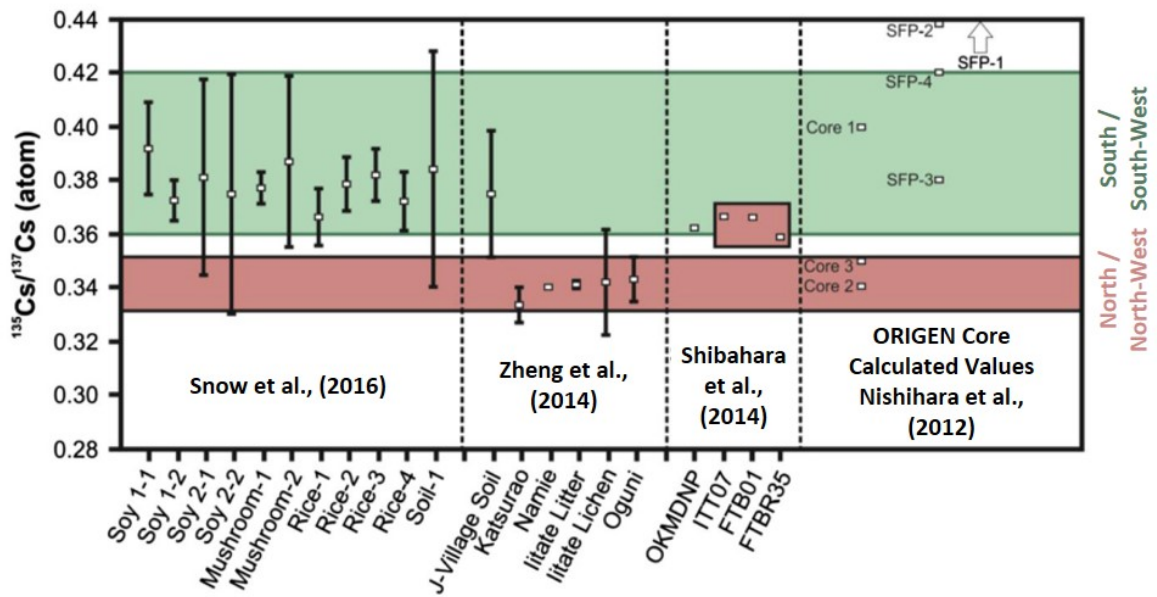
Figure 10.1: ^{135}Cs/^{137}Cs atomic (isotope) ratios derived from a range of organic samples (leaves, bark and sediment) obtained from positions to the north/north-west (red shading) and south/south-west (green shading) of the FDNPP by Snow et al., (2016) [43], Zheng et al., (2014) [162] and Shibahara et al., (2014) [161] - all are compared with ORIGEN estimates produced by Nishihara et al., (2012) [50]. *Modified from [43].*

distinctive one from another. It is these characteristic ratios that have allowed for the reactor unit provenancing of environmental contamination, as detailed in Section 2.2.5. An additional mechanism through which to study and attribute the radioactive material to a specific provenance, however, is via atomic ratios. Whereas activity ratios (non-destructively) utilise γ-ray emission peaks to derive a ratio indicative of composition, as detailed within Chapter 5, mass spectrometric methods (such as SIMS) destructively ionise the sample - counting the number (frequency) and mass of ions incident onto the systems ion-counting array. Whereas activity ratios represent a "quick" and "simple" means through which to analyse the composition of a γ-ray emitting radioactive material, it is widely-accepted that greater accuracy, more reliable and repeatable results, with less sample preparation and no requirement for long counting periods (typically 24 - 48 hours) can be attained using mass spectrometry techniques [189, 410]. Alongside the activity ratio for the strongly γ-ray emitting ^{134}Cs/^{137}Cs, Nishihara et al., (2012) [50], additionally predicted the corresponding atomic ratio of ^{135}Cs/^{137}Cs alongside the other fissionogenic isotopes.

The characteristic ratios (^{134}Cs/^{137}Cs activity and ^{135}Cs/^{137}Cs atomic) for Units 1 - 3 and the associated fuel storage ponds (FSP) 1 - 4 are detailed in Table 10.1. As per the ^{134}Cs/^{137}Cs activity ratios, a clear difference is apparent between the ratios ascribed to reactor Unit 1 and Units 2/3 - a result of the differing levels of fuel burn-up. In contrast to the Cs activity

ratios of the SFPs which are markedly different to the three reactor cores, there exists no clear separation in the ^{135}Cs/^{137}Cs atomic ratios between the cores and their associated FSPs - with the FSP of Unit 3 possessing a value bounded by those of reactor Unit 1 and reactor Units 2 and 3.

Unlike ^{134}Cs, which occurs with a half-life of only 2.065 years, ^{135}Cs is longer-lived with a half-life of 2.3 million years [52] - decaying through the emission of a low-energy β-particle into the stable ^{135}Ba. Owing to its lengthy half-life and low activity, ^{135}Cs represents less of a radiological hazard than ^{134}Cs and ^{137}Cs. This long-lived isotope is produced through the β-decay of ^{135}Xe. However, due to the precursor ^{135}Xe possessing; (i) a very high fission product yield (6.3333% for ^{235}U irradiated with thermal neutrons [133]) and, (ii) the greatest thermal neutron capture cross-section of any nuclide [52], this results in the near entirety (>90%) of the ^{135}Xe being rapidly transmuted into stable ^{136}Xe during routine reactor operations - with therefore little remaining to decay into ^{135}Cs [368, 411].

Arising from these source-term isotopic ratios calculated by Nishihara et al., (2012) [50], a number of works have sought to utilise the variation displayed by these values (Table 10.1) to attribute environmental contamination (across Fukushima Prefecture) to these differing sources. A summary plot detailing the results of a number of these studies is presented in Figure 10.1. Some of the earliest work of this type was performed by Shibahara et al., (2014) [161], who employed thermal ionisation mass spectrometry (TIMS) on grass, bark and moss samples collected from localities to the north, north-west and west of the FDNPP site. Despite illustrating a close-clustering of results (averaging a ^{135}Cs/^{137}Cs ratio of 0.364), such a value is not consistent with any inventory predictions (core or FSP), made by Nishihara et al., (2012) [50].

Subsequent work by Zheng et al., (2014) [162], conversely utilised a newly-developed triple-quadrupole inductively coupled plasma-mass spectrometer (ICP-MS) to determine the ^{135}Cs/^{137}Cs atomic ratios for a number of sampling sites located principally to the north-west of the FDNPP. In contrast to the work of Shibahara et al., (2014) [161], the isotope ratios for these samples better aligned with predicted values derived formerly from the ORIGEN calculations. The results excluded the possibility of material being sourced from any of the FSPs - with samples obtained from the north/north-west of the site shown to exhibit ^{135}Cs/^{137}Cs ratios indicative of a release from reactor Unit 2 at 0.341±0.002 (marginally below the Cs signature invoked for reactor Unit 3). To the south of the facility, however, a greater ^{135}Cs/^{137}Cs signature (0.375±0.024) was measured. The authors concluded that such a value could result from; (i) "significant deposition of radiocesium from Unit 1", or more-likely (ii) a "mixing of global fallout radiocesium with the FDNPP-sourced radiocesium". This second explanation was favoured owing to the previous detection of ≈10% fallout Pu ($^{239+240}$Pu) in this sample [143]. It was concluded, however, that more analysis was required to fully ascribe a provenance to this material.
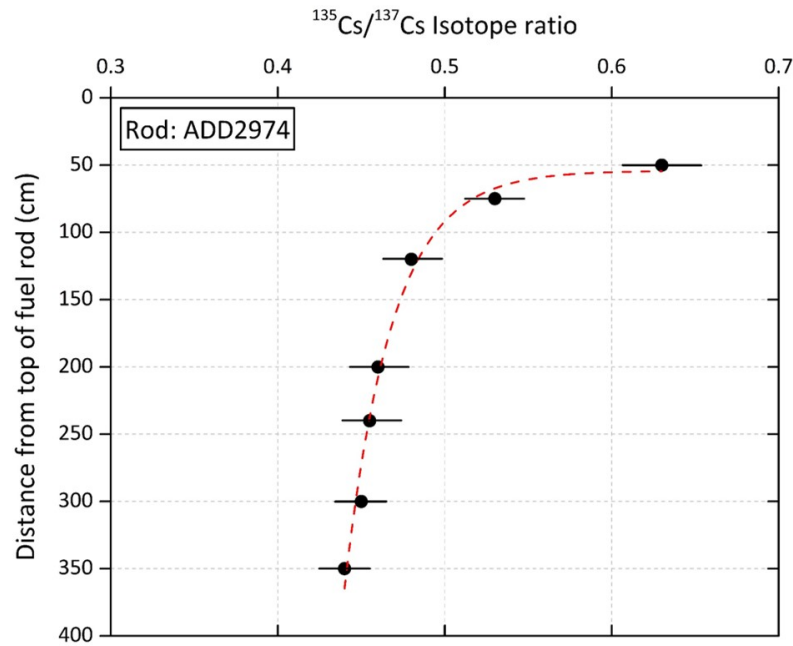
Figure 10.2: Measured variation in ^{135}Cs/^{137}Cs atomic ratio vertically down the length of a typical boiling water reactor (BWR) fuel rod. A corresponding increase in ^{137}Cs activity (Bq) was also observed at positions associated with the top of the fuel rod. *Data obtained from [53].*

A more recent study was undertaken by Snow et al., (2016) [43]. This work reported the further analysis of Fukushima-derived samples (soil and vegetation) using TIMS to provide ^{135}Cs/^{137}Cs isotopic ratios. While the samples in earlier works were obtained from localities within Fukushima Prefecture - ranging from 5 km to 70 km from the reactor site, the material studied by Snow et al., (2016) was obtained from "undisclosed locations across the Kanto region of Japan". Located 100 km - 250 km directly south of Fukushima Prefecture, the Kanto region comprises the entire Tokyo Metropolitan Area (TMA). Like the results obtained by Zheng et al., (2014) [162], a clustering of the ^{135}Cs/^{137}Cs isotope measurements was attained (Figure 10.1). However, owing to their contrasting provenance from the south/south-west of the FDNPP, an average ^{135}Cs/^{137}Cs isotopic value of 0.376±0.008 was obtained. The authors attribute this value to a source comprising mixed emissions from reactor Units 1, 2 and 3, but invoke the work of Guenther et al., (1991) [53], as a mechanism to account for a potentially high degree of spread between the isotope ratios.

Results of the work performed by Guenther et al., (1991) are shown graphically in Figure 10.2. Through the analysis of ^{135}Cs/^{137}Cs profiles down a typical BWR fuel rod, the isotopic ratio was observed to be significantly higher towards its top - where neutron fluxes are lower (preventing the transmutation of ^{135}Xe into ^{135}Cs). This ratio is observed to approach a more consistent value (indicative of the true degree of fuel burn-up) further down its length owing to the increased neutron flux experienced. Hence, the radiocesium composition "characteristic" of a

reactor is observed to vary according to the portion within the core from which the material was sourced - showing variation over the total integrated (average) core value predicted (via ORIGEN modelling). Alongside a fuel rod location-dependent variation in the radiocesium atomic ratio, this study also observed an increase in the total ^{137}Cs activity (Bq/g).

This work by Snow et al., (2016) [43], additionally examined the ^{134}Cs/^{137}Cs activity ratios of the suite of Kanto region samples, likewise comparing the results to the core inventory predictions made by Nishihara et al., (2012). Unlike previous plant-proximal studies (discussed in Chapter 2) which provided a clear attribution of the contaminations ^{134}Cs/^{137}Cs activity ratios to specific reactor unit events - this was not possible with Snow's values derived from analysis of more distally obtained samples. For all sample mediums (including soy-beans, mushrooms, rice and soil) an average ^{134}Cs/^{137}Cs activity ratio across all samples was determined to be 1.00±0.06 - therefore falling between all values derived by Nishihara et al., (2012) [50]. These results supported the authors earlier conclusions, that this material (acquired from considerable distances south and away from the main plume were the result of; (i) multiple reactor sources, but also potentially, (ii) variations in the radiocesium down the length of a single fuel rod.

Conclusions such as this support and highlight what is now regarded as the "best-practice" in the "nuclear forensic" analysis of radioactive samples [186, 189, 399], and hence why individual particles were the subject of this study. Unlike this aforementioned solution-based bulk-analysis of large (gram size) samples via TIMS and ICP-MS - whereby the contributions from individual sources are combined into one resultant signal, the analysis of individual particulate removes this summation and averaging - with the results obtained originating from a small and representative volume of material. As has been shown in the aforementioned works centred on the FDNPP accident; for determining Cs isotope ratios such a bulk-analysis approach makes specific reactor Unit attribution difficult and for Pu ratios, a discrimination from global fallout equally challenging.

10.2 Aims

Following the compositional and structural analysis performed using combined FIB and SEM-EDS, laboratory-based XRT and coincident SR-μ-XRF/SR-μ-XRT, this chapter had two principal goals. The first of which sought to employ additional synchrotron radiation techniques to interrogate the numerous high-density micron-scale particles (potentially of U composition) located within the sub-mm, silica-rich and fibrous-structured Unit 1 derived CF-01 sample.

Following this non-destructive analysis, the second portion of this chapter seeks to undertake destructive SIMS to further investigate the spatial distribution of any such U particles, as well as determining the isotopic composition of such inclusions within the CF-01 *ejecta particulate*. An accurate value for the ^{235}U/^{238}U isotopic ratio would exist as the key indicator for the

anthropogenic nature of the uranium contained within this particulate. With natural uranium (NU) containing 0.7 wt% ^{235}U, levels of between 3 wt% and 5 wt% ^{235}U would define any U as having an enrichment typical of that used in a light water reactor (LWR) [8, 11] - such as those at the FDNPP [25]. The potential existence of non-natural abundances of both ^{234}U and ^{236}U isotopes within such inclusions (the abundances of both are increased over naturally-occurring levels as a by-product of the fuel enrichment process) would further demonstrate its anthropogenic nature [21, 52]. This quantification would serve to refute the formerly suggested existence of U being the result of the naturally-occurring U (2 ppm) contained within the basaltic precursor material used to produce the Rockwool™ insulation [164].

The application of SIMS will also permit for the characteristic radiocesium ratio of the CF-01 particulate, collected north-west of the FDNPP close to its perimeter boundary (Figure 4.3), to be determined as well as that associated with the larger FT-13 material. This value can hence be evaluated with respect to the reactor inventory values attained through the ORIGEN core/FSP modelling of Nishihara et al., (2012) [50]. With the results obtained through SR-μ-XRF (described in Chapter 9) of the CF-01 material illustrating the distribution of Cs to be highly spatially discontinuous (Figure 9.17), SIMS is advantageous in permitting accurate mapping and depth-profiling into these previously identified Cs-rich regions. The application of SIMS will also be used to explore the wider isotopic composition and its variance within the representative particulate. Any observed elemental/isotopic discontinuity is anticipated to match that produced in the particle-wide SR-μ-XRF mapping, the results for Cs were shown in Figure 9.17.

In addition to isotopically evaluating the ^{135}Cs/^{137}Cs isotope ratio within the CF-01 material and confirming its provenance (released from Unit 1 as a consequence of its ^{134}Cs/^{137}Cs activity ratio [164]), isotopic analysis via SIMS will also be performed on the FT-13 particulate, to similarly assess through additional methodologies, its release source. As well as being considerably larger in diameter than the CF-01 particulate (2 mm in maximum dimension), this material was obtained directly to the west of the FDNPP (opposed to the north-west), but at a comparable distance from the reactors - as shown in Figure 4.4. The ^{134}Cs/^{137}Cs activity ratio analysis performed by Satou (2016) [164], has attributed it to the release that occurred from reactor Unit 2 - consistent with the radiocesium distribution (mapping) results of Nishizawa et al., (2015) [50], and Chino et al., (2016) [153] - as shown in Figure 2.10.

This utilisation of SIMS represents the first application of the technique to isotopically evaluate the composition of the larger individual *ejecta particulate*. While the aforementioned works analysed contaminated bulk organic samples [43, 161, 162], it was only during the Doctoral work of Satou (2016) [164], that SIMS was applied to the determination of radiocesium isotope (atomic) ratios within the spherical "Cs-balls" (termed *atmospheric particulate* in this work).

Through estimating the total amount of U that exists within one such large volume CF-01 fallout particle and combining this with the approximation of their depositional frequency from Satou (2016) [164], a crude but initial estimation of the total amount of actinide within the environment is possible within these contaminated regions.

10.3 Experimental methods

10.3.1 Synchrotron sample preparation

To analyse the CF-01 *ejecta particulate* formerly studied in Chapter 9, the same sample setup was used as in previous SR analysis. For this continued work, the particle was contained within the same double-layer of x-ray transparent adhesive Kapton™ film, supported on a stainless-steel pin and mounted onto a magnetic base - shown previously in Figure 9.1.

10.3.2 Synchrotron sample analysis

Two beamlines were employed for this analysis, used formerly to examine *ejecta material* or the considerably smaller, *atmospheric material*. Both located at the Diamond Light Source (DLS) synchrotron, a third generation facility operating with a nominal 300 mA current and 3 GeV beam energy, the I13-1 and I18 beamlines were used for tomography/fluorescence imaging and fluorescence imaging/micro-focus spectroscopy respectively. A full description of the optics located downstream of the sample environment for each experimental end-station is included in Section 5.4.5.2.

Tomography and fluorescence

Although U was not formerly identified during the prior analysis on the representative sub-mm particle, further SR-based analysis to investigate the micron-scale high-density particle inclusions was conducted on the I13-1 (coherence) beamline. For this subsequent work, the same methods were used as detailed in Section 9.3.6, although enhancements were made to the downstream optics setup for the fluorescence scans, following the earlier experiment.

The same three-dimensional XRT (absorption) rendering of the representative CF-01 particle generated previously in Chapter 9 was used as a surface on which to apply the new (enhanced) SR-μ-XRF mapping results.

As per the earlier SR-μ-XRF analysis on I13-1, Kirkpatrick-Baez mirrors were used to refine the incident (undulator-sourced) beam, however, to enable x-ray XRF mapping at increased spatial
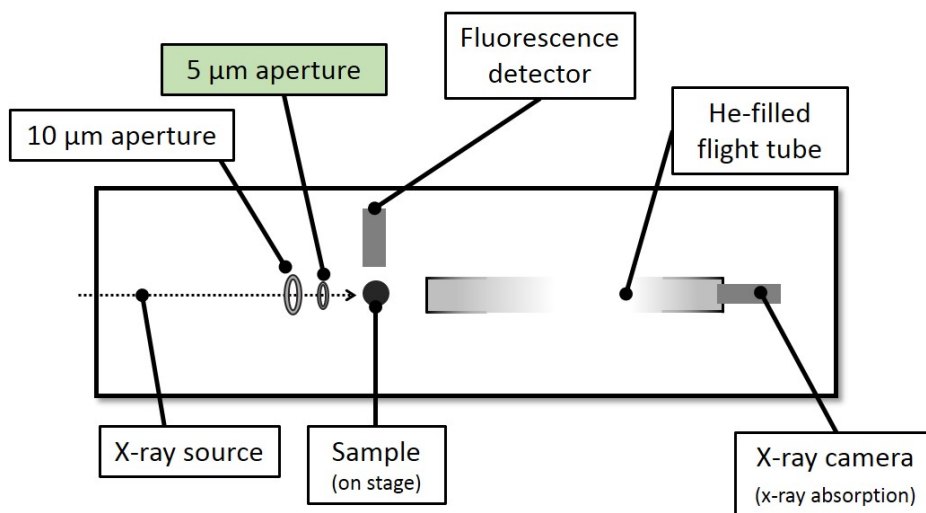
Figure 10.3: Plan view schematic (not to scale) of the revised setup at the I13-1 experimental end-station, the location of the newly installed 5 µm focusing aperture is highlighted.

resolutions above the 10 µm of the initial analysis, an additional 5 µm focusing aperture (pin-hole) was installed upstream of the sample - yet downstream of the previously singularly-used 10 µm pinhole. This larger, first, focusing aperture was installed principally to remove the undesired beam "wings" that resulted from the limited amount of source emittance (3.17 nm rad) and beam divergence that occurred as a function of the synchrotron storage ring and subsequent beamline optics [263]. The second, smaller, aperture located between the 10 µm pinhole and the sample served to further focus the beam as well as removing any additional "edge effects" that resulted from interactions with this proceeding pinhole. A plan view schematic of this enhanced setup is shown in Figure 10.3.

With this "enhanced" optical setup producing a better-focused x-ray beam than during the earlier work, to further enhance the resolution of the XRF mapping to match this optical advancement, a reduction in the step-size of the raster scan (via the sample stage step) was made - reduced from 10 µm to 2.5 µm. The sample 180° sample rotation (through 40 incremental steps) as per the previous SR-µ-XRF analysis, was again used. Owing to the region within which U was potentially contained having been speculated and resulting from the limited analysis time available on the beamline, only an isolated area of the sample 200 µm × 100 µm × 100 µm was scanned for elemental composition. To derive the SR-µ-XRF data, as for the earlier compositional analysis, a single element Vortex™ (Hitachi High Technology) fluorescence detector was used, positioned perpendicular to the sample and incident beam (Figure 10.3).

Taking into consideration the degree of sample absorption recorded at each stage position using the x-ray camera mounted directly behind the sample (used also for tomographic reconstructions)
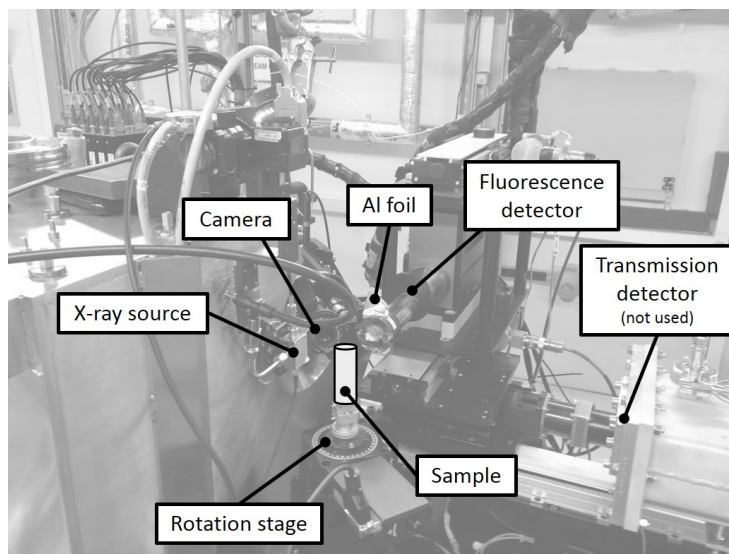
Figure 10.4: Labelled photograph of the I18 (micro-focus spectroscopy) experimental end-station.

the three-dimensional volume of U was reconstructed using the ordered-subset penalized maximum likelihood algorithm, with weighted linear and quadratic penalty algorithms in the TomoPy framework [373]. As per the earlier reconstructions, three-dimensional volumetric representations were rendered using the Avizo (FEI Company) software package [374]. The resulting spatial (pixel) resolution of the SR-μ-XRF U particle mapping during this latter analysis on the I13-1 beamline was 2.5 μm × 2.5 μm × 2.5 μm, a consequence of; (i) a smaller (better focused) beam size, and, (ii) the reduced stage step-size.

Micro-focus spectroscopy

SR-μ-XAS, as per the analysis on the *atmospheric particulate* described in Chapter 8 was performed on the representative CF-01 particle sample on the Diamond Light Source I18 (micro-focus spectroscopy) beamline. The same experimental setup was used as in the prior work, as detailed in Section 8.3.3, with a schematic of the end-station shown in Figure 10.4. Owing to the sub-mm thickness of the sample - which would result in the saturation of the beamlines downstream transmission detector, the perpendicular-mounted fluorescence detector was again used. To further reduce the intensity of the emission registered by this detector, a piece of 0.1 mm-thick high-purity Al-foil was placed over the face of detector - this reduced the signal intensity to levels to allow for appropriate dead-time (≈20%) of the six element SGX Sensortech Ltd. (Xspress-3™) Si-drift XRF detector.

After the approximate position of the sample (within the Kapton™ film "sandwich") was located using the optical camera on the beamline setup, initial XRF mapping was then performed. With the smallest beam-size afforded by the setup being 2 μm × 2 μm, the resulting pixel size of the

two-dimensional map was of the same spatial resolution when using a complimentary 2 μm stage step size. Using the maximum beam energy attainable by the I18 beamline, this mapping was performed at an incident energy of 21 keV - with a spectrum recorded at each individual scan position upon movement of the sample by a high-precision three-axis (+ rotation) stage (Thorlabs Inc.). The high source (photon) flux of the I18 beamline permitted for a per-pixel dwell time of only five seconds while generating maximum peak counts of >150,000 counts.

To permit for a calibration of these mapping results, a spectrum was additionally attained from the metallic support pin holding the Kapton™ film enclosed particle onto its magnetic base.

Following the identification of U-composition material within the two-dimensional XRF map of the particle, the XAS analysis was performed on the sample at these specific stage positions. To study the characteristic emission surrounding the U-L$_{III}$ edge at 17,167 eV, the incident x-ray beam energy was swept over the energy range of 17,025 eV to 17,510 eV - encompassing the pre-edge, emission-edge and extended-edge regions of the emission spectrum. For analytical efficiency, while still providing optimal spectral resolution, the energy steps of the scan "sweep" were varied over the 485 eV energy range. Between 17,025 eV and 17,140 eV - a 5 eV step was employed, reduced to 0.5 eV over the range 17,140 eV to 17,205 eV, before being coarsened (to 1 eV) between 17,205 eV and 17,252 eV, coarsened still further (to 2 eV steps) up to 17,400 eV and eventually at 2.5 eV increments up to the final energy value at 17,510 eV. To enhance the signal to noise ratio recorded within these scans, three repetitions were made for each particle inclusion over this energy window.

The interpretation of the two-dimensional XRF map was conducted using the Python multichannel analyser (PyMCA) [360]. As per the processing of the XAS data within Chapter 8; normalisation, deconvolution and linear combination peak-fitting to known reference materials were performed using the Demeter software package (version 0.9.24) [361]. This package contained the Athena and Artemis programs (for XANES and EXAFS analysis respectively), based upon the open-source IFEFFIT code [362, 363]. Spectroscopy standards for comparison were obtained from the library of reference materials contained within the International X-ray Absorption Spectroscopy (IXAS) XAFS Database [364], representing data from global synchrotron facilities.

10.3.3 Secondary ion mass spectrometry sample preparation

For the destructive SIMS analysis, both samples CF-01 and FT-13 were first diligently removed from their enclosing Kapton™ film, before being manipulated onto separate adhesive carbon discs. An electrically-conductive coating of Au was first applied to the sample prior to their SIMS analysis to negate against the samples electrically charging under the incident Ga$^+$ beam and high electrical sample biasing (positive or negative). This charging would adversely impact not

only upon the stability and rastering of the incident beam but also the resulting secondary ion emission and its subsequent detection and quantification.

For particle CF-01, prior to the SIMS analysis of both its bulk outer surface as well as the U particulate contained within the sample - a number of ion beam cuts were first made at grazing (oblique) angles into the material to remove the "excess" material from around/above the U-containing particles. To perform this, the FEI Helios NanoLab 600i DualBeam system was used. Commencing at a high incident Ga^+ beam energy of 16.0 nA (30 kV accelerating voltage and 4.12 mm working distance) a large (50 μm × 50 μm) trench cut was made, before a series of progressively decreasing beam currents, alongside the cleaning cross-section function of the instrument, were used to obtain a final finish free from the influence of ion beam "curtaining" or significant Ga^+ implantation. These cut surfaces were used to enable the targeting of regions of interest within sample CF-01 - as identified during earlier XRT and XRF analysis. In contrast, no surface preparation was performed prior to the SIMS analysis of the FT-13 *ejecta particulate* - which exhibited a contrastingly smooth and featureless surface form.

10.3.4 Secondary ion mass spectrometry analysis

All SIMS isotopic analysis was conducted using the in-house built magnetic sector (MS) SIMS instrument, utilising a primary Ga^+ ion beam to sputter the sample and produce the charged secondary ions from discrete areas. The electro-magnet downstream then filtered these ions based upon their mass, before they were then measured and the results quantified. Whilst spectrum across the entire mass range (0 amu - 300 amu) were collected, owing to the highly-characteristic ratios illustrative of their provenance, both Cs and U were the focus of the SIMS analysis.

The simplest methods of SIMS sample analysis used in this work was the generation of a mass spectrum from a region of interest, this was achieved by rastering the primary Ga^+ ion beam over an identified region of interest. Whilst the size of the regions sputtered varied, from 50 × 50 μm down to 10 × 10 μm, a consistent set of parameters were used to obtain each spectrum. The Ga^+ ion beam was set to an incident energy of 2.0 nA, with the magnet and detector stepping through the predefined mass window(s) in increments of 0.1 Da (atomic mass units) using a 1,000 ms dwell time on each (to obtain sufficient ion counts).

By rastering the beam over a predefined area and quantifying the mass of the secondary ion emissions at a specific location, a 2-dimensional image was produced. All ion mapping was performed at ×5000 magnification, with the resultant regions of interest measuring 40 μm × 40 μm. During ion mapping, the same incident ion beam current (2 nA) was used to generate the secondary species, however, the dwell time was reduced to 500 ms. For each map, a specific mass of interest was chosen, rather than the magnet alternating between varying mass units.

Multiple maps for different masses could be performed, although a change in the systems setup was required in each case. Features on the micron-scale were discernible on these SIMS maps.

The third mode of SIMS analysis employed the highly-destructive nature of the incident Ga^+ ion beam to etch into the sample to attain depth profiles for specific masses of interest. These profiles were able to detail variations in secondary ion (ejecta) composition with increasing etching (depth) into the material. Although etching depths of several microns can be readily-attained using the profiling functionality of the instrument, with greater etching depths, the influence of "edge" or "wall" effects become increasingly prevalent - with detected ion species originating not from the square region of interest, but from the oblique sides of the cut. To limit this detrimental influence, only depths of up to 10 μm were made into the sample (controlled via the total specified analysis time) - quantified fully post-analysis. As per the previous analysis techniques using the SIMS instrument, the same 2.0 nA primary Ga^+ ion beam energy was used, with a number of mass units of interest (up to six) profiled through the sample. The dwell time of the instrument was increased during this depth analysis to 5,000 ms per mass unit of interest, with the total analysis time set to three hours (to prevent the detrimental impact of "wall" effects). Each of these profiles was made at ×5000 magnification, resulting in a profile through an area 40 μm × 40 μm.

In addition to these three operational modes available on the in-house constructed SIMS instrument, a further function of the instrument (as with all other SIMS systems) is the ability of the setup to operate in either "positive" or "negative" bias modes. Such a biasing is the high voltage polarity (±4.5 kV in this instance) applied to the sample, which determines the proportions of either positive or negative ions that are generated [266]. During this analysis, both positive and negative bias SIMS were used to account for sample-specific differences in the production of secondary ions.

While EDS analysis of a sample allows for a (pseudo) quantitative compositional analysis to be derived [242], it is not a surface sensitive technique (sampling material at depths within the sample of up to 2 μm [239]). The opposite, however, is true of SIMS. Although permitting for depth sampling on the order of tens of nanometres, comparable quantifiable compositional information is not possible owing to inconsistent ion generation (and detection). Despite this, valuable information regarding the proportions (ratios) of different isotopes of the same element can be derived from SIMS due to their comparable ionisation behaviour under either positive or negative sample bias conditions. To obtain these values, the total areas bounded by the respective peaks (counts at that mass unit) are integrated, with these values ratioed.

10.4 Results

As in to Chapter 9, the initial results presented in Sections 10.4.1 to 10.4.3 of this chapter represent the analysis of the CF-01 (Unit 1 attributed) material, while the succeeding Section 10.4.4, details results obtained from the larger FT-13 and Unit 2 derived, *ejecta particulate*.

10.4.1 U and species distribution

The results of the combined SR-μ-XRF and SR-μ-XRT, highlighting the position of the U-containing inclusions, as determined on the I13-1 (coherence imaging) beamline, are shown by the green regions of the particles longitudinal sections shown in Figure 10.5. However, as previously stated, owing to time constraints on the I13-1 beamline, only a 200 μm × 100 μm × 100 μm region of the sample was further studied through XRF mapping at these enhanced spatial resolutions. From this reconstruction, the locations of the U particles are observed to be near-exclusively associated with the exterior circumference of the representative larger particle. Only one U-rich particle, however, is shown to be greater than 15 μm from the samples external (circumference) surface. All of the U-containing particles observed within this SR-μ-XRF scan (of the sub-region of the CF-01 particle) are additionally associated with the margins of the larger voids. Comparable in their location to both the peripheral Fe and cement composition fragments observed to exist embedded into the particles exterior surface in Chapter 9, the location of this U-composition material aligns with this works earlier conclusions. Not only did an explosive release event occur to produce structural reactor components, but also served to produce and incorporate the closely associated U reactor core material.

This abundance of U, located near-exclusively just below the outer circumference of the sub-mm CF-01 *ejecta particle*, serves as additional evidence to support the anthropogenic provenance of the species - rather than having originated as a constituent of the fibrous Rockwool™ precursor that surrounded the reactors steel PCV. As the fibrous form of the particle has been shown to still be evident (Sections 9.4.2 and 9.4.3), complete (total) melting of the material had not therefore taken place - with the resulting redistribution of species, however, not occurred. Therefore, this U material represents the surface incorporation of material as a consequence of a much later event.

From the compositional overlays taken at various longitudinal sections through the sample shown in Figure 10.5, it should be noted, however, that while the U particles are shown to exist with dimensions of up to 10 μm, the raw SR-μ-XRF mapping data details this actinide material to possess maximum dimensions <2.5 μm. This observed "coarsening" of the spatial resolution is a consequence of the post-processing algorithm used to derive the XRF maps. While the location of the U inclusion in the particles longitudinal sections shown in Figure 10.5 (taken at 0 μm, 20 μm and 40 μm up from the central horizontal axis), all detail an apparent U-rich particle

existing at the same position in all three images (at the base of the *ejecta particle*) - this however, represents a number of different, discrete particles. These multiple micron-scale particles exist as a clustering associated with the edge of a 70 µm diameter internal void.

Also highlighted (in blue) within the four longitudinal sections presented in Figure 10.5, are the regions of low void volume (porosity), identified formerly in Section 9.4.3 - corresponding to regions of cement composition. As expected for a volume of former structural material that had become incorporated into the partially-molten particle (during the final stages of the reactor buildings hydrogen explosion), no U composition particles are associated with this extensive CaO-rich region. A similar absence of the micron-scale U composition particles is similarly associated with the Fe-rich fragment (coloured orange in Figure 10.5), that was similarly embedded into the particles surface again during the ejection event. The incorporation of this angular, Fe composition fragment, into the partially-molten and softened material during the violent release event could afford a mechanism to account for the location of the single U-based particle, contained within the particles centre - identified in the section 40 µm from the particles median horizontal axis.
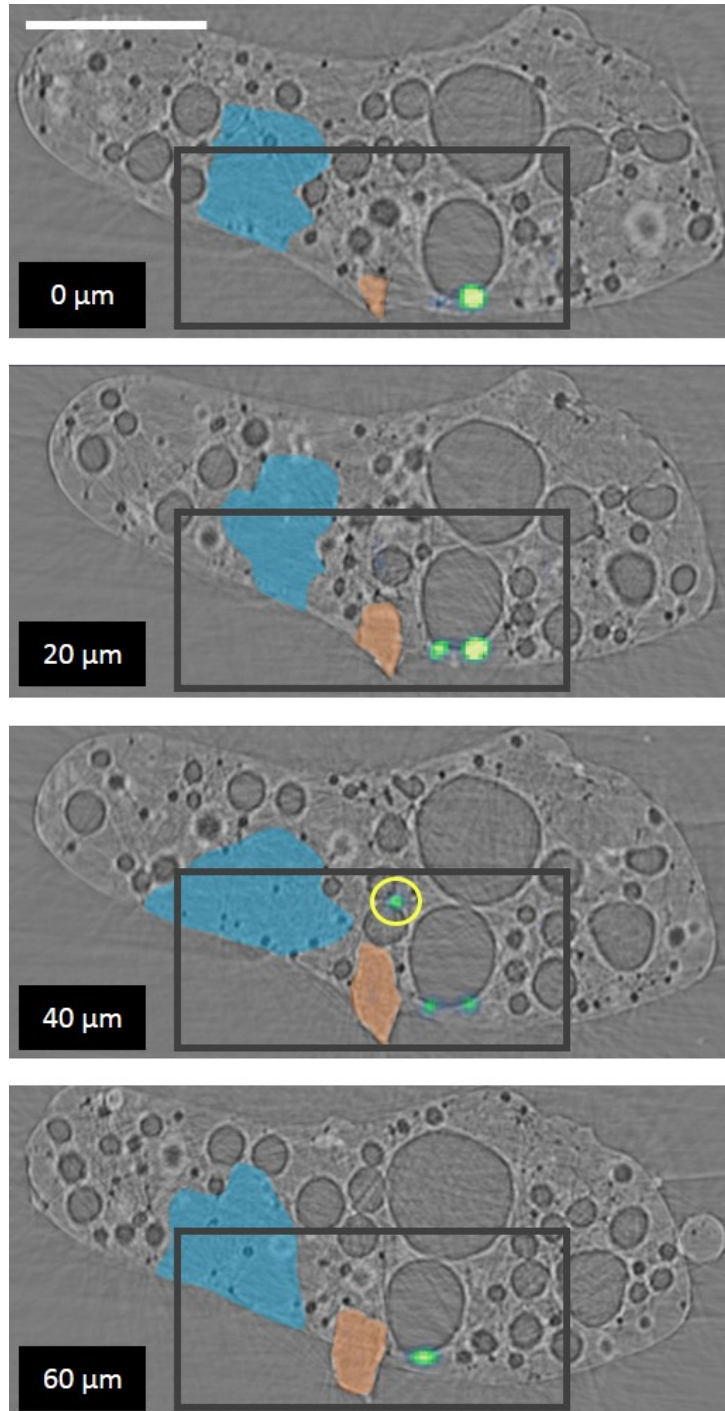
Figure 10.5: Compositional rendering of the SR-μ-XRF results of U mapping (green) overlain onto the SR-μ-XRT rendering of the CF-01 *ejecta particles* internal structure. Fluorescence mapping was performed only at high spatial resolution within the identified rectangular region. The values stated represent the distance of the horizontal section up from the central, longitudinal, tomographic slice through the sample volume. Blue shaded regions represent the location of cement composition regions with orange of those composed of Fe (steel), identified previously in Chapter 9. Scale bar = 100 μm.
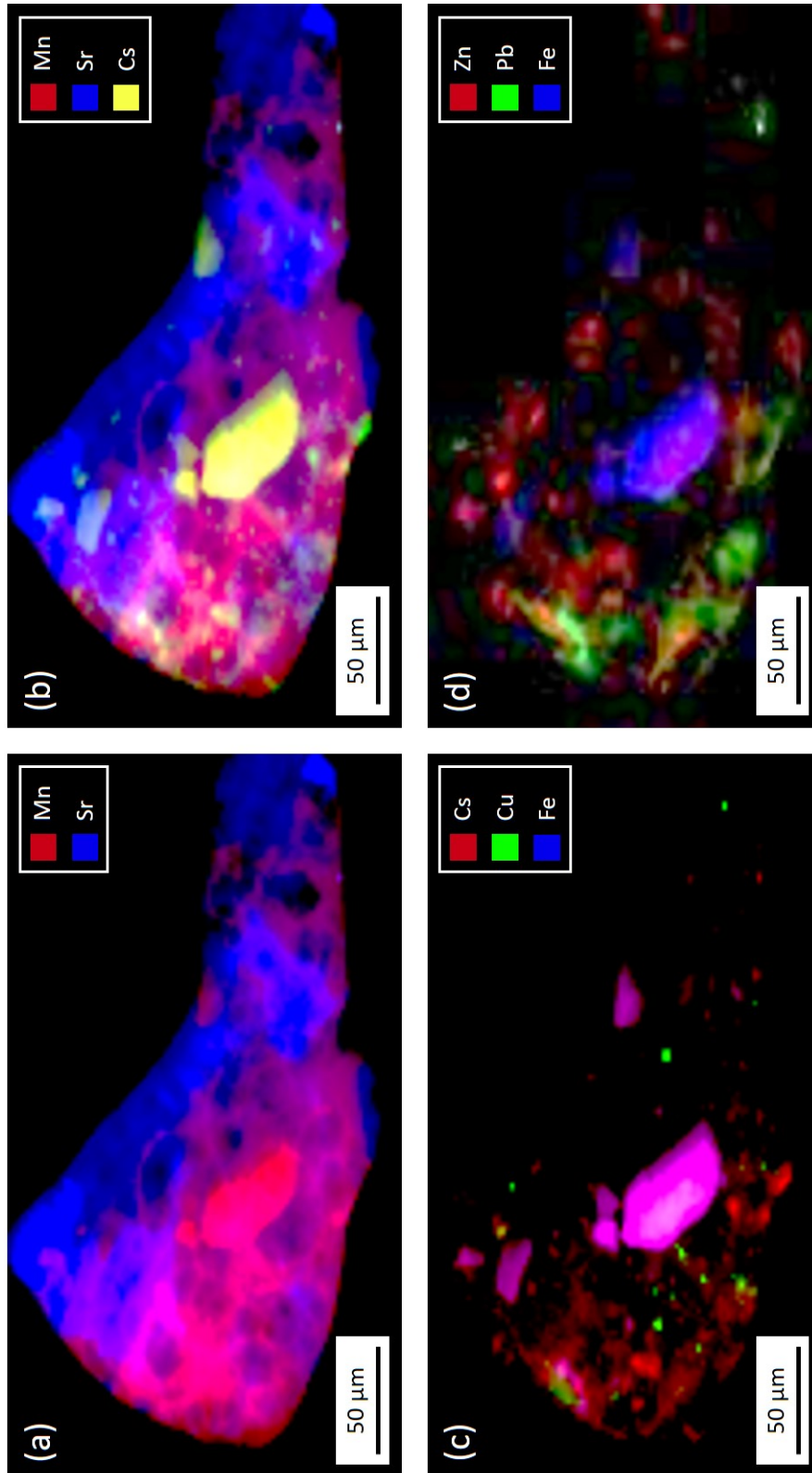
Figure 10.6: Two-dimensional SR-µ-XRF maps detailing the spatial distribution of Mn, Sr, Cs, Cu, Fe, Zn, and Pb within the representative sub-mm CF-01 *ejecta particle.*
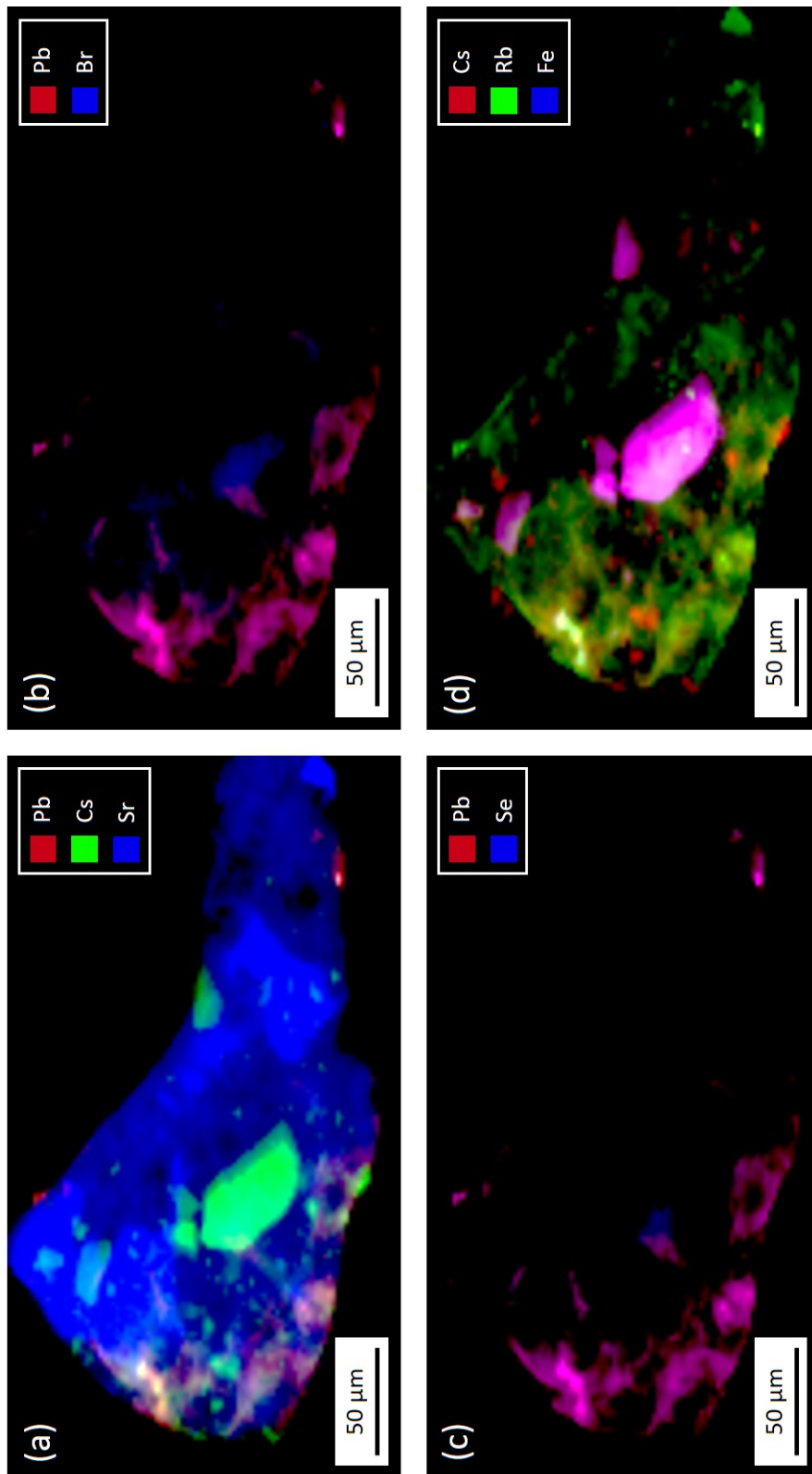
Figure 10.7: Two-dimensional SR-μ-XRF maps detailing the spatial distribution of Pb, Cs, Sr, Br, Se, Rb, and Fe within the representative sub-mm CF-01 *ejecta particle*.

While a valuable three-dimensional representation of the U distribution within the representative CF-01 *ejecta particulate* could be attained on the I13-1 beamline through multiple-projection analysis of the sample and the resulting rendering of µ-XRF data onto the earlier µ-XRT results, only a 2.5 µm XRF spatial resolution was possible using the beamlines best available experimental setup. Despite not allowing for the same three-dimensional rendering (due to the absence of sample rotation), the I18 beamline allowed for a slightly enhanced 2 µm × 2 µm pixel size over the entire particle, rather than a smaller, area of interest (as on the I13-1 beamline). This was only attainable due to the greater photon flux (2×10^{12} photons per second, at 10 keV) onto the sample than on the coherence beamline - with sufficient fluorescence yielded in the short dwell time (5 seconds) for each 2 µm × 2 µm pixel to constitute a full fluorescence spectrum. The two-dimensional XRF results showing the location and signal intensity of the distinct compositional regions within the entire CF-01 *ejecta particle* are shown in Figures 10.6 and 10.7, for the range of elements attainable/detected.

Although not depicted in these XRF results due to its characteristic x-ray emissions (1,739 eV and 1,835 eV) occurring below that attainable on the I18 beamline (minimum beam energy = 2,050 eV), Si was previously determined via sample-wide EDS analysis to be homogeneously distributed. This compositional homogeneity is observed to occur alongside considerable contributions from both Mn and Sr, as shown in Figure 10.6 (a), with the bulk of the particle-containing contributions from both elements in approximately equal concentrations. From the XRF map, little mixing of these elements is observed - with Mn concentrated within the bottom region of the particle and Sr conversely enriched in the top portion of the sample. These results complement those shown earlier in Figure 9.17.

The occurrence of Cs and its close association with the locations at which Fe is observed are shown in the XRF maps of Figures 10.6 (b) and (c). In addition to Cs being located in the large (surface protruding) Fe composition fragment identified and subsequently studied during the earlier synchrotron works (Section 9.4.3), the fission product species is also concentrated within a number of micron-scale regions, located towards the left-hand side region of the particle. These combined Cs and Fe-rich regions are, like the considerably larger particle, associated with the *ejecta particles* exterior. Also shown (coloured green) within Figure 10.6 (c) are micron-sized areas of elevated Cu concentration. While similarly located around the samples perimeter, these Cu-rich regions are not associated with the position of any other elements.

The spatial distribution of Fe, alongside Zn and also Pb is shown in Figure 10.6 (d). As is the case for the other elements, Zn is also distributed around the particles circumference, and like Cu, is found as mono-elemental regions uncorrelated with the locations of other elements - again agreeing with Chapter 9 results. Pb, in contrast, is found concentrated towards the left-hand portion of the particle - associated with many of the other elements.

A further XRF map detailing this samples exterior surface enrichment in Pb and Cs - distributed within a homogeneous background of Sr, is shown in Figure 10.7 (a). This co-existence of Pb, concentrated as isolated yet diffuse regions within the particle alongside other elements, is further shown in Figures 10.7 (b) and (c). In the former, the concentration of Pb (red) is plotted with that of the halogen element Br (blue). The purple colouration of the resulting overlay clearly illustrates the combined Pb-Br composition of the numerous isolated regions, found concentrated near-entirely around the particles left-most border.

In Figure 10.7 (c), the intensity of Pb (red) is plotted alongside the metalloid, Se (blue). Like Pb and Br in 10.7 (b), the purple colouration of the XRF elemental overlay details the co-existence of both Pb and Se, similarly concentrated in a number of regions close to the left edge of the particle. Combined, Pb, therefore, occurs associated with both Br and Se. These Pb-Br-Se regions are notably more diffuse in their appearance, with no clear edge structure/compositional boundary shown, unlike the Fe-Cs and Cu-rich regions. This disparity may, therefore, imply a difference in the form of these species contained within this CF-01 *ejecta particulate*. Hence, the Fe-Cs material may exist as solid (fragmented) particulate incorporated into the bulk (Si, Mn and Sr based) matrix, whereas the material composed of Pb-Se-Br may have undergone melting or a departure from a solid state ahead of its incorporation to yield such a highly-irregular and diffuse internal distribution.

Combined with the spatial distribution of both Cs and Fe, the distribution of Rb within the CF-01 *ejecta particle* is detailed in Figure 10.7 (d). Identical to Se and Br, Rb is additionally found associated with the location (and diffuse form) of Pb - observed distributed around the exterior of the particle, concentrated most significantly around its left-most perimeter.

While the XRF analysis on the I13-1 beamline resulted in the three-dimensional compositional mapping of the sample by generating fluorescence spectrum at multiple angles, the corresponding analysis on the I18 micro-focus spectroscopy beamline was only two-dimensional. Therefore, owing to the computed XRF signal from the latter I18 sample scan resulting from an averaging of the entire sample thickness, and not from the tomographically-integrated XRF mapping as on I13-1 beamline, the U signal from I18 was near-entirely masked by the spectral overlap from Rb. Whereas regions of U could themselves not be identified based upon their characteristic emissions from the sample, a number of regions (formerly identified as U on the I13-1 beamline), were shown to exhibit elevated Rb fluorescence intensity. No other fluorescence emissions from other actinides (e.g. Pu, Am or Np) were observed for this entire CF-01 *ejecta particle*, as these emission peaks would not overlap with those of Rb.
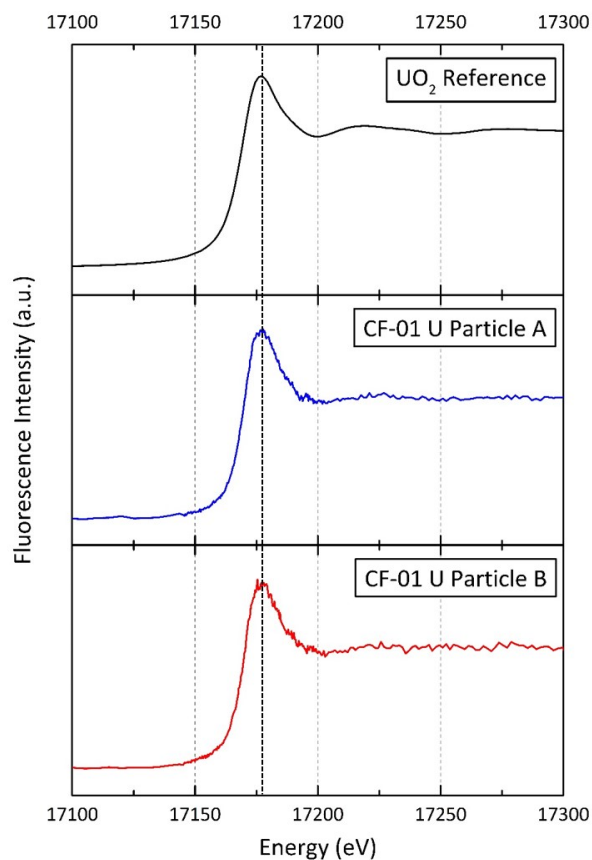
Figure 10.8: SR-μ-XANES analysis of two CF-01 included U particles (A and B) at the U-L$_{III}$ edge, alongside a reference UO$_2$ (Uraninite) spectrum.

10.4.2 U micro-focus spectroscopy

Despite having not been able to identify the spatial distribution of U during the I18 analysis, the location of U within the CF-01 particle sample was, however, successfully determined during the proceeding three-dimensional study on I13-1. As mentioned previously, these U-rich positions were also observed to show enhanced signal intensity around the Rb fluorescence region when mapped on the I18 beamline - confirming their location within the sample.

With no actinide other than U observed within the entire *ejecta particle*, XANES analysis was performed at the locations of two of these U particles. The results of this XANES analysis, alongside that of a reference UO$_2$ sample [412], are presented in Figure 10.8. Immediately apparent from these scans, over the 200 eV window across the U-L$_{III}$ edge (17,176 eV), is the similarity of the two sub-particles (A and B) contained within CF-01 to the reference UO$_2$ standard.
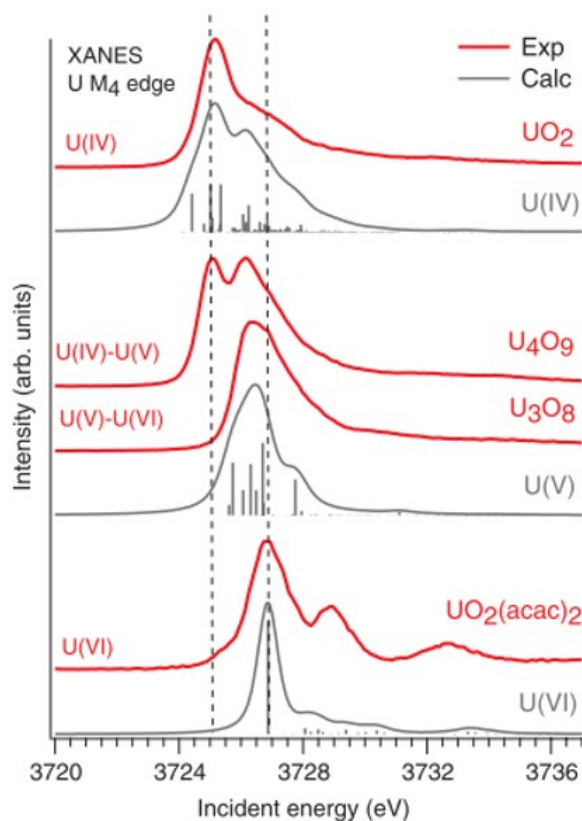
Figure 10.9: Comparison of experimental and calculated XANES spectrum at the U-M$_{IV}$ edge for differing U oxidation states. The dashed lines represent the energy positions of the main peaks corresponding to the U IV and VI oxidation states respectively. *Modified from [416]*.

The XANES spectra of both particle A and B, shown in Figure 10.8, are characterized by a broad "white line" (absorption edge) peaking around 17,176 eV before smoothly decreasing towards a minimum at 17,200 eV. This shape has been previously attributed to U(IV) oxidation state in uranium oxides and uranium composition glasses, whereas more oxidized forms; U(V) and U(VI) - typical of U in surface environments, are characterized by an increasingly asymmetrical shape, with a distinctive "shoulder" region apparent between 17,185 eV and 17,195 eV [413–415]. Although taken at the lower-energy U-M$_{IV}$ absorption edge, a representation of this change in the form of the XANES structure for differing U oxidation states (IV, V and VI) is shown in Figure 10.9, obtained during the study of Kvashnina et al., (2013) [416]. This same energy shift, as well as the occurrence of additional "shoulder" peaks on the higher-energy region of the XANES spectrum, is similarly observed on the U-L$_{III}$ edge - representing a broadening of the "white line".

Beam damage, characterised by a reduction of the "white line" intensity following tens of seconds of exposure to the high-energy (and flux) incident x-ray beam, has been previously reported

for Ca-Mg-Al-Si (CMAS) composition glasses by Halse (2014) [401]. While an edge intensity reduction was seen to occur, such a modification was not accompanied by an alteration in the overall XANES shape, that would have signified in these measurements, that a change in the oxidation state of the sample upon exposure to the x-ray beam has occurred. In this synchrotron analysis, the absorption spectrum remained completely unchanged over the total of 12 minutes of data collection. Therefore, consistent with the results of Halse (2014) [401], the effects of any beam-induced oxidation state changes associated with the U particles can be disregarded.

While the (IV) oxidation state of the U was determined, the analysis of the EXAFS that follow the U-L$_{III}$ absorption edge (detailing the atoms outwards co-ordination chemistry) was not possible. This resulted from the considerable signal to noise ratio within the fluorescence spectrum, a consequence of the large size of the incident beam (2 µm × 2 µm) in comparison the U particle but principally the total interaction volume (thickness) of the sample. If a larger particle were analysed, the x-ray beam would have interacted with a greater sample volume - resulting in a greater fluorescence signal (at the selected energy) over the finely-detailed, yet highly-informative, EXAFS region.

The application of synchrotron-based techniques for the analysis of Pu-containing material has been reported extensively, including within the works of Jernstrom et al., (2004) [417], and Salbu et al., (2001) [393]. In both works, a high (ng) detection sensitivity for Pu was reported during XRF mapping. With this material of reactor-origin, an ingrown (radiogenic) Pu component is likely to exist. However, as it (as well as other actinide elements) was not detected during this SR analysis, it, therefore, occurs at a very low concentration - below the limit of detection for this highly-sensitive and non-destructive technique.

10.4.3   Secondary Ion Mass Spectrometry

Isotopic analysis (advancing both the elemental and coordination chemistry analysis) of selected regions within the sub-mm CF-01 *ejecta particle* was obtained via SIMS. The formerly identified Cs and micron-scale U components of the material were considered the most characteristic of their provenance, and hence were the specific target of this analysis. A number of electron microscope images of the CF-01 particle following destructive SIMS analysis are shown in Figures 10.10 (a) to (d) - illustrating the micron-scale trenches that resulted from depth profiling over 40 µm × 40 µm regions into either the samples virgin or prior ion beam prepared surface. This depth profile milling was performed into either ion beam cut faces (Figure 10.10 (c)), and unprepared "virgin" surface regions of the particle (Figure 10.10 (d)).
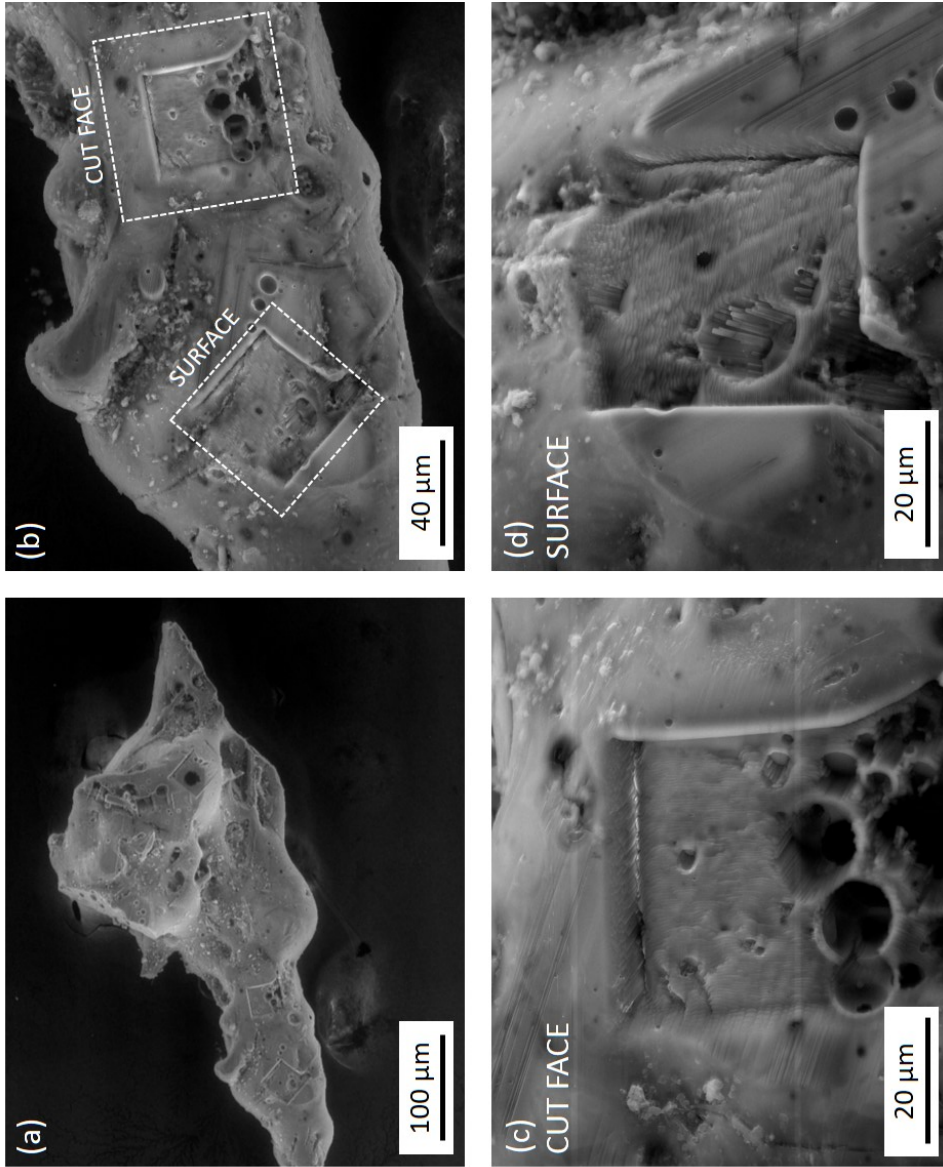
Figure 10.10: Secondary electron images of the features associated with the SIMS depth profiling into regions of the representative CF-01 particle; (a) entire sub-mm particle, (b) location of both surface (non ion beam prepared) and cut face (ion beam prepared) resultant depth profile trenches, (c) ion beam cut surface trench used for the compositional analysis of underlying features, and (d) depth profile trench on the uncut particles surface.
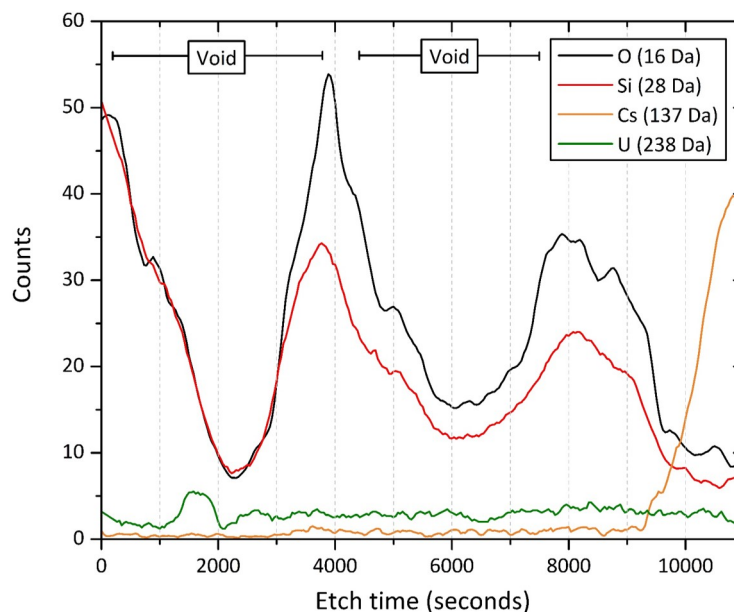
Figure 10.11: Positive bias SIMS depth profile through the previously ion beam prepared region of interest. The time (depth) variations in ion counts (concentration) for ^{16}O, ^{28}Si, ^{137}Cs and ^{238}U are shown.

With a region of interest (identified through the previous non-destructive methods) having been prepared (overlying material removed through ion beam milling), the first application of SIMS was to record a depth profile - encroaching into the sides of the μm-scale U inclusion and neighbouring Cs-rich region. The result of this positive-bias depth profile into the samples prior cut face is shown in Figure 10.11. Whereas a considerable variation in the abundance of both O and Si are observed over the duration of the depth profile, apparent is the transient fluctuation in the concentration of ^{238}U at the beginning of the analysis, alongside the more substantial increase in ^{137}Cs at the end of the scan. These compositional "spikes" hence confirm the results of the earlier non-destructive analyses - with a small, isolated region rich in U and a large Cs-rich region existing within the Si-based CF-01 *ejecta particle*. As marked on Figure 10.11, the mirrored reductions in Si and O ion intensity are associated with the locations of voids (pores) within the *ejecta particle*.

The difference in the measured intensities of the Cs and U masses results from the proportion (and relative depth) of each region sputtered by the primary Ga$^+$ ion beam. This is supported by the SIMS map for both ^{137}Cs and ^{238}U shown in Figure 10.12, again using the positive-bias mode of the SIMS instrument. With the U particle located in the wall of the trench, only the edge of the particle was dissected by the incident ion beam. This is in contrast to the Cs composition particle located at the base of the trench, therefore resulting in more of the particle being sputtered - with the emission of a greater number of secondary (ejecta) ions. The size of the U inclusion imaged

258
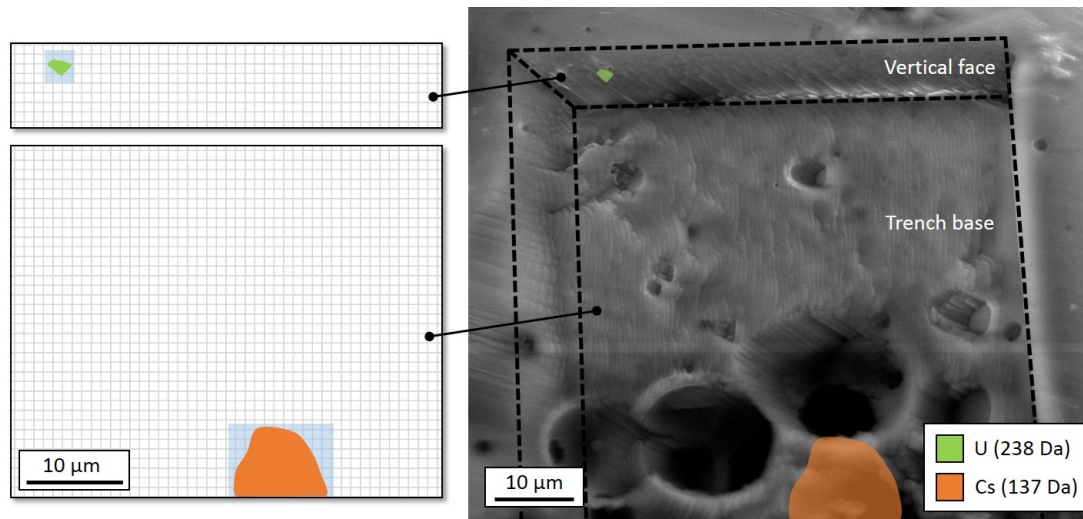
Figure 10.12: Positive-bias SIMS map detailing the location of U (238) and Cs (137), overlain onto a secondary electron image of the resulting ion beam etched trench. The regions where the spectrum presented in Figure 10.13 were obtained are additionally highlighted.

through SR-μ-XRF on the I13-1 beamline at the DLS is consistent with these SIMS results detailing its micron length-scale. The sub-angular form of this U particle is further highlighted in the SIMS map shown in Figure 10.12.

To determine the exact isotopic (atomic) composition of these two contrasting composition regions, spectra were derived from both regions (shown in Figure 10.12) over applicable mass windows comprising the various isotopes of interest. The resultant spectrum from the area comprising the more diffuse Cs composition region is shown in Figure 10.13, using the previously applied positive (left), as well as the negative (right) sample bias setup of the instrument. As shown in Figure 10.13, a number of readily-discernible peaks (between 134 amu and 137 amu) exist for the positive bias setting, however, no secondary ion peaks were detected within the same mass window when a negative sample bias voltage was employed. From positive SIMS analysis, prominent mass peaks are observed at mass units of 135 amu and 137 amu, with elevated ion counts above background yielding smaller peaks at 134 amu and 136 amu. Additional spectra using both positive (left) and negative (right) bias SIMS taken over an unprepared exterior portion (40 μm × 40 μm) of the sample are shown in Figure 10.14. For a region shown through earlier SR-μ-XRF analysis to contain no Cs component, no peaks across the Cs mass window were observed.

With stable Cs monoisotopic (^{133}Cs = 100% of natural abundance [52]), the other Cs isotopes are all fissionogenic and result from a nuclear origin. The abundances, and therefore the isotopic ratios at which these exist are dependent upon the degree of fuel burn-up. The largest mass peak

in Figure 10.13 occurs at ^{137}Cs. Decaying through the emission of a β^{-} particle to ^{137}Ba (via the brief intermediary step at ^{137m}Ba), despite possessing a moderate half-life of 30.17 years, a small component of ingrown (radiogenic) Ba will be present at 137 amu.

The other considerable Cs isotope contribution to the mass spectrum is from ^{135}Cs. Possessing a half-life of 2.3 million years [52], it is one of the longest-lived fission products [174]. The small peak within the window at 136 amu would be attributable to the short-lived and low fission product yield ^{136}Cs if measured rapidly after the release, however, due to the isotope possessing a half-life of only 13.16 days [52], the small yield produced would have subsequently decayed into the stable, radiogenic ^{136}Ba. The ingrowth of radiogenic ^{134}Ba will also have resulted following the β^{-} decay of ^{134}Cs (half-life = 2.065 years [52]) - with the peak at 134 amu therefore resulting predominantly from Ba, rather than the original fission product radiocesium.

As well as decaying to various isotopes of Ba, a number of stable Ba isotopes with competing masses to Cs are also encountered in nature (abundances shown in at.%): ^{130}Ba (0.1058 at.%), ^{132}Ba (0.1012 at.%), ^{134}Ba (2.417 at.%), ^{135}Ba (6.592 at.%), ^{136}Ba (7.853 at.%), ^{137}Ba (11.232 at.%) and ^{138}Ba (71.699 at.%) [418]. It is well accepted that owing to these comparable masses, both Cs and Ba are difficult to distinguish from one another in SIMS analysis [246]. However, the absence of a mass peak at 138 amu strongly implies that no ^{138}Ba was detected and therefore any contribution from stable ^{138}Ba (the most abundant of the Ba isotopes) as well as any radiogenically ingrown ^{138}Ba (from the rapid decay of the low fission yield ^{138}Cs) in this instance is very small or non-existent and therefore its contribution, can be neglected. The characteristic fission products of ^{134}Cs and ^{137}Cs, however, irrefutably confirms the Cs provenance as anthropogenic, rather than natural. This deficiency of natural Ba may represent its absence within the entire sample, however, in-line with the recent study of Ono et al., (2017) [190], it may conversely exist outside of the 40 µm × 40 µm region analysed in this instance.

Integration of the various peak areas from Figure 10.13 yields a number of distinct isotope ratios, detailed in Table 10.2. These decay-corrected values (to March 2011) of ^{134}(Cs+Ba*)/^{137}(Cs+Ba*), ^{135}Cs/^{137}(Cs+Ba*) and ^{137}(Cs+Ba*)/^{133}Cs determined during this work were 0.032, 0.397 and 0.002 respectively. These values are shown alongside the comparable SIMS isotopic analysis undertaken by Imoto et al., (2017) [371]. While the values for ^{134}(Cs+Ba*)/^{137}(Cs+Ba*) and ^{135}Cs/^{137}(Cs+Ba*) are consistent with those determined in this earlier work, the ^{137}(Cs+Ba*)/^{133}Cs value, however, does not correlate with the work of Imoto et al., (2017). Confirming the species distribution results of Section 9.4.5, this SIMS analysis corroborates the formerly implied near complete absence of a natural Cs component (^{133}Cs) contained in this CF-01 *ejecta particulate*.

The mass spectrum, across the 231 amu and 241 amu window, derived from positive bias SIMS on one of the micron-scale U particles contained within the CF-01 sample (identified formerly
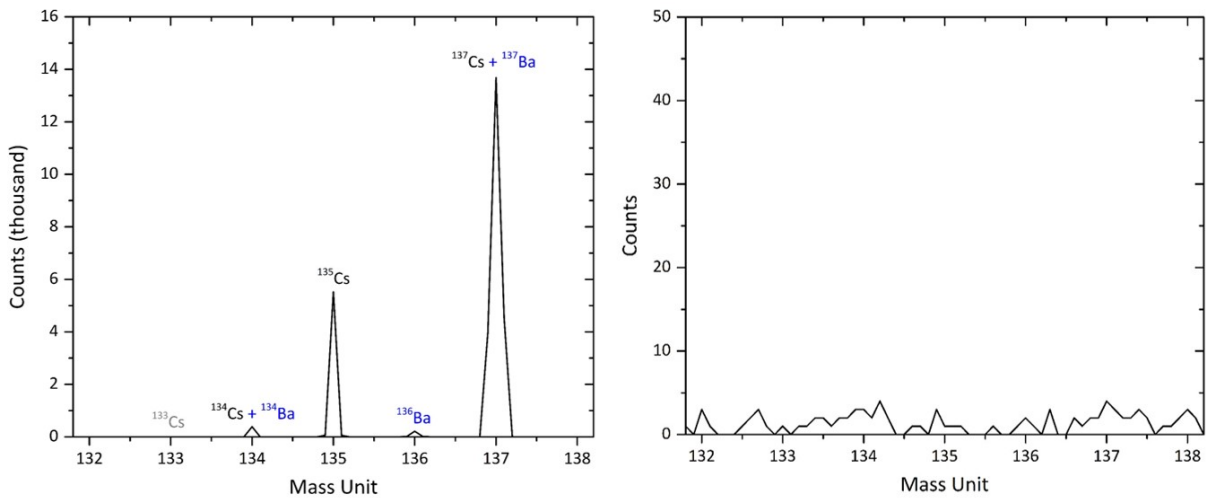
Figure 10.13: Cs isotopic spectrum obtained from the location of the Cs-rich inclusion identified in earlier depth profiling (Figure 10.11) and mapping (Figure 10.12), following ion beam preparation. Both positive (left) and negative (right) sample biases were used.
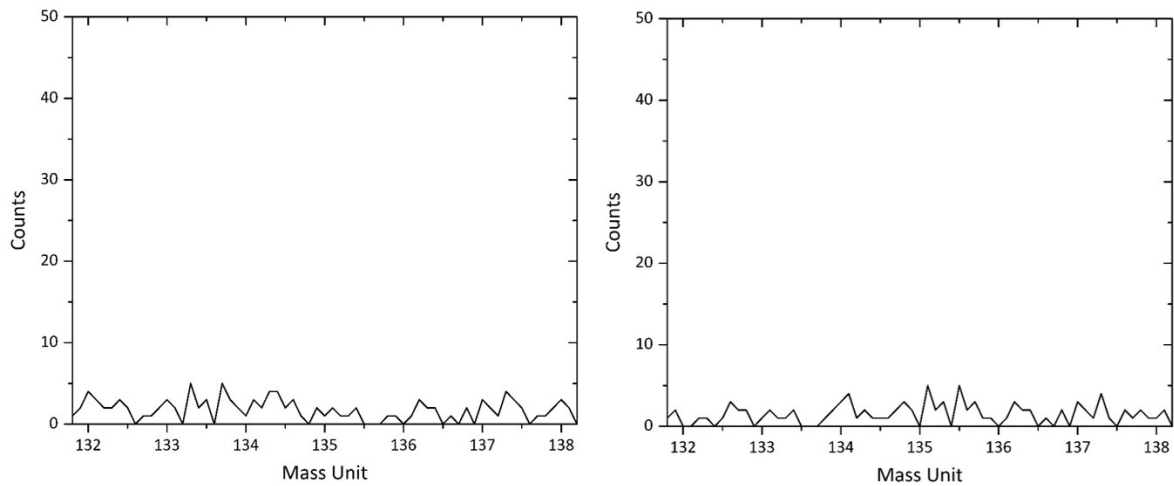
Figure 10.14: Mass spectrum obtained from the exterior (uncut/"virgin") surface of the CF-01 particle over the Cs mass window. Both positive (left) and negative (right) sample biases were used.

Isotopic ratio	Imoto et al., (2017) [371]	CF-01 ($\pm 2\sigma$)
^{134}(Cs+Ba*)/^{137}(Cs+Ba*)	0.02488 - 0.03184	0.032±0.0096
^{135}Cs/^{137}(Cs+Ba*)	0.3929 - 0.4011	0.397±0.012
^{137}(Cs+Ba*)/^{133}Cs	0.9119 - 0.9914	0.002±0.0005
^{235}U/^{238}U	0.029341 - 0.029584	0.0351±0.002

Table 10.2: Cs and U SIMS analysis results (decay-corrected to March 2011) from the respective regions of interest within the CF-01 *ejecta particle*, compared to those of Imoto et al., (2017) [371]. The inclusion of radiogenically-derived Ba species contributing to these values is shown (*).
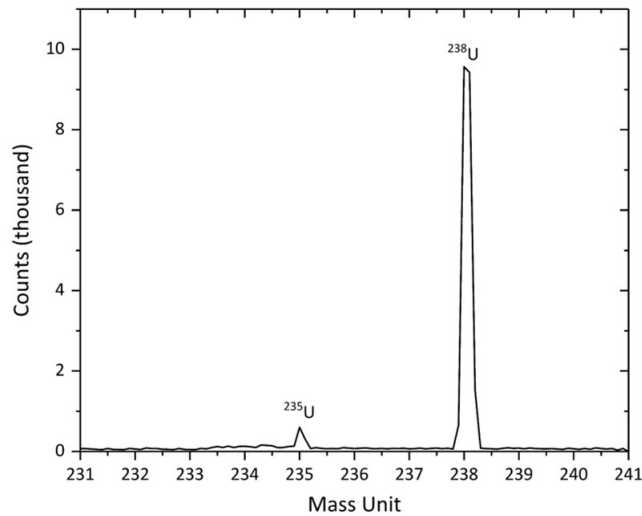
Figure 10.15: Positive bias SIMS spectrum obtained from the location of the U inclusion identified in earlier depth profiling (Figure 10.11) and mapping (Figure 10.12), following ion beam preparation.

in Figure 10.12), is shown in Figure 10.15. Unlike the Cs spectrum of Figure 10.13, where a number of mass peaks were detected, a single peak at 238 amu is dominant within this spectrum alongside a smaller 235 amu mass peak.

In contrast to the monoisotopic Cs, naturally-occurring U is constituted by a number of differing mass isotopes (abundances shown in atomic percent - at.%), consisting of; ^{234}U (0.005 at.%), ^{235}U (0.720 at.%) and the most-abundant ^{238}U (99.272 at.%) [365]. Alongside the raised abundances of specific U isotopes (e.g. ^{232}U, ^{233}U, ^{234}U, and ^{236}U), the key indicator of an anthropogenic (specifically reactor) source of U is its characteristic ^{235}U/^{238}U isotopic ratio. At any LWR facility, an enrichment in the fissile ^{235}U from approximately 0.7 wt%, to between 3 wt% and 5 wt% is required within the fuel to maintain criticality [21]. In the case of Unit 1 at the FDNPP, the ^{235}U enrichment varied between 3.4 wt% and 3.6 wt% - dependent upon its location within the core [25]. Apparent within the SIMS spectrum of Figure 10.15 is the larger magnitude ^{235}U peak than would otherwise be expected of a naturally-occurring U sample. Through integrating each peak area, a ^{235}U/^{238}U atomic ratio of 3.51 wt% is derived - indicative of typical light water reactor enrichment. This U isotopic ratio is comparable to that obtained by Imoto et al., (2017) [371], shown in Table 10.2.

Alongside the two ^{235}U and ^{238}U mass peaks, marginally elevated counts are also observed at 236 amu and 239 amu - likely representing U masses as hydride species (U-H). Across the entire 10 amu window between 231 amu and 241 amu, no other peaks are discernible.
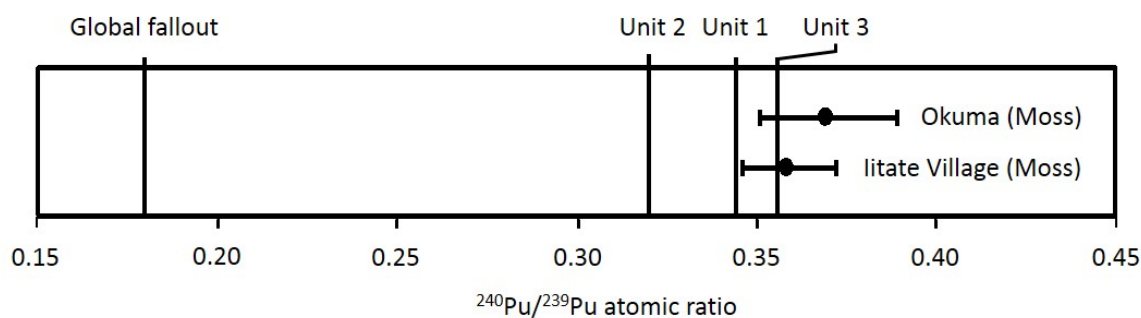
Figure 10.16: Comparison of the Pu isotope ratios of two samples (Okuma Town and Iitate Village) determined via ICP-MS, with core inventory values for reactor Units 1, 2 and 3 as well as global (background) atmospheric fallout. *Reference values from [50, 419].*

As encountered previously with regards to SR-μ-XAS analysis, despite likely existing as a (very small) component within the nuclear reactor sourced CF-01 *ejecta particle* sample, Pu was also not detected during this SIMS analysis. While, like Ba, this may represent a spatial inconsistency of the species within the particle, it could, however, be interpreted by the high limit of detection (LoD) and poor sensitivity of SIMS for such higher-mass (heavier) elements [246, 408]. It should be noted that while no Pu was detected in samples as part of this thesis, the application of ICP-MS as part of the work by Dunne and Martin et al., (in preparation) did conversely identify non-natural Pu signatures (^{240}Pu/^{239}Pu) in similar sample materials - indicative of their likely Fukushima origin rather than as a result of global fallout (Figure 10.16).

10.4.4 FT-13

The results of similar SIMS depth profiling on the unprepared surface of the larger FT-13 *ejecta particle* as was previously undertaken on the smaller, yet more angular CF-01 sample, are presented in Figure 10.17. As no particulate of actinide composition was determined to exist either on the surface or contained within this mm-scale radioactive material (Section 9.4.6), unlike the CF-01 samples, this SIMS analysis focused on quantifying the exterior distribution of fission product species.

From this surface, isotopic analysis (sputtering to a depth of 10 μm into the material), the concentrations of stable isotopes including; ^{28}Si, ^{40}Ca, ^{56}Fe, and ^{133}Cs are all observed to be uniform or non-existent in their concentration - although both Ca and Si display small depth-related reductions in their abundance. In contrast, the concentrations of the fission products of ^{90}Sr and ^{137}Cs, both exhibit a surface enrichment down to a depth corresponding to approximately 1.5 μm. Beyond this depth, secondary ions of neither isotope are detected within the sample.
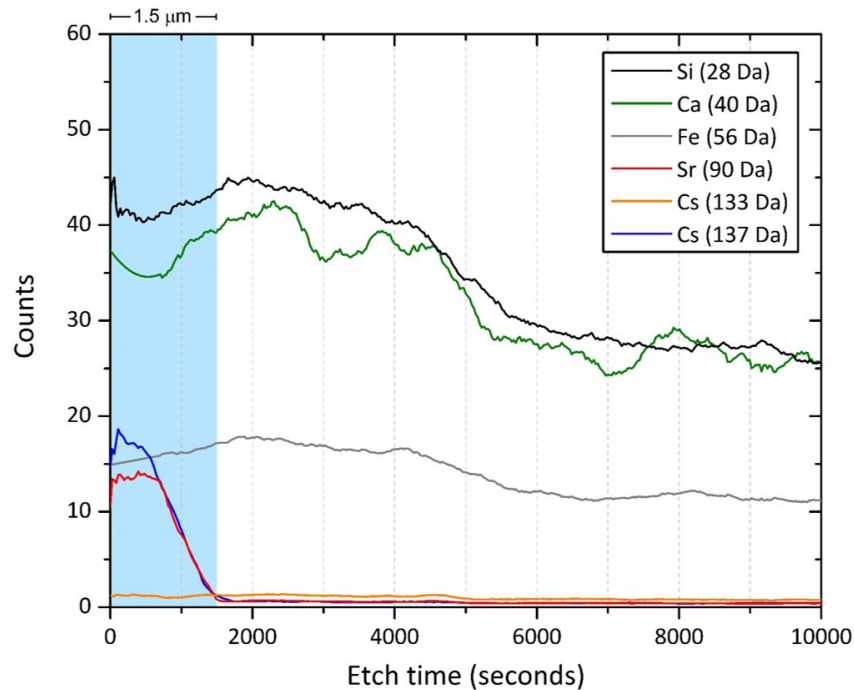
Figure 10.17: Positive bias SIMS depth profile through the uppermost surface of the mm-scale FT-13 *ejecta particle*. The time (depth) variations in ion counts (concentration) for ^{28}Si, ^{40}Ca, ^{56}Fe, ^{90}Sr, ^{133}Cs, and ^{137}Cs are shown. The position in the start of the depth profile at which the Cs isotope (atomic) ratios were derived, is identified (blue shading).

When the decay-corrected ^{135}Cs/^{137}Cs isotopic ratio, as derived from the uppermost 0.8 μm of the depth profile of Figure 10.17 is determined, a lesser value than that of the CF-01 material (0.397±0.0079), of 0.34±0.015 is derived. As determined for the CF-01 *ejecta particle*, the ^{137}Cs/^{133}Cs isotope ratio similarly occurs with a value close to zero, resulting from the non-detection and hence likely absence of naturally-occurring ^{133}Cs. Despite representing only an initial and rapid quantification of a small surface region of the FT-13 samples ^{135}Cs/^{137}Cs isotope ratio, this value is consistent with that predicted for reactor Unit 2 in the work of Nishihara et al., (2012) [50], having also been measured on micron-scale reactor Unit 2 derived material by Imoto et al., (2017) [371].

10.5 Discussion

CF-01 (Unit 1)

With the prior laboratory-based tomography results of the CF-01 *ejecta particulate* (Section 9.4.3), detailing the occurrence of numerous high atomic number (Z) particles associated with the sub-mm particles exterior-most circumference, synchrotron analysis on the I13-1 beamline at the DLS confirmed these preliminary qualitative results; with the micron-sized material composed of

U - located just below the surface of the sample. Complimentary analysis on the I18 beamline (also at the DLS) was able to derive phase information following the application of SR-µ-XANES.

Identical to the individual sub-micron U-based *atmospheric particulate* material formerly analysed in Section 8.4.3, this particle-included U was similarly shown to exist as UO_2 - with U in the chemically reduced IV oxidation state and therefore identical to that of the structure of nuclear fuel. This represents strong evidence to support the current rationalisation that a breach of the core containment had occurred [34], with the reactor building hydrogen explosion serving to distribute actinide material into the environment. Based on the measured $^{134}Cs/^{137}Cs$ activity ratio, this *ejecta particulate* is ascribed to have been sourced from reactor Unit 1 (when compared to the values produced following the core inventory modelling work of Nishihara et al., (2012) [50]). This sub-mm *ejecta particulate* was not derived from reactor Unit 2, however, in contrast to the bulk samples from which the U composition *atmospheric particulate* was isolated.

Alongside the SR-µ-XRF results obtained on the I13-1 beamline (Section 9.4.5), the results from this SR-µ-XRF mapping of the CF-01 *ejecta particle* from the I18 micro-focus spectroscopy beamline, as shown in Figures 10.6 and 10.7, serve as further evidence of the materials reactor provenance. These elemental maps highlight the co-existence of Cs in the sample with that of Fe, which together occur within the larger, highly-angular central particle as well as the numerous considerably smaller, yet similarly irregular, micron-scale inclusions. This fragmented form, combined with their surface location and composition further supports the conclusions made in Chapter 9, whereby such fragments were the result of material produced from a reactor-buildings hydrogen explosion embedding both reactor and structural components into Si-based thermal insulation materials that originally enclosed the RPV and had undergone a degree of melting. With only four known mineral species containing both Cs and Fe [354] (none of which have been found to exist within Japan), a natural origin of the Fe-Cs composition particulate can be near certainly disregarded - with the provenance of these inclusions, therefore, being anthropogenic and of reactor origin.

In addition to the Cs-containing Fe particles indicating a nuclear reactor source, the Sr-rich matrix within which this particulate is contained further invokes the materials reactor provenance and also a likely mechanism of formation. As detailed in the background discussions in Section 2.2.1, like Cs - Sr is produced as a fission product in extensive yields during reactor operation [133]. Alongside other gaseous species, it too would have existed at elevated levels in the Unit 1 PCV following the serious over-pressure venting of the RPV, that occurred shortly before the reactor buildings hydrogen explosion on the 12th March 2011. The particle-wide distribution of Sr, over the localised distribution of Cs (with Fe), is likely to result from the strong sorption of Cs onto the surfaces of Fe composition materials (including steels) [389], in contrast to the absence of such sorption behaviour shown by Sr.

This formation of such "poorly-soluble Fe-Cs forms" as defined by Al Rayyes et al., (1993) [389], would subsequently result in the environmental stability of Cs. Therefore, being strongly bound onto the surfaces of Fe-bearing materials, akin to the sorption of Cs onto clay and mica-type minerals [167, 168], the distribution of free and reactive Cs is, therefore, not of an environmental concern. Like the nanometre-sized clay and mica-bound Cs, which themselves are highly mobile in the environment, if this strongly Cs-bound Fe particulate were to be released from the surfaces of (or from inside) this particle, then it would be similarly readily-transported in suspension.

Although not as determinative of a reactor origin as other elements, Cu (similarly dispersed as micron-scale particles within the surface of the sub-mm CF-01 *ejecta particle*) occurs associated with various applications/processes typical of a nuclear reactor facility [35]. Alongside inducing embrittlement within RPV steels even under low radiation environments, Cu is more-extensively utilised in portions of a reactors water transport and heat-exchanger network [20, 35].

Unlike the γ-ray emitting Cs, the sole fission product isotope of Br (^{81}Br) is stable, with the fission products of Se being either similarly stable (^{77}Se, ^{78}Se, ^{80}Se and ^{82}Se) or decaying through a weak β^- decay (^{79}Se) into ^{79}Br, with a half-life of 3.27×10^5 years. Contrasting to the angular form of the Cs-containing Fe fragments - the Pb, Br and Se containing material is considerably more rounded/diffuse and less well-defined in its shape. As discussed formerly in Chapter 9, owing to its radiation shielding properties, but also its ductile nature, Pb was used extensively at the FDNPP to enclose the insulation material that surrounded each PCV and Suppression Chamber.

A mechanism to account for the diffuse form of these numerous Pb-based fragments, in addition to that of both Br and Se, can be ascribed to the volatilisation temperatures/boiling points of each of these elements. Unlike Fe, which possesses a melting point of 1538°C, Pb exhibits a considerably lower melting point of only 327.46°C [165]. As a consequence of this, at the elevated temperatures experienced during the LOCI at the FDNPP reactor Unit 1, the Pb shielding material reached temperatures sufficient to undergo significant melting. The large volume of Fe forming parts of the reactor and also the surrounding building, however, did not. During the subsequent reactor building hydrogen explosion, both Fe and Pb were fragmented and embedded into the fibrous Si thermal insulation, which itself reached temperatures sufficient to induce melting. At these reactor temperatures and pressures, both Br and Se would have existed in highly-mobile gaseous states [165], and would have readily combined with the partially-molten Pb.

As well as the incorporation of reactor-sourced Cs-bound Fe particulate, gaseous Sr and irregular-shaped Br-Se rich Pb material, there exists the aforementioned U fragments. Occurring in addition to these fission product and reactor materials distributed around the exterior region of the sub-mm *ejecta particulate*, this material is illustrative not only of elevated reactor

temperatures (expected as part of a LOCI), but also the structural/mechanical failure of the reactor cores fuel assemblies.

As part of the French-led VERCORS program [124], "significant" quantities of U were found deposited in various parts of the experimental "reactor network" that had been at around 830°C during a simulated LOCI scenario in the nearby reactor core. These results provided a crucial indication of the fuel assemblies rapid structural failure, its fragmentation and the subsequent mobility of U under accident/high temperature scenarios. The application of ICP-MS chemical analysis of the various simulation-derived samples revealed release values ranging from 1% to 10% for tests performed at the higher temperatures of 2330°C under differing (oxidising) conditions.

Having been classified as possessing a release behaviour synonymous of fission products with a "low volatility" in the work of Pontillon et al., (2010) [124], this VERCORS empirical study concluded that unlike Pu, Am and Cm - U may be released following a LOCI with release fractions of up to 10% in oxidising conditions. These oxidising, and high release conditions were experienced where considerable volumes of steam existed, due to the formation of UO_3 or various uranium hydroxide species. In addition to the temperature and oxidising conditions, the VERCORS severe accident program also concluded that factors such as burn-up, fuel-cladding interactions, nature of the fuel (UO_2 or MOX) and state of the fuel ("rod", "degraded rod" or "debris bed") served as further physical parameters to influence total fission product and actinide release.

As detailed in the description of the accident scenario in Section 1.3, the reactor Unit 1 core is believed to have reached temperatures in-excess of 2800°C by the early evening of the 11th March, in a steam-rich environment due to the lack of adequate core coolant supply. According to these VERCORS findings, under such high-temperature conditions, the U fuel would have begun to structurally degrade - with the production of solid (fine-scale) U particulate as a result. With core melting having reached completion by the morning of the 12th March and molten "corium" material falling through the base of both the RPV and PCV before eroding into the underlying concrete pedestal (Figure 1.3), a greater degree of this U particle volatilisation/fragment formation would have resulted [124].

While highly-oxidising conditions (in the reactor environment) were reported in the VERCORS study, the results of the U particulate from this thesis has shown the U to exist, however, as UO_2 - in the unoxidised and more chemically-reduced form. Rationalisations to account for this reduced form of U could be attributed to; (i) the significant reducing atmospheric overpressure resulting from the 130 kg of H_2 gas within/surrounding the reactor assembly [387], or (ii) O_2 gas serving as the limiting reagent, whereby the total mass of U was greater than the volume of O available to promote oxidation. The VERCORS project in contrast, utilised a single fuel assembly

within their experimental setup, therefore, issues concerning conclusions resulting from such simulations scalability require further consideration.

Estimates specific to the FDNPP reactor Unit 1 (employing MELCOR computational modelling combined with physical monitoring) by Sevon (2015) [420], determined that only 0.0004% of the core inventory was released into the environment over the 96-hours since the initiation of the LOCI. Assuming this release fraction (one significantly below that suggested through the VERCORS experiments) only 15 kg of the 77,100 kg of UO_2 (68,000 kg of U) originally located within the reactor core [25], was fragmented (or volatilised) and subsequently ejected during the reactor buildings hydrogen explosion. This work concluded that nearly all of the U, combined with other reactor materials (e.g. Zircaloy-4™ fuel cladding, stainless steel structural components and B_4C control rods) formed a 164,000 kg highly-radioactive "corium" mass that corroded through the base of the RPV and into the reactors underlying concrete pedestal. *(N.B. the exact quantity is likely never to ever be known due to the majority of this U existing as a once-molten corium mass in various positions around the base of the reactor Unit 1 RPV/PCV [54])*. The intense heat generated by the LOCI was also responsible for the melting of the Si-based insulation material located within close proximity to the reactor, into which the various species became combined.

In comparison to the SIMS analysis of "Cs micro-particles" (CMP's) by Imoto et al., (2017) [371], the results of which are shown alongside those determined during this work in Table 10.2, the atomic ratios for fissionogenic Cs are all in close agreement (with the exception of those ratios including ^{133}Cs). While an anthropogenic (Fukushima) origin of this material is shown by its radiocesium content, a specific reactor Unit origin can be further invoked based upon its Cs atomic (isotope) ratio when compared to those derived by the reactor inventory ORIGEN modelling of Nishihara et al., (2012) [50]. This atomic ratio based reactor Unit assignment represents a further mechanism to ascribe the landward contamination to a specific source, in addition to the radiocesium activity ratios described in Section 9.4.1.

One of these key "forensic" Cs isotope ratios is ^{135}Cs/^{137}Cs. As shown in Table 10.2 and also graphically in Figure 10.18, a decay-corrected (to the time of the release) ^{135}Cs/^{137}Cs atomic ratio of 0.397±0.012 determined in this work is consistent with the ^{135}Cs/^{137}Cs inventory value for Unit 1, as derived via the reactor core inventory modelling work of Nishihara et al., (2012) [50].

Although not as illustrative of a particular reactor source than the various high-yield, rapidly ingrown and short-lived fission product species (e.g. Cs, I, Ag, Sb and Te), the isotopic composition of U across a UO_2 fuel pellet and down the cores vertical length is considerably more consistent - exhibiting much less isotopic variability. Whereas compositional homogeneity is observed across the near-entire diameter of a standard 11 mm pressed and sintered fuel pellet post-irradiation - some variation (elementally, isotopically as well as structurally), is associated with the sub-mm
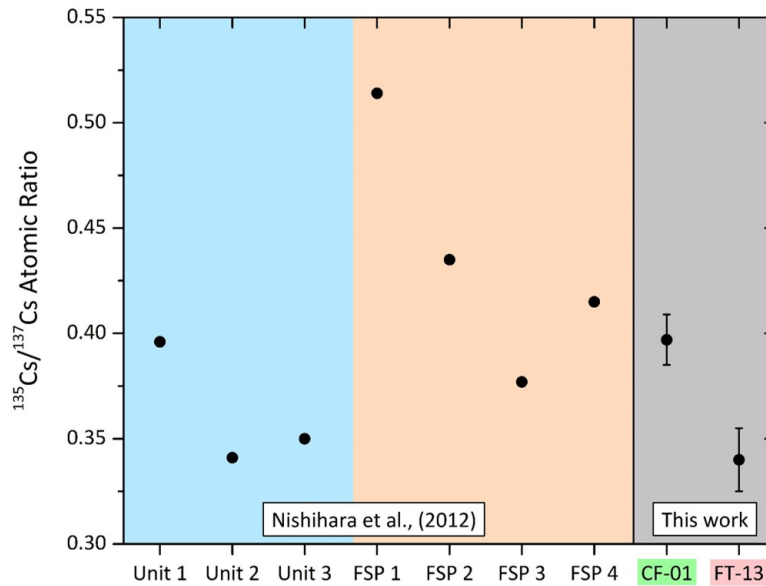
Figure 10.18: Comparison of the ^{135}Cs/^{137}Cs isotopic ratio of the Cs composition region in the CF-01 particulate alongside the reactor core inventory modelling values as determined by Nishihara et al., (2012) [50].

outermost region of its circumference. As detailed in the works of Buck et al., (2004) [23], and Bruno and Ewing (2006) [174], owing to the elevated thermal neutron fluxes experienced by the UO$_2$ fuel located closest to the surrounding Zr-C based cladding during reactor operation, (defined as the "rim-effect" by Spino and Papaioannou (2001) [421]), the degree of fuel burn-up is greatest. A schematic representation of a conceptual irradiated UO$_2$ fuel pellet, highlighting this high burn-up "rim-effect" portion, is shown in Chapter 8 (Figure 8.9).

Alongside a degradation in the structural integrity and hence the serviceable lifespan of the fuel as a result of its irradiation (associated with the pellets circumference), thermal neutrons are efficiently absorbed by the fertile ^{238}U in this high burn-up region. These optimised neutron absorption conditions led to the production of fissile ^{239}Pu [23]. This ^{239}Pu may capture further neutrons to yield other transuranic species (e.g. Am and Cm), or conversely undergo fission - with the build-up of a comparable yet marginally different suite of fission products.

From the SIMS analysis of the embedded U particle - established formerly from the SR-μ-XANES analysis to be U(IV) as UO$_2$, no masses other than those at 235 amu and 238 amu were detected. With a wt% ^{235}U of 3.51 wt%, this U inclusion is illustrative of; (i) an LEU fuel material, and also, (ii) this particulate having not originated from natural U (NU) contained within the precursor basalt-sourced Rockwool™ insulation - having been shown by Morgan and Lovering (1965) [390] to comprise approximately 0.2 ppm of the fibrous materials bulk composition.

With no other mass peaks aside from those at 235 amu and 238 amu, the results can be further invoked to attribute the material as originating from one of two potential sources. This particle inclusions could either have arisen from; (i) the central portion of an irradiated fuel pellet - where actinide species ingrowth had occurred (which would produce mass units other than 235 and 238) or, (ii) from the entire volume (including the pellets outermost circumference) of an unirradiated fuel pellet, recently installed with the reactor having not been extensively irradiated.

A graphical comparison of the wt% ^{235}U from reactor Units 1, 2 and 3, alongside this measured wt% ^{235}U within the CF-01 contained U micro-particle (as determined through SIMS analysis) is shown in Figure 10.19. The ^{235}U wt% values of the U contained within each of the three reactors fuel assemblies were obtained from records published by the plant's operator, TEPCO [25], as detailed formerly in Table 1.2. With the low (1.1 wt% - 1.3 wt%) ^{235}U of the 32 MOX fuel assemblies contained within Unit 3 excluded, the difference in the operational enrichment (wt% ^{235}U) between Unit 1 and Units 2 and 3 is apparent. From Figure 10.19, the micron-sized UO_2 particle shows a wt% ^{235}U value within the compositional range used in reactor Unit 1, distinct from fuel enrichment for both reactor Units 2 and 3. Alongside the SIMS isotopic ratio of the radiocesium contained within the particulate, this U signature serves as further evidence that the CF-01 was derived from reactor Unit 1. The integrity of the core must, therefore, have been sufficiently compromised for a component of the fuel to enter into the environment - with the majority having formed a mass of "corium" at the base of the PCV [54].

As they do not possess the same activity level (owing to their considerably longer half-lives) and therefore emit the intensity of characteristic and easily-detectable γ-rays, U, alongside many of the other actinide elements (e.g. Pu, Am and Cm) are often termed the "frequently forgotten radionuclides" [145] - with their existence and abundance quantifiable only through (destructive) mass spectrometry techniques. Resultantly, U "regardless of its enrichment level, represents a contrasting hazard owing to its chemotoxicity" [147, 422]. Such toxicity is apparent from its NFPA 704 classification, grouped within "Class 4" for Health [423], alongside hydrogen cyanide and hydrofluoric acid - whereby "very short exposure could cause death or major residual injury". It was only in 1999 that the extent of the toxicity of uranium dioxide was first established - absorbed through phagocytosis by the surfaces of the lungs [146].

Resulting from the SR-µ-XANES analysis of the CF-01 *ejecta particulate*, the U particles studied were observed to exist in the U(IV) oxidation state - characterised by the highly distinctive, symmetrical, absorption spectrum. Unlike the U(VI) oxidation state in which U also frequently exists, the IV redox state exhibits a far greater thermodynamic stability and is insoluble under environmental conditions [147]. It is this thermal stability and the relative insolubility of U(IV), in the form of UO_2, that allows for its use as the fuel within nuclear reactors.
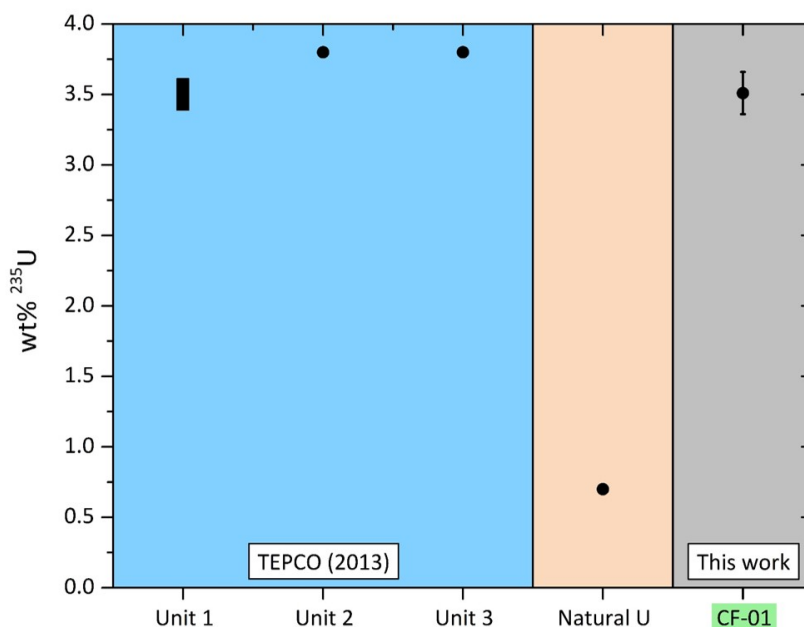
Figure 10.19: Comparison of the known FDNPP reactor Unit wt% ^{235}U levels (black) with that derived from the SIMS analysis of the U particle contained within the CF-01 sample (green). *U core inventory data of Units 1, 2 and 3 obtained from [25].*

As a consequence of the insoluble nature of these U(IV) particles, their leaching into environmental waters is considered to not represent an environmental hazard. A hazard would, however, result if a considerable volume of these particles were to become inhaled. If these particles were to additionally become oxidised to U(VI) (as U_3O_8), they would exist in a more soluble and hence readily transported (dissolved) state. As this small volume of U, occurring as embedded U particles, exists some microns below the surface of the Si-based *ejecta particle*, the risk of oxidation, release, dispersion and biological uptake is effectively eliminated. This *ejecta particulate* could be viewed as being analogous to a crude form of vitrified nuclear waste - whereby the nuclear material is enclosed within an impermeable glass; serving to not only eliminate the release of radiation but also prevent against species leaching and transportation over time [424].

FT-13

From the earlier laboratory-based XRT (confirmed through the application of Raman spectroscopy) detailing the amorphous internal volume of the FT-13 particle alongside a small number of Fe-based inclusions (Section 9.4.6), the analysis presented in this chapter conversely focused on the particles exterior-most surface. From the resulting SIMS analysis of the 2 mm diameter FT-13 *ejecta particle*, the primary fissionogenic isotope of Cs (^{137}Cs) was observed to exist entirely within an enriched outer "rind" - to a depth of circa. 1.5 μm. While this fission product isotope
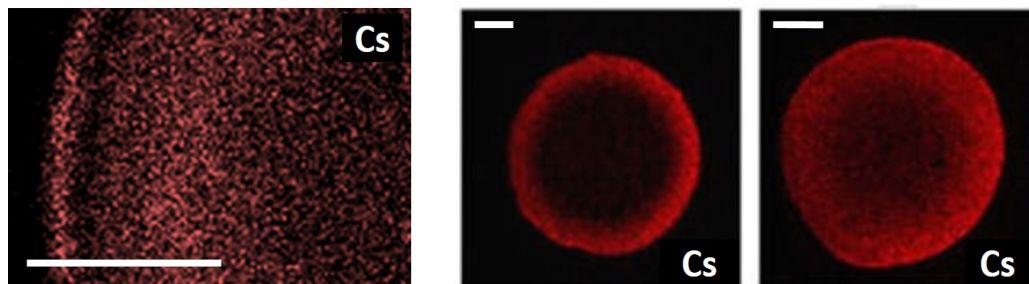
Figure 10.20: Cs EDS elemental mapping performed on micron-scale "Cs-ball" material. *Modified from [193] (left), and [194] (right)*. Scale bars = 0.5 µm.

was detected only during the very initial period of SIMS depth profiling, the existence of the primordial (stable) isotope of Cs (^{133}Cs) was not detected within the entire 10 µm section into the sample - therefore invoking either its abundance below the ppm LoD for SIMS analysis, or conversely its complete absence from the sample.

A comparison of the ^{135}Cs/^{137}Cs atomic ratio (determined from the outer surface) of this FT-13 *ejecta particulate* sample is plotted alongside the value derived from the CF-01 material, as well as the reactor core inventory values (for reactor Units 1, 2 and 3) resulting from the modelling work of Nishihara et al., (2012) [50], in Figure 10.18. Having been isolated from a site (Futaba Town) located at the very base of the primary contamination plume previously attributed via; (i) bulk isotopic analysis [48, 161, 162], (ii) regional mapping studies [69, 153] and more recently, (iii) preliminary single-particle quantification [164], to the FDNPP reactor Unit 2 - the ^{135}Cs/^{137}Cs isotopic ratio of this newly-discovered (yet significantly more sizeable) particle also aligns with the predicted core inventory value of reactor Unit 2 [50]. This initial isotopic quantification represents the very first analysis undertaken on such a mm-scale (Unit 2-derived) material, with particulates investigated from this reactor having formerly only been observed to have existed as micron-scale "Cs-balls" or similarly-sized, yet slightly angular material [191–194] - termed "Type-A" in the work of Satou (2016) [164].

When compared to the Cs distribution observed within the micron-scale "Cs-balls" of prior studies [193, 194], an analogous peripheral concentration is similarly evident (to 0.5 µm depths into the average 2 µm diameter sample. As formerly invoked in the study of Kogure et al., (2016) [194], the peripheral nature of the ^{137}Cs can be implied to result from the gaseous diffusion of the various Cs isotope species into the silicate glass particle after its solidification at a high temperature within the gas-filled atmosphere surrounding the reactor. Unlike the spherical micron-sized "Cs-balls", however, which were capable of being transported vast distances by the entraining air-masses [191, 192], such mechanisms did not permit for this mm-scale *ejecta particulate* to be carried far from the FDNPP site, resultantly deposited only 2 km from the site.

While the associated sample preparation and individual particle isolation involved in this highly-detailed isotopic analysis is considerably more extensive, time-consuming and inherently more costly than the bulk sediment, lichen and dust isotopic analysis that has to-date been widely undertaken [143, 161, 162, 327, 425], it does overcome issues when multiple isotopic contributions exist. This isotopic "dilution" of the primary signal of interest was encountered in the $^{235}U/^{238}U$ organic samples analysed by Shibahara et al., (2015) [141] - where naturally occurring U saturated any Fukushima-derived signal that may have existed. The multiple FDNPP reactor sources, combined with the residual global Pu background (from atmospheric weapons testing), resulted in multiple instances of end-member mixing being recorded on Fukushima-derived material in a number of studies [142, 143, 426]. Similar deconvolution of both reactor and global background fallout signals was additionally performed in works on Cs isotope ratios [163, 427], seeking to attribute sample contamination to a specific Fukushima reactor core source.

10.6 Conclusions and future work

The work described in this chapter represents an extension of the initial single particle analysis described in Chapter 9, as well as the very first application of targeted SR-μ-XANES and SIMS analysis of inclusions contained within the larger, Si-based, sub-mm representative *ejecta particulate*. This multi-technique analysis of microscopic regions of interest within the sample (analogous to searching for a "needle in a haystack") was only achieved through the accurate stage (and resultantly sample) positioning that allowed for the efficient correlation of the various techniques and their subsequent results. The following conclusions can, therefore, be drawn:

- Using cutting-edge materials analysis methods, it is possible to evaluate both the state (phase) and isotopic composition of single particles of interest - despite existing within a larger, enclosing, matrix.

- That the SIMS analysis of an isolated Cs-rich region supports earlier γ-ray spectroscopy ($^{134}Cs/^{137}Cs$ activity) results, with the complementary atomic ratio of $^{135}Cs/^{137}Cs$ being similarly illustrative of a signature characteristic of the FDNPP reactor Unit 1 when compared to estimates made in the work of Nishihara et al., (2012) [50].

- The U exists within the U(IV) oxidation state as uranium dioxide (UO_2). This form not only corresponds to the naturally-occurring Uraninite mineral but more notably is identical to that used as the fuel material within all light water reactors - the type involved in the numerous releases from the FDNPP.

273

- SIMS quantification confirmed these microscopic U particle inclusions as derived from the FDNPP - showing a wt% ^{235}U enrichment level matching that of the fuel contained in reactor Unit 1 of the FDNPP.

- The Unit 1 reactor core reached sufficiently high temperatures during the LOCI for its structural integrity to be compromised. In addition to the U failing - producing a volume of volatilised/fragmented fine-scale aerosol material, this heating resulted in the fuel material relocating (melting) from its initial position in the core assembly to the base of the RPV/PCV as a mass of "corium". This actinide material is believed, alongside the other gaseous fission product species and reactor components, to have combined with the Si-based material that insulated the PCV - which itself underwent significant melting as a result of the LOCI.

- As a result of the reactor building hydrogen explosion, structural components such as Fe (steel) and concrete (Chapter 9), were embedded into the very exterior of the Si-based particle - more peripherally than the U. This is believed to clearly define an event chronology - with the hydrogen explosion serving to produce Fe and concrete fragments which were then fused onto the surfaces of the Rockwool™ insulation sourced Si-based particulate.

- The micron-scale of the incorporated U fragments is consistent with the extensively studied microstructural size of UO_2 grains that combined constitutes nuclear fuel [23, 24]. As a consequence, the structural failure/fragmentation of the actinide fuel assemblies is seen as responsible for the observed existence of UO_2 on the surfaces of particulate possessing a Fukushima-derived radiocesium signature.

- The Cs content of the sample exists associated largely with the metallic Fe particulate (of various sizes), contained within the larger Si-rich particle. This association is likely the result of the known affinity that Cs shows for Fe [389].

- In contrast to the angular nature of the Fe particles; the Se and Br containing Pb regions were considerably more irregular in their form, postulated here to represent the incorporation of material (that unlike Fe) had undergone some degree of melting. The known lower melting point of metallic Pb over Fe supports such differences in the materials form.

- The IV oxidation state of the U is indicative of its environmental stability - being insoluble under typical conditions [147]. This form, therefore, implies that no U species leaching will result while the material remains unoxidised (chemically reduced).

- While insoluble due to its oxidation state, the existence of U as micron-scale particulate within the environment poses a notably health issue (if at total quantities greater than the <50 μm^3 in this instance) owing to its readily-inhalable nature [233], and absorption through phagocytosis by the vast surfaces of the lungs [146]. If existing at concentrations above the levels observed in this work (corresponding to hundreds of such micron-scale

particles), internal α-particle radiation exposure could also result if a large volume of these micron-scale actinide particles were inhaled.

- The enclosed nature of the U micro-particles, contained by the amorphous Si glass, will serve as a mechanism to reduce the likelihood of the actinide material from entering the environment. Any future fragmentation of such highly-porous particulate, analogous to naturally-occurring pumice [388], may contribute to the U fragments entering into the environment. However, the intact form of the *ejecta particle* analysed in this work would suggest a moderate degree of structural integrity to the material to prevent against its environmental breakup.

It should be noted that this high-resolution and multi-technique analysis has focused solely on a single particle deemed representative, isolated from a locality 2 km north-west of the site's reactors - part of a suite of similar *ejecta particles*. Whereas this material was selected due to its similarity (following electron microscope examination) to other such sub-mm particles - each of which were obtained from the same bulk sample, care must be taken when using these results in large-scale interpretations as they may not be wholly representative of the remainder of sub-mm particulate distributed within the environment. However, the results arising from this work have highlighted the occurrence of Fukushima-derived actinide material in the environment surrounding the plant. In addition to these results, the methods devised and employed in this chapter represent those that could be used during the further examination of Fukushima-derived or other nuclear-sourced fallout material.

The estimate for the UO_2 released from reactor Unit 1 provided by the MELCOR modelling of Sevon et al., (2015) [420], totalled 15.0 kg - or 0.0004% of the total core inventory. Through assuming the total UO_2 in a standard Unit 1 *ejecta particle* is consistent with the $\approx$50 µm^3 observed for this sample, before incorporating approximate particle depositional densities (from personal communications with Dr. Y. Satou of JAEA) and the total land area contaminated - a core release of approximately 12.9 kg of UO_2 is predicted. This value lies within 14% of the value predicted by Sevon et al., (2015), and serves to provide an initial (albeit approximate) validation of their results. Although such a quantity only represents a volume of UO_2 11 cm × 11 cm × 11 cm in size, it is not only U but also the various fission product elements and other actinide species that are contained within this release volume that represent a hazard [146, 147]. While a Fukushima U signature was encountered, it should be noted that U (in air, water and foodstuffs) occurs entirely naturally, with the United States Centre for Disease Control (CDC) summarising in addition to quantifying the known potential effects of prolonged (chronic) exposure to the actinide [311].

Following from this multi-technique analysis of a single *ejecta particle* - confirmed to have been derived from the FDNPP (and specifically reactor Unit 1), future work will focus on the

analysis of the other similarly-sourced particles to evaluate their consistency and therefore the conclusions of this study. As well as examining additional *ejecta particulate* samples through the same methods, the use of other analytical techniques is also planned including 3-Dimensional Atom Probe Tomography (3D-APT), ICP-MS, nano-focus SR-XAS, SR-μ-x-ray diffraction (XRD) and TIMS.

As proposed for the sub-μm U *atmospheric particulate* described in Chapter 8, one technique employable for the nano-meter scale compositional/phase analysis of this Si-based material will utilise the newly commissioned nano-focus spectroscopy beamline, I14, at the Diamond Light Source synchrotron. Whereas the I18 beamline was capable of 2 μm × 2 μm spatial resolutions, through the application of enhanced downstream optics, the I14 beamline can attain spatial resolutions (pixel sizes) down to 50 nm × 50 nm [263]. Hence, it will be possible to perform XRF mapping alongside XANES and potentially EXAFS point analysis at resolutions previously unattainable and with considerably less spectral noise.

To evaluate the isotopic ratio of the U material with a greater accuracy than the surface sensitive SIMS technique, the use of 3D-APT alongside solution or laser-ablation ICP-MS is also planned on regions of the sample determined to contain actinide material.

In order to investigate the potential influence of particle fragmentation on the release and dispersion of soluble or insoluble U into the environment, a number of environmental leaching studies are additionally planned. After first using a diamond (Microtome) cutting system to produce a number of particle sections, these slices will them be mounted onto the tips of glass support needles or onto TEM support grids before being placed into solutions analogous to environmentally observed fluids. Both SR-μ-XAS alongside subsequent solution nebulisation ICP-MS will then follow to determine; (i) if a U phase change had occurred, and, (ii) if U concentrations within the fluid had increased.

11

CONCLUSIONS AND FUTURE WORK

11.1 Thesis summary

In the years since the accident, despite considerable progress having been made in repairing the infrastructure and former reactor buildings on the FDNPP site by the plant's operators (TEPCO) - work to retrieve the previously molten corium material from inside each of the reactors RPV/PCV has yet to commence. Commendable activities have also occurred off-site - associated with the remediation of large areas of the less-highly contaminated Fukushima Prefecture. As a consequence, formerly excluded areas are becoming classified as safe, and ready for rehabitation.

While large portions of this *Special Decontamination Area* have been declassified, allowing citizens once displaced to return, a switch in focus to characterising the contamination across the more topographically challenging and heavily contaminated regions (closer to the plant) is needed.

In addition to considering the human health implications associated with the dose received from ionising radiation - the influence of the "frequently forgotten" (typically actinide) radionuclides has been somewhat overlooked, with the assumption (from the onset) that extremely low actinide volumes were released [155]. To ensure that an appropriate remediation and repopulation strategy is constructed, a thorough understanding of not only the form/state, distribution and concentration of the contamination but also its mobilisation and environmental longevity, is required to determine its full radiological and toxicological impact.

In contrast to the large number studies undertaken by Japanese research institutions and organisations, this work and the associated Fukushima-related publications represents that of a single UK-based PhD student. The results and conclusions from each chapter are hereby detailed:

Chapter 1

In this chapter, a background to the power generation operations and the infrastructure at the FDNPP was provided, alongside an overview of wider nuclear energy production in Japan. A description of the sequence of events and radiation releases that together constituted the accident were additionally provided. A summary of the material release estimates made after the accident was also detailed - these included extensive reactor core modelling in addition to evaluating the post-accident conditions of each reactor and its associated fuel storage ponds.

Chapter 2

A description of the radiation monitoring response to the accident was described; comprising initial high-altitude aerial surveys, leading to lower-altitude aerial platforms, foot-based, vehicular and oceanic survey types with time. The extensive evacuation areas that were instigated as a consequence of these surveys by the Government of Japan were also illustrated in this chapter in addition to the large-scale remediation activities (which are currently ongoing). A discussion of the various source attribution studies that have sought to delineate the landward contamination into that resulting from each distinct reactor Unit release was also included. Central to this source attribution was the forensic analysis of the particulate encountered within the environment as well as the radiocesium ratios (both activity and atomic) - a review of the studies to-date was also included in the final portion of this chapter.

Chapter 3

In addition to introducing the basic principles of radiation detection and the radiation detectors used in this work, this chapter firstly described the ground-based monitoring systems devised at the University of Bristol as part of this thesis as well as their calibration and initial testing. Alongside these "traditional" monitoring systems, the setup and calibration of a low-altitude unmanned aerial vehicle for radiation mapping, also produced at the University of Bristol, was additionally detailed. Through the application of test-sites in the UK and Japan, the idealised operational parameters and height normalisation processing to derive an on-ground dose-rate were together determined.

Chapter 4

In this chapter, the geographical locations and sample characteristics of the bulk organic material containing the micron/sub-micron *atmospheric particulate* was detailed. The same sample specifics pertaining to the sub-mm *ejecta particulate* (obtained from localities much closer

to the Fukushima facility) were also described as well as the multi-stage process employed to identify and separate these particles from the surrounding bulk sediment, lichen, moss or dust matrix.

Chapter 5

This chapter detailed the extensive suite of analytical instrumentation used throughout this thesis - applied to both the *atmospheric* and *ejecta* type particulate material.

Chapter 6

The results of contamination monitoring at selected sites around Fukushima Prefecture were presented. Through the use of ground-based, but more extensively from the low-altitude unmanned aerial vehicle (UAV) surveys capable of mapping γ-radiation intensity, it was determined that such Cs-containing fallout material was characterised by a high degree of environmental mobility. This ephemeral nature of such γ-emitting contamination was best-evidenced at sites for which previous remediation activities had occurred, prior to rapid re-contamination.

Radioactive "hot-spots" in each instance were associated where the solid material was trapped, or fluids transporting material would lose sufficient energy to deposit any particulate they carried. The application of this high-resolution site surveying permitted for the highly targeted collection of sample material for later use in this study.

Results from other sites highlighted the significant influence of water on the redistribution of radiocesium. This was attributed to; (i) the high clay/mica-type mineral content of Fukushima soils, (ii) the high affinity of Cs for sorption to the highly-reactive frayed-edge sites of such particles and, (iii) the ease of entrainment and transportation (mobility) of these fine-scale particles in fluvial systems.

Although remediation activities (e.g. scrubbing, sweeping and high-pressure washing) were observed to significantly reduce the overall contamination on horizontal (typically anthropogenic) surfaces such as roads, walls and isolated agricultural fields, the topographically extensive nature of Fukushima Prefecture was invoked to result in considerable and ongoing movement and relocation of the fallout-containing material. As a consequence of the easily remediated features being limited in their frequency (in comparison to the harder to decontaminate valleys, forests and sloping fields) across the Fukushima Prefecture, remediation is likely to continue within the contaminated regions for decades to come.

Chapter 7

In this chapter, the spatial distribution of *atmospheric particulate* (micron and sub-micron in maximum dimension, with a diverse elemental composition) sampled from across the Fukushima fallout region was examined. It was observed that across all particle compositions, a linear reduction in the average particle diameter occurred with increasing distance (along the length of the plume) from the FDNPP site. While this same size vs. distance correlation was determined for particulate of numerous compositions, the same linear decrease in average size was conversely not observed for others.

Resulting from; (i) the lack of a positive distance vs. average particle diameter correlation shown by potentially nuclear-sourced materials, (ii) a negative distance vs. average particle diameter correlation for other potentially nuclear-sourced particulate, and (iii) a strong positive distance vs. particle diameter correlation shown by similarly-sized particulate with a composition unattributable to a nuclear origin - other anthropogenic source(s) contributed to the particle populations observed. These non-nuclear derived anthropogenic particles (and their as yet undetermined source) would dilute or otherwise obscure any forensic particle signature attributable to a Fukushima release. However, irrespective of their source, the occurrence of micron-scale particulate of the compositions encountered could represent a health hazard owing to both their readily-inhalable nature and in some instances, their high level of chemotoxicity (e.g. Cd and U).

Chapter 8

Analysing the U-containing particulate formerly identified in Chapter 7, the work detailed in this chapter represented the first study to-date on the micron-scale actinide containing particles isolated from organic (substrate) materials. Despite being observed to exist at thirteen of the fourteen sampling locations, the U-containing material analysed in this initial study was collected from a single sampling site; the heavily-contaminated Iitate Village. To undertake this, a novel method for their removal and characterisation was first developed.

It was determined that the U-containing particulate from Iitate Village was anthropogenic in origin - and attributable to the release from the accident at the FDNPP. Isolated from an area contaminated exclusively by reactor Unit 2; the existence of U demonstrated that the reactor core and its surrounding containment had been compromised, despite the absence of an explosive release event - experienced by the other (1 and 3) reactor Unit buildings.

This occurrence is believed to represent a considerable health risk as a consequence of U chemotoxicity. Whereas the current "risk map", and therefore evacuation zones, are defined by the distribution of radiocesium and the resulting dose-rate, a re-evaluation (of the location

and extent of the various Fukushima evacuation zones) should be performed to incorporate the existence of this highly-toxic actinide material. As material irrefutably derived from the core of the FDNPP was observed to exist at a location 35 km for the site, it was suggested that more significant (size and activity) core material was likely to exist at localities closer to the plant boundary.

Chapter 9

In Chapter 9, a larger (sub-mm) *ejecta particle* attributed to have been derived for Unit 1 was analysed using a suite of high-resolution techniques. The carefully selected representative CF-01 particulate was observed to exhibit a highly-textured exterior surface (fibrous in appearance), with 24% of the particles total volume comprised of largely independent voids. Through the application of synchrotron radiation analysis techniques, Cs was shown to be distributed with considerable heterogeneity within the sample, concentrated as small, isolated regions around its exterior - strongly associated in the most part with the location of Fe (steel). These results correlated well with the very limited number of earlier Japanese x-ray based studies - each detailing a compositional heterogeneity (albeit at lower spatial resolutions) for such Unit 1 sourced material.

The periphery of the material contained both Ca and Fe rich zones - determined to represent the inclusion of both structural concrete (cement) and steel respectively. As a result also of synchrotron radiation analysis, the CF-01 particulate was shown to contain µm-sized particles of a high density material (believed U composition material) - similarly peripherally located (the analysis of which was detailed in Chapter 10). The formation mechanism for this CF-01 *ejecta material* was believed to have resulted from the immense heat and pressures generated in the PCV by the LOCI - alongside the rapid depressurisation of molten materials immediately proceeding the reactor buildings highly-energetic hydrogen explosion that occurred on the 12th March 2011.

As a consequence of the elevated temperatures that existed associated with the PCV at the time of the incident, the surrounding Si-based thermal insulation material would have undergone a degree of melting - exsolving volatile species to produce internal an gaseous volume. Existing within a "softened" state, the high pressure and temperature reactor-sourced gases (namely Cs) were coincidentally able to diffuse into (the periphery) of the material. The subsequent ignition of the flammable hydrogen component of these gases then caused the explosive fragmentation and dispersion of this insulation material, with the incorporation of similarly fragmented, structural material - the Fe component of which (through known Fe-Cs sorption) contained a more significant Cs content than had diffused (under pressure) into the particle volume.

It was observed that the larger diameter FT-13 sample, in contrast, possessed few of the features associated with the representative sub-mm CF-01 particulate. While similarly composed of a Si matrix, this Unit 2 sourced particle was shown, however, to contain no discernible internal porosity. As well as this void absence, no extensive surface or near-surface particulate existed (aside from a small number of near-pure Fe composition material), occurring at greater depths within the amorphous and structureless mm-sized particulate.

The different form of this FT-13 particle to the CF-01 material was invoked to have resulted from their contrasting source and hence formation mechanisms. Produced as a consequence of a PCV breach (and not a reactor building hydrogen explosion), this reactor Unit 2 sourced *ejecta particulate* was believed to have resulted from the similar melting of the Si-based insulation that surrounded the PCV (with the diffusion of gaseous and volatile Cs). However, following the more extensive melting of the fibrous Rockwool™ than that associated with the CF-01 material, the internal (fibrous) form, and porosity, were lost. The absence of extensive "embedded" fragments was a consequence of the unexplosive nature of the release.

Chapter 10

Further analysis of the CF-01 *ejecta particulate* was performed using SR-μ-XRF, SR-μ-XANES and SIMS isotopic analysis. The existence of Cs, associated with metallic Fe, was further shown. This correlation increased the confidence in the earlier results, and was suggested to represent the strong sorption of reactor-derived Cs onto the surfaces of Fe-based (steel) components. The bulk of the sample was also shown to contain a near-homogeneous Sr content alongside isolated Pb-based composition region, observed themselves to additionally contain both Br and Se.

The SR-μ-XANES analysis of the suspected micron-scale U particulate from Chapter 9 confirmed this material to be U(IV) as UO_2 - identical to that of nuclear fuel (but also the naturally-occurring Uraninite mineral). From SIMS analysis on one of these U particles, a non-natural U ratio was observed. This recorded U enrichment (3.51 wt% ^{235}U) was ascribed to result from material derived from Unit 1 at the FDNPP. The accompanying SIMS analysis of a Cs-rich region was similarly attributed to the FDNPP Unit 1, reinforcing this conclusion. Additional SIMS analysis of the FT-13 particle observed the distribution of radiocesium associated exclusively with the particles outermost circumference.

The U containing material was concluded to not represent a significant environmental hazard in its current glass encased form and insoluble oxidation state. However, the fragmentation of this particulate in the environment was invoked as a mechanism through which a release of this readily-inhalable and chemotoxic U could possibly (though not likely) occur. Although not directly detected due to limitations in instrument sensitivity, the occurrence of reactor-sourced U was

believed to illustrate the likely co-existence of other (toxic) actinide species (e.g. Pu, Am or Cm), themselves presenting far greater environmental implications.

11.2 Conclusions and implications for Fukushima

Examination of localities using an unmanned aerial vehicle (UAV) radiation survey system was illustrated - validated using comparable ground-based surveys. The platform was shown to be capable of examining regions of interest with metre-scale spatial resolution, comparable to the best resolutions otherwise attainable (on-ground). Alongside little or no dose exposure to an operator, the platform was proven to permit for the study of difficult or previously inaccessible locations.

The application of principally low-altitude UAV systems alongside on-ground radiological mapping of contamination has correlated with the findings of earlier speciation studies on the form and behaviour of fallout radiocesium. As a consequence of it's micron-scale grain size, this Cs-bound particulate was observed to be readily-mobilised under meteoric and fluvial conditions. This work has shown that whilst ionic (solution) Cs was immobilised through its binding onto solid surfaces, the readily transported nature of this fine-scale material (onto which it binds) represents a significant issue (and challenge) to the remediation effort. This material mobility can be viewed as highly-beneficial when associated with localities close to fluvial bodies, serving to reduce the overall contamination - whereby material was shown in this study (in support of other previous works) to be transported outwards into the Pacific Ocean, before being rapidly diluted [277].

This mobile particulate, however, was found to exhibit two specific behavioural caveats as part of this study. Firstly, at locations whereby fluids carrying the fine-scale Cs-bound particulate lost sufficient energy, the suspended materials they contained were deposited. The results obtained using the UAV highlighted significant radionuclide pre-concentrations (from an initially uniform contaminant distribution) at positions on a moderately-inclined site, containing a substantial irrigation network (typical of most crop producing sites of this type). The second, similar, behavioural anomaly was associated with the small number of buildings that exist, all surrounded by forested hillsides. Resulting from the significant surface features/textures shown by these buildings, fine-scale particulate-bound Cs was shown to have blown from these trees and become entrapped within gutters, tiles or in the roof-mounted solar panels.

This occurrence of particulate Cs represents a significant challenge in the large area remediation activities that are currently on-going across the *Special Decontamination Area* to reach the targeted dose-rates. Being highly-mobile, the re-contamination of previously remediated lower portions of hillsides as a consequence of downslope migration (slope instability) will invoke the dilemma of requiring the repetition of the costly and operator intensive decontamination

exercise. This will produce further volumes of LLW requiring adequate long-term disposal. As an additional consequence of its mobility, and as observed in this work, significant attention will be required when assessing contamination associated with buildings and other anthropogenic sinks for radioactive material (e.g. the sewage network).

Examination of particulate samples described in this work has demonstrated that they can be classified into either one of two distinct groupings; the smaller (µm to sub-µm sized) *atmospheric particulate* and the considerably larger (100's of µm in maximum dimension) *ejecta particulate*. The smaller (and generally more angular) material was characterised by a limited elemental composition, constituted by up to three (but more commonly a single) transition metal, post-transition metal, metalloid, lanthanide or actinide element - alongside various non-metals (O, P, S and Cl) and alkali/alkali earth elements (Na, K, Mg and Ca), believed to represent a background introduced by the sediments/organic matter within which it was contained and analysed. Whilst this work has shown a distance versus particle diameter relationship for material with certain compositions, the same trend was not, however, associated with *atmospheric particulate* of other compositions. This variance was attributed to contribution from one or more anthropogenic sources, unrelated to the FDNPP accident.

Subsequent work, examining a number of these U-containing *atmospheric particles*, through SR-µ-XANES, highlighted that each was formed of U(IV) as UO_2. This material was analogous in its structure not only to the naturally-occurring Uraninite mineral, but also that of nuclear fuel, and as such was invoked to have likely resulted from the FDNPP. These synchrotron results, suggesting a potential nuclear provenance, were validated by the observed existence of Cs - distributed homogeneously within a U-containing particle. The presence of these nano-scale U-Cs fragments confirmed that Fukushima-derived material exists within the environment as a consequence of a breach of the core-containing RPV and also the surrounding PCV. This observation correlated with the limited prior studies on the sub-µm U sourced from Unit 2 [192, 371] - although this work represented the first observation of such actinide material not enclosed within the centres of the now infamous "Cs-balls".

The larger *ejecta particulate* was in contrast, found to be more complex, both compositionally and structurally, than the smaller *atmospheric particulate*. Using non-destructive SEM, EDS, XRT, XRF and SR-µ-XANES alongside destructive FIB and SIMS analysis, various attributes of the representative CF-01 particle were shown - including the bulk of the particle being constituted of fibrous glassy Si-based material. This sub-mm particle had a complex internal structure comprised of a bimodal pore volume (constituting 24% of the total particle), while the particles exterior circumference was shown to contain fragments of both cement and steel. As well as other fission product species, the particle was additionally found (via SR-µ-XRF) to contain isolated (micron-sized) regions of Cs - associated with not only the smaller sized voids but also at the same

positions as the Fe composition inclusion particulate, together distributed around the largely Si-based particles perimeter.

Alongside Cs, using SR-μ-XRF, particles of U were observed to exist around the particles circumference. The additional application of SR-μ-XANES analysis on this U particulate found it existed in the U(IV) oxidation state, as UO_2. The wt% ^{235}U enrichment within one of these particles supported the $^{135}Cs/^{137}Cs$ atomic ratio and illustrated the material was sourced from the FDNPP reactor Unit 1.

This work has shown that it is possible to detect and extract individual micron-scale and sub-micron U particles within environmental media, even when such material was either enclosed within larger particulate or dispersed widely amongst sediment, dust or various organic bulk samples. The existence of radiocesium, bound to the surfaces of microscopic solid particles, will present a challenge to the large-scale remediation of the *Special Decontamination Area*. This materials mobility, combined with the topography of the region, will require repeated remediation activities be conducted at sites across Fukushima Prefecture, generating further volumes of contaminated surface-derived wastes.

Unlike the radioactivity hazard resulting from the existence of radiocesium in the environment, the presence of U represents a contrasting toxicology hazard, exacerbated by its readily-inhalable and ingestible particle size. Owing to the current evacuation and hence "risk map" being defined by the radiocesium dose-rate - whereby repopulation is permitted once permissible dose-rates are achieved (<20 mSv per annum [155]), this existence of chemotoxic U and a possible coexistence of other actinides, should warrant a redefinition of this "risk map" and the continuation or implementation of evacuation/restricted access areas.

It should be noted, however, that although dose-rates encountered across large regions of eastern Japan are now elevated above those before the FDNPP accident, locations with greater levels of naturally-occurring radioactivity exist. One such example is Cornwall in the south-west United Kingdom, which shows an elevated radioactive background across the entire region. Despite localities such as Tolgarrick Mill (employed as a calibration site in this thesis) exhibiting average dose-rates of >15 μSv h^{-1} (and a maximum of 215 μSv h^{-1}) from the decay of U-series elements, no evacuation orders or restrictions on habitation exist. With the majority of the plume region exhibiting dose-rates less than those measured in Cornwall, (as of November 2017), a repopulation of regions of Fukushima Prefecture contaminated exclusively by radiocesium (and not actinide species) represents a logical step in the regions recovery. This not only allows for citizens once displaced from their homes to return, but for the considerable financial cost associated with the remediation to be saved.

The mathematical assessment of the relocation measures employed following the FDNPP accident were examined (and compared to those which occurred in the aftermath of the Chernobyl accident) in the works of Waddington et al., (2017) [158], and Thomas et al., (2017) [428]. This Judgement or "J-value" evaluated any benefits to human life as a consequence of the evacuation against any detrimental health effects (on the population demographics) of such a mass-relocation. These studies concluded that based upon the current radiation distribution (solely of radiocesium) within Fukushima Prefecture, that the mass-evacuation of citizens should not have occurred - with the "life enhancement" brought about by such an evacuation being considerably less than the "life detraction" resulting from the stress of the relocation process. However, as this assessment does not consider the existence of actinide species within the environment - a reassessment of these conclusions is required with this new, crucial insight.

There are, however, limitations to the results presented in this thesis with respect to both the meter-scale and single-particle analysis. One limitation pertinent to the high-resolution (meter/sub-meter) mapping of radiation using the low altitude UAV, resulted from the innovative nature of the platform. Due to the UAV-mounted detection system performing surveys at altitudes not formerly employed, it was necessary to derive appropriate height normalisation algorithm(s). While ground-validated corrections were derived (and successfully applied in this study) for scenarios exhibiting either planer or point source geometries (or combinations of both), some divergence from predicted values was associated for a number of more complex radiation fields. Therefore, applying the current height normalisation procedures, to more intricate distribution scenarios would yield considerable uncertainty until further calibrations and modelling can be undertaken.

The limitation of the particulate analysis component of this study was the small number of particles, of both types, from which these conclusions were based. The U composition *atmospheric particulate* from the Iitate Village area was selected; (i) as a site known to have been contaminated exclusively by reactor Unit 2, and (ii) the bulk samples collected from the locality were found to contain a large volume of U composition fragments. To permit for the efficient and sequential multi-technique analytical process to be developed and subsequently performed, a decision was made to focus exclusively on a single representative "large" *ejecta particle* (CF-01) throughout this study. However, this single CF-01 sample was selected as it was representative of the entire suite of particulate isolated from the locality bordering the FDNPP site following initial pre-screening.

11.3 Future work

This thesis has presented an analysis of the March 2011 Fukushima Daiichi Nuclear Power Plant accident at two contrasting length-scales - highlighting, amongst other results, the complex form and composition of the *ejecta particulate* material. It also successfully demonstrated the

development and application of a multi-technique methodology (and necessary sample-handling procedure) for investigating such sub-mm material. There are limitations in this work, however, which are discussed above, some of these are overcome in the suggested future work:

1. Apply additional UAV calibration studies across multiple sites at a range of survey altitudes - each exhibiting differing radiation distributions. This is to provide additional data to validate/compound the height versus intensity calibration(s) described in this thesis.

2. Apply the low-altitude unmanned aerial vehicle to further characterise the transport and environmental mobility of radiocesium. This assessment is centred on determining the radiation intensity across agricultural sites, buildings and forests, otherwise inaccessible and therefore not readily assessed.

3. Extend the analysis of the micron-sized U composition material, from the one site in this work to the numerous other sites where this study observed similar U-containing material to exist, along the length of the main north-west trending (Unit 2) plume. This is to determine if the particulate (shown to increase in diameter with proximity to the FDNPP) can be attributed entirely to the power plant release, or from an alternate source.

4. Apply the analytical techniques described in this thesis to further similar samples that have been obtained from the Cambridge Filter Company (CF designation). This is to principally identify if any consistency exists in both the structure and composition of this particulate, collected from a single sampling location, attributed to the FDNPP reactor Unit 1.

5. Apply these same techniques to the similar sub-mm material, obtained from additional sites, likewise contaminated by the reactor building explosion that occurred from the FDNPP reactor Unit 1.

6. Undertake a solubility characterisation of the fallout particulate to determine the extent of any actinide (and other species) leaching should such *ejecta particulate* become fragmented.

7. With a sample of Unit 1 sourced material now analysed in addition to material attributed to Unit 2; apply analysis techniques developed and implemented in this thesis to any material subsequently isolated and attributed to the FDNPP reactor Unit 3. As this reactor core was operating with 32 MOX fuel assemblies, a discernible Pu signature, distinct from each of the other reactor Units, would likely be observed.

8. Apply these sample preparation and analysis techniques to "hot particles" from other worldwide sites. This could include materials from; (i) *Windscale and Sellafield* (assessing contributions from both Windscale fallout trapped in the Ravenglass (Seascale) Salt Marsh and effluent derived from both modern and historic activities at the Sellafield Ltd. nuclear

287

reprocessing site), (ii) *Palomares - Spain* and *Thule - Greenland* (aircraft crashes involving the transportation of thermonuclear weapons), and (iii) *Canadian Shield* (failed and crushed Russian Cosmos 954 satellite that widely-dispersed its Pu composition nuclear fuel-cell).

9. Utilise the I14 nano-focus XAS beamline at the Diamond Light Source to produce EXAFS data to determine the Fe-Cs co-ordination chemistry associated with the Fe-based fragment protruding from the surface of the representative CF-01 *ejecta particle*, examined extensively in this work.

A

RADIATION SURVEY METHOD COMPARISON

All values presented in this appendix are typical for each of the systems cited.

Manned Airborne

System mass (kg): >5,000

Example platforms: C12 (plane) and UH-1 (helicopter)

Flight duration (minutes): 120 - 300

Flight altitude (m): >150 (by law)

Survey length (m): >200,000

Velocity (m/s): 0 (hover) - 125

Detector payload (kg): >100

Spatial resolution (m^2): >250,000

Advantages: large survey areas, long flight durations, high-volume detector, extensive prior system applications, terrain independent, weather independent.

Limitations: expensive upkeep and operational costs, manual operation, strictly controlled by aviation law, radiation exposure to crew, requirement for trained pilots, poor spatial resolution.

References: [85, 86]

Unmanned Helicopter and Fixed-Wing

System mass (kg): 70

Example platform: Yamaha R-MAX

Flight duration (minutes): 90 - 360

Flight altitude (m): 50 - 100

Survey length (m): 3,000 - 5,000

Velocity (m/s): 0 (hover) - 15

Detector payload (kg): 10

Spatial resolution (m^2): 25

Advantages: no operator dose, fully-autonomous, terrain independent, low(er) cost of purchase and uptake than manned platform, prior agricultural applications, moderately sized detector.

Limitations: Operator training still required, greater operational altitude than UAV platform, adherence to aviation guidelines still required.

References: [93–95]

<div align="center">

Unmanned Aerial Vehicle (UAV)

</div>

System mass (kg): <7

Example platforms: University of Bristol AARM UAV and Virtual Robotics Italia UAV

Flight duration (minutes): approximately 45

Flight altitude (m): <15

Survey length (m): 1,000

Velocity (m/s): 0 (hover) - 8

Detector payload (kg): <1

Spatial resolution (m^2): <5

Advantages: no operator dose, fully-autonomous, low operational altitude, terrain independent, low-cost, simple operation, lightweight, minimal user training, rapid deployment, high spatial resolution.

Limitations: Small detector volumes (lower sensitivity/total count rates), limited flight durations, limited spatial coverage, young technology, highly weather dependent.

References: [100, 101, 429]

<div align="center">

Ground-Based

</div>

System mass (kg): N/A (must be transportable)

Example platforms: Safecast [105]

Flight duration (minutes): N/A

Flight altitude (m): N/A

Survey length (m): N/A

Velocity (m/s): N/A

Detector payload (kg): typically <1

Spatial resolution (m^2): <1

Advantages: very low cost, no requirement for "carrier" vehicle, readily deployable, extensive prior applications, little or no prior training required for application.

Limitations: Small detector volumes (lower sensitivity/total count rates), potentially significant radiation exposure to operators, bodily influence of radiation shielding upon results, slow rate of data acquisition, limited ground coverage and to accessible areas, terrain dependent.

References: [105]

Software used in the production of this Thesis

The software used during the analysis and associated visualisation of the data obtained during this thesis is hereby detailed.

FEI Amira-Avizo™ (version: 9.2) - Interactive visualisation and manipulation of 3-Dimensional data sets using a combination of visual programming (flows) and conventional scripted language.

Demeter (version: 0.9.26) - A suite of opnen-source software programmes (ATHENA, ARTEMIS and HEPHAESTUS) based around an further open-sourced set of perl modules with a user front-end using the IFEFFIT graphical environment. The combined suite allows for the representation, interrogation and quantification of x-ray absorption spectroscopy (XAS) data.

EDAX TEAM™ (version: 7.4) - An Energy Dispersive Spectroscopy (EDS) system for detector control, analysis and subsequent quantification of characteristic x-ray results from a scanning electron microscope. Corrections to data based upon the ZAF/eZAF algorithms are automatically undertaken within the software.

GEANT4 (version: 10.4) - Geant4 is an open-source toolkit for the simulation of the passage of particles through matter. Its areas of application include high energy, nuclear and accelerator physics, as well as studies in medical and space science.

ImageJ (version: 1.51w) - An open-sourced Java-based image processing program with architecture allowing for both software library-obtained as well as bespoke user-written macros and plugins to be utilised to manipulate various data and image formats.

KSpect™ (version: 18.4.201) - A multichannel analyser software application that acquires and displays the data from Kromek™ branded USB-based gamma-ray spectroscopy devices (e.g. SIGMA-50 and GR1).

LabVIEW™ (version: 2015 SP1) - A proprietary system design platform and development environment allowing for the visual (opposed to command-line based) programming language developed by National Instruments (NI). The environment features a large number of downloadable plugins to permit for the ready signal integration from a number of input software or hardware platforms.

OriginLab™ (version: 2018b) - A proprietary program for interactive scientific graphing, data manipulation and analysis. Capable of producing both 2D and 3D graphical representations, the software also includes a scripting language based upon the C/C++ compiled language (Origin C).

PyMCA (version: 5.3.1) - A stand-alone open-source graphical user interface (GUI) application and associated Python scripted tools developed at the European Synchrotron Radiation Facility (ESRF) used for the batch-processing, deconvolution and quantification of synchrotron x-ray fluorescence (XRF) data.

XM3D-Viewer™ (version: 2017.2) - Proprietary software from Zeiss Ltd. for the reconstruction, presentation and manipulation of large tomographic dataset obtained using the Zeiss Xradia Versa 520 X-ray Microscope (XRM).

Zeiss ZEN - Blue (version: 2.0) - Automated graphical analysis software for images obtained on Zeiss electron and optical microscopes. Size, volume and area analysis is automatically and simultaneous performed on uploaded images of .tiff or Zeiss proprietary formats.

C

DATA PRODUCED DURING THIS WORK

Data from this work is included on the CD enclosed at the rear of this Thesis.

NUCLEAR SECURITY REVIEW - ENERGY POLICY

The Future of Nuclear Security: Commitments and Actions - Power Generation and Stewardship in the 21st Century.

P.G. Martin, N.G. Tomkinson and T.B. Scott

Abstract

Since the terrorist events of the 11th September 2001, the world as it was once known was changed forever. It was these catastrophic terrorist actions over fifteen years ago that saw the dawn of a new era with heightened security across many everyday areas of society that had not previously witnessed such scrutiny or control. Coupling this elevated risk of physical and technical aggression with the ever-increasing global per capita energy demand - there has been witnessed a continually growing reliance on nuclear energy for baseline power generation, a form of electricity production that requires both the necessary international safeguards and controls for its safe use. As more and more of the global energy budget is provided by low-carbon sources (over polluting fossil fuels), the volume of nuclear material in existence will grow substantially - requiring considerable attention and policy to ensure its long-term safety and security.

This commentary describes the vast range of policy challenges faced by the nuclear industry resulting from the rapid technological advancements being made across society, and how these directly (and indirectly) affect global nuclear security, as well as providing a thorough discussion on how best these challenges may be overcome.

1.0 Introduction - A change in the global energy budget

With 2011 marking the year in which the world population first exceeded 7 billion , current estimates place 2021 as the year when 8 billion people will inhabit our planet [430, 431]. It may seem logical to conceive that the global energy requirement is a direct consequence of the total global population - with more people requiring access to electricity. Whilst the global population explosion is in-part responsible for our total energy requirement, it is the total energy consumption per capita (Figure D.1 (a)), that is the ultimate driver behind our total power requirements globally. Whereas at the beginning of the 1980's where the average person did not own a computer, several televisions and games consoles or large air-conditioning units, such items are now commonplace and have resulted in a near two-fold increase in the amount of energy used per person between 1980 and 2017 (Figure D.1 (a)).

Resulting from the considerable environmental impacts brought about by the burning of traditional fossil-fuels (coal, oil and natural gas), combined with their ever-declining availability (physically, and also through various geo-political circumstances) as well as considerable technological drivers, has led to a divestment in power produced through these means, and what is viewed by many as a "renaissance" in nuclear power [434–436]. Because of this increasing drive to liberate the vast quantities of energy stored within the atom, after a brief recession from 2010, the per capita proportion of nuclear power contributing to the global energy budget is increasing (Figure D.1 (b)). This resurgence in nuclear energy (albeit later that many foresaw) is similarly paired with a corresponding reduction in the proportion of fossil fuels consumed. As shown graphically within Figure D.1 (c), global fossil fuel consumption (per capita) has begun to decline - with this reduction enhanced further if China (the largest consumer of fossil fuels) is excluded (Figure D.1 (d)) [432].

However, despite this observed growth within the sector, is it the opinion of many that such a renaissance has not occurred and that any upturn in nuclear growth is considerably smaller than was once envisaged (or widely-sold). This is often ascribed to the fact that the building of new nuclear power plants is not economically viable via private investment, given the vast initial facility construction costs and the extended time for payback on such investment [437–439]. Works including these also cite the lack of large-scale facilities globally to deal with the wastes that are produced by the nuclear fuel cycle, in spite of the technological progress and new facilities witnessed in northern Europe (Sweden and Finland) [440].
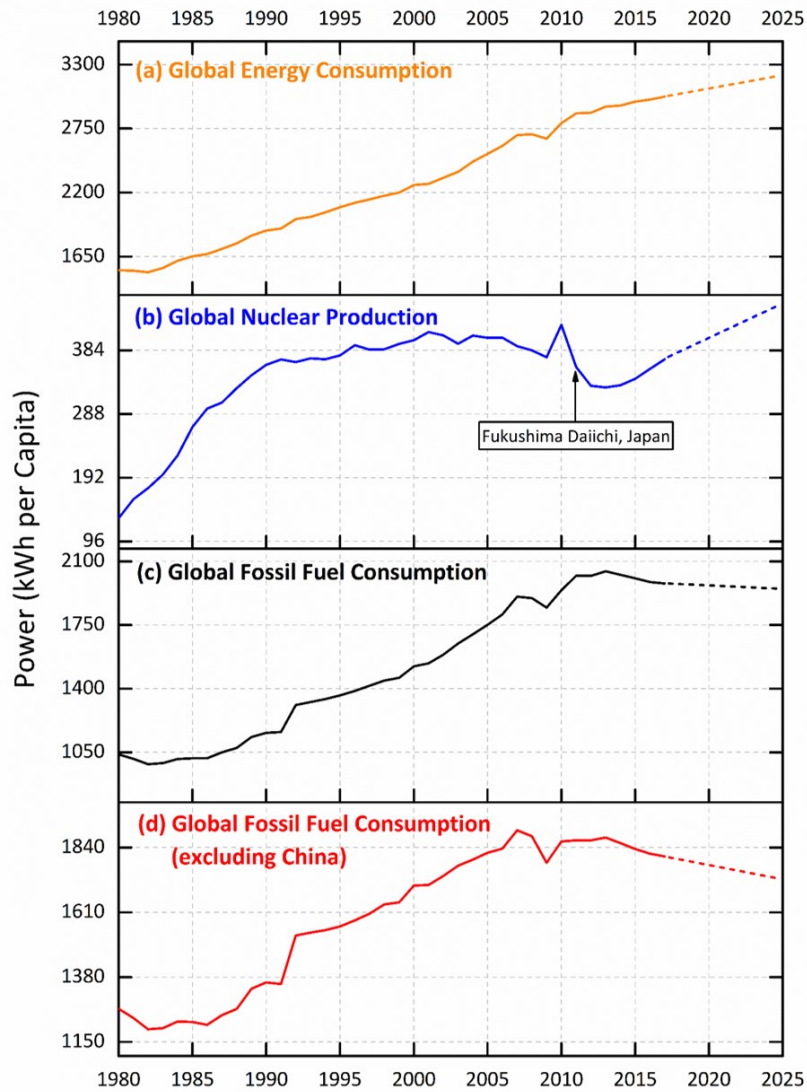
Figure D.1: Per-capita: (a) Global Energy Consumption, (b) Global Nuclear Power Production, (c) Global Fossil Fuel Production, and (d) Global Fossil Fuel Production - excluding China (energy statistics and population). *Data obtained from [430, 432, 433].*
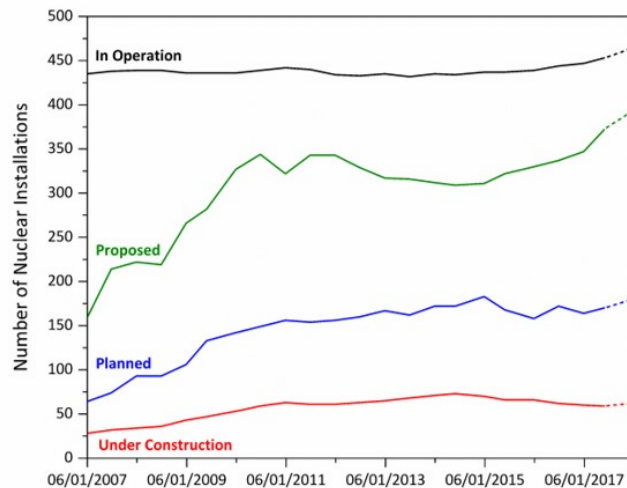
Figure D.2: Breakdown of global reactor inventory over time, an increase across all categories is observed. The following definitions are used in each case: "In Operation" - first connection to power distribution grid, "Under Construction" - first concrete poured at site, "Planned" - final approvals and funding in place and likely operational within 8-10 years and "Proposed" - initial plans made public and site selected for suitability studies. *Data obtained from [353, 433].*

Such resurgence in nuclear is further demonstrated by not only the total number of nuclear facilities operating globally, but also the total number of plants undergoing construction as well as those at the planning or initial design (proposal) stage, as shown graphically within Figure D.2. Following the 2011 Fukushima Daiichi Nuclear Power Plant accident in Japan, several countries elected to halt their nuclear programs, including Japan and Germany. Whilst this represented a significant number of facilities to enter shutdown - as is shown in Figure D.2, this was balanced by many reactors entering service in other countries. It is estimated that by 2035, approximately 130 reactors will enter retirement, however these will be replaced by nearly 300 new units - many of which will provide a considerably larger power-generating capacity [8, 353].

2.0 More material, more risk?

Consequently, with more nuclear reactors located in ever more countries, there exists (and will rise still further), a record amount of nuclear material of varying types (e.g. enrichment, form and radioactivity) distributed globally [353]. This presents considerable security, transport and health risks associated with all stages of the materials lifecycle; from fuel precursors through to spent fuel reprocessing, to wastes and final disposal. A plot illustrating the global uranium production directed into the fabrication of fresh nuclear fuel for use in reactors is shown within Figure D.3. Despite annual fluctuations in the volume of material entering fabrication, there is still evident a steady increase in material entering the nuclear fuel cycle.
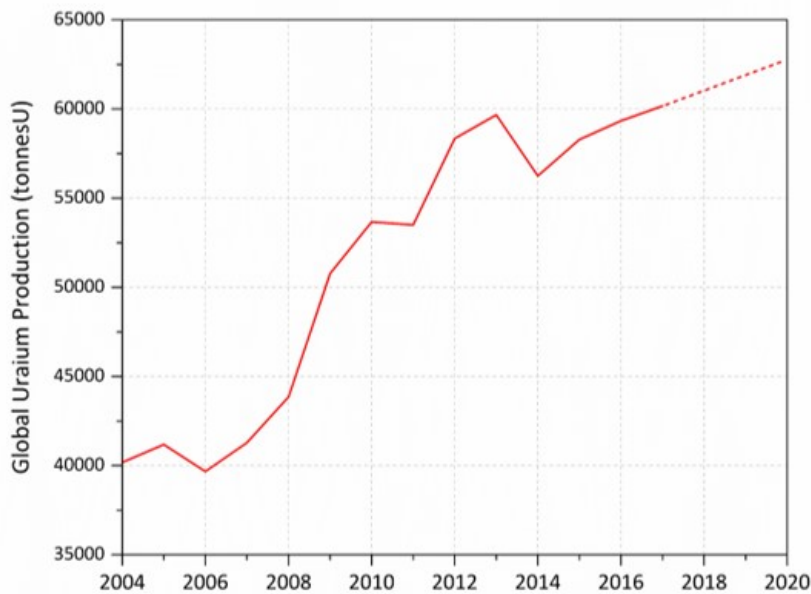
Figure D.3: Global uranium production (tons) directed to the production of new nuclear fuel assembles. *Data obtained from [353].*

Recent advancements in nuclear fission technology towards Small Modular Reactor (SMR) systems, arising principally from their lower projected construction costs and reduced proliferation risk makes them (for the first time) viable for private investment (World Nuclear Association, 2017b). These perceived benefits of SMR technology have led many to speculate that the number of such units will increase rapidly, to constitute a considerable component of many countries total nuclear reactor inventory (Figure D.4).

Unlike "traditional" fission reactors which generate power in the order of 1000 Mega Watt Electric (MWe), these off-site manufactured reactors are designed to be brought on-site fully-constructed and produce an electrical output of less than 300 MWe during peak operation. Whilst it may be the viewpoint of many that the wider distribution of smaller volumes of radiological material represents an improvement for safeguarding material from those wishing harm - with any potential attack yielding access to only a comparatively small volume of nuclear material, these reactors will still need to be kept highly-secure and therefore require an effective Nuclear Site Security Plan, following INFCIRC/225/Rev.5 recommendations [442], as for any other nuclear installation.

Accentuated by this portended rapid and extensive growth in SMR‚Äôs around the world due in no small part to the differing systems produced by a large number of vendors detailed in a recent publication by the National Nuclear Laboratory [441], several key challenges and threats to
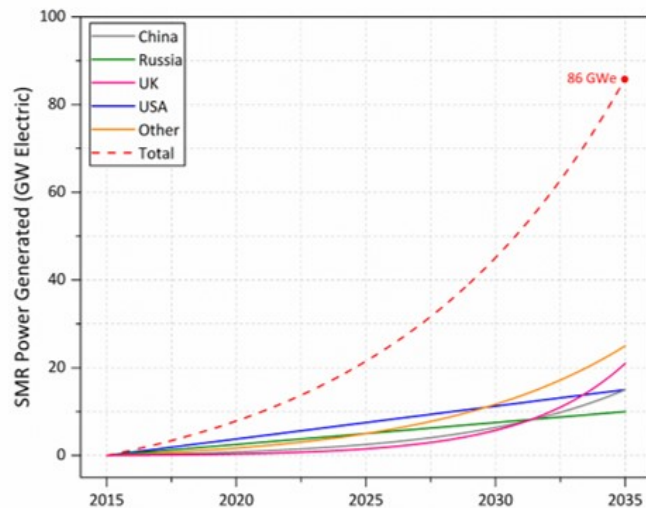
Figure D.4: Anticipated SMR growth forming part of global nuclear portfolio. Despite the apparent large uptake of small modular reactor technology to the year 2035, its share of the global nuclear energy generation market is small (world nuclear production in 2014 = 2.417×10^6 GWe). *Data obtained from [441].*

current (as well as future) nuclear security are apparent. As previously alluded to - the possibility of direct violent physical terrorism on nuclear infrastructure is considered the most obvious risk, and in the aftermath of recent global events, the threat of nuclear terrorism is now viewed by many international organisations to be as great as ever, as detailed in a number of summative works such as that of the Nuclear Threat Initiative (NTI), [443]. This "nuclear terrorism" can occur through actions such as direct physical attacks on nuclear power facilities, its transport network or the sites in which material is stored, potentially alongside coordinated cyber-attacks on the networks and systems that are utilised in the sector. Despite intense screening, the additional threat posed by insiders within these facilities cannot also be excluded. With terrorism defined not only as the use of violence, but also the threat of its use, suitable fear and anxiety exists even without any such acts ever occurring [444].

3.0 Keeping stock is keeping safe

Due to greater volumes of radiological material disseminated worldwide across the entire nuclear fuel cycle (from initial mining through to final waste reprocessing and storage), it becomes imperative for countries as well as regulatory organisations (such as the IAEA and Euratom) to accurately monitor radiological material, its location, form and enrichment state. Two related, yet contrasting aspects arising from this to impact future nuclear security are (i) smuggling: the act of moving material for monetary gain to criminal gangs and terrorist groups and (ii) proliferation: the spreading on nuclear material for weapons (typically clandestine) programmes.

The IAEA Incident and Trafficking Database (ITDB) [445], has reported a total of 2889 confirmed unauthorised possession and criminal activity incidents between 1993 and 2015 where material had been moved without authorisation and was intercepted by controlling authorities. Incidences where material has successfully been trafficked are obviously unreported, but it is highly likely that international policing efforts to prevent or intercept illicit trafficking of nuclear materials are not always successful. Such is evidenced by the regional variation in reported incidents made within the ITDB [445]. Whilst despite containing less nuclear material as a region [8], the total incidents of theft and loss within Asia is one-fiftieth of that of the USA, a disproportionality low amount.

With such growing risks associated with our future divestment in fossil fuel power; a central aim for the future of global nuclear security will be a strong commitment and requirement for (i) the physical and technical protection of nuclear materials, (ii) the meticulous accounting of nuclear materials, and (iii) the highly-accurate monitoring of nuclear sites and borders - incorporating a strong focus on evolving technologies, automation, robotics and the Internet of Things (IoT). However, whilst representing a key opportunity for improved safeguarding and monitoring, there lies a range of potential threats from each of these technologies (as is the case with any such system) if not employed for the correct means by those wishing harm through coordinated terrorist acts.

4.0 Threats and opportunities posed by new technologies

The rapid development of small but computationally powerful devices for a variety of industrial, domestic and recreational uses provides a rapidly evolving opportunity and threat register for nuclear facilities worldwide. As such, the topic of nuclear security is rarely out of the global media spotlight [446].

One such opportunity, but also a potential threat in the future of global nuclear security, is the rapidly evolving field of drone or unmanned aerial vehicle (UAV) technology. Accelerated markedly by the events at the Fukushima Daiichi Nuclear Power Plant in Japan, lightweight systems have been developed by a number of authors [95, 96, 226], each capable of achieving substantial flight durations and distances (>30 min and 10's of km). When combined with the range of existing available detection options, UAVs represent a means by which to gather large volumes of valuable data over nuclear sites or in response to radiological incidents. However, the availability of these systems to the public, coupled with the ease at which they are operated (using a combination of conventional hand-held remote controls and GPS way-points) has already been seen to impact upon operations surrounding airports - with numerous reports of unidentified aircraft or airspace incursions around the world [447].

The potential use of these systems for physical attacks (not only on nuclear institutions) has been viewed as significant by a UK think-tank [448], with a number of media articles also documenting recent global events [449, 450]. Possible scenarios range from (i) utilising drones to carry explosive materials into a nuclear site, potentially producing a criticality incident with the accurate targeting of key on-site facilities, and (ii) following the acquisition of radioactive material - using unmanned aerial systems to disperse this contaminant material over a wide area, or population centre.

Considerable recent advancements in artificial intelligence (AI) technology could prove beneficial for improving site monitoring using these UAVs and without the need for operator input and guidance. Conversely UAVs could also be employed in physical attacks [451]. In these cases, the UAV operator need not be in direct communication with the system during the attack with the drone targeting pre-defined positions on the ground. Whilst a lone, well targeted UAV system could cause moderate disruption and damage to a single item of nuclear infrastructure, a coordinated "swarm" could pose a much more substantial threat. The term "swarm" technology, was a concept introduced by Beni and Wang, (1993) [452], whereby multiple robotic systems can operate as a group independent of a human operator. UAV "swarms" could facilitate simultaneous coordinated attacks of a site/sites, using a significant number of airborne systems inbound from different heights, directions and at different speeds; in sufficient numbers such that existing defences would be overwhelmed.

The last ten years has also seen the accelerated advancement of battery technology with which to power these unmanned aerial platforms. As a result of considerable research effort from both industry and academia, the amount of electrical charge that can be stored within the same physical volume and weight has increased enormously [453]. Because of this, the typical survey duration possible with a UAV has grown, and hence accordingly, the distance from which attacks can take place has also increased.

4.1 Development of dynamic monitoring networks for nuclear monitoring

In addition to this remotely operated airborne technology, the use of other robotic systems, within advanced monitoring capabilities, contributes positively to the wider field of dynamic radiation monitoring. As a direct result of the extensive advancements that have occurred in radiation detectors and their miniaturisation, a powerful suite of technology now exists to enhance the current strength of nuclear security. This enhanced detection capability has enabled the production of "dynamic sensor networks", whereby a range of sensors can be deployed using a range of mobile platforms, all feeding back autonomously in near real-time to produce an extensive data network of a site or incident. The use of AI to process the numerous coincident

data streams, much like the human brain manages inputs from the body‚Äôs nervous system, means that temporal anomalies recorded by the sensors in the network representing a divergence from a known and calibrated baseline for the site can be rapidly verified and enacted upon.

As well as UAVs, mobile platforms able to carry these increasingly more capable radiation detection devices include humans and cars, however other (less mainstream) systems for dynamically monitoring radiation include hovercraft [454] and pipe-crawlers [455]. Current work to advance the scope of dynamic monitoring networks for nuclear security is investigating other remotely operated vehicles (ROVs) such as inflatable airships and miniaturised underwater submersibles.

Whereas dynamic sensor networks represent a means to actively "search" for radiation anomalies, their inherent complexity, with the required upkeep of the physical carrier platform, as well as the potential challenges in referencing their position over the duration of their survey means that static (fixed position) systems will always exist as a backbone within the future of nuclear site security onto which dynamic ones are incorporated. Again, with the recent progression in detector technology, numerous static systems that can be placed strategically around nuclear sites or dispersed within a public setting, for continual monitoring - typically based on gamma-ray detection [456, 457]. Typical examples of such systems include "portals" (typically large archways) and "pads" (everyday objects such as road cones, speed-humps and safety barriers) within both large arrays of highly-sensitive gamma-ray detectors can be installed to monitor for activity above normal background levels. Stemming from work at CERN (Large Hadron Collider), the application of muon tomography and scattering (utilising naturally occurring sub-atomic particles incident from space) for the detection as well as determination of the type of any radioactive source material, is a further detection method that now exists as part of the global nuclear security portfolio, most commonly for the scanning of entire shipping containers or large transport vehicles [458–460].

All of the detectors employed as part of dynamic systems are hence required to be both small and highly-portable, being widely dispersed via the aforementioned range of potential carriers to provide a wide spatial coverage. This distribution of hundreds, if not thousands (or hypothetically tens of thousands), of various sensor types and their real-time feedback to a single command point from where all of the information converges, is dependent on mass-network connectivity, the ability to stream (securely) data wirelessly at a sufficient rate and subsequently reprocess it efficiently [461]. Data acquired from static sensors presents less of an issue with regards to data transmission due to their fixed position over time, and hence less of a need for high-end data infrastructure and extensive coverage in the case of continually moving, dynamic systems. Through deploying this wide range of sensor options for monitoring, a "hub" from which all the platforms are capable from being dispersed and collating incoming data steam is required. This hub would typically act as a "node" via which data acquired by the systems would be collated

before transmission to a central data facility. There is also the potential for this technology to be used in a more covert method, to deliver a counter-proliferation capability, in identifying illicit nuclear weapons sites and materials.

4.2 Deployment of passive versus active sensors

Each of the detectors mentioned in the previous section may be referred to as "passive", whereby there is no external input of energy in order to stimulate the detection of any potential radioactive material [206, 462]. The contrasting type of system is what is termed "active". Unlike the smaller, cheaper and more readily transportable passive detectors, active type detectors require the production of highly penetrating beams to determine the internal structure of a large volume. Such systems include the use of neutrons, electron/neutron-induced gamma-flash or laser scanning to examine the contents of objects such as barrels and large containers [463, 464].

Like any electronic device; to enable it to function even for short periods it is required to receive power. For large, "active" devices this demand is considerable - with vast quantities needed for their operation, supplied through dedicated power networks. On the other hand, smaller "passive" devices which do not need to produce an activating source to detect radioactive material, call for markedly less power. As a result, potential exists for such low-power (static) devices (that remain stationary indefinitely) to benefit from advancements in long-term power supply for applications such as radiation store monitoring. Using natural radioactive decay; such as that associated with ^{238}Pu, ^{241}Am or more recently the β-decay of ^{14}C, a small but sufficient current can be produced to provide power to devices - acting as a "nuclear battery" to trickle-charge systems [465] (Patent Applications 17074485.6 and 62/504,012). The system (shown schematically within Figure D.5), using a diamond "tri-layer" surrounded by metallic contacts, has been invoked to be able to provide thousands of hours of current from materials otherwise considered as costly waste following power generation.

Current detector technology and the mechanisms by which to deploy it for continued nuclear security into the future have witnessed extensive progression over recent years, with great advancements in detector crystal production, miniaturisation and spectral resolution [466, 467]. With the explosion in the number of these detectors and limitless potential locations where they could be installed, the future will likely not lie in the detection hardware itself, but in their connectivity, automation, combined sensitivity and ultimately how best to utilise the "big data" generated by such a network of assorted sensor technology. Additional sensors can be incorporated alongside the radiation sensor in order to provide greater situational awareness around any detection incident. This enables a more detailed understand of what was in the area at the time of detection to help focus appropriate responses.
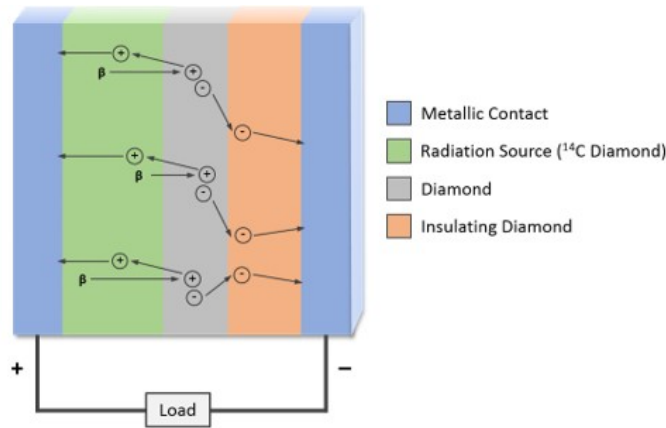
Figure D.5: Schematic of the proposed diamond battery, consisting of the multi-layer setup with differing forms of diamond (radioactive and stable) encased within metallic contacts. *Modified from [465].*

5.0 Data security and access

One of the fundamental questions to arise whenever nuclear site data is accumulated is how securely it is held, and who maintains a responsibility for its long-term security (stewardship). There are also additional issues centred on the correct data access and its presentation; making sure that those who require the data at varying levels are given the best and most complete access to it.

To produce high spatial resolution radiation monitoring with the greatest coverage achievable, data will be sourced from a range of not only different sensor types, but also different organisations and bodies. These organisations would typically include private companies such as power plants, reprocessing facilities and the operators of large indoor/outdoor event spaces in addition to public and law-enforcement groups. Whilst the data derived from these sources would constitute part of a combined data-map; certain data obtained from specific sites or found to constitute "interesting" or "abnormal" results may not be fully disclosed, representing issues surrounding data ownership and how information pertinent to nuclear security should be shared. To provide data into this combined system, complications arise surrounding its transmission and processing. Whilst the Internet of Things (IoT) is beginning to facilitate greater connectivity than ever before - revolutionising the data demand, questions need to be asked of how securely the considerable quantity of data originating from the extensive sensor network will be communicated back to locations where it is collected and monitored. Recent high-profile data hacks and system infiltrations of large companies have highlighted the vulnerability of many of what were assumed to be highly secure and well defended systems - comprising high-end encryption and cutting-edge software [468, 469]. With the production of a shared repository into which different groups and

organisations deposit their data as part of a larger collective, issues regarding the responsibility to protect and manage this data need be addressed. Through "Quantum Encryption" over traditionally employed mathematical encryption forms, this future form of data-handling will permit large data volumes to be transmitted securely with clear knowledge of whether any data had been intercepted on route [470, 471]. Attacks on computer networks as a result of the connected system are only a small portion of the negatives, however, that result from the IoT - with the 2015 Dell Annual Threat Report concluding that the number of attacks on corporate and industrial networks has been increasing by 100% year-on-year from 2013 [469].

Due to the range of differing sensors and carrier platforms that exist in addition to its transfer via the IoT, the data that is produced will vary considerably in its resolution and granularity. Relating back to the issue of data access and roles in future safeguarding; whereas the data may be collected at high resolution in many areas (and lower, more commonly at others), there represents the need to control (and streamline) what data is either seen by certain individuals and groups as well as the resolution at which they it. For example, those interested in the continual routine monitoring of buildings and individual sites such as plant operators will demand data at increased resolution than emergency response groups such as the UK's Cabinet Office Briefing Rooms (COBR) - where a wider overview of the data is demanded.

Indeed, The Sendai Framework argues that to "understand disaster risk" it is necessary to "promote real time access to reliable data, make use of spatial and local sensors, including geographic information systems (GIS), and use information and communications technology innovations to enhance measurement tools and the collection, analysis and dissemination of data". Risk mitigation must be built upon an empirically grounded understanding of the nature of the hazards, requiring an improvement of the integration of scientific knowledge into government and community decision-making [472].

6.0 Conclusion

In conclusion, whilst future risks to national and international nuclear security will still be posed by groups or individuals wanting to undertake direct physical violence or destruction, there will be a growing threat posed directly or in conjunction with physical attacks by more technologically-advanced methods. Whilst there still exists a credible threat from physical attacks on nuclear infrastructure or from groups dispersing acquired radioactive material within populated environments, the likelihood of an attack is considered to be low and the threat level remains relatively constant. However, as a deterrent and a representative illustration of capacity to prevent such attacks, a traditional armed and physical security presence will continue to be required on nuclear sites.

By contrast, the global evolution of smart technologies is unabated, with the world having evolved unrecognisably over the past half a century, mostly for good - with the invention and accessibility of the internet recognised as pivotal in our history. Despite the immense benefits that these technologies have brought to society, including quantifiable benefits for the nuclear sector, the IoT and smart technologies more widely may also be viewed as one of the greatest potential threats to global nuclear security over the foreseeable future. A comprehensive and joined up physical and cyber security plan (both covering the threat from an insider) is essential to counter the current threats to the global nuclear sector. Some arising technologies will present both a threat and an opportunity, e.g. the application of UAVs in routine nuclear/security monitoring and emergency/security assessment are of considerable promise, but at the same time present a security threat, as many nuclear sites are not currently fully prepared for the detection or prevention of coordinated incursions.

Ultimately, organisations responsible for nuclear safety and security must be obliged to stay up to date with both emerging physical and digital technologies that could enhance or pose a threat with respect to nuclear monitoring, security and safeguards. The further development of outcome based security regulation, placing the onus on the nuclear site to demonstrate security/system effectiveness, should encourage a more innovative approach to tackling the threat. Instead of the historical prescriptive approach to security regulation, a change in this methodology will encourage a stronger uptake of emerging beneficial technologies and stimulate the faster development of countermeasures against those which pose a threat. This will likely necessitate close liaison and resource sharing between defence and intelligence agencies, delivering further tangential benefits in other areas of national and international security outside of nuclear.

BIBLIOGRAPHY

[1] IAEA.
The International Nuclear and Radiological Event Scale User's Manual.
Vienna, Austria: International Atomic Energy Agency, 2008,
P. 218.
URL: http://www-pub.iaea.org/MTCD/Publications/PDF/INES2013web.pdf.

[2] IAEA.
"Technical Volume 1 of 5: Description and Context of the Accident".
In: *The Fukushima Daiichi Accident*.
Vienna, Austria: IAEA, 2015,
P. 238.
ISBN: 978-92-0-107015-9.
URL: http://www-pub.iaea.org/MTCD/Publications/PDF/AdditionalVolumes/
P1710/Pub1710-TV1-Web.pdf.

[3] A Bolsunovsky and D Dementyev.
"Evidence of the radioactive fallout in the center of asia (Russia) following the fukushima
nuclear accident".
In: *Journal of Environmental Radioactivity* 102 (Nov. 2011), pp. 1062–1064.
ISSN: 0265931X.
DOI: 10.1016/j.jenvrad.2011.06.007.
URL: http://www.sciencedirect.com/science/article/pii/S0265931X1100138X.

[4] O Masson et al.
"Tracking of airborne radionuclides from the damaged Fukushima Dai-ichi nuclear
reactors by European networks."
In: *Environmental Science & Technology* 45.18 (Sept. 2011), pp. 7670–7677.
ISSN: 1520-5851.
DOI: 10.1021/es2017158.
URL: http://dx.doi.org/10.1021/es2017158.

[5] TEPCO.
Overview of Facility of Fukushima Daiichi Nuclear Power Station.
2013.

URL: http://www.tepco.co.jp/en/nu/fukushima-np/outline_f1/index-e.html.

[6] TEPCO.
Glossary of a Nuclear Facility.
2017.
URL: http://www.tepco.co.jp/en/nu/fukushima-np/review/words-e.html.

[7] TEPCO.
Fukushima Nuclear Accident Analysis Report 2012.
Tech. rep.
Tokyo, 2012,
P. 503.
URL: http://www.tepco.co.jp/en/press/corp-com/release/betu12_e/images/120620e0104.pdf.

[8] IAEA.
IAEA Power Reactor Information System (PRIS).
2016.
URL: https://www.iaea.org/pris/.

[9] NRA.
Analysis of the TEPCO Fukushima Daiichi NPS Accident - Interim Report.
Tech. rep.
NRA, 2014,
P. 137.
URL: https://www.nsr.go.jp/data/000067237.pdf.

[10] World Nuclear Association.
Fukushima: Background on Fuel Ponds.
2016.
URL: http://www.world-nuclear.org/information-library/safety-and-security/safety-of-plants/appendices/fukushima-fuel-ponds-background.aspx.

[11] World Nuclear Association.
Fukushima: Background on Reactors.
2012.
URL: http://www.world-nuclear.org/information-library/safety-and-security/safety-of-plants/appendices/fukushima-reactor-background.aspx.

[12] GE Hitachi Nuclear Energy (GEH).
Nuclear Power Plants.
2017.
URL: https://nuclear.gepower.com/.

[13] JAIF (Japan Atomic Industrial Forum).

Nuclear Power in Japan.
Tech. rep.
2017.
URL: http://www.jaif.or.jp/en/npps-in-japan/.

[14] World Nuclear Association.
Nuclear Power in Japan.
2017.
URL: http://www.world-nuclear.org/information-library/country-profiles/countries-g-n/japan-nuclear-power.aspx.

[15] Phillip Y. Lipscy, Kenji E. Kushida, and Trevor Incerti.
"The Fukushima Disaster and Japan's Nuclear Plant Vulnerability in Comparative Perspective".
In: *Environmental Science & Technology* 47 (June 2013), pp. 6082–6088.
ISSN: 0013-936X.
DOI: 10.1021/es4004813.
URL: http://pubs.acs.org/doi/abs/10.1021/es4004813.

[16] World Nuclear Association.
Nuclear Power Plants and Earthquakes.
2017.
URL: http://www.world-nuclear.org/information-library/safety-and-security/safety-of-plants/nuclear-power-plants-and-earthquakes.aspx.

[17] T. Sagiya, S. Miyazaki, and T. Tada.
"Continuous GPS array and present-day crustal deformation of Japan".
In: *Pure and Applied Geophysics* 157 (2000), pp. 2303–2322.
ISSN: 00334553.
DOI: 10.1007/PL00022507.
URL: http://adsabs.harvard.edu/abs/2000PApGe.157.2303S.

[18] Japan Meteorological Agency.
Earthquake Information and Tsunami Advisories.
URL: http://www.jma.go.jp/en/quake/http://www.jma.go.jp/en/tsunami/.

[19] IAEA.
Environmental Consequences of the Chernobyl Accident and their Remediation: Twenty Years of Experience.
IAEA, 2006,
P. 166.
ISBN: 92-0-114705-8.

URL: http://www-pub.iaea.org/books/IAEABooks/7382/Environmental-Consequences-of-the-Chernobyl-Accident-and-their-Remediation-Twenty-Years-of-Experience.

[20] Samuel Glasstone and Alexander Sesonske.
      Nuclear Reactor Engineering: Reactor Design Basics / Reactor Systems Engineering.
      4th Ed.
      Springer US, 1994,
      P. 852.
      ISBN: 9781461358664.
      DOI: 10.1007/978-1-4615-2083-2.
      URL: http://www.springer.com/us/book/9781461575276.

[21] P. D. Wilson.
      The Nuclear Fuel Cycle : From Ore to Wastes.
      Oxford: Oxford University Press, 1996,
      P. 323.
      ISBN: 0198565402.
      URL: https://inis.iaea.org/search/search.aspx?orig_q=RN:28071286.

[22] Masaki Inoue and Takeo Asaka.
      Temperature and chemical history for spent fuel pools in Fukushima Dai-ichi Nuclear Power Station; Units 1 through 4 - In Japanese.
      Tech. rep.
      Japan Atomic Energy Agency, 2014,
      P. 46.
      DOI: 10.11484/jaea-review-2014-020.
      URL: http://jolissrch-inter.tokai-sc.jaea.go.jp/search/servlet/search?5041276&language=1.

[23] E. C. Buck, B. D. Hanson, and B. K. McNamara.
      "The geochemical behaviour of Tc, Np and Pu in spent nuclear fuel in an oxidizing environment".
      In: *Geological Society, London, Special Publications* 236.1 (Jan. 2004), pp. 65–88.
      ISSN: 0305-8719.
      DOI: 10.1144/GSL.SP.2004.236.01.05.
      URL: http://sp.lyellcollection.org/content/236/1/65.short.

[24] Peter C Burns, Rodney C Ewing, and Alexandra Navrotsky.
      "Nuclear fuel in a reactor accident."
      In: *Science* 335.6073 (Mar. 2012), pp. 1184–1188.
      ISSN: 1095-9203.
      DOI: 10.1126/science.1211285.

URL: http://www.sciencemag.org/content/335/6073/1184.

[25] TEPCO.
Fukushima Daiichi NPS - Information Portal.
2013.
URL: https://fdada.info/en/home2/accident2/specification2/.

[26] World Nuclear Association.
Safety of Nuclear Power Reactors.
2012.
URL: http://www.world-nuclear.org/info/Safety-and-Security/Safety-of-Plants/Fukushima-Accident/.

[27] Mark Simons et al.
"The 2011 magnitude 9.0 Tohoku-Oki earthquake: mosaicking the megathrust from seconds to centuries."
In: *Science* 332.6036 (July 2011), pp. 1421–1425.
ISSN: 1095-9203.
DOI: 10.1126/science.1206731.
URL: http://www.sciencemag.org/content/332/6036/1421.abstract.

[28] Shinzaburo Ozawa et al.
"Coseismic and postseismic slip of the 2011 magnitude-9 Tohoku-Oki earthquake."
In: *Nature* 475.7356 (June 2011), pp. 373–376.
ISSN: 0028-0836.
DOI: 10.1038/nature10227.
URL: http://www.nature.com/doifinder/10.1038/nature10227http://dx.doi.org/10.1038/nature10227.

[29] Thorne Lay et al.
"The Great Sumatra-Anadaman Earthquake of 26 December 2004."
In: *Science* 308 (May 2005), pp. 1127–1133.
ISSN: 00113891.
DOI: 10.1126/science.1112250.
URL: http://www.ncbi.nlm.nih.gov/pubmed/15905392.

[30] K Kurokawa et al.
"The National Diet of Japan: Fukushima Nuclear Accident Independent Investigation Commission."
In: *The National Diet of Japan* 1 (2012), p. 88.
URL: https://www.nirs.org/fukushima/naiic_report.pdf.

[31] Japan Meteorological Agency.
Monthly total of precipitation (mm) - Japan Meteorological Agency.

URL: http://www.data.jma.go.jp/obd/stats/etrn/view/monthly_s3_en.php?
block_no=47401&view=13.

[32] TEPCO.
Plant Status of Fukushima Daiichi Nuclear Power Station (as of 14:00 on March 18th 2011).
Tech. rep.
2011,
P. 4.
URL: http://www.tepco.co.jp/en/press/corp-com/release/11031803-e.html.

[33] TEPCO.
Measurement Data at Fukushima Daiichi Nuclear Power Station (in Japanese).
2011.
URL: http://www.tepco.co.jp/nu/fukushima-np/f1/data/2011/index-j.html.

[34] World Nuclear Association.
The Fukushima Daiichi Accident.
2017.
URL: http://www.world-nuclear.org/focus/fukushima/fukushima-accident.aspx.

[35] S.J. Zinkle and G.S. Was.
"Materials challenges in nuclear energy".
In: *Acta Materialia* 61.3 (Feb. 2013), pp. 735–758.
ISSN: 13596454.
DOI: 10.1016/j.actamat.2012.11.004.
URL: http://www.sciencedirect.com/science/article/pii/S1359645412007987.

[36] W.A Deer, R.A Howie, and J. Zussman.
An Introduction to the Rock-Forming Minerals.
Mineralogical Society of Great Britain and Ireland, Jan. 2013,
P. 495.
ISBN: 978-0903056-27-4.
DOI: 10.1180/DHZ.

[37] Tuomo Sevon.
"Molten core - Concrete interactions in nuclear accidents theory and design of an experimental facility".
In: *VTT Tiedotteita - Valtion Teknillinen Tutkimuskeskus* 2311 (2005), pp. 1–83.
ISSN: 12350605.
URL: http://www.ewp.rpi.edu/hartford/~flahid/EP/Other/Sevon.pdf.

[38] Nuclear Emergency Response Headquarters (Government of Japan).

Report of Japanese Government to the IAEA Ministerial Conference on Nuclear Safety - The Accident at TEPCO's Fukushima Nuclear Power Stations.
Tech. rep.
Toyko, 2011.
URL: http://japan.kantei.go.jp/kan/topics/201106/iaea_houkokusho_e.html.

[39] Yu Morino, Toshimasa Ohara, and Masato Nishizawa.
"Atmospheric behavior, deposition, and budget of radioactive materials from the Fukushima Daiichi nuclear power plant in March 2011".
In: *Geophysical Research Letters* 38 (Apr. 2011), p. 7.
ISSN: 00948276.
DOI: 10.1029/2011GL048689.
URL: http://doi.wiley.com/10.1029/2011GL048689.

[40] Georg Steinhauser et al.
"Post-Accident Sporadic Releases of Airborne Radionuclides from the Fukushima Daiichi Nuclear Power Plant Site". EN.
In: *Environmental Science & Technology* 49 (Nov. 2015), pp. 14028–14035.
URL: http://pubs.acs.org/doi/10.1021/acs.est.5b03155.

[41] Jiansong Wu et al.
"Analysis of ground deposition of radionuclides under different wind fields from the Fukushima Daiichi accident".
In: *Natural Hazards* (Feb. 2017), pp. 1–12.
ISSN: 0921-030X.
DOI: 10.1007/s11069-017-2777-7.
URL: http://link.springer.com/10.1007/s11069-017-2777-7.

[42] Haruo Tsuruta et al.
"First retrieval of hourly atmospheric radionuclides just after the Fukushima accident by analyzing filter-tapes of operational air pollution monitoring stations."
In: *Scientific Reports* 4.6717 (Jan. 2014), p. 10.
ISSN: 2045-2322.
DOI: 10.1038/srep06717.
URL: http://www.nature.com/srep/2014/141022/srep06717/full/srep06717.html.

[43] Mathew S Snow, Darin C Snyder, and James E Delmore.
"Fukushima Daiichi reactor source term attribution using cesium isotope ratios from contaminated environmental samples."
In: *Rapid Communications in Mass Spectrometry (RCM)* 30.4 (Feb. 2016), pp. 523–532.
ISSN: 1097-0231.
DOI: 10.1002/rcm.7468.

315

URL: http://www.ncbi.nlm.nih.gov/pubmed/26777683.

[44] IAEA.
Re-evaluation of INES rating; Effect to the Nuclear Facilities from the earthquake on east area of Japan.
Tech. rep.
Vienna: IAEA, 2012.
URL: https://www-news.iaea.org/ErfView.aspx?mId=b8d002ae-78cc-435b-a9c6-21860bdb46cc.

[45] Typhoon Lee et al.
"First detection of fallout Cs-135 and potential applications of 137Cs/135Cs ratios".
In: *Geochimica et Cosmochimica Acta* 57.14 (1993), pp. 3493–3497.
ISSN: 00167037.
DOI: 10.1016/0016-7037(93)90555-B.

[46] James E Delmore et al.
"Cesium isotope ratios as indicators of nuclear power plant operations."
In: *Journal of Environmental Radioactivity* 102.11 (Nov. 2011), pp. 1008–1111.
ISSN: 1879-1700.
DOI: 10.1016/j.jenvrad.2011.06.013.
URL: http://www.sciencedirect.com/science/article/pii/S0265931X11001561.

[47] V F Taylor, R D Evans, and R J Cornett.
"Preliminary evaluation of (135)Cs/(137)Cs as a forensic tool for identifying source of radioactive contamination."
In: *Journal of Environmental Radioactivity* 99.1 (Jan. 2008), pp. 109–118.
ISSN: 0265-931X.
DOI: 10.1016/j.jenvrad.2007.07.006.
URL: http://www.sciencedirect.com/science/article/pii/S0265931X07001890.

[48] Mathew S Snow and Darin C Snyder.
"135Cs/137Cs isotopic composition of environmental samples across Europe: Environmental transport and source term emission applications."
In: *Journal of Environmental Radioactivity* 151.1 (Jan. 2016), pp. 258–263.
ISSN: 1879-1700.
DOI: 10.1016/j.jenvrad.2015.10.025.
URL: http://www.sciencedirect.com/science/article/pii/S0265931X15301417.

[49] Darin C. Snyder et al.
"Radioactive cesium isotope ratios as a tool for determining dispersal and re-dispersal mechanisms downwind from the Nevada Nuclear Security Site".
In: *Journal of Environmental Radioactivity* 110 (2012), pp. 46–52.

ISSN: 0265931X.

DOI: 10.1016/j.jenvrad.2012.01.019.

[50] Kenji Nishihara, Hiroki Iwamoto, and Kenya Suyama.
Estimation of fuel compositions in Fukushima-Daiichi nuclear power plant (in Japanese).
Tech. rep.
Ibaraki, 2012,
P. 202.
URL: http://inis.iaea.org/Search/search.aspx?orig_q=RN:44087069.

[51] Allen G. Croff.
"Origen2: A Versatile Computer Code for Calculating the Nuclide Compositions and Characteristics of Nuclear Materials".
In: *Nuclear Technology* 62.3 (Sept. 1983), pp. 335–352.
URL: http://epubs.ans.org/?a=33257.

[52] CRC Press.
CRC Handbook of Chemistry and Physics - Table of Isotopes.
Ed. by W.M. Haynes.
96th Ed.
Boca Raton, Florida, 2015,
Pp. 11–2.
ISBN: 9781482208689.
URL: http://www.hbcpnetbase.com/.

[53] R.J. Guenther et al.
Characterization of spent fuel approved testing material–ATM-104.
Tech. rep.
Richland, WA: Pacific Northwest National Laboratory (PNNL), Dec. 1991,
P. 416.
DOI: 10.2172/138327.
URL: http://www.osti.gov/scitech/biblio/138327.

[54] TEPCO and IRID.
Reactor imaging technology for fuel debris detection by cosmic ray muon: measurement status report in Unit 1.
Tech. rep.
Tokyo, 2015,
P. 13.

[55] TEPCO and IRID.
Locating Fuel Debris inside the Unit 2 Reactor Using a Muon Measurement Technology at Fukushima Daiichi Nuclear Power Station.

Tech. rep.

Tokyo, 2016,

P. 9.

[56] TEPCO and IRID.

Locating Fuel Debris inside the Unit 3 Reactor Using a Muon Measurement Technology at Fukushima Daiichi Nuclear Power Station.

Tech. rep.

Tokyo, 2017,

P. 10.

URL: http://www.tepco.co.jp/en/nu/fukushima-np/handouts/2017/images/handouts_170727_01-e.pdf.

[57] IAEA.

"Technical Volume 5 of 5: Post Accident Recovery".

In: *The Fukushima Daiichi Accident*.

Vienna, Austria: IAEA, 2015,

P. 218.

ISBN: 978-92-0-107015-9.

URL: http://www-pub.iaea.org/MTCD/Publications/PDF/AdditionalVolumes/P1710/Pub1710-TV5-Web.pdf.

[58] TEPCO.

Nuclear Power Station - Fuel Removal from Unit 4 of Fukushima Daiichi NPS.

2017.

URL: http://www.tepco.co.jp/en/nu/fukushima-np/removal4u/index-e.html.

[59] TEPCO.

TEPCO Photo and Video Archive.

2017.

URL: http://photo.tepco.co.jp/en/index-e.html.

[60] Japanese Ministry of the Environment (Government of Japan).

Decontamination Guidelines, 2nd Edition 2013.

Tech. rep.

2013,

P. 246.

URL: http://josen.env.go.jp/en/framework/pdf/decontamination_guidelines_2nd.pdf.

[61] MEXT.

Extension Site of Distribution Map of Radiation Dose.

2011.

URL: http://ramap.jmc.or.jp/map/eng/.

[62] Japan Atomic Energy Agency (JAEA).
Database for Radioactive Substance Monitoring Data.
2017.
URL: http://emdb.jaea.go.jp/emdb/en/.

[63] NRA.
Comprehensive Radiation Monitoring Plan.
Tech. rep.
Tokyo, 2011,
P. 10.
URL: http://radioactivity.nsr.go.jp/en/contents/8000/7758/view.html.

[64] Kimiaki Saito and Yuichi Onda.
"Outline of the national mapping projects implemented after the Fukushima accident."
In: *Journal of Environmental Radioactivity* 139 (Jan. 2015), pp. 240–249.
ISSN: 1879-1700.
DOI: 10.1016/j.jenvrad.2014.10.009.
URL: http://www.sciencedirect.com/science/article/pii/S0265931X14003105.

[65] J.H. Hubbell and S.M. Seltzer.
Tables of X-Ray Mass Attenuation Coefficients and Mass Energy-absorption Coefficients; National Institute of Standards and Technology, Gaithersburg, MD. EN-US.
First.
2004.
URL: http://www.nist.gov/pml/data/xraycoef/.

[66] G. W. Grodstein.
X-ray attenuation coefficients from 100 keV to 100 MeV.
Tech. rep.
1957,
P. 58.

[67] Yukihisa Sanada and Tatsuo Torii.
"Aerial radiation monitoring around the Fukushima Dai-ichi Nuclear Power Plant using an unmanned helicopter."
In: *Journal of Environmental Radioactivity* 139 (Jan. 2015), pp. 294–249.
ISSN: 1879-1700.
DOI: 10.1016/j.jenvrad.2014.06.027.
URL: http://www.sciencedirect.com/science/article/pii/S0265931X14001994.

[68] Tomoyuki Furutani et al.

A Study on Micro-Scale Airborne Radiation Monitoring by Unmanned Aerial Vehicle for Rural Area Reform Contaminated by Radiation.

Tech. rep.

Keio University, 2014,

P. 9.

URL: http://www.ists.co.jp/wordpress_en/wp-content/uploads/Study-report.pdf.

[69] Yukiyasu Nishizawa et al.

"Distribution of the 134Cs/137Cs ratio around the Fukushima Daiichi nuclear power plant using an unmanned helicopter radiation monitoring system".

In: *Journal of Nuclear Science and Technology* 53.4 (Aug. 2015), pp. 1–7.

ISSN: 0022-3131.

DOI: 10.1080/00223131.2015.1071721.

URL: http://www.tandfonline.com/doi/abs/10.1080/00223131.2015.1071721.

[70] B.R.S. Minty, A.P.J. Luyendyk, and R.C. Brodie.

"Calibration and data processing for airborne gamma-ray spectrometry".

In: *Journal of Australian Geology & Geophysics* 17 (1997), pp. 51–62.

[71] James A. Pitkin and Joseph S. Duval.

"Design parameters for aerial gamma ray surveys".

In: *Geophysics* 45.9 (Sept. 1980), pp. 1427–1439.

ISSN: 0016-8033.

DOI: 10.1190/1.1441131.

URL: http://library.seg.org/doi/abs/10.1190/1.1441131.

[72] B.R.S. Minty.

"Fundamental of airborne gamma-ray spectrometry".

In: *Journal of Australian Geology & Geophysics* 17 (1997), pp. 39–50.

[73] D.C.W. Sanderson et al.

Environmental applications of airborne gamma spectrometry.

Tech. rep.

1995,

Pp. 71–91.

URL: http://www.iaea.org/inis/collection/NCLCollectionStore/_Public/27/025/27025425.pdf#page=26.

[74] J.H. Hubbell.

Photon Cross Sections, Attenuation Coefficients and Energy Absorption Coefficients from 10 keV to 100 GeV.

1969.

URL: http://www.nist.gov/data/nsrds/NSRDS-NBS29.pdf.

[75] UNSCEAR.
Sources, Effects and Risks of Ionizing Radiation.
Tech. rep.
New York: United Nations, 2013,
P. 322.
URL: http://www.unscear.org/unscear/en/publications.html.

[76] Civil Aviation Authority.
Small unmanned aircraft - Specific regulations about small drones.
2016.
URL: https://www.caa.co.uk/Commercial-industry/Aircraft/Unmanned-aircraft/
Small-unmanned-aircraft/.

[77] R. M. Moxham.
"Airborne radioactivity surveys in geologic exploration".
In: *Geophysics* 25.2 (Apr. 1960), pp. 408–432.
ISSN: 0016-8033.
DOI: 10.1190/1.1438711.
URL: http://library.seg.org/doi/10.1190/1.1438711.

[78] Joe S. Duval, Beverly Cook, and John A. S. Adams.
"Circle of Investigation of an Airborne Gamma-ray Spectrometer".
In: *Journal of Geophysical Research* 76.35 (Dec. 1971), pp. 8466–8470.
ISSN: 01480227.
DOI: 10.1029/JB076i035p08466.
URL: http://doi.wiley.com/10.1029/JB076i035p08466.

[79] D. Connor, P. G. Martin, and T. B. Scott.
"Airborne radiation mapping: overview and application of current and future aerial
systems".
In: *International Journal of Remote Sensing* 37.24 (Dec. 2016), pp. 5953–5987.
ISSN: 0143-1161.
DOI: 10.1080/01431161.2016.1252474.
URL: https://www.tandfonline.com/doi/full/10.1080/01431161.2016.1252474.

[80] Shin-ichi Okuyama et al.
"A Remote Radiation Monitoring System Using an Autonomous Unmanned Helicopter for
Nuclear Emergencies".
In: *Journal of Nuclear Science and Technology* 45.Supplement 5 (Aug. 2008), pp. 414–416.
ISSN: 0022-3131.
DOI: 10.1080/00223131.2008.10875877.

URL: http://dx.doi.org/10.1080/00223131.2008.10875877.

[81] Yukihisa Sanada, Tadashi Orita, and Tatsuo Torii.
"Temporal variation of dose rate distribution around the Fukushima Daiichi nuclear power station using unmanned helicopter".
In: *Applied Radiation and Isotopes* 118 (2016), pp. 308–316.
ISSN: 09698043.
DOI: 10.1016/j.apradiso.2016.09.008.
URL: http://www.sciencedirect.com/science/article/pii/S0969804316306868.

[82] Alex Malins et al.
"Fields of View for Environmental Radioactivity".
In: *Proceedings of the International Symposium on Radiological Issues for Fukushima's Revitalized Future*.
Sept. 2015,
Pp. 28–34.
URL: http://arxiv.org/abs/1509.09125http://www.rri.kyoto-u.ac.jp/anzen_kiban/outcome/Symposium'15_Proceedings_EN.pdf.

[83] R.L Grasty, K.L Kosanke, and R.S Foote.
"Fields of view of airborne gamma-ray detectors".
In: *Geophysics* 44.8 (Aug. 1979), pp. 1447–1457.
ISSN: 1070485X.
DOI: 10.1190/1.1441017.
URL: http://library.seg.org/doi/10.1190/1.1441017.

[84] A. J. Cresswell and D. C W Sanderson.
"The use of difference spectra with a filtered rolling average background in mobile gamma spectrometry measurements".
In: *Nuclear Instruments and Methods in Physics Research, Section A: Accelerators, Spectrometers, Detectors and Associated Equipment* 607.3 (2009), pp. 685–694.
ISSN: 01689002.
DOI: 10.1016/j.nima.2009.06.001.

[85] MEXT and US Department of Energy.
Results of the Airborne Monitoring by the Ministry of Education, Culture, Sports, Science and Technology and the U.S. Department of Energy. 6th May 2011.
Tech. rep.
2011,
P. 7.

[86] P Guss.

DOE response to the radiological release from the Fukushima Dai-ichi Nuclear Power Plant.

Tech. rep.

2011,

P. 34.

URL: http://hps.ne.uiuc.edu/rets-remp/PastWorkshops/2011/presentations/6C-DOEResponsetotheRadiologicalReleasefromtheFukushimaDaiichiNuclearPowerPlant.pdf.

[87]   MEXT.

Results of the Sixth Airborne Monitoring and Airborne Monitoring out of the 80km Zone of Fukushima Dai-ichi NPP.

Tech. rep.

2013,

P. 18.

URL: http://radioactivity.nsr.go.jp/en/list/307/list-1.html.

[88]   NRA.

Results of the Tenth Airborne Monitoring and Airborne Monitoring out of the 80km Zone of Fukushima Dai-ichi NPP.

Tech. rep.

2016,

P. 4.

URL: http://radioactivity.nsr.go.jp/en/list/307/list-1.html.

[89]   NRA.

Results of the Eleventh Airborne Monitoring and Airborne Monitoring out of the 80km Zone of Fukushima Dai-ichi NPP.

Tech. rep.

2017,

P. 4.

URL: http://radioactivity.nsr.go.jp/en/list/307/list-1.html.

[90]   I.J. Won and Dean Keiswetterg.

"Geophex Airborne Unmanned Survey System".

In: *Environmental Technology Development Through Industry Partnership*.

Morgantown, West Virginia, 1995,

P. 12.

DOI: 10.1190/1.1826814.

URL: http://www.iaea.org/inis/collection/NCLCollectionStore/_Public/27/040/27040829.pdfhttp://library.seg.org.proxy.library.carleton.ca/doi/pdf/10.1190/1.1826814.

[91] K. J. Hofstetter, D. W. Hayes, and M. M. Pendergast.
"Aerial robotic data acquisition system".
In: *Journal of Radioanalytical and Nuclear Chemistry Articles* 193.1 (May 1995), pp. 89–92.
ISSN: 02365731.
DOI: 10.1007/BF02041920.
URL: http://link.springer.com/10.1007/BF02041920.

[92] Jerry Towler, Bryan Krawiec, and Kevin Kochersberger.
"Radiation Mapping in Post-Disaster Environments Using an Autonomous Helicopter".
In: *Remote Sensing* 4.12 (July 2012), pp. 1995–2015.
ISSN: 2072-4292.
DOI: 10.3390/rs4071995.
URL: http://www.mdpi.com/2072-4292/4/7/1995/htm.

[93] Yamaha.
RMAX Type 1 / Type 1G.
URL: http://rmax.yamaha-motor.com.au/.

[94] Yukihisa Sanada et al.
"Radiation monitoring using an unmanned helicopter in the evacuation zone around the Fukushima Daiichi nuclear power plant". en.
In: *Exploration Geophysics* (Mar. 2014).
URL: http://library.seg.org/doi/abs/10.1071/EG13004.

[95] Yukihisa Sanada et al.
"Distribution of radioactive cesium measured by aerial radiation monitoring (in Japanese)".
In: *Hoshasen* 38.3 (2012), pp. 137–140.
URL: http://inis.iaea.org/Search/search.aspx?orig_q=RN:45050252.

[96] K Kurvinen et al.
"Design of a radiation surveillance unit for an unmanned aerial vehicle."
In: *Journal of Environmental Radioactivity* 81.1 (Jan. 2005), pp. 1–10.
ISSN: 0265-931X.
DOI: 10.1016/j.jenvrad.2004.10.009.
URL: http://www.sciencedirect.com/science/article/pii/S0265931X04003108.

[97] Roy Pöllänen et al.
"Radiation surveillance using an unmanned aerial vehicle".
In: *Applied Radiation and Isotopes* 67.2 (2009), pp. 340–344.
ISSN: 09698043.
DOI: 10.1016/j.apradiso.2008.10.008.
URL: http://www.sciencedirect.com/science/article/pii/S0969804308004831.

[98] K. Boudergui et al.

"Development of a drone equipped with optimized sensors for nuclear and radiological risk characterization".

In: *2011 2nd International Conference on Advancements in Nuclear Instrumentation, Measurement Methods and their Applications*.

IEEE, June 2011,

Pp. 1–9.

ISBN: 978-1-4577-0927-2.

DOI: 10.1109/ANIMMA.2011.6172936.

URL: http://ieeexplore.ieee.org/lpdocs/epic03/wrapper.htm?arnumber=6172936.

[99]   Nicolas Guenard, Tarek Hamel, and Laurent Eck.

"Control laws for the tele operation of an unmanned aerial vehicle known as an X4-flyer".

In: *IEEE International Conference on Intelligent Robots and Systems*.

IEEE, Oct. 2006,

Pp. 3249–3254.

ISBN: 142440259X.

DOI: 10.1109/IROS.2006.282432.

URL: http://ieeexplore.ieee.org/document/4058899/.

[100]   J W MacFarlane et al.

"Lightweight aerial vehicles for monitoring, assessment and mapping of radiation anomalies."

In: *Journal of Environmental Radioactivity* 136 (Oct. 2014), pp. 127–130.

ISSN: 1879-1700.

DOI: 10.1016/j.jenvrad.2014.05.008.

URL: http://www.sciencedirect.com/science/article/pii/S0265931X14001489.

[101]   Jacopo Aleotti et al.

"Unmanned aerial vehicle equipped with spectroscopic CdZnTe detector for detection and identification of radiological and nuclear material".

In: *2015 IEEE Nuclear Science Symposium and Medical Imaging Conference (NSS/MIC)*.

IEEE, Oct. 2015,

Pp. 1–5.

ISBN: 978-1-4673-9862-6.

DOI: 10.1109/NSSMIC.2015.7582264.

URL: http://ieeexplore.ieee.org/document/7582264/.

[102]   P.G. Martin et al.

"Low altitude unmanned aerial vehicle for characterising remediation effectiveness following the FDNPP accident".

In: *Journal of Environmental Radioactivity* 151 (Jan. 2016), pp. 58–63.

ISSN: 0265931X.

DOI: 10.1016/j.jenvrad.2015.09.007.

URL: http://www.sciencedirect.com/science/article/pii/S0265931X15301028.

[103] P.G. Martin et al.

"High-resolution radiation mapping to investigate FDNPP derived contaminant migration".

In: *Journal of Environmental Radioactivity* 164 (2016), pp. 26–35.

ISSN: 0265931X.

DOI: 10.1016/j.jenvrad.2016.06.025.

URL: http://linkinghub.elsevier.com/retrieve/pii/S0265931X16302284.

[104] FLYCAM UAV.

Airborne Radiation Detection.

2017.

URL: http://www.flycamuav.com/aerial-radiation-detection/.

[105] Safecast.

About Safecast.

2016.

URL: http://blog.safecast.org/about/.

[106] Misao Ikuta et al.

"Car-Borne Survey Using Ge Semiconductor Detector in the Chugoku Region of Japan".

In: *Japanese Journal of Health Physics* 47.3 (Aug. 2012), pp. 198–203.

ISSN: 0367-6110.

DOI: 10.5453/jhps.47.198.

URL: https://www.jstage.jst.go.jp/article/jhps/47/3/47_198/_article.

[107] Shuichi Tsuda et al.

Construction of a car-borne survey system for measurement of dose rates in air: KURAMA-II, and its application (in Japanese).

Tech. rep.

2013,

P. 68.

DOI: 10.11484/JAEA-Technology-2013-037.

URL: http://inis.iaea.org/Search/search.aspx?orig_q=RN:45066120.

[108] Tetsuji Imanaka et al.

"Early radiation survey of Iitate village, which was heavily contaminated by the Fukushima Daiichi accident, conducted on 28 and 29 March 2011."

In: *Health Physics* 102.6 (June 2012), pp. 680–686.

ISSN: 1538-5159.

DOI: 10.1097/HP.0b013e31824cfe18.

URL: http://www.ncbi.nlm.nih.gov/pubmed/22549322.

326

[109] Hamamatsu Photonics K.K.
Hamamatsu C12137-Series Specification.
Tech. rep.
Hamamatsu City, 2017,
P. 9.
URL: http://www.hamamatsu.com/us/en/product/alpha/R/4134/index.html.

[110] Alex Malins et al.
Topographic Effects on Ambient Dose Equivalent Rates from Radiocesium Fallout.
Tech. rep.
Feb. 2015,
P. 7.
URL: http://arxiv.org/abs/1502.03892.

[111] Masahide Ishizuka et al.
"Use of a size-resolved 1-D resuspension scheme to evaluate resuspended radioactive material associated with mineral dust particles from the ground surface".
In: *Journal of Environmental Radioactivity* 166.3 (2015), pp. 436–448.
ISSN: 18791700.
DOI: 10.1016/j.jenvrad.2015.12.023.

[112] Fulvio Amato et al.
"Short-term variability of mineral dust, metals and carbon emission from road dust resuspension".
In: *Atmospheric Environment* 74 (2013), pp. 134–140.
ISSN: 13522310.
DOI: 10.1016/j.atmosenv.2013.03.037.
URL: http://www.sciencedirect.com/science/article/pii/S1352231013002136.

[113] Harold Elford Jones and John Robert Cunningham.
Physics of Radiology, Fourth Edition.
4th Ed.
Springfield, Illinois, USA: Thomas Publishing, 1983,
P. 374.
ISBN: 0398046697.

[114] E. Buchanan et al.
"Operator related attenuation effects in radiometric surveys".
In: *Radiation Measurements* 86 (Mar. 2016), pp. 24–31.
ISSN: 13504487.
DOI: 10.1016/j.radmeas.2015.12.029.
URL: http://www.sciencedirect.com/science/article/pii/S1350448715301086.

[115] S. Endo et al.
"Measurement of soil contamination by radionuclides due to the Fukushima Dai-ichi Nuclear Power Plant accident and associated estimated cumulative external dose estimation".
In: *Journal of Environmental Radioactivity* 111 (Sept. 2012), pp. 18–27.
ISSN: 0265931X.
DOI: 10.1016/j.jenvrad.2011.11.006.
URL: http://dx.doi.org/10.1016/j.jenvrad.2011.11.006.

[116] Kimiaki Saito et al.
"Detailed deposition density maps constructed by large-scale soil sampling for gamma-ray emitting radioactive nuclides from the Fukushima Dai-ichi Nuclear Power Plant accident."
In: *Journal of Environmental Radioactivity* 139 (Apr. 2014), pp. 308–319.
ISSN: 1879-1700.
DOI: 10.1016/j.jenvrad.2014.02.014.
URL: http://www.sciencedirect.com/science/article/pii/S0265931X14000642.

[117] Michio Aoyama, Daisuke Tsumune, and Yasunori Hamajima.
"Distribution of 137Cs and 134Cs in the North Pacific Ocean: Impacts of the TEPCO Fukushima-Daiichi NPP accident".
In: *Journal of Radioanalytical and Nuclear Chemistry* 296.1 (Apr. 2013), pp. 535–539.
ISSN: 02365731.
DOI: 10.1007/s10967-012-2033-2.
URL: http://link.springer.com/10.1007/s10967-012-2033-2.

[118] Ken O Buesseler et al.
"Fukushima-derived radionuclides in the ocean and biota off Japan."
In: *Proceedings of the National Academy of Sciences of the United States of America* 109.16 (Apr. 2012), pp. 5984–5988.
ISSN: 1091-6490.
DOI: 10.1073/pnas.1120794109.
URL: http://www.pnas.org/content/109/16/5984.short.

[119] Georg Steinhauser, Alexander Brandl, and Thomas E Johnson.
"Comparison of the Chernobyl and Fukushima nuclear accidents: a review of the environmental impacts."
In: *Science of The Total Environment* 470-471 (Feb. 2014), pp. 800–817.
ISSN: 1879-1026.
DOI: 10.1016/j.scitotenv.2013.10.029.
URL: http://www.sciencedirect.com/science/article/pii/S004896971301173X.

[120] C. Ronneau, J. Cara, and D. Apers.

"The deposition of radionuclides from Chernobyl to a forest in Belgium".
In: *Atmospheric Environment* 21.6 (Jan. 1967), pp. 1467–1468.
ISSN: 00046981.
DOI: 10.1016/0004-6981(67)90094-7.
URL: http://www.sciencedirect.com/science/article/pii/0004698167900947.

[121]   G. Kirchner and C C Noack.
"Core History and Nuclide Inventory of the Chernobyl Core at the Time of Accident".
In: *Nuclear Safety* 29.1 (1988), pp. 1–5.
ISSN: 00295604.

[122]   G Ducros et al.
"Fission product release under severe accidental conditions: General presentation of the
program and synthesis of VERCORS 1-6 results".
In: *Nuclear Engineering and Design* 208.2 (2001), pp. 191–203.
ISSN: 00295493.
DOI: 10.1016/S0029-5493(01)00376-4.

[123]   Yves Pontillon and Gerard Ducros.
"Behaviour of fission products under severe PWR accident conditions. The VERCORS
experimental programme - Part 3: Release of low-volatile fission products and actinides".
In: *Nuclear Engineering and Design* 240.7 (July 2010), pp. 1867–1881.
ISSN: 00295493.
DOI: 10.1016/j.nucengdes.2009.06.025.
URL: http://www.sciencedirect.com/science/article/pii/S0029549309003161.

[124]   Yves Pontillon and Gerard Ducros.
"Behaviour of fission products under severe PWR accident conditions. The VERCORS
experimental programma - Part 2: Release and transport of fission gases and volatile
products".
In: *Nuclear Engineering and Design* 240.7 (July 2010), pp. 1853–1866.
ISSN: 00295493.
DOI: 10.1016/j.nucengdes.2009.06.024.
URL: http://www.sciencedirect.com/science/article/pii/S002954930900315X.

[125]   Yves Pontillon, Gerard Ducros, and P.P. Malgouyres.
"Behaviour of fission products under severe PWR accident conditions VERCORS experimental
programme - Part 1: General description of the programme".
In: *Nuclear Engineering and Design* 240.7 (July 2010), pp. 1843–1852.
ISSN: 00295493.
DOI: 10.1016/j.nucengdes.2009.06.028.
URL: http://www.sciencedirect.com/science/article/pii/S0029549309003148.

[126] P. von der Hardt and A. Tattegrain.
       "The Phebus fission product project".
       In: *Journal of Nuclear Materials* 188 (June 1992), pp. 115–130.
       ISSN: 00223115.
       DOI: 10.1016/0022-3115(92)90461-S.
       URL: http://linkinghub.elsevier.com/retrieve/pii/002231159290461S.

[127] OECD.
       Nuclear Fuel Behaviour in Loss-of-coolant Accident (LOCA) Conditions.
       Tech. rep.
       2009,
       P. 369.
       URL: https://www.oecd-nea.org/nsd/reports/2009/nea6846_LOCA.pdf.

[128] E.A.C. Crouch.
       "Fission-product yields from neutron-induced fission".
       In: *Atomic Data and Nuclear Data Tables* 19.5 (May 1977), pp. 417–532.
       ISSN: 0092640X.
       DOI: 10.1016/0092-640X(77)90023-7.
       URL: http://www.sciencedirect.com/science/article/pii/0092640X77900237.

[129] Jon M Schwantes, Christopher R Orton, and Richard A Clark.
       "Analysis of a nuclear accident: fission and activation product releases from the Fukushima
       Daiichi nuclear facility as remote indicators of source identification, extent of release, and
       state of damaged spent nuclear fuel."
       In: *Environmental Science & Technology* 46 (Aug. 2012), pp. 8621–8627.
       ISSN: 1520-5851.
       DOI: 10.1021/es300556m.
       URL: http://dx.doi.org/10.1021/es300556m.

[130] Simon V. Avery.
       "Fate of caesium in the environment: Distribution between the abiotic and biotic components
       of aquatic and terrestrial ecosystems".
       In: *Journal of Environmental Radioactivity* 30.2 (Jan. 1996), pp. 139–171.
       ISSN: 0265931X.
       DOI: 10.1016/0265-931X(96)89276-9.
       URL: http://linkinghub.elsevier.com/retrieve/pii/0265931X96892769.

[131] U.S. Atomic Energy Commission.
       *Theoretical Possibilities and Consequences of Major Accidents in Large Nuclear Power
       Plants*.
       Tech. rep.

Washington, 1957,

P. 105.

URL: http://hdl.handle.net/2027/uc1.b4164718.

[132] Rodney C Ewing and Takashi Murakami.

"Fukushima Daiichi More Than One Year Later".

In: *Elements* 8.2010 (2012), pp. 181–182.

ISSN: 1811-5209.

DOI: 10.2113/gselements.8.3.181.

URL: http://elements.geoscienceworld.org/content/8/3/181.abstract.

[133] IAEA.

Cumulative Fission Yields.

2017.

URL: https://www-nds.iaea.org/sgnucdat/c3.htm.

[134] UNSCEAR.

Sources and Effects of Ionizing Radiation: Volumes I & II.

Tech. rep.

New York: United Nations, 2000,

P. 1215.

URL: http://www.unscear.org/unscear/en/publications/2000_1.html.

[135] Masamichi Chino et al.

"Preliminary estimation of release amounts of 131I and 137Cs accidentally discharged from the Fukushima Daiichi nuclear power plant into the atmosphere". English.

In: *Journal of Nuclear Science and Technology* 48.7 (2011), pp. 1129–1134.

DOI: 10.3327/jnst.48.

URL: http://inis.iaea.org/Search/search.aspx?orig_q=RN:43013584.

[136] UNSCEAR.

Sources and Effects of Ionising Radiation.

Tech. rep.

New York: United Nations, 2008,

P. 245.

URL: http://www.unscear.org/unscear/en/publications.html.

[137] A. Stohl et al.

"Xenon-133 and caesium-137 releases into the atmosphere from the Fukushima Dai-ichi nuclear power plant: determination of the source term, atmospheric dispersion, and deposition".

In: *Atmospheric Chemistry and Physics* 12.5 (Mar. 2012), pp. 2313–2343.

ISSN: 1680-7324.

DOI: 10.5194/acp-12-2313-2012.

URL: http://www.atmos-chem-phys.net/12/2313/2012/acp-12-2313-2012.html.

[138]   J. I. Friese, R. F. Kephart, and D. D. Lucas.

"Comparison of radionuclide ratios in atmospheric nuclear explosions and nuclear releases from Chernobyl and Fukushima seen in gamma ray spectrometry".

In: *Journal of Radioanalytical and Nuclear Chemistry* 296.2 (May 2013), pp. 899–903.

ISSN: 02365731.

DOI: 10.1007/s10967-012-2213-0.

URL: http://link.springer.com/10.1007/s10967-012-2213-0.

[139]   Tetsuji Imanaka, Gohei Hayashi, and Satoru Endo.

"Comparison of the accident process, radioactivity release and ground contamination between Chernobyl and Fukushima-1".

In: *Journal of Radiation Research* 56.S1 (Dec. 2015), pp. 56–61.

ISSN: 13499157.

DOI: 10.1093/jrr/rrv074.

URL: http://www.ncbi.nlm.nih.gov/pubmed/26568603.

[140]   Y. Shibahara et al.

"235U/238U Isotopic ratio in plant samples from Fukushima Prefecture".

In: *Journal of Radioanalytical and Nuclear Chemistry* 303.2 (Sept. 2014), pp. 1421–1424.

ISSN: 0236-5731.

DOI: 10.1007/s10967-014-3542-y.

URL: http://link.springer.com/10.1007/s10967-014-3542-y.

[141]   Yuji Shibahara et al.

"Determination of isotopic ratios of plutonium and uranium in soil samples by thermal ionization mass spectrometry".

In: *Journal of Radioanalytical and Nuclear Chemistry* 307.3 (Oct. 2015), pp. 2281–2287.

ISSN: 0236-5731.

DOI: 10.1007/s10967-015-4551-1.

URL: http://link.springer.com/10.1007/s10967-015-4551-1.

[142]   Taeko Shinonaga et al.

"Airborne plutonium and non-natural uranium from the fukushima DNPP found at 120 km distance a few days after reactor hydrogen explosions."

In: *Environmental Science & Technology* 48.7 (Apr. 2014), pp. 3808–3814.

ISSN: 1520-5851.

DOI: 10.1021/es404961w.

URL: http://dx.doi.org/10.1021/es404961w.

[143]   Jian Zheng et al.

"Isotopic evidence of plutonium release into the environment from the Fukushima DNPP accident".

In: *Scientific Reports* 2.304 (Jan. 2012), p. 8.

ISSN: 2045-2322.

DOI: 10.1038/srep00304.

URL: http://www.nature.com/srep/2012/120308/srep00304/full/srep00304.html?WT.ec_id=SREP-639,638-20120402.

[144]   Stephanie Schneider et al.

"Radionuclide pollution inside the Fukushima Daiichi exclusion zone, part 2: Forensic search for the "Forgotten" contaminants Uranium-236 and plutonium".

In: *Applied Geochemistry* 85.B (2017), pp. 194–200.

ISSN: 08832927.

DOI: 10.1016/j.apgeochem.2017.05.022.

URL: http://www.sciencedirect.com/science/article/pii/S0883292717300896.

[145]   Georg Steinhauser.

"Fukushima's forgotten radionuclides: a review of the understudied radioactive emissions."

In: *Environmental Science & Technology* 48.9 (May 2014), pp. 4649–4663.

ISSN: 1520-5851.

DOI: 10.1021/es405654c.

URL: http://dx.doi.org/10.1021/es405654c.

[146]   J Timbrell.

Principles of biochemical toxicology.

3rd Ed.

CRC Press, 1999,

P. 404.

ISBN: 0-203-48417-7.

DOI: 10.1007/s13398-014-0173-7.2.

URL: https://books.google.co.uk/books?hl=en&lr=&id=ElriaDL4QcEC&oi=fnd&pg=PT10&dq=Principles+of+Biochemical+Toxicology.+Timbrell,+John&ots=Oo1cfAwIR4&sig=XqL6H9DiPNv7RNXe3yD88pcusRM.

[147]   Wolfgang Runde.

"The Chemical Interactions of Actinides in the Environment".

In: *Los Alamos Science* 26 (2000), pp. 392–411.

URL: http://library.lanl.gov/cgi-bin/getfile?26-39.pdf.

[148]   M. De Cort.

Atlas of caesium deposition on Europe after the Chernobyl accident.

Tech. rep.

IAEA, 1998.

URL: https://inis.iaea.org/search/search.aspx?orig_q=RN:37064773.

[149] L. Anspaugh, R. Catlin, and M Goldman.

"The global impact of the Chernobyl reactor accident".

In: *Science* 242 (Dec. 1988), pp. 1513–1519.

ISSN: 0036-8075.

DOI: 10.1126/science.3201240.

URL: http://www.sciencemag.org/content/242/4885/1513.short.

[150] Hideyuki Kawamura et al.

"Preliminary Numerical Experiments on Oceanic Dispersion of 131 I and 137 Cs Discharged into the Ocean because of the Fukushima Daiichi Nuclear Power Plant Disaster".

In: *Journal of Nuclear Science and Technology* 48.11 (Nov. 2011), pp. 1349–1356.

ISSN: 0022-3131.

DOI: 10.1080/18811248.2011.9711826.

URL: http://www.tandfonline.com/doi/abs/10.1080/18811248.2011.9711826.

[151] Geological Survey of Japan.

Geological Survey of Japan (GSJ), AIST.

Tech. rep.

Tokyo, 2015.

URL: https://www.gsj.jp/en/index.html.

[152] Geospatial Information Authority of Japan.

Maps & Geospatial Information.

2017.

URL: http://www.gsi.go.jp/ENGLISH/page_e30031.html.

[153] Masamichi Chino et al.

"Utilization of 134Cs/137Cs in the environment to identify the reactor units that caused atmospheric releases during the Fukushima Daiichi accident".

In: *Scientific Reports* 6.31376 (Aug. 2016), p. 14.

ISSN: 2045-2322.

DOI: 10.1038/srep31376.

URL: http://www.nature.com/articles/srep31376.

[154] METI.

Restricted Area, Deliberate Evacuation Area And Regions including Specific Spots Recommended for Evacuation.

2011.

URL: http://www.meti.go.jp/english/earthquake/nuclear/roadmap/pdf/evacuation_map_111125.pdf.

[155] Government of Japan.
Act on Special Measures Concerning the Handling of Radioactive Pollution.
Tokyo, 2011.

[156] METI.
Areas to which Evacuation Orders have been issued.
2015.
URL: http : / / www . meti . go . jp / english / earthquake / nuclear / roadmap / pdf / 150905MapOfAreas.pdf.

[157] Fukushima On The Globe.
Fukushima Hinansya: Evacuees by Number.
Tech. rep.
2014,
P. 20.
URL: http://fukushimaontheglobe.com/wp-content/uploads/fukushima_hinansya_ en.pdf.

[158] I. Waddington et al.
"J-value assessment of relocation measures following the nuclear power plant accidents at Chernobyl and Fukushima Daiichi".
In: *Process Safety and Environmental Protection* 112 (Nov. 2017), pp. 16–49.
ISSN: 09575820.
DOI: 10.1016/j.psep.2017.03.012.
URL: http://linkinghub.elsevier.com/retrieve/pii/S0957582017300782.

[159] Tomoyuki Takahashi.
Radiological issues for Fukushima's revitalized future.
2016,
P. 232.
ISBN: 9784431558484.
DOI: 10.1007/978-4-431-55848-4.
URL: http://link.springer.com/content/pdf/10.1007/978-4-431-55848-4.pdf.

[160] M Yamamoto et al.
"Isotopic Pu, Am and Cm signatures in environmental samples contaminated by the Fukushima Dai-ichi Nuclear Power Plant accident."
In: *Journal of Environmental Radioactivity* 132 (June 2014), pp. 31–46.
ISSN: 1879-1700.
DOI: 10.1016/j.jenvrad.2014.01.013.
URL: http://www.sciencedirect.com/science/article/pii/S0265931X14000162.

[161] Yuji Shibahara et al.

335

"Analysis of cesium isotope compositions in environmental samples by thermal ionization mass spectrometry - 1. A preliminary study for source analysis of radioactive contamination in Fukushima prefecture".
In: *Journal of Nuclear Science and Technology* 51.5 (Mar. 2014), pp. 575–579.
ISSN: 0022-3131.
DOI: 10.1080/00223131.2014.891954.
URL: http://www.tandfonline.com/doi/full/10.1080/00223131.2014.891954#.VZAU5PlVhBc.

[162] Jian Zheng et al.
"135Cs/137Cs Isotopic Ratio as a New Tracer of Radiocesium Released from the Fukushima Nuclear Accident".
In: *Environmental Science & Technology* 48 (May 2014), pp. 5433–5438.
ISSN: 0013-936X.
DOI: 10.1021/es500403h.
URL: http://dx.doi.org/10.1021/es500403h.

[163] Guosheng Yang, Hirofumi Tazoe, and Masatoshi Yamada.
"135Cs activity and 135Cs/137Cs atom ratio in environmental samples before and after the Fukushima Daiichi Nuclear Power Plant accident."
In: *Scientific Reports* 6.24119 (2016), p. 8.
ISSN: 2045-2322.
DOI: 10.1038/srep24119.
URL: http://www.nature.com/srep/2016/160407/srep24119/full/srep24119.html.

[164] Yukihiko Satou.
"Study of relationship between deposition of radioactive materials and radioactive particles in the difficult-to-return zone caused by the Fukushima Dai-ichi Nuclear Power Plant accident".
PhD thesis. University of Tsukuba, 2016,
P. 128.

[165] CRC Press.
CRC Handbook of Chemistry and Physics - Summary Properties of the Elements.
Ed. by W.M. Haynes.
96th Ed.
Boca Raton, Florida, 2015,
Pp. 4–11.
URL: http://hbcponline.com/faces/documents/04_01/04_01_0001.xhtml.

[166] Satoshi Mikami et al.

"Spatial distributions of radionuclides deposited onto ground soil around the Fukushima Dai-ichi Nuclear Power Plant and their temporal change until December 2012."
In: *Journal of Environmental Radioactivity* 139 (Jan. 2015), pp. 320–343.
ISSN: 1879-1700.
DOI: 10.1016/j.jenvrad.2014.09.010.
URL: http://www.sciencedirect.com/science/article/pii/S0265931X14002768.

[167]   B. L. Sawhney.
"Selective sorption and fixation of cations by clay minerals. A review".
In: *Clays and Clay Minerals* 20 (1972), pp. 93–100.
ISSN: 00098604.
DOI: 10.1346/CCMN.1972.0200208.

[168]   A. Cremers et al.
"Quantitative analysis of radiocaesium retention in soils".
In: *Nature* 335 (Sept. 1988), pp. 247–249.
ISSN: 0028-0836.
DOI: 10.1038/335247a0.
URL: http://dx.doi.org/10.1038/335247a0.

[169]   Hiroki Mukai et al.
"Speciation of radioactive soil particles in the Fukushima contaminated area by IP autoradiography and microanalyses."
In: *Environmental Science & Technology* 48.22 (Oct. 2014), 13053,Äì13059.
ISSN: 1520-5851.
DOI: 10.1021/es502849e.
URL: http://dx.doi.org/10.1021/es502849e.

[170]   R. Broda.
Gamma spectroscopy analysis of hot particles from the Chernobyl fallout.
Tech. rep.
1986,
P. 30.
URL: http://www.iaea.org/inis/collection/NCLCollectionStore/_Public/21/014/21014068.pdf.

[171]   L. Devell et al.
"Initial observations of fallout from the reactor accident at Chernobyl".
In: *Nature* 321.6067 (May 1986), pp. 192–193.
ISSN: 0028-0836.
DOI: 10.1038/321192a0.
URL: http://dx.doi.org/10.1038/321192a0.

[172]   Rolf Falk, Jorma Suomela, and Andor Kerekes.
        "A study of "hot particles" collected in Sweden one year after the chernobyl accident".
        In: *Journal of Aerosol Science* 19.7 (Jan. 1988), pp. 1339–1342.
        ISSN: 00218502.
        DOI: 10.1016/0021-8502(88)90168-1.
        URL: http://www.sciencedirect.com/science/article/pii/0021850288901681.

[173]   F.J. Sandalls, M.G. Segal, and N. Victorova.
        "Hot particles from Chernobyl: A review".
        In: *Journal of Environmental Radioactivity* 18.1 (Jan. 1993), pp. 5–22.
        ISSN: 0265931X.
        DOI: 10.1016/0265-931X(93)90063-D.
        URL: http://www.sciencedirect.com/science/article/pii/0265931X9390063D.

[174]   J. Bruno and R. C. Ewing.
        "Spent Nuclear Fuel".
        In: *Elements* 2.6 (Dec. 2006), pp. 343–349.
        ISSN: 1811-5209.
        DOI: 10.2113/gselements.2.6.343.
        URL: http://elements.geoscienceworld.org/content/2/6/343.short.

[175]   K. Edvarson, Kerstin Low, and J. Sisefsky.
        "Fractionation Phenomena in Nuclear Weapons Debris".
        In: *Nature* 184.4701 (Dec. 1959), pp. 1771–1774.
        ISSN: 0028-0836.
        DOI: 10.1038/1841771a0.
        URL: http://www.nature.com/doifinder/10.1038/1841771a0.

[176]   C.E. Adams, N.H. Farlow, and W.R. Schell.
        "The compositions, structures and origins of radioactive fall-out particles".
        In: *Geochimica et Cosmochimica Acta* 18 (Jan. 1960), pp. 42–56.
        ISSN: 00167037.
        DOI: 10.1016/0016-7037(60)90016-8.
        URL: http://www.sciencedirect.com/science/article/pii/0016703760900168.

[177]   J. Mackin et al.
        "Radiochemical analysis of individual fall-out particles".
        In: *Journal of Inorganic and Nuclear Chemistry* 15.1-2 (Sept. 1960), pp. 20–36.
        ISSN: 00221902.
        DOI: 10.1016/0022-1902(60)80005-X.
        URL: http://www.sciencedirect.com/science/article/pii/002219026080005X.

[178]   J.M. Kelley, L.A. Bond, and T.M. Beasley.

"Global distribution of Pu isotopes and 237Np".
In: *Science of The Total Environment* 237-238 (Sept. 1999), pp. 483–500.
ISSN: 00489697.
DOI: 10.1016/S0048-9697(99)00160-6.
URL: http://www.sciencedirect.com/science/article/pii/S0048969799001606.

[179] Qin-Hong Hu, Jian-Qing Weng, and Jin-Sheng Wang.
"Sources of anthropogenic radionuclides in the environment: a review."
In: *Journal of Environmental Radioactivity* 101.6 (June 2010), pp. 426–37.
ISSN: 1879-1700.
DOI: 10.1016/j.jenvrad.2008.08.004.
URL: http://www.sciencedirect.com/science/article/pii/S0265931X08001392.

[180] O C Lind et al.
"Characterization of U/Pu particles originating from the nuclear weapon accidents at
Palomares, Spain, 1966 and Thule, Greenland, 1968."
In: *Science of The Total Environment* 376.1-3 (Apr. 2007), pp. 294–305.
ISSN: 0048-9697.
DOI: 10.1016/j.scitotenv.2006.11.050.
URL: http://www.sciencedirect.com/science/article/pii/S0048969706009028.

[181] R Pöllänen et al.
"Multi-technique characterization of a nuclear bomb particle from the Palomares accident."
In: *Journal of Environmental Radioactivity* 90.1 (Jan. 2006), pp. 15–28.
ISSN: 0265-931X.
DOI: 10.1016/j.jenvrad.2006.06.007.
URL: http://www.sciencedirect.com/science/article/pii/S0265931X06000932.

[182] J. Garcia Lopez et al.
"Characterisation of hot particles remaining in soils from Palomares (Spain) using a
nuclear microprobe".
In: *Nuclear Instruments and Methods in Physics Research Section B: Beam Interactions
with Materials and Atoms* 260.1 (July 2007), pp. 343–348.
ISSN: 0168583X.
DOI: 10.1016/j.nimb.2007.02.044.
URL: http://www.sciencedirect.com/science/article/pii/S0168583X07004193.

[183] Daniel E Crean et al.
"Microanalytical X-ray imaging of depleted uranium speciation in environmentally aged
munitions residues."
In: *Environmental Science & Technology* 48.3 (Jan. 2014), pp. 1467–1474.
ISSN: 1520-5851.

DOI: 10.1021/es403938d.

URL: http://dx.doi.org/10.1021/es403938d.

[184] F.R. Livens and M.S. Baxter.
"Particle size and radionuclide levels in some west Cumbrian soils".
In: *Science of The Total Environment* 70 (Mar. 1988), pp. 1–17.
ISSN: 00489697.
DOI: 10.1016/0048-9697(88)90248-3.
URL: http://www.sciencedirect.com/science/article/pii/0048969788902483.

[185] R Pollanen.
"Nuclear fuel particles in the environment - characteristics, atmospheric transport and skin doses."
PhD thesis. University of Helsinki, 2002,
P. 147.
ISBN: 9517125283.
URL: http://www.iaea.org/inis/collection/NCLCollectionStore/_Public/33/043/33043484.pdf.

[186] Brit Salbu and Trygve Krekling.
"Characterisation of radioactive particles in the environment".
In: *The Analyst* 123.5 (Jan. 1998), pp. 843–850.
ISSN: 00032654.
DOI: 10.1039/a800314i.
URL: http://pubs.rsc.org/en/Content/ArticleLanding/1998/AN/A800314I.

[187] B. Salbu and O. C. Lind.
"Radioactive particles released from various nuclear sources".
In: *Radioprotection* 40 (June 2005), pp. 27–32.
ISSN: 0033-8451.
DOI: 10.1051/radiopro:2005s1-005.
URL: http://www.radioprotection.org/10.1051/radiopro:2005s1-005.

[188] Margaret West et al.
"2016 Atomic Spectrometry Update - a review of advances in X-ray fluorescence spectrometry and its applications".
In: *Journal of Analytical Atomic Spectrometry* 31.9 (2016), pp. 1706–1755.
ISSN: 0267-9477.
DOI: 10.1039/C6JA90034H.
URL: http://xlink.rsc.org/?DOI=C6JA90034H.

[189] IAEA.
Nuclear Forensics in Support of Investigations.

Vienna, 2015,

P. 80.

ISBN: 978-92-0-102115-1.

URL: http://www-pub.iaea.org/books/IAEABooks/10797/Nuclear-Forensics-in-Support-of-Investigations.

[190] Takahiro Ono et al.

"Investigation of the Chemical Characteristics of Individual Radioactive Microparticles Emitted from Reactor 1 by the Fukushima Daiichi Nuclear Power Plant Accident by Using Multiple Synchrotron Radiation X-ray Analyses".

In: *Bunseki Kagaku* 66.4 (2017), pp. 251–261.

ISSN: 0525-1931.

DOI: 10.2116/bunsekikagaku.66.251.

URL: https://www.jstage.jst.go.jp/article/bunsekikagaku/66/4/66_251/_article/-char/ja/.

[191] Kouji Adachi et al.

"Emission of spherical cesium-bearing particles from an early stage of the Fukushima nuclear accident."

In: *Scientific Reports* 3.2554 (Jan. 2013), p. 5.

ISSN: 2045-2322.

DOI: 10.1038/srep02554.

URL: http://www.nature.com/srep/2013/130830/srep02554/full/srep02554.html.

[192] Yoshinari Abe et al.

"Detection of uranium and chemical state analysis of individual radioactive microparticles emitted from the Fukushima nuclear accident using multiple synchrotron radiation X-ray analyses."

In: *Analytical Chemistry* 86.17 (Sept. 2014), pp. 8521–8525.

ISSN: 1520-6882.

DOI: 10.1021/ac501998d.

URL: dx.doi.org/10.1021/ac501998d.

[193] Noriko Yamaguchi et al.

"Internal structure of cesium-bearing radioactive microparticles released from Fukushima nuclear power plant".

In: *Scientific Reports* 6.20548 (Feb. 2016), p. 6.

ISSN: 2045-2322.

DOI: 10.1038/srep20548.

URL: http://www.nature.com/srep/2016/160203/srep20548/full/srep20548.html.

[194] Toshihiro Kogure et al.

"Constituent elements and their distribution in the radioactive Cs-bearing silicate glass microparticles released from Fukushima nuclear plant".
In: *Microscopy* 65.5 (Aug. 2016), pp. 451–459.
ISSN: 2050-5698.
DOI: 10.1093/jmicro/dfw030.
URL: http://jmicro.oxfordjournals.org/lookup/doi/10.1093/jmicro/dfw030.

[195]   Yukihiko Satou et al.
"First successful isolation of radioactive particles from soil near the Fukushima Daiichi Nuclear Power Plant".
In: *Anthropocene* 14 (June 2016), pp. 71–76.
ISSN: 22133054.
DOI: 10.1016/j.ancene.2016.05.001.
URL: http://linkinghub.elsevier.com/retrieve/pii/S2213305416300340.

[196]   Shogo Higaki et al.
"Discovery of non-spherical heterogeneous radiocesium-bearing particles not derived from Unit 1 of the Fukushima Dai-ichi Nuclear Power Plant , in residences five years after the accident".
In: *Journal of Environmental Radioactivity* 177 (2017), pp. 65–70.
ISSN: 0265-931X.
DOI: 10.1016/j.jenvrad.2017.06.006.
URL: http://www.sciencedirect.com/science/article/pii/S0265931X17302333.

[197]   Genki Furuki et al.
"Caesium-rich micro-particles: A window into the meltdown events at the Fukushima Daiichi Nuclear Power Plant".
In: *Scientific Reports* 7.42731 (Feb. 2017), p. 10.
DOI: 10.1038/srep42731.
URL: http://www.nature.com/articles/srep42731.

[198]   Antonella Balerna and Settimio Mobilio.
"Synchrotron Radiation: Basics, Methods and Applications".
In: *Introduction to Synchrotron Radiation*.
Berlin, Heidelberg: Springer Berlin Heidelberg, 2015,
P. 799.
ISBN: 9783642553158.
DOI: 10.1007/978-3-642-55315.
URL: http://link.springer.com/10.1007/978-3-642-55315-8_1.

[199]   Tetsuo Yasutaka, Wataru Naito, and Junko Nakanishi.

"Cost and effectiveness of decontamination strategies in radiation contaminated areas in Fukushima in regard to external radiation dose."
In: *PloS One* 8.9 (Jan. 2013), p. 11.
ISSN: 1932-6203.
DOI: 10.1371/journal.pone.0075308.
URL: http://journals.plos.org/plosone/article?id=10.1371/journal.pone.0075308.

[200] Japanese Ministry of the Environment (Government of Japan).
Management of off-site Waste Contaminated with Radioactive Materials due to the Accident at Fukushima Nuclear Power Stations.
Tech. rep.
Tokyo, 2012,
P. 33.
URL: https://www.env.go.jp/en/focus/docs/files/20121128-58.pdf.

[201] Sergey Fesenko et al.
"A Comparison of Remediation After The Chernobyl and Fukushima Daiichi Accidents."
In: *Radiation Protection Dosimetry* 312 (Nov. 2016), pp. 1–7.
ISSN: 1742-3406.
DOI: 10.1093/rpd/ncw312.
URL: http://www.ncbi.nlm.nih.gov/pubmed/27886996.

[202] Fukushima Reconstruction Agency.
Reconstruction from Nuclear Disaster & the History of Safety and Revitalization of Fukushima.
Tech. rep.
Fukushima Reconstruction Agency, 2017,
P. 16.
URL: http://www.reconstruction.go.jp/topics/main-cat1/20170427_huhyou-higai-husshoku_E.pdf#page=6.

[203] Tetsuo Yasutaka and Wataru Naito.
"Assessing cost and effectiveness of radiation decontamination in Fukushima Prefecture, Japan".
In: *Journal of Environmental Radioactivity* 151 (Jan. 2016), pp. 512–520.
ISSN: 18791700.
DOI: 10.1016/j.jenvrad.2015.05.012.
URL: http://linkinghub.elsevier.com/retrieve/pii/S0265931X15001575.

[204] UK National Audit Office.
Nuclear Decomissioning Authority - Progress on the Sellafield site: an update.

Tech. rep.

National Audit Office (NAO), 2015,

P. 31.

URL: http://www.parliament.uk/documents/commons-committees/public-accounts/
Progress-on-Sellafield-Site.pdf.

[205]   Japanese Ministry of the Environment (Government of Japan).

Environmental Remediation.

2017.

URL: http://josen.env.go.jp/en/#top03.

[206]   Glenn F. Knoll.

Radiation Detection and Measurement.

John Wiley & Sons, 2010,

P. 860.

ISBN: 0470131489.

DOI: 10.1017/CBO9781107415324.004.

[207]   P Leclair.

Gamma Ray Attenuation.

Tech. rep.

2010,

P. 16.

URL: http://faculty.mint.ua.edu/~pleclair/PH255/templates/formal/formal.
pdf.

[208]   Patricia E. Watson, Ian D Watson, and Richard D Bait.

"Total body water females estimated volumes for adult males and from simple anthropometric
measurements".

In: *The American Journal of Clinical Nutrition* 33.1 (1980), 27‚Äì39.

ISSN: 0002-9165.

[209]   Kromek Group PLC.

SIGMA Spec Sheet; Revision 6.

2015.

URL: http://www.kromek.com/downloads/sigma_rev6web.pdf.

[210]   Kromek Group PLC.

GR1 Spec Sheet; Revision 10.

2015.

URL: http://www.kromek.com/products_gr1spectrometer.asp.

[211]   National Physical Laboratory.

Intrinsic Photopeak Detection Efficiency as a Function of Energy: Kromek GR1.

Tech. rep.

Teddington: National Physical Laboratory, 2013,

P. 3.

[212] National Physical Laboratory.

Intrinsic Photopeak Detection Efficiency as a Function of Energy: Kromek SIGMA-50.

Tech. rep.

Teddington: National Physical Laboratory, 2015,

P. 2.

[213] Steven Bell.

"A comparison of emerging gamma detector technologies for airborne radiation monitoring".

In: *ANSRI 2016 Dublin*.

Dublin, Ireland, 2016,

P. 21.

URL: http://spacescience.ie/ansri2016/ansri2016_talks/31-VI-Bell.pdf.

[214] P.G. Martin et al.

"Development and validation of a high-resolution mapping platform to aid in the public awareness of radiological hazards".

In: *Journal of Radiological Protection* 38.1 (Jan. 2018), pp. 329–342.

ISSN: 0952-4746.

DOI: 10.1088/1361-6498/aaa914.

URL: http://iopscience.iop.org/article/10.1088/1361-6498/aaa914.

[215] Sakae Kinase et al.

"Changes in ambient dose equivalent rates around roads at Kawamata town after the Fukushima accident".

In: *Radiation Protection Dosimetry* 167 (Nov. 2015), pp. 1–4.

ISSN: 0144-8420.

DOI: 10.1093/rpd/ncv275.

URL: http://www.ncbi.nlm.nih.gov/pubmed/25953794.

[216] A. J. Cresswell et al.

"Demonstration of lightweight gamma spectrometry systems in urban environments".

In: *Journal of Environmental Radioactivity* 124 (2013), pp. 22–28.

ISSN: 0265931X.

DOI: 10.1016/j.jenvrad.2013.03.006.

[217] C. J. Moon.

"Geochemical exploration in Cornwall and Devon: a review".

In: *Geochemistry: Exploration, Environment, Analysis* 10.Williams 1954 (Aug. 2010), pp. 331–351.

345

ISSN: 1467-7873.

DOI: 10.1144/1467-7873/09-239.

URL: http://geea.lyellcollection.org/cgi/doi/10.1144/1467-7873/09-239.

[218] A. G. Darnley et al.
"Ages of Uraninite and Coffinite from South-West England".
In: *Mineralogical Magazine* 34.268 (1965), pp. 159–176.
ISSN: 0026-461X.
DOI: 10.1180/minmag.1965.034.268.13.
URL: http://www.minersoc.org/pages/Archive-MM/Volume_34/34-268-159.pdf.

[219] H.G. Dines.
The metalliferous mining region of South-West England.
London: HMSO, 1956.

[220] David Beamish.
"Environmental radioactivity in the UK: the airborne geophysical view of dose rate estimates."
In: *Journal of Environmental Radioactivity* 138 (Dec. 2014), pp. 249–263.
ISSN: 1879-1700.
DOI: 10.1016/j.jenvrad.2014.08.025.
URL: http://www.sciencedirect.com/science/article/pii/S0265931X14002598.

[221] Public Health England.
Guidance: Ionising radiation - dose comparision.
2011.
URL: https://www.gov.uk/government/publications/ionising-radiation-dose-comparisons/ionising-radiation-dose-comparisons.

[222] Leslie Rowsell Moore and Arthur E. Trueman.
"The Coal Measures of Bristol and Somerset".
In: *Quarterly Journal of the Geological Society* 93.1-4 (1937), pp. 195–240.
ISSN: 00167649.
DOI: 10.1144/GSL.JGS.1937.093.01-04.10.
URL: http://jgs.lyellcollection.org/content/93/1-4/195.short.

[223] The Coal Authority.
Coal Mining Report Ground Stability Report.
2017.
URL: https://www.groundstability.com/public/web/home.xhtml.

[224] Henry Thomas De La Beche.
Report on the Geology of Cornwall, Devon and West Somerset.
Longman, 1839,

P. 648.

[225] P.G. Martin et al.
"Radiological Assessment on Interest Areas on the Sellafield Nuclear Site via Unmanned Aerial Vehicle".
In: *Remote Sensing* 913.8 (Nov. 2016), p. 10.
ISSN: 2072-4292.
DOI: 10.3390/rs8110913.
URL: http://www.mdpi.com/2072-4292/8/11/913.

[226] P.G. Martin et al.
"The use of unmanned aerial systems for the mapping of legacy uranium mines".
In: *Journal of Environmental Radioactivity* 143 (May 2015), pp. 135–140.
ISSN: 0265931X.
DOI: 10.1016/j.jenvrad.2015.02.004.
URL: http://www.sciencedirect.com/science/article/pii/S0265931X15000314.

[227] P.G. Martin et al.
"In-situ removal and characterisation of uranium-containing particles from sediments surrounding the Fukushima Daiichi Nuclear Power Plant".
In: *Spectrochimica Acta Part B: Atomic Spectroscopy* 117 (Mar. 2016), pp. 1–7.
ISSN: 05848547.
DOI: 10.1016/j.sab.2015.12.010.
URL: http://www.sciencedirect.com/science/article/pii/S0584854715003006.

[228] AR2500 Acuity.
Acuity AR2500 Specification.
Tech. rep.
2014,
P. 2.
URL: www.acuitylaser.com.

[229] S. Agostinelli et al.
"GEANT4 - A simulation toolkit".
In: *Nuclear Instruments and Methods in Physics Research, Section A: Accelerators, Spectrometers, Detectors and Associated Equipment* 506 (2003), pp. 250–303.
ISSN: 01689002.
DOI: 10.1016/S0168-9002(03)01368-8.
URL: http://www.sciencedirect.com/science/article/pii/S0168900203013688,.

[230] ArduCopter.
Mission Planner Autopilot.
2018.

URL: http://ardupilot.org/planner/.

[231]   NRA.
Results of the Ninth Airborne Monitoring and Airborne Monitoring out of the 80km Zone of Fukushima Dai-ichi NPP.
Tech. rep.
NRA, 2015,
P. 4.
URL: http://radioactivity.nsr.go.jp/en/list/307/list-1.html.

[232]   M W Charles and J D Harrison.
"Hot particle dosimetry and radiobiology–past and present."
In: *Journal of Radiological Protection* 27.3A (Sept. 2007), pp. 97–109.
ISSN: 0952-4746.
DOI: 10.1088/0952-4746/27/3A/S11.
URL: http://stacks.iop.org/0952-4746/27/i=3A/a=S11.

[233]   C. Arden Pope III et al.
"Lung Cancer, Cardiopulmonary Mortality, and Long-term Exposure to Fine Particulate Air Pollution".
In: *JAMA* 287.9 (Mar. 2002), pp. 1132–1141.
ISSN: 0098-7484.
DOI: 10.1001/jama.287.9.1132.
URL: http://jama.jamanetwork.com/article.aspx?articleid=194704.

[234]   NRA.
Results of the Eighth Airborne Monitoring and Airborne Monitoring out of the 80km Zone of Fukushima Dai-ichi NPP.
Tech. rep.
NRA, 2014,
P. 3.
URL: http://radioactivity.nsr.go.jp/en/list/307/list-1.html.

[235]   Yuichi Onda et al.
"Soil sampling and analytical strategies for mapping fallout in nuclear emergencies based on the Fukushima Dai-ichi Nuclear Power Plant accident."
In: *Journal of Environmental Radioactivity* 139 (Jan. 2015), pp. 300–307.
ISSN: 1879-1700.
DOI: 10.1016/j.jenvrad.2014.06.002.
URL: http://www.sciencedirect.com/science/article/pii/S0265931X14001659.

[236]   IAEA.
"Technical Volume 4 of 5: Radiological Consequences".

In: *The Fukushima Daiichi Accident*.
Vienna, Austria: IAEA, 2015,
P. 262.
ISBN: 978-92-0-107015-9.
URL: http://www-pub.iaea.org/MTCD/Publications/PDF/AdditionalVolumes/
P1710/Pub1710-TV4-Web.pdf.

[237] B. Voutou and E. Stefanaki.
Electron Microscopy: The Basics.
Thessaloniki, 2008,
P. 11.
URL: https://optiki.files.wordpress.com/2013/03/electron-microscopythe-
basics.pdf.

[238] Chemistry: LibreTexts.
Electromagnetic Radiation.
2017.
URL: https://chem.libretexts.org/Core/Physical_and_Theoretical_Chemistry/
Spectroscopy/Fundamentals_of_Spectroscopy/Electromagnetic_Radiation.

[239] Joseph I. Goldstein et al.
*Scanning Electron Microscopy and X-Ray Microanalysis: A Text for Biologists, Materials
Scientists, and Geologists*.
2nd Ed.
New York: Plenum Press, 1992,
P. 807.

[240] Carl Zeiss NTS - Nano Technology System Division.
Zeiss SIGMA HD Product Manual.
Tech. rep.
Cambridge: Carl Zeiss Limited, 2014,
P. 132.
URL: https://www.zeiss.com/microscopy/int/products/scanning-electron-
microscopes/sigma.html.

[241] T E Everhart and R F M Thornley.
"Wide-band detector for micro-microampere low-energy electron currents".
In: *Journal of Scientific Instruments* 37.7 (July 1960), pp. 246–248.
ISSN: 10765670.
DOI: 10.1016/S1076-5670(04)33009-0.
URL: http://stacks.iop.org/0950-7671/37/.

[242] Dale E Newbury and Nicholas W M Ritchie.

"Is scanning electron microscopy/energy dispersive X-ray spectrometry (SEM/EDS) quantitative?"
In: *Scanning* 35.3 (Jan. 2012), pp. 141–68.
ISSN: 1932-8745.
DOI: 10.1002/sca.21041.
URL: http://www.ncbi.nlm.nih.gov/pubmed/22886950.

[243]   S. Kleindiek.
"Miniature three-axis micropositioner for scanning proximal probe and other applications".
In: *Journal of Vacuum Science & Technology B: Microelectronics and Nanometer Structures*
13.6 (Nov. 1995), p. 2653.
ISSN: 0734211X.
DOI: 10.1116/1.588043.
URL: http://scitation.aip.org/content/avs/journal/jvstb/13/6/10.1116/1.
588043.

[244]   R. L. Seliger et al.
"A high-intensity scanning ion probe with submicrometer spot size".
In: *Applied Physics Letters* 34.5 (Mar. 1979), pp. 310–312.
ISSN: 00036951.
DOI: 10.1063/1.90786.
URL: http://aip.scitation.org/doi/10.1063/1.90786.

[245]   M. W. Phaneuf.
"Applications of focused ion beam microscopy to materials science specimens".
In: *Micron* 30.3 (June 1999), pp. 277–288.
ISSN: 09684328.
DOI: 10.1016/S0968-4328(99)00012-8.
URL: http://linkinghub.elsevier.com/retrieve/pii/S0968432899000128.

[246]   EAG Laboratories.
Secondary Ion Mass Spectrometry (SIMS).
2017.
URL: https://www.eag.com/techniques/mass-spec/secondary-ion-mass-spectrometry-
sims/.

[247]   C. A. Volkert and A. M. Minor.
"Focused Ion Beam Microscopy and Micromachining".
In: *MRS Bulletin* 32.5 (2007), pp. 389–399.
ISSN: 0883-7694.
DOI: 10.1557/mrs2007.62.
URL: https://www.cambridge.org/core/journals/mrs-bulletin/article/focused-
ion-beam-microscopy-and-micromachining/53AD122BB293A13D1132A357834E0348.

[248] James W. Mayer and Ogden J. Marsh.
Applied Solid State Science: Advances in Materials and Device Research - Ion Implantation in Semiconductors.
Ed. by Raymond Wolfe.
New York: Academic Press, 1969,
Pp. 239–342.
URL: https://books.google.co.jp/books?hl=en&lr=&id=brU3BQAAQBAJ&oi=fnd&pg=PA239&dq=ion+implantation+semiconductor&ots=24Dfd6uMYe&sig=HntivbY-taMfE4p9IhnOECH5iBs.

[249] Steve Reyntjens and Robert Puers.
"A review of focused ion beam applications in microsystem technology".
In: *Journal of Micromechanics and Microengineering* 11.4 (July 2001), pp. 287–300.
ISSN: 0960-1317.
DOI: 10.1088/0960-1317/11/4/301.
URL: http://stacks.iop.org/0960-1317/11/.

[250] Carl Zeiss NTS - Nano Technology System Division.
Zeiss Crossbeam FIB-SEM Product Manual.
Tech. rep.
Cambridge: Carl Zeiss Limited, 2017,
P. 196.
URL: https://www.zeiss.com/microscopy/int/products/fib-sem-instruments.html.

[251] L. W. Swanson.
"Liquid metal ion sources: Mechanism and applications".
In: *Nuclear Instruments and Methods In Physics Research* 218.1 (Dec. 1983), pp. 347–353.
ISSN: 01675087.
DOI: 10.1016/0167-5087(83)91005-0.
URL: http://linkinghub.elsevier.com/retrieve/pii/0167508783910050.

[252] Chengge Jiao.
FIB and DualBeam Theory and Applications.
Tech. rep.
Oregon, USA: FEI Company, 2006,
P. 42.
URL: http://www.nanophys.kth.se/nanophys/facilities/nfl/secret-kth/fei-app-course/FibDualBTheoryApplCustomTrain.pdf.

[253] L. A. Giannuzzi and F. A. Stevie.
Introduction to Focused Ion Beams: Instrumentation, Theory, Techniques and Practice.

1st Ed.

New York: Springer US, 2005,

Pp. 1–12.

ISBN: 978-0-387-23116-7.

URL: http://link.springer.com/10.1007/0-387-23313-X_1.

[254] L Salvo et al.

"X-ray micro-tomography an attractive characterisation technique in materials science".

In: *Nuclear Instruments and Methods in Physics Research, Section B: Beam Interactions with Materials and Atoms*.

Vol. 200.

2003,

Pp. 273–286.

ISBN: 0168-583X.

DOI: 10.1016/S0168-583X(02)01689-0.

[255] Luc Salvo et al.

3D imaging in material science: Application of X-ray tomography.

Nov. 2010.

DOI: 10.1016/j.crhy.2010.12.003.

URL: http://www.sciencedirect.com/science/article/pii/S1631070510001660.

[256] Grant Bunker.

Introduction to XAFS: A Practical Guide to X-ray Absorption Fine Structure Spectroscopy.

Cambridge University Press, 2010,

P. 268.

ISBN: 9780521767750.

DOI: 10.1017/CBO9781107415324.004.

URL: http : / / www . cambridge . org / gb / academic / subjects / physics / condensed - matter - physics - nanoscience - and - mesoscopic - physics / introduction - xafs - practical - guide - x - ray - absorption - fine - structure - spectroscopy ? format = HB&isbn=9780521767750#C97Hu33zTmh1MZaG.97.

[257] Annibale Mottana and Augusto Marcelli.

"The Historical Development of X-ray Absorption Fine Spectroscopy and of Its Applications to Materials Science".

In: *History of Mechanism and Machine Science*.

Springer, Dordrecht, 2015,

Pp. 275–301.

ISBN: 978-94-017-9644-6.

DOI: 10.1007/978-94-017-9645-3{_}15.

URL: http://link.springer.com/10.1007/978-94-017-9645-3_15.

[258] Matthew Newville.
       Fundamentals of XAFS.
       Revision 1.
       2004.
       URL: http://xafs.org/Tutorials?action=AttachFile&do=get&target=Newville_
       xas_fundamentals.pdf.

[259] Wei Qun Shi et al.
       "Exploring actinide materials through synchrotron radiation techniques".
       In: *Advanced Materials* 26.46 (Dec. 2014), pp. 7807–7848.
       ISSN: 15214095.
       DOI: 10.1002/adma.201304323.
       URL: http://doi.wiley.com/10.1002/adma.201304323.

[260] J. A. Bearden.
       "X-ray wavelengths".
       In: *Reviews of Modern Physics* 39.1 (Jan. 1967), pp. 78–124.
       ISSN: 00346861.
       DOI: 10.1103/RevModPhys.39.78.
       URL: https://link.aps.org/doi/10.1103/RevModPhys.39.78.

[261] Carl Zeiss NTS - Nano Technology System Division.
       ZEISS Xradia 520 Versa 3D X-Ray Microscope.
       Tech. rep.
       Cambridge: Carl Zeiss Limited, 2017,
       P. 421.
       URL: https://www.zeiss.com/microscopy/int/products/x-ray-microscopy/zeiss-
       xradia-520-versa.html.

[262] Thermo Fisher Scientific.
       Thermo Scientific Niton FXL 950 Series Analysers.
       Tech. rep.
       Winchester: Niton UK Limited, 2017,
       P. 1.
       URL: https://www.thermofisher.com/order/catalog/product/NITONFXLXRF.

[263] Diamond Light Source Ltd.
       How Diamond Works - Diamond Light Source.
       2017.
       URL: http://www.diamond.ac.uk/Home/About/How-Diamond-Works.html.

[264] J.F.W. Mosselmans et al.
       "I18 - the microfocus spectroscopy beamline at the Diamond Light Source."

In: *Journal of Synchrotron Radiation* 16 (Nov. 2009), pp. 818–824.
ISSN: 1600-5775.
DOI: 10.1107/S0909049509032282.
URL: http://scripts.iucr.org/cgi-bin/paper?ia5044.

[265] Christoph Rau et al.
"Coherent imaging at the Diamond beamline I13".
In: *Physica Status Solidi (A) Applications and Materials Science* 208.11 (Nov. 2011),
pp. 2522–2525.
ISSN: 18626300.
DOI: 10.1002/pssa.201184272.
URL: http://doi.wiley.com/10.1002/pssa.201184272.

[266] F. L. Arnot and J. C. Milligan.
"A New Process of Negative Ion Formation".
In: *Proceedings of the Royal Society A: Mathematical, Physical and Engineering Sciences*
156.889 (Sept. 1936), pp. 538–560.
ISSN: 1364-5021.
DOI: 10.1098/rspa.1936.0166.
URL: http://rspa.royalsocietypublishing.org/cgi/doi/10.1098/rspa.1936.0166.

[267] Richard E. Honig.
"Sputtering of surfaces by positive ion beams of low energy".
In: *Journal of Applied Physics* 29.3 (Mar. 1958), pp. 549–555.
ISSN: 00218979.
DOI: 10.1063/1.1723219.
URL: http://aip.scitation.org/doi/10.1063/1.1723219.

[268] Richard C. Bradley.
"Secondary positive ion emission from metal surfaces".
In: *Journal of Applied Physics* 30.1 (Jan. 1959), pp. 1–8.
ISSN: 00218979.
DOI: 10.1063/1.1734952.
URL: http://aip.scitation.org/doi/10.1063/1.1734952.

[269] J. C. Vickerman and I. Gilmore.
Surface Analysis - The Principal Techniques.
2nd.
Wiley, 2009,
P. 686.
ISBN: 9780470721582.

DOI: 10.1002/9780470721582.

URL: http://doi.wiley.com/10.1002/9780470721582.

[270] Thermo Fisher Scientific.
Inductively Coupled Plasma Mass Spectrometry (ICP-MS).
2017.
URL: https://www.thermofisher.com/uk/en/home/industrial/mass-spectrometry/
inductively-coupled-plasma-mass-spectrometry-icp-ms.html.

[271] N.J. Harker.
"The corrosion of uranium in sealed environments containing oxygen and water vapour."
PhD thesis. University of Bristol, 2012.

[272] James F. Ziegler.
"SRIM-2003".
In: *Nuclear Instruments and Methods in Physics Research, Section B: Beam Interactions
with Materials and Atoms* 219-220 (June 2004), pp. 1027–1036.
ISSN: 0168583X.
DOI: 10.1016/j.nimb.2004.01.208.
URL: http://www.sciencedirect.com/science/article/pii/S0168583X04002587.

[273] Alex Malins et al.
"Evaluation of ambient dose equivalent rates influenced by vertical and horizontal
distribution of radioactive cesium in soil in Fukushima Prefecture."
In: *Journal of Environmental Radioactivity* 151 (Jan. 2016), pp. 38–49.
ISSN: 1879-1700.
DOI: 10.1016/j.jenvrad.2015.09.014.
URL: http://www.sciencedirect.com/science/article/pii/S0265931X15301089.

[274] Norikazu Kinoshita et al.
"Assessment of individual radionuclide distributions from the Fukushima nuclear accident
covering central-east Japan."
In: *Proceedings of the National Academy of Sciences of the United States of America* 108.49
(Dec. 2011), pp. 19526–19529.
ISSN: 1091-6490.
DOI: 10.1073/pnas.1111724108.
URL: http://www.pubmedcentral.nih.gov/articlerender.fcgi?artid=3241760&
tool=pmcentrez&rendertype=abstract.

[275] Jun Koarashi et al.
"Factors affecting vertical distribution of Fukushima accident-derived radiocesium in soil
under different land-use conditions."
In: *The Science of the Total Environment* 431 (Aug. 2012), pp. 392–401.

ISSN: 1879-1026.

DOI: 10.1016/j.scitotenv.2012.05.041.

URL: http://www.sciencedirect.com/science/article/pii/S0048969712007231.

[276] Keiko Tagami et al.
"Specific activity and activity ratios of radionuclides in soil collected about 20 km from the Fukushima Daiichi Nuclear Power Plant: Radionuclide release to the south and southwest."
In: *Science of The Total Environment* 409 (Oct. 2011), pp. 4885–4888.
ISSN: 1879-1026.
DOI: 10.1016/j.scitotenv.2011.07.067.
URL: http://www.sciencedirect.com/science/article/pii/S0048969711008321.

[277] Yosuke Yamashiki et al.
"Initial flux of sediment-associated radiocesium to the ocean from the largest river impacted by Fukushima Daiichi Nuclear Power Plant."
In: *Scientific Reports* 4.3714 (Jan. 2014), p. 7.
ISSN: 2045-2322.
DOI: 10.1038/srep03714.
URL: http://www.nature.com/srep/2014/140116/srep03714/full/srep03714.html?WT.ec_id=SREP-704-20140121_1.

[278] Mochamad Adhiraga Pratama et al.
"Future projection of radiocesium flux to the ocean from the largest river impacted by Fukushima Daiichi Nuclear Power Plant."
In: *Scientific Reports* 5.8408 (Jan. 2015), p. 9.
ISSN: 2045-2322.
DOI: 10.1038/srep08408.
URL: http://www.nature.com/srep/2015/150212/srep08408/full/srep08408.html.

[279] A S Rogowski and T Tamura.
"Movement of 137CS by Runoff Erosion and Infiltration on Alluvial Captina Silt Loam".
In: *Health Physics* 11.12 (1965), pp. 1333–1340.
ISSN: 15385159.
DOI: 10.1097/00004032-196512000-00010.
URL: http://journals.lww.com/health-physics/Abstract/1965/12000/Movement_of_137Cs_by_Runoff,_Erosion_and.10.aspx.

[280] D. E. Walling and T. A. Quine.
"Use of 137Cs measurements to investigate soil erosion on arable fields in the UK: potential applications and limitations".
In: *Journal of Soil Science* 42 (Mar. 1991), pp. 147–165.

356

ISSN: 00224588.

DOI: 10.1111/j.1365-2389.1991.tb00099.x.

URL: http://doi.wiley.com/10.1111/j.1365-2389.1991.tb00099.x.

[281] Rob N.J. Comans and Daryl E. Hockley.
"Kinetics of cesium sorption on illite".
In: *Geochimica et Cosmochimica Acta* 56 (Mar. 1992), pp. 1157–1164.
ISSN: 00167037.
DOI: 10.1016/0016-7037(92)90053-L.
URL: http://www.sciencedirect.com/science/article/pii/001670379290053L.

[282] E. De Jong, C. B. M. Begg, and R. G. Kachanoski.
"Estimates of soil erosion and deposition for some Saskatchewan soils".
In: *Canadian Journal of Soil Science* 63 (Aug. 1983), pp. 607–617.
ISSN: 0008-4271.
DOI: 10.4141/cjss83-061.
URL: http://pubs.aic.ca/doi/abs/10.4141/cjss83-061.

[283] ME Longmore et al.
"Mapping soil erosion and accumulation with the fallout isotope caesium-137".
In: *Soil Research* (1983).
URL: http://www.publish.csiro.au/paper/SR9830373.

[284] A. Konoplev et al.
"Behavior of accidentally released radiocesium in soil-water environment: Looking at Fukushima from a Chernobyl perspective".
In: *Journal of Environmental Radioactivity* 151 (Jan. 2016), pp. 568–578.
ISSN: 0265931X.
DOI: 10.1016/j.jenvrad.2015.06.019.
URL: http://www.sciencedirect.com/science/article/pii/S0265931X15300321.

[285] Klas Rosén, Ingrid Öborn, and Hans Lönsjö.
"Migration of radiocaesium in Swedish soil profiles after the Chernobyl accident, 1987-1995".
In: *Journal of Environmental Radioactivity* 46 (Oct. 1999), pp. 45–66.
ISSN: 0265931X.
DOI: 10.1016/S0265-931X(99)00040-5.
URL: http://www.sciencedirect.com/science/article/pii/S0265931X99000405.

[286] John R. Matzko et al.
"Observations on the Geology and Geohydrology of the Chernobyl Nuclear Accident Site, Ukraine".
In: *International Geology Review* 36.2 (Feb. 1994), pp. 203–211.

ISSN: 0020-6814.

DOI: 10.1080/00206819409465456.

URL: http://www.tandfonline.com/doi/abs/10.1080/00206819409465456.

[287]   Tetsuo Yasutaka et al.
"A GIS-based evaluation of the effect of decontamination on effective doses due to long-term external exposures in Fukushima."
In: *Chemosphere* 93.6 (Oct. 2013), pp. 1222–1229.
ISSN: 1879-1298.
DOI: 10.1016/j.chemosphere.2013.06.083.
URL: http://www.sciencedirect.com/science/article/pii/S0045653513009405.

[288]   Airi Mori et al.
"Assessment of residual doses to population after decontamination in Fukushima Prefecture".
In: *Journal of Environmental Radioactivity* 166 (2016), pp. 1–9.
ISSN: 0265931X.
DOI: 10.1016/j.jenvrad.2016.06.023.
URL: http://dx.doi.org/10.1016/j.jenvrad.2016.06.023.

[289]   J. Patrick Laceby et al.
"Do forests represent a long-term source of contaminated particulate matter in the Fukushima Prefecture?"
In: *Journal of Environmental Management* 183.3 (2016), pp. 742–753.
ISSN: 03014797.
DOI: 10.1016/j.jenvman.2016.09.020.
URL: http://www.sciencedirect.com/science/article/pii/S0301479716306661?via%3Dihub.

[290]   Siro Abe et al.
"Extensive Field Survey of Natural Radiation in Japan". English.
In: *Journal of Nuclear Science and Technology* 18.1 (Jan. 1981), pp. 21–45.
ISSN: 0022-3131.
DOI: 10.1080/18811248.1981.9733221.
URL: http://www.tandfonline.com/doi/abs/10.1080/18811248.1981.9733221#.VSvs9PnF98E.

[291]   Hiroaki Kato, Yuichi Onda, and Mengistu Teramage.
"Depth distribution of 137Cs, 134Cs, and 131I in soil profile after Fukushima Dai-ichi Nuclear Power Plant Accident."
In: *Journal of Environmental Radioactivity* 111 (Sept. 2012), pp. 59–64.
ISSN: 1879-1700.
DOI: 10.1016/j.jenvrad.2011.10.003.

URL: http://www.sciencedirect.com/science/article/pii/S0265931X11002426.

[292] Takeshi Ohno et al.
"Depth profiles of radioactive cesium and iodine released from the Fukushima Daiichi nuclear power plant in different agricultural fields and forests".
In: *Geochemical Journal* 46 (Nov. 2012), pp. 287–295.
ISSN: 0016-7002.
DOI: 10.2343/geochemj.2.0204.
URL: https://www.jstage.jst.go.jp/article/geochemj/46/4/46_2.0204/_article.

[293] Mengistu T Teramage et al.
"Vertical distribution of radiocesium in coniferous forest soil after the Fukushima nuclear power plant accident".
In: *Journal of Environmental Radioactivity* 137 (Nov. 2014), pp. 37–45.
ISSN: 18791700.
DOI: 10.1016/j.jenvrad.2014.06.017.
URL: http://www.sciencedirect.com/science/article/pii/S0265931X14001817.

[294] S. Staunton, C. Dumat, and A. Zsolnay.
"Possible role of organic matter in radiocaesium adsorption in soils".
In: *Journal of Environmental Radioactivity* 58 (Jan. 2002), pp. 163–173.
ISSN: 0265931X.
DOI: 10.1016/S0265-931X(01)00064-9.
URL: http://www.sciencedirect.com/science/article/pii/S0265931X01000649.

[295] N. Kamei-Ishikawa, S. Uchida, and K. Tagami.
"Distribution coefficients for 85Sr and 137Cs in Japanese agricultural soils and their correlations with soil properties".
In: *Journal of Radioanalytical and Nuclear Chemistry* 277.2 (Mar. 2008), pp. 433–439.
ISSN: 0236-5731.
DOI: 10.1007/s10967-007-7125-z.
URL: http://link.springer.com/10.1007/s10967-007-7125-z.

[296] Kaname Miyahara, Takayuki Tokizawa, and Shinichi Nakayama.
Overview of the Results of Fukushima Decontamination Pilot Projects.
Tech. rep.
2012,
P. 30.
URL: http://www-pub.iaea.org/iaeameetings/IEM4/30Jan/Miyahara.pdf.

[297] David Sanderson et al.

Validated radiometric mapping in 2012 of areas in Japan affected by the Fukushima-Daiichi nuclear accident.

Glasgow: The University of Glasgow, Jan. 2012,

P. 155.

ISBN: 9780852619377.

DOI: 10.5525/GLA.RESEARCHDATA.67.

URL: http://eprints.gla.ac.uk/86365/.

[298] P.G. Martin et al.

"3D unmanned aerial vehicle radiation mapping for assessing contaminant distribution and mobility".

In: *International Journal of Applied Earth Observation and Geoinformation* 52 (2016), pp. 12–19.

ISSN: 03032434.

DOI: 10.1016/j.jag.2016.05.007.

[299] Benjamin Chu.

Laser Light scattering: Basic Principles and Practice.

2nd Ed.

Dover Publications Inc., 2007,

P. 368.

ISBN: 0486457982.

URL: https://books.google.com/books?hl=en&lr=&id=1AvmDAAAQBAJ&oi=fnd&pg=PR9&dq=laser+light+scattering+study&ots=s8HmT_Et3-&sig=y0PqHylTM37tDCMPDJJ_Co110jk.

[300] Suchismita Mishra et al.

"Distribution and retention of Cs radioisotopes in soil affected by Fukushima nuclear plant accident".

In: *Journal of Soils and Sediments* 15 (Oct. 2014), pp. 374–380.

ISSN: 1439-0108.

DOI: 10.1007/s11368-014-0985-2.

URL: http://link.springer.com/10.1007/s11368-014-0985-2.

[301] Makoto Kaneko et al.

"Radioactive Cs in the Severely Contaminated Soils Near the Fukushima Daiichi Nuclear Power Plant".

In: *Frontiers in Energy Research* 3.37 (Sept. 2015), p. 10.

ISSN: 2296-598X.

DOI: 10.3389/fenrg.2015.00037.

URL: http://journal.frontiersin.org/article/10.3389/fenrg.2015.00037/abstract.

[302] Hiroki Mukai et al.
       "Cesium adsorption/desorption behavior of clay minerals considering actual contamination
       conditions in Fukushima."
       In: *Scientific Reports* 6.21543 (Jan. 2016), p. 7.
       ISSN: 2045-2322.
       DOI: 10.1038/srep21543.
       URL: http://www.nature.com/srep/2016/160212/srep21543/full/srep21543.html.

[303] Caroline Chartin et al.
       "Tracking the early dispersion of contaminated sediment along rivers draining the
       Fukushima radioactive pollution plume".
       In: *Anthropocene* 1 (Sept. 2013), pp. 23–34.
       ISSN: 22133054.
       DOI: 10.1016/j.ancene.2013.07.001.
       URL: http://www.sciencedirect.com/science/article/pii/S2213305413000088.

[304] Olivier Evrard et al.
       "Evolution of radioactive dose rates in fresh sediment deposits along coastal rivers draining
       Fukushima contamination plume."
       In: *Scientific Reports* 3.3079 (Jan. 2013), p. 6.
       ISSN: 2045-2322.
       DOI: 10.1038/srep03079.
       URL: http://www.nature.com/srep/2013/131029/srep03079/full/srep03079.html.

[305] S Nagao, M Kanamori, and S Ochiai.
       "Export of 134 Cs and 137 Cs in the Fukushima river systems at heavy rains by Typhoon
       Roke in September 2011".
       In: *Biogeosciences* 10 (2013), pp. 6125–6223.
       DOI: 10.5194/bg-10-6215-2013.
       URL: http://www.biogeosciences.net/10/6215/2013/bg-10-6215-2013.pdf.

[306] Shoji Hashimoto et al.
       "The total amounts of radioactively contaminated materials in forests in Fukushima,
       Japan."
       In: *Scientific Reports* 2 (Jan. 2012), p. 416.
       ISSN: 2045-2322.
       DOI: 10.1038/srep00416.
       URL: http://www.nature.com/srep/2012/120525/srep00416/full/srep00416.html.

[307] Satoshi Mikami et al.
       "The air dose rate around the Fukushima Dai-ichi Nuclear Power Plant: its spatial
       characteristics and temporal changes until December 2012."

361

In: *Journal of Environmental Radioactivity* 139 (Jan. 2015), pp. 250–259.

ISSN: 1879-1700.

DOI: 10.1016/j.jenvrad.2014.08.020.

URL: http://www.sciencedirect.com/science/article/pii/S0265931X14002549.

[308]   Alan J. Cresswell et al.

"Evaluation of forest decontamination using radiometric measurements".

In: *Journal of Environmental Radioactivity* 164 (2016), pp. 133–144.

ISSN: 0265931X.

DOI: 10.1016/j.jenvrad.2016.07.024.

URL: http://linkinghub.elsevier.com/retrieve/pii/S0265931X16302545.

[309]   Kazuya Tanaka et al.

"Local distribution of radioactivity in tree leaves contaminated by fallout of the radionuclides emitted from the Fukushima Daiichi Nuclear Power Plant".

In: *Journal of Radioanalytical and Nuclear Chemistry* 295.3 (Sept. 2012), pp. 2007–2014.

ISSN: 0236-5731.

DOI: 10.1007/s10967-012-2192-1.

URL: http://link.springer.com/10.1007/s10967-012-2192-1.

[310]   Nobuo Niimura et al.

"Physical properties, structure, and shape of radioactive Cs from the Fukushima Daiichi Nuclear Power Plant accident derived from soil, bamboo and shiitake mushroom measurements."

In: *Journal of Environmental Radioactivity* 139 (Jan. 2014), pp. 234–239.

ISSN: 1879-1700.

DOI: 10.1016/j.jenvrad.2013.12.020.

URL: http://www.sciencedirect.com/science/article/pii/S0265931X1300310X.

[311]   Centers for Disease Control and Prevention.

NIOSH Publications and Products.

2018.

URL: https://www.cdc.gov/niosh/pubs/default.html.

[312]   Petr Melnikov and Lourdes Zeia Zanoni.

Clinical effects of cesium intake.

June 2010.

DOI: 10.1007/s12011-009-8486-7.

URL: http://link.springer.com/10.1007/s12011-009-8486-7.

[313]   Yutaka Kanai.

"Monitoring of aerosols in Tsukuba after Fukushima Nuclear Power Plant incident in 2011."

In: *Journal of Environmental Radioactivity* 111 (Sept. 2012), pp. 33–37.

ISSN: 1879-1700.

DOI: 10.1016/j.jenvrad.2011.10.011.

URL: http://www.sciencedirect.com/science/article/pii/S0265931X11002505.

[314]   Helena Mala et al.
"Particle size distribution of radioactive aerosols after the Fukushima and the Chernobyl accidents."
In: *Journal of Environmental Radioactivity* 126 (Dec. 2013), pp. 92–98.
ISSN: 1879-1700.
DOI: 10.1016/j.jenvrad.2013.07.016.
URL: http://www.sciencedirect.com/science/article/pii/S0265931X13001732.

[315]   Olivier Masson et al.
"Size Distributions of Airborne Radionuclides from the Fukushima Nuclear Accident at Several Places in Europe."
In: *Environmental Science & Technology* 47.19 (Oct. 2013), pp. 10995–11003.
ISSN: 1520-5851.
DOI: 10.1021/es401973c.
URL: http://dx.doi.org/10.1021/es401973c.

[316]   World Health Organization.
Ten chemicals of major public health concern.
Tech. rep.
2016.
URL: http://www.who.int/ipcs/assessment/public_health/chemicals_phc/en/.

[317]   S. Yoshida et al.
"Determination of Major and Trace Elements in Japanese Rock Reference Samples by ICP-MS".
In: *International Journal of Environmental Analytical Chemistry* 63.3 (July 1996), pp. 195–206.
ISSN: 0306-7319.
DOI: 10.1080/03067319608026266.
URL: http://www.tandfonline.com/doi/abs/10.1080/03067319608026266.

[318]   Shin-ichi Yamasaki et al.
"Background levels of trace and ultra-trace elements in soils of Japan".
In: *Soil Science and Plant Nutrition* 47.4 (Dec. 2001), pp. 755–765.
ISSN: 0038-0768.
DOI: 10.1080/00380768.2001.10408440.
URL: http://www.tandfonline.com/doi/abs/10.1080/00380768.2001.10408440.

[319]   Tadashi Shimamura et al.
"Major to ultra trace elements in rainfall collected in suburban Tokyo".

In: *Atmospheric Environment* 41.33 (2007), pp. 6999–7010.

ISSN: 13522310.

DOI: 10.1016/j.atmosenv.2007.05.010.

[320]   Masato Iwashita et al.

"Determination of rare earth elements in rainwater collected in suburban Tokyo".

In: *Geochemical Journal* 45.3 (2011), pp. 187–197.

ISSN: 00167002.

DOI: 10.2343/geochemj.1.0121.

URL: http://jlc.jst.go.jp/DN/JST.JSTAGE/geochemj/1.0121?lang=en&from=CrossRef&type=abstract.

[321]   Naoki Furuta et al.

"Concentrations, enrichment and predominant sources of Sb and other trace elements in size classified airborne particulate matter collected in Tokyo from 1995 to 2004."

In: *Journal of Environmental Monitoring* 7.12 (2005), pp. 1155–1161.

ISSN: 1464-0325.

DOI: 10.1039/b513988k.

URL: http://xlink.rsc.org/?DOI=b513988khttp://www.ncbi.nlm.nih.gov/pubmed/16307066.

[322]   Yoshinari Suzuki, Tatsunosuke Suzuki, and Naoki Furuta.

"Determination of rare earth elements (REES) in airborne particulate matter (APM) collected in Tokyo, Japan, and a positive anomaly of europium and terbium."

In: *Analytical Sciences : The International Journal of The Japan Society for Analytical Chemistry* 26 (2010), pp. 929–935.

ISSN: 1348-2246.

DOI: JST.JSTAGE/analsci/26.929[pii].

URL: http://www.ncbi.nlm.nih.gov/pubmed/20834122.

[323]   S. Sakai et al.

World trends in municipal solid waste management.

Jan. 1996.

DOI: 10.1016/S0956-053X(96)00106-7.

URL: http://linkinghub.elsevier.com/retrieve/pii/S0956053X96001067.

[324]   Japanese Ministry of the Environment.

History and Current State of Waste Management in Japan.

Tech. rep.

Tokyo, 2014,

P. 32.

URL: https://www.env.go.jp/en/recycle/smcs/attach/hcswm.pdf.

364

[325]   M. Tanaka.
        "Reduction of and resource recovery from municipal solid waste in Japan".
        In: *Waste Management & Research* 10.5 (Oct. 1992), pp. 453–459.
        ISSN: 0734242X.
        DOI: 10.1016/0734-242X(92)90119-6.
        URL: http://linkinghub.elsevier.com/retrieve/pii/0734242X92901196.

[326]   V. Ramanathan et al.
        "Biomass Burning in the Tropics: Impact on Atmospheric Chemistry and Biogeochemical
        Cycles".
        In: *Science* 249.5549 (Dec. 2001), pp. 2119–2124.
        ISSN: 0036-8075.
        DOI: 10.1126/science.250.4988.1669.
        URL: http://www.ncbi.nlm.nih.gov/pubmed/17734705.

[327]   Aya Sakaguchi et al.
        "Isotopic compositions of (236)U and Pu isotopes in "black substances" collected from
        roadsides in Fukushima prefecture: fallout from the Fukushima Dai-ichi nuclear power
        plant accident."
        In: *Environmental Science & Technology* 48.7 (Apr. 2014), pp. 3691–3697.
        ISSN: 1520-5851.
        DOI: 10.1021/es405294s.
        URL: http://dx.doi.org/10.1021/es405294s.

[328]   WebMineral.
        Minerals by Chemical Composition.
        2017.
        URL: http://webmineral.com/chemical.shtml#.WN0y61UrJhE.

[329]   G. A. Sehmel.
        "Particle resuspension: A review".
        In: *Environment International* 4.2 (Jan. 1980), pp. 107–127.
        ISSN: 01604120.
        DOI: 10.1016/0160-4120(80)90005-7.
        URL: http://linkinghub.elsevier.com/retrieve/pii/0160412080900057.

[330]   Katsumi Shozugawa, Norio Nogawa, and Motoyuki Matsuo.
        "Deposition of fission and activation products after the Fukushima Dai-ichi nuclear power
        plant accident."
        In: *Environmental Pollution* 163 (Apr. 2012), pp. 243–247.
        ISSN: 1873-6424.
        DOI: 10.1016/j.envpol.2012.01.001.

URL: `http://www.sciencedirect.com/science/article/pii/S0269749112000024`.

[331] G. Le Petit et al.
"Analysis of Radionuclide Releases from the Fukushima Dai-Ichi Nuclear Power Plant Accident Part I".
In: *Pure and Applied Geophysics* 171.3-5 (Sept. 2012), pp. 629–644.
ISSN: 0033-4553.
DOI: `10.1007/s00024-012-0581-6`.
URL: `http://link.springer.com/10.1007/s00024-012-0581-6`.

[332] John. Emsley.
Nature's Building Blocks: An A-Z Guide to the Elements.
Oxford University Press, 2003,
P. 538.
ISBN: 0198503407.

[333] British Geological Survey.
Rare Earth Elements.
Tech. rep.
Nottingham: British Geological Survey, 2011,
P. 54.
URL: `www.bgs.ac.uk/downloads/start.cfm?id=1638`.

[334] Georgios Charalampides et al.
"Rare Earth Elements: Industrial Applications and Economic Dependency of Europe".
In: *Procedia Economics and Finance* 24 (2015), pp. 126–135.
ISSN: 22125671.
DOI: `10.1016/S2212-5671(15)00630-9`.
URL: `http://www.sciencedirect.com/science/article/pii/S2212567115006309`.

[335] R.L. Rudnick and S. Gao.
"Composition of the Continental Crust".
In: *Treatise on Geochemistry*.
Vol. 3.
Elsevier, 2003,
Pp. 1–64.
ISBN: 9780080437514.
DOI: `10.1016/B0-08-043751-6/03016-4`.
URL: `http://linkinghub.elsevier.com/retrieve/pii/B0080437516030164`.

[336] Yoshikazu Kikawada et al.
"Anomalous Uranium Isotope Ratio in Atmospheric Deposits in Japan".
In: *Journal of Nuclear Science and Technology* 46.12 (Dec. 2009), pp. 1094–1098.

ISSN: 0022-3131.

DOI: 10.1080/18811248.2009.9711621.

URL: http://www.tandfonline.com/doi/abs/10.1080/18811248.2009.9711621.

[337] Yoshikazu Kikawada et al.
"Origin of enriched uranium contained in Japanese atmospheric deposits".
In: *Natural Science* 4.11 (Nov. 2012), pp. 936–942.
ISSN: 2150-4091.
DOI: 10.4236/ns.2012.431122.
URL: http://www.scirp.org/journal/doi.aspx?DOI=10.4236/ns.2012.431122.

[338] Satoshi Yoshida et al.
"Concentrations of lanthanide elements, Th, and U in 77 Japanese surface soils".
In: *Environment International* 24.3 (Apr. 1998), pp. 275–286.
ISSN: 01604120.
DOI: 10.1016/S0160-4120(98)00006-3.
URL: http://linkinghub.elsevier.com/retrieve/pii/S0160412098000063.

[339] Katsumi Hirose and Yukio Sugimura.
"Concentration of uranium and the activity ratio of 234U/238U in surface air: Effect of atmospheric burn-up of Cosmos-954."
In: *Papers in Meteorology and Geophysics* 32.4 (Mar. 1981), pp. 317–322.
ISSN: 1880-6643.
DOI: 10.2467/mripapers.32.317.
URL: https://www.jstage.jst.go.jp/article/mripapers/32/4/32_4_317/_article.

[340] M. Aoyama, K. Hirose, and Y. Sugimura.
"Deposition of gamma-emitting nuclides in Japan after the reactor-IV accident at Chernobyl'".
In: *Journal of Radioanalytical and Nuclear Chemistry Articles* 116.2 (Dec. 1987), pp. 291–306.
ISSN: 0236-5731.
DOI: 10.1007/BF02035773.
URL: http://link.springer.com/10.1007/BF02035773.

[341] K. Hirose and Y. Sugimura.
"Plutonium isotopes in the surface air in Japan: Effect of Chernobyl accident".
In: *Journal of Radioanalytical and Nuclear Chemistry Articles* 138.1 (Jan. 1990), pp. 127–138.
ISSN: 0236-5731.
DOI: 10.1007/BF02049355.
URL: http://link.springer.com/10.1007/BF02049355.

[342] Satoshi Yoshida et al.

"Concentrations of uranium and ratios in soil and plant samples collected around the uranium conversion building in the JCO campus".

In: *Journal of Environmental Radioactivity* 50.1-2 (Aug. 2000), pp. 161–172.

ISSN: 0265931X.

DOI: 10.1016/S0265-931X(00)00075-8.

URL: http://www.sciencedirect.com/science/article/pii/S0265931X00000758.

[343] K. W. Nicholson.

"A review of particle resuspension".

In: *Atmospheric Environment* 22.12 (Jan. 1988), pp. 2639–2651.

ISSN: 00046981.

DOI: 10.1016/0004-6981(88)90433-7.

URL: http://linkinghub.elsevier.com/retrieve/pii/0004698188904337.

[344] K. W. Nicholson et al.

"The effects of vehicle activity on particle resuspension".

In: *Journal of Aerosol Science* 20.8 (Jan. 1989), pp. 1425–1428.

ISSN: 00218502.

DOI: 10.1016/0021-8502(89)90853-7.

URL: http://linkinghub.elsevier.com/retrieve/pii/0021850289908537.

[345] Alina Kabata-Pendias.

Trace Elements in Soils and Plants.

3rd Ed.

CRC Press, 2000,

P. 432.

ISBN: 0849315751.

DOI: 10.1201/b10158-25.

URL: https://www.crcpress.com/Trace-Elements-in-Soils-and-Plants-Third-Edition/Kabata-Pendias/p/book/9780849315756.

[346] Mark D. Hunsicker, Timothy R. Crockett, and Bode M A Labode.

"An overview of the municipal waste incineration industry in Asia and the former Soviet Union".

In: *Journal of Hazardous Materials* 47 (May 1996), pp. 31–42.

ISSN: 03043894.

DOI: 10.1016/0304-3894(95)00112-3.

URL: http://linkinghub.elsevier.com/retrieve/pii/0304389495001123.

[347] P. Fermo et al.

"The analytical characterization of municipal solid waste incinerator fly ash: Methods and preliminary results".

In: *Fresenius' Journal of Analytical Chemistry* 365.8 (Dec. 1999), pp. 666–673.
ISSN: 09370633.
DOI: 10.1007/s002160051543.
URL: http://link.springer.com/10.1007/s002160051543.

[348]   Richard L. Davison et al.
"Trace elements in fly ash. Dependence of concentration on particle size".
In: *Environmental Science & Technology* 8.13 (Dec. 1974), pp. 1107–1113.
ISSN: 0013-936X.
DOI: 10.1021/es60098a003.
URL: http://pubs.acs.org/doi/abs/10.1021/es60098a003http://dx.doi.org/10.
1021/es60098a003.

[349]   J. A. Campbell et al.
Separation and chemical characterization of finely-sized fly-ash particles.
July 1978.
DOI: 10.1021/ac50030a009.
URL: http://pubs.acs.org/doi/abs/10.1021/ac50030a009.

[350]   Chantel Block and Richard Dams.
"Study of Fly Ash Emission During Combustion".
In: *Environmental Science & Technology* 10 (Oct. 1976), pp. 1011–1017.
ISSN: 0013936X.
DOI: 10.1021/es60121a013.
URL: http://pubs.acs.org/doi/abs/10.1021/es60121a013.

[351]   Andrew P Ault et al.
"Single-particle SEM-EDX analysis of iron-containing coarse particulate matter in an
urban environment: sources and distribution of iron within Cleveland, Ohio."
In: *Environmental Science & Technology* 46 (May 2012), pp. 4331–4339.
ISSN: 1520-5851.
DOI: 10.1021/es204006k.
URL: http://dx.doi.org/10.1021/es204006k.

[352]   T. Christoudias and J. Lelieveld.
"Modelling the global atmospheric transport and deposition of radionuclides from the
Fukushima Dai-ichi nuclear accident". English.
In: *Atmospheric Chemistry and Physics* 13.3 (Feb. 2013), pp. 1425–1438.
ISSN: 1680-7324.
DOI: 10.5194/acp-13-1425-2013.
URL: http://www.atmos-chem-phys.net/13/1425/2013/acp-13-1425-2013.html.

[353]   World Nuclear Association.

World Nuclear Power Reactors & Uranium Requirements.

2017.

URL: http://www.world-nuclear.org/information-library/facts-and-figures/world-nuclear-power-reactors-and-uranium-requireme.aspx.

[354] Mindat.org.

Mineralogy Database - Mineral Collecting, Localities, Mineral Photos and Data.

2017.

URL: https://www.mindat.org/.

[355] A Bleise, P.R Danesi, and W Burkart.

"Properties, use and health effects of depleted uranium (DU): a general overview".

In: *Journal of Environmental Radioactivity* 64 (Jan. 2003), pp. 93–112.

ISSN: 0265931X.

DOI: 10.1016/S0265-931X(02)00041-3.

URL: http://www.sciencedirect.com/science/article/pii/S0265931X02000413.

[356] E. I. Hamilton.

"Depleted uranium (DU): A holistic consideration of DU and related matters".

In: *Science of the Total Environment* 281 (Dec. 2001), pp. 5–21.

ISSN: 00489697.

DOI: 10.1016/S0048-9697(01)01033-6.

URL: http://www.sciencedirect.com/science/article/pii/S0048969701010336.

[357] Kleindiek Nanotechnik GmbH.

MM3A-EM Micromanipulator Product Brochure.

Tech. rep.

Reutlingen, Germany, 2017,

P. 2.

URL: http://www.kleindiek.com/fileadmin/public/brochures/mm3a-em.pdf.

[358] S. Kleindiek, A. Rummel, and K Schock.

E-beam hardening SEM glue for fixation of small objects in the SEM.

2008,

Pp. 565–566.

URL: http://link.springer.com/chapter/10.1007/978-3-540-85156-1_283.

[359] Kleindiek Nanotechnik GmbH.

SEMGlu Product Brochure.

Tech. rep.

2017,

P. 2.

URL: http://www.kleindiek.com/fileadmin/public/brochures/semglu.pdf.

[360] V.A. Sole et al.
"A multiplatform code for the analysis of energy-dispersive X-ray fluorescence spectra".
In: *Spectrochimica Acta Part B: Atomic Spectroscopy* 62.1 (Jan. 2007), pp. 63–68.
ISSN: 05848547.
DOI: 10.1016/j.sab.2006.12.002.
URL: http://www.sciencedirect.com/science/article/pii/S0584854706003764.

[361] B Ravel and M Newville.
"ATHENA, ARTEMIS, HEPHAESTUS: data analysis for X-ray absorption spectroscopy using IFEFFIT."
In: *Journal of Synchrotron Radiation* 12 (July 2005), pp. 537–541.
ISSN: 0909-0495.
DOI: 10.1107/S0909049505012719.
URL: http://scripts.iucr.org/cgi-bin/paper?S0909049505012719.

[362] J. J. Rehr, R. C. Albers, and S. I. Zabinsky.
"High-order multiple-scattering calculations of x-ray-absorption fine structure".
In: *Physical Review Letters* 69.23 (Dec. 1992), pp. 3397–3400.
ISSN: 0031-9007.
DOI: 10.1103/PhysRevLett.69.3397.
URL: http://link.aps.org/doi/10.1103/PhysRevLett.69.3397.

[363] Matthew Newville.
"IFEFFIT : interactive XAFS analysis and FEFF fitting".
In: *Journal of Synchrotron Radiation* 8.2 (Mar. 2001), pp. 322–324.
ISSN: 0909-0495.
DOI: 10.1107/S0909049500016964.
URL: http://scripts.iucr.org/cgi-bin/paper?ph5149.

[364] International X-ray Absorption Society.
XAFS Materials Database.
2017.
URL: http://ixs.iit.edu/database/.

[365] P. De Bievre and P. D. P. Taylor.
"Table of the isotopic compositions of the elements".
In: *International Journal of Mass Spectrometry and Ion Processes* 123.2 (Feb. 1993), pp. 149–166.
ISSN: 01681176.
DOI: 10.1016/0168-1176(93)87009-H.
URL: http://www.sciencedirect.com/science/article/pii/016811769387009H.

[366] Samuel Glasstone.

The Effects of Nuclear Weapons. English.

Tech. rep.

Oak Ridge, TN: Office of Scientific and Technical Information, Feb. 1950,

P. 758.

DOI: 10.2172/972902.

URL: http://www.osti.gov/scitech/biblio/972902.

[367] Rudy J M Konings, Thierry Wiss, and Ondrej Benes.

"Predicting material release during a nuclear reactor accident."

In: *Nature Materials* 14.3 (Feb. 2015), pp. 247–252.

ISSN: 1476-1122.

DOI: 10.1038/nmat4224.

URL: http://dx.doi.org/10.1038/nmat4224.

[368] Mark Russell St. John Foreman.

"An introduction to serious nuclear accident chemistry".

In: *Cogent Chemistry* 1049111 (June 2015), p. 18.

URL: http://www.tandfonline.com/doi/abs/10.1080/23312009.2015.1049111.

[369] Tomohiro Endo, Shunsuke Sato, and Akio Yamamoto.

"Estimation of average burnup of damaged fuels loaded in Fukushima Dai-ichi reactors by using the 134Cs/137Cs ratio method."

In: *Symposium on Nuclear Data; 16-17 November 2011*.

Ed. by Hideo Harara et al.

IAEA, 2012,

Pp. 45–51.

DOI: 10.11484/jaea-conf-2012-001.

URL: http://jolissrch-inter.tokai-sc.jaea.go.jp/search/servlet/search?5035510.

[370] Yukihiko Satou.

"Radioactive particles in Fukushima".

In: *Goldschmidt 2016 - Yokohama (Japan)*.

Yokohama, Japan, 2016,

P. 1.

URL: https://goldschmidt.info/2016/uploads/abstracts/finalPDFs/A-Z.pdf.

[371] Junpei Imoto et al.

"Isotopic signature and nano-texture of cesium-rich micro-particles: Release of uranium and fission products from the Fukushima Daiichi Nuclear Power Plant".

In: *Scientific Reports* 7.5409 (July 2017), p. 12.

DOI: 10.1038/s41598-017-05910-z.

URL: http://www.ncbi.nlm.nih.gov/pubmed/28710475.

[372] C. Rau et al.
"The Diamond Beamline I13L for Imaging and Coherence".
In: *AIP Conference Proceedings*.
Vol. 1234.
2010,
Pp. 121–125.
ISBN: 9780735407824.
DOI: 10.1063/1.3463156.
URL: http://aip.scitation.org/doi/abs/10.1063/1.3463156.

[373] Doga Gursoy et al.
"TomoPy: A framework for the analysis of synchrotron tomographic data".
In: *Journal of Synchrotron Radiation* 21.5 (Sept. 2014), pp. 1188–1193.
ISSN: 16005775.
DOI: 10.1107/S1600577514013939.
URL: http://www.ncbi.nlm.nih.gov/pubmed/25178011.

[374] FEI Company.
Amira-Avizo 3D Software.
July 2017.
URL: https://www.fei.com/software/amira-avizo//.

[375] A. C. Ferrari and J. Robertson.
"Interpretation of Raman spectra of disordered and amorphous carbon".
In: *Physical Review B* 61.20 (May 2000), pp. 14095–14107.
ISSN: 0163-1829.
DOI: 10.1103/PhysRevB.61.14095.
URL: https://link.aps.org/doi/10.1103/PhysRevB.61.14095.

[376] HFW Taylor.
Cement Chemistry, Second Edition.
Aberdeen, Scotland: ICE Publishing, 1997,
P. 480.
ISBN: 0727725920.

[377] Ted Pella Inc.
Material Hardness Tables.
2017.
URL: https://www.tedpella.com/company_html/hardness.htm.

[378] Yohichi Gohshi et al.
"A Scanning X-Ray Fluorescence Microprobe with Synchrotron Radiation".

In: *Japanese Journal of Applied Physics* 26.2 - 8 (Aug. 1987), pp. 1260–1262.
ISSN: 0021-4922.
DOI: 10.1143/JJAP.26.L1260.
URL: http://stacks.iop.org/1347-4065/26/i=8A/a=L1260.

[379] H. Kleykamp.
"The chemical state of the fission products in oxide fuels".
In: *Journal of Nuclear Materials* 131.2-3 (Apr. 1985), pp. 221–246.
ISSN: 00223115.
DOI: 10.1016/0022-3115(85)90460-X.
URL: http://linkinghub.elsevier.com/retrieve/pii/002231158590460X.

[380] Robert H. Doremus.
Glass Science.
New York: Wiley, 1973.
ISBN: 9780122363078.
DOI: 10.1016/B978-0-12-236307-8.50011-9.
URL: http://www.sciencedirect.com/science/article/pii/B9780122363078500119.

[381] Bulent Ozturk.
"Hybrid effect in the mechanical properties of jute/rockwool hybrid fibres reinforced phenol formaldehyde composites".
In: *Fibers and Polymers* 11.3 (June 2010), pp. 464–473.
ISSN: 12299197.
DOI: 10.1007/s12221-010-0464-3.
URL: http://link.springer.com/10.1007/s12221-010-0464-3.

[382] A. M. Zihlif and G. Ragosta.
"A Study on the Physical Properties of Rock Wool Fiber-Polystyrene Composite".
In: *Journal of Thermoplastic Composite Materials* 16.3 (May 2003), pp. 273–283.
ISSN: 00000000.
DOI: 10.1177/0892705703016003005.
URL: http://jtc.sagepub.com/cgi/doi/10.1177/0892705703016003005.

[383] Rockwool Limited.
Deleterious Materials Data Sheet.
Cardiff, 2017.
URL: http://www.rockwool.co.uk/technical-support/documentation/datasheets/.

[384] IARC Working Group on the Evaluation of Carcinogenic Risk to Humans.
IARC Monographs Programme on the Evaluation of Carcinogenic Risks To Humans: Man-Made Mineral Fibres.
Tech. rep.

1988,

P. 309.

URL: https://www.ncbi.nlm.nih.gov/books/NBK316364/pdf/Bookshelf_NBK316364.
pdf.

[385] Rudolf Klingholz.
"Technology and production of man-made mineral fibres".
In: *Annals of Occupational Hygiene* 20.2 (Oct. 1977), pp. 153–159.
ISSN: 00034878.
DOI: 10.1093/annhyg/20.2.153.
URL: https://academic.oup.com/annweh/article/20/2/153/178697/TECHNOLOGY-
AND-PRODUCTION-OF-MANMADE-MINERAL.

[386] P.G. Martin et al.
"Analysis of external surface irregularities on Fukushima-derived fallout particles".
In: *Frontiers in Energy Research* 5.25 (2017), p. 9.
ISSN: 2296-598X.
DOI: 10.3389/FENRG.2017.00025.
URL: http://journal.frontiersin.org/article/10.3389/fenrg.2017.00025.

[387] J. Yanez, M. Kuznetsov, and a. Souto-Iglesias.
"An analysis of the hydrogen explosion in the Fukushima-Daiichi accident".
In: *International Journal of Hydrogen Energy* 40.25 (July 2015), pp. 8261–8280.
ISSN: 03603199.
DOI: 10.1016/j.ijhydene.2015.03.154.
URL: http://linkinghub.elsevier.com/retrieve/pii/S0360319915008009.

[388] A.G. Whitham and R.S.J. Sparks.
"Pumice".
In: *Bulletin of Volcanology* 48.4 (Aug. 1986), pp. 209–223.
ISSN: 02588900.
DOI: 10.1007/BF01087675.
URL: http://link.springer.com/10.1007/BF01087675.

[389] A.H Al Rayyes et al.
"Radiocaesium in hot particles: Solubility vs. chemical speciation".
In: *Journal of Environmental Radioactivity* 21 (Jan. 1993), pp. 143–151.
ISSN: 0265931X.
DOI: 10.1016/0265-931X(93)90051-8.
URL: http://www.sciencedirect.com/science/article/pii/0265931X93900518.

[390] J. W. Morgan and J. F. Lovering.

375

"Uranium and thorium abundances in the basalt cored in mohole project (Guadalupe site)".

In: *Journal of Geophysical Research* 70.18 (Sept. 1965), pp. 4724–4725.

ISSN: 01480227.

DOI: 10.1029/JZ070i018p04724.

URL: http://doi.wiley.com/10.1029/JZ070i018p04724.

[391] George H Coleman.

The Radiochemistry of Plutonium.

Tech. rep.

Livermore, CA (United States): Lawrence Livermore National Laboratory (LLNL), Sept. 1965,

P. 192.

DOI: 10.2172/4516515.

URL: http://www.osti.gov/servlets/purl/4516515/.

[392] M. Dozol and R. Hagemann.

"Radionuclide migration in groundwaters: Review of the behaviour of actinides".

In: *Pure and Applied Chemistry* 65.5 (Jan. 1993), pp. 1081–1102.

ISSN: 0033-4545.

DOI: 10.1351/pac199365051081.

URL: http://www.degruyter.com/view/j/pac.1993.65.issue-5/pac199365051081/pac199365051081.xml.

[393] B. Salbu et al.

"High energy X-ray microscopy for characterisation of fuel particles".

In: *Nuclear Instruments and Methods in Physics Research Section A: Accelerators, Spectrometers, Detectors and Associated Equipment* 467-468 (July 2001), pp. 1249–1252.

ISSN: 01689002.

DOI: 10.1016/S0168-9002(01)00641-6.

URL: http://www.sciencedirect.com/science/article/pii/S0168900201006416.

[394] O C Lind et al.

"Characterization of uranium and plutonium containing particles originating from the nuclear weapons accident in Thule, Greenland, 1968."

In: *Journal of Environmental Radioactivity* 81.1 (Jan. 2005), pp. 21–32.

ISSN: 0265-931X.

DOI: 10.1016/j.jenvrad.2004.10.013.

URL: http://www.sciencedirect.com/science/article/pii/S0265931X04003297.

[395] O C Lind et al.

"Micro-analytical characterisation of radioactive heterogeneities in samples from Central Asian TENORM sites."
In: *Journal of Environmental Radioactivity* 123 (Sept. 2013), pp. 63–70.
ISSN: 1879-1700.
DOI: 10.1016/j.jenvrad.2012.02.012.
URL: http://www.sciencedirect.com/science/article/pii/S0265931X12000641.

[396]   Daniel E. Crean et al.
"Expanding the nuclear forensic toolkit: chemical profiling of uranium ore concentrate particles by synchrotron X-ray microanalysis".
In: *RSC Advances* 5.107 (Oct. 2015), pp. 87908–87918.
ISSN: 2046-2069.
DOI: 10.1039/C5RA14963K.
URL: http://pubs.rsc.org/en/Content/ArticleHTML/2015/RA/C5RA14963K.

[397]   Gabriele Tamborini et al.
"Application of secondary ion mass spectrometry to the identification of single particles of uranium and their isotopic measurement".
In: *Spectrochimica Acta Part B: Atomic Spectroscopy* 53.9 (Aug. 1998), pp. 1289–1302.
ISSN: 05848547.
DOI: 10.1016/S0584-8547(98)00121-9.
URL: http://www.sciencedirect.com/science/article/pii/S0584854798001219.

[398]   Maria Betti, Gabriele Tamborini, and Lothar Koch.
"Use of Secondary Ion Mass Spectrometry in Nuclear Forensic Analysis for the Characterization of Plutonium and Highly Enriched Uranium Particles".
In: *Analytical Chemistry* 71 (July 1999), pp. 2616–2622.
ISSN: 0003-2700.
DOI: 10.1021/ac981184r.
URL: http://dx.doi.org/10.1021/ac981184r.

[399]   Maria Betti et al.
Analysis of Environmental Radionuclides.
Vol. 11.
Radioactivity in the Environment.
Elsevier, 2008,
Pp. 355–370.
ISBN: 9780080449883.
DOI: 10.1016/S1569-4860(07)11011-1.
URL: http://www.sciencedirect.com/science/article/pii/S1569486007110111.

[400]   Gabriele Tamborini and Maria Betti.

"Characterisation of Radioactive Particles by SIMS".

In: *Microchimica Acta* 132.2-4 (Apr. 2000), pp. 411–417.

ISSN: 0026-3672.

DOI: 10.1007/s006040050088.

URL: http://link.springer.com/10.1007/s006040050088.

[401]   H. R. Halse.

"Using synchrotron radiation to determine the oxidation state of uranium in magmas".

PhD thesis. Imperial College London, 2014,

P. 300.

URL: https://spiral.imperial.ac.uk/handle/10044/1/19423.

[402]   S Torok et al.

"Characterization and speciation of depleted uranium in individual soil particles using microanalytical methods".

In: *Spectrochimica Acta Part B: Atomic Spectroscopy* 59.5 (May 2004), pp. 689–699.

ISSN: 05848547.

DOI: 10.1016/j.sab.2004.02.003.

URL: http://www.sciencedirect.com/science/article/pii/S0584854704000473.

[403]   Nicholas S. Lloyd et al.

"Precise and accurate isotopic analysis of microscopic uranium-oxide grains using LA-MC-ICP-MS".

In: *Journal of Analytical Atomic Spectrometry* 24 (May 2009), pp. 752–758.

ISSN: 0267-9477.

DOI: 10.1039/b819373h.

URL: http://pubs.rsc.org/en/Content/ArticleHTML/2009/JA/B819373H.

[404]   L. A. Lewis et al.

"Spatially-resolved analyses of aerodynamic fallout from a uranium-fueled nuclear test".

In: *Journal of Environmental Radioactivity* 148 (2015), pp. 183–195.

ISSN: 18791700.

DOI: 10.1016/j.jenvrad.2015.04.006.

[405]   J. Jernstrom et al.

"Characterization and source term assessments of radioactive particles from Marshall Islands using non-destructive analytical techniques".

In: *Spectrochimica Acta Part B: Atomic Spectroscopy* 61.8 (Aug. 2006), pp. 971–979.

ISSN: 05848547.

DOI: 10.1016/j.sab.2006.09.002.

URL: http://www.sciencedirect.com/science/article/pii/S0584854706002515.

[406]   Terry F. Hamilton et al.

"Frequency distribution, isotopic composition and physical characterization of plutonium-bearing particles from the Fig-Quince zone on Runit Island, Enewetak Atoll".
In: *Journal of Radioanalytical and Nuclear Chemistry* 282.3 (Dec. 2009), pp. 1019–1026.
ISSN: 02365731.
DOI: 10.1007/s10967-009-0237-x.
URL: http://link.springer.com/10.1007/s10967-009-0237-x.

[407]   R. Pollanen et al.
"Analysis of radioactive particles from the Kola Bay area".
In: *The Analyst* 126.5 (Jan. 2001), pp. 724–730.
ISSN: 00032654.
DOI: 10.1039/b101099i.
URL: http://pubs.rsc.org/en/Content/ArticleHTML/2001/AN/B101099I.

[408]   Igor V. Veryovkin et al.
"Mass spectrometry on the nanoscale with ion sputtering based techniques: What is feasible?"
In: *Nuclear Instruments and Methods in Physics Research, Section B: Beam Interactions with Materials and Atoms* 261 (Aug. 2007), pp. 508–511.
ISSN: 0168583X.
DOI: 10.1016/j.nimb.2007.04.058.
URL: http://linkinghub.elsevier.com/retrieve/pii/S0168583X07008221.

[409]   J. Truyens, E.A. Stefaniak, and Y. Aregbe.
"NUSIMEP-7: uranium isotope amount ratios in uranium particles".
In: *Journal of Environmental Radioactivity* 125 (Nov. 2013), pp. 50–55.
ISSN: 0265931X.
DOI: 10.1016/j.jenvrad.2013.02.008.
URL: http://www.sciencedirect.com/science/article/pii/S0265931X13000453.

[410]   IAEA.
Advances in Destructive and Non-Destructive Analysis for Environmental Monitoring and Nuclear Forensics.
Vienna: IAEA, 2004,
P. 114.
ISBN: 92-0-110203-8.
URL: http://www-pub.iaea.org/books/IAEABooks/6795/Advances-in-Destructive-and-Non-Destructive-Analysis-for-Environmental-Monitoring-and-Nuclear-Forensics.

[411]   W. E. Burcham.
Nuclear Physics: An Introduction.

379

McGraw-Hill, 1963,

P. 739.

URL: https://books.google.co.uk/books/about/Nuclear_Physics.html?id= tB5RAAAAMAAJ&pgis=1.

[412] Susan A. Cumberland et al.
"Characterization of uranium redox state in organic-rich eocene sediments".
In: *Chemosphere* 194 (Dec. 2017), pp. 602–613.
ISSN: 00456535.
DOI: 10.1016/j.chemosphere.2017.12.012.
URL: http://linkinghub.elsevier.com/retrieve/pii/S0045653517319732.

[413] Boris Kosog et al.
"Oxidation state delineation via U L III-edge XANES in a series of isostructural uranium coordination complexes".
In: *Inorganic Chemistry* 51.14 (July 2012), pp. 7940–7944.
ISSN: 00201669.
DOI: 10.1021/ic3011234.
URL: http://pubs.acs.org/doi/10.1021/ic3011234.

[414] J. Petiau et al.
"Delocalized versus localized unoccupied 5f states and the uranium site structure in uranium oxides and glasses probed by x-ray-absorption near-edge structure".
In: *Physical Review B* 34.10 (Nov. 1986), pp. 7350–7361.
ISSN: 01631829.
DOI: 10.1103/PhysRevB.34.7350.
URL: https://link.aps.org/doi/10.1103/PhysRevB.34.7350.

[415] S. V. Stefanovsky et al.
"Oxidation state and coordination environment of uranium in sodium iron aluminophosphate glasses".
In: *Doklady Physical Chemistry* 468.1 (May 2016), pp. 76–79.
ISSN: 0012-5016.
DOI: 10.1134/S0012501616050043.
URL: http://link.springer.com/10.1134/S0012501616050043.

[416] K. O. Kvashnina et al.
"Chemical State of Complex Uranium Oxides".
In: *Physical Review Letters* 111.25 (Dec. 2013), p. 5.
ISSN: 0031-9007.
DOI: 10.1103/PhysRevLett.111.253002.
URL: http://link.aps.org/doi/10.1103/PhysRevLett.111.253002.

[417] J. Jernstrom et al.
"Non-destructive characterisation of low radioactive particles from Irish Sea sediment
by micro X-ray synchrotron radiation techniques: micro X-ray fluorescence (u-XRF) and
micro X-ray absorption near edge structure (u-XANES) spectroscopy".
In: *Journal of Analytical Atomic Spectrometry* 19.11 (Nov. 2004), p. 1428.
ISSN: 0267-9477.
DOI: 10.1039/b409991e.
URL: http://pubs.rsc.org/en/Content/ArticleHTML/2004/JA/B409991E.

[418] O. Eugster, F. Tera, and G. J. Wasserburg.
"Isotopic analyses of barium in meteorites and in terrestrial samples".
In: *Journal of Geophysical Research* 74.15 (July 1969), pp. 3897–3908.
ISSN: 01480227.
DOI: 10.1029/JB074i015p03897.
URL: http://doi.wiley.com/10.1029/JB074i015p03897.

[419] E. P. Hardy, P. W. Krey, and H. L. Volchok.
"Global inventory and distribution of fallout plutonium".
In: *Nature* 241.5390 (Feb. 1973), pp. 444–445.
ISSN: 0028-0836.
DOI: 10.1038/241444a0.
URL: http://www.nature.com/doifinder/10.1038/241444a0.

[420] Tuomo Sevon.
"A MELCOR model of Fukushima Daiichi Unit 1 accident".
In: *Annals of Nuclear Energy* 85 (Nov. 2015), pp. 1–11.
ISSN: 03064549.
DOI: 10.1016/j.anucene.2015.04.031.
URL: http://linkinghub.elsevier.com/retrieve/pii/S0306454915002315.

[421] J. Spino and D. Papaioannou.
"Lattice parameter changes associated with the rim-structure formation in high burn-up
UO2 fuels by micro X-ray diffraction".
In: *Journal of Nuclear Materials* 281.2-3 (Oct. 2000), pp. 146–162.
ISSN: 00223115.
DOI: 10.1016/S0022-3115(00)00236-1.
URL: http://www.sciencedirect.com/science/article/pii/S0022311500002361.

[422] Guogang Jia et al.
"Concentration, distribution and characteristics of depleted uranium (DU) in the Kosovo
ecosystem: A comparison with the uranium behavior in the environment uncontaminated
by DU".

In: *Journal of Radioanalytical and Nuclear Chemistry* 260.3 (2004), pp. 481–494.
ISSN: 02365731.
DOI: 10.1023/B:JRNC.0000028206.70671.70.
URL: http://link.springer.com/10.1023/B:JRNC.0000028206.70671.70.

[423] National Fire Protection Association.
NFPA 704: Standard System for the Identification of the Hazards of Materials for Emergency Response.
Tech. rep.
2017.
URL: http://www.nfpa.org/codes-and-standards/all-codes-and-standards/list-of-codes-and-standards/detail?code=704.

[424] W. G. Burns et al.
"Effects of radiation on the leach rates of vitrified radioactive waste".
In: *Journal of Nuclear Materials* 285 (Jan. 1982), pp. 130–132.
ISSN: 00223115.
DOI: 10.1016/0022-3115(82)90424-X.
URL: http://www.nature.com/doifinder/10.1038/295130a0.

[425] Aya Sakaguichi et al.
"Isotopic determination of U, Pu and Cs in environmental waters following the Fukushima Daiichi Nuclear Power Plant accident".
In: *Geochemical Journal* 46.4 (Nov. 2012), pp. 355–360.
ISSN: 0016-7002.
DOI: 10.2343/geochemj.2.0216.
URL: https://www.jstage.jst.go.jp/article/geochemj/46/4/46_2.0216/_article.

[426] Jian Zheng, Keiko Tagami, and Shigeo Uchida.
"Release of plutonium isotopes into the environment from the Fukushima Daiichi Nuclear Power Plant accident: what is known and what needs to be known."
In: *Environmental Science & Technology* 47 (Sept. 2013), pp. 9584–9595.
ISSN: 1520-5851.
DOI: 10.1021/es402212v.
URL: http://dx.doi.org/10.1021/es402212v.

[427] Yuji Shibahara et al.
"Analysis of cesium isotope compositions in environmental samples by thermal ionization mass spectrometry-3".
In: *Journal of Nuclear Science and Technology* 54.2 (Sept. 2016), p. 9.
ISSN: 0022-3131.

DOI: 10.1080/00223131.2016.1223560.

URL: https://www.tandfonline.com/doi/full/10.1080/00223131.2016.1223560.

[428] P.J. Thomas.

"Quantitative guidance on how best to respond to a big nuclear accident".

In: *Process Safety and Environmental Protection* 112 (Nov. 2017), pp. 4–15.

ISSN: 09575820.

DOI: 10.1016/j.psep.2017.07.026.

URL: http://linkinghub.elsevier.com/retrieve/pii/S0957582017302410.

[429] Carina Cai et al.

"Designing a Radiation Sensing UAV System".

In: *2016 IEEE Systems and Information Engineering Design Symposium (SIEDS)*.

Apr. 2016,

Pp. 165–169.

ISBN: 9781509009701.

DOI: 10.1109/SIEDS.2016.7489292.

URL: http://ieeexplore.ieee.org/lpdocs/epic03/wrapper.htm?arnumber=7489292.

[430] The World Bank.

Total World Population.

2017.

URL: http://data.worldbank.org/indicator/SP.POP.TOTL.

[431] United Nations Department of Economic and Social Affairs - Population Division.

World Population Prospects.

2015.

URL: https://esa.un.org/unpd/wpp/.

[432] The Shift Project Data Portal.

Breakdown of Electricity Generation by Energy Source.

2017.

URL: http://www.tsp-data-portal.org/Breakdown-of-Electricity-Generation-by-Energy-Source.

[433] IAEA.

IAEA Safeguards Overview - Comprehensive Safeguards Agreements and Additional Protocols.

2017.

URL: https://www.iaea.org/publications/factsheets/iaea-safeguards-overview.

[434] Robin W. Grimes and William J. Nuttall.

"Generating the Option of a Two-Stage Nuclear Renaissance".

In: *Science* 329.5993 (2010), pp. 799–803.

ISSN: 0036-8075.

DOI: 10.1126/science.1188928.

URL: http://science.sciencemag.org/content/329/5993/799.

[435] Gail H. Marcus and Alan E. Levin.
"New Designs for the Nuclear Renaissance".
In: *Physics Today* 55.4 (Apr. 2002), pp. 54–60.
ISSN: 00319228.
DOI: 10.1063/1.1480783.
URL: http://physicstoday.scitation.org/doi/10.1063/1.1480783.

[436] William J. Nuttall.
Nuclear Renaissance: Technologies and Policies for the Future of Nuclear Power.
IOP, 2005,
P. 313.
ISBN: 0750309369.
DOI: 10.1063/1.2180180.
URL: https://books.google.co.jp/books?hl=en&lr=&id=qi_wlX2WuHgC&oi=fnd&
pg=PR9&dq=nuclear+renaissance&ots=YS3Y0jZZg3&sig=_AGQVaDZZy9G_KoSnzOzwXfSbjE#
v=onepage&q=nuclearrenaissance&f=false.

[437] Peter Bradford.
"Honey, I Shrunk the Renaissance: Nuclear Revival, Climate Change, and Reality".
In: *Electricity Policy* (2004), p. 9.
URL: http://www.electricitypolicy.com/bradford-10-15-10.2-final.pdf.

[438] Paul Brown.
Voodoo Economics and the Doomed Nuclear Renaissance.
Tech. rep.
London, 2008,
P. 36.
URL: http://www.mng.org.uk/gh/resources/voodoo_economics.pdf.

[439] Shashi van de Graaff.
"Understanding the nuclear controversy: An application of cultural theory".
In: *Energy Policy* 97 (Oct. 2016), pp. 50–59.
ISSN: 03014215.
DOI: 10.1016/j.enpol.2016.07.007.
URL: http://linkinghub.elsevier.com/retrieve/pii/S0301421516303597.

[440] Robert Darst and Jane I. Dawson.

"Waiting for the Nuclear Renaissance: Exploring the Nexus of Expansion and Disposal in Europe".

In: *Risk, Hazards & Crisis in Public Policy* 1.4 (Jan. 2010), pp. 47–80.

ISSN: 1944-4079.

DOI: 10.2202/1944-4079.1047.

URL: http://doi.wiley.com/10.2202/1944-4079.1047.

[441]   National Nuclear Laboratory (NNL).

Small Modular Reactors (SMR) Feasibility Study.

Tech. rep.

Workington, Cumbria: National Nuclear Laboratory (NNL), 2014,

P. 64.

URL: http://www.nnl.co.uk/media/1627/smr-feasibility-study-december-2014.pdf.

[442]   IAEA.

Report of the International Mission on Remediation of Large Contaminated Areas Off-site the Fukushima Dai-ichi NPP.

2011,

P. 81.

ISBN: 9789290058908.

[443]   Nuclear Threat Initiative (NTI).

Radiological Security Progress Report.

Tech. rep.

Washington, 2016,

P. 32.

URL: http://www.nti.org/analysis/reports/radiological-security-progress-report/.

[444]   North Atlantic Treaty Organisation (NATO).

Glossary of Term And Definitions.

Tech. rep.

Brussels, Belgium, 2014,

P. 443.

URL: https://nso.nato.int/nso/zPublic/ap/aap6/AAP-6.pdf.

[445]   IAEA.

IAEA Incident and Trafficking Database (ITDB).

2015.

URL: http://www-ns.iaea.org/security/itdb.asphttp://www-ns.iaea.org/downloads/security/itdb-fact-sheet.pdf.

[446] BBC News.
Hacks 'probably compromised' UK industry - 18th July 2017.
2017.
URL: http://www.bbc.com/news/technology-40642962.

[447] Federal Aviation Authority (FAA).
Runway Safety Statistics: Runway Incursion Totals.
2016.
URL: http://www.faa.gov/airports/runway_safety/statistics/.

[448] The Remote Control Project.
The hostile use of drones by non-state actors against British targets.
Tech. rep.
2016,
P. 24.
URL: http://remotecontrolproject.org/wp-content/uploads/2016/01/Hostile-use-of-drones-report_open-briefing.pdf.

[449] Jack Nicas.
Criminals, Terrorists Find Uses for Drones, Raising Concerns.
New York, Jan. 2015.
URL: https://www.wsj.com/articles/criminals-terrorists-find-uses-for-drones-raising-concerns-1422494268.

[450] Joby Warrick.
Nuclear Security: Use of weaponized drones by ISIS spurs terrorism fears.
Washington, Feb. 2017.
URL: https://www.washingtonpost.com/world/national-security/use-of-weaponized-drones-by-isis-spurs-terrorism-fears/2017/02/21/9d83d51e-f382-11e6-8d72-263470bf0401_story.html?utm_term=.f6742c6fd459.

[451] Jack Clark.
"Bloomberg: Why 2015 Was a Breakthrough Year in Artificial Intelligence".
In: *Bloomberg Technology* (2015), p. 2.
URL: https://www.bloomberg.com/news/articles/2015-12-08/why-2015-was-a-breakthrough-year-in-artificial-intelligence.

[452] Gerardo Beni and Jing Wang.
"Swarm Intelligence in Cellular Robotic Systems".
In: *Robots and Biological Systems: Towards a New Bionics? NATO ASI Series* 102.2 (1993),
pp. 703–712.
ISSN: 0258-1248.
DOI: 10.1007/978-3-642-58069-7{_}38.

URL: http://link.springer.com/10.1007/978-3-642-58069-7_38.

[453]   Bruno Scrosati and Jurgen Garche.
         Lithium batteries: Status, prospects and future.
         2010.
         DOI: 10.1016/j.jpowsour.2009.11.048.

[454]   D. G. Jones et al.
         "Distribution of 137Cs and inventories of 238Pu, (239/240)Pu, 241Am and 137Cs in Irish
         Sea intertidal sediments".
         In: *Journal of Environmental Radioactivity* 44 (Aug. 1999), pp. 159–189.
         ISSN: 0265931X.
         DOI: 10.1016/S0265-931X(98)00133-7.
         URL: http://linkinghub.elsevier.com/retrieve/pii/S0265931X98001337.

[455]   H.T. Roman, B.A. Pellegrino, and W.R. Sigrist.
         "Pipe crawling inspection robots: an overview".
         In: *IEEE Transactions on Energy Conversion* 8.3 (1993), pp. 576–583.
         ISSN: 08858969.
         DOI: 10.1109/60.257076.
         URL: http://ieeexplore.ieee.org/lpdocs/epic03/wrapper.htm?arnumber=257076.

[456]   Ruizhong Lin, Zhi Wang, and Youxian Sun.
         Wireless sensor networks solutions for real time monitoring of nuclear power plant.
         2004.
         DOI: 10.1109/WCICA.2004.1343280.
         URL: http://ieeexplore.ieee.org/lpdocs/epic03/wrapper.htm?arnumber=
         1343280.

[457]   Kunihiko Nabeshima et al.
         "Real-time Nuclear Power Plant Monitoring with Neural Network".
         In: *Journal of Nuclear Science and Technology* 35.2 (Feb. 1998), pp. 93–100.
         ISSN: 0022-3131.
         DOI: 10.1080/18811248.1998.9733829.
         URL: http://www.tandfonline.com/doi/abs/10.1080/18811248.1998.9733829.

[458]   P Baesso et al.
         "High resolution muon tracking with resistive plate chambers".
         In: *Journal of Instrumentation* 7 (Nov. 2012), p. 11.
         ISSN: 1748-0221.
         DOI: 10.1088/1748-0221/7/11/P11018.
         URL: http://stacks.iop.org/1748-0221/7/i=11/a=P11018?key=crossref.
         72ee26eba08d154d632b60af80f6edaf.

[459] Konstantin N. Borozdin et al.
"Surveillance: Radiographic imaging with cosmic-ray muons."
In: *Nature* 422 (Mar. 2003), pp. 277–278.
ISSN: 00280836.
DOI: 10.1038/422277a.
URL: http://www.nature.com/doifinder/10.1038/422277a.

[460] C. Thomay et al.
"Passive 3D Imaging of Nuclear Waste Containers with Muon Scattering Tomography".
In: *Journal of Instrumentation* 03008.2 (Mar. 2016), pp. 4–6.
ISSN: 1748-0221.
DOI: 10.1088/1748-0221/11/03/P03008.
URL: http://stacks.iop.org/1748-0221/11/i=03/a=P03008?key=crossref.
644876ad51763d3a06565ad322c7151b.

[461] Jane K. Hart and Kirk Martinez.
"Environmental Sensor Networks: A revolution in the earth system science?"
In: *Earth-Science Reviews* 78.3-4 (2006), pp. 177–191.
ISSN: 00128252.
DOI: 10.1016/j.earscirev.2006.05.001.

[462] N. Tsoulfanidis and S. Landsberger.
Measurement and Detection of Radiation, Fourth Edition.
4th Ed.
CRC Press, 2015,
P. 606.
ISBN: 1482215497.
URL: https://books.google.co.uk/books?hl=en&lr=&id=zRjSBQAAQBAJ&oi=fnd&
pg=PP1&ots=ValJlvS7qj&sig=4JJ67_m48q6yyUCo1JsNuU_q2pU.

[463] Nicolas Estre et al.
"High-energy X-ray imaging applied to non destructive characterization of large nuclear
waste drums".
In: *2013 3rd International Conference on Advancements in Nuclear Instrumentation,
Measurement Methods and Their Applications, ANIMMA 2013*.
IEEE, June 2013,
Pp. 1–6.
ISBN: 9781479910472.
DOI: 10.1109/ANIMMA.2013.6727987.
URL: http://ieeexplore.ieee.org/document/6727987/.

[464] Christopher P. Jones et al.

"Evaluating laser-driven Bremsstrahlung radiation sources for imaging and analysis of nuclear waste packages".
In: *Journal of Hazardous Materials* 318 (2016), pp. 694–701.
ISSN: 18733336.
DOI: 10.1016/j.jhazmat.2016.07.057.

[465] EPSRC.
EPSRC (EP/K030302/1).
2013.
URL: http://gow.epsrc.ac.uk/NGBOViewGrant.aspx?GrantRef=EP/K030302/1.

[466] R. Carchon et al.
"Gamma radiation detectors for safeguards applications".
In: *Nuclear Instruments and Methods in Physics Research, Section A: Accelerators, Spectrometers, Detectors and Associated Equipment* 579.1 (2007), pp. 380–383.
ISSN: 01689002.
DOI: 10.1016/j.nima.2007.04.086.

[467] Qiushi Zhang et al.
"Progress in the development of CdZnTe unipolar detectors for different anode geometries and data corrections".
In: *Sensors* 13.2 (2013), pp. 2447–2474.
ISSN: 14248220.
DOI: 10.3390/s130202447.
URL: http://www.mdpi.com/1424-8220/13/2/2447/htm.

[468] BBC News.
Yahoo 'state' hackers stole data from 500 million users.
2016.
URL: http://www.bbc.co.uk/news/world-us-canada-37447016.

[469] Dell.
Dell Security Annual Threat Report | 2015.
Tech. rep.
2015,
Pp. 1–16.
URL: https://software.dell.com/docs/2015-dell-security-annual-threat-report-white-paper-15657.pdf.

[470] P. Oscar Boykin and Vwani Roychowdhury.
"Optimal Encryption of Quantum Bits".
In: *Physical Review A* 67 (Apr. 2000), p. 12.
ISSN: 1050-2947.

DOI: 10.1103/PhysRevA.67.042317.

URL: http://link.aps.org/doi/10.1103/PhysRevA.67.042317.

[471] Henry Chen et al.

"Spectral response of THM grown CdZnTe crystals".

In: *IEEE Transactions on Nuclear Science*.

Vol. 55.

June 2008,

Pp. 1567–1572.

ISBN: 0018-9499.

DOI: 10.1109/TNS.2008.924089.

URL: http://ieeexplore.ieee.org/stamp/stamp.jsp?tp=&arnumber=4545082.

[472] United Nations Office for Disaster Risk Reduction.

Sendai Framework for Disaster Risk Reduction 2015 - 2030.

Tech. rep.

Geneva, Switzerland: The United Nations Office for Disaster Risk Reduction, 2015,

P. 38.

URL: http://www.preventionweb.net/files/43291_sendaiframeworkfordrren.pdf.